FINAL REPORT
U.S. Department of Energy

COLLOID-FACILITATED TRANSPORT OF RADIONUCLIDES THROUGH THE VADOSE ZONE

Principal Investigator:

Markus Flury
Department of Crop and Soil Sciences
Washington State University

Collaborators:

James B. Harsh
Department of Crop and Soil Sciences
Washington State University

John F. McCarthy
Center for Environmental Biotechnology
University of Tennessee

Peter C. Lichtner
Geoanalysis—Earth and Environmental Sciences
Los Alamos National Laboratory

John M. Zachara
Environmental Molecular Science Laboratory
Pacific Northwest National Laboratories

Project Number:
70135

Grant Number:
DE-FG07-99ER62882

Project Duration:
September 15, 2002 to September 14, 2005
(no-cost extension until September 14, 2006)

Contents

1 Executive Summary

The main purpose of this project was to advance the basic scientific understanding of colloid and colloid-facilitated Cs transport of radionuclides in the vadose zone. We focused our research on the hydrological and geochemical conditions beneath the leaking waste tanks at the USDOE Hanford reservation. Specific objectives were (1) to determine the lability and thermodynamic stability of colloidal materials, which form after reacting Hanford sediments with simulated Hanford Tank Waste, (2) to characterize the interactions between colloidal particles and contaminants, i.e., Cs and Eu, (3) to determine the potential of Hanford sediments for *in situ* mobilization of colloids, (4) to evaluate colloid-facilitated radionuclide transport through sediments under unsaturated flow, (5) to implement colloid-facilitated contaminant transport mechanisms into a transport model, and (6) to improve conceptual characterization of colloid-contaminant-soil interactions and colloid-facilitated transport for clean-up procedures and long-term risk assessment.

We have previously shown that upon contact with simulated waste tank solutions, Hanford sediments change their mineralogical composition. Certain minerals, i.e., quartz, smectite, and kaolinite, are partially dissolved, and new mineral phases, i.e., the feldspathoids cancrinite and sodalite, are formed. We have characterized these mineral transformations and clarified the mineral transformation pathways. The new minerals were mainly in the colloidal size fraction (diameter less than 2 μm), had a negative surface charge, and were microporous, meaning they contained small pores. When Cs was present during the formation of the minerals, contaminants, like Cs, could be trapped inside the mineral structure.

Transport experiments under water saturated and unsaturated conditions showed that the colloids were mobile in Hanford sediments. As the water saturation of the sediments decreased, the amount of colloids transported also decreased. The colloids had the ability to enhance the migration of the radionuclide Cs; however, Cs initially sorbed to colloids was desorbed during

transport through uncontaminated Hanford sediments. The finding that Cs was stripped off the colloids during the transport through uncontaminated sediments implies that colloids will likely not be an effective carrier for Cs, unless the Cs is incorporated into the mineral structure of the colloids such that the radionuclide cannot desorb from the colloids. Nevertheless, it appears that the amount of Cs that can be transported by mobile colloids beneath Hanford waste tanks is limited. Colloids will not be able to move the bulk mass of Cs through the vadose zone at Hanford.

Colloid stability studies indicate that Hanford sediment form stable colloidal suspensions when suspended in Hanford sediment pore waters. Colloid stability was assessed by determination of the critical coagulation concentration, i.e., the chemical electrolyte concentration at which colloidal suspensions flocculate and settle out (become unstable). Although in the stable mode, Hanford colloids will settle out of solution after extended periods of time (months to years). Given the low recharge rates at Hanford range, which from near 0 to more than 100 mm/year, and the long travel times for rainwater to reach the groundwater of more than 40 years, it appears that colloidal transport is unlikely to occur if colloids are initially to be suspended close to the soil surface by infiltrating rainwater. However, if preferential flow or transient flow occurs, then colloidal transport may become more important.

The results of this project have also led to improvements of our fundamental understanding of colloid transport and mobilization under unsaturated flow conditions in porous media. We have found that colloid attachment to the liquid-gas interface is not that relevant and that colloids rather attached near the triple phase interface where air, water, and solid phases meet. We have also found that capillary forces are the most dominant forces governing colloid release in unsaturated porous media. These results help to advance our understanding of colloid fate and transport in unsaturated porous media.

2 Comparison of Actual Accomplishments with Goals and Objectives of the Project

Objective 1: Determine the lability and thermodynamic stability of colloidal materials, which form after reacting Hanford sediments with simulated Hanford Tank Waste

When Hanford tank waste contacts sediments, minerals are dissolved and new minerals precipitate. Three types of colloidal materials were formed upon reaction of tank waste solutions with sediments: (1) altered native minerals of colloidal size, (2) newly precipitated phases, and (3) precipitates formed during titration of supernatant solutions. Different minerals in the Hanford sediments reacted differently with simulated tank solutions: some (e.g., kaolinite) were completely or partially dissolved. Others, like quartz and feldspar, were partially dissolved. Still others (biotite), were resistant towards solution. The newly formed colloidal phases were identified as zeolites, sodalites, and cancrinites.

Because Hanford tank waste wastes have variable chemistry, we have systematically investigated the effects of solution chemistry (NaOH concentrations, Si:Al ratio, presence of cations and anions, and temperature) on mineral formation and transformations. We have clarified the mineral transformation pathways. Cancrinite and sodalite were the two stable mineral phases, whereas allophane and LTA zeolite formed as transition phases. The concentration of NaOH and type of anion were determinative in mineral formation and transformation.

Cancrinite and sodalite likely form when Hanford tank waste leaks into subsurface sediments. Their morphology and crystallinity will vary with alkalinity, salinity, and the Si/Al ratio, which also vary during waste-sediment reactions. Temperature affects the reaction rates, but not the reaction pathways. The negative charge of the colloids at pH values typical for the Hanford vadose zone (pH$>$7) suggests that the colloids likely form stable, mobile suspensions, that they are not electrostatically attracted to the dominantly negatively-charged Hanford sediments (however, cations such as Cs will electrostatically attach to the colloids).

Objective 2: Characterize the interactions between initially-formed colloids, their dissolution/alteration products, and native colloidal particles with contaminants in batch experiments under various ionic strength and pH conditions

Cesium sorption studies showed that the colloids formed from secondary mineral phases had higher sorption affinity for Cs than did the original minerals. We determined how much Cs is incorporated into the secondary phases, and how much is subsequently released by desorption. In zeolite and allophane, most of the incorporated Cs (94–99%) was readily exchangeable with Na or K, whereas Ca was less effective in replacing Cs: only 65–85% of the Cs could be replaced. In cancrinite and sodalite, a large fraction of the incorporated Cs was not easily exchangeable with Na, K, or Ca: only 1–57% of the Cs could be exchanged. The desorption kinetics experiments showed that Cs desorbs quickly from zeolite. Cesium desorption from cancrinite, sodalite, and

allophane, however, was slow, suggesting that Cs was trapped in cages and channels. Effective diffusion coefficients for Cs in cancrinite and sodalite were in the order of 10^{-14} m^2/s, and for zeolite in the order of 10^{-9} m^2/s.

Europium serves as a homologue to study the geochemistry of trivalent actinides such as Am(III) and Cm(III) in the wastes. We studied the sorption of Eu^{3+} at relatively high concentration (millimolar) on smectite and calcite and identified and characterized the precipitated solid phases of Eu^{3+}. We further investigated inhibition of the precipitation by ligands EDTA and humic acid. Smectite and calcite were mixed with Eu^{3+} solutions for up to one year in either capped or open centrifuge tubes. When twice the CEC equivalent of Eu^{3+} was added, about 50% of the added Eu^{3+} was sorbed by smectite in the pH range 3–5.5. Infrared, X-ray diffraction, and electron microscopic analyses imply that short-range ordered $Eu(OH)_3$ nano particles precipitated on smectite when pH was raised above 6. Sorption of Eu^{3+} in the interlayer of smectite was observed in the entire pH range (3–10) as evidenced by the expansion of the d(001) space of smectite from 1.2 nm to 1.5 nm. The EDTA ligand reduced Eu^{3+} sorption by nearly two-thirds in the pH range 4–10. This retardation effect was weakened at low pH and was insignificant at pH$<$3. Infrared analysis showed increasing formation of a neutral Eu-EDTA complex on smectite at lower pH. When europium reacted with calcite in open air for one year without agitation, nearly 100% of added $Eu(NO_3)_3$ precipitated as hydrated carbonate $Eu_2(CO_3)_3 \cdot 3\,H_2O$ with a trace amount of Ca^{2+} coprecipitated within this phase. When Eu^{3+}-calcite suspension was agitated by shaking, another solid carbonate phase $EuOHCO_3$ precipitated rapidly (within one day). Presence of EDTA and humic acid completely inhibited the formation of the europium carbonate phases. Under the natural pH condition (around 8) of the Hanford sediment, it is likely that Eu^{3+} forms carbonate and hydroxide precipitates.

Objective 3: Determine the potential of Hanford sediments for in situ mobilization of colloids for different types of sediments and different leaching scenarios

Colloid transport through Hanford sediments is affected by ionic strength and water flow rate. These effects were quantified with column experiments using colloids formed by reacting waste solutions with Hanford sediments. Colloids were transported largely unretarded through the sediment, and a portion seemed to be irreversibly attached to minerals inside the column.

Transport during unsaturated conditions clearly caused more colloidal particles to be trapped inside the column than under saturated conditions. Interestingly, the colloid breakthrough curves do not show a plateau, but rather the concentrations in the outflow steadily increase after initial breakthrough. Model analyses assuming physical non-equilibrium and mobile-immobile flow regions inside the columns revealed that the steady increase is due to physical non-equilibrium. With unsaturation, the initial colloid breakthrough still occurs at about one pore volume, indicating that colloids are not retarded inside the column—that is, they travel with the velocity of the water. Less colloidal material was transported as sediment water content decreased.

A series of column experiments were conducted to investigate coupled effect of flow rate

and ionic strength on transport and mobilization of a model colloid (montmorillonite) in a model porous medium (Accusand). We found that the ionic strength effect was largely dependent upon the inflow rate. Increased influx rate caused more colloids to move through the silica sand in the higher than lower ionic strength solutions, suggesting that the hydrodynamic interaction can significantly overcome the electrostatic interaction, and high flux velocity frequently occurring in the preferential flow pathways may cause mobilization of the colloids that are otherwise immobilized or travel only a short distance at high ionic strength. A main mechanism responsible for the release pulse was inferred to be colloid remobilization driven by capillary forces. Consideration of energy barrier, friction and capillary forces, and depletion interaction suggests that colloid transport depends on the porous structure/roughness of the *in situ* colloids on the collector surfaces, as well as the interaction between the *in situ* and introduced colloids. Our study indicates that transient flow is an important condition for causing the coupling of the physical and chemical mechanisms of colloid transport, and mechanistic understanding on co-transport of foreign and *in situ* colloids under various conditions is very critical for site remediation.

Objective 4: Evaluate colloid-facilitated radionuclide transport through sediments under different degrees of water saturation in packed and undisturbed sediment columns

Saturated- and unsaturated column experiments were used to investigate effects of colloids on Cs transport. The colloids facilitated the transport of Cs through Hanford sediments. Due to the non-linearity of Cs sorption, colloid-facilitated Cs transport was more pronounced at low Cs concentration than at high Cs concentration. Absent colloids, no Cs moved through the 10-cm long columns. Cs transport absent colloids was only seen under high ionic strength. Cesium that had been pre-associated with colloids was stripped off during transport through the sediments. The higher the flow rates, the less Cs was stripped off, indicating that Cs desorption is at least partly residence-time dependent. Depending on the flow rate, up to 70% of the initially sorbed Cs desorbed from colloidal carriers and was captured in the stationary sediments. Less Cs was stripped off colloids under unsaturated than under saturated flow conditions at similar flow rates. This was likely due to the reduced colloid-sediment collision or increased fraction of Cs-bearing colloids in water-immobile regions as water content decreased and water flow was divided between mobile and immobile regions.

Applying these results to the Hanford site, it seems unlikely that colloids will have moved Cs to the depths observed under the tanks. If Cs is reversibly attached to colloids by ion-exchange, Cs would likely be stripped as the colloids move through uncontaminated sediments—unless Cs is irreversibly bound in cages of feldspathoids. The possibility of colloids to be transported from the soil surface down into the ground water at the tank farms appears minimal, unless water contents and flow rates are locally and temporally increased (e.g., by snow melt or by artificial infiltration caused by past waste management practices).

Objective 5: Implement colloid-facilitated contaminant transport mechanisms and thermodynamic stability constants for colloids into a reactive chemical transport model, and verify model simulations with experimental transport data

The reactive transport model FLOTRAN was used to simulate Cs transport in column experiments. Discrepancies between model and experiment indicated that kinetic limitations may be present in the ion exchange reactions and that the local equilibrium assumption adopted by FLOTRAN may not be valid. We modified FLOTRAN to include kinetic ion exchange reactions—a major restructuring of the code, because the global implicit scheme utilized by FLOTRAN only solved the aqueous species transport equations in a coupled manner, whereas to simulate kinetic ion exchange, sorbed species needed to be solved simultaneously with the aqueous component equations. In addition, a kinetic reaction subroutine was written to calculate the reaction term for kinetic ion exchange equations.

FLOTRAN was applied to column experiments involving simulated tank waste using a 1.4 M NaOH + 3.7 M $NaNO_3$ + 0.125 M $NaALO_4$ solution to investigate migration of Cs through Hanford sediment columns at temperatures of 22^oC and 50^oC. The Pitzer model was used for activity coefficient corrections. Results indicated a complex behavior of species concentrations eluted from the column. The initial breakthrough of Cs was well reproduced in the calculations using ion exchange coefficients obtained from an independent study. One puzzling aspect of the experiments, however, was that nitrate did not behave as a nonreactive tracer as expected and as predicted by the model. The model calculations, however, were based on a fully saturated column rather than an initially dry column. To partially compensate for this, the initial fluid composition was set to the composition of the observed breakthrough concentrations.

Objective 6: Improve conceptual characterization of colloid-contaminant-soil interactions and colloid-facilitated transport for clean-up procedures and long-term risk assessment

Conditions favorable for colloid generation and release exist at the Tank Farms, when high ionic strength waste solutions are displaced by low ionic strength pore water. We experimentally simulated such a situation. Colloidal particles were mobilized during the change of ionic strength. Mobilized colloids consisted mainly of quartz, mica, illite, kaolinite, and chlorite. Mobilized colloids carried a fraction of the Cs along. Colloid stability was assessed with two different methods: batch turbidity and dynamic light scattering. Critical coagulation concentrations (CCCs) were determined for pure Na and pure Ca electrolyte solutions and for mimicked Hanford vadose zone pore waters with varying sodium adsorption ratios (SAR). Lower initial colloid concentrations and shorter settling times gave larger CCCs. The CCCs determined from the dynamic light scattering, where diluted colloidal suspensions are used, were not dependent on settling time and arbitrary CCC criteria—dynamic light scattering is therefore the preferred method to measure colloid stability. The stability of natural colloids was intermediate between pure kaolinite and montmorillonite.

We conclude that colloids in the Hanford vadose zone form stable suspensions, i.e., are in the slow-aggregation regime. Nonetheless, due to their probable long travel times in the zone, nearly all colloids will aggregate and be removed from the water column before reaching groundwater levels.

In regard to colloid-facilitated transport of Cs, it appears that if Cs is sorbed on the outer surfaces of colloids, Cs will be stripped off from the colloids as they move through uncontaminated sediments. This will limit the amount and distance of Cs transport in the vadose zone.

3 Summary of Project Activities

This section provides a summary of the experimental methods and results of the project. A detailed account of these activities is given in the attached technical manuscripts in the Appendix.

3.1 Research Objectives

The goal of this project was to improve the basic understanding of the role of colloids in facilitating the transport of contaminants in the vadose zone. We focussed on three major thrusts: (1) thermodynamic stability and mobility of colloids formed by reactions of sediments with highly alkaline tank waste solutions, (2) colloid-contaminant interactions, and (3) *in situ* colloid mobilization and colloid-facilitated contaminant transport occurring in Hanford sediments. As contaminants to study colloid-facilitated transport, we have selected Cs and Eu. The specific objectives were to:

1. Determine the lability and thermodynamic stability of colloidal materials, which form after reacting Hanford sediments with simulated Hanford Tank Waste.

2. Characterize the interactions between initially-formed colloids, their dissolution/alteration products, and native colloidal particles with contaminants in batch experiments under various ionic strength and pH conditions.

3. Determine the potential of Hanford sediments for *in situ* mobilization of colloids for different types of sediments and different leaching scenarios.

4. Evaluate colloid-facilitated radionuclide transport through sediments under different degrees of water saturation in packed and undisturbed sediment columns.

5. Implement colloid-facilitated contaminant transport mechanisms and thermodynamic stability constants for colloids into a reactive chemical transport model, and verify model simulations with experimental transport data.

6. Improve conceptual characterization of colloid-contaminant-soil interactions and colloid-facilitated transport for clean-up procedures and long-term risk assessment.

3.2 Experimental Methods

3.2.1 Overall Research Design

The objectives of this study were accomplished through a series of batch and transport experiments in combination with mathematical modeling. Batch studies were conducted to study sediment dissolution and re-precipitation of secondary minerals. Batch studies were also conducted to study sorption of Cs and Eu on mineral surfaces. Transport studies were conducted to study

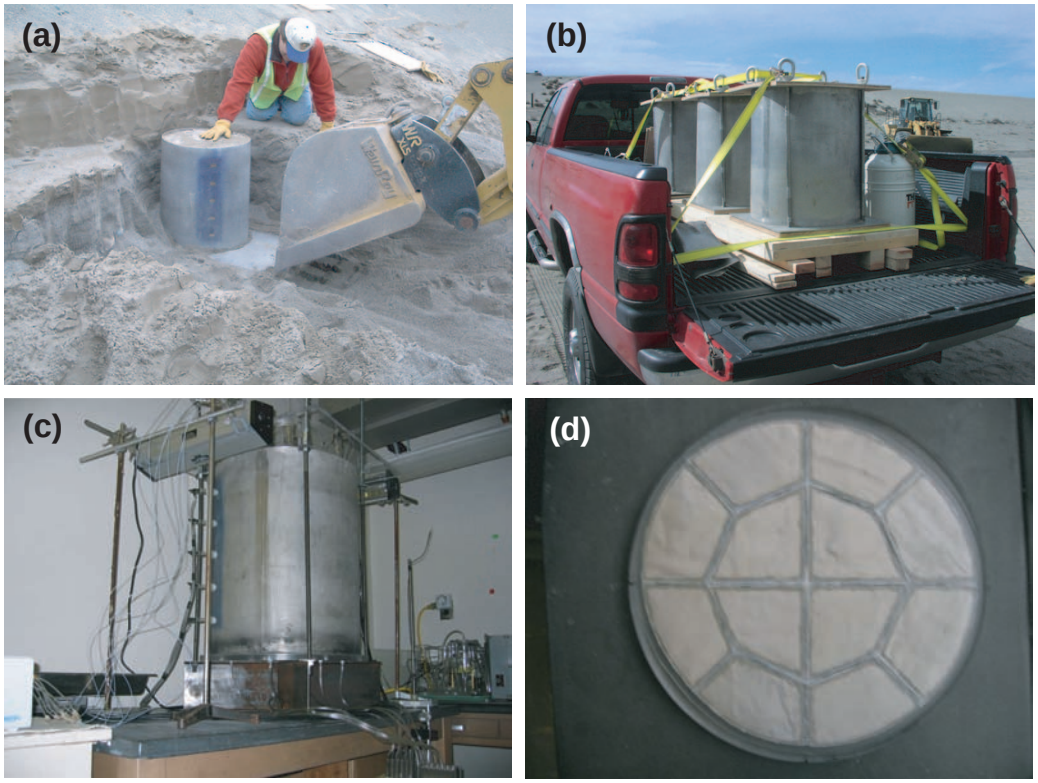

Figure 1. Sampling of meso-scale undisturbed sediment cores from the ERDF site at Hanford (a,b), laboratory setup (c), and bottom plate (d).

mobility and *in situ* mobilization of colloids from sediments. We conducted these experiments with well-defined sand media as well as with natural sediments from the Hanford Site. We used repacked as well as undisturbed Hanford sediments.

3.2.2 Sediments

Bulk sediments used in this study were collected from the submarine pit (218-E-12B) and the ERDF pit at the Hanford site. These sediments are representative, both in texture and mineralogy, of the material underlying the immediate vicinity of the S-SX (single-shell) tank farm at Hanford. These sediments have been used by other EMSP investigators and extensive characterization data are given elsewhere [*Serne et al.*, 2002a]. In two sampling campaigns in April and May 2003, we sampled three large undisturbed soil cores (Fig. 1a,b). The core sediments represent the two major sediment facies occurring in the Hanford formation: a coarse-pebbly sand and a finer-textured sand. These cores were setup in the laboratory for unsaturated transport experiments (Fig. 1c,d).

Table 1. Composition of simulated tank waste (STW), prepared at room temperature (20 to 22°C), and experimental conditions of batch experiments.

Designation of solution	NaOH	$NaAlO_4$ (mol/kg)	$NaNO_3$	pH	Temperature[a] (°C)	Time[a] (days)	Designation of colloids formed
Control[b]	0	0	0	7.1[b]	50	40	colloid 0
STW1	1.4	0.125	3.7	14.2[c]	50	25, 40	colloid 1
STW2	2.8	0.125	3.7	14.5[c]	50	40	colloid 2
STW3	1.4	0.25	3.7	14.2[c]	50	40	colloid 3
STW4	2.8	0.25	3.7	14.5[c]	50	40	colloid 4

[a]Temperature and duration of batch reactions with sediments.
[b]Distilled water.
[c]Determined by titration which measures non-carbonate alkalinity (NCA).

3.2.3 Objective 1: Sediment Dissolution and Colloid Formation

(*References:* Deng et al., 2006a,b,d; Mashal et al., 2004; 2005a,b; Zhao et al., 2004)

We studied mineral dissolution and colloid formation with pure model minerals and natural Hanford sediments under a series of different simulated tank waste. For most of the studies, we used four simulated tank waste, which are high in NaOH, $NaNO_3$, and $NaAlO_2$ (Table 1) and reacted the model minerals and sediments for various time periods and at different temperatures.

Given that there is a wide range of chemical compositions of simulated tank waste, we also studied mineral formation and transformation by systematically varying anion composition and OH concentrations of simulated tank solutions. A series of batch experiments were conducted by reacting soluble Si with different simulated tank waste solutions. This approach allowed us to obtain pure precipitates that could be characterized in detail.

We also assessed the relative dissolution resistance of common silicate minerals in simulated tank waste. The mineral resistance to caustic solutions was predicted based on solution compositions and solubility product constants. The predictions were compared to experimental observations obtained from a Hanford fine sand and several model minerals (muscovite, biotite, smectite, illite, vermiculite, and chlorite) reacted with simulated tank wastes.

The products of the mineral dissolution and re-precipitation reactions were analyzed with X-ray diffraction (XRD), Fourier transform infrared (FTIR) spectroscopy, scanning electron microscopy (SEM), solid state NMR, electrophoretic mobility, and BET surface area. Chemical modeling was performed with the GMIN code.

3.2.4 Objective 2: Characterization of the Interactions between Cs and Eu and Sediments and Reaction Products

(*References:* Deng et al., 2006c; Flury et al., 2004; Mon et al., 2006; Zhao et al., 2004)

We determined the sorption of Cs and Eu to unreacted and reacted Hanford sediments and model minerals. Cesium sorption was determined in batch experiments as a function of solution pH in the range of 3 to 11. Cesium sorption was also investigated using column experiments with 1, 10, 100, and 1000 mM NaCl electrolyte solutions. Sorption isotherms were constructed from batch equilibrium experiments and the batch-derived sorption parameters were compared with column breakthrough curves. Column transport experiments were analyzed with a two-site equilibrium-nonequilibrium model.

During formation of secondary precipitates, contaminants like Cs can be incorporated into the porous mineral structure of the precipitates. We determined the resistance of incorporated Cs^+ to ion exchange and the mobility and diffusion coefficient of Cs^+ in the minerals. We measured the Cs^+ desorption kinetics from water-washed minerals using a batch reactor technique. The kinetic ion exchange experiments were conducted with Na^+ electrolyte solutions. To check the distribution of cations in minerals during the ion exchange reaction, we mapped the elemental distribution in the minerals with X-ray energy dispersive spectroscopy. ^{133}Cs magic-angle spinning nuclear magnetic resonance (MAS-NMR) was used to assess Cs mobility inside the minerals. The effective diffusion coefficient of Cs^+ in the minerals was estimated using the following radial diffusion equation, which describes diffusion within porous particles [*Crank*, 1975].

Europium can precipitate as its own colloidal phase or sorb to subsurface minerals. To identify the precipitated solid phases on surfaces of clay minerals and calcite that occur in Hanford sediments we investigated precipitation and adsorption of Eu in presence of EDTA and humic acids. After reacting with Eu solutions, the minerals were analyzed with X-ray diffraction, scanning electron microscopy, and X-ray energy dispersive spectroscopy.

3.2.5 Objective 3: Determine the potential of Hanford sediments for in situ mobilization of colloids for different types of sediments and different leaching scenarios

(*References:* Chen and Flury, 2005; Chen et al., 2005; Czigany et al., 2005b; Shira et al., 2006; Zhuang et al., 2006a,b)

We studied colloid interactions with the liquid-gas and the solid-liquid interfaces in a porous medium. Column experiments were conducted under steady-state water flow conditions with effective water saturations ranging from 0.56 to 1.0. Four types of colloidal particles were used: native Hanford colloids, Hanford colloids reacted with waste tank solutions, pure kaolinite, and pure Na-montmorillonite. Colloid transport was described by the mobile-immobile region model accounting for first-order colloid removal from the mobile region. Using the extended DLVO theory, free energies of Lifshitz-van der Waals, electrostatic and Lewis acid/base interactions between colloids, sediments and the liquid-gas interface were calculated based on their independently determined surface thermodynamic properties.

A series of column experiments were conducted to investigate coupled effect of flow rate and ionic strength on transport and *in situ* mobilization of a model colloid (montmorillonite) in a

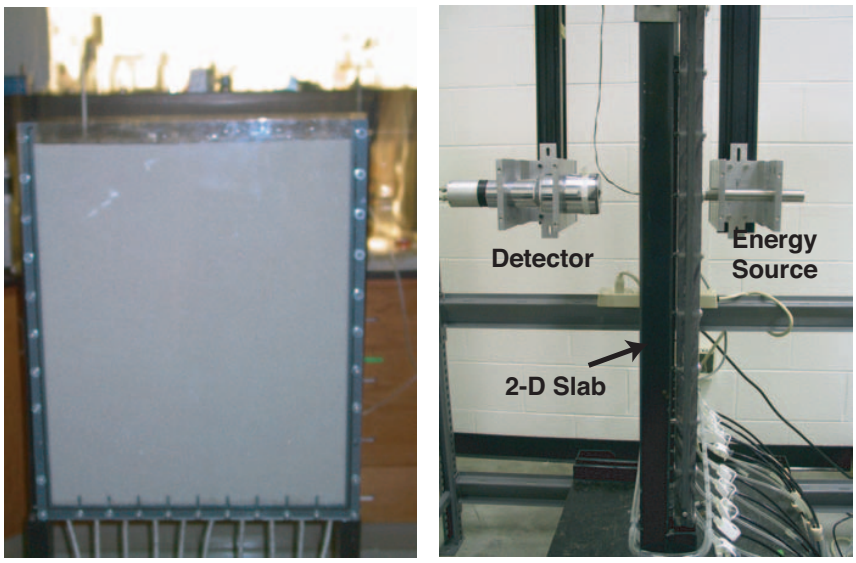

Figure 2. Front view and side view of 2-D slab Hele Shaw cell setup with the γ-ray attenuation device.

model porous medium (Accusand). The effects of transient flow on mobilization of colloids from the Hanford sediments were evaluated with irrigation experiments (two columns under water-saturated and eight under water-unsaturated flow conditions) by introducing a certain volume of the injection solution with varying solution ionic strength, irrigation rate, and infiltration frequency (a single continuous infiltration event, or multiple infiltration/drainage pulses).

We also studied the impacts of transient flow regimes and horizontal sediment layering on colloid transport. A transparent Hele-Shaw cell was employed in our 2-D experiments (Fig. 2). To monitor the spatiotemporal variation of sand water content, we used a gamma-ray attenuation system. Two sets of experiments were performed to demonstrate the effect of layering-structure on colloid transport in sands. One was transport of montmorillonite (Mt) in homogeneous coarse sand, and the other was in the same sand but with a 1.5-cm thick fine sand layer. Total concentrations of colloids (Mt plus in-situ silica colloid) were determined, whereas Mt concentration was analyzed with ICP based on Al measurement.

The effect of infiltration into an initially dry sediment on *in situ* mobilization was simulated using repacked Hanford sediment column where inflow was applied using a sprinkler consisting of 12 hypodermic needles. The bottom of the column was equipped with a single-layer nylon membrane. Five 3-mm diameter holes were evenly distributed along the perimeter 2 cm above the bottom of the column to allow air to escape during infiltration events. The column itself was mounted on an electronic load-cell to monitor the overall gravimetric water content. A constant tension of -10 cm-H_2O was maintained at the bottom of the column using a hanging water column. We used deionized water as the infiltrating solution to simulate low ionic strength rainwater.

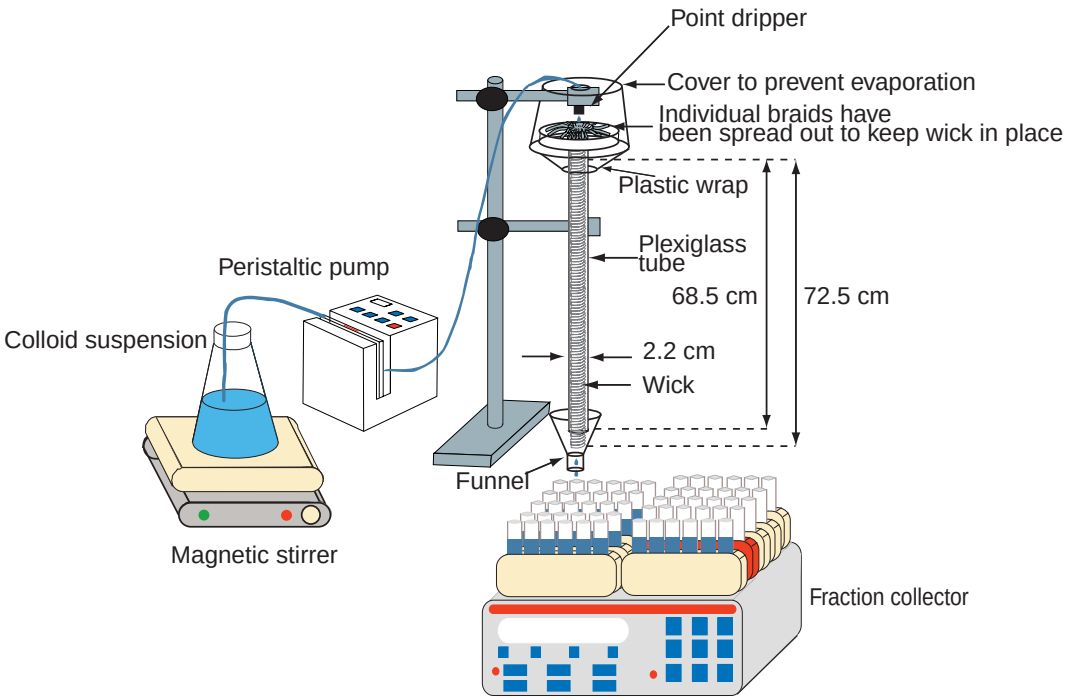

Figure 3. Experimental setup for the wick experiments.

Infiltration experiments were conducted with different flow rates and by sequentially increasing the flow rates (and consequently increasing the water contents). In total, we conducted the following 5 series of column experiments: Series 1: initial flow rate of 0.018 cm/min, then step-wise increase of the flow rate to 0.036 cm/min, 0.072 cm/min, 0.144 cm/min and 0.288 cm/min; Series 2: initial flow rate of 0.036 cm/min, then step-wise increase to 0.072 cm/min, 0.144 cm/min and 0.288 cm/min; Series 3: initial flow rate of 0.072 cm/min, then step-wise increase to 0.144 cm/min and 0.288 cm/min; Series 4: initial flow rate of 0.144 cm/min, then increase to 0.288 cm/min; Series 5: flow rate of 0.288 cm/min.

Fiberglass wicks are frequently used to sample pore water and determine water fluxes in soils. We evaluated the performance of fiberglass wicks to sample colloids. Different colloids were used for the wick testing: feldspathoids, ferrihydrite, montmorillonite, kaolinite, and a mixture of mineral colloids extracted from a coarse calcareous sediment. The colloids were dispersed in either a buffered Na_2CO_3/$NaHCO_3$ solution (ionic strength 6.7 mM, pH 10) or deionized water. Colloid breakthrough curves through 77-cm long fiberglass wicks were determined for three different flow rates. A typical setup for the fiberglass wick testing is shown in (Fig. 3).

3.2.6 *Objective 4: Evaluate colloid-facilitated radionuclide transport through sediments under different degrees of water saturation in packed and undisturbed sediment columns*

(*References:* Chen and Flury, 2005; Czigany et al., 2005b)

Saturated and unsaturated column experiments were used to investigate effects of colloids on Cs and Eu transport. We investigated whether, and to what extent, colloidal particles can facilitate the transport of ^{137}Cs at Hanford. We used colloidal materials isolated from Hanford sediments. Transport experiments were conducted under variably-saturated, steady-state flow conditions in repacked, 20 cm long Hanford sediment columns, with effective water saturations ranging from 0.2 to 1.0. Under water-saturated conditions, we conducted a series of experiments with different Cs loadings on the colloids at the same pore water velocity (10 cm/min). Under water-unsaturated conditions, the Cs loading on the colloids was kept constant, but we varied the effective water saturation S_e in increments of 0.1 by decreasing effective water content from 1.0 to 0.2.

Europium was used as an analogue of the trivalent actinides, i.e., plutonium and americium. We synthesized Europium hydroxycarbonate, and introduced it to an unsaturated laboratory column packed with Hanford sediments. We conducted the following two sets of column experiments. For the first set of experiments, we flushed the column with europium hydroxycarbonate synthesized in advance with different concentrations at a fixed flow rate of 0.018 cm/min. We used synthesized europium hydroxycarbonate at concentrations of 0.80, 1.42, 2.83, and 5.66 mg/L. For each run, a new sediment column was used. For the second set of experiments, we flushed the column with europium hydroxycarbonate at a fixed concentration of 2.83 mg/L but variable flow rates.

Conditions favorable for colloid generation and release exist at the Tank Farms, when high ionic strength waste solutions are displaced by low ionic strength pore water. We experimentally simulated such a situation. Colloidal particles were mobilized during the change of ionic strength. Mobilized colloids consisted mainly of quartz, mica, illite, kaolinite, and chlorite. Mobilized colloids carried a fraction of the Cs along. Colloid stability was assessed with two different methods: batch turbidity and dynamic light scattering. Critical coagulation concentrations (CCCs) were determined for pure Na and pure Ca electrolyte solutions and for mimicked Hanford vadose zone pore waters with varying sodium adsorption ratios (SAR). Lower initial colloid concentrations and shorter settling times gave larger CCCs. The CCCs determined from the dynamic light scattering, where diluted colloidal suspensions are used, were not dependent on settling time and arbitrary CCC criteria—dynamic light scattering is therefore the preferred method to measure colloid stability. The stability of natural colloids was intermediate between pure kaolinite and montmorillonite.

3.2.7 *Objective 5: Implement Colloid-facilitated Contaminant Transport Mechanisms into a Reactive Transport Model*

(*References:* Chen et al., 2005)

We modified the two-region transport model [*van Genuchten and Wagenet*, 1989] to describe colloid transport in unsaturated porous media. From our previous [*Cherrey et al.*, 2003] and current experimental observations, we have evidence that there is no colloid deposition at the liquid-solid interface. We believe that retained colloids in the column are either captured at the liquid-gas interface by film-straining [*Lenhart and Saiers*, 2002] or captured at the solid-liquid-gas three phase interface due to physical constraint [*Crist et al.*, 2004*; Chen and Flury*, 2005]. These colloid-capturing actions most likely occur from the mobile region. Thus, we assume that colloids are only deposited within the mobile region only:

$$\frac{\partial(\theta_m c_m)}{\partial t} + \frac{\partial(\theta_{im} c_{im})}{\partial t} = \frac{\partial}{\partial z}\left(\theta_m D_m \frac{\partial c_m}{\partial z}\right) - \frac{\partial(q_m c_m)}{\partial z} - \theta_m \lambda_m c_m \quad (1)$$

$$\frac{\partial(\theta_{im} c_{im})}{\partial t} = \alpha(c_m - c_{im}) \quad (2)$$

where c_m, c_{im} refer to the colloid concentrations in the mobile and immobile phases, respectively, θ_m and θ_{im} refer to the mobile and immobile water, respectively, q_m denotes the Darcy velocity of the mobile water, λ_m the colloid deposition coefficient from the mobile water phase, D_m the colloid dispersion coefficient in the mobile phase, and α the colloid transfer coefficient between mobile and immobile water. Taking the water content constant and using dimensionless variables, we can write equations 1 and 2 as

$$\beta\frac{\partial C_m}{\partial T} + (1-\beta)\frac{\partial C_{im}}{\partial T} = \frac{1}{Pe}\frac{\partial^2 C_m}{\partial Z^2} - \frac{\partial C_m}{\partial Z} - \mu_m C_m \quad (3)$$

$$(1-\beta)\frac{\partial C_{im}}{\partial T} = \omega(C_m - C_{im}) \quad (4)$$

where the upper case C's denote dimensionless colloid concentrations ($C_m = c_m/c_0$ and $C_{im} = c_{im}/c_0$) with c_0 being the colloid concentration in the inflow. The dimensionless time is defined as $T = vt/L$, and the space as $Z = z/L$, where L is the length of the column. The dimensionless parameters are defined as

$$\beta = \frac{\theta_m}{\theta} \quad \text{(Fraction of mobile water)} \quad (5)$$

$$Pe = \frac{vL}{\beta D_m} \quad \text{(Peclet number)} \quad (6)$$

$$\omega = \frac{\alpha L}{\theta v} \quad \text{(Mass transfer coefficient)} \quad (7)$$

$$\mu_m = \frac{\beta\lambda_m L}{v} = \frac{\lambda_m L}{v_m} \quad \text{(Deposition coefficient)} \quad (8)$$

where $v = q_m/\theta$ is the pore water velocity, $\theta = \theta_m + \theta_{im}$, and $v_m = v/\beta$.

The reactive transport model FLOTRAN was used to simulate Cs transport in column experiments. Discrepancies between model and experiment indicated that kinetic limitations may be present in the ion exchange reactions and that the local equilibrium assumption adopted by FLOTRAN may not be valid. FLOTRAN currently does not simulate kinetic ion exchange reactions. FLOTRAN was applied to column experiments involving simulated tank waste using a 1.4 M NaOH + 3.7 M $NaNO_3$ + 0.125 M $NaALO_4$ solution to investigate migration of Cs through Hanford sediment columns at temperatures of 22^{o}C and 50^{o}C. The Pitzer model was used for activity coefficient corrections.

3.3 Principal Results

3.3.1 Objective 1: Sediment Dissolution and Colloid Formation

(*References:* Deng et al., 2006a,b,d; Mashal et al., 2004; 2005a,b; Zhao et al., 2004)

Three types of colloidal materials were formed upon reaction of tank waste solutions with sediments: (1) altered native minerals of colloidal size, (2) newly precipitated phases, and (3) precipitates formed during titration of supernatant solutions. Different minerals in the Hanford sediments reacted differently with simulated tank solutions: some (e.g., kaolinite) were completely or partially dissolved. Others, like quartz and feldspar, were partially dissolved. Still others (biotite), were resistant towards solution. The newly formed colloidal phases were identified as zeolites, sodalites, and cancrinites (Fig. 4).

Because these wastes have variable chemistry, we have systematically investigated the effects of solution chemistry (NaOH concentrations, Si:Al ratio, presence of cations and anions, and temperature) on mineral formation and transformations. We have elucidated the mineral transformation pathways (Fig. 5). Cancrinite and sodalite were the two stable mineral phases, whereas allophane and LTA zeolite formed as transition phases. The concentration of NaOH and type of anion were determinative in mineral formation and transformation.

Cancrinite and sodalite likely form when Hanford tank waste leaks into subsurface sediments. Their morphology and crystallinity will vary with alkalinity, salinity, and the Si/Al ratio, which also vary during waste-sediment reactions. Temperature affects the reaction rates, but not the reaction pathways. The negative charge of the colloids at pH values typical for the Hanford vadose zone (pH$>$7) suggests that the colloids likely form stable, mobile suspensions, that they are not electrostatically attracted to the dominantly negatively-charged Hanford sediments. However, cations such as Cs will electrostatically attach to the colloids.

Theoretical predictions and experimental observations indicate that quartz was the most labile mineral in simulated tank waste. Amphibole, pyroxene, and chlorite were the most stable phases. The relative resistance of the minerals in the alkaline solutions increased in the following order: quartz $<$ kaolinite $<$ smectite $<$ illite $<$ vermiculite $<$ mica $<$ feldspars $<$ chlorite, am-

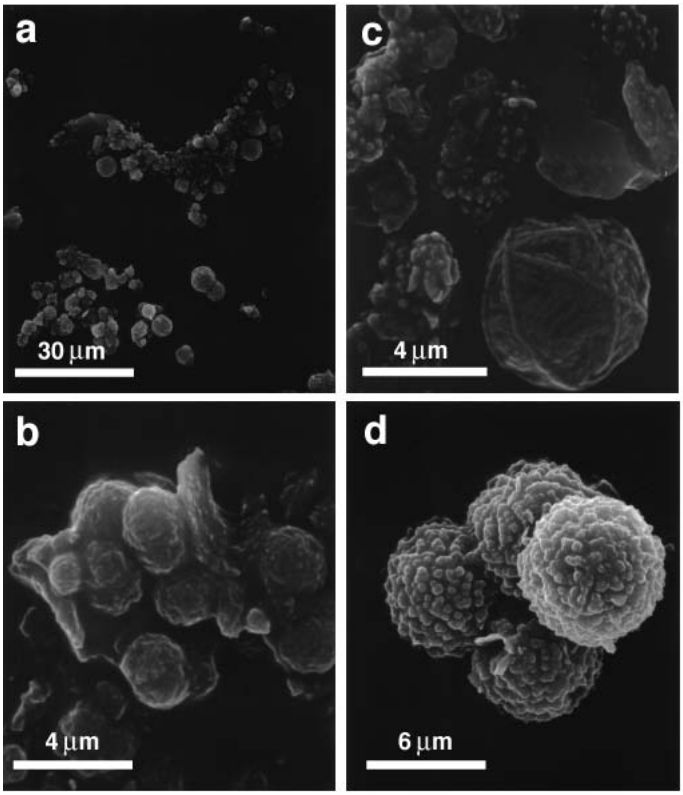

Figure 4. Scanning electron images of colloidal material in reacted Hanford sediments with simulated tank waste (from Mashal et al., 2004).

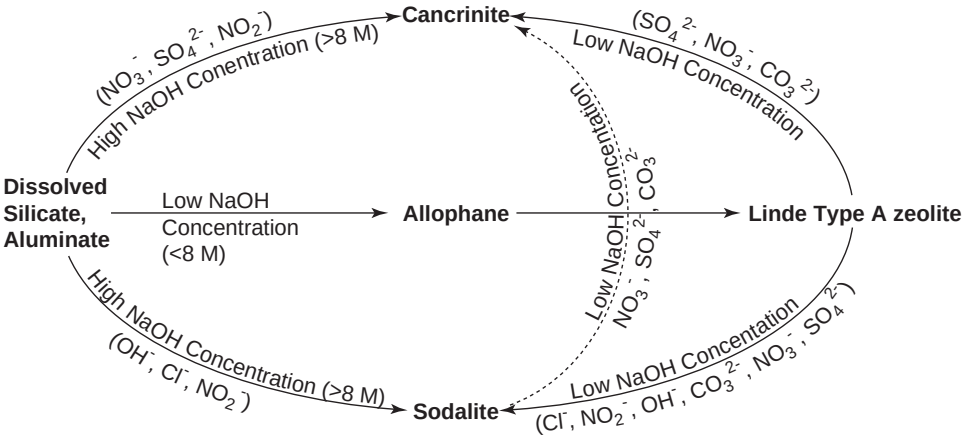

Figure 5. Mineral transformation pathways in the simulant solutions mimicking Hanford tank waste solutions (from Deng et al., 2006c).

phiboles, pyroxenes. This order is nearly opposite to the resistance of the minerals in soils under well-drained conditions. An example of mineral etching is shown in (Fig. 6).

3.3.2 Objective 2: Characterization of the Interactions between Cs and Eu and Sediments and Reaction Products

(*References:* Deng et al., 2006c; Flury et al., 2004; Mon et al., 2006; Zhao et al., 2004)

Cesium sorption studies showed that the newly-formed colloids had higher sorption affinity for Cs than did the original minerals. The feldspathoid products sorbed nearly an order of magnitude more Cs than the unaltered kaolinite; however, Na and Ca strongly competed for sorption sites. At low concentration (0.01 mol_c/L) Ca was more competitive than Na, but at higher concentration (0.1 mol_c/L), Na was more competitive than Ca and displaced most of the Cs. Cesium sorption to Hanford sediments in both batch and column experiments was best described with a nonlinear Freundlich isotherm. The column experiments indicated that Cs transport in Hanford sediments occurred under two-site equilibrium and nonequilibrium sorption. Effective retardation factors of Cs during transport through Hanford sediments were reduced by a factor of 10 when the ionic strength increased from 100 to 1000 mM.

We determined how much Cs is incorporated into the secondary phases, and how much is subsequently released by desorption. In zeolite and allophane, most of the incorporated Cs (94–99%) was readily exchangeable with Na or K, whereas Ca was less effective in replacing Cs: only 65–85% of the Cs could be replaced. In cancrinite and sodalite, a large fraction of the incorporated Cs was not easily exchangeable with Na, K, or Ca: only 1–57% of the Cs could be exchanged (Fig. 7). The desorption kinetics experiments showed that Cs desorbed quickly from zeolite. Cesium desorption from cancrinite, sodalite, and allophane, however, was slow, suggesting that Cs was trapped in cages and channels. Effective diffusion coefficients for Cs in cancrinite and sodalite were in the order of 10^{-14} m^2/s, and for zeolite in the order of 10^{-9} m^2/s. The high resistance of incorporated Cs^+ to desorption in sodalite and cancrinite may have twofold implications to the DOE Hanford site: on one hand, the minerals can immobilize the Cs^+, on the other hand, the minerals can be secondary contaminant sources when they became chemically unstable with respect to the pore water of the sediments.

We conducted studies on Eu precipitation onto various mineral surfaces. Eu has properties similar to other trivalent radionuclides, like Am and Cm. Europium precipitated as $Eu(OH)_3$ on the surfaces of clay minerals when pH>6. Europium precipitated as $Eu_2(CO_3)_3$ and $EuOHCO_3$ on the surfaces of calcite. Under the natural pH condition (around 8) of the Hanford sediment, it is likely that Eu forms precipitates on surfaces of clay minerals and calcite. In pH range 3 to 5.5, nearly 50% of Eu was adsorbed by smectite and the adsorption did not show significant variation with pH, suggesting a strong interaction between Eu and the mineral. When pH>6, Eu precipitated a short-range ordered $Eu(OH)_3$; the particle size was in the nanometer range (Fig. 8). The presence of EDTA inhibited the precipitation of $Eu(OH)_3$. The precipitation of Eu on calcite

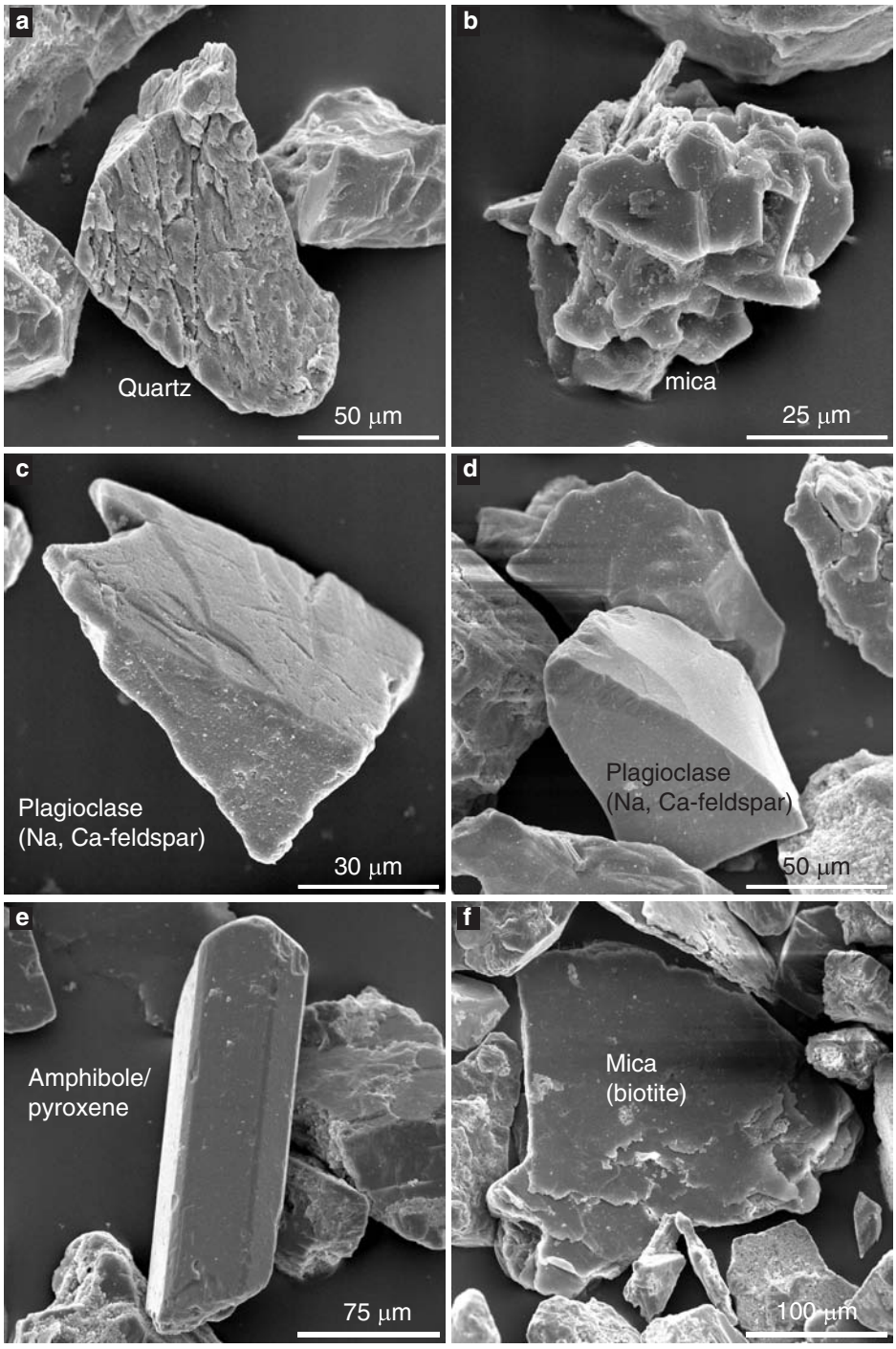

Figure 6. Scanning electron microscopy images of (a-d) light ($<$2.97 g cm^{-3}) and (e-f) heavy ($>$2.97 g cm^{-3}) minerals in sand fraction of the Hanford sediment reacted with STW4. (a) a quartz particle showing etched graves, (b) a K-containing mineral (mica or k-feldspar) showing etching along edges, (c) and (d) Ca-containing minerals (Ca-feldspar) showing weak or no etching on surfaces, (e) and (f) Ca-containing mineral (amphiboles and pyroxenes) were nearly unattacked.

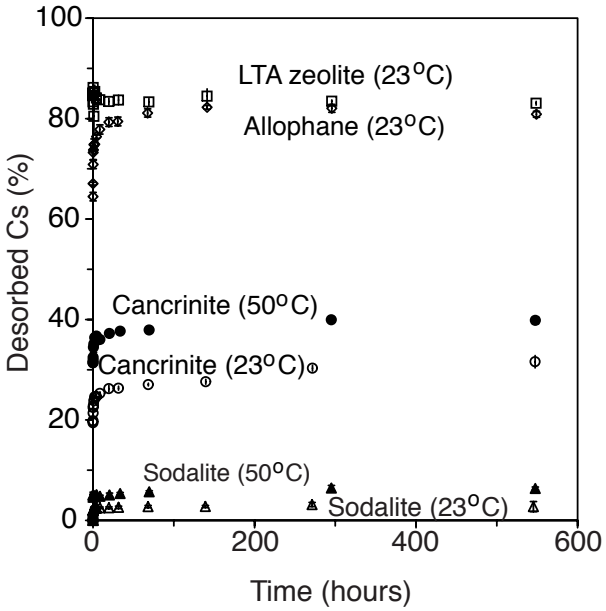

Figure 7. Desorption of Cs^+ from the four Cs-incorporated minerals: cancrinite, sodalite, LTA zeolite, and allophane. Desorption is expressed as percentage of initial amount of Cs^+ present in minerals (water-washed minerals).

was affected by partial pressure of CO_2. When Eu solution was mixed with calcite in a closed system for three days, dissolution of calcite and new precipitates were observed. On the contrary, when Eu solution was mixed with calcite in an open system, only calcite dissolution was observed within the first eight weeks and $Eu_2(CO_3)_3 3H_2O$ formed after nearly one year of reaction. Under the natural pH condition (around 8) in the Hanford sediment, it is likely that Eu forms $Eu(OH)_3$ precipitates. The presence of ligands may inhibit the precipitation of $Eu(OH)_3$, but it does not significantly reduce the adsorption of Eu on smectite (Fig. 9).

3.3.3 Objective 3: Determine the potential of Hanford sediments for in situ mobilization of colloids for different types of sediments and different leaching scenarios

(*References:* Chen and Flury, 2005; Chen et al., 2005; Czigany et al., 2005b; Shira et al., 2006; Zhuang et al., 2006a,b)

Our previous results have shown that colloids and colloid-associated Cs can be mobilized from water-saturated sediments when the ionic strength of the infiltration solution decreases [*Flury et al.*, 2002]. However, under saturated flow, colloid transport is more pronounced than under unsaturated flow. Colloid deposition increased with decreasing system saturation. Under constant chemical conditions, colloids deposited within the column could quantitatively be recovered in the column outflow by re-saturating the column after each unsaturated-flow breakthrough.

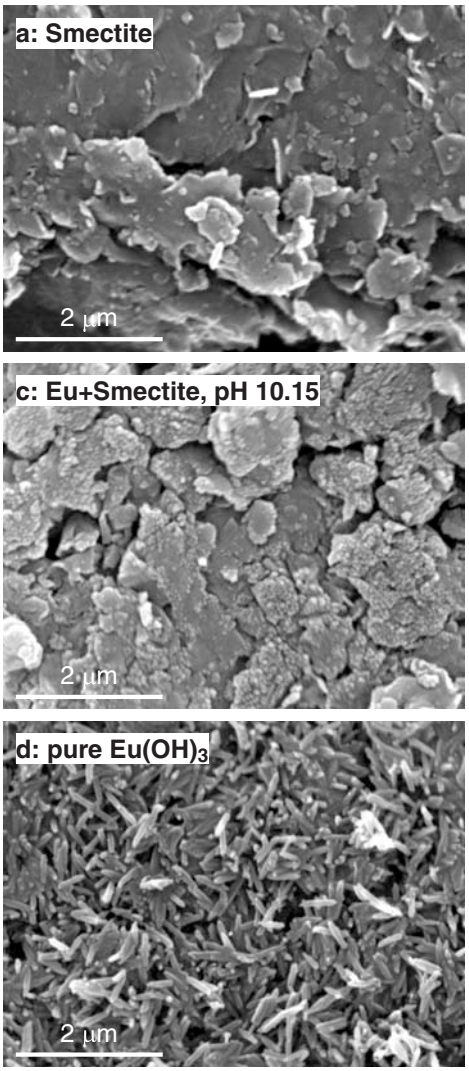

Figure 8. SEM images of (a) starting smectite, (b) small $Eu(OH)_3$ particles precipitated on smectite surfaces at pH 10.15, and (c) pure $Eu(OH)_3$ precipitated in solution without smectite.

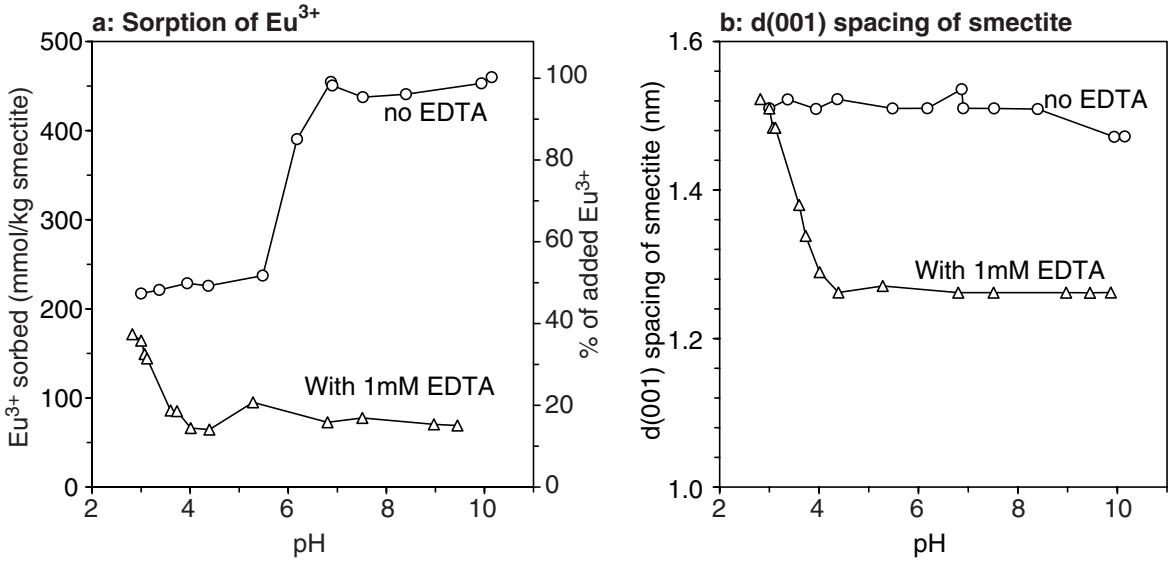

Figure 9. (a) Amount of europium sorbed by smectite at different pH and (b) the d(001) spacings of resulting smectite samples.

Through microscopic observations in a glass micromodel containing suspended air bubbles, we found that colloids did not adhere to the liquid-gas interface. Using the extended DLVO theory, free energies of Lifshitz-van der Waals, electrostatic and Lewis acid/base interactions between colloids, sediments and the liquid-gas interface were calculated based on their independently determined surface thermodynamic properties. Experimental results and surface thermodynamic calculations support the hypothesis that colloids were retained near thin water films of thickness comparable to the colloid diameters.

In the study where a series of column experiments were conducted to examine the effect of irrigation pattern on releases of in-situ colloids in two Hanford sediments under saturated and unsaturated transient flow conditions, we show that during transient flow more in-situ colloids were released than during steady state flow. The number of short-term hydrological pulses proved more vital than total irrigation volume or persistence time length for increasing the amount of mobilized in-situ colloids. However, increasing ionic strength diminished this effect. At an irrigation rate equal to 5% of the saturated hydraulic conductivity, transient multi-pulse flow in 2 mM $NaNO_3$ was equivalent to a fifty-fold reduction of solution ionic strength (from 100 mM to 2 mM) in a single pulse flow in terms of their positive effects on in-situ colloid mobilization. However, in subsequent irrigation pulses, effluent colloid concentrations were much lower at the low than the high irrigation rates, due likely to rate-limited detachment of the tightly (more chemically) attached colloids, which is subject to the hydrodynamic forces overcoming the DLVO forces. The experiments also indicate that mechanical straining of colloids in the fine sand greatly decreased

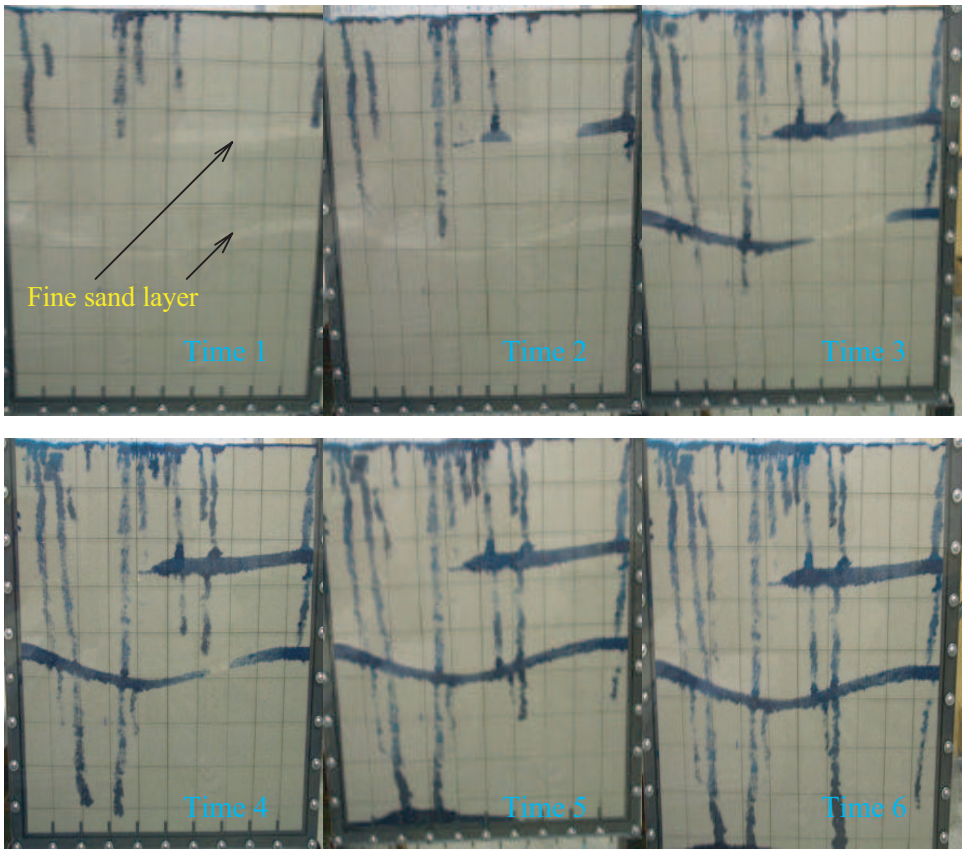

Figure 10. Spatial and temporal evolution of flow patters in multi-layered sand system.

the amount of mobilized colloids, although the fine sand contained about one order of magnitude greater concentration of the in-situ colloids than the coarse sand. This highlights that transient flow is critical for in-situ colloid mobilization, and implies that long-term assessment of colloid release should consider the rainfall pattern and geometrical structure of flow pathways.

A 2-dimensional Hele-Shaw cell for studying colloid transport in texturally layered sediment systems. We have used pure silica sand layers, and results show that preferential flow of water is prevalent and triggerred by the textural boundaryes (Fig. 10). Preferential flow fingers can merged if encountering a fine sand layer. However, new fingers can be generated when water or colloids enter a coarse sand below a fine sand layer. We believe that subsequent redistribution of the water and colloids largely depends on the pattern and intensity of irrigation to the layered sands. This will help us understand colloid mobilization in Hanford sediments, and suggests that we need a systematic study of sediment layering at the site if we are to predict subsurface transport.

During infiltration of a low ionic strength solution (simulated rainfall) into dry Hanford sediments, colloids were eluted by the infiltrating water with the peak colloid concentrations in the outflow coinciding with the arrival of the infiltration front (Fig. 11). At the same initial water

content, a larger flow rate led to a greater amount of colloids released from the column. Colloid elution curves had a steep breakthrough front and a pronounced tailing. The cumulative amount of colloids released was linearly proportional to the column water content established after steady-state flow rates were achieved. We used the advection-dispersion equation with a first-order colloid release reaction to analyze the experimental data. The colloid release rate coefficient increased nearly linearly with the increase of water content. Elution pH and electric conductivity in the column outflow decreased with elapsed time, but the electrophoretic mobility of eluted colloids did not vary significantly with time. We calculated forces exerted on colloids and found that electrostatic and Lifshitz-van der Waals interactions, calculated based on the DLVO theory, and hydrodynamic forces, were all less important than capillary forces in controlling colloid release.

The evaluation of fiberglass wicks for colloid sampling in the vadose zone showed that flow rate, pH, and colloid type affected colloid breakthrough. Colloid recovery in the effluent was higher at pH 10 than at pH 7, and increased with increasing flow rate. The mixture of mineral colloids extracted from sediment moved almost conservatively through the wicks; the colloid recoveries ranged from 88 to $\approx$100% for pH 7 and 10, respectively. Ferrihydrite at pH 10 moved conservatively with recoveries ranging from 95 to $\approx$100%. All other colloids; however, showed lower mass recoveries. At pH 10, colloid recovery ranged from 55% for montmorillonite to $\approx$100% for ferrihydrite and the mixture of mineral colloids, whereas at pH 7, the recovery ranged from $<$5% for kaolinite and ferrihydrite to $\approx$100% for the mixture of mineral colloids. These results suggest that for certain conditions and colloid types, fiberglass wicks can be an acceptable tool for colloid sampling in the vadose zone. However, under many conditions studied here colloids were significantly retained inside the wicks, and consequently, the use of wicks for colloid sampling in the vadose zone must be considered with caution.

3.3.4 Objective 4: Evaluate colloid-facilitated radionuclide transport through sediments under different degrees of water saturation in packed and undisturbed sediment columns

(*References:* Chen and Flury, 2005; Czigany et al., 2005b)

Cesium, pre-associated with colloids, was stripped off during transport through the sediments. The higher the flow rates, the less Cs was stripped off, indicating, in part, that Cs desorption from carrying colloids was a residence-time dependent process. Depending on the flow rate, up to 70% of the initially sorbed Cs desorbed from colloidal carriers and was captured in the stationary sediments. Less Cs was stripped off colloids under unsaturated than under saturated flow conditions at similar flow rates. This phenomenon was likely due to the reduced availability of sorption sites for Cs on the sediments as the water content decreased and water flow was divided between mobile and immobile regions.

There was a general trend that less Cs desorbed from colloids during transport as water flow rates increased (Figure 12), likely because of the smaller residence times at higher flow rates.

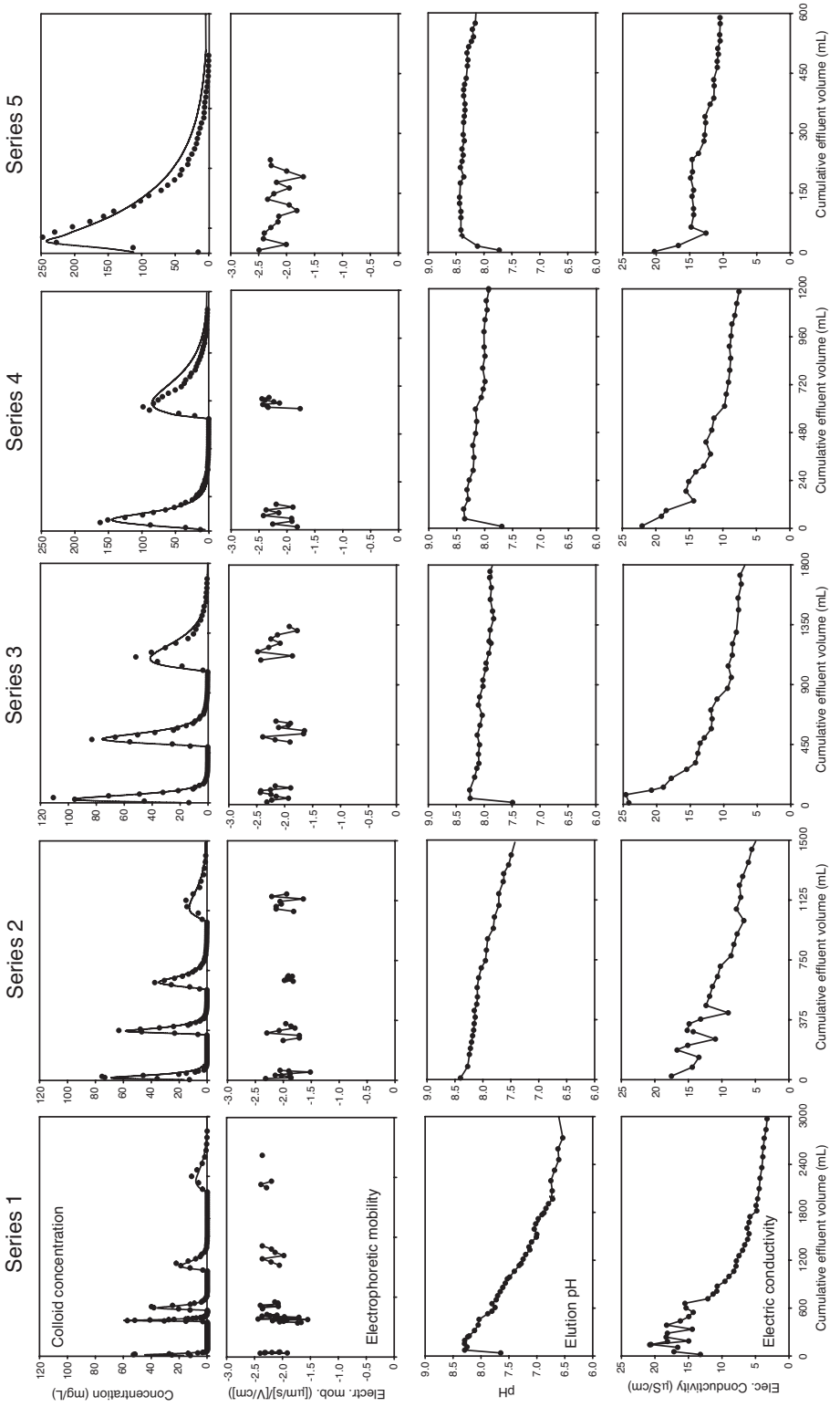

Figure 11. Colloid release breakthrough curves for the 5 series of experiments with initial flow rates of 0.018, 0.036, 0.072, 0.144 and 0.288 cm/min, respectively. For the colloid breakthrough curves, symbols are measured colloid concentrations and lines are model simulations.

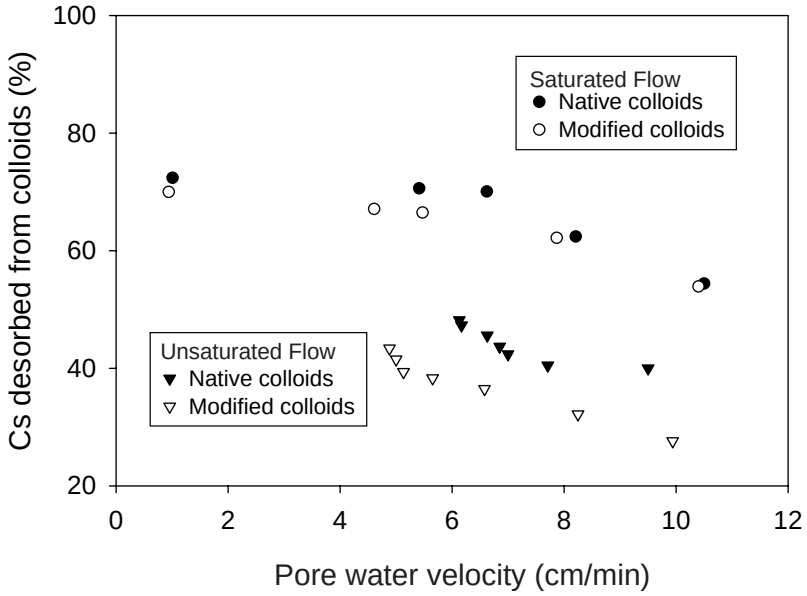

Figure 12. Cesium desorbed from colloids during transport through sediment column as a function of the measured pore water velocity $v = q_m/\theta$.

However, under similar flow rates, less Cs desorbed from colloids during unsaturated flow than during saturated flow. We think that during unsaturated flow, less Cs sorption sites on the sediments are available to strip off the Cs from colloids because less sediment surface area is in contact with the mobile flow regions. Furthermore, as the water content decreased, the immobile water fraction increased, indicating that colloids moved through a smaller effective cross-section of the porous medium. That would further decrease the amount of sediment sorption sites available to strip Cs from the colloids.

Europium was found to be eluted with the infiltrating pore water and peak europium concentrations coincided with the colloid breakthroughs, indicating europium transport was facilitated by colloids. Larger flow rates led to increased colloid mobilization and europium elusion. We used MINTEQ, a geochemical equilibrium speciation model, to simulate europium speciation in solution.

According to both the batch turbidity and the dynamic light scattering results, the CCC of natural Hanford colloids was intermediate between that of the kaolinite and montmorillonite clay mineral standards. This suggests that the clay mineral standards can be used to bracket the behavior of natural Hanford colloids. In contrast to the batch studies, the light scattering studies did not reveal differences in colloidal stability between coarse and fine Hanford colloids.

The results of our colloid stability experiments and the measured pore water compositions in vadose zone Hanford sediments indicate that colloids likely form stable suspensions in vadose zone Hanford sediments. However, the colloidal stability, as defined by the CCC does, not nec-

essarily imply that colloids stay suspended for sufficiently long times to play a relevant role for contaminant transport. Long-term stability experiments indeed indicated that colloids from the Hanford sediments will form stable suspensions for several weeks, but over longer time periods, colloids will settle out from suspension. After about 16 weeks, on average 90% of the colloidal mass settled out from suspension.

We conclude that colloids in the Hanford vadose zone form stable suspensions, i.e., are in the slow-aggregation regime. Nonetheless, due to their probable long travel times in the zone, nearly all colloids will aggregate and be removed from the water column before reaching groundwater levels.

3.3.5 Objective 5: Implement Colloid-facilitated Contaminant Transport Mechanisms into a Reactive Transport Model

(*References:* Lichtner et al., 2004; Chen et al., 2005)

The nitrate and colloid data from column experiments could be well described with the two-region model and the results suggest a significant fraction of immobile water when the effective water saturation dropped below 0.8. Under water saturated conditions, both native and modified colloids were quantitatively recovered and no colloids were deposited inside the column. When the column became unsaturated, colloids began to be retained in the sediment. At an effective water saturation of 0.2, $\approx$60% of colloids were retained within the column. These colloids were mostly likely retained at the liquid-gas-solid three phase interface.

Results of FOLTRAN applications to reactive transport experiments indicated a complex behavior of species concentrations eluted from the column. Shown in Figure 13 are breakthrough curves for Cs^+, Na^+, and NO_3^-. Results indicated a complex behavior of species concentrations eluted from the column. The initial breakthrough of Cs was well reproduced in the calculations using ion exchange coefficients obtained from an independent study [*Steefel et al.*, 2003*; Lichtner et al.*, 2004]. One puzzling aspect of the experiments, however, was that nitrate did not behave as a nonreactive tracer as expected and as predicted by the model. The model calculations, however, were based on a fully saturated column rather than an initially dry column. To partially compensate for this, the initial fluid composition was set to the composition of the observed breakthrough concentrations.

Ion exchange reactions are usually considered to have fast, reversible, reaction kinetics governed by electrostatic attraction. However, when taking place on colloids ion exchange reactions appear to exhibit irreversibility, for example sorption of plutonium on colloids as observed at the Nevada Test Site [*Kersting et al.*, 1999]. To account for such irreversibility, a kinetic description of ion exchange rates is needed.

Ion Exchange Reactions

The simplest approach to developing a kinetic formulation of ion exchange is to assume simple reaction kinetics in which the rate is equal to the difference between the forward and

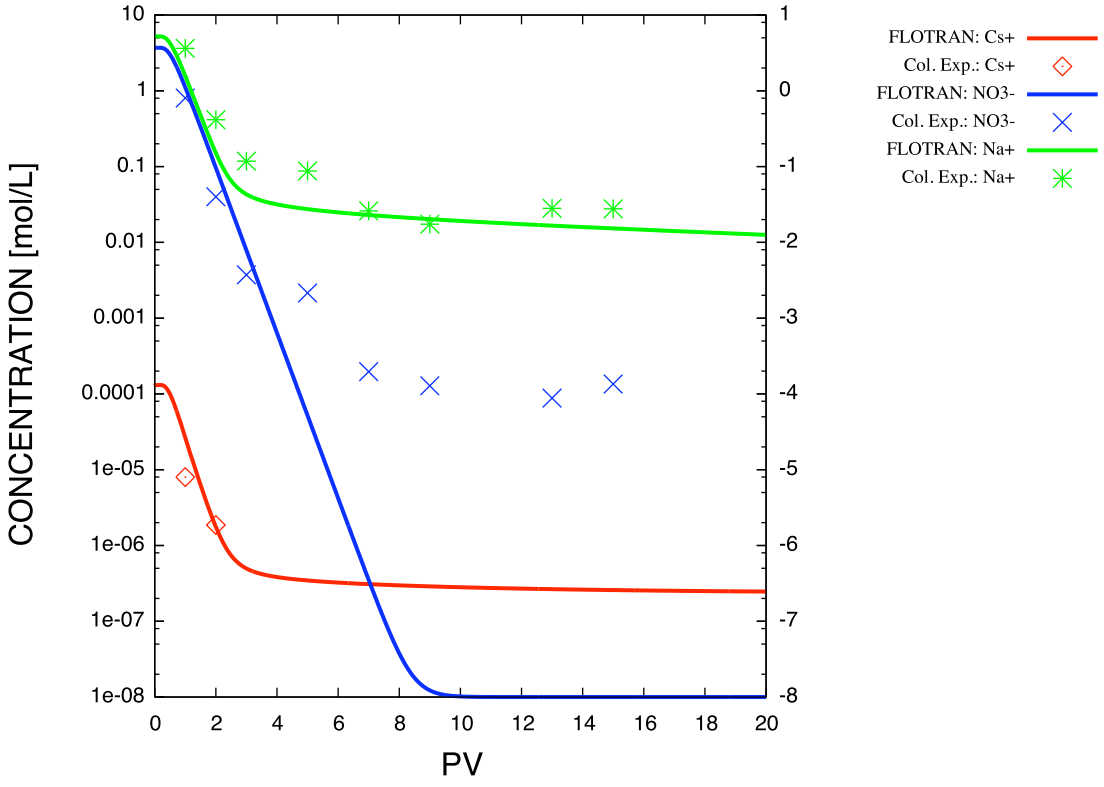

Figure 13. Breakthrough curves for Cs^+, Na^+, and NO_3^- plotted as a function of eluted pore volumes and compared with column data.

backward rates with concentrations raised to powers of the reaction stoichiometric coefficients. This form of the rate law, however, is not unique (with the exception of monovalent exchange) and depends on the stoichometry used to write the exchange reaction. As long as the rate law is consistent with the equilibrium state of the reaction, the correctness of the form of the rate law cannot be ascertained without further experiment effort. In particular, the form of the rate law cannot be deduced from the reaction stoichiometry alone, but requires additional experimental data as is well known from the theory of kinetics. However, rate laws which violate conservation of charge can be eliminated even though they may reproduce the correct equilibrium state.

Two equivalent forms of ion exchange reactions for the purposes of equilibrium calculations are in common use. One form is given by

$$\frac{1}{z_{j_0}}\mathcal{A}_{j_0} + \frac{1}{z_j}\big(X_m\big)_{z_j}\mathcal{A}_j \;\rightleftharpoons\; \frac{1}{z_j}\mathcal{A}_j + \frac{1}{z_{j_0}}\big(X_m\big)_{z_{j_0}}\mathcal{A}_{j_0}, \tag{9a}$$

and the other by

$$z_j\mathcal{A}_{j_0} + z_{j_0}\big(X_m\big)_{z_j}\mathcal{A}_j \;\rightleftharpoons\; z_{j_0}\mathcal{A}_j + z_j\big(X_m\big)_{z_{j_0}}\mathcal{A}_{j_0}, \tag{9b}$$

obtained by multiplying the former reaction by the product $z_{j_0} z_j$. The quantities z_{j_0} and z_j denote the valencies of cations $\mathcal{A}_{j_0}$ and $\mathcal{A}_j$, with reference cation denoted by the subscript j_0 and the subscript $j \neq j_0$ represents all other cations. Species $\left(X_m\right)_{z_j} \mathcal{A}_j$ indicates sorption of the jth cation associated with the mth mineral on the surface exchange site X_m. Only in the case of monovalent exchange ($z_{j_0} = z_j = 1$) are the two forms identical.

The respective mass action equations are given by

$$K_{j_0 j} = \left(\frac{X_{j_0}^m}{a_{j_0}}\right)^{1/z_{j_0}} \left(\frac{a_j}{X_j^m}\right)^{1/z_j}, \tag{10a}$$

and

$$\widetilde{K}_{j_0 j} = \left(\frac{X_{j_0}^m}{a_{j_0}}\right)^{z_j} \left(\frac{a_j}{X_j^m}\right)^{z_{j_0}}, \tag{10b}$$

where, using the Gaines-Thomas convention, the equivalent fractions X_k^m are defined by

$$X_k^m = \frac{z_k S_k^m}{\sum_l z_l S_l^m} = \frac{z_k}{\omega_m} S_k^m, \quad \sum X_k^m = 1, \tag{11}$$

with ω_m the site concentration associated with the mth mineral defined by

$$\omega_m = \sum_k z_k S_k^m. \tag{12}$$

The site concentration ω_m is related to $\mathcal{Q}_m$, the cation exchange capacity (CEC) with units mol/kg, associated with the mth mineral, by the expression

$$\omega_m = \varphi_m \rho_m \mathcal{Q}_m, \tag{13}$$

with mineral density ρ_m and volume fraction φ_m.

Typically, an average exchange capacity $\mathcal{Q}$ is defined for the bulk rock, related to the contribution from individual minerals $\mathcal{Q}_m$ by the summation

$$\mathcal{Q} = \sum_m \chi_m \mathcal{Q}_m, \tag{14}$$

where χ_m denotes the mass fraction of the mth mineral given by

$$\chi_m = \frac{\varphi_m \rho_m}{\sum_{m'} \varphi_{m'} \rho_{m'}}. \tag{15}$$

The average site concentration ω is related to $\mathcal{Q}$ by the expression

$$\omega = (1 - \varphi) \rho_s \mathcal{Q}, \tag{16}$$

with porosity φ and solid density ρ_s given by

$$\rho_s = \frac{1}{1-\varphi}\sum_m \varphi_m \rho_m, \tag{17}$$

and

$$1-\varphi = \sum_m \varphi_m. \tag{18}$$

The average site concentration ω is related to the mineral site concentrations ω_m by the sum

$$\omega = \sum_m \omega_m, \tag{19}$$

where the bulk site concentration averaged over different minerals making up the rock aggregate satisfies

$$\omega = \sum_j z_j S_j, \tag{20}$$

with the total site concentration S_j equal to

$$S_j = \sum_m S_j^m. \tag{21}$$

For equivalent exchange $(z_j = z)$, an explicit expression exists for the sorbed concentrations given by

$$S_j^m = \frac{\omega_m}{z}\frac{k_j^m C_j}{\sum k_l^m C_l}, \tag{22}$$

where C_k denotes the kth cation concentration. This expression follows directly from the mass action equations and conservation of exchange sites. Note that the bulk sorbed concentration does not have the same form as the individual mineral contributions unless the selectivity coefficients k_j^m are the same for each mineral, in which case

$$S_j = \frac{\omega}{z}\frac{k_j C_j}{\sum k_l C_l}. \tag{23}$$

Kinetic Rate Laws

The kinetic reaction rate for reaction (9a) has the following form

$$I_{j_0 i}^m = k_{j_0 j}^{mf} a_{j_0}^{1/z_{j_0}} \left(X_j^m\right)^{1/z_j} - k_{j_0 j}^{mb} a_j^{1/z_j} \left(X_j^m\right)^{1/z_{j_0}}, \tag{24a}$$

and for reaction (9b) the form

$$\widetilde{I}_{j_0 j}^m = \widetilde{k}_{j_0 j}^{mf} a_{j_0}^{z_j} \left(X_j^m\right)^{z_{j_0}} - \widetilde{k}_{j_0 j}^{mb} a_i^{z_{j_0}} \left(X_{j_0}^m\right)^{z_j}. \tag{24b}$$

where $k_{j_0j}^{mf}$, $k_{j_0j}^{mb}$, $\widetilde{k}_{j_0j}^{mf}$, and $\widetilde{k}_{j_0j}^{mb}$ denote the forward and backward rate constants associated with the mth mineral, respectively. Although the reaction rates I_{j_0j} and $\widetilde{I}_{j_0j}$ corresponding to reactions (9a) and (9b) are not simply related, the equilibrium constants for the corresponding reactions are related by the expression

$$\widetilde{K}_{j_0j}^m = \left(K_{j_0j}^m\right)^{z_{j_0}z_j}. \tag{25}$$

The ratio of the forward and backward rate constants are equal to the equilibrium constants according to

$$K_{j_0j}^m = \frac{k_{j_0j}^{mf}}{k_{j_0j}^{mb}}, \tag{26}$$

and similarly for $\widetilde{K}_{j_0j}^m$.

Another form of the kinetic rate law analogous to transition state theory is to write the reaction rate as

$$I_{j_0j}^m = -k_{j_0j}^{mb}\mathcal{P}_{j_0j}^m\left(1 - K_{j_0j}^m Q_{j_0i}^m\right), \tag{27}$$

where the prefactor $\mathcal{P}_{j_0j}^m$ and ion activity product $Q_{j_0j}^m$ are defined by

$$\mathcal{P}_{j_0j}^m = a_j^{z_{j_0}}\left(X_{j_0}^m\right)^{z_j}, \tag{28}$$

and

$$Q_{j_0j}^m = \frac{a_{j_0}^{1/z_{j_0}}\left(X_j^m\right)^{1/z_i}}{a_j^{1/z_i}\left(X_j^m\right)^{1/z_{j_0}}}. \tag{29}$$

Equilibrium holds if $K_{j_0j}^m Q_{j_0j}^m = 1$. In this form the rate is equivalent to Eqn. (24a). However, setting $\mathcal{P}_{j_0j}^m$ equal to a constant or some other form dictated by experiment, leads to alternative rate laws with the identical equilibrium state.

Multicomponent Mass Conservation Relations Involving Colloids

Mass conservation equations for a multicomponent system involving colloid-facilitated transport and including homogeneous aqueous reactions, mineral precipitation and dissolution, and ion exchange reactions with the form given in (9a) using cation $\mathcal{A}_{j_0}$ as reference cation are given by

$$\frac{\partial}{\partial t}\varphi\Psi_{j_0} + \boldsymbol{\nabla}\cdot\left(\boldsymbol{q}\Psi_{j_0} - \varphi D\boldsymbol{\nabla}\Psi_{j_0}\right) = -\frac{1}{z_{j_0}}\sum_{j\neq j_0,\,m} I_{j_0j}^m - \frac{1}{z_{j_0}}\sum_{j\neq j_0,\,c} I_{j_0j}^c - \sum_m \nu_{j_0m}I_m, \tag{30a}$$

$$\frac{\partial}{\partial t}\varphi\Psi_j + \boldsymbol{\nabla}\cdot\left(\boldsymbol{q}\Psi_j - \varphi D\boldsymbol{\nabla}\Psi_j\right) = \frac{1}{z_j}\sum_m I_{j_0j}^m + \frac{1}{z_j}\sum_c I_{j_0j}^c - \sum_m \nu_{jm}I_m, \tag{30b}$$

for aqueous primary species. The sums over indices m and c run over all minerals and colloids present in the system. Individual primary species concentrations are denoted by C_j and the total

concentration Ψ_j is defined by

$$\Psi_j = C_j + \sum_i \nu_{ji} C_i, \tag{31}$$

where the sum is over secondary species with concentrations C_i related by the mass action relations

$$C_i = \gamma_i^{-1} K_i \prod_j \left(\gamma_j C_j\right)^{\nu_{ji}}, \tag{32}$$

to primary species concentratins C_j. Quantities K_i, $\gamma_{j,i}$, ν_{ji} denote the equilibrium constant, activity coefficients for primary and secondary species, and stoichiometric reaction coefficients. Mineral reaction rates I_m have the form

$$I_m = -k_m a_m \big(1 - K_m Q_m\big), \tag{33}$$

motivated by transition state theory with equilibrium constant K_m and ion activity product Q_m, Sorbed concentrations for minerals and colloids obey the conservation equations

$$\frac{\partial S_{j0}^m}{\partial t} = \frac{1}{z_{j_0}} \sum_{j \neq j_0} I_{j_0 j}^m, \tag{34a}$$

$$\frac{\partial S_j^m}{\partial t} = -\frac{1}{z_j} I_{j_0 j}^m, \tag{34b}$$

for minerals, and

$$\frac{\partial S_{j0}^c}{\partial t} + \boldsymbol{\nabla} \cdot \left(\boldsymbol{q}_c S_{j0}^c\right) = \frac{1}{z_{j_0}} \sum_{j \neq j_0} I_{j_0 j}^c, \tag{35a}$$

$$\frac{\partial S_j^c}{\partial t} + \boldsymbol{\nabla} \cdot \left(\boldsymbol{q}_c S_j^c\right) = -\frac{1}{z_j} I_{j_0 j}^c, \tag{35b}$$

for colloids labeled with superscript c, where the colloid velocity $\boldsymbol{q}_c$ may be different from the fluid velocity $\boldsymbol{q}$.

Similar expressions hold for the exchange reactions of the form of reactions (9b) but with different stoichiometric exchange coefficients

$$\frac{\partial}{\partial t}\varphi \Psi_{j_0} + \boldsymbol{\nabla} \cdot \left(\boldsymbol{q} \Psi_{j_0} - \varphi D \boldsymbol{\nabla} \Psi_{j_0}\right) = -\sum_{i \neq j_0,\, m} z_j \widetilde{I}_{j_0 j}^m - \sum_m \nu_{j_0 m} I_m, \tag{36a}$$

$$\frac{\partial}{\partial t}\varphi \Psi_{j} + \boldsymbol{\nabla} \cdot \left(\boldsymbol{q} \Psi_{j} - \varphi D \boldsymbol{\nabla} \Psi_{j}\right) = z_{j_0} \sum_m \widetilde{I}_{j_0 j}^m - \sum_m \nu_{i m} I_m, \tag{36b}$$

with sorbed concentrations for minerals

$$\frac{\partial S_{j_0}^m}{\partial t} = \sum_{i \neq j_0} z_j \widetilde{I}_{j_0 j}^m, \tag{37a}$$

$$\frac{\partial S_j^m}{\partial t} = -z_{j_0} \widetilde{I}_{j_0 j}^m. \tag{37b}$$

and colloids

$$\frac{\partial S_{j_0}^c}{\partial t} + \boldsymbol{\nabla} \cdot \left(\boldsymbol{q}_c S_{j_0}^c \right) = \sum_{i \neq j_0} z_j \widetilde{I}_{j_0 j}^c, \tag{38a}$$

$$\frac{\partial S_j^c}{\partial t} + \boldsymbol{\nabla} \cdot \left(\boldsymbol{q}_c S_j^c \right) = -z_{j_0} \widetilde{I}_{j_0 j}^c. \tag{38b}$$

Eliminating the exchange rates from the primary species equations gives the following partial differential equation for primary species concentrations

$$\frac{\partial}{\partial t}\left(\varphi \Psi_j + \sum_m S_j^m + \sum_c S_j^c \right) + \boldsymbol{\nabla} \cdot \left(\boldsymbol{q} \Psi_j + \sum_c \boldsymbol{q}_c S_j^c - \varphi D \boldsymbol{\nabla} \Psi_j \right) = -\sum_m \nu_{jm} I_m. \tag{39}$$

This equation is valid for all exchangeable cations and for both forms of the exchange reactions.

It follows that for both formulations charge is conserved. Multiplying Eqn. (39) by the valence of the jth species and summing over all species gives

$$\left(\frac{\partial}{\partial t} \varphi + \boldsymbol{\nabla} \cdot \boldsymbol{q} - \varphi D \boldsymbol{\nabla} \right) \sum_j z_j \Psi_j = 0. \tag{40}$$

This is a consequence of neutrality of minerals ($\sum_j z_j \nu_{jm} = 0$), and conservation of exchange sites according to the result

$$\frac{\partial \omega_m}{\partial t} = \frac{\partial \omega_c}{\partial t} = 0. \tag{41}$$

implying that the cation exchange capacity of the porous medium is constant. The surface area for sorption is related to mineral abundances which may change over time and space due to precipitation/dissolution reactions.

It should be noted that for the often employed rate equation of the form

$$I_j = -k_j \left(S_j - K_j^D \Psi_j \right), \tag{42}$$

with rate constant k_j and where K_j^D denotes the distribution coefficient, which yields the correct relation between sorbed and aqueous concentrations at equilibrium ($S_j = K_j^D \Psi_j$), this rate law does *not* conserve charge.

Retardation

It follows from the primary species transport equations that for approximately constant distribution coefficients giving the ratio of sorbed to aqueous concentrations for mineral and colloid sorption, that the migration of each cation is retarded by the factor $\mathcal{R}_j$ defined as

$$\mathcal{R}_j = \frac{1 + \sum_m K_j^m + \sum_c K_j^c}{1 + \sum_c f_c K_j^c}, \tag{43}$$

where $f_c = q_c/q$, and distribution coefficients K_j^m and K_j^c for minerals and colloids, respectively, are defined by

$$K_j^m = \frac{1}{\varphi \Psi_j} S_j^m, \tag{44}$$

and

$$K_j^c = \frac{1}{\varphi \Psi_j} S_j^c. \tag{45}$$

For $f_c = 1$, $\mathcal{R}_j$ simplifies to

$$\mathcal{R}_j = 1 + \frac{\sum_m K_j^m}{1 + \sum_c K_j^c}. \tag{46}$$

Thus according to this latter expression, for $\sum_c K_j^c \gg \sum_m K_j^m \gg 1$, colloids effectively eliminate retardation. However, for sorption on colloids to effectively compete with mineral surfaces, generally requires high colloid concentrations (Honeyman and Ranville, 2002).

Numerical Implementation

An initial attempt to modify FLOTRAN [*Lichtner*, 2001] to implement sorption kinetics did not succeed because of major restructuring of the code that was required. The global implicit scheme utilized by FLOTRAN only solved the aqueous primary species transport equations in a coupled manner, whereas to simulate kinetic ion exchange, sorbed species needed to be solved simultaneously with the aqueous primary species equations. A new approach is currently being implemented which requires only minor modifications to the existing code, achieved by storing the existing residual and Jacobian arrays into new arrays that are dimensioned to include the sorbed species. However, to implement the correct kinetic rate law, new data will be needed to constrain the form of the rate law for ion exchange (or surface complexation) reactions on colloids or mineral surfaces. Presently, there does not exist sufficient data for this purpose for the complex fluids encountered at the Hanford site.

3.3.6 Objective 6: Improve conceptual characterization of colloid-contaminant-soil interactions and colloid-facilitated transport

Many of the radioactive contaminants sorb strongly to subsurface minerals and are therefore considered fairly immobile. Colloids can potentially facilitate the movement of such contaminants, provided colloids are present, sorb contaminants strongly, form stable suspensions, and are mo-

bile in the subsurface. All of these conditions must be met if colloid-facilitated transport is a relevant transport mechanism.

The results of our colloid stability experiments and the measured pore water compositions in vadose zone Hanford sediments indicate that colloids likely form stable suspensions in vadose zone Hanford sediments. However, the colloidal stability, as defined by the CCC does, not necessarily imply that colloids stay suspended for sufficiently long times to play a relevant role for contaminant transport. Long-term stability experiments indeed indicated that colloids from the Hanford sediments will form stable suspensions for several weeks, but over longer time periods, colloids will settle out from suspension. After about 16 weeks, on average 90% of the colloidal mass settled out from suspension.

Measured recharge rates at Hanford range from near 0 to more than 100 mm/year, depending on variation in precipitation, soil type, and vegetation cover [*Gee et al.*, 1992]. One of the most contaminated locations at Hanford, the waste tank area, has some of the highest recharge rates, because of the coarse-textured sediment used for backfill and the absence of vegetation. In addition, the "umbrella effect", i.e., the runoff and redirection of water due to the presence of the tanks, enhances the local recharge rates. The thickness of the Hanford vadose zone, where the waste tanks are located, varies from 40 to 100 m [*Gee and Heller*, 1985; *McKinley et al.*, 2001]. Assuming the worst-case scenario of a shallow vadose zone (40-m thickness), a high recharge rate (100 mm/year), and an average volumetric water content of 10%, the travel time of the recharge water is 40 years. Over this time period, colloidal suspensions at the Hanford site will not be stable. Estimations based on measured aggregation rates show that after 40 years only up to 0.08% of the initially suspended colloids remain in suspension.

At the Hanford site, an important question is whether Cs that has leaked into the vadose zone can reach the underlying groundwater. From core sampling in the S-SX tank farm, we know that peak concentrations of ^{137}Cs are located at 25 to 26-m depth below ground, with traces of ^{137}Cs found up to 38 m below ground [*Serne et al.*, 2002b; *Serne et al.*, 2002c]. Based on the results of our laboratory study it is unlikely that colloids were responsible for the movement of the Cs to these depths. If Cs is reversibly attached to to colloids by ion-exchange, Cs would likely be stripped off the colloids as the colloids move through uncontaminated sediments. The sediments underlying Hanford waste tanks sorb Cs with high affinity [*Zachara et al.*, 2002; *McKinley et al.*, 2001], and this would provide an effective means of opposing colloid-facilitated Cs transport. Other studies have indeed shown that the current location of Cs under Hanford SX waste tanks can be explained by chromatographic solution phase transport in a high electrolyte waste solution [*Knepp*, 2002; *Steefel et al.*, 2003; *Lichtner et al.*, 2004].

In addition, colloid transport itself is restricted in the vadose zone, and with decreasing moisture content, the restriction becomes more obvious. In this study, we show that $\approx$55 to 60% of initially present colloids are retained in the column at an effective water saturation of 0.2. At the Hanford site, gravimetric water saturations in sediments of the Hanford formation underlying the S-SX waste tanks range from 0.04 to 0.17 kg/kg [*Serne et al.*, 2002b], and the thickness of

the vadose zone varies from 40 to 100 m [*Gee and Heller*, 1985*; McKinley et al.*, 2001]. The possibility of colloids to be transported from the soil surface to the ground water at the Hanford tank farms appears minimal, unless water contents and flow rates are locally and temporally increased by snow melt events or artifical infiltration caused by past waste management practices.

4 Products Developed

4.1 Publications Published in Peer-Reviewed Journals (in inverse chronological order)

1. Deng, Y., M. Flury, J. B. Harsh, and A. R. Felmy, and O. Qafoku, Cancrinite and sodalite formation in the presence of Cesium, Potassium, Magnesium, Calcium, and Strontium in Hanford tank waste simulants, *Appl. Geochem.*, (in press), 2006a.

2. Deng, Y., J. B. Harsh, M. Flury, J. Young, and J. S. Boyle, Mineral formation during simulated leaks of Hanford waste tanks, *Appl. Geochem., 21*, 1392–1409, 2006b.

3. Shira, J. M., B. C. Williams, M. Flury, S. Czigany, and M. Tuller, Sampling silica and ferrihydrite colloids with fiberglass wicks under unsaturated flow conditions, *J. Environ. Qual., 35*, 1127–1134, 2006.

4. Mon, J., Y. Deng, M. Flury, and J. B. Harsh, Cesium incorporation and diffusion in cancrinite, sodalite, zeolite, and allophane, *Micropor. Mesopor. Mat., 86*, 277–287, 2006.

5. Chen, G., M. Flury, J. B. Harsh, and P. C. Lichtner, Colloid-facilitated transport of cesium in variably-saturated Hanford sediments, *Environ. Sci. Technol., 39*, 3435–3442, 2005.

6. Chen, G., and M. Flury, Retention of mineral colloids in unsaturated porous media as related to their surface properties. *Colloids Surf. Physicochem. Eng. Aspects, 256*, 207–216, 2005.

7. Czigany, S., M. Flury, and J. B. Harsh, Colloid stability in vadose zone Hanford sediments. *Environ. Sci. Technol., 39*, 1506–1512, 2005a.

8. Czigany, S., M. Flury, J. B. Harsh, B. C. Williams, and J. M. Shira, Suitability of fiberglass wicks to sample colloids from vadose zone pore water. *Vadose Zone J., 4*, 175–183, 2005b.

9. Mashal, K., J. B. Harsh, M. Flury, and A. R. Felmy, Analysis of precipitates from reactions of hyperalkaline solutions with soluble silica. *Appl. Geochem., 20*, 1357–1367, 2005a.

10. Mashal, K., J. B. Harsh, and M. Flury, Clay mineralogical transformations over time in Hanford sediments reacted with simulated tank waste. *Soil Sci. Soc. Am. J., 69*, 531–538, 2005b.

11. Mashal, K., J. B. Harsh, M. Flury, A. R. Felmy, and H. Zhao, Colloid formation in Hanford sediments reacted with simulated tank waste. *Environ. Sci. Technol., 38*, 5750–5756, 2004.

12. Lichtner, P. C., S. Yabusaki, K. Pruess, and C. I. Steefel, Role of competitive cation exchange on chromatographic displacement of cesium in the vadose zone beneath the Hanford S/SX tank farm, *Vadose Zone J., 3*, 203–219, 2004.

13. McCarthy, J. F., and L. D. McKay, Colloid transport in the subsurface: past, present, and future challenges *Vadose Zone J., 3*, 326–337, 2004.

14. Crist, J. T, J. F. McCarthy, Y. Zevi, P. Baveye, J. A. Troop, and T. S. Steenhuis, Pore-scale visualization of colloid transport and retention in partly saturated porous media. *Vadose Zone J., 3*, 444–450, 2004.

15. Flury, M., S. Czigany, G. Chen, and J. B. Harsh, Cesium migration in saturated silica sand and Hanford sediments as impacted by ionic strength. *J. Contam. Hydrol., 71*, 111–126, 2004.

16. Zhuang, J., Y. Jin, and M. Flury, Comparison of natural colloid and kaolinite transport in porous media. *Vadose Zone J., 3*, 395–402, 2004.

17. Zhao, H., Y. Deng, J. B. Harsh, M. Flury, and J. Boyle, Alteration of kaolinite to cancrinite and sodalite by simulated Hanford Tank Wastes and its impact on cesium retention. *Clays Clay Miner., 52*, 1–13, 2004.

18. Flury, M., J. B. Harsh, and J. B. Mathison, Miscible displacement of salinity fronts: Implications for colloid mobilization. *Water Resour. Res., 39*, 1373, doi:10.1029/2003WR002491, 2003.

19. Zhuang, J., M. Flury, and Y. Jin, Colloid-facilitated Cs transport through water-saturated Hanford sediment and Ottawa sand. *Environ. Sci. Technol., 37*, 4905–4911, 2003.

20. Cherrey, K. D., M. Flury, and J. B. Harsh, Nitrate and colloid transport through coarse Hanford sediments under steady state, variably saturated flow. *Water Resour. Res., 39*, 1165, doi:10.1029/2002WR001944, 2003.

    (Correction published in *Water Resour. Res., 40*, W03901, doi:10.1029/2004WR003066, 2004.)

4.2 Unpublished Reports and Publications in Preparation

1. Zhuang, J., J. F. McCarthy, E. Perfect, J. Tyner, M. Flury, T. S. Steenhuis, The coupled effect of flux rate and ionic strength on transport of colloid through porous media during unsaturated transient flow. (in preparation), 2006a.

2. Zhuang, J., J. F. McCarthy, E. Perfect, J. Tyner, and M. Flury, *In situ* colloid mobilization in Hanford sediments under unsaturated transient flow condition: Effect of irrigation pattern. (in preparation), 2006b.

3. Deng, Y., J. B. Harsh, M. Flury, and J. S. Boyle, Precipitation and adsorption of europium on smectite and calcite, (in preparation), 2006c.

4. Deng, Y., H. Zhao, J. B. Harsh, M. Flury, and J. S. Boyle, Resistance of silicate minerals to alkaline waste simulants, (in preparation), 2006d.

4.3 Web Sites

The following web sites provide information about the project. The general web site is

`http://akasha.wsu.edu`.

A list of publication is given at

`http://akasha.wsu.edu/~flury/publications.html`.

Project information is given at

`http://akasha.wsu.edu/~flury/research/colloid.html`.

Literature Cited

Chen, G., and M. Flury, Retention of mineral colloids in unsaturated porous media as related to their surface properties, *Colloids Surf. Physicochem. Eng. Aspects, 256*, 207–216, 2005.

Cherrey, K. D., M. Flury, and J. B. Harsh, Nitrate and colloid transport through coarse Hanford sediments under steady state, variably saturated flow, *Water Resour. Res., 39*, 1165, doi:10.1029/2002WR001944, 2003.

Crank, J., *The Mathematics of Diffusion*, 2nd ed., Clarendon Press, Oxford University Press, Oxford, 1975.

Crist, J. T., J. F. McCarthy, Y. Zevi, P. C. Baveye, J. A. Troop, and T. S. Steenhuis, Pore-scale visualization of colloid transport and retention in partially saturated porous media, *Vadose Zone J., 3*, 444–450, 2004.

Flury, M., J. B. Mathison, and J. B. Harsh, *In situ* mobilization of colloids and transport of cesium in Hanford sediments, *Environ. Sci. Technol., 36*, 5335–5341, 2002.

Gee, G. W., and P. R. Heller, *Unsaturated water flow at the Hanford site: A review of literature and annotated bibliography*, Pacific Northwest National Laboratory, Richland, WA, 1985.

Gee, G. W., M. J. Fayer, M. L. Rockhold, and M. D. Campbell, Variations in recharge at the Hanford site, *Northwest Sci., 66*, 237–250, 1992.

Kersting, A. B., D. W. Efurd, D. L. Finnegan, D. J. Rokop, D. K. Smith, and J. L. Thompson, Migration of plutonium in ground water at the Nevada Test Site, *Nature, 397*, 56–59, 1999.

Knepp, A. J., *Field Investigation Report for Waste Management Area S-SX*, RPP-7884, Rev. 0, CH2M HILL Hanford Group, Inc., Richland, Washington, 2002.

Lenhart, J. J., and J. E. Saiers, Transport of silica colloids through unsaturated porous media: experimental results and model comparisons, *Environ. Sci. Technol., 36*, 769–777, 2002.

Lichtner, P. C., *FLOTRAN User Manual*, LA-UR-01-2349, Los Alamos National Laboratory report, Los Alamos, New Mexico, 2001.

Lichtner, P. C., S. Yabusaki, K. Pruess, and C. I. Steefel, Role of competitive cation exchange on chromatographic displacement of cesium in the vadose zone beneath the Hanford S/SX tank farm, *Vadose Zone J., 3*, 203–219, 2004.

McKinley, J. P., C. J. Zeissler, J. M. Zachara, R. J. Serne, R. M. Lindstrom, H. T. Schaef, and R. D. Orr, Distribution and retention of Cs-137 in sediments at the Hanford Site, Washington, *Environ. Sci. Technol., 35*, 3433–3441, 2001.

Serne, R. J., B. N. Bjornstad, H. T. Schaef, B. A. Williams, D. C. Lanigan, D. G. Horton, R. E. Clayton, A. V. Mitroshkov, V. L. LeGore, M. J. O'Hara, C. F. Brown, K. E. Parker, I. V. Kutnyakov, J. N. Serne, G. V. Last, S. C. Smith, C. W. Lindenmeier, J. M. Zachara, and D. S. Burke, *Characterization of Vadose Zone Sediment: Uncontaminated RCRA Borehole Core Samples and Composite Samples*, Pacific Northwest National Laboratory, US Department of Energy, PNNL-13757-1, Richland, Washington, 2002a.

Serne, R. J., R. E. Clayton, I. V. Kutnyakov, G. V. Last, V. L. LeGore, T. C. Wilson, H. T. Schaef, M. J. O'Hara, K. B. Wagnon, D. C. Lanigan, C. F. Brown, B. A. Williams, C. W. Lindenmeier, R. D. Orr, D. S. Burke, and C. C. Ainsworth, *Characterization of Vadose Zone Sediment: Borehole 41-09-39 in the S-SX Waste Management Area*, Pacific Northwest National Laboratory, US Department of Energy, PNNL-13757-3, Richland, Washington, 2002b.

Serne, R. J., R. E. Clayton, I. V. Kutnyakov, G. V. Last, V. L. LeGore, T. C. Wilson, H. T. Schaef, M. J. O'Hara, K. B. Wagnon, D. C. Lanigan, C. F. Brown, B. A. Williams, C. W. Lindenmeier, R. D. Orr, D. S. Burke, and C. C. Ainsworth, *Characterization of Vadose Zone Sediment: Slant Borehole SX-108 in the S-SX Waste Management Area*, Pacific Northwest National Laboratory, US Department of Energy, PNNL-13757-4, Richland, Washington, 2002c.

Steefel, C. I., S. Carroll, P. Zhao, and S. Roberts, Cesium migration in Hanford sediment: a multisite cation exchange model based on laboratory transport experiments, *J. Contam. Hydrol., 67*, 219–246, 2003.

van Genuchten, M. T., and R. J. Wagenet, Two-site/two-region models for pesticide transport and degradation: Theoretical development and analytical solutions, *Soil Sci. Soc. Am. J., 53*, 1303–1310, 1989.

Zachara, J. M., S. C. Smith, C. Liu, J. P. McKinley, R. J. Serne, and P. L. Gassman, Sorption of Cs^+ to micaceous subsurface sediments from the Hanford Site, USA, *Geochim. Cosmochim. Acta, 66*, 193–211, 2002.

Appendix: Reprints of Publications

- Zhuang, J., J. F. McCarthy, E. Perfect, J. Tyner, and M. Flury, *In situ* colloid mobilization in Hanford sediments under unsaturated transient flow condition: Effect of irrigation pattern. (in preparation), 2006.
- Zhuang, J., J. F. McCarthy, E. Perfect, J. Tyner, M. Flury, T. S. Steenhuis, The coupled effect of flux rate and ionic strength on transport of colloid through porous media during unsaturated transient flow. (in preparation), 2006.
- Deng, Y., H. Zhao, J. B. Harsh, M. Flury, and J. S. Boyle, Resistance of silicate minerals to alkaline waste simulants, (in preparation), 2006.
- Deng, Y., M. Flury, J. B. Harsh, and A. R. Felmy, and O. Qafoku, Cancrinite and sodalite formation in the presence of Cesium, Potassium, Magnesium, Calcium, and Strontium in Hanford tank waste simulants, *Appl. Geochem.*, (in press), 2006.
- Deng, Y., J. B. Harsh, M. Flury, J. Young, and J. S. Boyle, Mineral formation during simulated leaks of Hanford waste tanks, *Appl. Geochem., 21*, 1392–1409, 2006.
- Shira, J. M., B. C. Williams, M. Flury, S. Czigany, and M. Tuller, Sampling silica and ferrihydrite colloids with fiberglass wicks under unsaturated flow conditions, *J. Environ. Qual., 35*, 1127–1134, 2006.
- Mon, J., Y. Deng, M. Flury, and J. B. Harsh, Cesium incorporation and diffusion in cancrinite, sodalite, zeolite, and allophane, *Micropor. Mesopor. Mat., 86*, 277–287, 2006.
- Chen, G., M. Flury, J. B. Harsh, and P. C. Lichtner, Colloid-facilitated transport of cesium in variably-saturated Hanford sediments, *Environ. Sci. Technol., 39*, 3435–3442, 2005.
- Chen, G., and M. Flury, Retention of mineral colloids in unsaturated porous media as related to their surface properties, *Colloids Surf. Physicochem. Eng. Aspects, 256*, 207–216, 2005.

  (Correction published in *Colloids Surf. Physicochem. Eng. Aspects, 256*, 207–216, 2006.)
- Czigany, S., M. Flury, and J. B. Harsh, Colloid stability in vadose zone Hanford sediments, *Environ. Sci. Technol., 39*, 1506–1512, 2005.
- Czigany, S., M. Flury, J. B. Harsh, B. C. Williams, and J. M. Shira, Suitability of fiberglass wicks to sample colloids from vadose zone pore water, *Vadose Zone J., 4*, 175–183, 2005.

- Mashal, K., J. B. Harsh, M. Flury, and A. R. Felmy, Analysis of precipitates from reactions of hyperalkaline solutions with soluble silica, *Appl. Geochem., 20*, 1357–1367, 2005.
- Mashal, K., J. B. Harsh, and M. Flury, Clay mineralogical transformations over time in Hanford sediments reacted with simulated tank waste, *Soil Sci. Soc. Am. J., 69*, 531–538, 2005.
- Mashal, K., J. B. Harsh, M. Flury, A. R. Felmy, and H. Zhao, Colloid formation in Hanford sediments reacted with simulated tank waste, *Environ. Sci. Technol., 38*, 5750–5756, 2004.
- McCarthy, J. F., and L. D. McKay, Colloid transport in the subsurface: past, present, and future challenges. *Vadose Zone J., 3*, 326–337, 2004.
- Crist, J. T, J. F. McCarthy, Y. Zevi, P. Baveye, J. A. Troop, and T. S. Steenhuis, Pore-scale visualization of colloid transport and retention in partly saturated porous media. *Vadose Zone J., 3*, 444–450, 2004.
- Flury, M., S. Czigany, G. Chen, and J. B. Harsh, Cesium migration in saturated silica sand and Hanford sediments as impacted by ionic strength. *J. Contam. Hydrol., 71*, 111–126, 2004.
- Zhuang, J., Y. Jin, and M. Flury, Comparison of natural colloid and kaolinite transport in porous media, *Vadose Zone J., 3*, 395–402, 2004.
- Zhao, H., Y. Deng, J. B. Harsh, M. Flury, and J. Boyle, Alteration of kaolinite to cancrinite and sodalite by simulated Hanford Tank Wastes and its impact on cesium retention, *Clays Clay Miner., 52*, 1–13, 2004.
- Flury, M., J. B. Harsh, and J. B. Mathison, Miscible displacement of salinity fronts: Implications for colloid mobilization, *Water Resour. Res., 39*, 1373, doi:10.1029/2003WR002491, 2003.
- Zhuang, J., M. Flury, and Y. Jin, Colloid-facilitated Cs transport through water-saturated Hanford sediment and Ottawa sand, *Environ. Sci. Technol., 37*, 4905–4911, 2003.
- Cherrey, K. D., M. Flury, and J. B. Harsh, Nitrate and colloid transport through coarse Hanford sediments under steady state, variably saturated flow, *Water Resour. Res., 39*, 1165, doi:10.1029/2002WR001944, 2003.

  (Correction published in *Water Resour. Res., 40*, W03901, doi:10.1029/2004WR003066, 2004.)

In-situ Colloid Mobilization in Hanford Sediments under Unsaturated Transient Flow Conditions: Effect of Irrigation Pattern

JIE ZHUANG[1], JOHN F. MCCARTHY[1], EDMUND PERFECT[1], JOHN TYNER[2], MARKUS FLURY[3], AND TAMMO S. STE ENHUIS[4]

[1]*Department of Earth and Planetary Sciences, Center for Environmental Biotechnology, The University of Tennessee, Knoxville, TN 37996*
[2]*Department of Biosystems Engineering and Environmental Science, The University of Tennessee, Knoxville, TN 37996*
[3]*Department of Crop and Soil Sciences, Center for Multiphase Environmental Research Washington State University, Pullman, WA 99164*
[4]*Department of Biological and Environmental Engineering, Cornell University, Ithaca, NY 14853*

Abstract

Colloid transport is a potential means for facilitated off-site relocation of radioactive wastes at the Hanford site of Washington State. In this study, a series of column experiments were conducted to examine the effect of irrigation pattern on releases of *in-situ* colloids in two Hanford sediments under saturated and unsaturated transient flow conditions and its dependence on solution ionic strength, irrigation rate and sediment texture. The results show that during transient flow more *in-situ* colloids were released than during steady state flow. The number of short-term hydrological pulses proved more vital than total irrigation volume or persistence time length for increasing the amount of mobilized *in-situ* colloids. However, increasing ionic strength diminished this effect. At an irrigation rate equal to 5% of the saturated hydraulic conductivity, transient multi-pulse flow in 2 mM $NaNO_3$ was equivalent to a fifty-fold reduction of solution ionic strength (from 100 mM to 2 mM) in a single pulse flow in terms of their positive effects on *in-situ* colloid mobilization. However, in subsequent irrigation pulses, effluent colloid concentrations were much lower at the low than the high irrigation rates, due likely to rate-limited detachment of the tightly (more chemically) attached colloids, which is subject to the hydrodynamic forces overcoming the DLVO forces. The experiments also indicate that mechanical straining of colloids in the fine sand greatly decreased the amount of mobilized colloids, although the fine sand contained about one order of magnitude greater concentration of the *in-situ* colloids than the coarse sand. This study highlights that transient flow is critical for *in-situ* colloid mobilization, and implies that long-term assessment of colloid release should consider the rainfall pattern and geometrical structure of flow pathways.

Key words: Colloid mobilization, Transient flow, Hanford sediment, Flow pattern, Ionic strength, Flow rate

Introduction

Colloids are ubiquitous in subsurface formations (McCarthy and Degueldre, 1992), and can be detritally contained in the parent geologic material or authigenically formed *in-situ* by geochemical alterations of thermodynamically unstable primary mineral phases, or by precipitation of inorganic solid phases (McCarthy and Zachara, 1989). Natural or

anthropogenic disturbances can promote the formation of colloids as well as the mobilization of pre-existing colloids (Gschwend et al., 1990; McCarthy and Zachara, 1989; Newman, 1990; Ryan, 1992; Ryan and Elimelech, 1996; Ryan and Gschwend, 1990), or introduce colloids from waste sites (Bunn et al., 2002; Seaman and Bertsch, 2000, McCarthy and Zachara, 1989; Newman et al., 1993; Seaman et al., 1995; Grolimund et al., 2001; Wan et al., 2004). Once mobilized, colloids can migrate significant distances and appreciably enhance the transport of adsorbed contaminants. Colloid transport and its potential to enhance subsurface contaminant transport have been well documented at various scales (Mills et al., 1991; Ryan and Elimelech, 1996; Kretzschmar et al., 1999; Ryan et al., 2000; McGechan and Lewis, 2002). Numerous laboratory-scale experiments have demonstrated that mobilization of colloids can enhance contaminant transport (Bunn et al., 2002; Flury et al., 2002; Newman et al., 1993; Seaman and Bertsch, 2000; Sen et al., 2002; Zhuang et al., 2003). The importance of colloids in facilitating the field-scale transport of contaminants has been well established in studies of radionuclide migration at contaminated sites (Buddemeier and Hunt, 1988; Bunn et al., 2002; Kersting et al., 1999). The fraction of colloids that disperses in water has been used as an input parameter for predicting colloid leaching and colloid-facilitated transport through the vadose zone (Jarvis et al., 1999; Villholth et al., 2000).

Three main types of factors are recognized to affect colloid mobilization. These are composition of the aqueous phase, properties of colloids and media, and physical and chemical conditions of flow. Results of field studies demonstrate that soil colloids can be released in high concentrations during rainfall events, presumably due to chemical and hydrodynamic perturbations associated with the advancing wetting front (Pilgrim and Huff, 1983; Kaplan et al., 1993; Grant et al., 1996; Ryan et al., 1998; Jarvis et al., 1999; Laubel et al., 1999; Worrall et al., 1999; El-Farhan et al., 2000). High solution pH and low ionic strength proved favorable for colloid dispersion (Rengasamy, 1983; Kaplan et al., 1996; Kjaergaard et al., 2004). It has also been reported that clays with higher density of surface electric charge exhibit greater dispersibility (Seta and Karathanasis, 1996). Hydrodynamic interaction controlled by flow velocity is another mechanism governing colloid mobilization in porous media. Rapid flow through fractures (Degueldre et al., 1989), rapid infiltration of rainfall (Kaplan et al., 1993), and increases in pumping rate during sampling (Puls et al., 1992; Backhus et al., 1993; Kearl et al., 1994) can produce higher colloid concentrations in groundwater as expected from theoretical and laboratory investigations of model systems (Hubbe, 1985; Sharma et al., 1992; Das et al., 1994). Furthermore, colloid-release processes are complicated by non-uniform distribution of the concentration of naturally deposited colloids in soil profiles, as well as spatiotemporal variations of soil moisture content and pore water velocity. The relationships between colloid release and changes in moisture content and pore water velocity are not constant, but vary over the course of infiltration and drainage (Ryan et al., 1998).

Most of the previous studies that have examined colloid mobilization have been conducted in saturated systems, and the few that considered unsaturated systems have focused principally on steady-state flow conditions (Kretzschmar et al., 1999). Such conditions, however, do not necessarily represent the natural flow regime because the subsurface exhibits intermittent infiltrations, spatiotemporal variability of soil moisture, non-uniform distributions of colloid concentration and size, transient flow, and chemical perturbation. Under natural condition,

transient flow regimes can be triggered by rainfall, irrigation, or snowmelt. The temporal variability in moisture content and pore water velocity that characterize transient flow regimes drives colloid mobilization, accelerating release rates beyond that which would be predicted on the basis of steady-flow experiments (Kaplan et al., 1993; Ryan et al., 1998; El-Farhan et al., 2000). Although progress has been made toward quantifying the mobilization processes of colloids in porous media (McDowell-Boyer, 1992; Ryan and Elimelech, 1996; Swartz and Gschwend, 1998), transient flow of colloids has not been well-examined (Saiers, 2003), especially for *in-situ* colloids in natural sediments. Our understanding of complicated colloid-sediment interactions and our ability to predict mobilization of *in-situ* colloids in natural subsurface sites are still limited.

Radioactive materials have leaked from underground waste tanks at the Hanford Reservation located in the southeast of Washington State, and mobility of the radionuclides is currently of great concern for the quality of groundwater and vadose zone environments. A number of studies showed that colloid particles can potentially facilitate the movement of radionuclides like Cs-137 (Flury et al., 2002; Zhuang et al., 2003; Chen et al., 2005), and thus suggest that colloid movement must be considered in long-term risk assessment and management of waste at Hanford. Hanford soils are generally coarse and layered in structure, so limited precipitation (95-313 mm/year) can infiltrate readily and then redistribute via subsurface flows. The infiltration and recharge are largely controlled by rainfall and sediment texture (Gee, 1987). Subject to the regular pattern of local weather (wet and cool in winters, and hot and dry in summers) or abrupt events (e.g., thunderstorms), water flow perturbation (e.g., wetting and drying, preferential flow) may take place in the Hanford vadose zone and affect *in-situ* colloid mobilization by means of some mechanisms different from those identified under steady-state flow conditions. At present, mechanisms controlling colloid release and transport under unsaturated transient flow conditions are still unclear or ill-defined, though the processes under saturated flow conditions have been mechanistically examined. In addition, the effect of soil wetting and drying on colloid release and transport may be superimposed upon effect of solution chemistry in the vadose zone. This is because Hanford colloids can be remobilized during the waste leaking when high ionic strength tank liquors (Serne, 1998) are diluted by low ionic strength pore water (Flury et al., 2002).

In this study, we explore the role of transient flow in mobilizing the *in-situ* colloids from unsaturated Hanford sediments. We hypothesize that multi-pulse transient irrigation is much more important than single-pulse continuous irrigation for *in-situ* colloid release and transport. A series of laboratory-scale column experiments were carried out to characterize the effects of irrigation pattern in relation to solution ionic strength, irrigation rate, and sediment texture. Relevant mechanisms are discussed based on the experimental observations.

Materials and Methods

Porous Materials. Two Hanford sediments (fine sand and coarse sand) were used as the porous media in all the column experiments. The sediments, free of radionuclide contamination and representative of the material underlying the Hanford waste tanks, were collected from ERDF pit between the Hanford 200 East and West areas at the U.S. DOE Hanford Reservation in south-central Washington State. The main clay minerals of the sediments include mica, illite, smectite, vermiculite, quartz, feldpars, and pyroxene (Mashal et

al, 2004). The total carbon contents of the coarse and fine sands, as measured with a Shimadzu TOC-V organic carbon analyzer, are 1.5 and 4.2 g kg^{-1}, respectively. Prior to the experiments, both sediments were sieved to remove pebbles larger than 1 cm in diameter. The remainder was then lightly rinsed for triple times with distilled water in a water-to-soil ratio 2:1 in a plastic pan, to remove the excessive amount of unattached fine material. After the rinsing procedure the sediments were dried at 60 ^{o}C for use in the column experiments.

Water-washing of the sands prior to the experiments was because our initial experiments demonstrated that there was a sufficient amount of readily mobilized fine material in the sediments to quickly clog the nylon mesh at the bottom of the column during the transport experiments. The clogging precluded us to maintain a stable lower boundary hydrological condition. We realize this pre-cleaning might make the experimental sediments differ from the natural ones due to loss of a fraction of fine materials. To provide a reference for the *in-situ* colloid concentration, we dispersed three grams of the original and water-washed Hanford sediments in 20-mL deionized water using a probe ultrasonicator (Make, Fisher Sci. Inc.) at 10 Watts for one minute. The suspension was allowed to settle before the suspended particles smaller than 2 μm were extracted according to the gravitational separation method (Gee and Or, 2002). Using a spectrophotometer as described below, the concentrations of the extracted colloids was measured to be 597.3±60.4 and 237.4±29.1 μg g^{-1} soil for the unwashed and washed coarse sand, respectively, and 7511.6±806.1 and 3859.5±450.6 μg g^{-1} soil for the unwashed and washed fine sand, respectively. It is obvious that 40% and 50% of the <2 μm colloids were still remained in the water-cleaned coarse and fine sediments, respectively. This amount of the colloids was assumed to be adequate for examining the effect of irrigation pattern on *in-situ* colloid mobilization.

Physical properties of the two sands are plotted in Figure 1. Grain size distribution of the sediments was determined by sieving the sediments through a stacked set of metal mesh sieves. Water retention characteristics of the coarse and fine sediments were determined from the drying curves measured with a Tempe pressure cell (Soil Moisture Equipment Inc., Model 1400B1M2-3) (Dane and Hopmans, 2002); the bulk densities of the samples for these measurements were 1.60 Mg m^{-3} the coarse and 1.42 Mg m^{-3} for fine sand . These bulk densities were similar to those of the packed sand columns used in the colloid mobilization and transport experiments. The saturated hydraulic conductivity (K_s) of the two sediment samples was determined using a constant-head method (Klute and Dirksen, 1986). Pore size distribution was estimated from the water characteristics of the sands using the Young-Laplace equation.

Figure 1

Experimental Setup and Procedures

Column Construction and Pre-equilibrium. The unsaturated column setup used in this study is illustrated in Figure 2. The system consisted of a peristaltic pump, soil column, liquid sprinkler, fraction collector, as well as vacuum source and vacuum control valve. The column was constructed of clear Schedule-40 polyvinylchloride pipe that was 2-cm in inner diameter and 60 cm in length. A nylon membrane with 20-μm pore size and 6.4 kPa air-entry value (Spectra/Mesh, Spectrum Laboratories, Inc.) was sealed on the bottom plate of the column to maintain capillary pressure at the bottom of the sand columns. To avoid possible puncture of the nylon membrane by the jagged Hanford sediments, a thin layer (<1 mm) of glass fiber was

put above the membrane prior to packing sand to the column. The bottom of the column was sealed by gluing on a flat-bottomed PVC fitting with a small barb.

Figure 2

To mimic the *in-situ* soil moisture condition of sediments at the Hanford site (approximately 4 to 20% volumetric moisture; Serne et al., 2002), we wetted the Hanford sands to about 4% gravimetric water content (6.4% volumetric water content and 16% saturation of the packed sands) by gently misting a pan containing a known dry weight of sediments using a cold mist humidifier. The pan was sealed overnight to uniformly distribute the moisture within the sediment. The damp sand was then packed in the column in 2-cm increments and tapped between layers to obtain a more uniform packing; care was taken to avoid drying of the sand during the packing procedure. The total soil water content of the column was calculated. The column was mounted vertically between a gamma-ray source and detector mounted on two computer-controlled linear actuators. Before starting an irrigation experiment, a 10-mL syringe was used to inject 2-3 mL water into tubing on the barbed fitting at the bottom of the column to just saturate the 20-μm nylon mesh so it would maintain a 6.4 kPa air-entry tension on the sediment. Before any irrigation experiments were initiated, the initial moisture distribution within the column was allowed to equilibrate to a constant tension (-5.5 kPa) overnight by connecting the barbed fitting at the end of the column to a sealed beaker that was attached to a vacuum chamber (CL-040, Soil Measurement Systems, Tucson, AZ) and vacuum control valves (Type 70, Bellofram Corp., Newell, WV).

Transient Irrigation Experimental Design and Procedures. The effects of transient flow on mobilization of colloids from the Hanford sediments were evaluated in a series of column irrigation experiments (two columns under water-saturated and eight under water-unsaturated flow conditions) by introducing a certain volume of the injection solution with varying solution ionic strength, irrigation rate, and infiltration frequency (a single continuous infiltration event, or multiple infiltration/drainage pulses). The infiltration solution was $NaNO_3$ prepared using particle-free deionized (-18 M-ohm) water at either 2 mM or 100 mM ionic strength, and adjusted to pH 7 using $NaHCO_3$. Two different levels of irrigation rates were used in the study. They were ~5 and ~94 mm h^{-1}, equivalent to 0.3% and 5% saturated hydraulic conductivity (K_s) of the coarse sand, respectively, and the rate 5 mm h^{-1} corresponded to ~10% of the K_s of the fine sand. All experiments were conducted at room temperature (22±1 ^{o}C). A summary of the experimental conditions for all the columns is provided in Table 1.

Table 1

An irrigation experiment was initiated by introducing an injection solution into the packed column upward from the bottom (saturated experiments) or downward from the top (unsaturated experiments) of the column using a peristaltic pump. In the water-saturated experiments, the pump was directly connected to the bottom of the column and the 150-mL effluent (~ 2 pore volumes) was collected from the top using a fraction collector. In the water-unsaturated experiments, the pump was attached via Tygon tubing to a sprinkler system consisting of an injection chamber (1.9-cm inner diameter and 3-cm height) with seven 26-gauge hypodermic needles arranged uniformly across the bottom of the chamber and sealed with silicone sealant. A short length of thin Teflon tubing attached to the barb at the bottom of

the column was connected to the vacuum chamber in which the fraction collector was sealed. The unsaturated experiment was initiated by positioning the sprinkler system over the top of the sediment column. The lower boundary tension of the water-unsaturated column was maintained at –5.5 kPa for the entire course of the water-unsaturated experiments. When an expected volume of effluent had been collected, the pump was stopped, and the column was top-covered and allowed to drain overnight under the tension into a tube on the fraction collector. Hence, the entire course of the unsaturated flow was composed of two phases: an infiltration phase and a drainage phase. In one set of experiments (termed single-infiltration), the continuous injection was ceased when 150-mL effluent from the fine sand column or 200-mL effluent from the coarse sand column was collected, and the column was then allowed to drain overnight. In a second series of experiments (termed multi-pulse infiltration), the 150- or 200-mL effluent was collected in a series of three or four sequential infiltration-drainage events. Each pulse was identically applied as that described for the single-infiltration case, except that only 50-mL solution (~ 1 pore volume) was collected before the infiltration was terminated and the column allowed to drain overnight under the tension.

In each of the irrigation events, when drainage out the bottom of the column ceased (less than 0.1 mL h^{-1}), samples collected in the fraction collector were taken out and weighed to determine the volume eluted. Examination of the colloid mass on the nylon membrane indicated that removal of the colloids by the nylon membrane was negligible. Colloids within each sample were resuspended with a vortexer and the concentration of colloids was analyzed with a UV-visible spectrophotometer (DU Series 640, Beckman Instruments, Inc., Fullerton, CA) at 360 nm wavelength (El-Farhan et al., 2000; Flury et al., 2002; Saiers and Lenhart, 2003;). The turbidity data were subsequently converted into the colloid concentration using a calibration curve, which was constructed using colloidal material (<2 μm) that was dispersed in distilled water by over-night shaking Hanford sediments that had been prepared for packing the columns as described earlier.

In-Situ Water Content Measurement Using Gamma-Ray Attenuation. A custom-built gamma-ray attenuation system (Ferraz and Mansell, 1979) was used to monitor the spatial and temporal distribution of soil water before and during the transient irrigation experiments. We continuously monitored the *in-situ* water content of the sediments at two locations (25- and 45-cm depths of the packed sand). The volumetric water content was determined at these locations based on the attenuation of gamma-radiation by water. The gamma-ray source is a 240-mCi Am^{241} source (Isotope Products Laboratories; PO8); source collimation is provided by a 3-mm diameter hole in the end of the tungsten rod. A NaI(TI) gamma-rays detector and photo-multiplier tube (Bicron, 3m3/3, Newbury, OH) is collimated using a 10-mm diameter hole in a lead shield placed in front of the detector. The sand column was placed between source and detector. The source and detector were mounted to a computer-controlled linear actuator (Bislide 15 inch; MN-0150-E01-21) with a stepping motor, and a micro-stepping . Further details of the gamma-ray system are available in Tyner and Brown (2004). The prepared and pre-equilibrated columns were first scanned vertically for ten cycles prior to irrigation to determine the gamma-ray attenuation due to the sediment and the initial moisture content. The counting time was ten seconds at each depth. Based on the distance of the energy source from the column, the 10-second counting warranted the measurement deviation less than 10% of the actual volumetric water content. Total time for one cycle of the scanning was

about 3 minutes. During irrigation, changes in water content at those locations reflected the spatial and temporal variations in the moisture content via the Lambert-Beer equation (Oostrom et al., 2002) and the known mass attenuation coefficient of water μ_w. Our experimentally determined value of μ_w agreed well with the theoretical value, indicating that the system is well collimated.

Results and Discussion

Effect of Flow Pattern on the In-situ Colloid Mobilization and Its Dependence on Solution Ionic Strength. Figures 3a and 3b present the effects of multi-pulse infiltration and single-infiltration on mobilization of *in-situ* colloids in Hanford sediments at two solution ionic strengths (2 and 100 mM). In both cases, mobilization of the *in-situ* colloids in each irrigation event was similar: a considerable amount of the *in-situ* colloids was leached out of the columns along with the initial breakthrough of the injected liquid, followed by a decrease of colloid concentration in the effluent to a constant low level and afterward a secondary concentration peak of colloids near the end of the drainage phase. The drainage-induced secondary peak seemed small and inconsistent in magnitude among the infiltration pulses. In the multi-pulse infiltration, the concentrations of the primary peaks of colloid concentrations observed for the irrigation events after the first one remarkably declined, while the constant tailing concentrations remained similar for all the infiltration pulses. Water content data presented in Figures 4 and 5 indicate that colloid release significantly took place as soil water increased during infiltration or decreased during drainage. The results clearly indicate that hydrological pulses were positively associated to the colloid effluent purge. The transient flow mobilized more colloids than the steady-state flow. Plotting of cumulative mass of the effluent colloids against cumulative volume of outflow for both flow patterns suggests that the pulse number of infiltration is more vital than total irrigation volume for increasing the total amount of the colloids leached from the Hanford sediments (Figure 3c). Note that an implicit process basing this rule is transient perturbation of flow, which can render jumps of both physical and chemical potentials at liquid-solid interfaces.

Figure 3

Figures 3b and 3c also display a significant ionic strength effect. Compared to the 2 mM solution, the primary peak of colloid concentrations were higher but decreased much more rapidly in the 100 mM solution. This indicates that change of chemical potential arising from increasing ionic strength concentrated the releasable colloids (then they moved together) but reduced the kinetic release rate of the chemically adsorbed colloids (then colloid concentration leveled off rapidly). Cumulative curves for the two flow patterns and two ionic strengths (Figure 3c) show that at 5% K_s irrigation rate, multi-pulse infiltration of 100 mM $NaNO_3$ solution was equivalent to a fifty-fold reduction of ionic strength (from 100 mM to 2 mM) in single-infiltration in terms of positive effects of the two factors (flow pattern and ionic strength) on colloid mobilization.

The above results agree with the previous studies (Jacobsen et al., 1997; Ryan et al., 1998; Schelde et al., 2002; de Jonge et al., 2004), which were conducted using undisturbed soils where macropore flow occured. We realize that the results of the repacked columns in this study may not be comparable to those of undisturbed columns. However, the results for flow

rate effect as reported below suggest that macropore flow might still occur in the columns packed with coarse Hanford sand due to initial non-uniform distribution of water contents between macropore and micropore, as well as coarse texture of the sediment in which flow was significantly subject to gravity effect. Physical and chemical perturbations resulted from the transient flow were assumed to be primarily responsible for the peak concentrations of the released colloids (McDowell-Boyer, 1992; El-Farhan et al., 2000; Blume et al., 2005). However, mechanisms dominating the transient flow effects may vary with flow stages and depend on many factors, such as, source colloid concentration, initial water content, chemical condition, sediment texture, flow velocity, pore straining, and preferential attachment of colloids to moving air-water interfaces (Bradford et al., 2002; Saiers and Lenhart, 2003). As documented in the literature, *in-situ* colloid mobilization is driven by net interaction energy, which is defined by the sum of hydrodynamic forces, electrostatic double-layer (EDL) force, van der Waals force, and short-range solvation or steric force (McDowell-Boyer, 1992; Ryan and Elimelech, 1996; Ruckenstein and Prieve, 1976; Israelachvili and McGuiggan, 1988). The colloid release pattern as shown in Figure 3 is presumably attributed to a coupling of two mechanisms. One is the physical dispersion of the readily releasable colloids to the fluid streamlines, since increase of moisture content (Figures 4 and 5) could cause a jump of local soil water potential with the changes of water configuration or dimensions in the size-varying pore system. The hydrological non-equilibrium resulted from the transient flow could reduce capillary attraction of colloids to the liquid/solid interfaces, and consequently promote release of colloids into pore water (Kaplan et al., 1993; El-Farhan et al., 2000). It can be seen from Figures 4 and 5 that occurrence of high release rates of colloids always followed the changes of sand water contents. The observation indicates that transient flow characteristic of potential jump was critical for colloid release (Figures 4 and 5). A second mechanism is due to the abrupt loss of chemical equilibrium. Change of ionic atmosphere near or on the colloid surfaces can affect the electric double layer (EDL) interaction between particle-surface and particle-particle through surface-charge screening effect. Low ionic strength (2 mM) favors an increase of the magnitude of repulsive EDL potential between like-charged colloids and mineral grains, leading to release of attached colloids (Israelachvili and McGuiggan, 1988), and vice versa for the effect of high ionic strength (100 mM). Therefore, releasable colloids decreased directly with increasing ionic-strength (Kallay et al., 1987; Elimelich and O'Melia, 1990a; Ryan and Gschwend, 1994). This explains the observed slower decline of the colloid effluent concentrations from the primary peaks in 2 mM solution than that in 100 mM solution (Figures 3a, b).

As infiltration proceeded, the flow approached and finally reached a steady state both hydrologically and chemically. Under the steady state condition, the energy barrier to detachment persisted, thereby hindering release of many colloids. The detachment of colloids was then subject to a rate-limited chemical process with low and constant release rates (Lenhart and Saiers, 2002). As illustrated in Figures 4 and 5, a secondary peak of colloid effluent concentrations occurred during the drainage,. Similar phenomena have also been microscopically imaged and theoretically explained by Crist et al. (2004, 2005). As water drained downward slowly, the mobile colloids could be accumulated and moved with the water front and ultimately produced a peak of colloid concentration at the outlet. This drainage-facilitated colloid remobilization stresses the importance of hydrological perturbation in facilitating *in-situ* colloid mobilization during both infiltration and drainage.

Figures 4 and 5

Effect of Irrigation Rate. Figure 6 illustrates the effect of irrigation rate on mobilization of the *in-situ* colloids in the coarse Hanford sand during unsaturated transient flow. The initial surge of water was associated with very high colloid concentrationsColloid effluent concentrations were generally lower at the low (0.3% K_s) than at the high (5% K_s) irrigation rates, showing a significant flow rate effect.

Figure 6

In the initial two pulses of irrigation, the observation that a similar amount of colloids was mobilized at 0.3% K_s and 5% K_s irrigation rates suggests that the water contents during these two irrigation rates were similar. The measured water contents of sand corresponding to the first effluent sample were 0.16 m^3 m^{-3} (40% water saturation) and 0.23 m^3 m^{-3} (60% water saturation) for the 0.3% K_s and 5% K_s irrigation rates, respectively. However, when the flow was steady-state, the sand water contents at both flow rates were ~0.23 m^3 m^{-3}. After the sediment was sufficiently eluted by an infiltration-drainage cycle with the water saturation reaching as high as ~60% during most of the elution time, the soil water could distribute much more uniformly in the porous medium compared to the initial water condition of the packed sediment. The improved connectivity of water in the column after the leaching would considerably reduce the macropore flow, and made the colloid migration responsive to the hydrodynamic shear stress triggered by change of flow rate. This can explain the significant effect of flow rate on colloid mobilization as observed in the irrigation events after the first two pulses. The observed effect of flow rate is also supported by a few of existing studies. McDowell-Boyer (1992) conducted detachment experiments with quartz and feldspar sand-packed columns, and found an increase of the mobilization of a polystyrene latex microsphere (1.46 μm) with increasing flow rate. Kaplan et al (1993) characterized the particles mobilized by water infiltrating through soil horizons from the U.S. Department of Energy's Savannah River site near Aiken, South Carolina. They reported that the abundance of mobilized particles and the size of the mobilized particles both increased with increasing flow rate during the rainfall simulation, as expected from hydrodynamic detachment theory. Batra et al. (2001) found that the hydrodynamic force for detachment theoretically increased as the surface asperity size approached the separation distance.

In addition to soil water condition, status of colloid mobility is another factor that may determine the flow rate effect. In terms of affinity of colloid attachment on porous media, *in-situ* colloids can be roughly categorized into two groups: readily releasable colloids that are physically attached to sediments by capillary forces of water films, and adhesive colloids that are chemically attached. Readily releasable colloids are can be easily be detached due to the reduction of the capillary forces if water content increases. . Even a light rainfall can still mobilize a significant amount of *in-situ* colloids if most of them are readily releasable. In contrast, if a soil contains a relatively low concentration of colloids and a dominant fraction is chemically attached, water content effect on colloid desorption and relocation would increase.

Effect of Time Interval between Transient Irrigation Pulses. Figure 7 compares the release pattern of colloids and their cumulative amounts under two time intervals for drainage.

A long-time drainage (15-day) between the irrigation pulses caused a higher primary peak of colloid release concentration but a steeper decline from the peak level than a short-time drainage (one-day) (Figure 7a). This is likely contingent to water redistribution (i.e., downward movement of water film) during drainage. As water slowly traveled to the lower part of the column under gravity, colloids reversibly attached at air-water or near air-water-solid interfaces were remobilized with the moving water and gradually accumulated in the deeper sand. As the drainage time elongated, colloid concentration increased in the sand near the outlet. Consequently, a higher initial peak and a shorter tailing of colloid effluent concentration were observed after the long-time than the short-time drainages during the following elution event. Similarity of the cumulative release curves for both time intervals is due mainly to equivalence of total amount of the colloids available for mobilization under the drainage in the two columns (Figure 7b). We thus infer that the primary peak of colloid release concentration might increase more if the drainage time were longer than 15-day as tested, but the increase of peak concentration would depend on the total amount of mobile colloids. This result implies that the effect of multi-pulse infiltration on *in-situ* colloid mobilization can be preserved for a long time (at least 15 days as tested in the study), and individual rainfall events in the whole year are perhaps cumulative with respect to their impact on *in-situ* colloid mobilization.

Figure 7

Effect of Soil Texture. Figure 8 demonstrates the *in-situ* colloid mobilization in two textured Hanford sediments during single saturated infiltration and multi-pulse unsaturated infiltration. Under both flow conditions, more colloids were released from the coarse sand than from the fine sand, and the discrepancy mainly occurred in the first 60-mL elution of the saturated flow or in the first event of the multi-pulse unsaturated infiltration (Figure 8a, b). Saturated condition greatly facilitated *in-situ* colloid release from both sands, and considerably enlarged the texture effect, in comparison to the unsaturated flow (Figure 8c, d). Factors leading to dependence of colloid release to sand texture may include source colloid concentration, water content, pore size, and pore velocity of flow in the sediments. The experiments as described earlier show that the source concentration of *in-situ* colloids (<2 μm) in the fine sand was ~1.2 order of magnitude higher than that in the coarse sand. The steady-state water content was also higher in the fine sand (~0.30 m^3/m^3) than in the coarse sand (~0.23 m^3/m^3). Based on previous studies (Kretzschmar, 1999; McCarthy and McKay, 2004), these two factors should have caused higher effluent concentration of colloids from the fine sand than from the coarse sand columns. This however was not supported by the experimental results as shown in Figure 8. Therefore, pore size and pore velocity might be the dominant factors rendering different behaviors of the *in-situ* colloid mobilization in the two sands. The pore size distribution was estimated using the Young-Laplace equation from the drying curve of the sand water characteristics. The coarse sand had much larger pores than the fine sand (Figure 1). The larger size of pores could reduce the mechanical straining (pore channel and throat clogging) of colloids and cause greater volume of active flow of the infiltrating water. As a result, coarse texture favored detachment of *in-situ* colloids and their subsequent mobilization. As documented by Bradford et al. (2002), mechanical straining of colloid transport significantly decreases with increasing pore size. The mechanical straining effect was also indirectly substantiated by the results of saturated flow experiments as shown in Figures 8d and 9. The resulted relative concentration (C/C_0) of the colloids in the effluent of

coarse sand column was more than one order of magnitude higher than that of fine sand column. This indicates that mechanical straining, which is subject to pore sizes of sediments, played a major role in decreasing the mobilization of *in-situ* colloids in the fine sand. Although pore velocity of the flow was not a factor responsible for the difference of two sands in colloid release during the saturated flow, it might affect the mobilization of *in-situ* colloids under saturated flow condition. This suggests that water flowed faster in the coarse sand than in the fine sand, and the larger pore velocity might enhance the transport of colloids in the coarse sand compared to the fine sand (Zhuang et al., 2004). Therefore, the mechanical straining should be considered as a primary mechanism resulting in less colloid release from the finer textured sand, and pore velocity might be a secondary factor affecting the transient unsaturated mobilization of the *in-situ* colloids.

Figures 8 and 9

In conclusion, *in-situ* colloid mobilization is very significantly subject to transient perturbations of infiltrations. Regardless of the time interval between the infiltration pulses, number of multi-pulse infiltration determines the cumulative amount of mobilized colloids, and this effect increases with decreasing ionic strength. Irrigation rate proved more important for detachment of the relatively tightly attached colloids than the readily releasable ones. This follows the mechanism that the detachment of tightly (chemically) attached colloids is due to the overcoming of hydrodynamic forces to the DLVO forces, while the release of the readily releasable colloids is due to the reduction of capillary force of water films on the sediments. The study reveals that both infiltration and drainage can cause colloid mobilization due to flow-triggered jump of physical and chemical potentials, but infiltration plays a primary role while effect of drainage is secondary. Transient mobilization of colloids also depends on the water content and geometry of the flow pathways. Readily releasable colloids require a lower critical water content for mobilization than the tightly attached colloids. Pore structure is a key factor in influencing the mode of the association of colloidal particles and their transport behaviors. Mechanical straining of colloids has shown to be the primary mechanism responsible for the less colloid mobilization in finer textured Hanford sand; and hence, coarsening of sediment texture is more effective in facilitating colloid mobilization when *in-situ* colloid concentration is higher. This study may have significant implications for characterizing colloid migration at the Hanford site, since Hanford sediment profiles exhibit vastly heterogeneous layering structure, varying flow velocity field, as well as non-uniform distribution of sedimental chemistry and *in-situ* colloid concentrations.

Acknowledgements

This work was supported by the Environmental Management Science Program, U.S. Department of Energy under Grant No. DE-FG07-99ER62882.

Literature Cited

Batra, A.; Paria, S.; Manohar, C.; Khilar, K.C. Removal of surface adhered particles by surfactants and fluid motions. *AIChEJ.* **2001**, *47*, 2557-2565.

Backhus, D.A.; Ryan, J.N.; Groher, D.M.; MacFarlane, J.K.; Gschwend, P.M. Sampling colloids and colloid-associated contaminants in groundwater. *Ground Water* **1993**, *31*, 466-479.

Bergendahl, J.A.; Grasso, D. Mechanistic basis for particle detachment from granular media. *Environ. Sci.Technol.* **2003**, *37)*, 2317-2322.
Bradford, S.A.; Yates, S.R.; Bettahar, M.; Simunek, J. Physical factors affecting the transport and fate of colloids in saturated porous media. *Warer Resour. Res*. **2002**, *38*, 1327, doi:10.1029/2002WR001340.
Buddemeier R. W.; Hunt J. R. Transport of Colloidal Contaminants in Groundwater: Radionuclide Migration at the Nevada Test Site. *Appl. Geochem.* **1988**, 3(5), 535-548.
Bunn R. A.; Magelky R. D.; Ryan J. N.; Elimelech M. Mobilization of natural colloids from an iron oxide-coated sand aquifer: Effect of pH and ionic strength. *Environ. Sci. Technol.* **2002**, *36(3)*, 314-322.
Chan, D.Y.C.; Henry, J.D.; White, L.R. The interaction of colloidal particles collected at fluid interfaces. *J. Colloid Interface Sci*. **1981**, *79*, 410-418.
Chapman, H.D. Cation-exchange capacity. In *Methods of Soil Analysis. Part 2. Agron. Monogr. 9*; ASA and SSSA, Madison, WI., 1965; pp 891-901.
Chen, G.; Flury, M.; Haesh, J.B.; Lichtner, P.C. Colloid-facilitated transport of cesium in variably-saturated Hanford sediments. *Environ. Sci. Technol.* **2005**, *39*, 3435-3442.
Chen, G.; Flury, M.; McCarthy, J.F. In situ colloid mobilization in unsaturated Hanford sediment flow. *Water Resour. Res.* **In review.**
Blume, T.; Weisbrod, N.; Selker, J.S. On the critical salt concentrations for particle detachment in homogeneous sand and heterogeneous Hanford sediments. *Geoderma* **2005**, *124(1-2)*, 121-132.
Dane, J.H.; Hopmans, J.M. Pressure cell. In *Methods of Soil Analysis. Part 4-Physical Methods*; Dane, J.H., Topp, G.C., Eds.; ASA and SSSA, Madison, WI. 2002; pp 684-688.
Das, S.K.; Schechter, R.S.; Sharma, M.M. The role of surface-roughness and contact deformation on the hydrodynamic detachment of particles from surfaces. *J. Colloid Interface Sci*. **1994**, *164(1)*, 63-77.
Degueldre, C.; Baeyens, B.; Goerlich, W.; Riga, J.; Verbist, J.; Stadelmann, P. Colloids in water from a subsurface fracture in granitic rock, Grimsel Test Site, Switzerland. *Geochim. Cosmochim. Acta.* **1989**, *53(3)*, 603-610.
de Jonge, L.W.; Moldrup, P.; Rubaek, G.H.; Schelde, K.; Djurhuus, J. Particle leaching and particle-facilitated transport of phosphorus at field scale. *Vadose Zone J.* **2004**, *3 (2)*, 462-470.
El-farhan, Y.H.; Denovio, N.M.; Herman, J.S.; Hornberger, G.M. Mobilization and transport of soil particles during infiltration experiments in an agricultural field, Shenandoah Valley, Virginia. *Environ. Sci. Technol*. **2000**, *34*, 3555-3559.
Elimelech, M.; O'Melia, C.R. Kinetics of deposition of colloidal particles in porous media. *Environ. Sci. Technol.* **1990**, *24*, 1528-1536.
Ferraz, E. S. B.; Mansell, R. S. Determining water content and bulk density of soil by gamma ray attenuation methods. In *Technical Bullent #807*; University of Florida, Gainesville, FL., 1979; pp 51.
Flury, M.; Mathison, J.B.; Harsh, J.B. In situ mobilization of colloids and transport of cesium in Hanford sediments. *Environ. Sci. Technol*. **2002**, *36*, 5335-5341.
Gee, G.W. Recharge at the Hanford site: Status report. Technical report, PNNL, Richland, WA. **1987**.
Gee, G.W.; Or, D. Particle-size analysis. In *Methods of Soil Analysis. Part 4-Physical Methods*; Dane, J.H., Topp, G.C., Eds.; ASA and SSSA, Madison, WI. 2002; pp 269-278.
Grant, R.; Laubel, A.; Kronvang, B.; Andersen, H.E. Svendsen, L.M., and Fuglsang, A. Loss dissolved and particulate phosphorus from arable catchments by subsurface drainage. *Water Res*. **1996**, *30*, 2633-2642.
Grolimund, D.; Borkovec, M.; Barmettler, K.; Sticher, H. Colloid-facilitated transport of strongly sorbing contaminants in natural porous media: A laboratory column study. *Environ. Sci. Technol*. **1996**, *30 (10)*, 3118-3123.
Grolimund, D.; Barmettler, K.; Borkovec, M. Release and transport of colloidal particles in natural porous media 2. Experimental results and effects of ligands. *Water Resour. Res*. **2001**, *37*, 571-582.

Gschwend P. M.; Backhus D. A.; MacFarlane J. K.; Page A. L. Mobilization of Colloids in Groundwater Due to Infiltration of Water at a Coal Ash Disposal Site. *J. Contamin. Hydrol*. **1990**, *6*, 307-320.

Hubbe, M.A. Detachment of colloidal hydrous oxide spheres from flat solids exposed to flow. 2. Mechanism of release. *Colloids Surf*., A **1985**, *16(3-4)*, 249-270.

Israelachvili, J.N.; McGuiggan, P.M. Forces between surfaces in liquids. *Science* **1988**, *241*, 795-800.

Jacobsen, O.H.; Moldrup, C.L.; Konnerup L.; Petersen, L.W. Particle transport in macropores of undisturbed soil columns. *J. Hydrol*. **1997**, *196*, 185-203.

Jarvis, N.J.; Bergström, L.; Dik, P.E. Modeling water and solute transport in macroporous soil. II. Chloride breakthrough under non-steady flow. *J. Soil Sci.* **1991**, *42*, 71-81.

Jarvis, N.J.; Villholth, K.G.; Ulen, B. Modeling particle mobilization and leaching in macroporous soil. *Eur. J. Soil. Sci*. **1999**, *50*, 621-632.

Kallay, N.; Barouch, E.; Matijevic, E. Diffusional detachment of colloidal particles from solid-solution interfaces. *Adv. Colloid Interface Sci.* **1987**, *27*, 1-42.

Kaplan, D.I.; Bertsch, P.M.; Adriano, D.C.; Miller, W.P. Soil-borne mobile colloids as influenced by water flow and organic carbon. *Environ. Sci. Technol.* **1993**, *27*, 1193-1200.

Kaplan, D.I.; Sumner, M.E.; Bertsch, P.M.; Adriano, D.C. Chemical conditions conducive to the release of mobile colloids from Ultisol profiles. *Soil Sci. Soc. Am. J.* **1996**, *60*, 269-274.

Kearl, P.M.; Korte, N.E.; Stites M.; Baker, J. Field comparison of micropurging vs. traditional groundwater sampling. *Ground Water Monitoring and Remediation* **1994,** 14(4), 183-190.

Kersting A. B.; Efurd D. W.; Finnegan D. L.; Rokop D. J.; Smith D. K.; Thompson J. L. Migration of plutonium in ground water at the Nevada Test Site. *Nature* **1999**, *397(6714)*, 56-59.

Kjaergaard, C.; Moldrup, P.; de Jonge, L.W.; Jacobsen, O.H. Colloid mobilization and transport in undisturbed soil columns. II. The role of colloid dispersibility and preferential flow. *Vadose Zone J*. **2004**, *3 (2)*, 424-433.

Klute, A.; Dirksen, C. Hydraulic conductivity and diffusivity: laboratory methods. In *Methods of Soil Analysis: Part I*; ASA and SSSA, Madison, WI., 1986; pp 687-734.

Kralchevsky, P.A.; Nagayama, K. Capillary interactions between particles bound to interfaces, liquid films and biomembranes. *Adv. Colloid Interface Sci*. **2000**, *85*, 145-192.

Kralchevsky, P.A.; Paunov, V.N.; Ivanov, I.B.; Nagayama, K. Capillary meniscus interaction between colloidal particles attached to a liquid-fluid interface. *J. Colloid Interface Sci.* **1992**, *151*, 79-94.

Kretzschmar, R.; Borkovec, M.; Grolimund, D.; Elimelech, M. Mobile subsurface colloids and their role in contaminant transport. *Adv. Agron*. **1999**, *66*, 121-193.

Laedgsmand, M.; Villholth, K.G.; Ullum, M.; Jensen, K.H. Processes of colloid mobilization and transport in macroporous soil monoliths. *Geoderma* **1999**, *93*, 33-59.

Laubel, A.; Jacobsen, O.H.; Kronvang, B.; Grant, R.; Andersen H.E. Subsurface drainage loss of particles and phosphorus from field plot experiments and a title-drained catachment. *J. Environ. Qual*. **1999**, *28*, 576-584.

Lenhart, J.J.; Saiers, J.E. Transport of silica colloids through unsaturated porous media: experimental results and model comparisons. *Environ. Sci. Technol*. **2002**, *36*, 769-777.

Mashal, K., Harsh, J.B., Flury, M., Felmy, A. R and Zhao, H. Colloid formation in Hanford Sediments reacted with simulated tank waste, *Environ. Sci. Technol.* **2004**, *38*, 5750-5756.

McCarthy, J.F.; Zachara, J.M. Subsurface transport of contaminants-mobile colloids in the subsurface environment may alter the transport of contaminants. *Environ. Sci. Technol.* **1989**, *23*, 496-502.

McCarthy J. F.; Degueldre C. Sampling and characterization of groundwater colloids for studying their role in the subsurface transport of contaminants. In *Environmental Particles, Vol. II*; Buffle, J., van Leeuwen, H., Eds.; Lewis Publishers, 1992; pp 79-109.

McCarthy, J.F.; McKay, L.D. Colloid transport in the subsurface: past, present, and future challenges. *Vadose Zone J*. **2004**, 3, 326-337.

McDowell-Boyer, L.M. Chemical mobilization of micro-sized particles in saturated porous media under steady flow conditions. *Environ. Sci. Technol.* **1992**, *26*, 586-593.

McGechan, M.B.; Lewis, D.R. Transport of particulate and colloid-sorbed contaminants through soil, part 1: General principles. *Biosystems Engineering* **2002**, *83(3)*, 255-273.
McKay, L.D.; Sandford, W.E.; Strong, J.M. Field-scale migration of colloidal tracers in a fractured shale saprolite. *Ground Water* **2000**, *38*, 139-147.
Mills, W.B.; Liu, S.; Fong, F.K. Literature-review and model (COMET) for metals transport in porous-media. *Ground Water* **1991**, *29(2)*, 199-208.
Mohanty, B.P.; Bowman, R.S.; Hendrickx, J.M.H.; Simunek, J.; van Genuchten, M.Th. Preferential transport of nitrate to a tile drain in an intermittent-flood-irrigated field: Model development and experimental evaluation. *Water Resour. Res.* **1998**, *34*, 1061-1076.
Newman M. E. Effects of Alterations in Groundwater Chemistry on the Mobilization and Transport of Colloids, Clemson University. 1990.
Newman, M.E.; Elzerman, A.W.; Looney, B.B. Facilitated transport of selected metals in aquifer material packed-columns. *J. Contam. Hydrol* **1993**, *14(3-4)*, 233-246.
Nikolaides, M.G.; Bausch, A.R.; Hsu, M.F.; Dinsmore, A.D.; Brenner, M.P.; Gay., C.; Weitz, D.A. Electric-field-induced capillary attraction between like-charged particles at liquid interfaces. *Nature* **2002**, *420*, 299-301.
Oostrom, M.; Dane, J. H.; Lenhard, R. J. Fluid contents. In *Methods of Soil Analysis – Part 4 Physical Methods*; Dane, J.H., G. C. Topp, G.C., Eds.; ASA and SSSA, Madison, WI., 2002; pp 1539-1563.
Petersen, C.T.; Holm, J.; Koch, C.B.; Jensen, H.E.; Hansen, S. Movement of pendimethalin, ioxynil and soil particles to field drainage tites. *Pest. Manage. Sci*. **2003**, *59*, 85-96.
Pilgrim, D.H.; Huff, D.D. Suspended sediment in rapid subsurface stormflow on a large field plot. *Earth Surf. Proc. Landforms* **1983**, *8*, 451-463.
Puls, R.W.; Clark, D.A.; Bledsoe, B.; Powell, R.M.; Paul, C.J. Metals in groundwater-sampling artifacts and reproducibility. *Hazardous Wastes and Hazardous Materials* **1992**, *9(2)*, 149-162.
Ramsay, J.D.F. The role of colloids in the release of radionuclides from nuclear waste. *Radiochim. Acta* **1988**, *44*, 165-170.
Ravisangar, V.; Brouckaert, B.M.; Amirtharajah, A.; Sturm, T.W. The role of solution chemistry in the stability and detachment of cohesive kaolinite particles. *Water Sci. Technol.*: *Water Supply 1*, **2001**, 25-32.
Rengasamy, P. Clay dispersion in relation to changes in the electrolyte-composition of dialyzed red-brown earths. *J. Soil Sci.* **1983**, *34 (4)*, 723-732 1983
Rousseau, M.; Di Pietro, L. ; Angulo-Jaramillo, R. ; Tessier, D.; Cabibel, B. Preferential transport of soil colloidal particles: Physiochemical effects on particle mobilization. *Vadose Zone J.* **2004**, *3*, 247-261.
Ruckenstein, E.; Prieve, D.C. Adsorption and desorption of particles and their chromatographic-seperation. *AIChEJ.* **1976**, *22*, 276-283.
Roy, S.B.; Dzombak, D.A. Colloid release and transport processes in natural and model porous media. *Colloid Surf., A* **1996**, *107*, 245-262.
Ryan J. N.; Gschwend P. M. Colloid Mobilization in Two Atlantic Coastal Plain Aquifers: Field Studies. *Water Resour. Res*. **1990**, *26(2)*, 307-332.
Ryan J. N. Clay colloid mobilization in an iron oxide-coated sand. Ph.D. Thesis, Massechusetts Institute of Technology. 1992.
Ryan, J.N.; Gschwend, P.M. Effects of ionic strength and flow rate on colloid release: Relating kinetics to intersurface potential energy. *J. Colloid Interface Sci*. **1994**, *164*, 21-34.
Ryan, J.N.; Elimelech, M. Colloid mobilization and transport in groundwater. *Colloid Surf., A* **1996**, *107*, 1-56.
Ryan. J.N.; Illangasekare, T.H.; Litaor, M.I.; Shannon, R. Particle and plutonium mobilization in macroporous soils during rainfall simulations. *Environ. Sci. Technol.* **1998**, *32*, 476-482.
Ryan, J.N.; Elimelech, M.; Baeseman, J.L.; Magelky, R.D. Silica-coated titania and zirconia colloids for subsurface transport field experiments. *Environ. Sci. Technol.* **2000**, *34(10)*, 2000-2005.

Saiers, J.E.; Hornberger, G.M. The influence of ionic strength on the facilitated transport of cesium by kaolinite colloids. *Water Resour. Res*. **1999**, *25*, 1713-1727.
Saiers, J.E.; Hornberger, G.M. The role of colloidal kaolinite in the transport of cesium through laboratory sand columns. *Water Resour. Res*. **1996**, *32 (1)*, 33-41.
Saiers, J.E.; Lenhart, J.J. Ionic-strength effects on colloid transport and interfacial reactions in partially saturated porous media. *Water Resour. Res*. **2003**, *39*, 1256, doi: 10.1029/2002WR001887.
Saiers, J.E. Colloid mobilization and transport winthin unsaturated porous media under transient-flow conditions. *Water Resour. Res*. **2003**, *39*, 1019, doi: 10.1029/2002WR001370.
Kätterer, T.; Schmied, B.; Abbaspour, K.C.; Schulin, R. Single- and dual-porosity modeling of multiple tracer transport through soil columns: effects of initial moisture and mod of application. *Euro. J. Soil Sci*. **2001**, *52*, 25-36.
Seaman, J.C.; Bertsch, P.M.; Miller, W.P. Chemical controls on colloid generation and transport in a sandy aquifer. *Environ. Sci. Technol*. **1995**, *29(7)*, 1808-1815.
Seta, A.K.; Karathanasis, A.D. Water dispersible colloids and factors influencing their dispersibility from soil aggregates. *Gerdoma* **1996**, *74*, 255-266.
Schelde, K.; Moldrup, P.; Jacobsen, O.H.; de Jonge, H.; de Jonge, L.W.; Komatsu, T. Diffusion-limited mobilization and transport of natural colloids in macroporous soil. *Vadose Zone J*. **2002**, *1*, 125-136.
Seaman J. C.; Bertsch P. M. Selective colloid mobilization through surface-charge manipulation. *Environ.Sci. Technol*. **2000**, *34(17)*, 3749-3755.
Sen T. K.; Mahajan S. P.; Khilar K. C. Colloid-associated contaminant transport in porous media: 1. Experimental studies. *AICHEJ.* **2002**, *48(10)*, 2366-2374.
Serne, R. J.; Clayton, R.E.; Kutnyakov, I.V.; Last, G.V.; LeGore, V.L.; Wilson, T.C.; Schaef, H.T.; O'Hara, M.J.; Wagnon, K.B.; Lanigan, D.C.; Brown, C.F.; Williams, B.A.; Lindenmeier, C.W.; Orr, R.D.; Burke, D.S.; Ainsworth, C.C. Characterization of Vadose Zone Sediment: Borehole 41-09-39 in the S-SX Waste Management Area, Pacific Northwest National Laboratory, US Department of Energy, PNNL-13757-3, Richland, Washington. 2002.
Serne, R.J.; Zachara, J.M.; Burke, D.S. Chemical Information on Tank Supernatants, Cs Adsorption from Tank Liquids onto Hanford Sediments, and Field Observation of Cs Migration from Past Tank Leaks; PNNL-11495/UC-510. 1998.
Sharma, M.M.; Chamoun, H.; Sita Rama Sarma, D.S.H.; Schechter, R.S. Factors controlling the hydrodynamic detachment of particles from surfaces. *J. Colloid Interface Sci*. **1992**, *149(1)*, 121-134.
Stamou, D.; Duschl, C.; Johannsmann, D. Long-range attraction between colloidal spheres at the air-water interface: The consequence of an irregular meniscus. *Phys. Rev. E* **2000**, *62*, 5263-5272.
Swartz, C.H.; Gschwend, P.M. Mechanisms controlling release of colloids to groundwater in a Southeastern Coastal Plain aquifer sand. *Environ. Sci. Technol*. **1998**, *32*, 1779-1785.
Tyner, J. S.; G. O. Brown. Improvements to estimating unsaturated soil hydraulic properties from horizontal infiltration. *Soil Sci. Soc. Am. J*. **2004**, *68(1)*, 1-6.
Vanderborght, J.; Jacques, D.; Feyen, J. Deriving transport parameters from transient flow leaching experiments by approximate steady-state flow convection-dispersion models. *Soil Sci. Soc. Am. J*. **2000**, *64*, 1317-1327.
Villholth, K.G.; Jarvis, N.J.; Jacobsen, O.H.; de Jonge, H. Field investigations and modeling of particle-facilitated pesticide transport in macroporous soil. *J. Environ. Qual.* **2000**, *29*, 1298-1309.
Wan J. M.; Tokunaga T. K.; Saiz E.; Larsen J. T.; Zheng Z. P.; Couture R. A. Colloid formation at waste plume fronts. *Environ. Sci. Technol*. **2004**, *38(22)*, 6066-6073.
Wickmann, H.H.; Korley, J.N. Colloid crystal self-organization and dynamics at the air/water interface. *Nature* **1998**, *393*, 445-447.
Worrall, F.; Parker, A.; Rae, J.E.;Johnson, A.C. A study of suspended and colloidal matter in the leachate from lysimeters and its role in pesticide transport. *J. Environ. Qual.* **1999**, *28*, 595-604.
Zhuang, J.; Nakayama, K.; Yu, G.R.; Miyazaki, T. Predicting unsaturated hydraulic conductivity of soil based on some basic soil properties. *Soil & Tillage Research*, **2001**, *59(3-4)*, 143-154.

Zhuang, J.; Flury, M.; Jin, Y. Colloid-facilitated cesium transport through water-saturated Hanford sediments and Ottawa sand. *Environ. Sci. Technol.* **2003**, *37*, 4905-4911.
Zhuang, J.; Jin, Y., Flury, M. Comparison of Hanford colloid and kaolinite transport in porous media. *Vadose Zone J.* **2004**, *3(2)*, 395-402.

TABLE 1. Parameters of the in-situ colloid mobilization experiments

Exp.#	Sand texture	Flow pattern*	Irrigation rate		Ionic strength (mM)	Time Interval (day)	Initial water content (% g/g)	Bulk density (Mg/m^3)	Porosity
			$\%K_s$	mm/h					
1	Coarse	MI-Unsat	5	93.8	2	1	3.79	1.55	0.42
2	Coarse	SI-Unsat	5	93.8	2	0	4.23	1.59	0.40
3	Coarse	MI-Unsat	5	93.8	100	1	3.94	1.60	0.40
4	Coarse	SI-Unsat	5	93.8	100	0	3.34	1.54	0.42
5	Coarse	MI-Unsat	0.3	5.3	2	1	4.01	1.62	0.39
6	Coarse	SI-Unsat	0.3	5.3	2	0	3.89	1.58	0.41
7	Fine	MI-Unsat	9.2	4.2	2	1	3.20	1.40	0.45
8	Coarse	MI-Unsat	5	93.8	2	15	3.51	1.57	0.41
9	Fine	SI-Sat	11.7	5.3	2	0	3.62	1.59	0.38
10	Coarse	SI-Sat	0.3	5.0	2	0	3.86	1.67	0.37

* MI: multi-pulse infiltration; SI: single infiltration; Unsat: water-unsaturated downward flow condition; Sat: water-saturated upward flow condition.

FIGURE LEGENDS:

FIGURE 1. Soil physical properties of the two Hanford sands used in the column experiments. K_s is saturated hydraulic conductivity.

FIGURE 2. A schematic of the unsaturated experimental column system

FIGURE 3. Colloid release from coarse Hanford sand as affected by flow pattern and solution ionic strength at an irrigation rate of 93.8 mm/h (5% K_s).

FIGURE 4. Variations of soil water content (θ) and colloid release rate (CRR) during multi-pulse infiltration in 2 mM $NaNO_3$ solution at an irrigation rate of 5% K_s (93.8 mm/h) (Exp. #1). CRR is defined as the mass of colloids released from unit soil cross area along with unit amount of liquid effluent.

FIGURE 5. Variations of soil water content (θ) and colloid release rate (CRR) during multi-pulse infiltration in100 mM $NaNO_3$ solution at an irrigation rate of 5% K_s (93.8 mm/h) (Exp. #3).

FIGURE 6. Effect of irrigation rate on the in-situ colloid release from coarse Hanford sand in 2 mM $NaNO_3$.

FIGURE 7. Effect of time interval of irrigation pulses on in-situ colloid mobilization in coarse Hanford sand in 2 mM $NaNO_3$ at an irrigation rate of 5% K_s (93.8 mm/h).

FIGURE 8. Effect of soil texture on in-situ colloid release in 2 mM $NaNO_3$ at a low irrigation rate of 5 mm/h. The rate is equivalent to 0.3% K_s of the coarse Hanford sand, and 9.2% K_s of the fine Hanford sand. Note the scales of Y-axis are different between the unsaturated and saturated results.

FIGURE 9. Relative concentrations of the in-situ colloids released from two textured sands under saturated flow condition in 2 mM $NaNO_3$ at a low flow rate of 5 mm/h. Source colloid concentration was measured in deionized water using sedimentation method for the < 2 μm colloids.

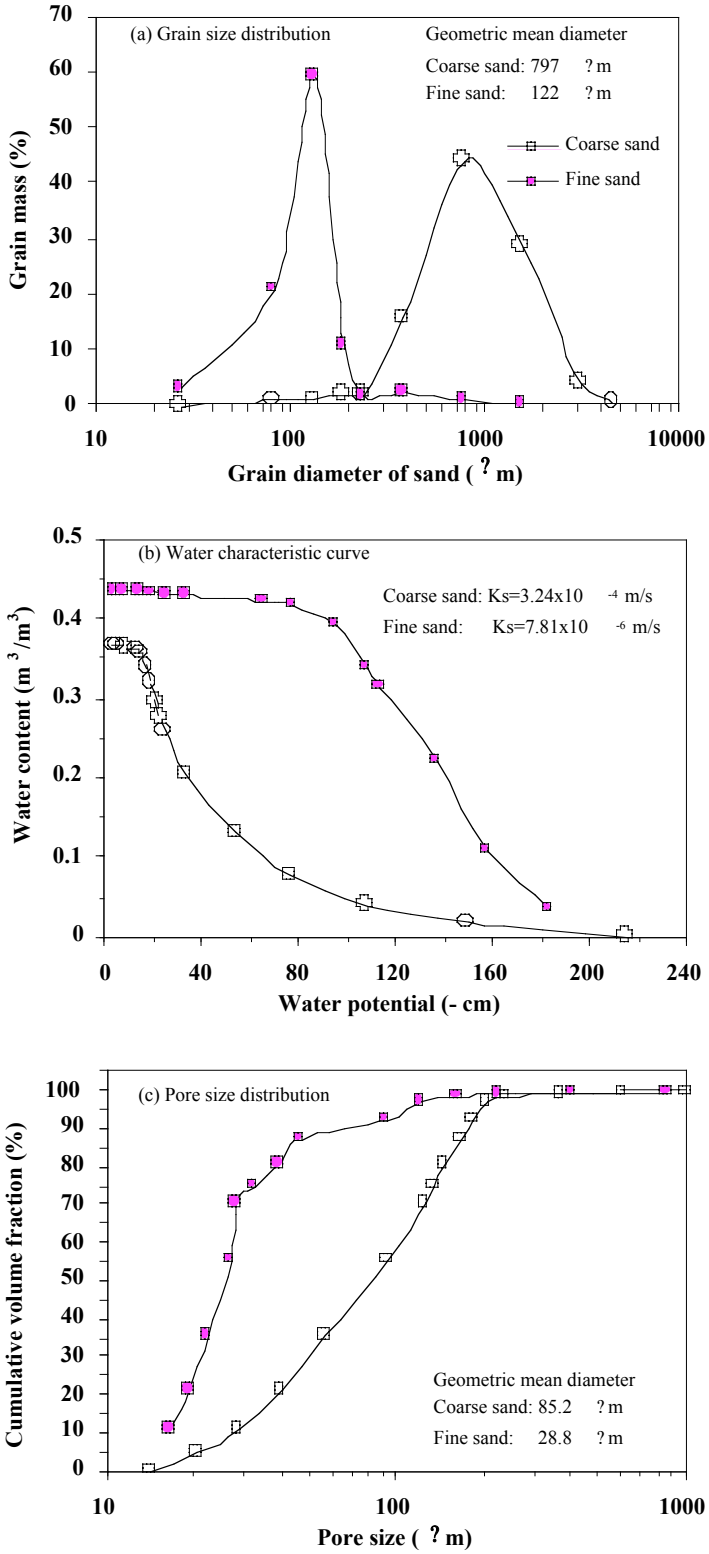

FIGURE 1. Soil physical properties of the two Hanford sands used in the column experiments. K_s is saturated hydraulic conductivity.

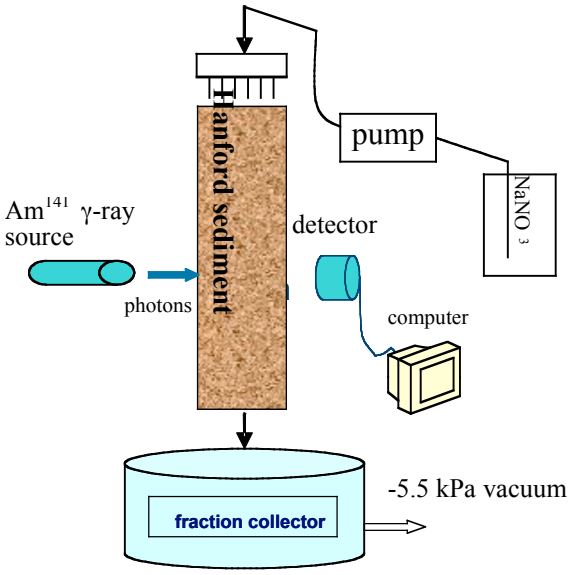

FIGURE 2. A schematic of the unsaturated experimental column system

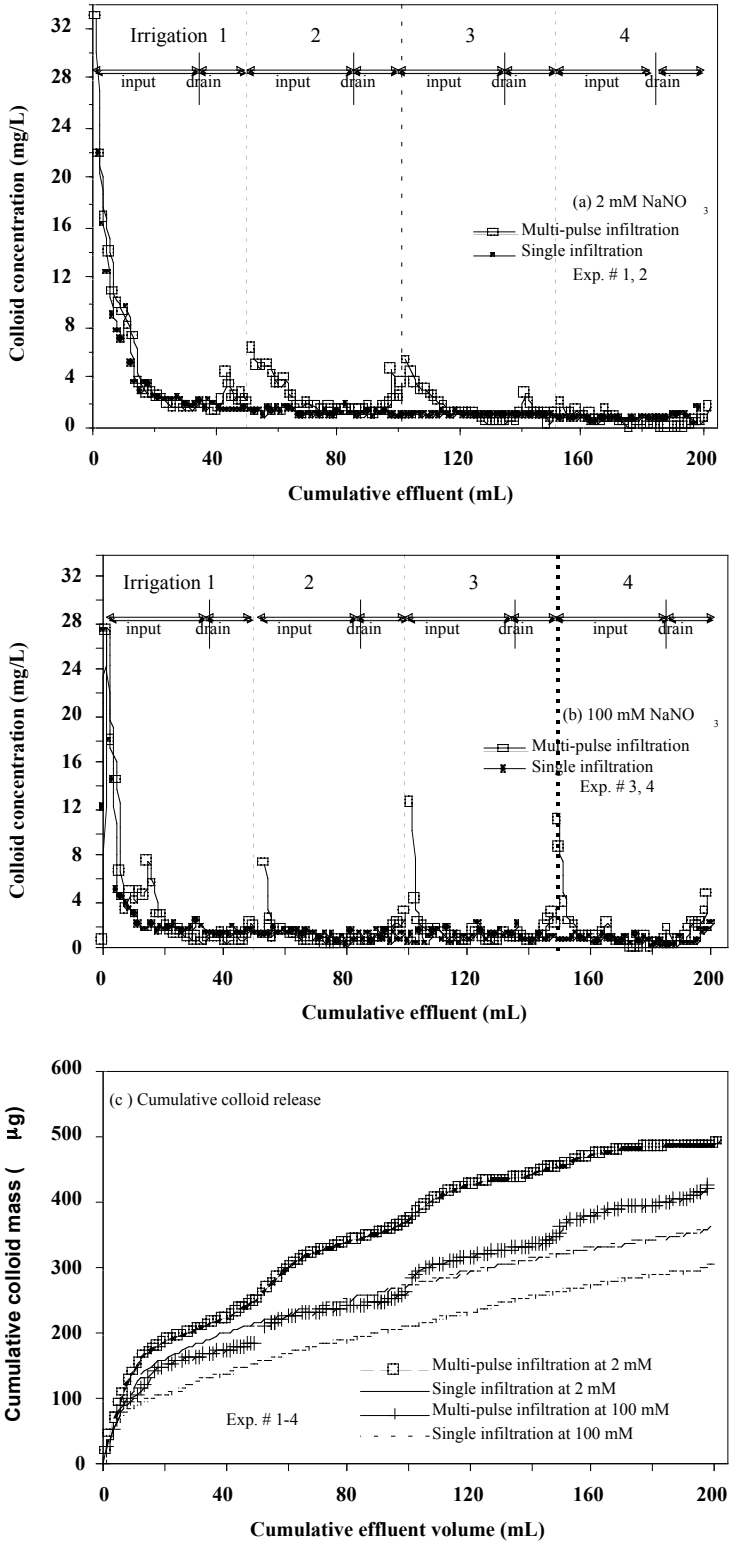

FIGURE 3. Colloid release from coarse Hanford sand as affected by flow pattern and solution ionic strength at an irrigatio rate of 93.8 mm/h (5% K_s).

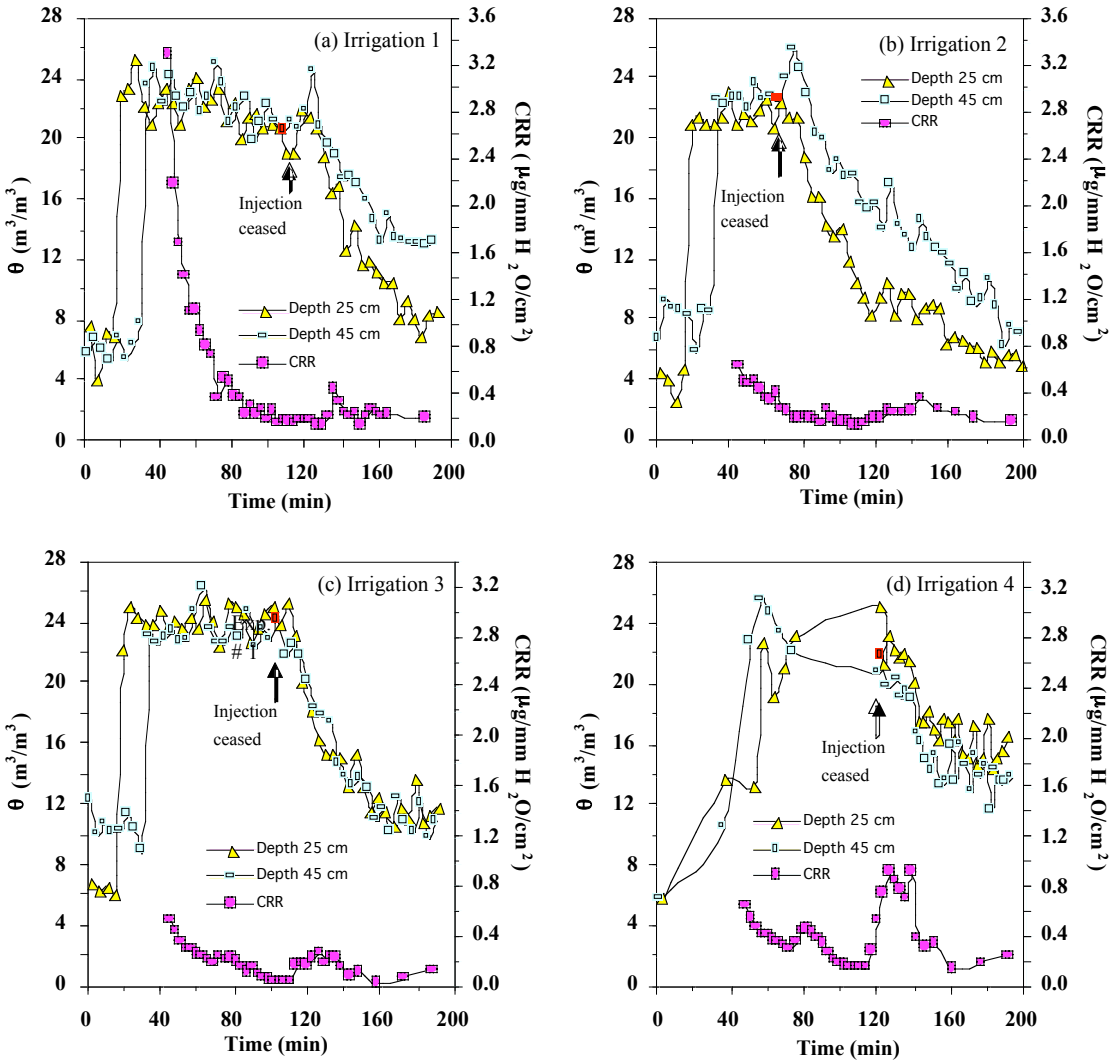

FIGURE 4. Variations of soil water content (θ) and colloid release rate (CRR) during multi-pulse infiltration in 2 mM $NaNO_3$ solution at an irrigation rate of 5% K_s (93.8 mm/h) (Exp. #1). CRR is defined as the mass of colloids released from unit soil cross area along with unit amount of liquid effluent.

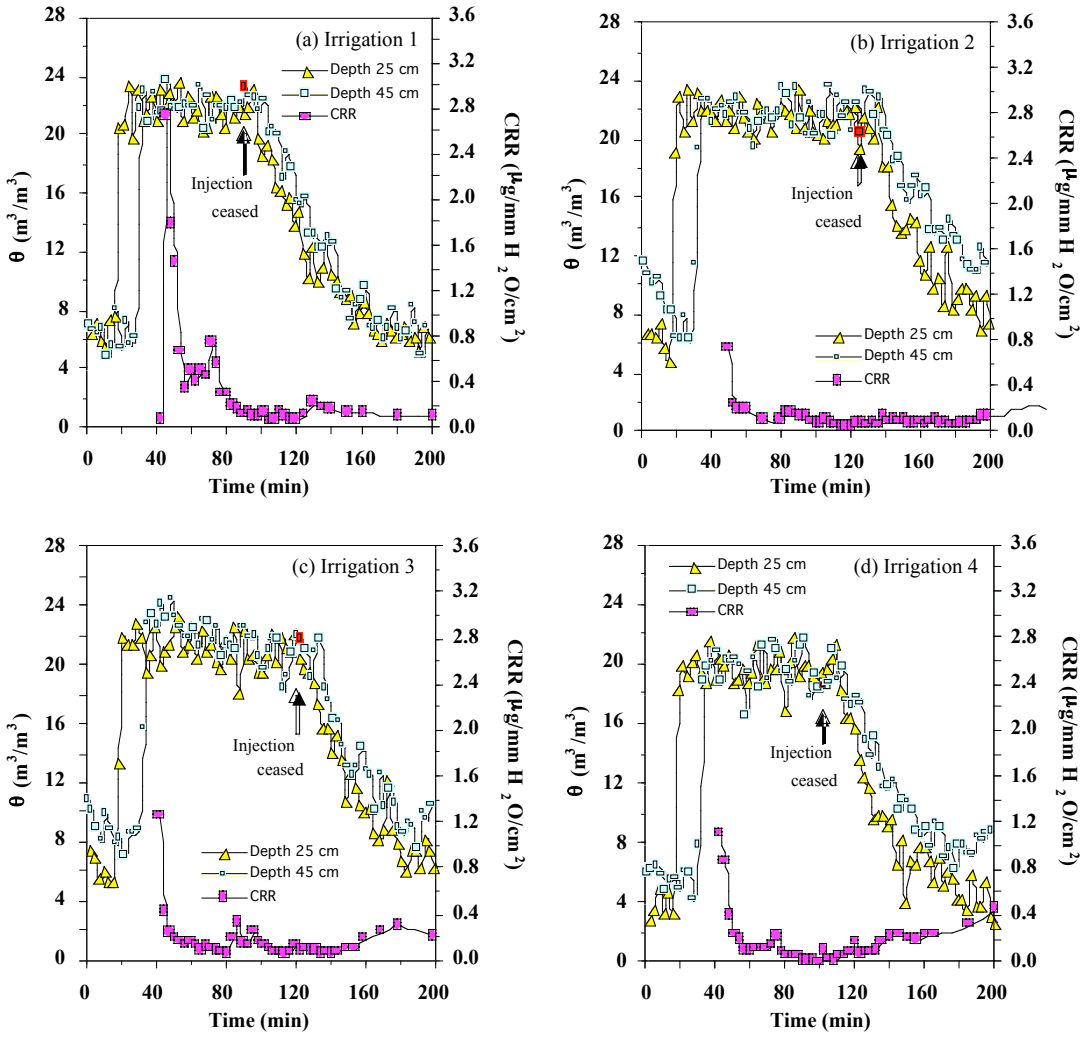

FIGURE 5. Variations of soil water content (θ) and colloid release rate (CRR) during multi-pulse infiltration in100 mM $NaNO_3$ solution at an irrigation rate of 5% K_s (93.8 mm/h) (Exp. #3)

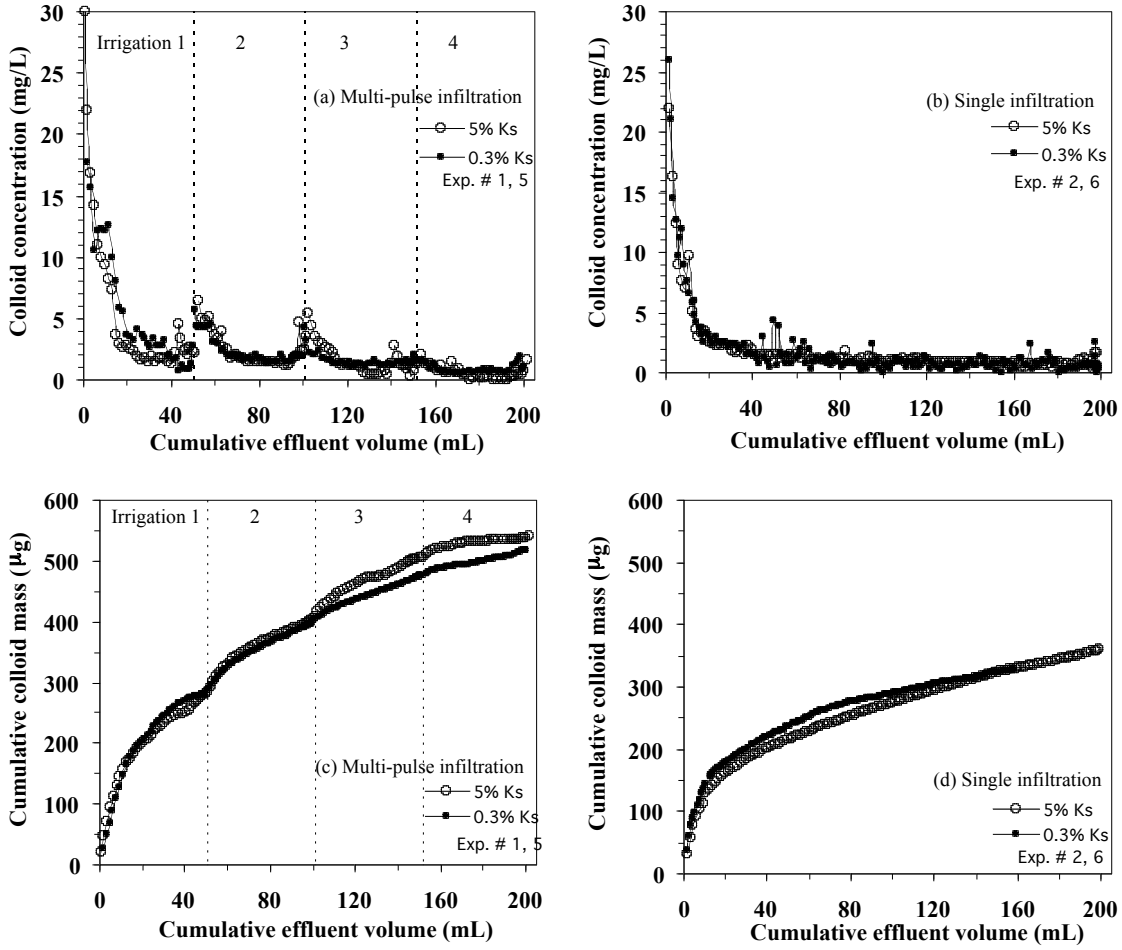

FIGURE 6. Effect of irrigation rate on the in-situ colloid release from coarse Hanford sand in 2 mM $NaNO_3$

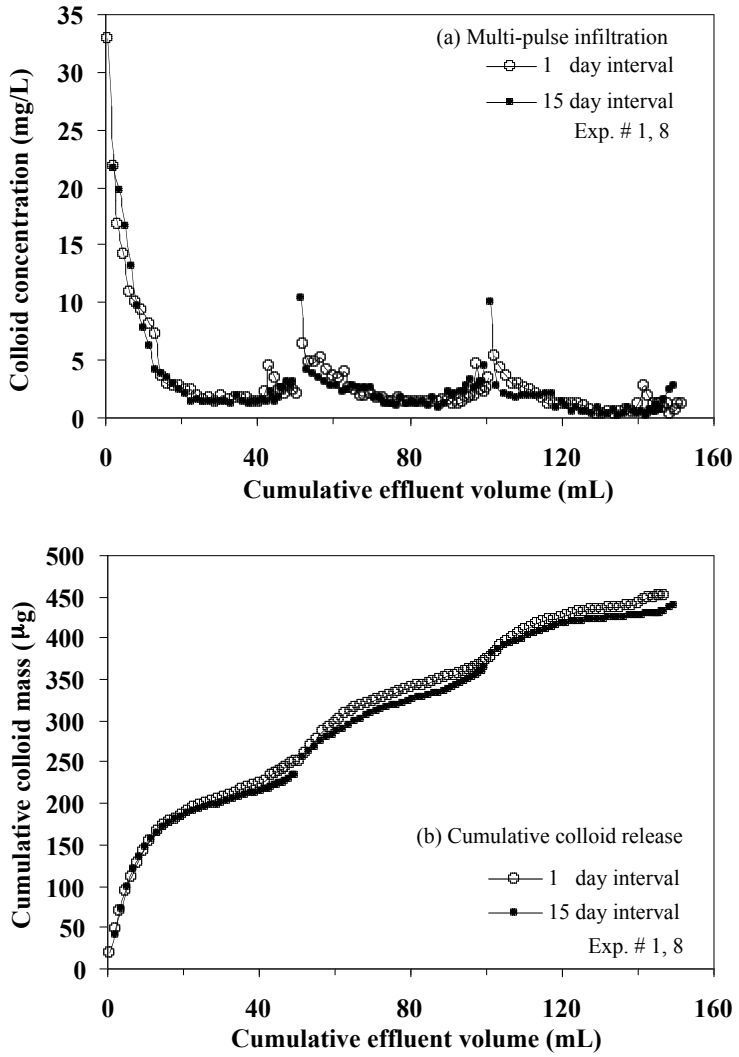

FIGURE 7. Effect of time interval of irrigation pulses or in-situ colloid mobilization in coarse Hanford sand in 2 mM $NaNO_3$ at an irrigation rate of 5% K_s (93.8 mm/h).

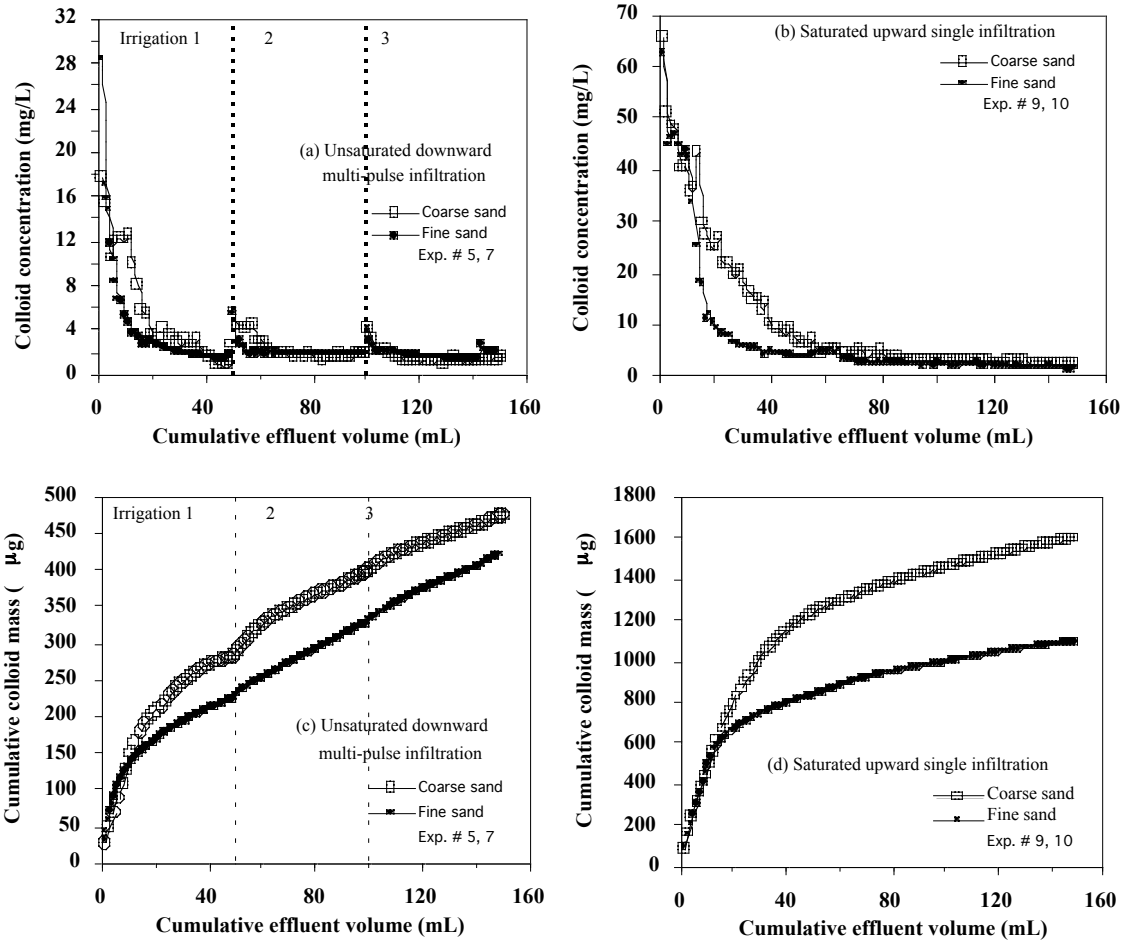

FIGURE 8. Effect of soil texture on in-situ colloid release in 2 mM $NaNO_3$ at a low irrigation rate of 5 mm/h. The rate is equivalent to 0.3% K_s of the coarse Hanford sand, and 9.2% K_s of the fine Hanford sand. Note the scales of Y-axis are different between the unsaturated and saturated results.

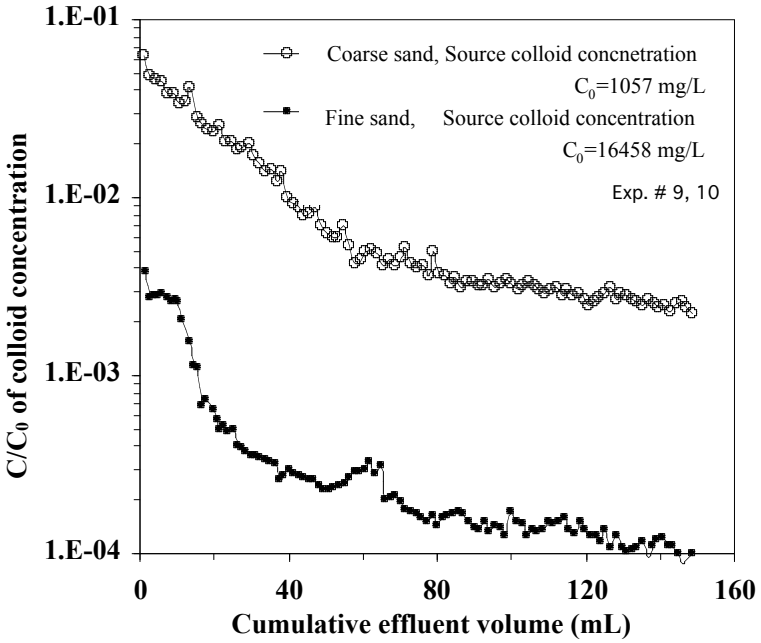

FIGURE 9. Relative concentrations of the in-situ colloids released from two textured sands under saturated flow condition in 2 mM $NaNO_3$ at a low flow rate of 5 mm/h. Source colloid concentration was measured in deionized water using sedimentation method for the < 2 μm^{22} colloids.

The coupled effect of flux rate and ionic strength on transport of colloid through porous media during unsaturated transient flow

Jie Zhuang[1], John F. McCarthy[1], Ed Perfect[1], John Tyner[2], Markus Flury[3], and Tammo S. Steenhuis[4],

[1]Center for Environmental Biotechnology, Department of Earth and Planetary Sciences, The University of Tennessee, Knoxville, TN 37996
[2]Department of Biosystem Engineering and Environmental Sciences, The University of Tennessee, Knoxville, TN 37996
[3]Department of Crop and Soil Sciences, Center for Multiphase Environmental Research, Washington State University, Pullman, WA 99164
[4]Department of Biological and Environmental Engineering, Cornell University, Ithaca, NY 14853

Abstract

Understanding colloid transport in porous media is critical for assessing migration of contaminants because colloids are potential vectors of many contaminants. In this study, a series of column experiments were conducted to investigate coupled effect of flux rate and ionic strength on transport and mobilization of montmorillonite particles in a model porous medium under unsaturated transient flow conditions. It was found that the ionic strength effect greatly depended on infiltration rate of colloid suspension. Enhanced hydrodynamic effect due to increase of infiltration rate, which favors colloid mobilization, turned out to be able to overcome the electrostatic attachment of colloids resulting from increased solution ionic strength. During drainage of water from the packed porous medium, secondary release peaks of the colloid appeared in both phases of colloid injection and elution. The peaking occurred larger in the solution with higher ionic strength. The result suggests that water redistribution, which caused dimensional change of surface and corner water, played a significant role in remobilizing the attached colloids. Presence of in-situ silica colloids in the medium was identified to decrease transport of the introduced montmorillonite colloids in 2 mM $NaNO_3$ solution. In general, the study stresses that colloid transport and mobilization were determined by coupled physical and chemical mechanisms during unsaturated transient flow, such as rainfall and irrigation, and transient water flow can facilitate colloid transport and mobilization, compared to steady-state flow.

1. Introduction

Accurate knowledge of colloid mobilization and transport in natural and technological systems is of primary importance in assessment and prediction of colloid-facilitated contaminant migration [*McCarthy and Zachara*, 1989; *Grolimund et al.*, 1996; *Zhuang et al.*, 2003]. In the past several decades, considerable advances have been made on understanding the processes and mechanisms of colloid deposition and transport through laboratory and field studies, as well as numerical modeling [*McDowell-Boyer et al.*, 1986; *Saiers and Hornberger*, 1994; *Johnson et al.*, 1996; *McGechan et al.*, 2002]. It has been recognized that colloid mobilization is a function of many factors, which include properties of colloid and medium phases [*Bradford et al.*, 2002; *Zhuang et al.*, 2004], solution chemistry [*Gamerdinger and Kaplan*, 2001], and flow conditions [*McDowell-Boyer*, 1992; *James and Chrysikopoulos*, 2000; *Lenhart and Saiers*, 2002]. However,

complex natural environmental conditions greatly preclude a complete characterization of colloid transport in vadose zones. Studies that are conducted under conditions similar to natural processes are thus becoming increasingly essential and important. The natural transport processes are typically featured with transient flow, variable water saturation, and affluence of in-situ colloids.

As so far, most of studies on colloid transport have been carried out under steady-state flow conditions, and many important mechanisms have been examined. Nonetheless, transient flow is more prevalent in soils, particularly top soils, than steady-state flow. . Several recent studies have addressed transient transport by aiming to reveal the influence of physical and chemical perturbations on colloid mobilization and transport. Saiers and Lenhart [2003] and Chen et al. [2005] reported that stepwise increase of flow rates during unsaturated flow can substantially increase colloid transport. Crist et al [2004, 2005] and Zevi et al. [2005] visualized redistribution of colloids driven by water-film flow or/and corner flow during drainage. They found that air/water meniscus/solid interface, instead of air-water interface, plays a critical role in retaining colloids in unsaturated porous media. Their results suggest that any changes of water configurations in porous media would cause colloid remobilization. However, the transient transport of colloids may also be subject to additional physical and chemical conditions of the flow, because net forces acting on the colloids largely depend on hydrodynamic and electrostatic forces that are determined by flux rate and solution ionic strength, respectively. Systematic study on the interactions of various factors is thus essential for comprehensive understanding and prediction of colloid transport. To our knowledge, combined effect of flux rate and ionic strength on transient transport of colloids remains unexamined yet.

Significant interaction may exist between in-situ and introduced colloids during their transport. This is because collision and attachment efficiencies of the introduced colloids heavily rely on the surface characteristics of matrix, and the in-situ colloids, especially those attached on matrix surfaces, can physically impact morphological structure of the liquid/solid interface at nano- and micro-scales (e.g., increase of surface roughness). In-situ colloids may promote or reduce transport of the invading colloids, depending on specific flow conditions and difference in surface characteristics between the native and the foreign colloids. *Weroński et al*. [2003] reported that transport of a latex colloid increased with increasing concentration of silica colloids in the liquid phase. Co-transport of in-situ and introduced colloids are believed to extensively occur in most of the natural contaminated sites. Unfortunately, very few studies have so far been made to examine interaction of two colloids during transport, due mainly to technical difficulty in separating one colloid from the other in characterization. It would be thus very interesting to explore the effect of in-situ colloids on transport of the invading colloids, particularly under transient flow condition. The observation will provide important information regarding mobilization of in-situ colloids for realistic risk assessment of site-specific contaminant transport.

The objective of this study was to examine the coupled effect of flux rate and ionic strength, and the effect of in-situ colloids on transport of an introduced colloid under water-unsaturated transient flow conditions. We hypothesize that electrostatic interaction of colloid with solid surfaces depends on hydrodynamic effects, and transient water flow can enhance colloid transport and mobilization.

2. Materials and Method

2.1 Porous Medium and Colloid

A model silica sand with a trade name as Accusand (grade 20/30, Unimin Corporation, Le Sueur, MN, USA), was used as the porous medium in the transport experiments. The sand grains are uniform with a d_{50} diameter of 0.71 ± 0.02 mm and a cation exchange capacity of 0.57 cmol/kg as provided by the Unimin Corporation. The total carbon content was analyzed to be 0.3 g/kg using Shimadzu TOC-V organic carbon analyzer with a solid sample module. Saturated hydraulic conductivity was determined to be 784±11 cm/h using a constant-head method [Klute and Dirksen, 1986]. Drying curve of water retention characteristics was characterized with a Tempe pressure cell (Soil Moisture Equipment Inc., Model 1400B1M2-3) [Dane and Hopmans, 2002], and described as $\theta = (0.348\text{-}0.016)[1+(0.0744\psi)^{8.47}]^{-0.882}$, with θ the volumetric water content (m^3/m^3) and ψ the absolute value of soil water potential in cm H_2O. Prior to the experiments, the sand was rinsed with deionized water until no particles suspended in the liquid phase as verified by turbidity measurement. The cleaned sand was then oven-dried at 60°C for experimental use.

The experimental colloid was montmorillonite, a 2:1 clay extensively present in soils. To obtain particles smaller than 1-μm, the original Na-rich montmorillonite powder (SWy-2, purchased from The Source Clays Respository, Boulder, Colorado) was first dispersed using a probe ultrasonicator at 10 Watts for 10 min , and then the <1-μm particles were extracted in deionized water according to the gravitational separation method [Gee and Or, 2002]. After being concentrated in a polypropylene beaker at 60°C, the montmorillonite slurry was kept in a refrigerator (6°C) for subsequent preparation of each experimental colloid suspension. Particle size distribution of the colloids in water was measured with BI-XDCW X-ray Disc Centrifuge System (Brookhaven Instruments Corp., Holtsville, New York) and plotted along with chemical composition of the particles in Figure 1. Averaged colloid sizes and zeta potentials at different solutions were characterized with a ZetaPals analyzer (Brookhaven Instrument Ltd.).

Figure 1

2.2 Breakthrough Experiments

One-dimensional column experiments were conducted under unsaturated transient flow condition to investigate the effects of flux rate, solution ionic strength and in-situ silica colloids on deposition and transport of montmorillonite (Table 1). The column system used in the study was similar to that as illustrated in *Zhuang et al.* [2005]. The column was made of clear Schedule-40 PVC pipe, with 2-cm inner diameter and 60-cm height. In the experiments, a nylon membrane with 20-μm pore size and -6.4 kPa air-entry value (Spectra/Mesh, Spectrum Laboratories, Inc.) was placed on the base of the column to control capillary tension (-5.5 kPa) through a vacuum system. The vacuum system consisted of a vacuum chamber (CL-040, Soil Measurement Systems, Tucson, AZ) and vacuum control valves (Type 70, Bellofram Corp., Newell, WV). Teflon tubing was used throughout the system except for a portion of tygon tubing used in the peristaltic pump. When the column was packed, a deaerated $NaNO_3$ background solution (pH 7, 2 to100 mM) was pre-introduced into the column from its bottom to a certain

height. Then, the sand was slowly poured into the column as 1-cm increments while stirred with a plastic rod to ensure uniform packing and to avoid air entrapment in the column. Before running of each experiment, the packed column was flushed with deaerated $NaNO_3$ solution to precondition the columns for the breakthrough experiments. The flushing removed the colloids residing in the columns, established a steady-state flow, and standardized background ionic strength and pH. Five pore volumes of the $NaNO_3$ solution were injected to flush the column for complete removal of the in-situ silica colloids. However, in the experiments aiming to examine the in-situ colloid effect on montmorillonite transport, only one pore volume of the solution flew through the column for keeping a certain level of residual of the in-situ colloids. Following the flush, the column was equilibrated under a vacuum pressure (-5.5 kPa) for overnight, with column-top covered by a sparsely punctured Parafilm. The averaged sand water content was determined to be 0.035 m^3/m^3 after the hydrological equilibrium was reached. The transport experiment was initiated by pumping the input solution, which was composed of the $NaNO_3$ background solution along with the experimental colloid (250 mg/L), into the column at a constant surface flux rate. The influent reservoir was constantly stirred during the entire course of experiments. After six to ten pore volumes (depending on the sand water content for a similar total influx volume at different irrigation rates) of injection of the colloid suspension, the irrigation was ceased and the water was allowed to drain out of the column under the negative tension for 15 h. Elution with colloid-free $NaNO_3$ solution was performed after drainage ceased. Again, the drainage began with stopping of the injection of clear solution, after the effluent colloid concentration returned to a baseline level determined at the beginning of each experiment. During the experiments, the effluents were collected from the bottom of the column into 10-mL glass test tubes in regular time intervals using a fraction collector. Room temperature was maintained at 22±1^{o}C during the experiments.

Table 1

2.3 Analysis of Colloid Concentrations

We determined the montmorillonite concentration (Mt) by measuring aluminum concentration of each sample using ICP-MS (IRIS Intrepid II XSP, Thermo Electron Co.) at wavelength 308.96 nm. This is because crystal montmorillonite contains a specific percentage of aluminum but in the silica sand aluminum content was negligible as measured. Figure 1a shows the measured aluminum-montmorillonite calibration curve. The total colloid concentration (montmorillonite plus silica) was determined using a UV-VIS spectrophotometer at 360 nm (DU Series 640, Beckman Instruments, Inc., Fullerton, CA) from the calibration curves of the respective colloids. Based on the absorbance (A) of the total colloids from the UV-VIS analysis and the montmorillonite concentration (Mt) measured using ICP, silica colloid concentration (Si) in each sample was computed with the formula: $A=a_1\mathrm{Mt}+a_2\mathrm{Si}$, where a_1 and a_2 are the slope coefficients of the UV-VIS calibration curves for montmorillonite and silica colloids, respectively. The silica colloids for predetermination of the calibration curve were collected by flushing the packed sand.

2.4 In-situ Water Content Measurement Using Gamma-ray Attenuation System

A custom-built gamma-ray attenuation system was used to monitor the spatial and temporal distribution of water before and during transient irrigation experiments. Unlike other methods

used to monitor water tension, such as tensiometers, the gamma-ray system is non-invasive, thus avoiding concerns about disturbance of the sediment. We continuously monitored the in-situ water content of the packed sand at four depths (25, 35, 48 and 57 cm) of the vertical columns. The gamma-ray source was a 240-mCi Am^{241} source (Isotope Products Laboratories; PO8); source collimation was provided by a 3-mm diameter hole in a tungsten shield. A NaI(TI) gamma-ray detector and photo-multiplier tube (Bicron, 3m3/3, Newbury, OH) were collimated using a 10-mm diameter hole in a lead shield. The system included a computer controlled multi-channel analyzer (MCA) (Princeton Gamma-Tech; MCA 2100R, Oak Ridge, TN). The porous media chamber was placed between the source and the detector, which were mounted to a computer-controlled linear actuator (Bislide 15 inch; MN-0150-E01-21) with stepping motor (Advanced Micro Systems; AMS23-150-2), micro-stepping driver (Advanced Micro Systems; DR-4M), and PC bus step motor controller (Advanced Micro Systems; PCMC). The system was programmed to scan the selected four locations of the column throughout the irrigation and drainage experiments using software-controlled motors and a data acquisition system. Further details of the gamma-system are given by Tyner and Brown, 2004.

The preequilibrated columns were scanned vertically for ten cycles prior to irrigation to determine the gamma-ray attenuation due to the sediment and the initial moisture content. The counting time was ten seconds at each depth. Based on the distance of the energy source from the column, the 10-second counting time led to an accuracy of ±10% of the actual water content. Total time for one cycle of the scanning was about 3 min including the traveling time of actuator between the depths. Spatial and temporal changes in sand moisture content during the irrigation and drainage were calculated with the Lambert-Beer equation [Oostrom et al., 2002] and the known mass attenuation coefficient of water μ_w. Our experimentally determined value of μ_w agreed well with the theoretical value, indicating that the system was well collimated.

3. Results and Discussion

3.1 Water Infiltration and Drainage at Different Flux Rates

Figure 2 shows that the maximum or stable water saturation of the packed sand increased with increasing flux rate, with the saturation degrees being 0.30, 0.38, and 0.47 for the flux rates of 0.5%, 5%, and 10% K_s (K_s, saturated hydraulic conductivity), respectively. The travel times of the wetting fronts to reach the bottom of the column were 4.5, 7, 38 minutes at the flux rates of 10%, 5%, and 0.5% K_s. Note that once there occurred an outflow, the water condition within the column also became stable, suggesting a steady state transport of the colloids during the period between the initial outflow and the beginning of drainage. Figure 2 shows that the drainage rate depended on the specific irrigation rate. It took about 100 minutes for the water saturation established at 0.5% K_s influx rate to return to its initial value before the infiltration, while about 60 and 40 minutes elapsed for completing the same processes at 5% and 10% K_s influx rates, respectively. These results clearly indicate that the rate of water distribution or redistribution was dependent on specific flux rate.

Figure 2

3.1 Effect of Ionic Strength on Colloid Transport and Elution

Transient transport and elution of montmorillonite colloids through the silica sand at three flux rates (0.5%, 5%, and 10% K_s) and three ionic strengths (2, 20, and 100 mM $NaNO_3$) are compared in Figure 3. In the injection phases of most of the experiments (Figure 3a, c and e), the colloid concentrations exhibited a rising trend in the initial effluents, and then climbed up to a stable level after outflow of ~10-mL of colloid suspension. The low colloid concentration in the beginning caused by attachment of colloids on the sand surface; yet stabilization of the effluent concentration at a high level implies arrival of a kinetic equilibrium for colloid attachment and that the attached colloids would repulse the adsorption of incoming colloids [*Song and Elimelech*, 1993; *Johnson and Elimelech*, 1995]. It is shown that low ionic strength favored the colloid transport with stable C/C_0 values, for instance, reaching ~0.95 and ~0.6 C/C_0 in 2 and 20 mM solutions, respectively, at irrigation rate of 0.5% K_s. This sharply contrasted to the very low effluent concentration (only ~0.05-0.1 C/C_0) observed in 100 mM solution at the same flux rate. Evidently, reduction of electrostatic repulsion between the particle and the sand surface due to increasing ionic strength increased the colloid deposition [e.g., *Compere et al.*, 2001; *Gamerdinger and Kaplan*, 2001].

In the elution phases of the experiments (Figure 3b, d and f), the effluent concentrations of montmorillonite peaked coincidently with the initial breakthrough of the introduced colloid-free solution, followed by a rapid decline of the concentration to a constant low level after ~10-mL of cumulative outflow. The peaking is considered due to build-up of the colloid concentration in the moving wetting front and limited reattachment of the released colloids during the transport as mechanistically illustrated in Figure 4a.. Since more colloids are retained in the porous media at higher ionic strength, larger concentration peaking are usually observed when eluting the columns through which colloids have previously transported in higher ionic strength solution. This explains the observed higher elution peak of montmorillonite concentration in 100 mM than in 2 and 20 mM solutions.

Figure 3 and Table 2

3.2 Drainage-induced Colloid Mobilization

As depicted in Figure 3, water drainage induced a release peak of colloids in both the colloid injection phase and the elution phase, particularly in the solutions with higher ionic strengths (20 and 100 mM). This might be caused by slow movement of water films as well as dimensional change of corner-water ducts during water drainage/redistribution [*Crist et al.*, 2004; 2005]. Figure 4b illustrates that during the slow drainage colloids in immobile water had adequate time to diffuse into mobile water, and asymmetric capillary forces exerted around colloid due to deformation of air-water interface could also drag the deposited colloids into the thick moving water phase [*Kralchevsky et al.*, 1992; *Kralchevsky and Nagayama*, 2000]. Consequently, the mobile colloids were accumulated in the downward-moving thick water films and finally eluted out of the column with an abrupt increase of concentration. Similar to the behavior of retained colloids in the elution process (Figure 3b, d, and f), the drainage effect in the injection phase increased with increasing concentration of colloids residing at interfaces within the column (Figure 3a, c, and e). Figure 3 demonstrates that drainage-induced colloid mobilization (the release peaks) tended to be larger at higher ionic strength (e.g., 100 mM). These results imply that configurational change of interfacial water or pore-water arising from infiltration, drainage, or any other type of hydrodynamic perturbations (e.g., flow rate change) are key mechanisms controlling colloid mobilization and remobilization. Instable air-water interfaces under

unsaturated transient flow condition are thus expected to increase mobilization of colloids that are otherwise retained at the air-water or/and air-water-solid interface under unsaturated steady-state flow condition.

3.3 Interplay between the Flux Rate Effect and the Ionic Strength Effect

Hydrodynamic interaction, which is subject to flux rate, is one of the main mechanisms controlling colloid transport in porous media [*Ryan and Gschwend*, 1994; *Kretzschmar et al.*, 1997; *Zhuang et al.*, 2004]. Figure 4 shows a combined effect of flux rate and ionic strength on transport of montmorillonite through the packed sand. Stabilized breakthrough C/C_0 (Figure 4a) and recovery rates (Figure 4b) of colloids indicate that high velocity promoted both transport and elution of the colloids, and the relative hydrodynamic effect increased with increasing ionic strength of solution that represents the chemical effect. The interplay of these hydrodynamic and chemical effects can be attributed to several mechanisms: colloid size effect, counteracting of the hydrodynamic and electrostatic forces, and water content effect. It is well known that instability and aggregation of colloidal particles in the solution with high ionic strength can lead to increase of their effective sizes [*Czigany et al.*, 2005]. Particle sizes of montmorillonite used in this study were measured to be 439±6, 512±8, 709±13, 1572±75 μm in deionized water, 2 mM, 20 mM, and 100 mM $NaNO_3$ solutions, respectively. Larger particles have proved more sensitive to change of hydrodynamic forces, because particle Peclet number, a ratio of convection to diffusion, is greater for larger particles [*Ko et al.*, 2000; *Zhuang et al.*, 2004].

Colloid deposition is also determined by the overcoming of hydrodynamic force to electrostatic force. In the solution with low ionic strength, the strong electrostatic repulsion between the colloid and the sand made the majority of colloids suspend in the mobile liquid phase; thereby net increase of the number of transported colloids was limited as the flux rate increased. On the contrary, in the solution with high ionic strength, colloids were subject to reduced electrostatic repulsion between the colloid and the sand, resulting in enhanced colloid deposition. In this case, larger hydrodynamic force arising from higher flux rate could play a greater role in promoting colloid transport, compared to the case with low ionic strength.

Additionally, flux rate effect and ionic strength effect might interplay through the mechanism of water content effect. Many Increased water content reduces mechanical straining of colloids in the unsaturated porous media due to expansion of flow pathways (thin water films and corner-water ducts) and enhanced pore-water continuity at high water content [*Wan and Tokunage*, 1997; *Lenhart and Saiers*, 2002; *Saiers and Lenhart*, 2003, Gao et al., 2006]. Therefore, at high flux rate, deposited colloids at high ionic strength that otherwise transported through the unsaturated sand medium at low ionic strength [*Kretzschmar et al.*, 1997; *Compere et al.*, 2001] could disperse into the flowing phase of liquid.

An implication of the overcoming of hydrodynamic interaction to electrostatic interaction at high flux rate is that critical electrolyte concentration for colloid coagulation or immobilization in bulk porous media [*Ravisangar et al*., 2001; *Blume et al.*, 2005] may not apply to the scenario with preferential flow or fracture flow. This is because flow velocity and water content in these flow channels are usually much higher than the bulk media [*McKay et al.*, 2000; *Wang et al*.,

2004]. Preferential flow under transient flow condition requires higher critical electrolyte concentration for immobilizing colloids. Site risk assessment and modeling of colloid-facilitated contaminant transport should thus account for the coupled effect between flux rate and ionic strength, particularly in the coarse-textured and fracture-affluent vadose zones.

Figure 4

4. Conclusions

Increasing influx rate increased colloid transport through the silica sand, and the effect became more significant in the higher than lower ionic strength solutions. The result suggests that the hydrodynamic interaction significantly overcame the electrostatic interaction, and high flux velocity frequently occurring in the preferential flow pathways might cause remarkable mobilization of the colloids that are otherwise immobilized or travel only a short distance in bulk porous medium in high ionic strength solution. The study identified transient flow as an important condition for strengthening the coupling effect. It was found that water drainage/redistribution induced a secondary peak of colloid release. The main mechanism responsible for the release peaking was inferred to be colloid remobilization driven by capillary force that was reinforced by dimensional change of water films during the drainage. The experimental results also show that in-situ silica colloid reduced transport of the invading montmorillonite particles in 2 mM $NaNO_3$ solution, with potential mechanisms including energy barrier, friction and capillary forces, and depletion interaction. The in-situ colloid effect suggests that colloid transport depends on porous structure/roughness formed by attachment of in-situ colloids on collector surfaces, as well as the interaction between the in-situ and introduced colloids.

Acknowledgement
The study was supported by the Environmental Management Science Program, U.S. Department of Energy under Grant No. DE-FG07-02ER63496.

References

Batra, A., S. Paria, C. Manohar, and K.C. Khilar (2001), Removal of surface adhered particles by surfactants and fluid motions. AIChEJ, 47, 2557-2565.

Bhattacharjee, S., C.H. Ko, and M. Elimelech. (1998), DLVO Interaction between rough surfaces. Langmuir, 14, 3365-3375.

Blume, T., N. Weisbrod, and J.S. Selker (2005), On the critical salt concentrations for particle detachment in homogeneous sand and heterogeneous Hanford sediments. Geoderma, 124(1-2), 121-132.

Bradford, S.A., S.R. Yates, M. Bettahar, and J. Simunek (2002), Physical factors affecting the transport and fate of colloids in saturated porous media. Water Resour. Res., 38, 1327, doi:10.1029/2002WR001340.

Chan, D.Y.C., J.D. Henry and L.R. White (1981), The interaction of colloidal particles collected at fluid interfaces. J. Colloid Interf. Sci., 79, 410-418.

Chen, G., M. Flury, and J.F. McCarthy (2005), In-situ colloid mobilization under unsaturated transient flow condition. Water Resour. Res., (In Review).

Compere, F., G. Porel, and F. Delay. (2001), Transport and retention of clay particles in saturated porous media: Influence of ionic strength and pore velocity. J. Contamin. Hydrol., 49, 1-21.

Crist, J.T., Y. Zevi, J.F. McCarthy, J.A. Throop, and T.S. Steenhuis (2005), Transport and retention mechanisms of colloids in partially saturated porous media. Vadose Zone J., 4, 184-195.

Crist, J.T., J.F. McCarthy, Y. Zevi, P. Baveye, J.A. Throop, and T.S. Steenhuis (2004), Pore-scale visualization of colloid transport and retention in partly saturated porous media. Vadose Zone J., 3, 444-450.

Czigany, S., M. Flury, and J.B. Harsh (2005), Colloid stability in vadose zone Hanford sediments. Environ. Sci. Technol., 39, 1506-1512.

Das, S.K., R.S. Schechter, and M.M. Sharma (1994), The role of surface-roughness and contact deformation on the hydrodynamic detachment of particles from surfaces. J. Colloid Interf. Sci., 164(1), 63-77.
El-Farhan, Y.H., N.M. Denovio, J.S. Herman, and G.M. Hornberger (2000), Mobilization and transport of soil particles during infiltration experiments in an agricultural field, Shenandoah Valley, Virginia. Environ. Sci. Technol., 34, 3555-3559.
Elimelech, M., and C.R. O'Melia (1990), Effect of particle-size on collision efficiency in the deposition of Brownian particles with electrostatic energy barriers. Langmuir, 6, 1153-1163.
Gamerdinger, A.P., and D.I. Kaplan (2001), Colloid transport and deposition in water-saturated Yucca Mountain tuff as determined by ionic strength. Environ. Sci. Technol., 35, 3326-3331.
Grolimund, D., M. Borkovec, K. Barmettler, and H. Sticher (1996), Colloid-facilitated transport of strongly sorbing contaminants in natural porous media: A laboratory column study. Environ. Sci. Technol., 30, 3118-3123.
Jacobsen, O.H., Moldrup, C.L., Konnerup L., and Petersen, L.W. (1997), Particle transport in macropores of undisturbed soil columns. J. Hydrol., 196, 185-203.
James, S.C., and C.V. Chrysikopoulos (2000), Transport of polydisperse colloids in a saturated fracture with spatially variable aperture. Water Res. Resour., 36, 1457-1465.
Jenkins, P., and M. Snowden (1996), Depletion flocculation in colloidal dispersions. Adv. Colloid Interf. Sci., 68, 57-96.
Johnson, P.R., and M. Elimelech (1995), Dynamics of colloid deposition in porous media: Blocking based on random sequential adsorption. Langmuir, 11, 801-812.
Johnson, P.R., N. Sun, and M. Elimelech (1996), Colloid transport in geochemically heterogeneous porous media: Modeling and measurements. Environ. Sci. Technol., 30, 3284-3293.
Ko, C.H., S. Bhattacharjee, and M. Elimelech (2000), Coupled influence of colloidal and hydrodynamic interactions on the RSA dynamic blocking function for particle deposition onto packed spherical collectors. J. Colloid Interf. Sci., 229, 554-567.
Kokkoli, E., and Zukoski, C.F. 1998. Langumuir 14, 1189-1195
Kralchevsky, P.A., V.N. Paunov, I.B. Ivanov, and K. Nagayama (1992), Capillary meniscus interaction between colloidal particles attached to a liquid-fluid interface. J. Colloid Interf. Sci., 151, 79-94.
Kralchevsky, P.A., and K. Nagayama (2000), Capillary interactions between particles bound to interfaces, liquid films and biomembranes. Adv. Colloid Interf. Sci., 85, 145-192.
Kretzschmar, R., K. Barmettler, D. Grolimund, Y.D. Yan, M. Borkovec, and H. Sticher (1997), Experimental determination of colloid deposition rates and collision efficiencies in natural porous media. Water Resour. Res., 33, 1129-1137.
Lenhart, J.J., and J.E. Saiers. (2002), Transport of silica colloids through unsaturated porous media: experimental results and model comparisons. Environ. Sci. Technol., 36, 769-777.
Lenhart, J.J., and J.E. Saiers (2003), Colloid mobilization in water-saturated porous media under transient chemical conditions. Environ. Sci. Technol., 37, 2780-2787.
Litton, G.M., and T.M. Olson (1996), Particle size effects on colloid deposition kinetics: evidence of secondary minimum deposition. Coolods and Surfaces A, 107, 273-283.
McCarthy, J.F., and J.M. Zachara (1989), Subsurface transport of contaminants-mobile colloids in the subsurface environment may alter the transport of contaminants. Environ. Sci. Technol., 23, 496-502.
McDowell-Boyer, L.M. (1992), Chemical mobilization of micro-sized particles in saturated porous media under steady flow conditions. Environ. Sci. Technol., 26, 586-593.
McDowell-Boyer, L.M, J.R. Hunt, and N. Sitar (1986), Particle-transport through porous-media. Water Resour. Res., 22,1901-1921.
McGechan, M.B., and D.R. Lewis (2002), Transport of particulate and colloid-sorbed contaminants through soil, Part 1: General Principles. Biosystems Engineering, 83, 255-273.
McKay, L.D., R.W. Gillham, and J.A. Cherry (1993), Field experiments in a fractured clay till. 2. solute and colloid transport. Water Resour. Res., 29, 3879-3890.
Ravisangar, V., Brouckaert, B.M., Amirtharajah, A., and Sturm, T.W. 2001. The role of solution chemistry in the stability and detachment of cohesive kaolinite particles. Water Sci. Technol.: Water supply 1, 25-32.
Ryan, J.N., and Gschwend, P.M. (1994), Effects of ionic strength and flow rate on colloid release: Relating kinetics to intersurface potential energy. J. Colloid Interface Sci., 164, 21-34.
Ryan, J.N., and M. Elimelech (1996), Colloid mobilization and transport in groundwater. Colloid Surf. A 107:1-56.
Ryan. J.N., T.H. Illangasekare, M.I. Litaor, and R. Shannon (1998), Particle and plutonium mobilization in macroporous soils during rainfall simulations. Environ. Sci. Technol., 32, 476-482.
Ryan, J.N., M. Elimelech, J.L. Baeseman, and R.D. Magelky (2000), Silica-coated titania and zirconia colloids for

subsurface transport field experiments. Environ. Sci. Technol. 34:2000-2005.
Saiers, J.E., and G.M. Hornbereger (1994), First- and second-order kinetics approaches for modeling the transport of colloidal particles in porous media. Water Resour. Res., 30(9), 2499-2506.
Saiers, J.E., and J.J. Lenhart (2003), Ionic-strength effects on colloid transport and interfacial reactions in partially saturated porous media. Water Resour. Res., 39, 1256, doi: 10.1029/2002WR001887.
Saiers, J.M., and J.J. Lenhart (2003) Colloid mobilization and transport within unsaturated porous media under transient-flow conditions. Water Resour. Res., 39 (1), 1019, doi:10.1029/2002WR001370.
Schelde, K., P. Moldrup, O.H., Jacobsen, H. de Jonge, L.W. de Jonge, and T. Komatsu (2002), Diffusion-limited mobilization and transport of natural colloids in macroporous soil. Vadose Zone J., 1, 125-136.
Schroth, M.H., S.J. Ahearn, J.S. Selker, and J.D. Istok (1996), Characterization of Miller-similar silica sands for laboratory hydrologic studies, Soil Sci. Soc. Am. J., 60, 1331-1339.
Seebergh, J.E., and J.C. Berg (1994), Depletion flocculation of aqueous electrosterically-stabilized latex dispersions. Langmuir, 10, 454-463.
Shellenberger, K., and B.E. Logan (2002), Effect of molecular scale roughness of glass beads on colloidal and bacterial deposition. Environ. Sci. Technol., 36(2), 184-189.
Song, L.F., and M. Elimelech (1993), Dynamics of colloid deposition in porous-media-Modeling the role of retained particles. Colloid Surf. A, 73, 49-63.
Tabor, D. (1977), Surface forces and surface interactions. J. Colloid Interface Sci., 58, 2-13.
Walz, J.Y. (1998), The effect of surface heterogeneities on colloidal forces. Adv. Colloid Interface. Sci., 74, 119-168.
Wan, J., and T. Tokunaga. (1997), Film straining of colloids in unsaturated porous media: Conceptual model and experimental testing. Environ. Sci. Technol., 31, 2413-2420.
Wang, Z., W.A. Jury, A. Tuli, and D.J. Kim (2004), Unstatble flow during redistribution: controlling factors and practical implications. Vadose Zone J., 3, 549-559.
Weroński, P., J.Y. Walz, and M. Elimelech (2003), Effect of deposition interactions on transport of colloidal particles in porous media. J. Colloid Interf. Sci., 262, 372-383.
Zevi Y., Dathe A., McCarthy JF, Richards BK, and Steenhuis TS. 2005. Distribution of colloid particles onto interfaces in partly saturated sand. Environ. Sci. Technol. 39: 7055-7064.
Zhuang, J., M. Flury, and Y. Jin (2003), Colloid-facilitated cesium transport through water-saturated Hanford sediments and Ottawa sand. Environ. Sci. Technol., 2003, 37, 4905-4911.
Zhuang, J., Y. Jin, and M. Flury (2004), Comparison of Hanford colloid and salinity transport in porous media. Vadose Zone J., 3(2), 395-402.
Zhuang, J., M.F. McCarthy, E. Perfect, J.S. Tyner, M. Flury, and T.S. Steenhuis (2005), In-situ colloid mobilization in Hanford sediments under unsaturated transient flow condition: Effect of irrigation pattern. Environ. Sci. Technol. (In review).

Table 1 Column Experimental Conditions

Exp. No.	Irrigation rate (%Ks)	Irrigation rate mm/h	Ionic strength (mM)	In-situ silica (mg/L)	Initial water content (m^3/m^3)	Bulk density (Mg/m^3)	Porosity
1	0.5	51.9	2	low	2.90	1.82	0.32
2	0.5	51.9	2	high	3.10	1.76	0.35
3	0.5	51.9	20	low	3.54	1.81	0.33
4	0.5	51.9	100	low	3.41	1.82	0.33
5	5	515.7	2	low	3.05	1.82	0.33
6	5	515.7	2	high	3.18	1.78	0.34
7	5	515.7	20	low	3.40	1.82	0.33
8	5	515.7	100	low	3.43	1.81	0.33
9	10	1031.4	2	low	3.25	1.78	0.34
10	10	1031.4	20	low	3.17	1.81	0.33
11	10	1031.4	100	low	3.60	1.82	0.33

Table 2 Colloid size and zeta potential at different ionic strengths

Solution	Effective diameter (μm)	Zeta potential (mv)
Deionized water	436.8±6.0	-43.8±1.7
2 mM $NaNO_3$	512.2±7.8	-40.25±0.8
20 mM $NaNO_3$	708.9±12.7	-31.3±+4.1
100 mM $NaNO_3$	1572.5±75.2	-24.6±1.0

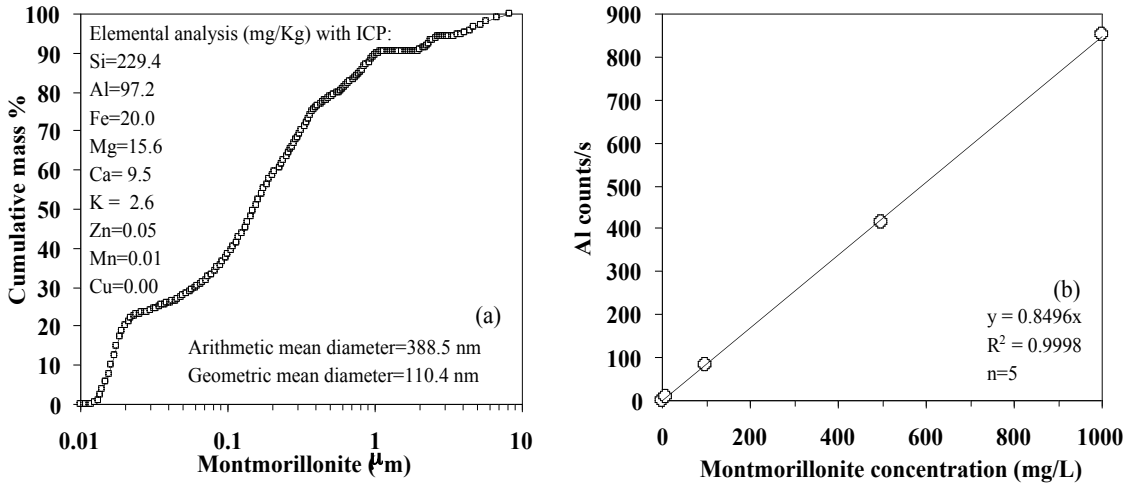

Figure 1. Particle size distribution and chemical composition of the montmorillonite colloids in deic
water (a), and calibration curve determined by measuring Al content in montmorillonite with ICP-M

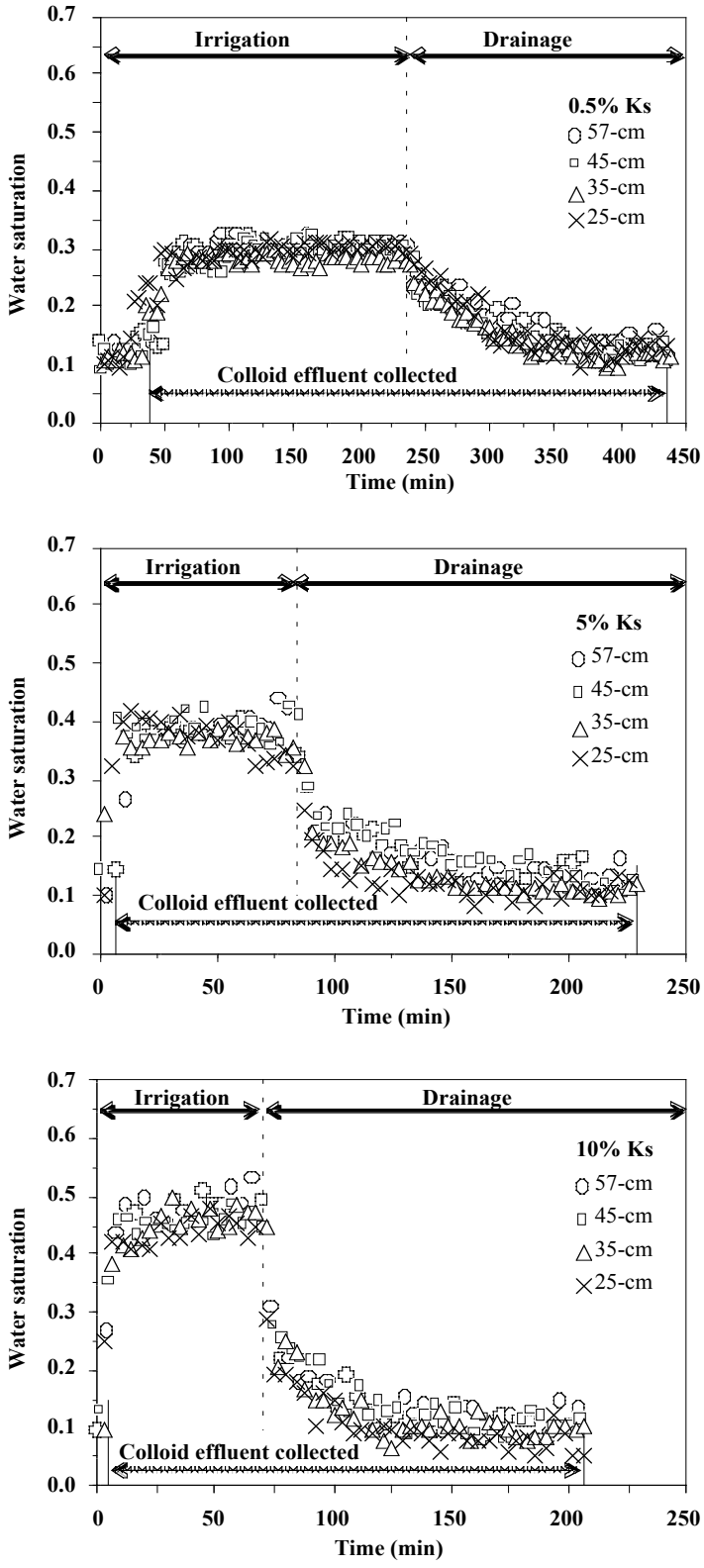

Figure 2. Temporal change of water saturation at different depths of the column during irrigation and drainage

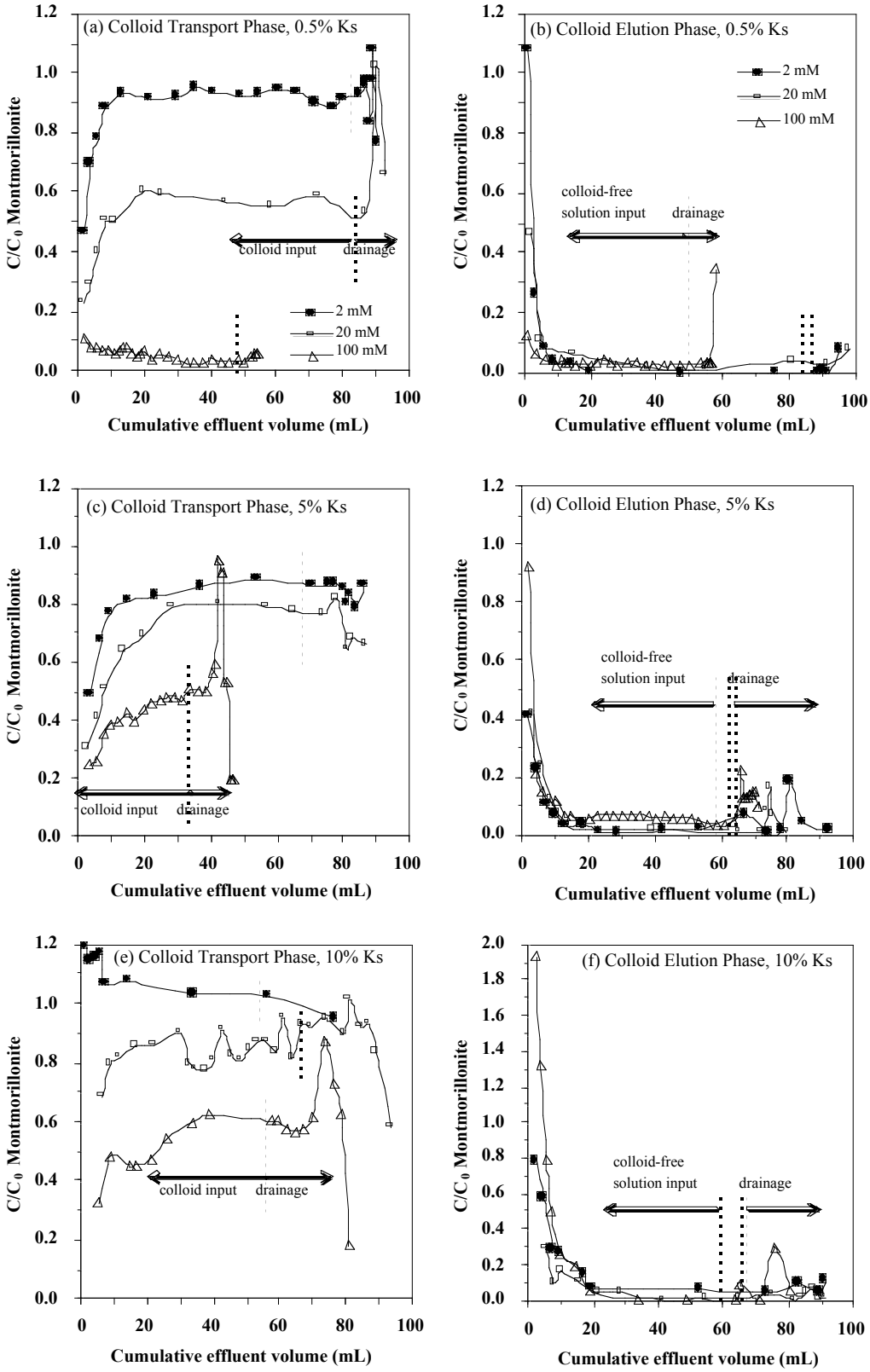

Figure 3. Effects of ionic strength and flux rate on mobilization of montmorillonite colloid silica sand under unsaturated transient flow condition

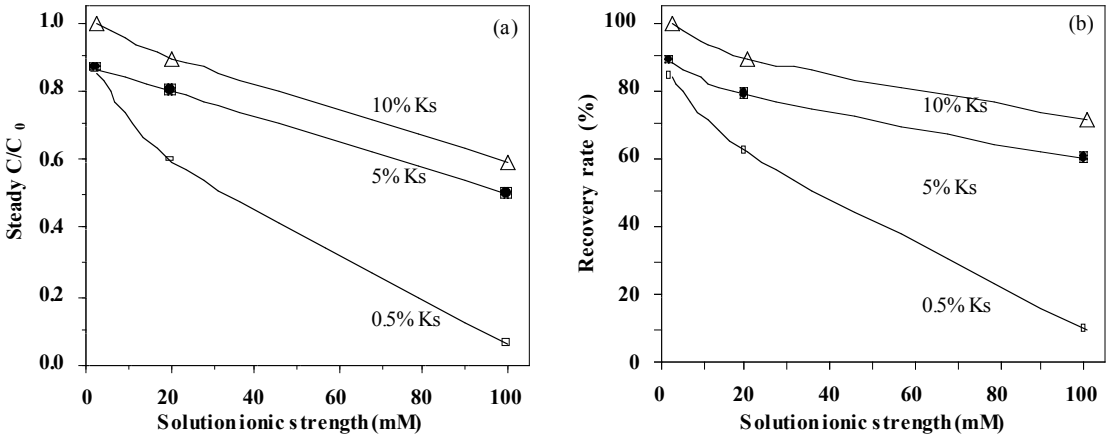

Figure 4. Interdependence of ionic strength and flow rate in influencing transport of montmorillonite through the silica sand under unsaturated transient flow condition

Resistance of Silicate Minerals to Alkaline Waste Simulants

Youjun Deng[1,*], Hongting Zhao[2], Kholoud Mashal[3], James B. Harsh[1], Markus Flury[1], and Jeffrey Boyle[1]

[1]Department of Crop and Soil Sciences, Center for Multiphase Environmental Research, Washington State University, Pullman, WA 99164-6420

[2]Current address: Sandia National Laboratories, MS-0779, Albuquerque, NM 87185

[3]Current address: The Hashemite University, The Institute of Land, Water and Environment, Department of Land Management, Zarqa 13115, Jordan

[*]Corresponding author:

Youjun Deng

Department of Crop and Soil Sciences

Washington State University

Pullman, WA 99164-6420

Phone: 1-509-335-9692

Fax: 1-509-335-8674

E-mail: yjdeng@mail.wsu.edu

ABSTRACT

Silicate minerals exposed to highly-alkaline solutions from high-level radioactive waste leaks have different dissolution resistance. Selective dissolution of the minerals will influence the solution chemistry and the precipitation of new solid phases, which can alter the sorption and transport of contaminants present in the wastes. The objective of this study was to elucidate the relative dissolution resistance of common silicate minerals in highly-alkaline and saline solutions that have chemical compositions similar to the high-level radioactive wastes at the US Department of Energy, Hanford Site, Washington. The mineral resistance to caustic solutions was predicted based on solution compositions and solubility product constants. The predictions were compared to experimental observations obtained from a Hanford fine sand and several model minerals (muscovite, biotite, smectite, illite, vermiculite, and chlorite) reacted with simulated tank wastes (STW). Reacted sediments and model minerals were characterized with scanning electron microscopy, X-ray diffraction, and Fourier transform infrared spectroscopy. Theoretical predictions and experimental observations indicate that quartz was the most labile mineral in the alkaline solutions. Amphibole, pyroxene, and chlorite were the most stable phases. The relative resistance of the minerals in the alkaline solutions increased in the following order: quartz < kaolinite < smectite < illite < vermiculite < mica < feldspars < chlorite, amphiboles, pyroxenes. This order is nearly opposite to the resistance of the minerals in soils under well-drained conditions. The relative resistance revealed that the major dissolving minerals are Si-rich quartz and fine-sized clay minerals. This information is useful for understanding the interaction between alkaline tank wastes and the underlying sediments and for accurately predicting the fate of leaking nuclear wastes.

INTRODUCTION

Silicates are major minerals in most soils and sediments. Their resistance and weathering sequence under well-drained conditions at a natural pH (4.5–8.2) have been extensively studied and are well known (e.g., Jackson and Sherman, 1953; Allen and Hajek, 1989). Sometimes, these minerals are exposed to highly alkaline solutions (pH>10) in either a constrained environment or under special anthropogenic conditions. The dissolution resistance of silicate minerals to highly alkaline solutions is different from their resistance to weathering in most soils and sediments. The resistance difference will result in selective dissolution of the minerals and formation of new minerals. The changes in surface properties of the sediment minerals along with the formation of new mineral phases can alter the sorption and transport of heavy metals, radionuclides, organics, and other contaminants.

Wastes generated during uranium processing and plutonium extraction at the US Department of Energy (DOE) Hanford Site, Washington, were stored in underground tanks. Many of these storage tanks have leaked, and more than 3800 m^3 of high-level radioactive wastes have leaked into the vadose zone (Gephart and Lundgren, 1998). The waste solutions had high pH (as high as 15), high ionic strength (could be saturated with respect to $NaNO_3$ and $NaNO_2$), and high aluminate concentration (>0.1 M) (Serne et al., 1998). Numerous simulation experiments have shown that silicate minerals can be dissolved by the caustic tank leaks and new silicate solids, including cancrinite, sodalite, and Linde Type A zeolite, formed (e.g., Kaplan et al., 1998; Serne et al., 1998; Bickmore et al., 2001; McKinley et al., 2001; Chorover et al., 2003; Kaplan et al., 2003; Qafoku et al., 2003a,b, 2004; Zhao et al., 2004; Mashal et al., 2004, 2005a,b; Choi et al., 2005a,b; Um et al., 2005). These simulation experiments focused on the solution chemistry or the new mineral phases, but little is known

about the relative dissolution resistance of various minerals of the sediments to the alkaline wastes.

Quartz is partially dissolved by solutions in the pH range of 13 to 14 at about 90 °C and cancrinite formed on the surfaces of quartz (Bickmore et al., 2001; Um et al., 2005). Kaolinite is also vulnerable to dissolution by alkaline simulants and converted to cancrinite and sodalite (e.g., Chorover et al., 2003; Zhao et al., 2004). Smectite dissolved much slower than kaolinite (Bauer and Berger, 1998); but, like kaolinite, smectite has been used as a silicate source to form various zeolites at high pH (e.g., Breck, 1974), therefore, smectite dissolves appreciably in alkaline solutions. Biotite appeared to be more resistant to alkaline solutions than quartz and kaolinite because the concentration of dissolved silicate from biotite was not high enough to form new crystalline phases (Samson et al., 2005). Bauer et al. (1998) observed that illite and K-feldspar formed in alkaline solutions at the expense of kaolinite, implying that illite and K-feldspar are stable or metastable in the alkaline solutions. Anorthite (a Ca-feldspar) could be dissolved by high alkaline solutions, but the dissolution was much less than that of a sediment taken from the Hanford Site (Shade, 1974), suggesting that anorthite was much less soluble than some minerals in the sediment.

Temperature is critical in the dissolution of silicate minerals. For example, Choquette et al. (1991) investigated the dissolution of quartz, feldspars (oligoclase, labradorite, and microcline), biotite, chlorite, amphiboles (hornblende and actinolite), and pyroxenes (diopside and augite) at 23 and 80 °C. From scanning electron microscopy (SEM) observation, they found that none of the tested rock-forming silicate minerals were dissolved by 1 M NaOH solution at 23 °C even after 265 days of reaction. However, distinct surface etching was observed on quartz and some feldspars within seven days at 80 °C, and potassium depletion

from biotite was observed. They also observed that amphiboles, pyroxenes, and chlorite did not react with the alkaline solutions even at the elevated temperature. Increasing temperature and alkalinity increased the dissolution rate of kaolinite and nearly complete dissolution was achieved at 80 °C after 8 weeks of reaction with simulants containing 1.4 or 2.8 molal NaOH (Zhao et al., 2004).

Chemical compositions of alkaline solutions after reacting with sediments can be used to deduce dissolution information about minerals. According to Mashal et al. (2004), when simulants containing 1.4 or 2.8 molal NaOH and 0.125 or 0.25 molal $Al(OH)_4^-$ reacted with a Hanford sediment for 40 days at 50 °C, the major chemical composition changes can be summarized as follows: (1) the concentration of dissolved silicate steadily increased to 0.2–0.3 molal; (2) aluminate was depleted to about 0.0008 molal; (3) the concentration of dissolved K^+ reached 0.03 molal; (4) the concentration of Ca^{2+} and Mg^{2+} were three to four orders of magnitude lower than that of K^+; and (5) the concentration of Fe was about one order of magnitude lower than that of K^+. Similar concentration changes in Si, Al, K, and Fe were reported by Qafoku et al. (2003b). These chemical composition data suggest that the major dissolving minerals in the sediment are Si-rich phases, presumably quartz. The data also suggest some K-bearing minerals were dissolved. The dissolution of Ca- or Mg-bearing minerals cannot be analyzed from the chemical composition of the solution because precipitation of $Ca(OH)_2$ and $Mg(OH)_2$ may control the concentrations of Ca^{2+} and Mg^{2+}.

It is expected that the relative dissolution resistance is controlled by both the thermodynamic stability and the kinetics of dissolution. In natural sediments and soils, minerals rarely reach equilibrium with respect to one another. We expect similar non-equilibrium or pseudo-equilibrium would occur under alkaline conditions. Those minerals that are farthest

from equilibrium with respect to the alkaline solutions are hypothesized to be the most labile. Minerals that are more stable in sediments and soils might be less resistant to the alkaline solutions. The objective of this study was to elucidate the relative dissolution resistance of common silicate minerals in alkaline solutions that have chemical composition similar to high-level radioactive wastes at the Hanford Site, Washington.

MATERIALS AND METHODS

Experimental approaches

We studied, both theoretically and experimentally, the dissolution resistance of common silicate minerals in alkaline solutions. We calculated (1) the theoretical equilibrium activities of silicate and aluminate of common silicate minerals in simulated tank waste that has reacted with the Hanford sediment and (2) the saturation indices of four simulants with respect to the common silicate minerals in the sediment. We also compared the predicted resistance with observations made on a Hanford sediment and several model minerals. In the simulation experiments, we used two strategies to simplify the comparison. One approach was to fractionate the reacted sediment samples according to particle size and density, the other one was to use model minerals with impurities.

Theoretical prediction of relative stability of silicate minerals in alkaline solutions

To predict the relative stability of common silicate minerals in alkaline solutions, activity diagram of the minerals were constructed. Because the major chemical composition changes in the reacting simulants are the enrichment of silicate and depletion of aluminate, the re-

lationship between soluble silicate and aluminate was our main concern. As many sediment minerals such as amphiboles, pyroxenes, and feldspars have varying chemical compositions and different solubilities, we used ideal minerals in the calculations. Tremolite was used to represent amphibole, diopside to represent pyroxenes, anorthite to represent Ca-feldspars (Table 1). $< Table\ 1 >$

Based on the supernatant compositions of four simulants (STW1-STW4) reacted with a Hanford sediment at 50 °C for 40 days (Mashal et al., 2004), we used the GMIN chemical equilibrium model to calculate the activities of aqueous species (Felmy, 1995; Mashal et al., 2004). For the activity diagram construction, the activities of the major species except silicate and aluminate were fixed to the calculated values from measured concentrations of the species in reacted simulant STW4. We assumed that the activity of Mg^{2+} was at equilibrium with $Mg(OH)_2$; and Fe^{3+} with $Fe(OH)_3$. These assumptions appeared to be valid because $Mg(OH)_2$, and $Fe(OH)_3$ have been observed in simulation experiments (Choquette et al., 1991; Deng et al., 2006a). Our calculations suggest that, in pH 13-14 solutions, $H_2SiO_4^{2-}$ is the dominant silicate species in the observed Si concentration range (<0.4 molar) (Qafoku et al., 2003b; Mashal et al., 2004) and $Al(OH)_4^-$ is the dominant aluminum species, and therefore, only the activities of $H_2SiO_4^{2-}$ and $Al(OH)_4^-$ were used in the activity diagram. In Table 1, the saturation indices (SI) of the supernatants with respect to each silicate mineral phase were normalized as

$$\frac{\log_{10} SI}{N} = \frac{\log_{10}(IAP/k)}{N} \tag{1}$$

where IAP is the ion activity product, k is the equilibrium constant (solubility product), and N is the total number of ions in the dissolution reaction (Mashal et al., 2004).

According to the transition state theory (e.g., Lasaga, 1981; Aagaard and Helgeson,

1982; Devidal et al., 1997), mineral dissolution rate depends on the saturation index when the solution is close to saturation with respect to the mineral. When the dissolution reactions are written as in Table (1), the net dissolution rate r of a mineral is determined by its forward (dissolution) rate $\overrightarrow{r}$ and chemical affinity A

$$r = \overrightarrow{r}\left[1 - e^{(-\frac{A}{\sigma RT})}\right] \tag{2}$$

where σ is the average stoichiometric number, which is equal to the ratio of destruction rate of an intermediate activated complex relative to the overall dissolution rate; R is the universal gas constant; T is temperature in Kelvin; and A is the chemical affinity defined as

$$A = \ln \frac{IAP}{k} = 0.434 \log_{10}(SI) \tag{3}$$

Equation (2) suggests that when a solution is far from saturation with respect to the mineral [$\log_{10}(SI) << 0$], the net dissolution rate of a mineral should be independent of the saturation index, and $r \approx \overrightarrow{r}$; but when the solution is close to the saturation [$\log_{10}(SI) \approx 0$], the net dissolution rate should be proportional to the chemical affinity and $\log_{10}(SI)$, and

$$r \approx \overrightarrow{r}\left[\frac{A}{\sigma RT}\right] \propto \overrightarrow{r} \log_{10}(SI) \tag{4}$$

Therefore, a mineral should be more resistant, i.e. dissolves more slowly, when the solution is close to equilibrium with the mineral.

Sediment and model minerals

A sediment sample and several model minerals were reacted with alkaline simulants. The sediment sample was a silty fine sand sediment from the Hanford Formation and was taken from a trench wall at the Submarine Site 218-E-12B at the DOE Hanford Site. A detailed

description of the sediment is given by Serne et al. (2002). The sand and silt fractions of the sediment consisted of quartz (nearly 80% wt), plagioclase feldspar, K-feldspar, mica (biotite and muscovite), chlorite, amphibole, and iron oxide (magnetite); the clay fraction, of smectite, chlorite, mica/illite, kaolinite, quartz, and trace amounts of other minerals (Table 2). The sediment sample was air dried and the <2 mm fraction was collected after passing through a sieve. < *Table* 2 >

Reaction of the sediment and model minerals with alkaline simulants

Four simulated tank wastes (STW) (Table 3) were prepared according to Mashal et al. (2004). One hundred gram of a Hanford fine sand sediment or 10 g of model minerals were mixed with each simulant solution in a 250 mL Nalgene polypropylene bottle. The simulant was reacted with the sediment for one month at 80 °C and with the model minerals for up to three months at 50 °C or 80 °C. After reacting with the simulants, the sediments and model minerals were separated by centrifugation. Excess electrolytes in the samples were removed by dialysis against deionized water. The reacted sediment samples were further fractionated as follows: the 50–2000 μm sand fraction was separated with a sieve; and the 2–50 μm silt fraction and <2 μm clay fraction were separated by sedimentation. Light (<2.97 g cm^{-3}) and heavy (>2.97 g cm^{-3}) minerals of the sand fractions were separated by suspending the sands in 1,1,2,2-tetrabromoethane (density=2.967 g cm^{-3}) using a procedure similar to that described by Cady et al. (1986). Magnetic minerals were collected with a hand magnet. The solid samples were dried at 80 °C. < *Table* 3 >

Characterization of reacted sediments and model minerals

Scanning electron microscopic (SEM) imaging and X-ray diffraction (XRD) analysis were conducted for each of the reacted sediments and the model minerals. Micrograph imaging was performed on a Hitachi S-570 SEM , energy dispersive spectra were recorded on a FEI Sirion field emission SEM, and powder XRD were collected on a Philips XRG 3100 diffractometer (Philips Analytical Inc., Mahwah NJ, USA). Fourier transform infrared (FTIR) analysis was conducted for the clay fractions of the sediment samples on a Perkin Elmer Spectrum GX FTIR System. For FTIR, 1 mg clay was mixed with 100 mg KBr and the mixture was pressed into a pellet. The FTIR spectra were recorded with the transmission mode and a resolution of 1 cm^{-1}.

RESULTS AND DISCUSSION

Predicted stability from saturation indices and activity diagram

Most of the saturation indices of minerals in the four supernatants (Table 1) are negative, indicating that the solutions were undersaturated with respect to most of the minerals such as quartz, kaolinite, feldspars (albite, anorthite, K-feldspar), and smectite; and therefore, these minerals should be dissolved. However, the solutions were oversaturated with respect to chlorite, tremolite, diopside and these minerals should be stable. The saturation indices of the solution with respect to mica and vermiculite are close to zero, suggesting mica and vermiculite should be stable in the solutions too. The activity diagram (Fig. 1) reveals that: (1) the solubility of most minerals, such as quartz, kaolinite, feldspars (anorthite, albite, K-feldspar), mica (muscovite), and illite, in alkaline simulant solutions are higher than that of cancrinite and sodalite, suggesting these silicate phases should dissolve and convert to

cancrinite and sodalite; (2) chlorite, tremolite (an amphibole), and diopside (a pyroxyene) are less soluble than cancrinite and sodalite, implying they should be the most resistant phases in the alkaline solutions. (3) it is impossible for all of the mineral phases to reach equilibrium with respect to one another; (4) at different aluminate activities. e.g., during the aluminate depletion process as observed in the simulation experiments, the relative stability of minerals would differ: at high aluminate activities [e.g., $\log_{10}\left(\mathrm{Al(OH)}_4^-\right) > -1$], the solubilities of the minerals fall in the order: quartz > kaolinite > illite > albite, K-feldspar > smectite > anorthite > vermiculite > muscovite > tremolite > diopside > chlorite; at low aluminate activities, [e.g., $\log_{10}\left(\mathrm{Al(OH)}_4^-\right) < -5$], the solubilities are: kaolinite > illite > anorthite > muscovite > quartz >albite, K-feldspar > vermiculite > chlorite > tremolite > diopside; (5) if the supernatant was at equilibrium with quartz (the dominant mineral in the sediment), the calculated silicate activity would be 1.8, which is 2.5 orders of magnitude higher than the calculated activities from measured concentrations, suggesting that the reacted alkaline solutions were undersaturated with respect to quartz; (6) the cancrinite and sodalite lines nearly overlap with each other, this might be why they often coexist in many alkaline solutions reported (e.g., Chorover et al., 2003; Qafoku et al., 2003a, 2004; Zhao et al., 2004; Mashal et al., 2004, 2005a,b; Choi et al., 2005b; Um et al., 2005; Deng et al., 2006a,b). Most of the mineral resistances deduced from the saturation indices and the activity diagram are consistent with the observations made in simulation experiments. Quartz (Bickmore et al., 2001; Um et al., 2005), kaolinite (Chorover et al., 2003; Zhao et al., 2004), and smectite (Bauer and Berger, 1998) dissolved appreciably but biotite (Samson et al., 2005), amphibole, pyroxene, and chlorite (Choquette et al., 1991) did not. The stability of feldspars appears to be under-estimated by the activity diagram; this might be the result of its slow dissolution

rate $\overrightarrow{r}$. < *Fig.* 1 >

Dissolution of Hanford Sediment

Size fraction analysis (Table 4) indicates that, after the sediment reacted with the simulants, the content of the clay fraction increased while the content of the sand fraction decreased, yet the texture of the sediment was not changed. After reacting with the simulants, the color of the sediment did not show distinct changes. The unreacted and reacted sediment were light brownish gray with a Munsell color index of 2.5Y 6/2.5-2.5Y 7/2.5, suggesting no significant quantities of iron oxide formed in the sediments. All minerals identified in the unreacted sediment remained in the reacted sediments. New minerals, cancrinite and sodalite, were found in the clay fraction. < *Table* 4 >

Sand and Silt Fractions

Our XRD analysis indicates that the mineral compositions of the sand and silt fractions were not dramatically altered by the caustic waste solutions. Every mineral identified in the sand fraction of the unreacted sediment remained in the reacted sediment samples. There was little difference in the mineral compositions among the sediment samples reacted with the four simulants (STW1 to STW4). Light minerals (<2.97 g cm^{-3}) accounted for 91 to 94% weight of the sand fraction. As identified by XRD analysis, the light minerals were quartz, mica (muscovite), and feldspars; and the heavy minerals (>2.97 g cm^{-3}) were mica (biotite), amphibole, pyroxene, chlorite, and iron oxide. Minor amounts (<0.5% by weight) of heavy magnetic minerals were present in the sand fractions of both the unreacted and reacted sediment samples.

When the sediment was reacted with STW4, the SEM micrographs showed distinct etching graves on surfaces of quartz particles (Fig. 2a) and some etching along the edges of K-bearing minerals (muscovite, Fig. 2b), but very little or no etching on the surfaces of plagioclase (Na, Ca-feldspars, Fig. 2c,d) in the light sand fraction. No distinct etching marks were found on surfaces of any heavy minerals in the sand fraction (Fig. 2e,f). Mineral phases in the micrographs were identified with energy dispersive X-ray spectra (Figs. 3). Similar morphological changes and stability were also observed on the sediments reacted with simulants STW1, STW2, and STW3 (images not shown). The morphological observation is consistent with the reported resistances of quartz (Bickmore et al., 2001; Um et al., 2005), amphibole, pyroxene (Choquette et al., 1991), and Ca-feldspar anorthite (Shade, 1974) in alkaline solutions. < *Fig.* 2 >
< *Fig.* 3 >

The same mineral phases as in the sand fractions were also identified in the silt fractions of the unreacted and the reacted sediments by XRD analysis (data not shown). Microscopic examination showed that quartz was the most labile mineral as indicated by its etching graves on surfaces; no distinct etching marks were found on surfaces of Ca-containing minerals. Heavy minerals (amphiboles, pyroxenes, and chlorite) were the most stable phases. This observation is consistent with the prediction based on the saturation index (Table 1) and activity diagram (Fig. 1).

Clay Fraction

Minerals in the clay fraction of the unreacted Hanford sediment were mica (illite), chlorite, smectite, quartz, and feldspars as identified by XRD analysis (Fig. 4) and kaolinite by FTIR analysis (Fig. 5). After reacting with the simulants, all these mineral phases remained while

cancrinite and sodalite formed. Although it was difficult to quantify the mass change of each mineral, it is evident from the relative peak heights of XRD and FTIR spectra that smectite, kaolinite, and quartz concentrations decreased. Dissolution of clay minerals resulted in distinct morphological changes: the unreacted clay particles showed dominant platy morphology and the reacted clay particles showed aggregates formed from needle- or grain-shaped particles (cancrinite and sodalite) (Fig. 6). It appears that the alkalinity of the simulants determined the dissolution rate of the minerals. The FTIR spectra (Fig. 5) suggest that more kaolinite (3696 cm^{-1} and 3620 cm^{-1} bands) and quartz (798 and 778 cm^{-1} bands) were dissolved when NaOH concentration was increased from 1.4 to 2.8 molal. The XRD and FTIR analyses revealed that more smectite, kaolinite, and quartz were dissolved when the alkalinity was increased. Our results and those reported in the literature consistently show that the clay-sized quartz, kaolinite (Chorover et al., 2003; Zhao et al., 2004), and smectite (Bauer and Berger, 1998) are labile to the alkaline solutions.

< *Fig.* 4 >
< *Fig.* 5 >
< *Fig.* 6 >

Dissolution of Model Minerals

The model minerals had different dissolution resistance to the caustic simulants. Mica, chlorite, and vermiculite were more resistant than smectite and illite. The XRD analysis indicates that model minerals muscovite, biotite, vermiculite, and chlorite were well preserved in simulant STW4. Their XRD patterns did not show distinct changes after reacting with the simulant and no new crystalline phases were detected by XRD (Fig. 7). Any changes in the morphologies of reacted muscovite, biotite, vermiculite, and chlorite were indiscernible from the original minerals (Fig. 8). Likewise, no changes could be discerned by XRD and SEM analyses following reaction with the other three simulants (STW1-STW3).

< *Fig.* 7 >
< *Fig.* 8 >

Smectite and illite were less resistant. The XRD analysis revealed that cancrinite and sodalite formed at the expense of these minerals (Fig. 9), suggesting they served as the Si and Al source for the new mineral phases. The SEM micrographs (Fig. 10) indicates that cancrinite and sodalite were much smaller than the original clay minerals. The relative abundance of cancrinite and sodalite to the original minerals in the 2.8 molal OH^- simulants were higher than those in the 1.4 molal OH^- simulants, suggesting that the dissolution of the original minerals increased with increasing alkalinity. Increasing temperature from 50 °C to 80 °C also promoted dissolution of the original minerals and the formation of cancrinite and sodalite (e.g., the SWy smectite in Fig. 9). < *Fig.* 9 >

< *Fig.* 10 >

The XRD analysis revealed that the quartz present in SWy-1 was completely dissolved, but mica survived in the alkaline solutions (Fig. 9), suggesting the resistance order of the three minerals were: quartz < smectite < mica. Both quartz and illite in the illite sample were only partly dissolved by the alkaline solutions. The observations with the model minerals suggest that the overall resistance order of the minerals were: quartz < smectite < illite < vermiculite < muscovite, biotite, chlorite.

Observed and predicted mineral stabilities

By and large, the observed relative resistance of the minerals agreed well with the prediction based on the activity diagram (Fig. 1): quartz, kaolinite, and smectite were less resistant than mica and chlorite. The observed and predicted resistance of the minerals agree well with those reported in the literature (Shade, 1974; Choquette et al., 1991; Bauer and Berger, 1998; Bickmore et al., 2001; Chorover et al., 2003; Zhao et al., 2004; Um et al., 2005). The activity diagram (Fig. 1) shows that not all of the minerals can reach equilibrium with re-

spect to one another and most of them should convert to cancrinite. The experimental results with the Hanford sediment suggest that none of the minerals were completely dissolved. It is unlikely that complete dissolution will occur because the solution, over time, becomes saturated or oversaturated with respect to many other minerals. If Al is depleted by cancrinite/sodalite formation, high-concentration Si will remain in solution, thereby, preventing further dissolution of Si-rich minerals.

CONCLUSIONS

Based on results reported in the literature, our experimental observations with model and sediment minerals, and the theoretical predictions, we conclude that the relative resistance and dissolution sequence of quartz and silicate minerals in highly-alkaline solutions are, by and large, opposite to the order of their resistance and weathering sequence in natural soils under well-drained conditions. The dissolution resistance of the mineral in highly-alkaline solutions increased with the following order: quartz $<$ kaolinite $<$ smectite $<$ illite $<$ vermiculite $<$ mica $<$ feldspars $<$ chlorite, amphiboles, pyroxenes. As in natural soils and sediments, kinetics plays an important role in the dissolution, almost none of the silicate minerals reached equilibrium with the alkaline solutions. Our data help to understand mineral dissolution and precipitation reactions that occur when Hanford tank waste or other highly alkaline solutions leak into the subsurface.

ACKNOWLEDGEMENTS

This work was supported by the Environmental Management Science Program, U.S. Department of Energy under contract DE-FG07-99ER62882. We thank the Electron Microscopy

Center and the Department of Geology at Washington State University for the use of SEM and FTIR equipments. We thank Dr. Andrew R. Felmy of Pacific Northwest National Laboratory for allowing using the activity data in the calculation of saturation indices (Table 1).

REFERENCES

Aagaard, P., and H.C. Helgeson. 1982. Thermodynamic and kinetic constraints on reaction rates among minerals and aqueous solutions. i. theoretical considerations. Am. J. Sci. 282:237–285.

Allen, B.L., and B.F. Hajek. 1989. Mineral occurrence in soil environments. p. 199–278., *In* J.B. Dixon and S.B. Weed (ed.), Minerals in Soil Environments, 2 ed. Soil Science Society of America, Madison, Wisconsin, USA.

Bauer, A., and G. Berger. 1998. Kaolinite and smectite dissolution rate in high molar KOH solutions at 35° and 80°C. Appl. Geochem. 13:905–916.

Bauer, A., B. Velde, and G. Berger. 1998. Kaolinite transformation in high molar KOH solutions. Appl. Geochem. 13:619–629.

Bickmore, B.R., K.L. Nagy, J.S. Young, and J.W. Drexler. 2001. Nitrate-cancrinite precipitation on quartz sand in simulated Hanford tank solutions. Environ. Sci. Technol. 35:4481–4486.

Breck, D.W. 1974. Zeolite Molecular Sieves: Structure, Chemistry, and Use. John Wiley, New York.

Cady, J.G., L.P. Wilding, and L.R. Drees. 1986. Petrographic microscope techniques. p. 185–218., *In* A. Klute (ed.), Methods of Soil Analysis: Part 1, Physical and Mineralogical Methods. SSSA Book Series, No. 5, 2nd ed. Soil Science Society of America, Inc., Madison, Wisconsin, USA.

Chipera, S.J., and D.L. Bish. 2001. Baseline studies of the Clay Minerals Society source clays: powder X-ray diffraction analyses. Clays Clay Miner. 49:398–409.

Choi, S., M.K. Amistadi, and J. Chorover. 2005a. Clay mineral weathering and contaminant dynamics in a caustic aqueous system I. Wet chemistry and aging effects. Geochim. Cosmochim. Acta 69:4425–4436.

Choi, S., G. Crosson, K.T. Mueller, S. Seraphin, and J. Chorover. 2005b. Clay mineral weathering and contaminant dynamics in a caustic aqueous system II. Mineral transformation and microscale partitioning. Geochim. Cosmochim. Acta 69:4437–4451.

Choquette, M., M.A. Berubé, and J. Locat. 1991. Behavior of common rock-forming minerals in a strongly basic sodium hydroxide solution. Can. Mineral. 29:163–173.

Chorover, J., S. Choi, M.K. Amistadi, K.G. Karthikeyan, G. Crosson, and K.T. Mueller. 2003. Linking cesium and strontium uptake to kaolinite weathering in simulated tank waste leachate. Environ. Sci. Technol. 37:2200–2208.

Deng, Y., M. Flury, J.B. Harsh, and J.S. Young. 2006a. Cancrinite and sodalite formation in the presence of cesium, potassium, magnesium, calcium, and strontium in Hanford tank waste simulants. Appl. Geochem. (in revision).

Deng, Y., J.B. Harsh, M. Flury, J.S. Young, and J.S. Boyle. 2006b. Mineral formation during simulated leaks of Hanford waste tanks. Appl. Geochem. (in revision).

Devidal, J.L., J. Schott, and J.L. Dandurand. 1997. An experimental study of kaolinite dissolution and precipitation kinetics as a function of chemical affinity and solution composition at 150 degrees c, 40 bars, and ph 2, 6.8, and 7.8. Geochim. Cosmochim. Acta 61:5165–5186.

Felmy, A.R. 1995. GMIN, a computerized chemical equilibrium program using a constrained minimization of the Gibbs free energy: summary report. p. 377–407., *In* Chemical Equilibrium and Reaction Models, No. SSSA Special Publication 42. Soil Science Society of America, Inc., Madison, Wisconsin.

Gephart, R.E., and R.E. Lundgren. 1998. Hanford Tank Cleanup: A Guide to Understanding the Technical Issues. Battelle Press, Columbus, 4th ed.

Jackson, M.L., and G.D. Sherman. 1953. Chemical weathering of minerals in soils. Adv. Agron. 5:219–318.

Kaplan, D.I., K.E. Parker, and J.C. Ritter. 1998. Effects of Aging Quartz Sand and Hanford Sediment with Sodium Hydroxide on Radionuclide Sorption Coefficients and Sediment Physical and Hydrologic Properties: Final Report for Substask 2a. Pacific Northwest National Laboratory, PNNL-11965, Richland, Washington.

Kaplan, D.I., R. Serne, J. Schefer, R.M. Lindstrom, K.E. Parker, A.T. Owen, D.E. McCready, and J.S. Young. 2003. The Influence of Glass Leachate on the Hydraulic, Physical, Mineralogical and Sorptive Properties of Hanford Sediment. Pacific Northwest National Laboratory, PNNL-14325, Richland, Washington.

Kittrick, J.A. 1971. Stability of montmorillonite: I. Belle Fourche and Clay Spur montmorillonites. Soil Sci. Soc. Am. Proc. 35:140–145.

Lasaga, A.C. 1981. Transition state theory. p. 135–169., *In* A.C. Lasaga and R.J. Kirkpatrick (ed.), Kinetics of Geochemical Processes. Reviews in Mineralogy and Geochemistry, No. 8. Mineralogical Society of America, Washington, D.C.

Lindsay, W.L. 1979. Chemical equilibria in soils. Wiley, New York.

Mashal, K., J.B. Harsh, and M. Flury. 2005a. Clay mineralogical transformations over time in Hanford sediments reacted with simulated tank waste. Soil Sci. Soc. Am. J. 69:531–538.

Mashal, K., J.B. Harsh, M. Flury, and A.R. Felmy. 2005b. Analysis of precipitates from reactions of hyperalkaline solutions with soluble silica. Appl. Geochem. 20:1357–1367.

Mashal, K., J.B. Harsh, M. Flury, A.R. Felmy, and H. Zhao. 2004. Colloid formation in Hanford sediments reacted with simulated tank waste. Environ. Sci. Technol. 38:5750–5756.

McKinley, J.P., C.J. Zeissler, J.M. Zachara, R.J. Serne, R.M. Lindstrom, H.T. Schaef, and R.D. Orr. 2001. Distribution and retention of ^{137}Cs in sediments at the Hanford Site, Washington. Environ. Sci. Technol. 35:3433–3441.

Park, H., and P. Englezos. 1999. Thermodynamic modeling of sodium aluminosilicate formation in aqueous alkaline solutions. Ind. Eng. Chemical Resorc. 38:4959–4965.

Parkhurst, D.L., and C. Appelo. 1999. Users guide to PHREEQC (version 2) a computer program for speciation, batch-reaction, one-dimensional transport, and inverse geochem-

ical calculations. Technical Report Water-Resources Investigations Report 99-4259, U.S. Department of the Interior, U.S. Geological Survey.

Qafoku, N.P., C.C. Ainsworth, J.E. Szecsody, D.L. Bish, J.S. Young, D.E. McCready, and O.S. Qafoku. 2003a. Aluminum effect on dissolution and precipitation under hyperalkaline conditions: II. Solid phase transformations. J. Environ. Qual. 32:2364–2372.

Qafoku, N.P., C.C. Ainsworth, J.E. Szecsody, and O.S. Qafoku. 2003b. Aluminum effect on dissolution and precipitation under hyperalkaline conditions: I. Liquid phase transformations. J. Environ. Qual. 32:2354–2363.

Qafoku, N.P., C.C. Ainsworth, J.E. Szecsody, and O.S. Qafoku. 2004. Transport-controlled kinetics of dissolution and precipitation in the sediments under alkaline and saline conditions. Geochim. Cosmochim. Acta 68:2981–2995.

Samson, S.D., K.L. Nagy, and W.B. Cotton III. 2005. Transient and quasi-steady-state dissolution of biotite at 22-25 °C in high pH, sodium, nitrate, and aluminate solutions. Geochim. Cosmochim. Acta 69:399–413.

Serne, R.J., B.N. Bjornstad, H.T. Schaef, B.A. Williams, D.C. Lanigan, D.G. Horton, R.E. Clayton, A.V. Mitroshkov, V.L. Legore, M.J. O'Hara, C.F. Brown, K. Parker, I.V. Kutnyakov, J.N. Serne, G.V.. Last, S.C. Smith, C.W. Lindenmeier, J.M. Zachara, and B. D. 2002. Characterization of Vadose Zone Sediment: Uncontaminated RCRA Borehole Core Samples and Composite Samples. Pacific Northwest National Laboratory, PNNL-13757-1, Richland, WA.

Serne, R.J., J.M. Zachara, and D.S. Burke. 1998. Chemical information on tank supernatants, Cs adsorption from tank liquids onto Hanford sediments, and field observations of Cs mi-

gration from past tank leaks. Technical Report PNNL-11498/UC-510, Pacific Northwest National Laboratory.

Shade, J.W. 1974. Reaction of Hanford sediments with synthetic waste: A reconnaissance study. Technical Report ARH-CD-176, Atlantic Richfield Hanford Company.

Um, W., R.J. Serne, S.B. Yabusaki, and A.T. Owen. 2005. Enhanced radionuclide immobilization and flow path modifications by dissolution and secondary precipitates. J. Environ. Qual. 34:1404–1414.

Xu, S., and J.B. Harsh. 1992. Alkali cation selectivity and surface charge of 2:1 clay minerals. Clays Clay Miner. 40:567–74.

Zhao, H., Y. Deng, J.B. Harsh, M. Flury, and J.S. Boyle. 2004. Alteration of kaolinite to cancrinite and sodalite by simulated Hanford tank waste and its impact on cesium retention. Clays Clay Miner. 52:1–13.

Table 1: Equilibrium constants used in activity diagram (Fig. 1) construction and the normalized saturation indices (SI) of four simulated tank waste solutions (STW1, STW2, STW3, STW4), which reacted with a Hanford sediment at 50 °C for 40 days, with respect common silicate minerals.

Component	Reactions	$\log_{10} k$	$\log_{10}(SI)/N$ [f]			
			STW1	STW2	STW3	STW4
Quartz	$SiO_2 + 2OH^- \rightleftharpoons H_2SiO_4^{2-}$	1.02[a]	-0.62	-0.78	-0.67	-0.79
Kaolinite	$Al_2Si_2O_5(OH)_4 + 6OH^- + H_2O \rightleftharpoons 2H_2SiO_4^{2-} + 2Al(OH)_4^-$	0.035[a]	-0.62	-0.86	-0.74	-0.86
Albite	$NaAlSi_3O_8 + 6OH^- + 2H_2O \rightleftharpoons Na^+ + Al(OH)_4^- + 3H_2SiO_4^{2-}$	-3.00[a]	-0.21	-0.37	-0.29	-0.37
Anorthite	$CaAl_2Si_2O_8 + 4OH^- + 4H_2O \rightleftharpoons Ca^{2+} + 2Al(OH)_4^- + 2H_2SiO_4^{2-}$	-9.71[a]	-0.39	-0.67	-0.55	-0.64
Diopside	$CaMgSi_2O_6 + 2H_2O \rightleftharpoons Ca^{2+} + Mg^{2+} + 2H_2SiO_4^{2-}$	-26.11[a]	1.61	1.32	1.47	1.38
Tremolite	$Ca_2Mg_5Si_8O_{22}(OH)_2 + 2OH^- + 6H_2O \rightleftharpoons 2Ca^{2+} + 5Mg^{2+} + 8H_2SiO_4^{2-}$	-99.43[a]	1.42	1.17	1.32	1.19
K-feldspar	$KAlSi_3O_8 + 6OH^- + 2H_2O \rightleftharpoons K^+ + Al(OH)_4^- + 3H_2SiO_4^{2-}$	-5.57[a]	-0.17	-0.32	-0.25	-0.33
K-mica	$KAl_3Si_3O_{10}(OH)_2 + 8OH^- + 4H_2O \rightleftharpoons K^+ + 3Al(OH)_4^- + 3H_2SiO_4^{2-}$	-12.40[a]	0.04	-0.17	-0.09	-0.17
Chlorite	$Mg_5Al_2Si_3O_{10}(OH)_8 + 4H_2O \rightleftharpoons 5Mg^{2+} + 2Al(OH)_4^- + 3H_2SiO_4^{2-} + 2OH^-$	-74.02[a]	1.06	0.82	0.94	0.82
Illite	$K_{0.6}Mg_{0.25}Al_{2.3}Si_{3.5}O_{10}(OH)_2 + 8.2OH^- + 3H_2O$ $\rightleftharpoons 0.6K^+ + 0.25Mg^{2+} + 2.3Al(OH)_4^- + 3.5H_2SiO_4^{2-}$	-5.97[a]	-0.43	-0.64	-0.54	-0.64
Smectite	$[(Si_{7.87}Al_{0.13})(Al_{3.03}Mg_{0.58}Fe(III)_{0.45})O_{20}(OH)_4]^{0.56-} + 17.66OH^-$ $+4.26H_2O \rightleftharpoons 3.16Al(OH)_4^- + 0.58Mg^{2+} + 0.45Fe(OH)_4^- + 7.87H_2SiO_4^{2-}$	-16.31[b]	-0.20	-0.40	-0.29	-0.40
Vermiculite	$K_{0.1}Ca_{0.06}Mg_{2.71}Fe(II)_{0.02}Fe(III)_{0.46}Al_{1.14}Si_{2.91}O_{10}(OH)_2 + 4.18H_2O$ $+1.86OH^- \rightleftharpoons 0.1K^+ + 0.06Ca^{2+} + 2.71Mg^{2+} + 0.02Fe^{2+} + 0.46Fe(OH)_4^-$ $+1.14Al(OH)_4^- + 2.91H_2SiO_4^{2-}$	-38.65[c]	0.18	-0.06	0.07	-0.07
Cancrinite	$Na_6Si_6Al_6O_{24} \cdot 2NaNO_3 \cdot 4H_20 + 8H_2O + 12OH^-$ $\rightleftharpoons 8Na^+ + 6Al(OH)_4^- + 6H_2SiO_4^{2-} + 2NO_3^-$	-36.2[d]	0.43	0.29	0.32	0.29
Sodalite	$Na_6Si_6Al_6O_{24} \cdot 2NaOH \cdot 2H_2O + 10H_2O + 10OH^-$ $\rightleftharpoons 8Na^+ + 6Al(OH)_4^- + 6H_2SiO_4^{2-}$	-36.64[e]	0.45	0.33	0.34	0.33
Portlandite	$Ca(OH)_2 \rightleftharpoons Ca^{2+} + 2OH^-$	-5.2[a]				
Brucite	$Mg(OH)_2 \rightleftharpoons Mg^{2+} + 2OH^-$	-11.16[a]				
$Fe(OH)_3$	$Fe(OH)_3 + 3H^+ \rightleftharpoons Fe^{3+} + 3H_2O$	3.54[c]				
Al^{3+}	$Al^{3+} + 4H_2O \rightleftharpoons Al(OH)_4^- + 4H^+$	-22.7[a]				
H_4SiO_4	$H_4SiO_4 \rightleftharpoons H_2SiO_4^{2-} + 2H^+$	-23.0[a]				

[a] according to Parkhurst and Appelo (1999); [b] calculated from Kittrick (1971); [c] calculated from Lindsay (1979);
[d] according to Bickmore et al. (2001); [e] according to the adjusted value of Park and Englezos (1999);
[f] calculated from the compositions of simulated tank wastes of Mashal et al. (2004).

Table 2: Mineral composition of Hanford sediment and model mineral samples.

Sample	Mineral Composition	Reference[d]
Hanford sediment[a]	Quartz, plagioclase, biotite, muscovite, chlorite, amphiboles, pyroxenes	Serne et al. (2002)
Biotite (Canada)[b]	Biotite	
Muscovite (North Carolina)[b]	Muscovite	
Vermiculite (South Africa)[b]	Vermiculite	Xu and Harsh (1992)
Chlorite (Michigan)[b]	Chlorite	
SAz[c]	Smectite, quartz, mica, feldspar	Chipera and Bish (2001)
SWy-1[c]	Smectite, quartz, mica	Chipera and Bish (2001)
Illite (Fithian, Illinois)[b]	Illite, quartz	

[a]Collected at the Hanford site, Washington;

[b] purchased from Ward's Natural Science Establishment, Inc. Rochester, New York

[c] purchased from Clay Minerals Society, current address: Purdue University, West Lafayette, Indiana

[d] references provide mineral characterization data

Table 3: Chemical composition of simulated tank waste (STW).

Simulant	NaOH	$NaAlO_2$	$NaNO_3$
	molal		
STW1	1.4	0.125	3.7
STW2	2.8	0.125	3.7
STW3	1.4	0.25	3.7
STW4	2.8	0.25	3.7

Table 4: Texture of sediment before and after reacting with four simulated tank wastes.

Simulant	Content (g kg^{-1})						Texture (USDA)
	Sand				Silt	Clay	
	Heavy (> 2.97 g cm^{-3})		Light (< 2.97g cm^{-3})	Total			
	Magnetic	Nonmagnetic					
Unreacted	3	52	645	700	273	28	Sandy loam
STW1	3	33	616	652	271	77	Sandy loam
STW2	3	51	568	623	307	70	Sandy loam
STW3	3	53	635	691	261	48	Sandy loam
STW4	4	55	590	649	279	73	Sandy loam

List of Figures

Figure 8. Scanning electron microscopy images of (a) biotite, (b) muscovite, (c) chlorite, and (d) vermiculite after reacting with STW4 for two months at 50 °C.

Figure 9. X-ray diffraction patterns of illite and smectites before and after reacting with STW4 for one month at 50 or 80 °C.

Figure 10. Scanning electron microscopy images of smectite (SWy-1) (a) before and (b) after reacting with STW4; and illite (c) before and (d) after reacting with STW4 for two months at 50 °C.

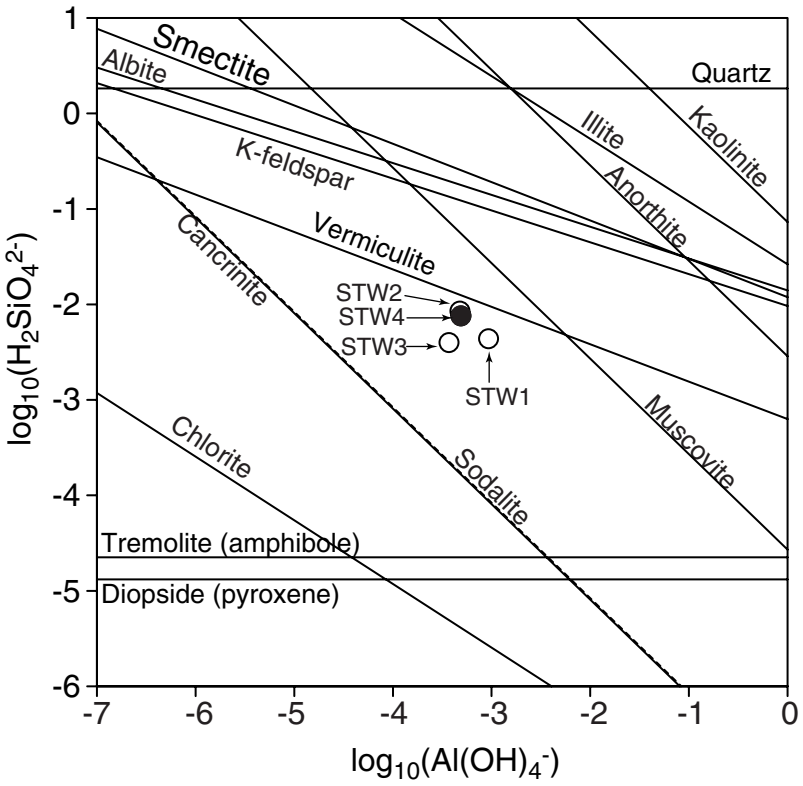

Figure 1: Activity diagram of silicate minerals in simulant STW4 (activities: H_2O, 0.92; H^+, 1.2×10^{-13}; Na^+, 1.61; Mg^{2+}, 7.5×10^{-11}; K^+, 0.013; Ca^{2+}, 5.1×10^{-7}; OH^-, 0.42; NO_3^-, 0.84). The calculated activities from measured concentrations of silicate and aluminate in four simulants (STW1 to STW4) are indicated with arrows.

1 ———————————————————————————————-

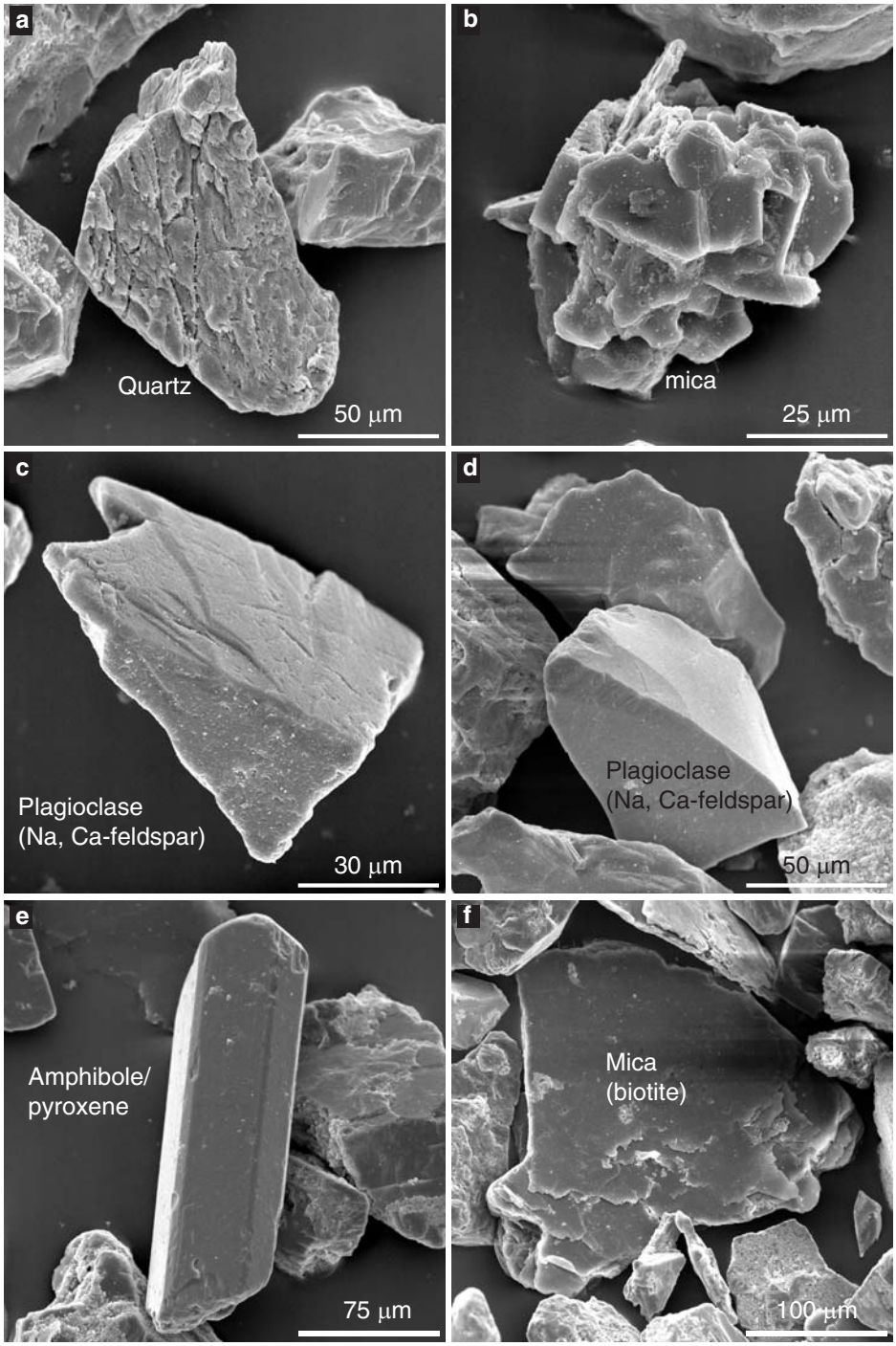

Figure 2: Scanning electron microscopy images of (a-d) light (<2.97 g cm^{-3}) and (e-f) heavy (>2.97 g cm^{-3}) minerals in sand fraction of the Hanford sediment reacted with STW4. (a) a quartz particle showing etched graves, (b) a K-containing mineral (mica or k-feldspar) showing etching along edges, (c) and (d) Ca-containing minerals (Ca-feldspar) showing weak or no etching on surfaces, (e) and (f) Ca-containing mineral (amphiboles and pyroxenes) were nearly unattacked.

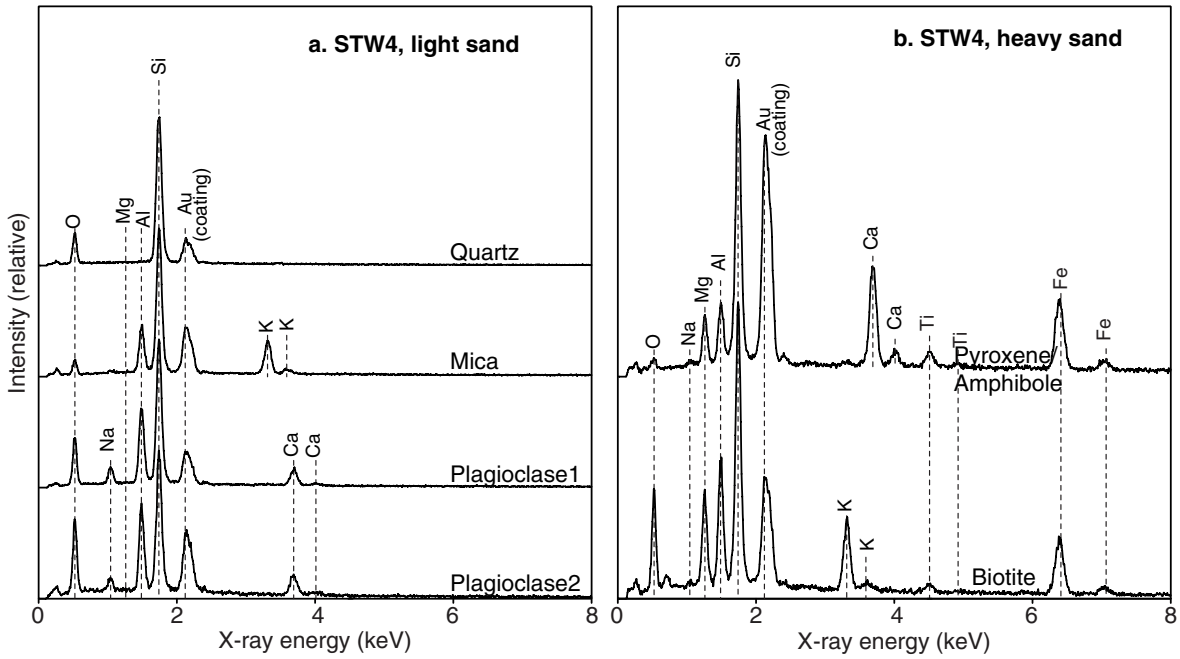

Figure 3: Energy dispersive X-ray spectra of (a) light minerals ($<$2.97 g cm^{-3}) and (b) heavy minerals ($>$2.97 g cm^{-3}) in sand fraction of the Hanford sediment reacted with STW4.

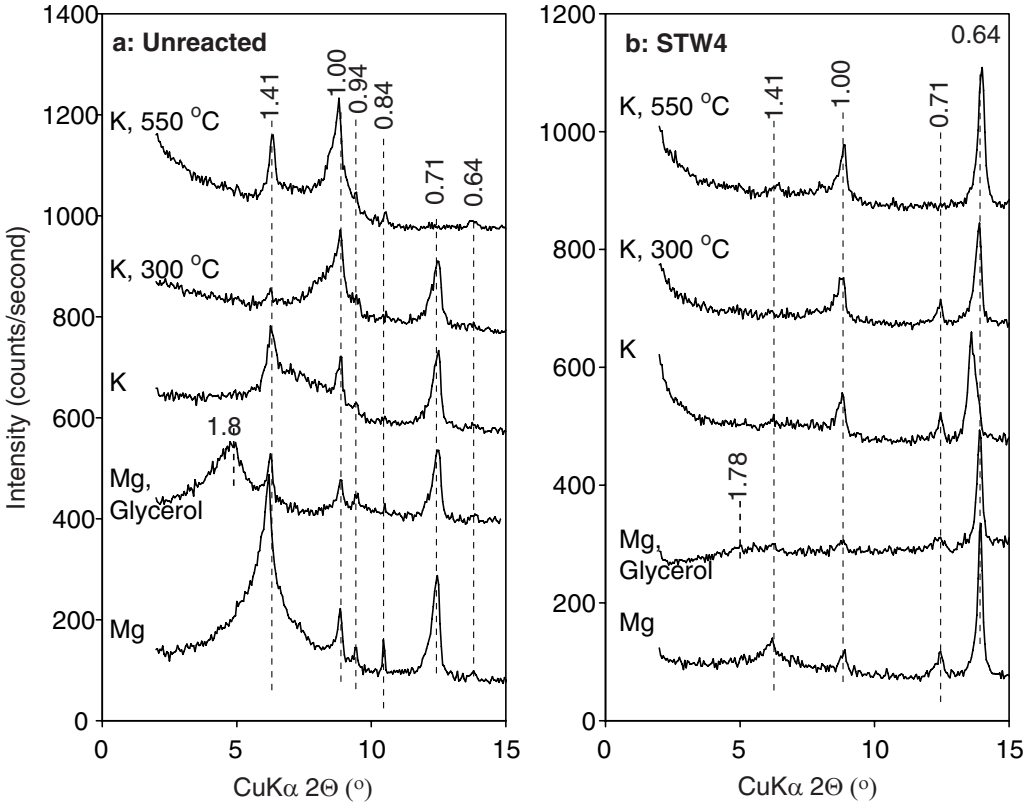

Figure 4: X-ray diffraction patterns of clay fractions of Hanford sediment before and after reacting with STW4. For XRD, the clays were exposed to Mg, K saturation, glycerol solvation, heat treatments as indicated in the graphs.

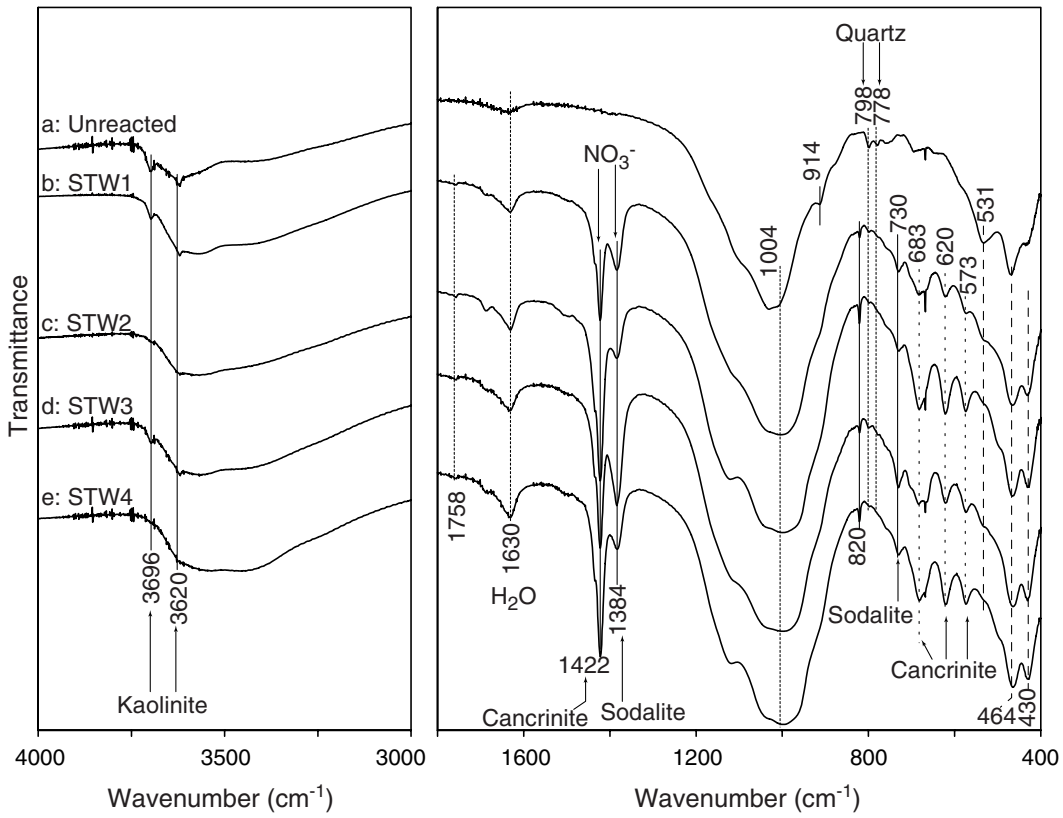

Figure 5: Fourier transform infrared spectra of the clay fractions of Hanford sediment before and after reacting with the simulated tank wastes.

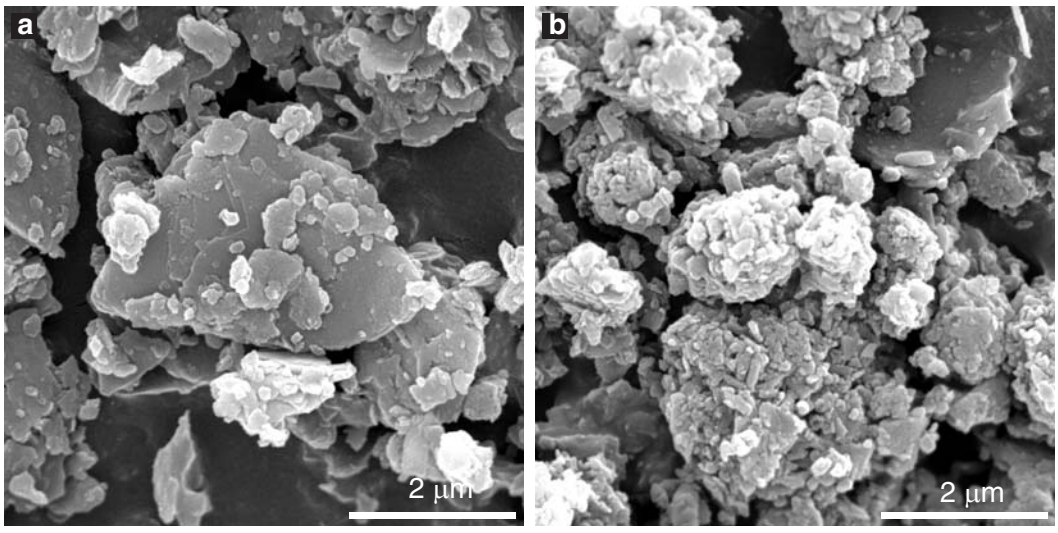

Figure 6: Scanning electron microscopy images of clay fractions of Hanford sediment (a) before and (b) after reacting with STW4.

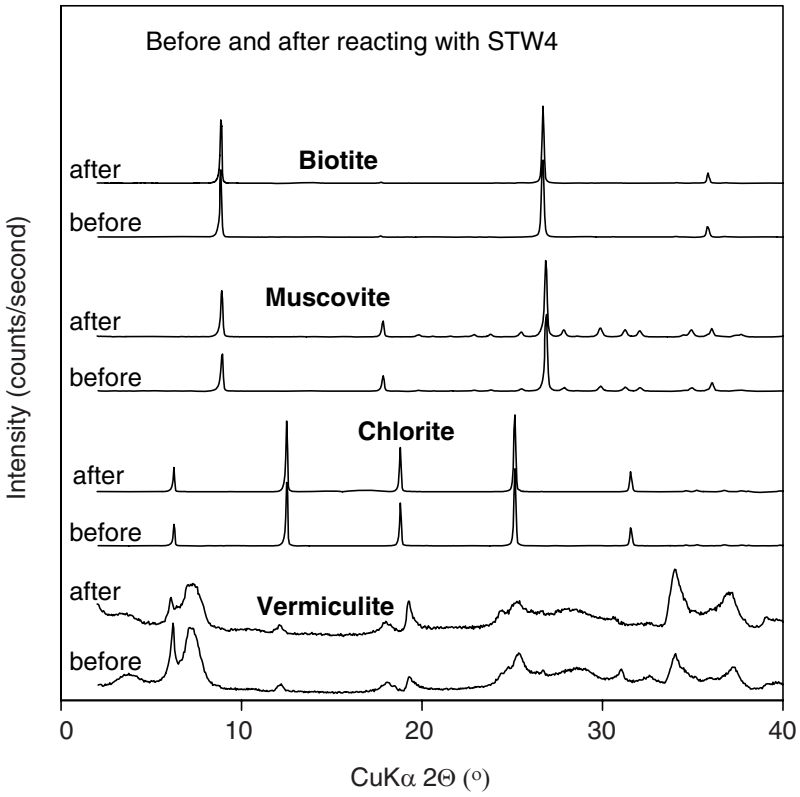

Figure 7: X-ray diffraction patterns of biotite, muscovite, chlorite, and vermiculite before and after reacting with STW4 for two months at 50 °C.

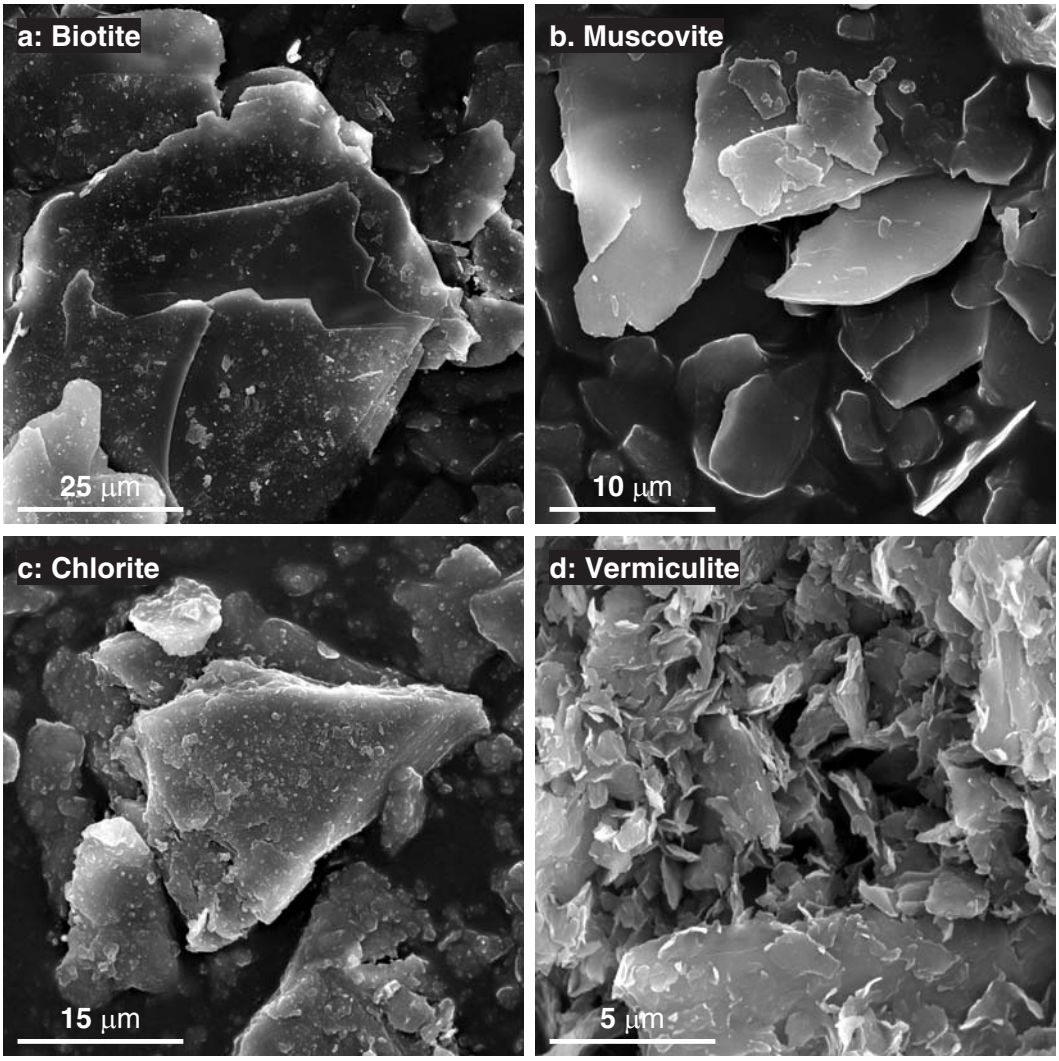

Figure 8: Scanning electron microscopy images of (a) biotite, (b) muscovite, (c) chlorite, and (d) vermiculite after reacting with STW4 for two months at 50 °C.

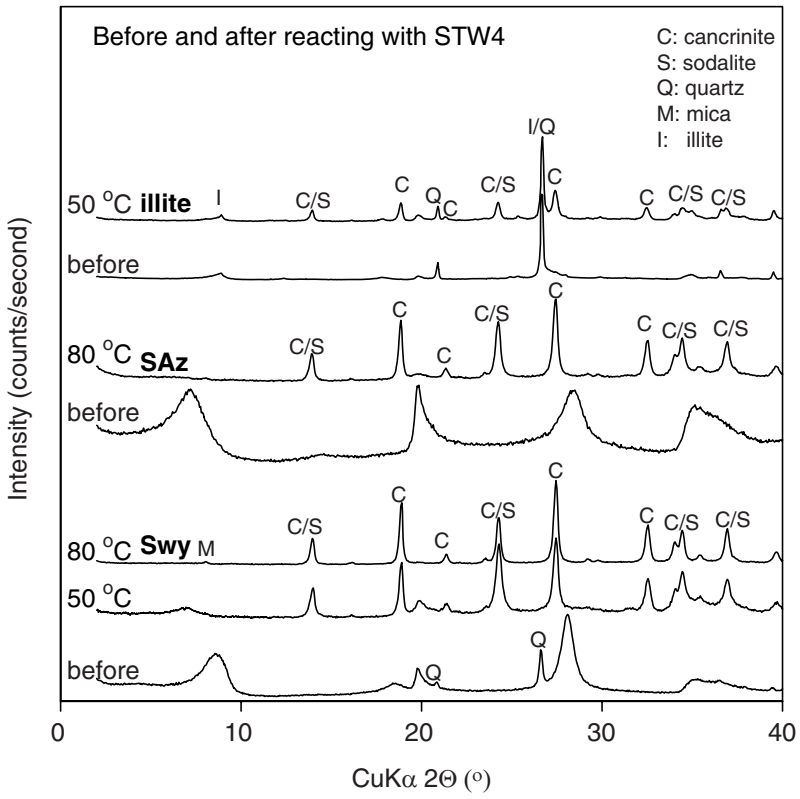

Figure 9: X-ray diffraction patterns of illite and smectites before and after reacting with STW4 for one month at 50 or 80 °C.

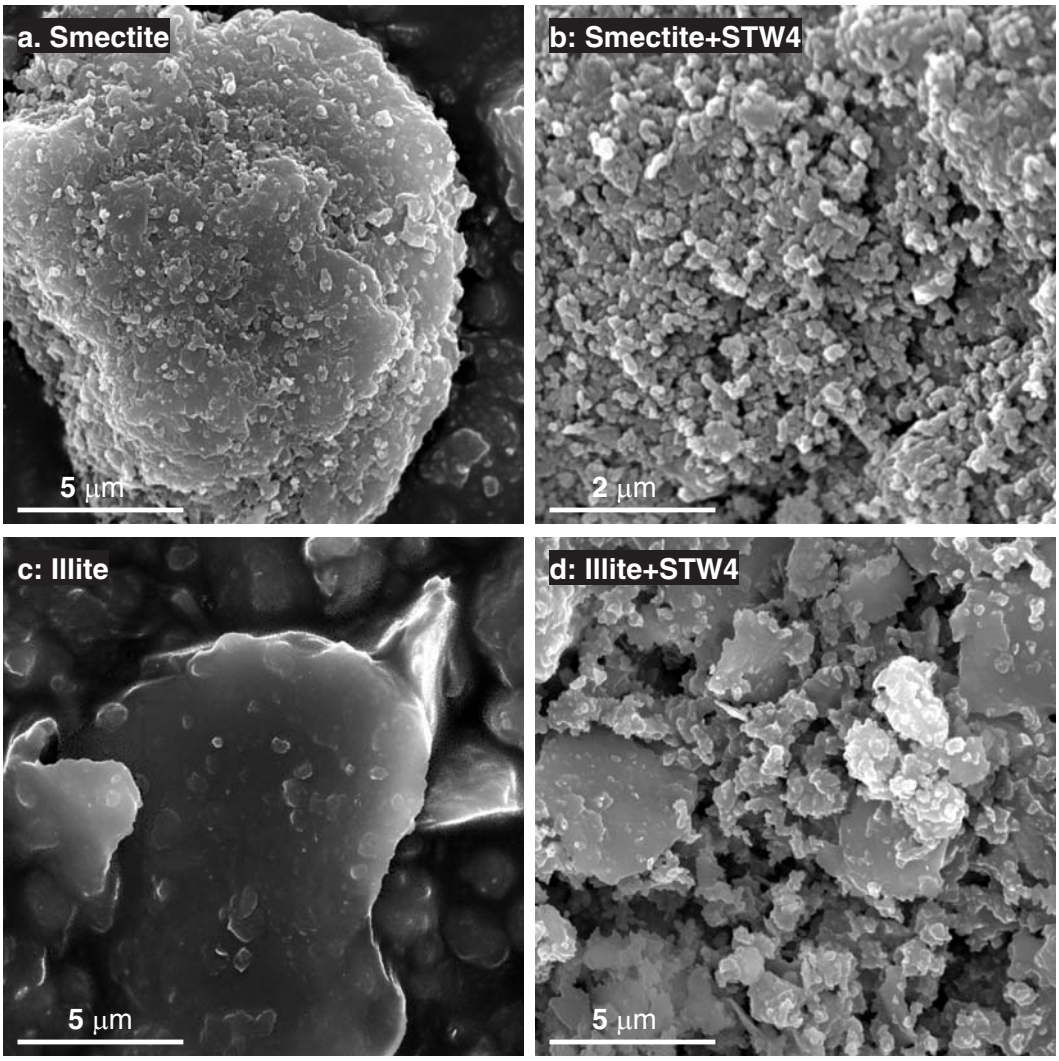

Figure 10: Scanning electron microscopy images of smectite (SWy-1) (a) before and (b) after reacting with STW4; and illite (c) before and (d) after reacting with STW4 for two months at 50 °C.

Available online at www.sciencedirect.com
ScienceDirect
Applied Geochemistry xxx (2006) xxx–xxx
Applied Geochemistry
www.elsevier.com/locate/apgeochem

Cancrinite and sodalite formation in the presence of cesium, potassium, magnesium, calcium and strontium in Hanford tank waste simulants

Youjun Deng [a], Markus Flury [a], James B. Harsh [a,*], Andrew R. Felmy [b], Odeta Qafoku [b]

[a] *Department of Crop and Soil Sciences, Center for Multiphase Environmental Research, Washington State University, Pullman, WA 99164-6420, United States*
[b] *Pacific Northwest National Laboratory, Environmental Molecular Science laboratory, Richland, WA 99352, United States*

Received 12 May 2005; accepted 27 June 2006
Editorial handling by M. Gascoyne

Abstract

High-level radioactive tank waste solutions that have leaked into the subsurface at the US Department of Energy Hanford Site, Washington, are chemically complex. Here, the effect of five cations, Cs^+, K^+, Sr^{2+}, Ca^{2+} and Mg^{2+}, on mineral formation and transformation pathways under conditions mimicking Hanford tank leaks is investigated. Sodium silicate was used to represent the dissolved silicate from sediments. The silicate was added into a series of simulants that contained 0.5 M aluminate, 1 M or 16 M NaOH, and the NO_3 salts of the cations. The precipitates were monitored by X-ray diffraction, scanning electron microscopy, and X-ray energy dispersive spectroscopy. In the 1 M NaOH simulants, low concentration of Cs^+ (<100 mM) did not affect the formation of lepispheric cancrinite and sodalite, whereas only highly crystalline cancrinite formed when Cs^+ concentration was $\geqslant$250 mM. An unidentified feldspathoid or zeolite intermediate phase was observed in the presence of high concentrations of Cs^+ (500 mM). The presence of K^+ did not alter, but slowed, the formation of cancrinite and sodalite. The presence of divalent cations led to the formation of metastable or stable silicates, aluminates, hydroxides, or aluminosilicates. The formation of these intermediate phases slowed the formation of cancrinite and sodalite by consuming OH^-, silicate, or aluminate. Compared with the concentrations used in this study, the concentrations of radioactive Cs^+ and Sr^{2+} in the tank solutions are much lower and divalent cations (Ca^{2+} and Mg^{2+}) released from sediments likely precipitate out as hydroxides, silicates or aluminates; therefore, the authors do not expect that the presence of these monovalent and divalent cations significantly affect the formation of cancrinite and sodalite in the sediments underneath the leaking waste tanks.
Published by Elsevier Ltd.

1. Introduction

At the US DOE Hanford site, underground high-level radioactive waste tanks have leaked more than 3800 m^3 of solution into the vadose zone (Gephart

* Corresponding author. Fax: +1 509 335 8674.
E-mail address: harsh@wsu.edu (J.B. Harsh).

0883-2927/$ - see front matter Published by Elsevier Ltd.
doi:10.1016/j.apgeochem.2006.06.019

and Lundgren, 1998; Lichtner and Felmy, 2003). The waste solutions are characterized by high alkalinity (OH^- concentration up to >8.5 M), high ionic strength (up to saturation with $NaNO_3$), and high concentration of aluminate (up to 3.4 M) (Serne et al., 1998; Lichtner and Felmy, 2003). Nitrate and NO_2^- are the major inorganic anions other than the OH^- in most of the tanks and 5.5 M NO_3^- and 4.4 NO_2^- M have been reported in some SX tanks (Lichtner and Felmy, 2003). Other anionic species, such as Cl^-, CO_3^{2-} and SO_4^{2-}, also occur in the tanks. Sodium is the dominant cation in the tank supernatants; its concentration was reported to be as high as 19 M (Lichtner and Felmy, 2003). Other cations are present in the tanks at much lower concentrations. The concentrations of Ca^{2+} and K^+ in the SX-108 tank were 33 and 74 mmol L^{-1}, respectively (Lichtner and Felmy, 2003). Cesium-137 and ^{90}Sr are the major radioactive elements in the tank wastes with radioactivities as high as 0.3 and 0.15 Ci L^{-1}, respectively (Serne et al., 1998), whereas their chemical concentrations in the tank supernatants are in the range of 10^{-6} to 10^{-4} M (Lichtner and Felmy, 2003).

When contacted by the tank waste solutions following a leak, silicate minerals in the sediments can be dissolved by the hyperalkaline solutions and release $H_2SiO_4^{2-}$, $Al(OH)_4^-$, and other structural ions such as K^+, Mg^{2+} and Ca^{2+}. Previous experiments indicate that K^+ concentration in reacted solution reached 13 mmol L^{-1} when 1 L of tank simulant contacted 1 kg of a Hanford sediment, whereas the concentrations of Ca^{2+} and Mg^{2+} were three orders of magnitude smaller than that of K^+ (Mashal et al., 2004). Similar solution compositions have been reported in column experiments with Hanford sediment (Qafoku et al., 2004). Experiments with Hanford sediments and model minerals indicate that feldspathoids, cancrinite and sodalite can form in the alkaline solutions (Kaplan et al., 1998, 2003; Bickmore et al., 2001; Chorover et al., 2003; Qafoku et al., 2003, 2004; Mashal et al., 2004; Choi et al., 2005a,b; Um et al., 2005).

In these experiments, the chemical compositions of simulants are generally simple compared with the Hanford tank wastes. A systematic investigation of the mineral transformations as a function of the chemical composition of tank waste, temperature and time is needed. This paper focuses on the effects of cation composition on the mineral transformation in the alkaline solutions. In a parallel study, the authors investigated the effects of anion type, alkalinity, salinity and temperature (Deng et al., in press). In those experiments, using the Na salts of varying types of anions, it was observed that, when NaOH concentration was <8 M, the mineral transformation pathway was: short-range ordered aluminosilicate → Linde Type A (LTA) zeolite → sodalite and/or cancrinite.

Cations may affect the reaction paths because they can form ion pairs with anions in solution, and the size of these ion pairs may not fit into the cages of the feldspathoids or zeolite. For example, Chorover et al. (2003) reported that cancrinite, sodalite and chabazite formed when kaolinite was reacted with waste simulants containing 10^{-5} to 10^{-3} M Cs^+ and Sr^{2+}. Bosnar et al. (2004) identified Li^+ and Na^+ as structure-forming cations and K^+, Rb^+ and Cs^+ as structure-breaking cations in the nucleation and crystal growth of zeolites. In addition to their effect on the formation of feldspathoids and zeolite, it is expected that divalent or higher valent cations will precipitate as hydroxide, aluminate or silicate phases. Under alkaline conditions, other silicate minerals, such as dioctahedral palygorskite and trioctahedral sepiolite (Singer, 1989), zeolite (Ming and Mumpton, 1989), and various 1:1 and 2:1 phyllosilicates (Dixon and Schulze, 2002) can form as well.

The objective of this study was to investigate the effect of cations on mineral formation and transformation pathways under conditions mimicking Hanford tank leaks. Specifically, the authors investigate (1) what types of minerals form in the presence of different cations, namely Cs^+, K^+, Sr^{2+}, Ca^{2+} and Mg^{2+}; (2) how the mineral transformation pathways are affected by the cations; and (3) how cations determine the crystallinity of cancrinite and sodalite.

2. Materials and methods

2.1. Modeling

To determine the thermodynamically stable solid phases in the presence of the dominant waste tank solution cations and the common cations released from sediments, the GMIN chemical equilibrium model was used to calculate the saturation indices (SI) of suspected solid phases at the ion activities and temperature (80 °C) of simulated waste solutions. When thermodynamic data were available, the equilibrium constant k_2 at 80 °C (T_2) was calculated from the known constant k_1 and enthalpy ΔH^0

Please cite this article in press as: Deng, Y. et al., Cancrinite and sodalite formation in the presence of ..., Appl. Geochem. (2006), doi:10.1016/j.apgeochem.2006.06.019

at temperature T_1 (e.g., 25 °C) using the van't Hoff equation

$$\ln\left(\frac{k_2}{k_1}\right) = -\frac{\Delta H^0}{R}\left(\frac{1}{T_2} - \frac{1}{T_1}\right) \quad (1)$$

where R is the universal gas constant. Predictions were compared to precipitates formed in solutions designed to simulate tank leach conditions.

2.2. Tank waste simulant preparation

Cesium and Sr^{2+} are the major radioactive elements found in the waste tanks, whereas K^+, Ca^{2+} and Mg^{2+} exist in tank waste and are also the major cations in the sediment minerals. Only the nitrate salt form of these cations was used in the simulants. Two NaOH concentration levels were chosen, 1 and 16 M, to mimic the low and high alkalinity of the tank waste. Sodium silicate was used to represent dissolved silicate from sediments. The silicate solution was mixed with tank waste simulants in polypropylene bottles and the precipitates were periodically monitored with X-ray diffraction, electron microscopy, and X-ray energy dispersive spectroscopy. The simulation experiments were performed at 80 °C.

In simulation experiments, 10 mL of warm (80 °C) NaOH solution, containing sodium silicate (Na_2SiO_3) and one nitrate salt of Cs^+, K^+, Mg^{2+}, Ca^{2+}, or Sr^{2+}, were mixed with 10 mL of NaOH solution containing sodium aluminate ($NaAlO_2$). The concentrations of the anions in the starting mixtures were: 0.175 M $H_2SiO_4^{2-}$, 0.5 M $Al(OH)_4^-$, 0.5 M NO_3^-, 1 or 16 M OH^-. The concentrations of the cations were either 0.25 M Sr^{2+}, 0.25 M Ca^{2+}, 0.25 M Mg^{2+}, or 0.5 M K^+. Cesium concentration was varied as 0.1, 1, 10, 50, 100, 250 and 500 mM in 1 M NaOH solutions, but only one concentration level, 500 mM Cs^+, was used in the simulant containing 16 M NaOH. When $CsNO_3$ concentration was <500 mM, NaNO3 was added to make up a total of 0.5 M NO_3^- in the simulants. Sodium silicate ($Na_2SiO_3 \cdot 9\,H_2O$) and $Ca(NO_3)_2$ were purchased from Fisher Scientific; sodium aluminate ($NaAlO_2$) was from STREM Chemicals (Newburyport, MA); other compounds were from Sigma-Aldrich. All chemicals were used as received. The sodium aluminate is of technical grade whereas all other compounds are of ACS reagent grade.

Each simulant mixture was stored in a capped 30-mL Nalgene polypropylene bottle at 80 ± 2 °C. To sample the precipitates, the bottle was shaken by hand for 2 min to suspend the particles. About 1 mL of suspension from each bottle was transferred to a centrifuge tube. The phases were separated by centrifugation (12,000g, 5 min). Precipitates in the tubes were washed 3 times by mixing with 30 mL of deionized water each time, shaken for 1 h or longer, and centrifuged. The precipitates were finally dried at 50 °C.

2.3. Characterization of precipitates

The precipitates were analyzed with a diffractometer equipped with a graphite monochromater and with Cu-Kα radiation (Philips XRG 3100, Philips Analytical Inc., Mahwah NJ). Step scan mode was employed in the analysis. Step size was set as 0.05°2θ, and the scan time was set to 5 s at each step. Mineral identification was performed by matching the observed XRD peaks and the published peaks of known minerals. The following minerals were matched: cancrinite (Buhl and Löens, 1996), sodalite (Sieger et al., 1991), amesite [$(Mg_2Al)[(Si, Al)O_5](OH)_4$] (Steinfink and Brunton, 1956), brucite [$Mg(OH)_2$] (Zhukhlistov et al., 1997), Ca hydrogarnet [$Ca_3Al_2(OH)_{12}$] (Lager et al., 1987), portlandite [$Ca(OH)_2$] (ICDD, 1974, card 4-733), Ca aluminate hydrate [$Ca_3Al_2O_6 \cdot (8–12)H_2O$] (ICDD, 1974, card 2-0083), Ca silicate hydrate [$xCaO \cdot SiO_2 \cdot yH_2O$] (ICDD, 1974, card 6-0010), Sr silicate hydrate [$Sr_3Si_2O_7 \cdot 4H_2O$] (ICDD, 1974, card 6-0473), and Sr hydrogarnet [$Sr_3Al_2(OH)_{12}$, or $Sr_3Al_2O_6 \cdot 6H_2O$] (Nevskii et al., 1982).

Microscopic analysis was performed on a Hitachi S-570 scanning electron microscope (SEM), and a LEO982 and a FEI SIRION field emission scanning electron microscopes (FESEM). The X-ray energy dispersive (EDS) spectra and elemental mapping were recorded on the FESEM. Electron micrographs showed generally uniform morphology of precipitates, and the images shown in this manuscript are representative for the precipitates formed, unless indicated otherwise.

3. Results

3.1. Mineral formation prediction

The saturation indices (Table 1) showed that all the starting simulants were supersaturated with respect to cancrinite and sodalite, suggesting that either or both cancrinite and sodalite could form in the simulants and that the nature of cations

Table 1
Saturation indices (SI)of starting simulants containing different cations with respect to suspected solid phases

Component	Reactions	$\log_{10}k$ (80 °C)	$\log SI = \log_{10}IAP - \log_{10}k$ (at 80 °C)				
			Cs^+	K^+	Ca^{2+}	Mg^{2+}	Sr^+
Gibbsite	$Al(OH)_3 + OH = Al(OH)_4^-$	0.11[a]	0.49	0.57	0.44	0.42	0.53
Cancrinite	$Na_6Si_6Al_6O_{24} \cdot 2NaNO_3 \cdot 4H_2O + 8H_2O + 12OH^- \rightleftharpoons 8Na^+6Al(OH)_4^- + 6H_2SiO_4^{2-} + 2NaO_3^-$	36.9[b]	20.6	19.8	20. 9	21.0	19.71
Sidlite	$Na_6Si_6Al_6O_{24} \cdot 2NaOH \cdot 2H_2O + 10H_2O + 10OH^- \rightleftharpoons 8Na^+6Al(OH)_4^- + 6H_2SiO_4^{2-}$	39.2[c]	23. 6	22.9	23.5	23.7	22.7
Portlandite	$Ca(OH)_2 \rightleftharpoons Ca^{2+} + 2OH^-$	5.69[a]			2.53		
Brucite	$Mg(OH)_2 \rightleftharpoons Mg^{2+} + 2OH^-$	11.2[a]				7.5	
	$Sr(OH)_2 \cdot 8H_2O \rightleftharpoons Sr^{2+} + 2OH^- + 8H_2O$	3.68[d]					0.66
Tobermorite like	$Sr_5Si_6O_{16}(OH)_2 \cdot 5H_2O + 5H_2O \rightleftharpoons 5Sr^{2+} + 6H_3SiO_4^- + 4OH^-$	38.0[e]					15.8

[a] Calculated using van't Hoff equation; the values of log K and enthalpy at standard state were taken from Parkhurst and Appelo (1999).
[b] Based on equilibrium constant of Bickmore et al. (2001)and enthalpy of Liu et al. (2005).
[c] Based on equilibrium constant and enthalpy of Park and Englezos (1999).
[d] Constant at 25 °C (Felmy et al., 1998).
[e] Constant at 20–23 °C (Felmy et al., 2003).

would not affect the formation of these two phases. The saturation indices also indicated that $Ca(OH)_2$ could form in the presence of Ca^{2+}, $Mg(OH)_2$ in the presence of Mg^{2+}, and $Sr(OH)_2 \cdot H_2O$ and a tobermorite-like Sr silicate $Sr_5Si_6O_{16}(OH)_2 \cdot 5H_2O$ in the presence of Sr^{2+}.

3.2. Observed mineral transformation in 1 M NaOH solutions

When the silicate and aluminate simulants containing 1 M NaOH were mixed together, white precipitate formed instantly. The white precipitate did not yield distinct X-ray diffraction peaks, suggesting it is a short-range ordered aluminosilicate phase.

3.2.1. Minerals formed in the presence of 0.1–500 mM Cs^+

3.2.1.1. XRD and SEM. When the starting Cs^+ concentration was ⩽100 mM, both cancrinite and sodalite formed within 1 week (Fig. 1a). No other minerals were detected by XRD. The precipitates formed after 8 weeks of reaction had similar X-ray diffraction patterns (Fig. 1b) to those after 1 week

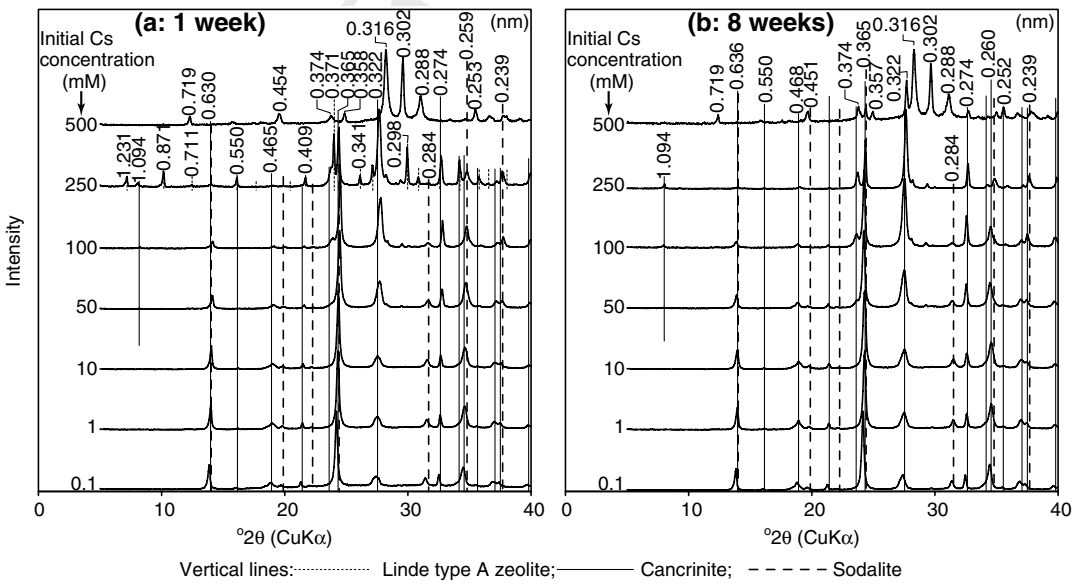

Fig. 1. The X-ray diffraction patterns of precipitates formed in the presence of 0.1–500 mM $CsNO_3$ in 1 M NaOH after (a) one and (b) 8 weeks of reaction.

Please cite this article in press as: Deng, Y. et al., Cancrinite and sodalite formation in the presence of ..., Appl. Geochem. (2006), doi:10.1016/j.apgeochem.2006.06.019

of reaction. Cancrinite and sodalite formed in the presence of $\leqslant 100$ mM $CsNO_3$ showed lepispheric morphology (Fig. 2a and b). There were no distinct morphological changes during the 8 weeks of reaction.

When initial $CsNO_3$ concentration was increased to 250 mM, LTA zeolite remained in the precipitate after 1 week of reaction but disappeared within 8 weeks (Fig. 1a and b). The LTA zeolite in the 1-week precipitate was characterized by its compact morphology (Fig. 2c). Cancrinite was the only mineral identified by XRD analysis after 8 weeks of reaction (Fig. 1b, the second pattern from top) and there were more tiny hexagonal cancrinite needles in the lepispheres formed (Fig. 2d). The highly-symmetric hexagonal needle shape reflected cancrinite's hexagonal symmetry ($P6_3$) (Buhl et al., 2000) and is an indication of high crystallinity.

When initial $CsNO_3$ concentration was increased to 500 mM, an unidentified mineral phase was observed after 1 week of reaction (Fig. 1a, top pattern). The XRD peak positions of the precipitate matched those of a Cs-containing mineral formed by mixing 3 M NaOH and kaolinite reported by Barrer et al. (1968). In that reference, the mineral was termed zeolite D, a chabazite-like mineral. The authors are not certain that this is the correct mineral identification because the peak positions do not match those of any known chabazite. This mineral was most likely a zeolite because ion exchange experiments indicated that Cs^+ and Na^{2+} in it are more readily exchangeable (data not

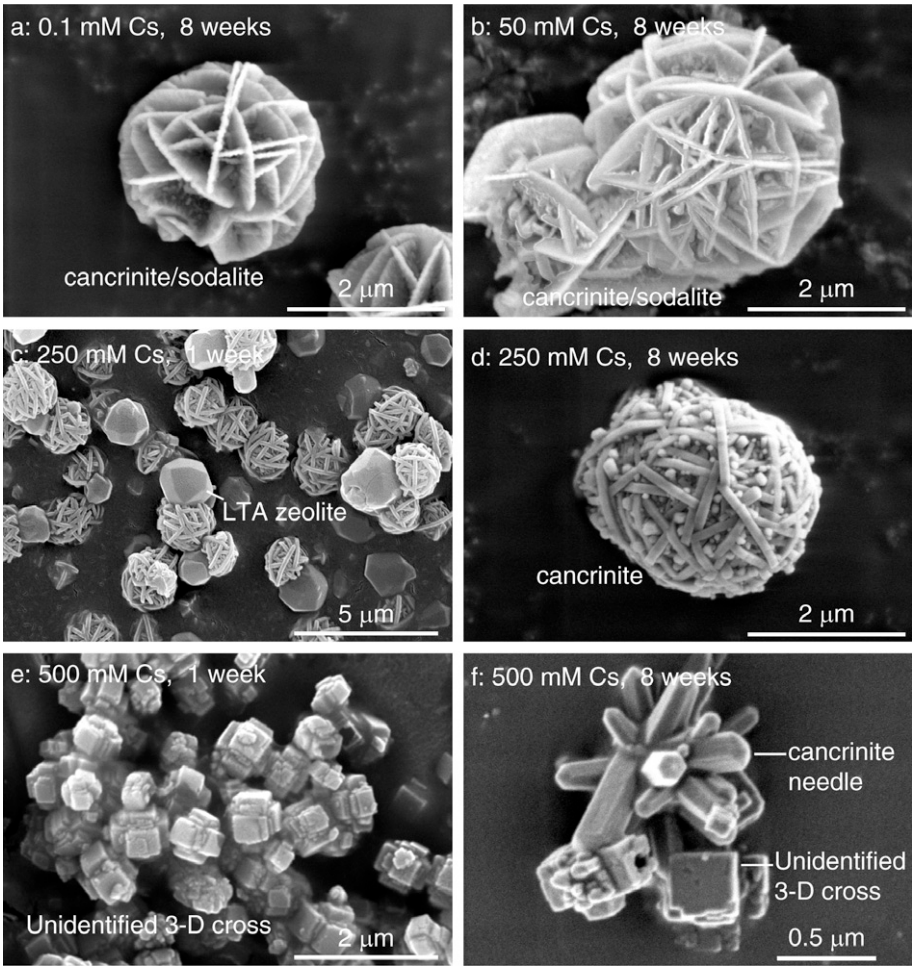

Fig. 2. The SEM images of precipitates formed in the presence of 0.1–500 mM $CsNO_3$ in 1 M NaOH solutions, after 1 or 8 weeks of reaction.

Please cite this article in press as: Deng, Y. et al., Cancrinite and sodalite formation in the presence of ..., Appl. Geochem. (2006), doi:10.1016/j.apgeochem.2006.06.019

shown) than those in feldspathoids (Mon et al., 2005). This mineral had a three-dimensional cross morphology (Fig. 2e). After 8 weeks of reaction, cancrinite appeared (Fig. 1b, top pattern) at the expense of the unidentified mineral.

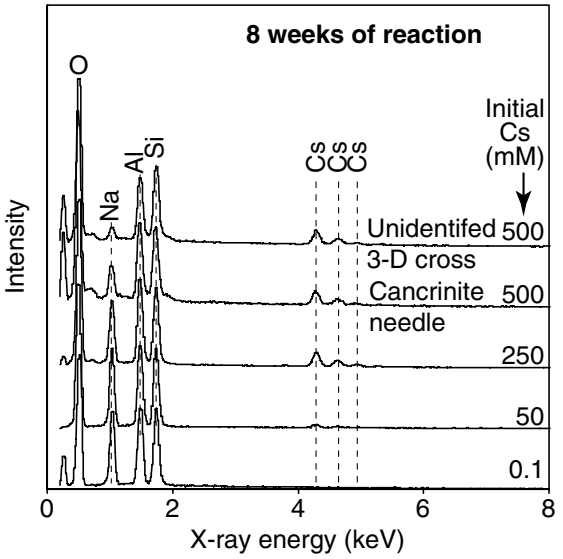

Fig. 3. Energy dispersive spectra of precipitates formed in 1 M NaOH solutions in the presence of 0.1–500 mM $CsNO_3$, after 8 weeks of reaction.

3.2.1.2. Crystallinity of cancrinite and preference of cancrinite over sodalite. Fig. 1 reveals that the diffraction intensities at 0.322 and 0.274 nm, relative to the peak at 0.365 nm, increased with increasing initial Cs^+ concentration. The 0.322 and 0.274 nm peaks belong to the (121) and (400) diffractions of cancrinite and highly crystalline cancrinite has stronger diffractions at these two positions (Buhl and Löens, 1996). The diffraction intensity difference and the hexagonal needle shape of the particles indicate that the presence of $CsNO_3$ in the alkaline solutions favors the formation of highly-crystalline cancrinite.

3.2.1.3. EDS and elemental mapping. The EDS analysis indicates that Al and Si peaks were roughly equal in intensity for the cancrinite/sodalite lepispheres and the cancrinite needles (Fig. 3). The Cs^+ intensity increased with starting Cs^+ concentration, whereas the Na signal weakened. Elemental mapping (Fig. 4) on cancrinite formed in the presence of 250 mM $CsNO_3$ indicates that Cs, Na and Al are homogeneously distributed in the particles. Other elements such as O and Si have the same distribution as Al and, therefore, are not shown. The EDS data and elemental mapping of cancrinite suggest that Cs^+ can be incorporated at the sites that

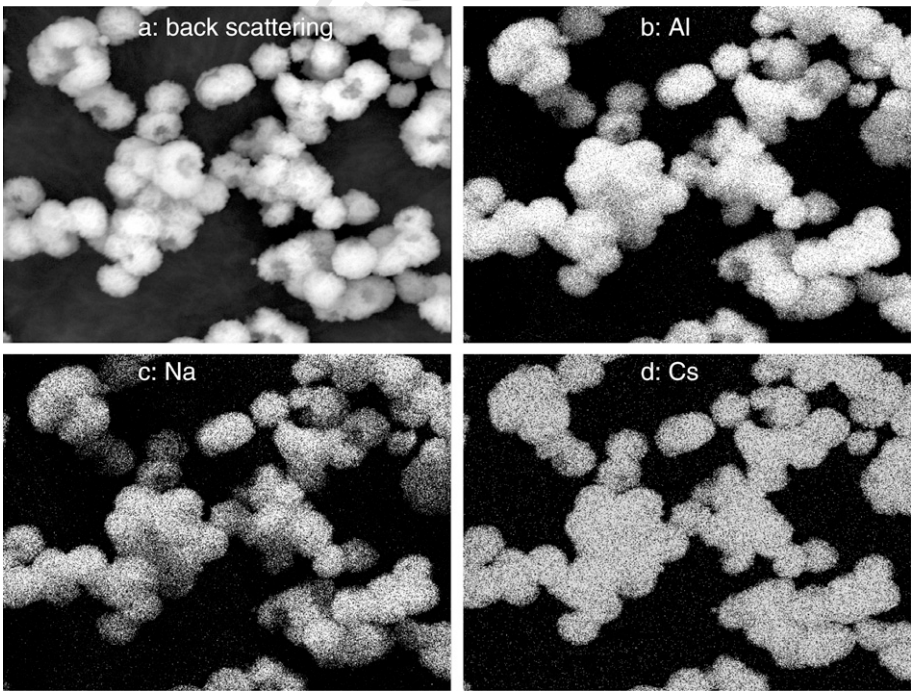

Fig. 4. Elemental mapping of cancrinite formed in 1 M NaOH solutions in the presence of 250 mM $CsNO_3$, after 8 weeks of reaction.

Please cite this article in press as: Deng, Y. et al., Cancrinite and sodalite formation in the presence of ..., Appl. Geochem. (2006), doi:10.1016/j.apgeochem.2006.06.019

are normally occupied by Na^+. The EDS intensities of Na and Cs did not exactly match; this is likely caused by the different volatilization rates of the elements to electron beam bombardment, e.g., Na volatilizes more rapidly than other elements (Bickmore et al., 2001), and the rough surfaces of the powdery samples. Rough surface enhances the difference of volatilization rates and, therefore, it limits the strict quantitative analysis. The distribution difference between Na and Cs in Fig. 4 is not sufficient to conclude that they have different distributions.

3.2.2. Minerals formed in the presence of 0.5 M K^+

The presence of 0.5 M K^+ in 1 M NaOH solution slowed down the formation of cancrinite and sodalite. The LTA zeolite remained in the precipitate after 1 week of reaction (Fig. 5, bottom spectrum). The SEM image also indicates that both LTA zeolite, cancrinite and sodalite existed in the precipitates (Fig. 6a). The LTA zeolite particles were more or less rounded (Fig. 6a) suggesting dissolution. After 8 weeks of reaction, only cancrinite and sodalite lepispheres remained in the precipitates (Fig. 6b).

3.2.3. Minerals formed in the presence of 0.25 M Mg^{2+}, Ca^{2+} or Sr^{2+}

The XRD analyses indicate that both cancrinite and sodalite formed within 1 week in the presence of Mg^{2+} or Ca^{2+} (Fig. 5). It took more time to form cancrinite in the presence of Sr^{2+}. Several other silicates, aluminates, aluminosilicates and hydroxides of these divalent cations formed too.

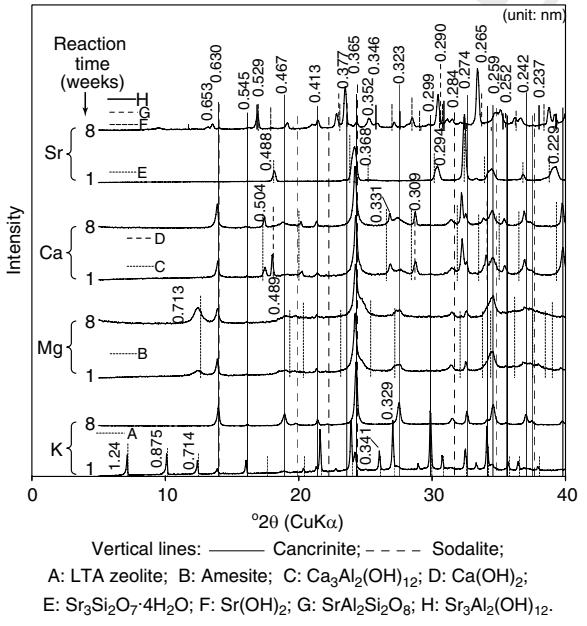

Fig. 5. The XRD patterns of precipitates formed in 1 M NaOH solutions in the presence of different cations.

Amesite, $[(Mg_2Al)[(Si, Al)O_5](OH)_4]$, a trioctahedral 1:1 phyllosilicate mineral, formed in the presence of Mg^{2+}. The broadness of the amesite peaks at 0.712, 0.46, and 0.36 nm indicates that the crystallinity of this mineral was poor. The particles formed in the presence of Mg^{2+} were only a few tenths of a μm in diameter and irregular in shape (Fig. 6c), confirming that the minerals were poorly crystalline. The XRD patterns (Fig. 5), the morphology (Fig. 6d), and EDS spectra (Fig. 7) of the particles did not show distinct changes after 8 weeks of reaction, showing that amesite was a stable or metastable mineral phase in addition to cancrinite and sodalite when Mg^{2+} was present.

When Ca^{2+} was present, a Ca hydrogarnet $[Ca_3Al_2(OH)_{12}]$ and portlandite $[Ca(OH)_2]$ in addition to cancrinite and sodalite, were identified by XRD (Fig. 5). The cancrinite and sodalite formed were typical lepispheres (Fig. 6c). Given the EDS spectrum in Fig. 7, the larger round particles (>10 μm, Fig. 6d) are probably the Ca-hydrogarnet identified in the XRD pattern. There were weak Si peaks on the EDS spectra of the large Ca-hydrogarnet and the EDS spectra of cancrinite/sodalite lepispheres showed weak Ca peaks (Fig. 7). The $Ca(OH)_2$ precipitate could be dissolved in water when the samples were extensively washed. The Ca-hydrogarnet appeared stable in the 1 M NaOH simulants. The XRD (Fig. 5), morphological (Fig. 6e and f), and EDS (Fig. 7) results did not show distinct changes from week 1 to week 8.

When Sr^{2+} was present in the simulants, XRD peaks at 0.488, 0.368, 0.429, 0.274 nm (Fig. 5) approximately matched a Sr silicate hydrate $Sr_3Si_2O_7 \cdot 4\,H_2O$ (ICDD, 1974, card 6-0473). The EDS spectrum (Fig. 7) confirmed the occurrence of a Sr silicate phase with large angular morphology (Fig. 6g). No cancrinite or sodalite was evident after 1 week of reaction from the XRD or SEM. After 8 weeks of reaction, part of the Sr silicate hydrate remained in the precipitates. The XRD peaks (Fig. 5) indicate that Sr hydrogarnet $[Sr_3Al_2(OH)_{12}$ or $Sr_3Al_2O_6 \cdot 6H_2O]$, $Sr(OH)_2$, $SrAl_2Si_2O_8$, and other unidentified crystals formed. The Sr-hydrogarnets were large and round, and had abundant voids at the surfaces and within the particles (Fig. 6h). The EDS spectrum of the

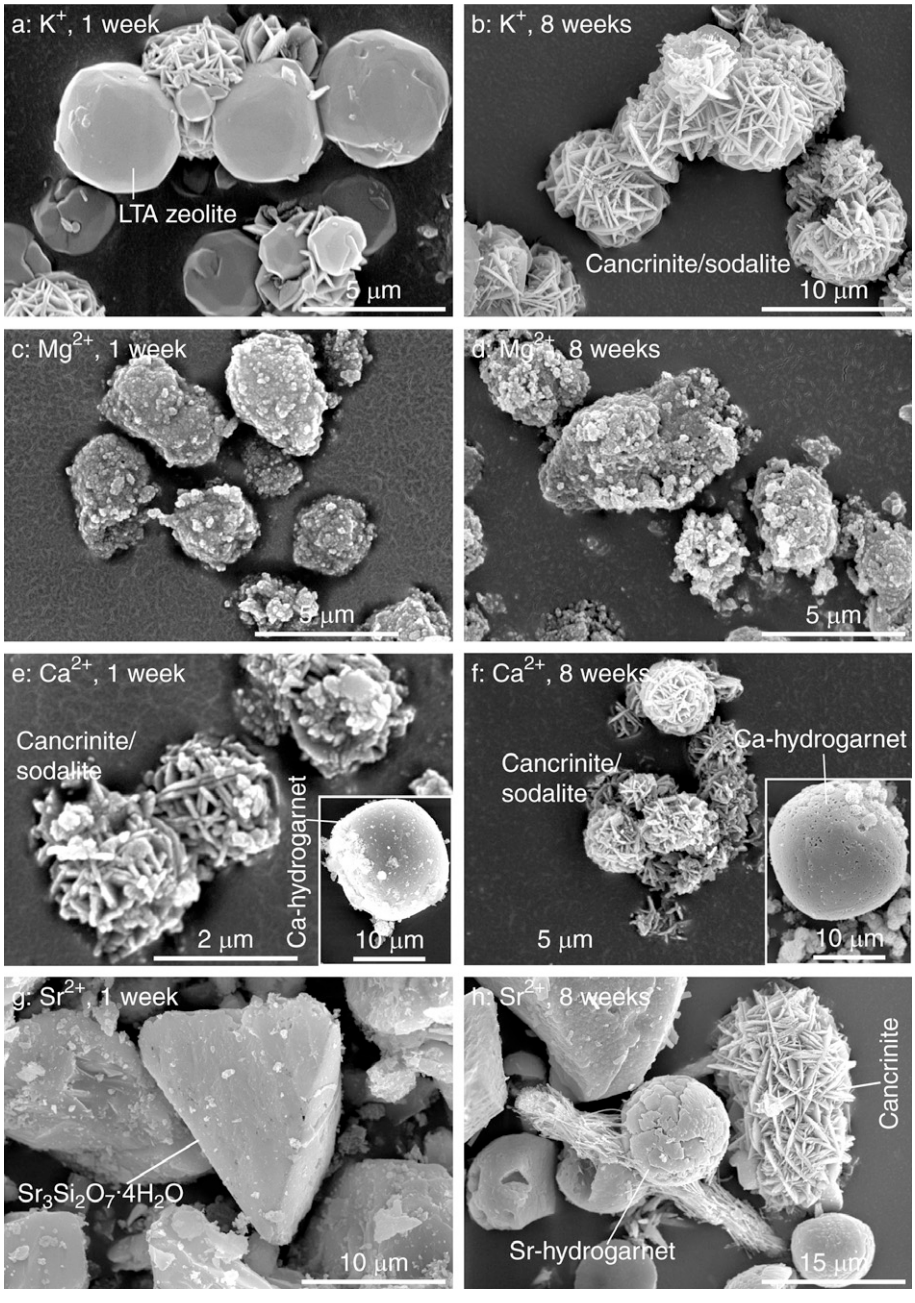

Fig. 6. The SEM images of precipitates formed in the presence of different cations in 1 M NaOH solutions.

Sr-hydrogarnet (Fig. 7) confirmed the presence of Al and Sr in the particle. Because the peaks of Si (1.739 kev, Kα) and Sr (1.806 keV, Lα) are too close to be resolved, it is difficult to determine if Si occurred in this phase. A few lepispheric particles were observed in the precipitates after 8 weeks of reaction (Fig. 6h), and the EDS spectrum indicates they are cancrinite/sodalite.

3.3. Observed mineral transformation in 16 M NaOH solutions

3.3.1. Minerals formed in the presence of 0.5 M K^+ or Cs^+

The XRD patterns (Fig. 8) indicate that only cancrinite formed in the 16 M NaOH solution in the presence of 0.5 M K^+ or Cs^+. The strong

Please cite this article in press as: Deng, Y. et al., Cancrinite and sodalite formation in the presence of ..., Appl. Geochem. (2006), doi:10.1016/j.apgeochem.2006.06.019

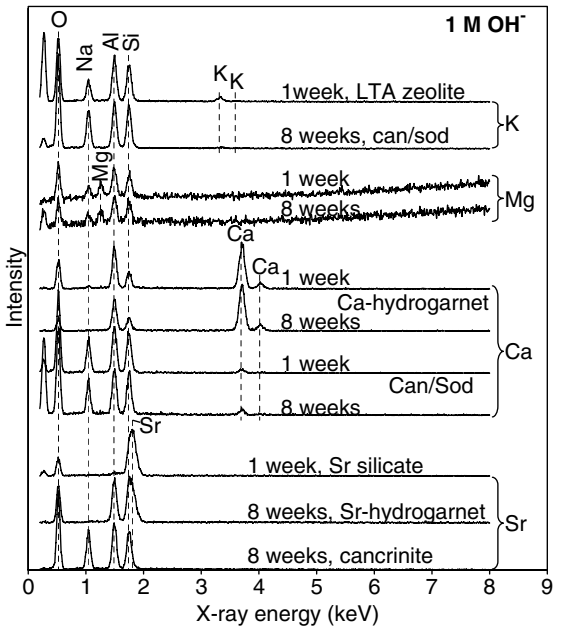

Fig. 7. Energy dispersive spectra of LTA zeolite, cancrinite/sodalite, $Mg(OH)_2$, Ca-hydrogarnet, Sr-silicate, Sr-hydrogarnet formed in 1 M NaOH in the presence of 0.5 M Cs^+ or K^+, 0.25 M Mg^{2+}, Ca^{2+}, or Sr^{2+}.

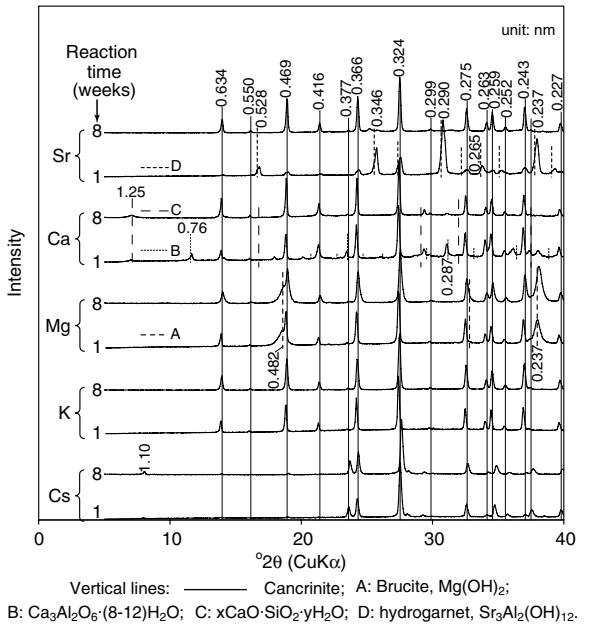

Fig. 8. The XRD patterns of precipitates formed in 16 M NaOH solutions in the presence of different cations after 1 and 8 weeks of reaction.

(121) diffraction at 0.324 nm relative to the (300) diffraction at 0.366 nm is an indication of high crystallinity of cancrinite. Cancrinite formed in the presence of Cs^+ had weaker diffractions at 0.634 nm (110), 0.469 nm (101), and 0.416 nm (210), but stronger diffraction at 0.377 nm (201) and 1.10 nm (100). The (100) peak normally does not show in the XRD patterns due to the high

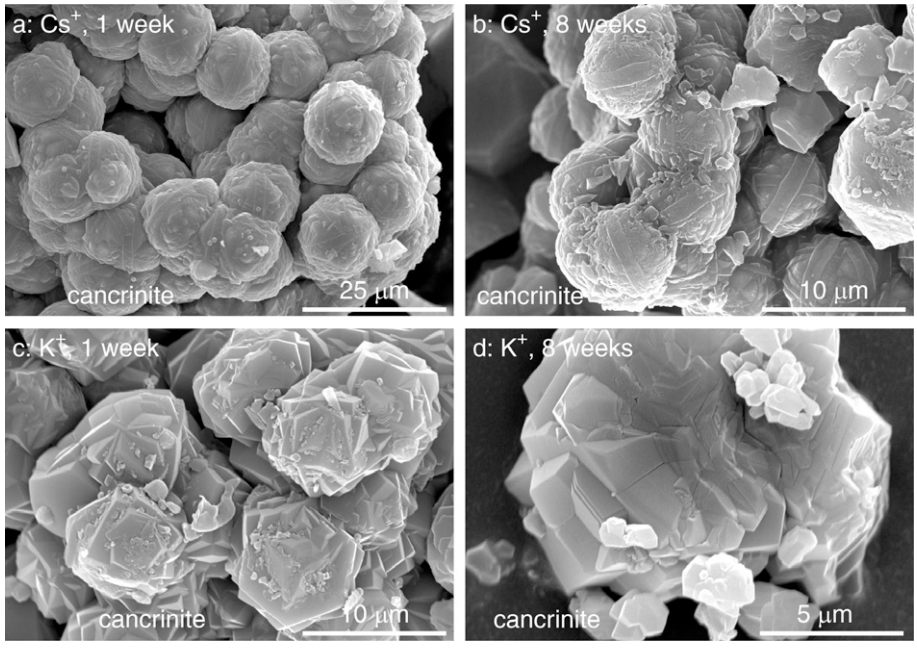

Fig. 9. The SEM images of cancrinites formed in the presence of 0.5 M Cs^+ or K^+ in 16 M NaOH solutions.

Please cite this article in press as: Deng, Y. et al., Cancrinite and sodalite formation in the presence of ..., Appl. Geochem. (2006), doi:10.1016/j.apgeochem.2006.06.019

symmetry of the crystal (hexagonal, $P6_3$ in space group, Buhl et al., 2000). The XRD patterns of cancrinite formed in the presence of 0.5 M $CsNO_3$ matched a Cs–Li-analogue of cancrinite reported by Fechtelkord et al. (2001). Their Rietveld structure refinements revealed that $Cs^+$was exclusively located in the ε-cage of cancrinite (Fechtelkord et al., 2001).

Cancrinite formed in the presence of Cs^+ appeared as balls surrounded by "bandages" (Fig. 9a), and these "bandages" are likely the edges of thick cancrinite disks. Cancrinite (Fig. 9c) formed in the presence of K^+ had the same morphology as $NaNO_3$-cancrinite. Analyses with XRD (Fig. 8) and SEM (Fig. 9) did not reveal obvious differences between the cancrinite formed after 1 week of reaction and 8 weeks of reaction; indicating highly crystalline cancrinite formed rapidly in the 16 M NaOH solutions.

3.3.2. Minerals formed in the presence of 0.25 M Mg^{2+}, Ca^{2+} or Sr^{2+}

When divalent cations Mg^{2+}, Ca^{2+} or Sr^{2+} were present in the 16 M NaOH simulants, highly-crystalline cancrinite formed. These cancrinites had similar XRD patterns (Fig. 8) and morphologies (Fig. 10). Other mineral phases, either as an intermediate phase or as a stable phase, were observed in the precipitates. The non-cancrinite minerals are discussed as follows:

When 0.25 M Mg^{2+} was present in the simulants, Mg^{2+} precipitated out as brucite, $Mg(OH)_2$. The brucite appeared stable or metastable in the 16 M NaOH simulants; it persisted after 8 weeks of reaction. The broad XRD diffraction peaks of brucite indicate poor crystallinity. The small crumbs in Fig. 10a and b are probably brucite particles; they often adhered to larger cancrinite crystals. The EDS analysis showed different Mg abundances

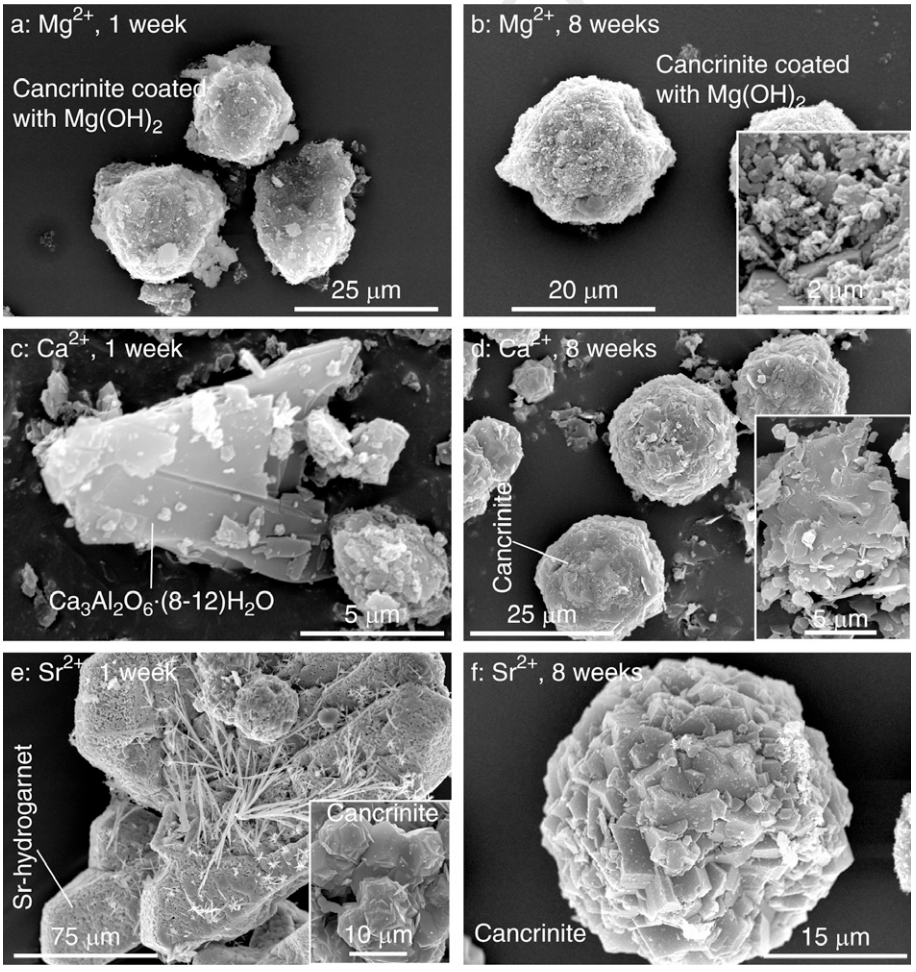

Fig. 10. The SEM images of precipitates formed in the presence of 0.25 M Mg^{2+}, Ca^{2+}, or Sr^{2+} in 16 M NaOH solutions.

Please cite this article in press as: Deng, Y. et al., Cancrinite and sodalite formation in the presence of ..., Appl. Geochem. (2006), doi:10.1016/j.apgeochem.2006.06.019

between the small particle-rich area and the relative clean area of cancrinite (Fig. 11). The precipitates did not show distinct morphological changes within 8 weeks (Fig. 10b).

When Ca^{2+} was present in the simulant, a Ca aluminate hydrate [$Ca_3Al_2O_6 \cdot (8–12)H_2O$] and a Ca silicate hydrate [$xCaO \cdot SiO_2 \cdot yH_2O$; $x \approx 1$ and y is variable] formed as indicated by the XRD analysis (Fig. 8). The Ca aluminate hydrate (Ca-hydrogarnet) might contain a trace amount of Si (Fig. 11). The Ca aluminate hydrate disappeared from the precipitates within 8 weeks, whereas Ca silicate hydrate remained (Fig. 8). The EDS spectrum indicates that the angular particles with smooth surfaces in the 1-week precipitates (Fig. 10c) were Ca aluminate hydrate; they were not observed in the 8-week precipitates. The flakes, some of which coated larger cancrinite particles, might be Ca silicate hydrate (Fig. 10d).

After 1 week of reaction, a Sr hydrogarnet, $Sr_3Al_2(OH)_{12}$, formed in the presence of Sr^{2+} (Fig. 8). The Sr hydrogarnet particles (Fig. 10e) had the same porous morphology as those formed in 1 M NaOH (Fig. 6h). A few cancrinite particles were found in the 1-week precipitates, and cancrinite had the typical euhedral morphology of highly crystalline $NaNO_3$-cancrinite (Fig. 10e, inset). After 8 weeks of reaction, the Sr hydrogarnet disappeared and only cancrinite (Fig. 10f) remained.

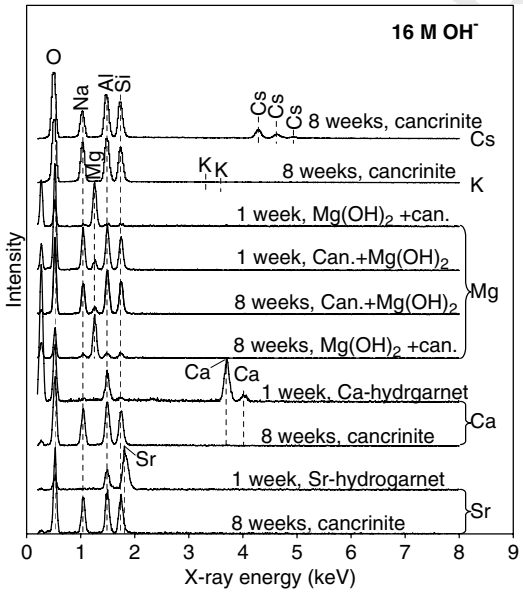

Fig. 11. Energy dispersive spectra of highly-crystalline cancrinite, Ca-hydrogarnet, Sr-hydrogarnet formed in 16 M NaOH in the presence of 0.5 M Cs^+ or K^+, 0.25 M Mg^{2+}, Ca^{2+}, or Sr^{2+}.

3.4. Incorporation of cations in cancrinite and sodalite

The EDS analysis indicates that cations can be incorporated into cancrinite, but they showed different abilities to enter the feldspathoids. The K^+ signal in the EDS spectrum of cancrinite formed in the presence of 0.5 M KNO_3 in 16 M NaOH is negligible (Fig. 11). In the starting 1 M NaOH simulant, the K/Na molar ratio is 1:3.7 while the K/Na molar ratio of the EDS signals of the cancrinite and sodalite lepispheres is <1:40 (Fig. 7). These data suggest that the cancrinite or sodalite tend to exclude K^+ from the structure in the presence of high soluble Na^+. This is consistent with the observation that K^+ concentration was three orders of magnitude higher than those of Ca^{2+} and Mg^{2+} in the supernatant solution when Hanford sediments contacted alkaline simulants (Mashal et al., 2004). In the 16 M NaOH simulants, the Cs/Na ratio is 1:17, whereas the Cs/Na ratio of EDS signal in cancrinite formed in the presence of 0.5 M $CsNO_3$ is about 1:3 (Fig. 11). This suggests that, during the crystallization of cancrinite, Cs^+ is a stronger competitor for the internal cage or channel sites of cancrinite than K^+. The EDS spectra of cancrinites formed in 16 M NaOH simulants showed negligible Ca or Sr peaks (Fig. 11). The signals in cancrinites/sodalites formed in 1 M NaOH were also weak (Fig. 7), suggesting the divalent cations were not incorporated into cancrinite in large quantities. This observation agrees with the paucity of divalent cations in natural cancrinite, in which the Ca:Na molar ratio is less than 1:6 (Mozgawa, 2001).

4. Discussion

4.1. Consistence and discrepancy between prediction and observation

The observed formation of cancrinite, sodalite, $Ca(OH)_2$, $Mg(OH)_2$ and $Sr(OH)_2$ in the simulated tank waste solutions was consistent with the model predictions (Table 1), yet the predicted tobermorite-like Sr silicate was not observed in the experiment. Several crystalline phases such as the unidentified zeolite, Ca- and Sr-hydrogarnets, amesite, Sr aluminosilicate were not predicted by the software GMIN because they are not present in the thermodynamic database.

4.2. Mineral transformation pathways

Cancrinite was the dominant stable mineral phase formed in the simulants. The major mineral transformations observed in the presence of different cations were similar to the transformations observed in the Na^+-only system: an amorphous aluminosilicate phase → LTA zeolite → cancrinite/sodalite.

Based on the equations described by Barnes et al. (1999), the formation of cancrinite and sodalite in the presence of monovalent cations K^+or Cs^+ is written as:

$$6Al(OH)_4^- + 6H_2SiO_4^{2-} + (6+y-x)\,Na^+ + xM^+ + yNO_3^- \leftrightarrows [Na^+_{(6+y-x)}, M^+_x]Si_6Al_6O_{24}\cdot yNO_3^- + 12OH^- + 12H_2O \quad (2)$$

where M^+ denotes the monovalent non-Na cations. The maximum of y is 2 as observed in pure $NaNO_3$-cancrinite (Buhl and Löens, 1996). Cancrinite and sodalite have the same stoichiometry, therefore, Eq. (2) describes the formation of both of cancrinite and sodalite. A similar equation can be used to describe the formation of cancrinite and sodalite in the presence of divalent cations (M^{2+}= Mg^{2+}, Ca^{2+}or Sr^{2+}):

$$6Al(OH)_4^- + 6H_2SiO_4^{2-} + (6+y-x)Na^+ + xM^+ + yNO_3^- \leftrightarrows [Na^+_{(6+y-2x)}, M^{2+}_x]Si_6Al_6O_{24}\cdot yNO_3^- + 12OH^- + 12H_2O \quad (3)$$

Both equations illustrate the competition among cations for exchange sites.

4.3. Formation of intermediate silicate, aluminate, and hydroxide phases

Depending on the type of cation present, different intermediate or stable mineral phases were observed. Formation of silicates (Sr^{2+}, Ca^{2+}), aluminate (Sr^{2+}, Ca^{2+}), hydroxide (Ca^{2+}, Mg^{2+}, Sr^{2+}), and aluminosilicates slowed the transformation rate, yet enhanced the crystallinity of cancrinite and the dominance of cancrinite over sodalite. Based on the minerals identified in this experiment, the formation of the intermediate or stable phases in addition to cancrinite and sodalite can be written as follows:

(1) *Formation of silicates:* Both $Ca^{2+}$and Sr^{2+} precipitated out as silicates, but Mg^{2+}did not:

$$xCa^{2+} + H_2SiO_4^{2-} + yH_2O \rightleftharpoons xCaO\cdot SiO_2\cdot(y+1)H_2O \quad (4)$$

$$3Sr^{2+} + 2H_2SiO_4^{2-} + 2OH^- + H_2O \rightleftharpoons Sr_3Si_2O_7\cdot 4H_2O \quad (5)$$

The Ca-silicate was less labile than the Sr-silicate.

(2) *Formation of aluminates:* Two polymorphs of Ca-aluminate and one type of Sr aluminate (Sr-hydrogarnet) formed in 1 and 16 M NaOH solutions:

$$3Ca^{2+} + 2Al(OH)_4^- + 4OH^- + (2-6)H_2O \rightleftharpoons Ca_3Al_2O_6\cdot(8-12)H_2O \quad (6)$$

$$3Ca^{2+} + 2Al(OH)_4^- + 4OH^- \rightleftharpoons Ca_3Al_2(OH)_{12}\ \text{(Ca-hydrogarnet)} \quad (7)$$

$$3Sr^{2+} + 2Al(OH)_4^- + 4OH^- \rightleftharpoons Sr_3Al_2(OH)_{12}\ \text{or}\ Sr_3Al_2O_6\cdot 6H_2O \quad (8)$$

The Sr-hydrogarnet was more labile than Ca-aluminate, and Ca-aluminate was more labile than Ca-silicate.

(3) *Formation of hydroxides:* All of the divalent cations (Ca^{2+}, Mg^{2+} and Sr^{2+}) precipitated as hydroxides:

$$Mg^{2+} + 2OH^- \rightleftharpoons Mg(OH)_{2(\text{brucite})} \quad (9)$$

$$Ca^{2+} + 2OH^- \rightleftharpoons Ca(OH)_2 \quad (10)$$

$$Sr^{2+} + 2OH^- \rightleftharpoons Sr(OH)_2 \quad (11)$$

(4) *Formation of aluminosilicates:* Strontium precipitated out as aluminosilicates in 1 M NaOH solutions, and the precipitate later converted to Sr aluminate. When Mg^{2+} was present in the simulants, poorly crystalline amesite formed.

$$2Al(OH)_4^- + 2H_2SiO_4^{2-} + Sr^{2+} \rightleftharpoons SrAl_2Si_2O_8 + 4OH^- + 4H_2O \quad (12)$$

$$2Al(OH)_4^- + H_2SiO_4^{2-} + Mg^{2+} \rightleftharpoons (Mg_2Al)[(Si,Al)O_5](OH)_{4(\text{amesite})} + 3H_2O \quad (13)$$

Reactions (4)–(13) have two opposite effects on the main mineral transformation pathway: all of these reactions reduce the concentration of the divalent cations in the solutions and, therefore, reduce their competition for the cage or channel sites in cancrinite and sodalite. At the same time, Reactions (4)–(13) consume OH^- from solution, which may slow down the

main mineral transformation rate because OH^- is the mineralization agent in forming cancrinite and sodalite (Deng et al., in press). Reactions (4), (5), (12), and (13) decrease the concentration of silicate, and Reactions (6)–(8) and (13) reduce the concentration of aluminate in the solutions. The decrease in silicate and aluminate concen trations depresses the formation of LTA zeolite, cancrinite and sodalite.

4.4. Crystallinity and dominance of cancrinite

This experiment indicates that the crystallinity of cancrinite was enhanced in the presence of Cs^+ and Sr^{2+}. Sodalite formation was inhibited in the presence of high concentrations of CsNO3. This is likely due to a size match requirement between the cations and the cages. Sodalite has only one type of cage (β-cage) which contains 4 monovalent cations (e.g., Na^+) with a central anion (e.g., Cl^-). The ionic radius of Cs^+ (0.169 nm) might be too large for it to fit into this cage. Cancrinite contains the slightly larger ε-cage and a 12-membered ring structure in which Cs^+ cations and the divalent cations may fit. The similarity of cancrinite formed in 16 M NaOH in the presence of K^+, Mg^{2+} $Ca^{2+}$and $Sr^{2+}$to $NaNO_3$-cancrinite indicates the weak effect of these cations on the formation and structure of cancrinite at high NaOH concentration, likely because of competition from Na^+ ions.

Similar to the effect of Cs^+ and Sr^{2+} observed in this experiment, Barney (1976) reported that the presence of a small amount of fission products in radioactive waste did not affect the formation of cancrinite. He observed that (1) only cancrinite formed when Cs^+ is $\leqslant$0.37 M and Sr^{2+} $\leqslant$0.1 M; (2) pollucite ([Cs,Na]$AlSi_2O_6$) and an unknown mineral phase formed when Cs^+ concentration was above 0.75 M; (3) Sr hydrogarnet formed when Sr^{2+} concentration was in the range of 0.38–1.30 M; and (4) $SrCO_3$ formed when CO_3^{2-} appeared in the simulants. Barney (1976) predicted that the incorporated Cs^+ and Sr^{2+} could not be released except by decomposition of the feldspathoids with acids.

4.5. Implications for Hanford tank waste leaks

Given the low concentrations (10^{-6} to 10^{-4} M) of Cs^+ and Sr^{2+} in the tank waste compared with the concentration used in this study, and the slow release of K^+, $Ca^{2+}$and Mg^{2+} from sediments contacting the tank waste, these cations will not likely dramatically change mineral transformation sequence of short-range ordered aluminosilicate → LTA zeolite → cancrinite/sodalite in low-concentration NaOH solutions. The presence of these cations, however, will direct the formation of highly-crystalline cancrinite. The higher pref1erence of Cs^+ incorporation, and the small size as well as higher crystallinity of the Cs-incorporated cancrinite may affect the transport of Cs^+ in the sediment. The precipitation of the intermediate phases will slow down the formation of the feldspathoids, but does not seem to affect the adsorption or incorporation of monovalent cations like Cs^+ in their structures. By and large, the presence of cations other than Na^+ will not affect the formation of the two major types of minerals, cancrinite and sodalite, upon contact of waste solutions with subsurface sediment at the Hanford site. Mineral transformations revealed by this experiment are consistent with simulation experiments with Hanford sediments. Cancrinite and sodalite were the major products in the experiments conducted by Qafoku et al. (2003, 2004) and Mashal et al. (2004). The intermediate phases, however, were not confirmed by these experiments, presumably due to the low concentrations of the cations.

5. Uncited references

Felmy et al. (1998), Felmy et al. (2003), Liu et al. (2005), Park and Englezos (1999) and Parkhurst and Appelo (1999).

Acknowledgements

This research was supported by the Office of Science (BER), US Department of Energy, Grant No. DE-FG07-99ER62882 and by the Inland Northwest Research Alliance. Some of the SEM analysis was performed at the Electron Microscopy Center, Washington State University. James S. Young performed FESEM analysis. FESEM and EDS analyses were carried out in the Environmental Molecular Sciences Laboratory (a national scientific user facility sponsored by the US DOE Office of Biological and Environmental Research) located at Pacific Northwest National Laboratory, operated by Battelle for the DOE.

References

Barnes, M.C., Addai-Mensah, J., Gerson, A.R., 1999. The kinetics of desilication of synthetic spent Bayer liquor seeded with cancrinite and cancrinite/sodalite mixed-phase crystals. J. Cryst. Growth 200, 251–264.

Barney, G.S., 1976. Fixation of radioactive waste by hydrothermal reactions with clays. In: Campbell, M.H. (Ed.), High-Level Radioactive Waste Management, Advances in Chemistry Series, vol. 153. American Chemical Society, Washington, DC, pp. 108–125.

Barrer, R.M., Cole, J.F., Sticher, H., 1968. Chemistry of soil minerals. V. Low temperature hydrothermal transformations of kaolinite. J. Chem. Soc. (A) 1968, 2475–2485.

Bickmore, B.R., Nagy, K.L., Young, J.S., Drexler, J.W., 2001. Nitrate-cancrinite precipitation on quartz sand in simulated Hanford tank solutions. Environ. Sci. Technol. 35, 4481–4486.

Bosnar, S., Antonić-Jelić, T., Bronić, J., Krznarić, I., Subotić, B., 2004. Influence of anions on the kinetics of zeolite A crystallization: a population balance analysis. J. Cryst. Growth 267, 270–282.

Buhl, J.-C., Löens, J., 1996. Synthesis and crystal structure of nitrate enclathrated sodalite $Na_8[AlSiO_4]_6(NO_3)_2$. J. Alloys Compd. 235, 41–47.

Buhl, J.-C., Stief, F., Fechtelkord, M., Gesing, T.M., Taphorn, U., Taake, C., 2000. Synthesis, X-ray diffraction and MAS NMR characteristics of nitrate cancrinite $Na_{7.6}[AlSiO_4]6(NO_3)_{1.6}(H_2O)_2$. J. Alloys Compd. 305, 93–102.

Choi, S., Amistadi, M.K., Chorover, J., 2005a. Clay mineral weathering and contaminant dynamics in a caustic aqueous system I. Wet chemistry and aging effects. Geochim. Cosmochim. Acta 69, 4425–4436.

Choi, S., Crosson, G., Mueller, K.T., Seraphin, S., Chorover, J., 2005b. Clay mineral weathering and contaminant dynamics in a caustic aqueous system II. Mineral transformation and microscale partitioning. Geochim. Cosmochim. Acta 69, 4437–4451.

Chorover, J., Choi, S., Amistadi, M.K., Karthikeyan, K.G., Crosson, G., Mueller, K.T., 2003. Linking cesium and strontium uptake to kaolinite weathering in simulated tank waste leachate. Environ. Sci. Technol. 37, 2200–2208.

Deng, Y., Harsh, J.B., Flury, M., Young, J.S., Boyle, J.S., in press. Mineral formation during simulated leaks of Hanford waste tanks. Appl. Geochem.

Dixon, J.B., Schulze, D.G., 2002. Soil Mineralogy with Environmental ApplicationsSSSA Book Series, vol. 7. Soil Science Society of America Inc., Madison, Wisconsin, USA.

Fechtelkord, M., Posnatzki, B., Buhl, J.-C., Fyfe, C.A., Groat, L.A., Raudsepp, M., 2001. Characterization of synthetic Cs–Li cancrinite grown in a butanediol-water system: an NMR spectroscopic and Rietveld refinement study. Am. Mineral. 86, 881–888.

Felmy, A.R., Dixon, D.A., Rustad, J.R., Mason, M.J., Onishi, L.M., 1998. The hydrolysis and carbonate complexation of strontium and calcium in aqueous solution. Use of molecular modeling calculations in the development of aqueous thermodynamic models. J. Chem. Thermodyn. 30, 1103–1120.

Felmy, A.R., Mason, M.J., Gassman, P.L., McCready, D.E., 2003. The formation of Sr silicates at low temperature and the solubility product of tobermorite-like $Sr_5Si_6O_{16}(OH)_2 \cdot 5H_2O$. Am. Mineral. 88, 73–79.

Gephart, R.E., Lundgren, R.E., 1998. Hanford Tank Cleanup: A Guide to Understanding the Technical Issues, fourth ed. Battelle Press, Columbus.

ICDD, 1974. Powder Diffraction File. International Center for Diffraction Data, Newtown Square, PA.

Kaplan, D.I., Parker, K.E., Ritter, J.C., 1998. Effects of Aging Quartz Sand and Hanford Sediment with Sodium Hydroxide on Radionuclide Sorption Coefficients and Sediment Physical and Hydrologic Properties: Final Report for Substask 2a. Pacific Northwest National Laboratory, PNNL-11965, Richland, Washington.

Kaplan, D.I., Serne, R., Schefer, J., Lindstrom, R.M., Parker, K.E., Owen, A.T., McCready, D.E. Young, J.S., 2003. The Influence of Glass Leachate on the Hydraulic, Physical, Mineralogical and Sorptive Properties of Hanford Sediment. Pacific Northwest National Laboratory, PNNL-14325, Richland, Washington.

Lager, G.A., Armbruster, T., Faber, J., 1987. Neutron and X-ray diffraction study of hydrogarnet $Ca_3Al_2(O_4H_4)_3$. Am. Mineral. 72, 756–765.

Lichtner, P.C., Felmy, A.R., 2003. Estimation of Hanford SX tank waste compositions from historically derived inventories. Comput. Geosci. 29, 371–383.

Liu, Q., Xu, H., Navrotsky, A., 2005. Nitrate cancrinite: synthesis, characterization, and determination of the enthalpy of formation. Micropor. Mesopor. Mater. 87, 146–152.

Mashal, K., Harsh, J.B., Flury, M., Felmy, A.R., Zhao, H., 2004. Colloid formation in Hanford sediments reacted with simulated tank waste. Environ. Sci. Technol. 38, 5750–5756.

Ming, D.W., Mumpton, F.A., 1989. Zeolites in soils. In: Dixon, J.B., Weed, S.B. (Eds.), Minerals in Soil Environments, second ed. Soil Science Society of America, Madison, Wisconsin, USA, pp. 873–912.

Mon, J., Deng, Y., Flury, M., Harsh, J.B., 2005. Cesium incorporation and diffusion in cancrinite, sodalite, zeolite, and allophane. Micropor. Mesopor. Mater. 86, 277–286.

Mozgawa, W., 2001. The relation between structure and vibrational spectra of natural zeolites. J. Mol. Struct. 596, 129–137.

Nevskii, N.N., Ivanov-Emin, B.N., Nevskaya, N.A., Kaziev, G.Z., Belov, N., 1982. Crystal structure of strontium hydrogarnets. Dokl. Akad. Nauk SSSR 264, 857–858.

Park, H., Englezos, P., 1999. Thermodynamic modeling of sodium aluminosilicate formation in aqueous alkaline solutions. Ind. Enginer. Chem. Resourc. 38, 4959–4965.

Parkhurst, D.L., Appelo, C., 1999. Users guide to PHREEQC (version 2) a computer program for speciation, batch-reaction, one-dimensional transport, and inverse geochemical calculations. U.S. Dept. Interior, U.S. Geol. Surv.

Qafoku, N.P., Ainsworth, C.C., Szecsody, J.E., Bish, D.L., Young, J.S., McCready, D.E., Qafoku, O.S., 2003. Aluminum effect on dissolution and precipitation under hyperalkaline conditions: II. Solid phase transformations. J. Environ. Qual. 32, 2364–2372.

Qafoku, N.P., Ainsworth, C.C., Szecsody, J.E., Qafoku, O.S., 2004. Transport controlled kinetics of dissolution and precipitation in the sediments under alkaline and saline conditions. Geochim. Cosmochim. Acta 68, 2981–2995.

Serne, R.J., Zachara, J.M., Burke, D.S., 1998. Chemical information on tank supernatants, Cs adsorption from tank liquids onto Hanford sediments, and field observations of Cs migration from past tank leaks. Pacific Northwest National Laboratory.

Please cite this article in press as: Deng, Y. et al., Cancrinite and sodalite formation in the presence of ..., Appl. Geochem. (2006), doi:10.1016/j.apgeochem.2006.06.019

Sieger, P., Wiebcke, M., Felsche, J., Buhl, J.C., 1991. Orientational disorder of the nitrite anion in the sodalite sodium aluminum silicate nitrite ($Na_8[AlSiO_4]_6(NO_2)_2$). Acta Crystallog., Sect. C: Cryst. Struct. Commun. 47, 498–501.

Singer, A., 1989. Palygorskite and sepiolite group minerals. In: Dixon, J.B., Weed, S.B. (Eds.), Minerals in Soil Environments, second ed. Soil Science Society of America, Madison, Wisconsin, USA, pp. 829–872.

Steinfink, H., Brunton, G., 1956. The crystal structure of amesite. Acta Cryst. 9, 487–492.

Um, W., Serne, R.J., Yabusaki, S.B., Owen, A.T., 2005. Enhanced radionuclide immobilization and flow path modifications by dissolution and secondary precipitates. J. Environ. Qual. 34, 1404–1414.

Zhukhlistov, A.P., Avilov, A.S., Ferraris, D., Zvyagin, B.B., Plotnikov, V.P., 1997. Three-site disordered statistical distribution of hydrogen in the brucite structure $Mg(OH)_2$, based on electron diffractometric data. Kristallograf. 42, 841–845.

Please cite this article in press as: Deng, Y. et al., Cancrinite and sodalite formation in the presence of ..., Appl. Geochem. (2006), doi:10.1016/j.apgeochem.2006.06.019

Available online at www.sciencedirect.com
SCIENCE DIRECT®
Applied Geochemistry 21 (2006) 1392–1409
Applied Geochemistry
www.elsevier.com/locate/apgeochem

Mineral formation during simulated leaks of Hanford waste tanks

Youjun Deng [a], James B. Harsh [a,*], Markus Flury [a], James S. Young [b], Jeffrey S. Boyle [a]

[a] *Department of Crop and Soil Sciences, Center for Multiphase Environmental Research, Washington State University, Pullman, WA 99164-6420, United States*
[b] *Pacific Northwest National Laboratory, Environmental Molecular Sciences Laboratory, Richland, WA 99352, United States*

Received 3 September 2005; accepted 4 May 2006
Editorial handling by M. Gascoyne
Available online 11 July 2006

Abstract

Highly-alkaline waste solutions have leaked from underground tanks at the US DOE Hanford Site, Washington, causing mineral dissolution and re-precipitation upon contact with subsurface sediments. The main mineral precipitation and transformation pathways were studied in solutions mimicking tank leak conditions at the US DOE Hanford Site. In batch experiments, Si-rich solutions, representing dissolved silicate minerals, were mixed with caustic tank simulants. The tank wastes encompass a large range of chemical compositions. The effect of the following factors on mineral transformations were investigated: temperature (22, 50 and 80 °C), concentration of NaOH (from 0 to 16 M), 6 types of common inorganic anions in the tank supernatant, concentration of $NaNO_3$ (the most abundant electrolyte in the tanks), and the Si/Al ratio in the starting solutions. Precipitates were characterized by X-ray diffraction (XRD), scanning electron microscopy (SEM), and Fourier transform infrared (FT-IR) spectroscopy. A general mineral transformation pathway was observed: poorly crystalline aluminosilicate → Linde Type A (LTA) zeolite → cancrinite/sodalite. Cancrinite and sodalite were the two stable mineral phases. The concentration of NaOH and the type of anion played the determinative roles in mineral formation and transformation. Increasing NaOH concentration and temperature favored the formation of cancrinite and sodalite. Cancrinite formed in the presence of NO_3^- or SO_4^{2-}; sodalite formed in the presence of Cl^- or NO_2^-. The experiments indicate that (1) NaOH is a mineralization agent in the mineral transformation and the anions served as templates in the formation of cancrinite and sodalite by forming ion-pairs with Na^+ and (2) cancrinite and sodalite with various morphologies and crystallinity should form in the contaminated sediments.

1. Introduction

During nearly 40 years of U processing and Pu extraction, a large amount of radioactive waste has been generated at the US Department of Energy Hanford Site in Washington State. The waste was stored in 177 underground tanks on site (Crowley, 1997; Gephart and Lundgren, 1998). Sixty-seven of the single-shell carbon–steel tanks are suspected to have leaked 3800 m^3 or more liquid containing over 10^6 Ci of ^{137}Cs into the underlying sediments

* Corresponding author. Fax: +1 509 335 8674.
E-mail address: harsh@wsu.edu (J.B. Harsh).

0883-2927/$ - see front matter © 2006 Elsevier Ltd. All rights reserved.
doi:10.1016/j.apgeochem.2006.05.002

(Gephart and Lundgren, 1998). The waste solutions have concentrated NaOH (up to 8 M or more) and have been shown to alter and dissolve minerals occurring at the Hanford site (Kaplan et al., 1998, 2003; Serne et al., 1998; Bickmore et al., 2001; McKinley et al., 2001; Chorover et al., 2003; Qafoku et al., 2003a,b, 2004). Kaolinite, quartz, feldspar and smectite can be partially or completely dissolved by simulated tank solutions (Bickmore et al., 2001; Chorover et al., 2003; Zhao et al., 2004; Mashal et al., 2004).

In addition to the dissolution of minerals present in the sediments, new poorly crystalline and crystalline phases have been observed in simulation experiments mimicking Hanford tank leaks (Table 1). The reported new phases are bayerite, poorly crystalline materials, cancrinite, sodalite and chabazite. The dissolution of the sediments and the precipitation of the new phases alter the sorption behavior of radionuclides in the sediments. Radionuclides can be incorporated in and sorbed to the new mineral phases (Chorover et al., 2003; Zhao et al., 2004; Um et al., 2005; Mon et al., 2005). The new phases are likely not stable with respect to the chemical composition of the natural pore water in the sediments; therefore, they can become contaminant sources in the future. This paper is focused on the role of solution composition, temperature, and time in the formation of new mineral phases.

The reported studies suggest that mineral transformation in the sediments can be generalized into two main processes: (1) dissolution of silica and aluminosilicate minerals, e.g.:

$$SiO_{2(quartz)} + 2OH^- = H_2SiO_4^{2-} \quad (1)$$

$$Al_2Si_2O_5(OH)_{4(kaolinite)} + 6OH^- + H_2O = 2Al(OH)_4^- + 2H_2SiO_4^{2-} \quad (2)$$

and (2) precipitation of poorly crystalline materials, feldspathoids, e.g., cancrinite and sodalite, and zeolites:

$$6Al(OH)_4^- + 6H_2SiO_4^{2-} + 8Na^+ + 2NO_3^- = Na_6Si_6Al_6O_{24} \cdot 2NaNO_{3(cancrinite)} + 12OH^- + 12H_2O \quad (3)$$

Cancrinite, sodalite, and Linde Type A zeolite (also called Linde A zeolite, or Zeolite A) have identical framework stoichiometry – $[Si_6Al_6O_{24}]^{6-}$. The minerals are structurally related, differing only in the stacking sequences of the secondary building units.

The waste composition varies considerably among Hanford tanks (Serne et al., 1998; Lichtner and Felmy, 2003). It is expected that during a leak, different waste solutions will cause different dissolution and precipitation reactions in the sediments. For instance, mineral dissolution, as indicated by Si released into the solution phase, was enhanced with increasing NaOH concentration (Kaplan et al., 1998, 2003; Qafoku et al., 2004). The types of anions present will likely affect the formation of new minerals, and thus indirectly affect the dissolution of the sediments. The temperature in the vicinity of the tanks was estimated to be as high as 120 °C, and in the sediments 20 m below the tanks could be as high as 70 °C (Pruess et al., 2002). The effect of temperature on mineral transformation was not explicitly considered in most of the previous simulation experiments with Hanford sediments. The authors have observed that increasing temperature increased the rates of kaolinite dissolution and feldspathoid formation (Zhao et al., 2004).

Most previous work has considered the minerals formed from a mixture of tank simulants with solid phases – either Hanford sediments or model minerals (Table 1). This prevents rigorous control over Si/Al ratio, cation, and anion compositions. Furthermore, most studies limited NaOH concentration to one or two values and anions to $OH^-$and NO_3^-. Although NaOH concentrations in the tanks appeared to exceed 10 M (Buck and McNamara, 2004), no studies have used concentrations >4 M. Because only a narrow range of chemical compositions was simulated, the general principles of the mineral transformations, particularly, the functions of the individual waste components in the mineral transformation, have not been delineated. Given the large variation and the complexity of tank waste composition, it is important to systematically study the mineral transformation as a function of waste composition, temperature, and time.

Here, the precipitation and transformation of cancrinite, sodalite, LTA zeolite, and poorly crystalline aluminosilicates in tank waste simulants are investigated. The overall goal was to deduce the mineral transformation pathways. The specific objectives were (1) to determine the effects of alkalinity, salinity, electrolyte type, temperature, and time on the crystallographic and morphological properties of the precipitates and (2) to elucidate structure-directing roles of anions in the formation of cancrinite and sodalite.

Table 1
Precipitates formed in simulation experiments mimicking Hanford tank leaks

Starting material	Simulant composition				Temperature	New precipitates	Reference
	OH^-	Al	Anions	Cations			
Hanford sediment	1.5 M	0.6 M	6 M NO_3^-, 0.67 M NO_2^-, 0.27 M Cl^-	4.75 M Na^+	20, 32, 60, 83 °C	Bayerite ($Al(OH)_3$)	Serne et al. (1998)
	1 M	0.005–0.22 M	1 M NO_3^-	~2 M Na^+	50 °C	Cancrinite, sodalite	Qafoku et al. (2003b)
	1, 4 M	0.05, 0.165 M	1 M NO_3^-, 0.19, 1.93 mM CrO_4^{2-}	~2, 5 M Na^+	50 °C	Cancrinite	Qafoku et al. (2004)
	1.4, 2.8 mol/kg	0.125, 0.25 mol/kg	3.7 mol/kg NO_3^-	5.2–6.8 mol/kg Na^+	50 °C	Cancrinite, sodalite	Mashal et al. (2004)
	0.1–1.4 mol/kg	3.7,125 mmol/kg	0,3.7 mol/kg NO_3^-	0.1–5.2 mol/kg Na^+	25 and 50 °C	Cancrinite, sodalite,zeolite A	Mashal et al. (2005a)
	1.47 M	0.805 M	4.72 M NO_3^-, 0.17 M CO_3^{2-}, 0.84 M NO_2^-, 0.06 M SO_4^{2-}	8.05 M Na^+	20, 70 °C	Cancrinite, zeolite,bayerite	Wan et al. (2004)
	1.04 M	0.01 M	2 M NO_3^-	~3 M Na^+	90 °C	Cancrinite, analcime	Um et al. (2005)
Quartz (+biotite)	0.1, 1 M	5, 10 mM	0.5–4 M NO_3^-	2.1–3 M Na^+	89 °C	Cancrinite	Bickmore et al. (2001)
	1.04 M	0.01 M	2 M NO_3^-	~3 M Na^+	90 °C	Cancrinite	Um et al. (2005)
Kaolinite	1 mol/kg	0.05 mol/kg	1 mol/kg NO_3^-	2 mol/kg Na^+, 10^{-5}– 10^{-3} M Cs^+, Sr^{2+}	Room *T*	Chabazite, sodalite, cancrinite	Chorover et al. (2003)
	1.4, 2.8 mol/kg	0.125, 0.25 mol/kg	3.7 mol/kg NO_3^-	5.2–6.8 mol/kg Na^+	50, 80 °C	Cancrinite, sodalite	Zhao et al. (2004)
Tetraethyl orthosilicate	0.7,1.4 mol/kg	6.5-125 mmol/kg	1.5 mol/kg NO_3^-	2.2–3.1 mol/kg Na^+	50 °C	Cancrinite, sodalite, zeolite A	Mashal et al. (2005b)

2. Materials and methods

2.1. Mineral synthesis

The approach was to obtain pure precipitates that could be characterized in detail. Sodium silicate ($Na_2SiO_3 \cdot 9H_2O$, Fisher Scientific) was used to represent the dissolved Si from the sediments (see reactions (1) and (2)). The silicate solution was reacted with tank simulants of various chemical composition, and the precipitates were characterized after specified reaction periods. The concentrations used in the experiments were guided by reported concentrations of dissolved Si in Hanford sediments (Qafoku et al., 2004) and Na^+, OH^-, and anion concentrations in waste tanks (Serne et al., 1998; Lichtner and Felmy, 2003).

Silicate concentration were varied from 0.018 M to 0.175 M and aluminate concentration from 0.005 M to 0.5 M. The corresponding Si/Al molar ratio was varied from 0.35 to 35 (Table 2). During the investigation of the effects of other factors, only one concentration level was used, 0.175 M for silicate and 0.5 M for aluminate, in the simulants.

Sodium silicate and sodium aluminate ($NaAlO_2$, STREM Chemicals, Newburyport, MA) were dissolved in 0, 1, or 16 M NaOH solutions separately and warmed to desired temperatures (22, 50 or 80 °C). The silicate and aluminate solutions (20 or 40 mL total) were mixed with different ratios in Nalgene polypropylene bottles containing different additional anions (Table 2). The bottles were capped and kept at 22, 50 or 80 °C without shaking. At the time of analysis, the bottles were shaken by hand and about 1 mL of suspension was taken and centrifuged at 1.2×10^4g for 5 min. The supernatant was decanted and the precipitates were washed 3 times with distilled water by shaking and centrifuging. After the last washing, the particles were suspended in water and about 1 mL suspension was pipetted onto a quartz or glass slide and dried at 50 °C for X-ray diffraction (XRD) analysis. The rest of the sample was dried in the centrifuge tube at 50 °C. To test whether heating would induce mineral alteration, samples that were freeze-dried, air-dried, and heated at 50 °C and 150 °C were compared with XRD and SEM analyses. No mineral transformation was observed during these drying processes.

To study the effects of NO_3^-, NO_2^-, CO_3^{2-}, PO_4^{3-}, Cl^- and SO_4^{2-} on mineral transformation, two sets of simulants were used. In the first set, the solutions contained only one type of anion; in the second set, the solutions contained 2–6 types of anions. The combination of the anions in the second set was based on their abundance in tank waste. The average abundance of the anions in the SX waste tanks decreased in the order: $NO_3^- > NO_2^- > CO_3^{2-} > PO_4^{3-} > Cl^- > SO_4^{2-}$ (Serne et al., 1998). Nitrate and NO_2^- were chosen for the 2-anion mixture; NO_3^-, NO_2^-, and CO_3^{2-} were chosen for the 3-anion mixture; and successively, one more anion was included following the abundance order.

2.2. Characterization of precipitates

2.2.1. Mineral identification and quantification by X-ray diffraction

The XRD analysis was performed with Cu Kα radiation on a Philips diffractometer equipped with a graphite monochromator and a θ-compensation slit (Philips XRG 3100, Philips Analytical Inc., Mahwah, NJ). The instrument was operated at 35 kV and 30 mA. A step size of 0.05° 2θ and a

Table 2
Chemical compositions of simulants, reaction temperatures, and sampling time

Experiments		NaOH (M)	Anion[a]	$H_2SiO_4^{2-}$ (M)	$Al(OH)_4^-$ (M)	Temperature (°C)	Sampling time (weeks)
Investigating factor	Values of the factor						
Time	5 min, 2, 6 h, 1, 2, 4 days, 1, 2, 3, 4, 6, 8, 12, 16, 24, 32 weeks	1	NO_3^-	0.175	0.5	22, 50, 80	Varied
NaOH concentration	0, 0.125, 0.25, 0.5, 1, 2, 4, 8, 16 M	Varied	NO_3^-	0.175	0.5	80	1, 4, 8, 16, 32
Type of anion	NO_3^- NO_2^-, CO_3^{2-}, PO_4^{3-}, Cl^-, SO_4^{2-}	1, 16	Varied	0.175	0.5	80	4, 8, 16, 32
Multiple types of anions	Mixture of 2–6 anions	1	Varied	0.175	0.5	80	4, 8, 16, 32
$NaNO_3$ concentration	0, 0.125, 0.5, 1, 2, 4, 8 M and saturated	1		0.175	0.5	80	4, 8, 16, 32
Silicate concentration	0.018, 0.044, 0.088, 0.131, 0.175 M	1	NO_3^-	varied	0.5	80	4
Aluminate concentration	0.005, 0.05, 0.125, 0.25, 0.5 M	1	NO_3^-	0.175	varied	80	4

[a] 0.5 M for monovalent anions, 0.25 M for divalent anions, and 0.17 M for PO_4^{3-}.

dwell time of 5 s at each step were used in the step scan mode. The particles on the slides did not show strong orientation preference.

Mineral quantification was based on the linear relationship between diffraction intensity, I, and the weight fraction of a mineral phase, w, (Moore and Reynolds, 1997). The ratio of the diffraction intensities of two minerals can be written as (Moore and Reynolds, 1997):

$$\frac{I_1}{I_2} = \frac{k_1 w_1}{k_2 w_2} = k\frac{w_1}{w_2} \tag{4}$$

where k_1 and k_2 are constants depending on diffraction angle and chemical formula of the mineral, and $k = \frac{k_1}{k_2}$.

The constant k was obtained from a series of standards, which were prepared by pairwise mixing of known amounts of poorly crystalline aluminosilicate, cancrinite, sodalite and LTA zeolite. For the mineral standards, poorly crystalline aluminosilicate, LTA zeolite, sodalite, and cancrinite were synthesized in very similar solutions as the simulants. The XRD and SEM imaging analyses (data not shown) indicated that the poorly crystalline aluminosilicate and LTA zeolite standards were pure and sodalite standards contained trace amounts of cancrinite (<5% by weight). Pure cancrinite with small particle size (< 2 μm) that resembled those commonly observed in the simulants was not obtained; instead, a mixture of cancrinite and sodalite was formed. The weight fraction of cancrinite in this mixture was delineated from XRD analysis by adding known amounts of sodalite to the mixture. The 101, 121, and 400 diffraction peaks of cancrinite, the 310 and 200 diffraction peaks of sodalite, and the 110, 111, 220, and 330 diffraction peaks of LTA zeolite were used for the quantification. These peaks are unique for the individual crystalline phases. The

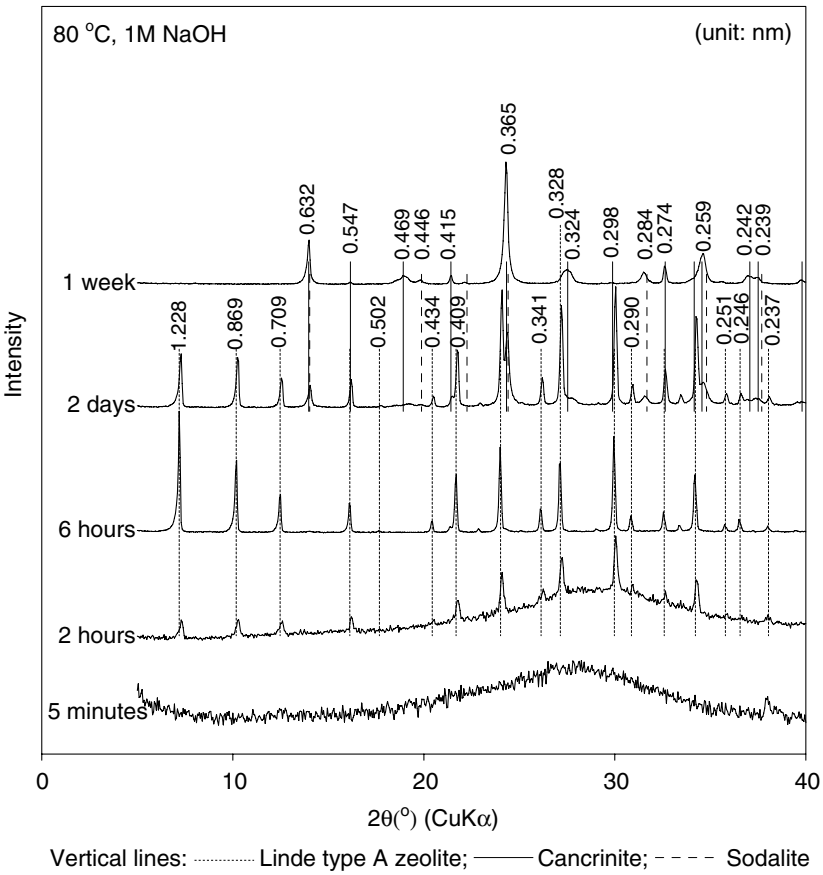

Fig. 1. XRD patterns of the precipitates formed at different stages at 80 °C in 1 M NaOH in the presence of 0.5 M NO_3^-. Precipitates formed after longer reaction time had similar patterns as the 1-week precipitate. Peak positions of LTA zeolite (Wyckoff, 1968), cancrinite (Buhl et al., 2000), and sodalite (Sieger et al., 1991) are marked with vertical lines.

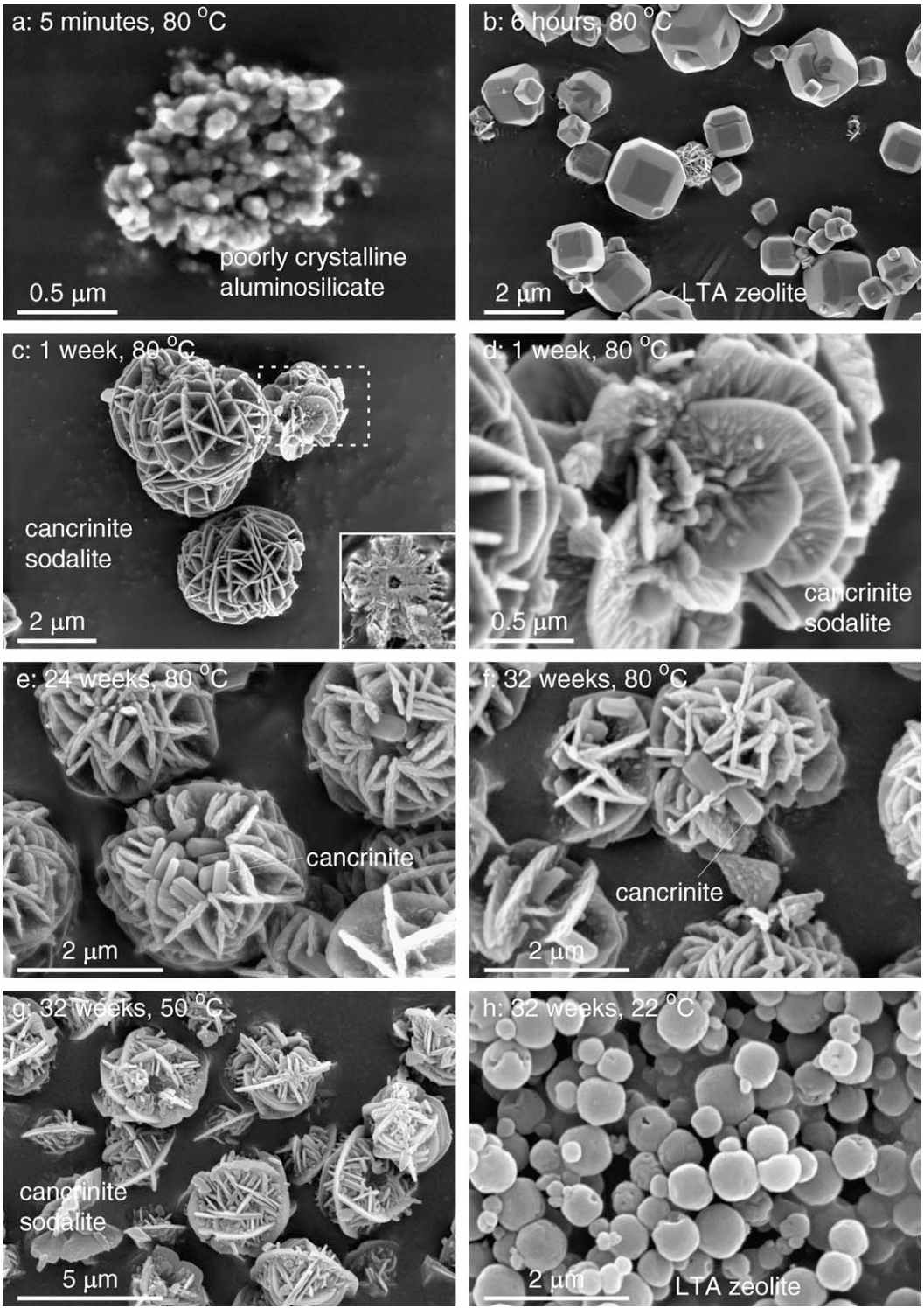

Fig. 2. SEM images of precipitates formed at different stages in simulants containing 1 M NaOH and 0.5 M NO_3^-. (a–f): at 80 °C, the inset in (c) is a sectioned lepisphere and (d) is an enlargement of the outlined area in (c); (g) at 50 °C for 32 weeks; and (h) at 22 °C for 32 weeks.

approach of Hermans and Weidinger (1961) was followed to estimate poorly crystalline aluminosilicate based on its broad diffraction peak near 0.3 nm.

2.2.2. Electron microscopy

Micrographs were recorded on a Hitachi S-570 scanning electron microscope (SEM) and a LEO982 field emission scanning electron microscope (FESEM). The X-ray energy dispersive spectroscopy (EDS) analysis was performed on the FESEM with an Oxford ISIS energy dispersive X-ray detector. Powder samples were directly mounted on carbon tabs and sputter coated with Au for analysis on the SEM and with carbon for the FESEM. Some samples were embedded in LR White resin (London Resin Company, Ltd., Reading, Berkshire, England) and sectioned with a diamond knife. The EDS spectra were often checked on several particles, but due to the similarity among the particles, only one spectrum for each sample is reported.

2.2.3. FT-IR spectra analyses

Fourier transform infrared (FT-IR) spectra were recorded on a Perkin–Elmer Spectrum GX 162 FT-IR System spectrometer with a resolution of 1 cm^{-1}. A mid-IR range deuterated triglycine sulfate (TGS) detector was used. The optic bench, detector, and sample chamber of the instrument were purged with dry and low-CO_2 air produced by a Whatman Lab Gas Generator (Haverhill, MA). Precipitates (0.5–2 mg) were mixed with 150 mg dry KBr and the mixtures pressed into pellets with a hydraulic press. The pellets were heated to 150 °C for at least 12 h to reduce moisture and then were cooled to room temperature in a desiccator before IR analysis.

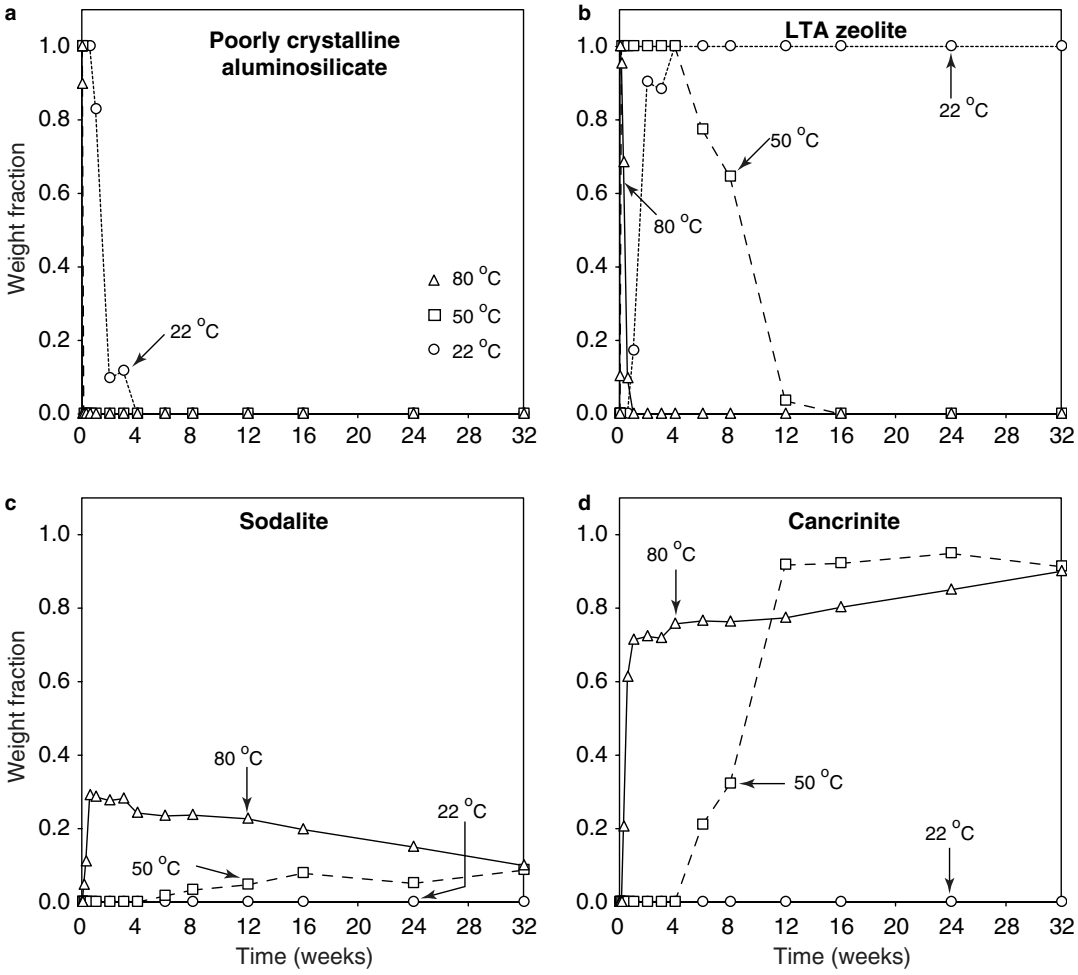

Fig. 3. Weight fractions of poorly crystalline aluminosilicate, LTA zeolite, sodalite, and cancrinite formed at 22, 50 and 80 °C in simulants containing 1 M NaOH and 0.5 M NO_3^-.

3. Results

3.1. Mineral transformation in 1 M NaOH in the presence of 0.5 M NO_3^-

A white precipitate formed instantly when a 1 M NaOH solution containing silicate was mixed with a 1 M NaOH solution containing aluminate at 22, 50 and 80 °C. At all temperatures, a similar sequence of mineral formation/transformation was observed. Typical XRD patterns for 80 °C are shown in Fig. 1. The initial precipitates did not have distinct X-ray diffraction peaks (e.g., the 5-min pattern in Fig. 1), suggesting that they are, at best, poorly crystalline aluminosilicate materials. This phase converted to LTA zeolite, and then to cancrinite and sodalite (Fig. 1).

The poorly crystalline aluminosilicate precipitates had small size (<0.1 μm in diameter) and uniform shape (Fig. 2a). The LTA zeolite particles were corner-truncated (111 form) or edge-truncated (110 form) cubes (Fig. 2b). The cancrinite and sodalite particles were lepispheres composed of intergrown thin disks or blades (Fig. 2c–f). The lepispheres were hollow in the center (Fig. 2c, inset). After longer reaction time, small needle-shaped hexagonal cancrinite appeared on the disks (Fig. 2e,f).

The mineral formation/transformation rates increased with temperature. This is shown by plotting the weight fractions of the minerals as a function of reaction time (Fig. 3). There appears to be no net conversion of sodalite to cancrinite at 50 °C, i.e., the weight ratio of sodalite-to-cancrinite remained constant after the dissolution of LTA zeolite. The ratio decreased at 80 °C, suggesting continuous transformation of sodalite to cancrinite. The mineral transformation at the three temperatures were:

$$\text{At } 22\,^{\circ}\text{C}: \text{Poorly crystalline aluminosilicate} \xrightarrow{\sim 1\ \text{week}} \text{LTA zeolite.}$$

$$\text{At } 50\,^{\circ}\text{C}: \text{Poorly crystalline aluminosilicate} \xrightarrow{<1\ \text{day}} \text{LTA zeolite} \xrightarrow{\sim 6\ \text{weeks}} \text{cancrinite} + \text{sodalite}$$

$$\text{At } 80\,^{\circ}\text{C}: \text{Poorly crystalline aluminosilicate} \xrightarrow{<2\ \text{h}} \text{LTA zeolite} \xrightarrow{<1\ \text{day}} \text{cancrinite} + \text{sodalite} \xrightarrow{<32\ \text{weeks}} \text{cancrinite}$$

The morphologies of particles formed at 22 and 50 °C were similar to those formed at 80 °C. The LTA zeolite had similar morphology as shown in Fig. 2b, except LTA zeolite formed at 22 °C was more rounded than at 50 °C and 80 °C (Fig. 2h). The LTA zeolite particles formed at 22 °C did not show distinct morphological changes even after 2 years of reaction.

3.2. Effect of NaOH concentration on mineral transformations

The effects of NaOH concentration can be summarized as follows: (1) increasing NaOH concentration

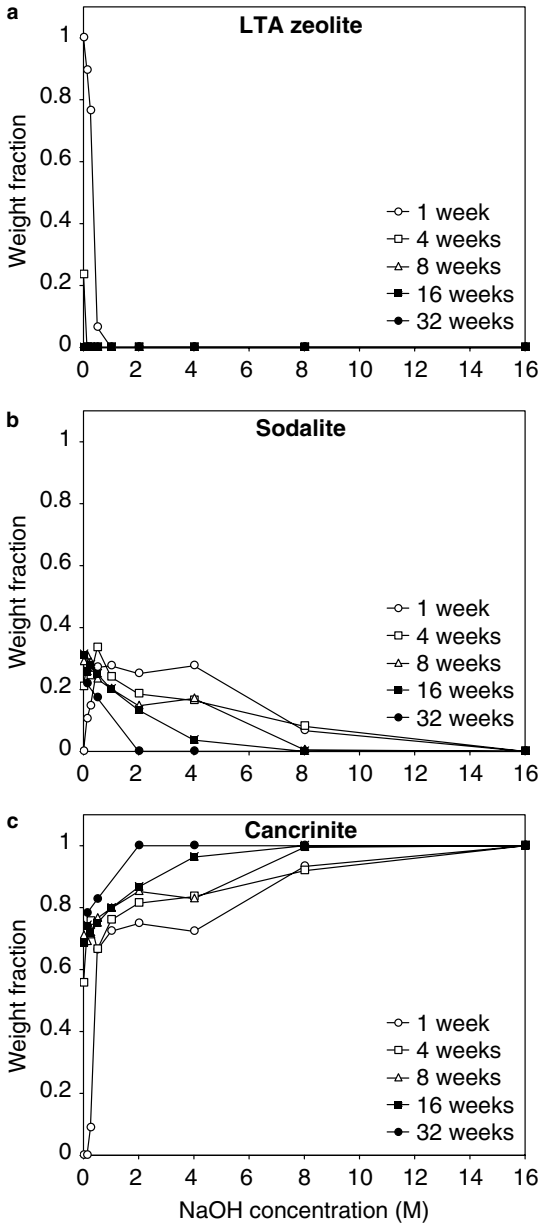

Fig. 4. Weight fractions of: (a) LTA zeolite; (b) sodalite and (c) cancrinite formed in solutions of different NaOH concentration in the presence of 0.5 M NO_3^- at 80 °C.

increased the mineral transformation rate and (2) the morphologies and sizes of cancrinite and sodalite varied with NaOH concentration.

In the simulants containing <8 M NaOH, the mineral transformations were the same as for the case of 1 M NaOH discussed above. The dissolution of LTA zeolite was more rapid at increasing NaOH concentrations (Fig. 4a). The weight fraction of sodalite initially increased with NaOH concentration for <1 M NaOH but decreased for >1 M NaOH (Fig. 4b). The differences were due to the increased transformation rate from LTA zeolite to sodalite/cancrinite as NaOH concentration was increased. The weight fraction of cancrinite consistently increased with increasing NaOH concentration and with reaction time (Fig. 4c). After 32 weeks of reaction, cancrinite was the only mineral left in simulants containing >2 M NaOH. In 16 M NaOH, cancrinite was the only mineral observed. These results suggest that, in the presence of $NaNO_3$, cancrinite is stable in concentrated NaOH solutions but sodalite is not.

Three types of morphologies for cancrinite and sodalite were observed when the NaOH concentration was varied: lepispheres, small needles or bars, and well-crystallized euhedral particles. Increasing

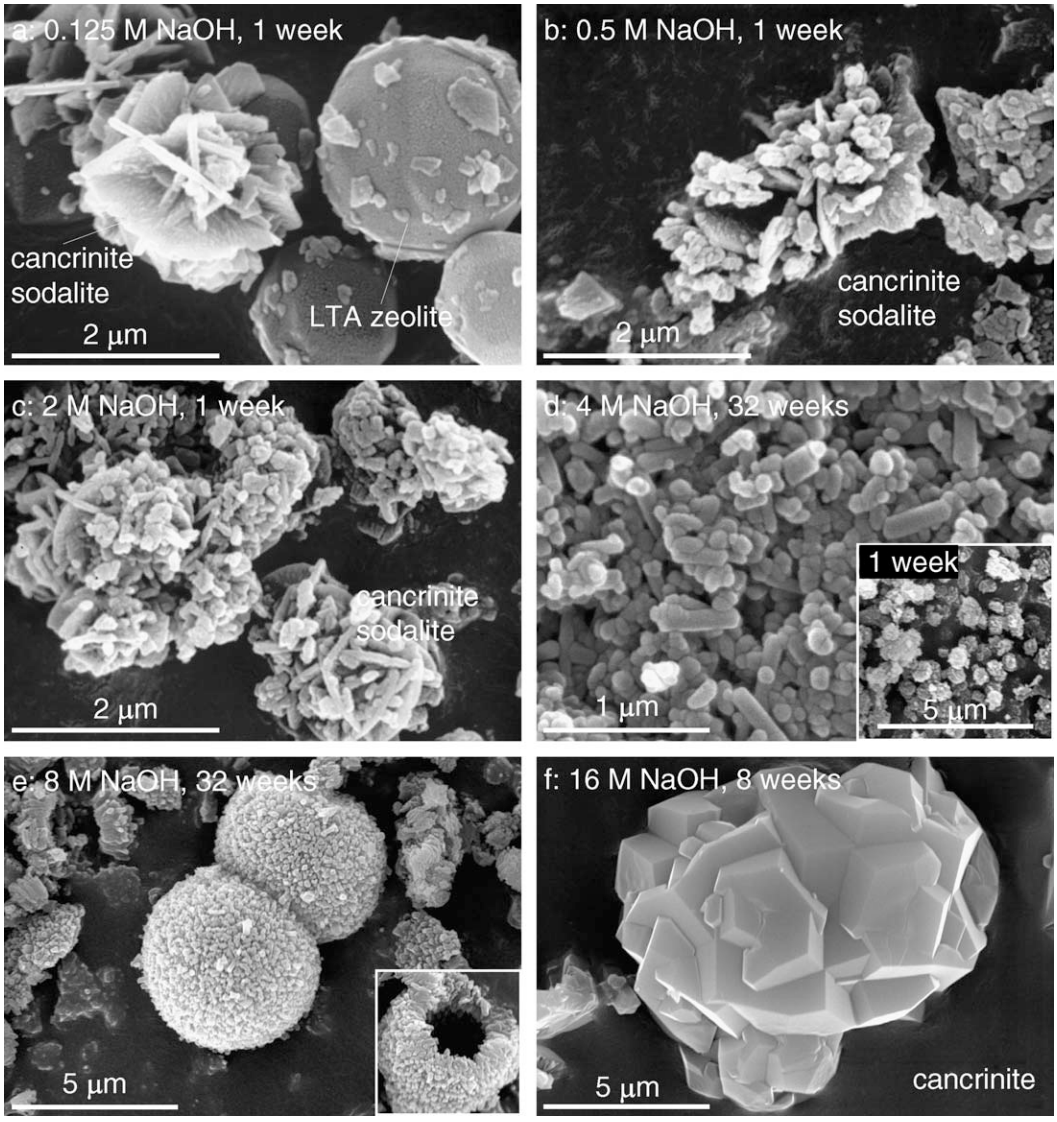

Fig. 5. SEM images of precipitates formed in solutions of different NaOH concentration in the presence of 0.5 M NO_3^-, after 1 week of reaction unless indicated otherwise.

NaOH concentration increased the symmetry, the particle size of the crystals, or both. Lepispheric cancrinite and sodalite formed when NaOH concentration was <4 M (Fig. 5a–c). The lepispherical precipitates formed in 4 M NaOH were smaller than those formed at lower NaOH concentration (Fig. 5d, inset); after longer reaction time (e.g., 32 weeks), only small needle-shaped hexagonal cancrinite formed in 4 M NaOH (Fig. 5d). Small, aggregated particles were observed in 8 M NaOH (Fig. 5e). Cancrinite formed in 16 M NaOH solutions were generally larger and more developed toward euhedral crystals (Fig. 5f),suggesting higher crystallinity. Mineral transformation rates, the symmetry of the crystals, and the particle size of the precipitates suggest that NaOH is a mineralization agent in the formation of cancrinite in the presence of $NaNO_3$.

3.3. Structure-directing roles of anions in cancrinite and sodalite formation

Anions $NO_3^-, NO_2^-, CO_3^{2-}, PO_4^{3-}, Cl^-$ and SO_4^{2-} in the simulants affected (1) the formation rate and dominance of cancrinite and sodalite and (2) the morphologies of cancrinite and sodalite. No matter what anions were present, poorly crystalline aluminosilicate and LTA zeolite formed as intermediate precipitates. The rate of conversion from LTA zeolite to cancrinite and/or sodalite decreased in the following order: $NaNO_3$,Na_2SO_4 > Na_2CO_3 > NaCl, $NaNO_2$ > NaH_2PO_4,OH^- only (Fig. 6a).

The relative abundance and stability of sodalite and cancrinite were affected by the types of anions. Only sodalite formed in solutions containing Cl^- or NO_2^- after 16 weeks. The sodalite did not convert to cancrinite in these two solutions after another 16 weeks of reaction (Fig. 6b), indicating that sodalite was nonlabile. Both sodalite and cancrinite formed in the presence of CO_3^{2-} and SO_4^{2-} within 4 weeks. Highly crystalline and nearly pure cancrinite developed in the presence of SO_4^{2-} (Fig. 6b,c). The simulant containing PO_4^{3-} had nearly identical mineral phase transformations as the solution with only OH^-; they had the slowest transformation rates compared to the other electrolytes; and the precipitates were dominantly sodalite (Fig. 6b,c).

Cancrinite and sodalite had different morphologies in the presence of different anions. Sodalite formed in the presence of Na_2CO_3 (16 weeks), NaH_2PO_4 (32 weeks), or NaOH alone (32 weeks)

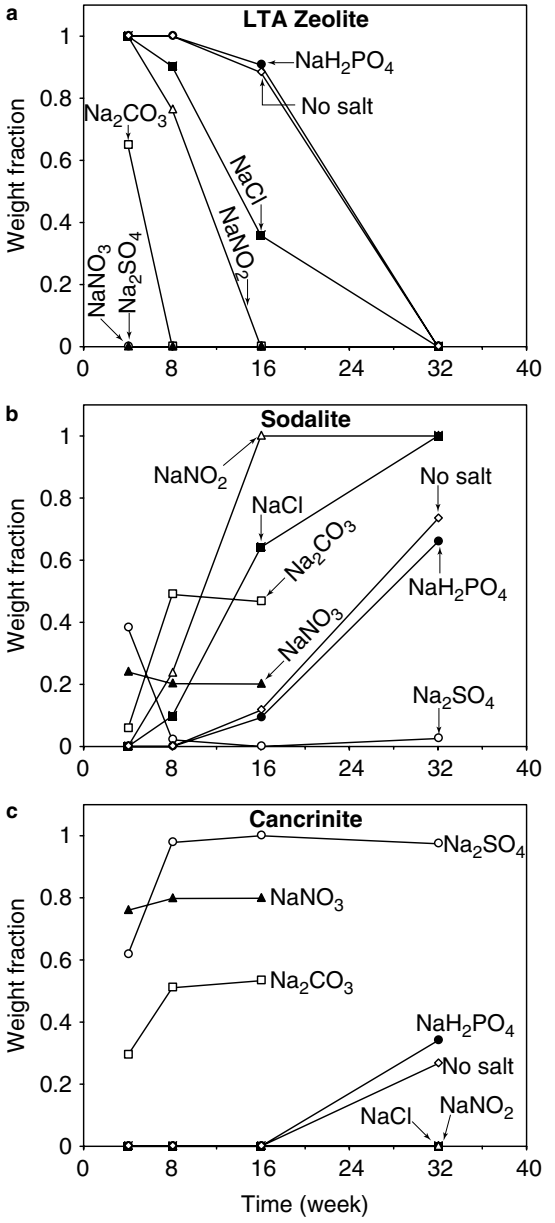

Fig. 6. Weight fractions of: (a) LTA zeolite; (b) sodalite and (c) cancrinite formed in 1 M NaOH solutions at 80 °C in the presence of different types of anions.

had similar thin platy morphology (Fig. 7b–e). Pure sodalite that formed in the presence of NaCl or $NaNO_2$ had similar wedge-shaped blade structures (Fig. 7f,g). After 16 weeks of reaction in the presence of Na_2SO_4, the cancrinite particles developed to stable, euhedral hexagonal bars (Fig. 7h).

When two or more types of anions were added simultaneously, the formation rate of sodalite and cancrinite were determined by the stronger

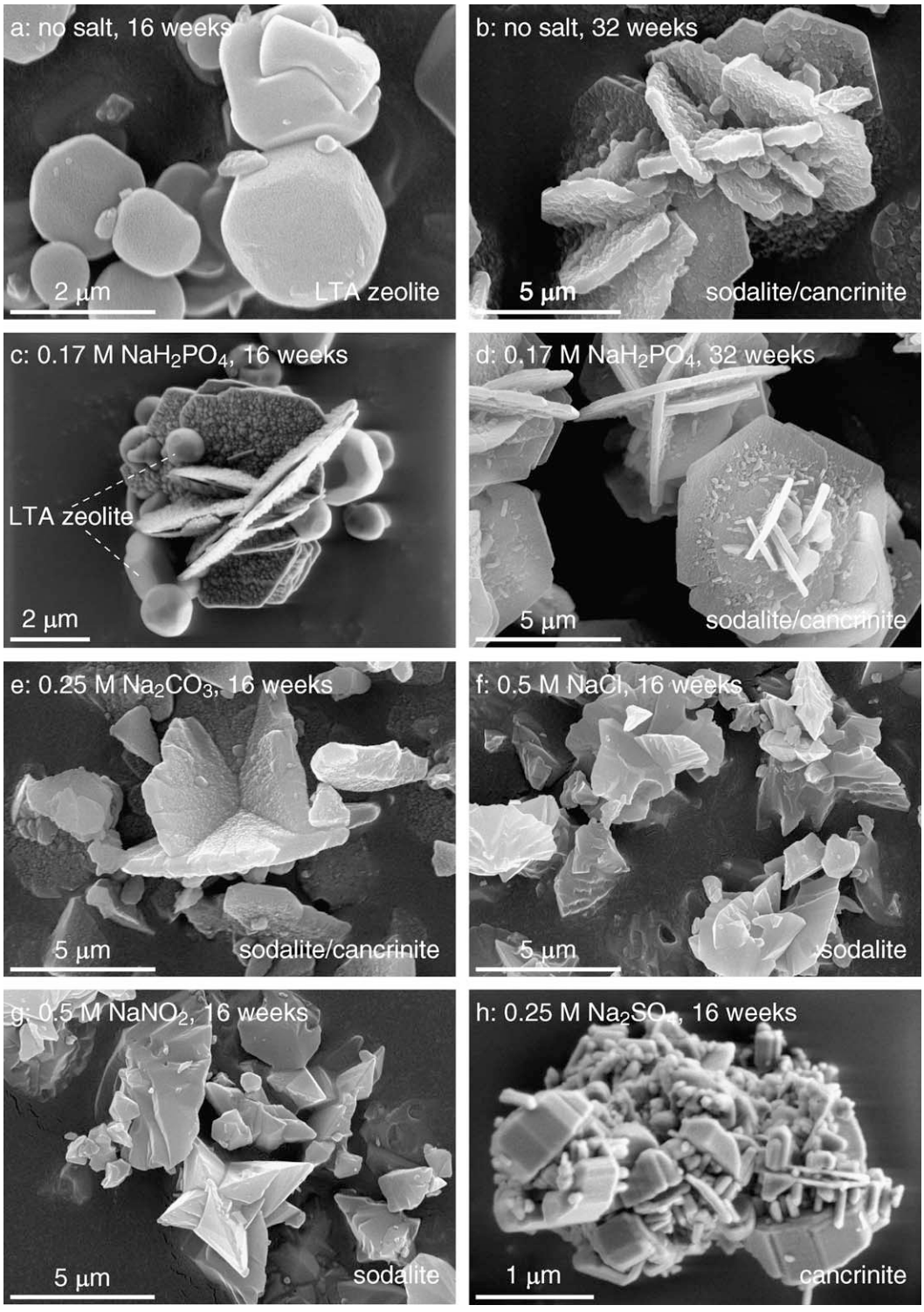

Fig. 7. SEM images of precipitates formed in 1 M NaOH solutions at 80 °C in the presence of different types of anions.

structural-directing anions, namely NO_3^- and SO_4^{2-}. The XRD patterns (data not shown) of the precipitates formed in the presence of multiple anions were similar to each other, and did not show distinct changes from week 4 to week 32. The morphologies of precipitates were also similar to each other and

were characterized by lepispheric and fine-grain morphology similar to those shown in Fig. 5a–c.

3.4. Effect of $NaNO_3$ concentration on mineral transformation in 1 M NaOH solutions

When the $NaNO_3$ concentration was increased, the XRD patterns showed two trends: (1) the patterns became more noisy and the peaks became broader and weaker, indicating that less crystalline minerals formed; and (2) sodalite peaks (e.g., 0.284 nm) weakened and disappeared when $NaNO_3$ was >8 M. The weight fraction of sodalite and cancrinite could not be quantified due to the poor signal to noise ratios in some of the XRD patterns.

The FT-IR spectra (Fig. 8a) of the precipitates that formed in high-concentration $NaNO_3$ solutions resembled the cancrinite/sodalite lepispheres formed in the presence of 0.5 M $NaNO_3$ in terms of band positions. Both cancrinite (e.g., 621 and 574 cm^{-1}) and sodalite (e.g., 730, 706 and 664 cm^{-1}) bands were present. Sodalite bands weakened compared to cancrinite bands but did not disappear when $NaNO_3$ concentration was increased. The cancrinite and sodalite formed in the presence of high concentrations of $NaNO_3$ had small size and elongated morphology (Fig 8b). After 32 weeks of reaction, the morphology of the precipitates did not show distinct changes.

3.5. Effect of Si/Al ratio on mineral transformation in 1 M NaOH solutions

The starting concentrations of silicate and aluminate in the simulants affected the abundance and the crystallinity of cancrinite to sodalite. Both XRD and FT-IR analyses revealed that cancrinite dominated the precipitates when the aluminate concentration was $\leqslant$0.125 M and the Si/Al molar ratio was $\geqslant$1.4 (Fig. 9). Cancrinite particles that formed in solutions with high Si/Al molar ratio (1.4–35) showed rod-shaped morphology (Fig. 10a,b), suggesting high crystallinity. Both cancrinite and sodalite formed in the simulants when aluminate

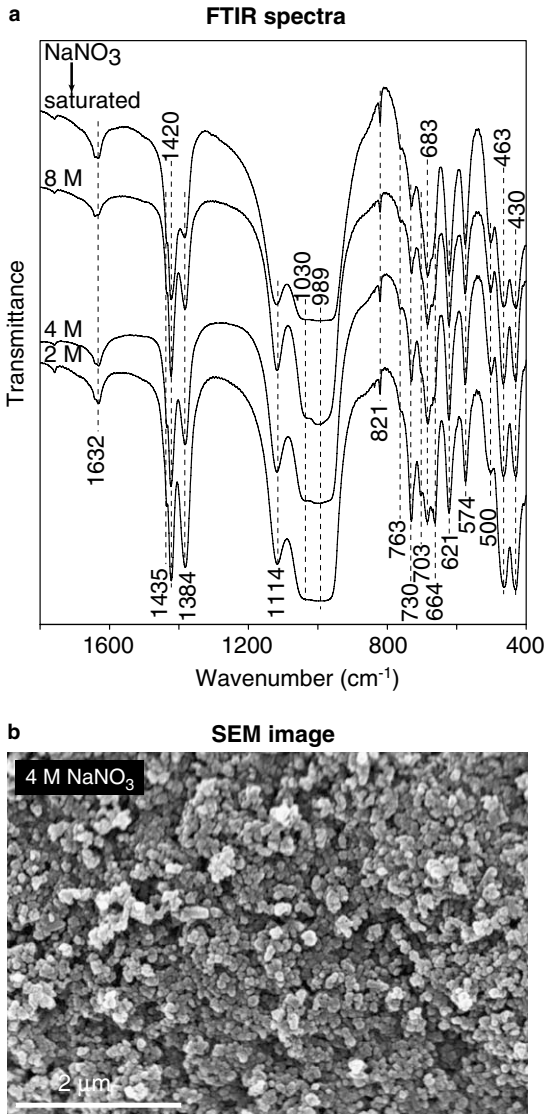

Fig. 8. (a) FT-IR spectra of precipitates formed in 1 M NaOH solutions with 0 M to saturated $NaNO_3$ at 80 °C and (b) cancrinite/sodalite formed in 1 M NaOH solution in the presence of 4 M $NaNO_3$ after 32 weeks of reaction at 80 °C.

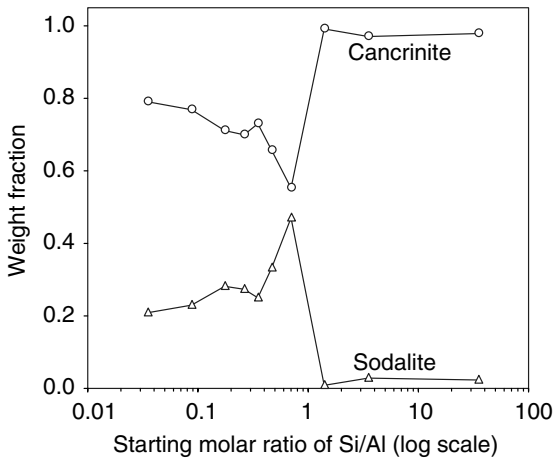

Fig. 9. Weight fractions of sodalite and cancrinite formed in 1 M NaOH solutions at 80 °C with different starting Si/Al molar ratios, after 4 weeks of reaction.

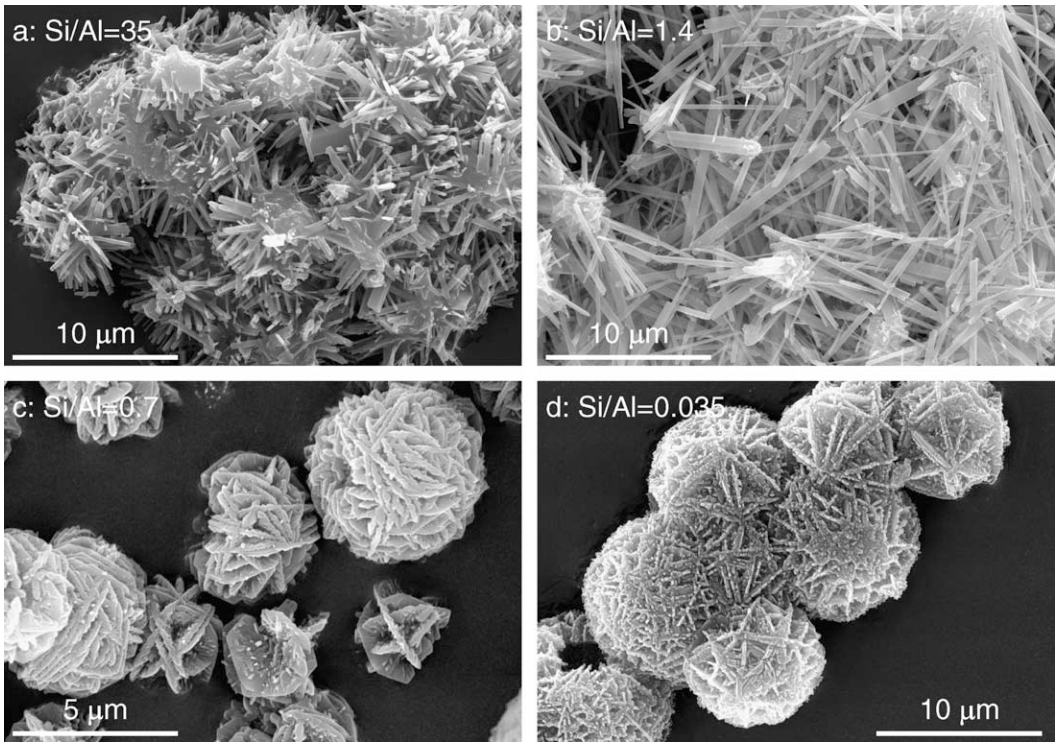

Fig. 10. SEM images of cancrinite and sodalite formed in 1 M NaOH solutions at 80 °C with different starting Si/Al molar ratios, after 4 weeks of reaction.

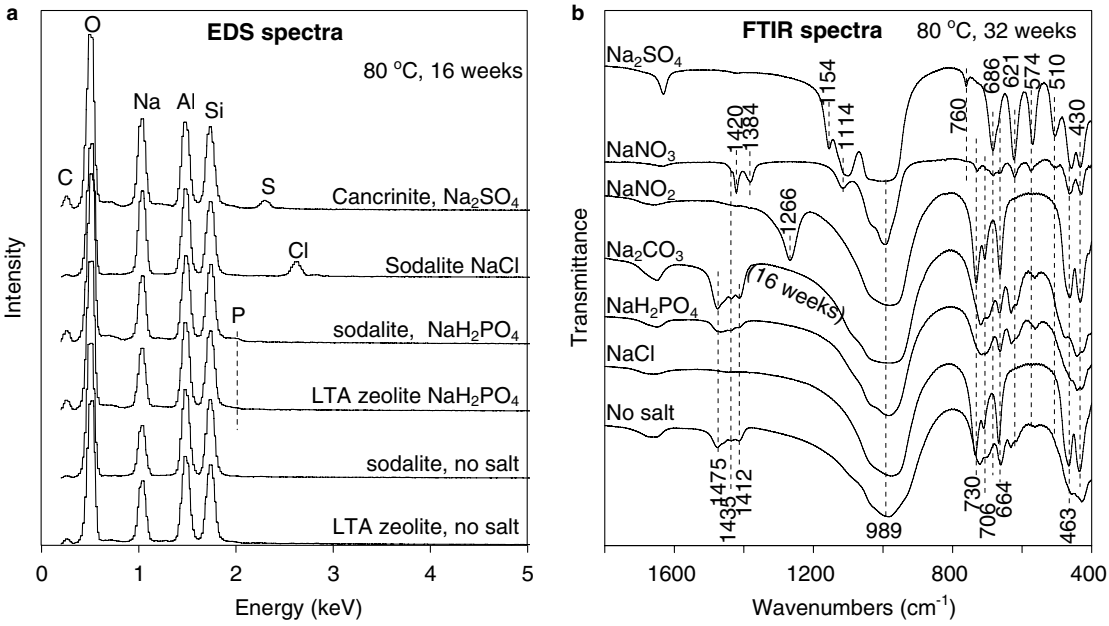

Fig. 11. (a) EDS and (b) FT-IR spectra of precipitates formed in 1 M NaOH solutions at 80 °C in the presence of different types of anions. FT-IR spectra were recorded after 32 weeks of reaction unless indicated otherwise.

concentration was greater than 0.125 M and the Si/Al ratio was <1.4, regardless of the concentration of the silicate. Cancrinite and sodalite formed with Si/Al ratio <1.4 had typical lepispheric morphology (Fig. 10c,d). These results suggest that a silicate-rich but Al-depleted solution favored the formation of

highly crystalline cancrinite. A similar observation was made in experiments with Hanford sediments (Qafoku et al., 2003b): when Si/Al molar ratios were in the range of 0.096–0.284, lepispheric cancrinite/sodalite formed, and when the Si/Al ratio was 14.2, rod-like precipitates (most likely cancrinite) formed.

3.6. Incorporation of anions into cancrinite and sodalite

The EDS and FT-IR spectra indicate that anions were incorporated into cancrinite and sodalite. The EDS spectra (Fig. 11a) suggest that SO_4^{2-} was incorporated into cancrinite when Na_2SO_4 was present, and Cl^- was incorporated into sodalite when NaCl was present. Incorporation of NO_3^-, NO_2^- and CO_3^{2-} in cancrinite or/and sodalite was confirmed by the occurrence of the $\nu 3$ IR bands (1266–1450 cm^{-1}) of the anions in the minerals (Fig. 11b and Table 3). The EDS and FT-IR analyses suggest that PO_4^{3-} was not incorporated into cancrinite or sodalite. None of the anions were detected in LTA zeolite by EDS or FT-IR analysis.

Table 3
Assignments of infrared bands of cancrinite, sodalite, and incorporated anions

Band (cm^{-1})	Cancrinite[a]	Sodalite[a]	Incorporated anions[†]
3639			ν, OH^- in sodalite
1475			ν_3, CO_3^{2-}
1435			ν_3, CO_3^{2-}
1420			ν_3, NO_3^- in cancrinite
1412			ν_3, CO_3^{2-}
1384			ν_3, NO_3^- in sodalite
1266			ν_3, NO_2^- in sodalite
1154			ν_3, SO_4^{2-} in cancrinite
1114	ν_a, Al–O–Si		
1030	ν_a, Al–O–Si	ν_a, Al–O–Si	
989	ν_a, Al–O–Si	ν_a, Al–O–Si	
821			δ, NO_3^-
760	ν_s, Al–O–Si		
730		ν_s, Al–O–Si	
706		ν_s, Al–O–Si	
686	ν_s, Al–O–Si		
664		ν_s, Al–O–Si	
621	Double ring[b]		
574	Double ring[b]		
510	δ, T–O		
463	δ, T–O	δ, T–O	
430	δ, T–O	δ, T–O	

Vibrations: ν, stretching; δ, bending.
Symmetry: a, asymmetric; s, symmetric. T = Si or Al.
[a] From Barnes et al. (1999b); [†]from Nyquist et al. (1997).
[b] Parallel 4- or 6-membered rings.

4. Discussion

4.1. Mineral transformation pathways

The mineral phases and morphologies demonstrate that several factors, i.e., NaOH concentration, type of anion, Si/Al ratio, salinity, and temperature, affected the mineral transformation rates and the stability of the end products. By and large, in low concentrations of NaOH (<8 M), the minerals formed in the following sequence: poorly crystalline aluminosilicate, LTA zeolite, lepispheric cancrinite/sodalite, and needle-shaped cancrinite. The distinct morphology and particle size differences among poorly crystalline aluminosilicate, LTA zeolite, and cancrinite/sodalite suggest that the nucleation and crystallization of the crystals were mediated through the solution. Mineral transformations did not occur in the solid state. A similar solution-mediated mechanism was reported in the study of mineral transformation in spent Bayer liquor (Barnes et al., 1999a). The LTA zeolite formed at the expense of poorly crystalline aluminosilicate. Both cancrinite and sodalite formed simultaneously when LTA zeolite was dissolving (Fig. 3). The conversion between sodalite and cancrinite appeared to be slow in <1 M NaOH solutions. Similar slow conversion from sodalite to cancrinite was reported by others (Barnes et al., 1999b,c). The authors propose the mineral transformation pathways shown in Fig. 12. In Na salt dominated systems, NaOH concentration and the type of anion play critical roles in determining the types of final minerals. Both sodalite and cancrinite could form in the alkaline solutions depending on the types of anions present. When NaOH concentration was high, cancrinite formed in the presence of NO_3^- or SO_4^{2-}; sodalite formed in the presence of OH^-, Cl^-, or CO_3^{2-}. When NaOH concentration was <8 M, cancrinite and sodalite were still the end minerals, yet poorly crystalline aluminosilicate and LTA zeolite occurred as intermediate phases. Sulfate favored the formation of cancrinite whereas Cl^- or NO_2^- favored the formation of sodalite. Frequently, both cancrinite and sodalite formed jointly in the solutions with low NaOH concentrations (e.g., 1 M NaOH).

The increasing formation rate of cancrinite and sodalite with increasing NaOH concentration indicates that NaOH was a mineralization agent in the formation of the minerals. Increasing OH^- concentration increased the dissolution of precursors

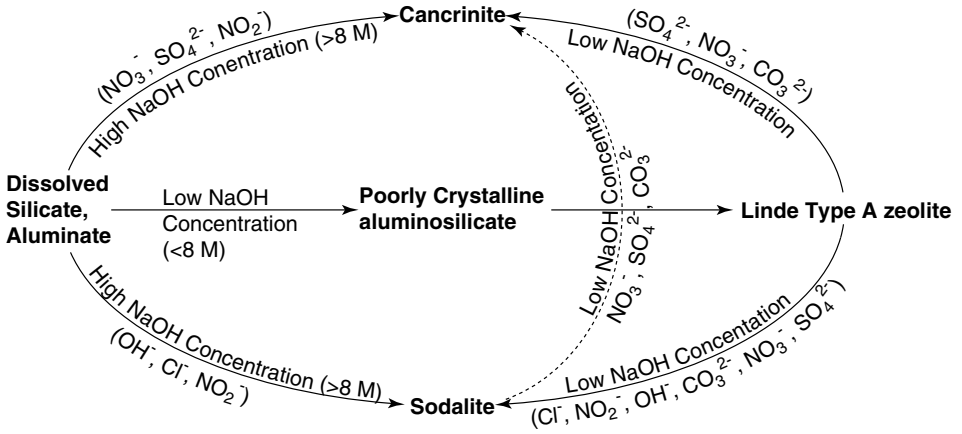

Fig. 12. Mineral transformation pathways in the simulant solutions mimicking Hanford tank waste solutions.

(poorly crystalline aluminosilicate and LTA zeolite), moreover, increasing NaOH concentration also ensured that the species of Al was in the tetrahedral form $Al(OH)_4^-$ in the solution. Both effects facilitated the formation of the feldspathoids.

4.2. Structure-directing role of anions in forming cancrinite and sodalite

The mineral phases observed in this study suggest that Cl^- and NO_2^- directed the nucleation of sodalite and SO_4^{2-} directed the nucleation of cancrinite. Some anions, such as CO_3^{2-} and NO_3^- can be the templates for both cancrinite and sodalite, with NO_3^- more likely to favor cancrinite formation. Phosphate was not involved in the formation of cancrinite or sodalite. The mineral transformation rates suggested that NO_3^- and SO_4^{2-} are stronger structure-directing anions, i.e., the minerals formed within a shorter time, than Cl^- and NO_2^-. When multiple types of anions were present, NO_3^- and SO_4^{2-} played the dominant role in nucleation and crystallization of cancrinite and sodalite.

The template role of the anions in the nucleation of cancrinite and sodalite is likely determined by (1) the size matching requirement between the anion-Na^+ ion pairs and the cages or channels of the feldspathoids and (2) the charge balance requirements between the ion pairs, cage-Na^+, and the framework. The negative charges on the framework of sodalite require 3 alkali metal cations to stay within each β-cage. Without incorporating an anion in the center of the β-cage, the 3 alkali cations are adjacent to each other, and this arrangement will not be stable due to the electrostatic repulsion among the cations (Rabo, 1976). The presence of an anion in the center, which in turn requires another alkali cation to balance the charge, will compensate the direct cation-cation repulsion. The 4 alkali cations are tetrahedrally coordinated to the center anion forming a highly symmetric tetrahedron inside each cage (Rabo, 1976). The tetrahedral coordination inside every β-cage of sodalite is not favored by divalent or trivalent anions because these anions would bring more cations into the cage to balance their charges, and therefore, will not fit the size matching requirement. This is likely why sulfate-or carbonate-sodalite converted to cancrinite and phosphate could not be incorporated into sodalite.

In cancrinite, the ion pairs can stabilize the one-dimensional channel as a "backbone" (Fechtelkord et al., 2001). It has been observed that the incorporated anions, such as CO_3^{2-}, OH^- and SO_4^{2-} in natural cancrinite, and sulfide, thiosulfate or selate in synthetic cancrinite, stay in the wide main channel, whereas the small-cages host only cations and water molecules (Buhl et al., 2000). Corroborating the finding that PO_4^{3-} did not serve as the template, Buck and McNamara (2004) reported that PO_4^{3-} was absent in cancrinite formed in the sludge of a waste tank at the Hanford site, even though PO_4^{3-} was present in the tank supernatant.

Similar template roles of anions in the formation of cancrinite and sodalite have been reported by Barrer (1982) and Bosnar et al. (2004). They reported that Cl^-, Br^-, I^-, ClO_3^-, ClO_4^- and

$HCOO^-$ induced the crystallization of sodalite, whereas $SO_4^{2-}, NO_3^-, SeO_4^2, CrO_4^2, MoO_4^{2-}$ and MnO_4^- induced the crystallization of cancrinite.

4.3. Similarities and discrepancies with reported studies

The findings that NaOH acts as a mineralization agent and that the anion-Na ion pairs serve as the structure-directing templates in the formation of cancrinite and sodalite corroborate and generalize the observations of previous studies. Cancrinite formed when tank waste simulants reacted with either model minerals or with Hanford sediments (Table 1). Sodalite was observed in some of these simulation experiments when NaOH concentration was in the range of 1–3 M (Chorover et al., 2003; Qafoku et al., 2003b; Zhao et al., 2004; Mashal et al., 2004). Lepispheres were the most common morphologies observed for the feldspathoids in these published studies. Small hexagonal needle or rod-shaped cancrinite has also been reported with model minerals (Bickmore et al., 2001) and the Hanford sediments (Qafoku et al., 2004).

The proposed mineral transformation pathways are supported by other studies with alkaline solutions. For example, in spent Bayer liquor that contains a high concentration of CO_3^{2-}, the solid phase precipitated in the order LTA zeolite, sodalite and cancrinite at elevated temperatures (as high as 240 °C) in 3.7 M NaOH (Barnes et al., 1999a,b; Gerson and Zheng, 1997; Zheng et al., 1997).

The authors note differences between these results and those summarized in Table 1. Bayerite or chabazite were not observed. In most of the simulation experiments listed in Table 1, no poorly crystalline aluminosilicate and LTA zeolite were reported. The absence of these two solid phases in most of the experiments is probably caused by the fast mineral transformation rates under the favored conditions used in those simulations: e.g., elevated temperature; high concentrations of $NaNO_3$ and NaOH; and, perhaps the presence of other cations (e.g., Cs^+, Sr^{2+} and other cations released from sediments).

In this study, the solution compositions were extended to the extreme possible in the tank environments while maintaining a controlled system. The results show that while cancrinite and/or sodalite remain as at least metastable products in all systems, anion type and OH concentration affect the rate of formation, crystallinity, and relative stability of the end products.

5. Implication for Hanford waste tank leaks

Even though the experimental system is simple in terms of chemical composition compared to an actual Hanford tank leak, the conclusions are applicable to the reactions between the leaks and the sediments at the Hanford site because they share the same chemistry.

During a tank leak, the NaOH concentrations, the types of anions and temperature varied considerably with time. According to the mineral transformation pathways postulated here, it is speculated that cancrinite and sodalite would form in the contaminated sediments. The morphological changes observed here suggest that at least two types of cancrinite, lepispheric and needle-shaped particles can form when NaOH $\leqslant$8 M. The morphological changes of the cancrinite and sodalite as a function of the starting Si/Al ratio suggest that feldspathoids with different crystallinity formed when the leaked solutions contacted the sediments. Because quartz is the major mineral in Hanford sediments, it is likely that dissolved silicate concentrations increased when the high alkaline waste solution contacted the sediments but, at same time, aluminate concentrations decreased due to the formation of feldspathoids. This has been confirmed in simulation experiments with sediments (Qafoku et al., 2003a; Mashal et al., 2004).

Cancrinite, sodalite, LTA zeolite, and poorly crystalline aluminosilicate were observed in the experiment, yet none of these minerals has been confirmed from the borehole samples taken underlying the tanks (Serne et al., 2002a,b,c; Knepp, 2002). The experiments indicate that under conditions similar to Hanford tank leaks, cancrinite and sodalite would likely be small granular or needle-shaped particles, which may be diffcult to observe in a sediment matrix. Moreover, the quantity of the feldspathoids formed in the sediments may be small and, therefore, not detectable by common analysis methods. Liu et al. (2003) checked weathered mica particles isolated from the contaminated sediment under SX tank farm and found that weakly weathered mica was coated with fibrous precipitates whereas highly weathered mica was completely encrusted with secondary phases. These precipitates could be dissolved by acidified ammonium oxalate solutions, which indicates they are unstable at low pH (Liu et al., 2003). The authors have shown that cancrinite and sodalite are not stable under acidic conditions (Zhao et al., 2004).

McKinley et al. (2002) analyzed samples from a SX-108 slant borehole and suggested chabazite, a Ca-bearing zeolite, might be present in one of the samples. Cancrinite has been reported to occur in the tank sludge when silicon (e.g., diatomaceous earth) was present in the tanks (Crowley, 1997). Recently, Buck and McNamara (2004) have detected lepispheric cancrinite in the sludge of a Hanford waste tank. These results imply that feldspathoids or zeolitic minerals have likely formed in the contaminated sediments. Whether they have been weathered away under current pore water conditions or whether they have not been revealed by analytical methods, remains to be determined.

Acknowledgements

This research was supported by the Office of Science (BER), US Department of Energy, Grant No. DE-FG07-05ER62882 and by the Inland Northwest Research Alliance. We thank the Electron Microscopy Center and the Department of Geology at Washington State University for the use of SEM, TEM and FT-IR equipment. The FESEM and EDS analyses were performed in the Environmental Molecular Sciences Laboratory (a national scientific user facility sponsored by the US DOE Office of Biological and Environmental Research) located at Pacific Northwest National Laboratory, operated by Battelle for the DOE.

References

Barnes, M.C., Addai-Mensah, J., Gerson, A.R., 1999a. The mechanism of the sodalite to cancrinite phase transformation in synthetic spent Bayer liquor. Micropor. Mesopor. Mater. 31, 287–302.

Barnes, M.C., Addai-Mensah, J., Gerson, A.R., 1999b. A methodology for quantifying sodalite and cancrinite phase mixtures and the kinetics of the sodalite to cancrinite phase transformation. Micropor. Mesopor. Mater. 31, 303–319.

Barnes, M.C., Addai-Mensah, J., Gerson, A.R., 1999c. The solubility of sodalite and cancrinite in synthetic spent Bayer liquor. Colloid Surf. A-Physicochem. Eng. Asp. 157, 101–116.

Barrer, R.M., 1982. Hydrothermal Chemistry of Zeolites. Academic Press, London, UK.

Bickmore, B.R., Nagy, K.L., Young, J.S., Drexler, J.W., 2001. Nitrate-cancrinite precipitation on quartz sand in simulated Hanford tank solutions. Environ. Sci. Technol. 35, 4481–4486.

Bosnar, S., Antonić-Jelić, T., Bronić, J., Krznarić, I., Subotić, B., 2004. Influence of anions on the kinetics of zeolite A crystallization: a population balance analysis. J. Cryst. Growth 267, 270–282.

Buck, E.C., McNamara, B.K., 2004. Precipitation of nitrate-cancrinite in Hanford tank sludge. Environ. Sci. Technol. 38, 4432–4438.

Buhl, J.-C., Stief, F., Fechtelkord, M., Gesing, T.M., Taphorn, U., Taake, C., 2000. Synthesis, X-ray diffraction and MAS NMR characteristics of nitrate cancrinite $Na_{7.6}[AlSiO_4]_6(NO_3)_{1.6}(H_2O)_2$. J. Alloy. Compd. 305, 93–102.

Chorover, J., Choi, S., Amistadi, M.K., Karthikeyan, K.G., Crosson, G., Mueller, K.T., 2003. Linking cesium and strontium uptake to kaolinite weathering in simulated tank waste leachate. Environ. Sci. Technol. 37, 2200–2208.

Crowley, K.D., 1997. Nuclear waste disposal: the technical challenges. Phys. Today 50, 32–39.

Fechtelkord, M., Posnatzki, B., Buhl, J.-C., 2001. Synthesis of basic cancrinite in a butanediol–water system. Chem. Mater. 13, 1967–1975.

Gephart, R.E., Lundgren, R.E., 1998. Hanford Tank Cleanup: A Guide to Understanding the Technical Issues, 4th ed. Battelle Press, Columbus.

Gerson, A.R., Zheng, K., 1997. Bayer process plant scale: transformation of sodalite to cancrinite. J. Cryst. Growth 171, 209–218.

Hermans, P.H., Weidinger, A., 1961. On the determination of the crystalline fraction of polyethylenes from X-ray diffraction. Makromol. Chem. 144, 24–36.

Kaplan, D.I., Parker, K.E., Ritter, J.C., 1998. Effects of Aging Quartz Sand and Hanford Sediment with Sodium Hydroxide on Radionuclide Sorption Coeffcients and Sediment Physical and Hydrologic Properties: Final Report for Subtask 2a. Pacific Northwest National Laboratory, PNNL-11965, Richland, Washington.

Kaplan, D.I., Serne, R., Schefer, J., Lindstrom, R.M., Parker, K.E., Owen, A.T., McCready, D.E., Young, J.S., 2003. The Influence of Glass Leachate on the Hydraulic, Physical, Mineralogical and Sorptive Properties of Hanford Sediment. Pacific Northwest National Laboratory, PNNL-14325, Richland, Washington.

Knepp, A.J., 2002. Field Investigation Report for Waste Management Area S-SX. RPP-7884, Rev. 0, CH2M HILL Hanford Group, Inc., Richland, Washington.

Lichtner, P.C., Felmy, A.R., 2003. Estimation of Hanford SX tank waste compositions from historically derived inventories. Comput. Geosci. 29, 371–383.

Liu, C., Zachara, J.M., Smith, S.C., McKinley, J.P., Ainsworth, C.C., 2003. Desorption kinetics of radiocesium from subsurface sediments at Hanford Site, USA. Geochim. Cosmochim. Acta 67, 2893–2912.

Mashal, K., Harsh, J.B., Flury, M., Felmy, A.R., Zhao, H., 2004. Colloid formation in Hanford sediments reacted with simulated tank waste. Environ. Sci. Technol. 38, 5750–5756.

Mashal, K., Harsh, J.B., Flury, M., 2005a. Clay mineralogical transformations over time in Hanford sediments reacted with simulated tank waste. Soil Sci. Soc. Am. J. 69, 531–538.

Mashal, K., Harsh, J.B., Flury, M., Felmy, A.R., 2005b. Analysis of precipitates from reactions of hyperalkaline solutions with soluble silica. Appl. Geochem. 20, 1357–1367.

McKinley, J.P., Zeissler, C.J., Zachara, J.M., Serne, R.J., Lindstrom, R.M., Schaef, H.T., Orr, R.D., 2001. Distribution and retention of ^{137}Cs in sediments at the Hanford Site, Washington. Environ. Sci. Technol. 35, 3433–3441.

McKinley, J.P., Zachara, J.M., Gassman, P.L., Ainsworth, C.C., Arey, B., McKinley, S., Schaef, T., Smith, S.C., Kimberling,

J., Bish, D.L., 2002. Appendix D2. S-SX site mineralogy. In: Knepp, A.J. (Ed.), Field Investigation Report for Waste Management Area S-SX. RPP-7884, Rev. 0, CH2M HILL Hanford Group, Inc., Richland, Washington.

Mon, J., Deng, Y., Flury, M., Harsh, J.B., 2005. Cesium incorporation and diffusion in cancrinite, sodalite, zeolite, and allophane. Micropor. Mesopor. Mater. 86, 277–286.

Moore, D.M., Reynolds, R.C.J., 1997. X-ray Diffraction and the Identification and Analysis of Clay Minerals, 2nd ed. Oxford University Press, Oxford.

Nyquist, R.A., Putzig, C.L., Leugers, M.A., 1997. Infrared Spectra, The Handbook of Infrared and Raman Spectra of Inorganic Compounds and Organic Salts, vol. 3. Academic Press, San Diego.

Pruess, K., Yabusaki, S., Steefel, C., Lichtner, P., 2002. Fluid flow, heat transfer, andsolute transport at nuclear waste storage tanks in the Hanford vadose zone. Vadose Zone J. 1, 68–88.

Qafoku, N.P., Ainsworth, C.C., Szecsody, J.E., Qafoku, O.S., 2003a. Aluminum effect on dissolution and precipitation under hyperalkaline conditions: I. Liquid phase transformations. J. Environ. Qual. 32, 2354–2363.

Qafoku, N.P., Ainsworth, C.C., Szecsody, J.E., Bish, D.L., Young, J.S., McCready, D.E., Qafoku, O.S., 2003b. Aluminum effect on dissolution and precipitation under hyperalkaline conditions: II. Solid phase transformations. J. Environ. Qual. 32, 2364–2372.

Qafoku, N.P., Ainsworth, C.C., Szecsody, J.E., Qafoku, O.S., 2004. Transport controlled kinetics of dissolution and precipitation in the sediments under alkaline and saline conditions. Geochim. Cosmochim. Acta 68, 2981–2995.

Rabo, J.A., 1976. Salt occlusion in zeolite crystals. In: Rabo, J.A. (Ed.), Zeolite Chemistry and Catalysis, ACS Monograph, 171. Academic Press, San Diego, pp. 332–349.

Serne, R.J., Zachara, J.M., Burke, D.S., 1998. Chemical information on tank super natants, Cs adsorption from tank liquids onto Hanford sediments, and field observations of Cs migration from past tank leaks. Pacific Northwest National Laboratory, Richland, Washington.

Serne, R.J., Last, G.V., Gee, G.W., Schaef, H.T., Lanigan, D.C., Lindenmeier, C.W., Clayton, R.E., LeGore, V.L., Orr, R.D., O'Hara, M.J., Brown, C.F., Burke, D.S., Owen, A.T., Kutnyakov, I.V., Wilson, T.C., 2002a. Characterization of Vadose Zone Sediment: Borehole 41-09-39 in the S-SX Waste Management Area. Pacific Northwest National Laboratory, PNNL-13757-3, Richland, Washington.

Serne, R.J., Last, G.V., Schaef, H.T., Lanigan, D.C., Lindenmeier, C.W., Ainsworth, C.C., Clayton, R.E., LeGore, V.L., O'Hara, M.J., Brown, C.F., Orr, R.D., Kutnyakov, I.V., Wilson, T.C., Wagnon, K.B., Williams, B.A., Burke, D.S., 2002b. Characterization of Vadose Zone Sediment: Slant Borehole SX-108 in the S-SX Waste Management Area. Pacific Northwest National Laboratory, PNNL-13757-4, Richland, Washington.

Serne, R.J., Schaef, H.T., Bjornstad, B.N., Lanigan, D.C., Gee, G.W., Lindenmeier, C.W., Clayton, R.E., LeGore, V.L., Orr, R.D., O'Hara, M.J., Brown, C.F., Last, G.V., Kutnyakov, I.V., Burke, D.S., Wilson, T.C., Williams, B.A., 2002c. Characterization of Vadose Zone Sediment: Borehole 299-W23-19 [SX-115] in the S-SX Waste Management Area. Pacific Northwest National Laboratory, PNNL-13757-2, Richland, Washington.

Sieger, P., Wiebcke, M., Felsche, J., Buhl, J.C., 1991. Orientational disorder of the nitrite anion in the sodalite sodium aluminum silicate nitrite ($Na_8[AlSiO_4]_6(NO_2)_2$). Acta Crystallog., Sect. C: Cryst. Struct. Commun. 47, 498–501.

Um, W., Serne, R.J., Yabusaki, S.B., Owen, A.T., 2005. Enhanced radionuclide immobilization and flow path modifications by dissolution and secondary precipitates. J. Environ. Qual. 34, 1404–1414.

Wan, J., Tokunaga, T.K., Saiz, E., Larsen, J.T., Zheng, Z., Couture, R.A., 2004. Colloid formation at waste plume fronts. Environ. Sci. Technol. 38, 6066–6073.

Wyckoff, R.W.G., 1968, 2nd ed.Crystal Structures, Vol. 4 Wiley, New York.

Zhao, H., Deng, Y., Harsh, J.B., Flury, M., Boyle, J.S., 2004. Alteration of kaolinite to cancrinite and sodalite by simulated Hanford tank waste and its impact on cesium retention. Clays Clay Miner. 52, 1–13.

Zheng, K., Gerson, A.R., Addai-Mensah, J., Smart, R.S.C., 1997. The influence of sodium carbonate on sodium aluminosilicate crystallization and solubility in sodium aluminate solutions. J. Cryst. Growth 171, 197–208.

Published online May 31, 2006

Sampling Silica and Ferrihydrite Colloids with Fiberglass Wicks under Unsaturated Conditions

Jason M. Shira, Barbara C. Williams,* Markus Flury, Szabolcs Czigány, and Markus Tuller

ABSTRACT

The suitability of passive capillary samplers (PCAPS) for collection of representative colloid samples under partially saturated conditions was evaluated by investigating the transport of negatively and positively charged colloids in fiberglass wicks. A synthetic pore water solution was used to suspend silica microspheres (330 nm in diameter) and ferrihydrite (172 nm in diameter) for transport experiments on fiberglass wicks. Breakthrough curves were collected for three unsaturated flow rates with silica microspheres and one unsaturated flow rate with ferrihydrite colloids. A moisture characteristic curve, relating tensiometer measurements of matric potential to moisture content, was developed for the fiberglass wick. Results indicate that retention of the silica and the ferrihydrite on the wick occurred; that is, the wicks did not facilitate quantitative sampling of the colloids. For silica microspheres, 90% of the colloids were transmitted through the wicks. For ferrihydrite, 80 to 90% of the colloids were transmitted. The mechanisms responsible for the retention of the colloids on the fiberglass wicks appeared to be physicochemical attachment and not thin-film, triple-phase entrapment, or mechanical straining. Visualization of pathways by iron staining indicates that flow is preferential at the center of twisted bundles of filaments. Although axial preferential flow in PCAPS may enhance their hydraulic suitability for sampling mobile colloids, we conclude that without specific preparation to reduce attachment or retention, fiberglass wicks should only be used for qualitative sampling of pore water colloids.

The vadose zone is an important source of colloids and contaminants (Sprague et al., 2000). Transport of colloids is collectively influenced by the stability of colloidal material (tendency to stay suspended), the hydrodynamics of porous media, and the tendency for retention to occur in the soil or rock medium. Colloid stability is affected by elemental composition (Mayer and Jarrell, 1996), aqueous phase pH, ionic strength (Saiers and Lenhart, 2003), and electrolyte speciation (Liu et al., 1995; McCarthy et al., 2002). At least two mechanisms for retention occur: attachment and straining. Attachment is usually assumed to be the primary mechanism for retention in porous media. Attachment can be due to electrostatic, van der Waals, hydrogen bonding, and hydrophobic interactions. The mechanism of straining may be due to mechanical trapping when pore throats are too small to permit passage (McDowell-Boyer et al., 1986; Bradford et al., 2002), or, at lower moisture contents in the vadose zone, may result from thin film entrapment or entrapment at air–water–solid (AWS) interfaces (Wan and Tokunaga, 1997; Jin et al., 2000; Lenhart and Saiers, 2002; Crist et al., 2004). Hydrodynamic properties of the porous medium such as the saturated hydraulic conductivity (K_s), unsaturated hydraulic conductivity [$K(\theta)$], pore water velocity (v), and pore geometry govern the residence time of the pore water solution and pathway that a given colloid may take.

Sampling of colloids from pore water, particularly in the vadose zone, is challenging. The negative water potentials that persist in the vadose zone make retrieval of representative samples of colloids difficult. Aqueous samples are collected from the vadose zone with suction samplers (suction lysimeters), zero-tension samplers (zero-tension lysimeters), or passive capillary samplers (PCAPS). PCAPS collect pore water via a wick, the top end of which is unraveled and pressed against the underside of the horizon to be sampled. Installation of PCAPS is similar to that of zero-tension lysimeters. An access trench is excavated along the study site with horizontal tunnels to install the PCAPS. The use of PCAPS in vadose zone sampling has been studied in detail with respect to solute and flux sampling (Holder et al., 1991; Poletika et al., 1992; Boll et al., 1992; Brandi-Dohrn et al., 1996; Goyne et al., 2000; Louie et al., 2000; Gee et al., 2002, 2003) and also with respect to mobile–immobile pore water (Landon et al., 1999). We assumed a priori that passive capillary samplers (PCAPS), as opposed to suction and zero-tension samplers, have the best chance of yielding a representative sample for reasons described below.

Suction samplers have inherent limitations with respect to conservative transport of colloids. First, colloids may be mechanically strained or attached in the porous tip of the sampler. Second, the application of a vacuum may induce an unrepresentative geochemical condition, such as a geochemical gradient, around the suction sampler. If the vacuum pulls high-ionic-strength water from dead-end pores or smaller pore spaces that had not been contributing to flow at the pre-suction gradient, mobile colloids could flocculate. In other settings, the dispersion of colloids from aggregates could result from a decrease of ionic strength as a result of reduced solute residence

J.M. Shira, Department of Environmental Science, University of Idaho, Moscow, ID 83844. Current address: Washington State Department of Ecology, Olympia, WA 98504. B.C. Williams, Department of Biological and Agricultural Engineering, University of Idaho, Moscow, ID 83844-0904. M. Flury and S. Czigány, Department of Crop and Soil Sciences, Center for Multiphase Environmental Research, Washington State University, Pullman, WA 99164. S. Czigány, current address: Department of Physical Geography, Geographical Institute, University of Pécs, Hungary. M. Tuller, Soils and Land Resources Division, University of Idaho, Moscow, ID 83844-2339. Received 25 Apr. 2005. *Corresponding author (barbwill@uidaho.edu).

Published in J. Environ. Qual. 35:1127–1134 (2006).
Technical Reports: Vadose Zone Processes and Chemical Transport
doi:10.2134/jeq2005.0136

677 S. Segoe Rd., Madison, WI 53711 USA

Abbreviations: AWS, air–water–solid; PCAPS, passive capillary sampler; SEM–EDS, scanning electron microscopy–energy dispersive spectrometry.

time. Finally, if the suction imposed is significantly stronger than the ambient soil matrix potential, colloids may be physically sheared from aggregates.

Zero-tension samplers also have potential limitations for sampling of colloids. Zero tension samplers operate only if a zone of saturation has collected above the sampling device. As water percolates through the profile, flow lines are routed about the zone of saturation due to change in boundary conditions (Abdou and Flury, 2004). Routing biases collection of flux, chemical (dissolved) or colloid (suspended) samples.

Because fiberglass wicks alleviate the boundary condition problems described above, we test if they are suitable for colloid sampling. The degree to which fiberglass wick PCAPS attenuate colloid transport was recently studied in a similar investigation concurrent with this one (Czigány et al., 2005). In both the Czigány study and this one, different moisture contents (flow rates) for transport of negatively charged colloids were compared by evaluation of breakthrough curves, and examination of the transport of positively charged ferrihydrite was performed. In addition, the Czigány et al. (2005) investigation specifically tested negatively charged ferrihydrite, natural colloids, feldspathoids, montmorillonite, and kaolinite. Unique contributions added by our investigation here include development of a moisture characteristic curve and collection of tensiometer data along the length of the wick during the experiments to explicitly relate retention to moisture content, transport tests of monodisperse solutions of microspheres, and comparison of experimental results to calculations of thin-film thickness. The fiberglass wick products used in the two studies differed slightly in terms of cross-sectional area, and therefore in the magnitude of K_s. The conclusions of the Czigány et al. (2005) investigation were that flow rate, pH, and colloid type affected colloid breakthrough, and that the utility of using wicks for reliable sampling was therefore limited.

In another investigation of colloid transport through wicks, Biddle et al. (1995) concluded that PCAPS transmit representative samples of mobile colloids. However, in that study a colloidal suspension was collected from the field site with a PCAPS and then tested for retention in a laboratory wick experiment. If straining or attachment of colloid material occurred during the original collection of soil solution, those colloids will not have been present for the subsequent retention test, and attenuation of colloids may, therefore, have been underrepresented in the retention test.

In this study, we investigated the transport of positively and negatively charged colloids in fiberglass wicks at near-saturated and unsaturated conditions. We hypothesized that (i) negatively charged silica microspheres would be conservatively transmitted at flow rates equal to the saturated hydraulic conductivity (K_s) of the fiberglass wick and (ii) that at progressively lower flow rates than the saturated flux that the colloids would be increasingly retained, indicating thin-film straining or triple-phase (AWS) entrapment. These hypotheses were tested with transport experiments conducted at different flow rates and with different colloids (silica and ferrihydrite).

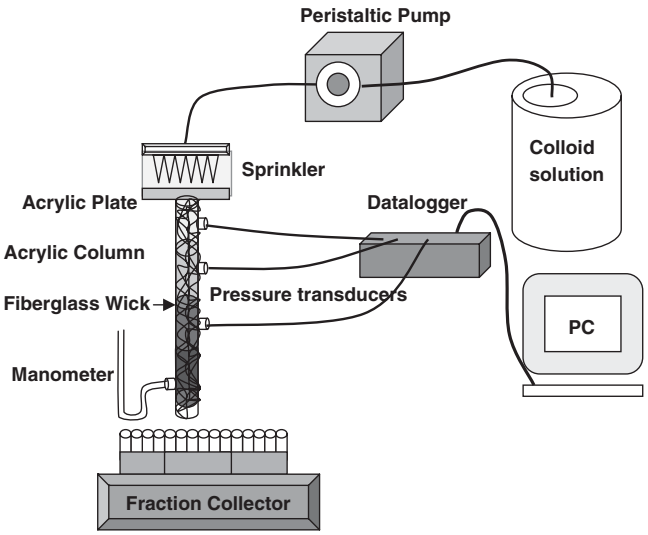

Fig. 1. Setup for unsaturated wick colloid transport experiments.

MATERIALS AND METHODS

Column Design

A 47-cm-long column of 1.27-cm-thick acrylic tubing was designed to house the 50-cm-long, 9.5-mm-diameter fiberglass wick (no. 1380; Pepperell Braiding, Pepperell, MA). At the top of the acrylic tube a 6- × 6-cm acrylic plate was secured to provide a mounting platform for the fiberglass wicks (Fig. 1). The fiberglass wicks were unraveled and radially extended to the edges of the acrylic plate, then secured with silicone sealer around the edge. A sprinkler head consisting of 12 hypodermic needles was used to apply inflow solution to the wick surface. Aluminum foil enclosed the area around the sprinkler and splayed-out wick to reduce evaporation from the sprinkler and wick top.

Tensiometers

Matric potential varied from some negative value at the top of the wick, to zero at the bottom of the wick, depending on the water flux being transmitted (the maximum flux being equal to the saturated hydraulic conductivity of the wick). Matric potential was measured with tensiometers to verify steady state conditions during transport experiments, determine moisture content along the wick, and provide the basis for calculation of pore water velocities. Tensiometers were mounted on the column at four locations (7, 27, 37, and 47.5 cm from the bottom of wick). The tensiometers consisted of a ceramic tip (0652X07-B1M3; Soil Moisture Corp., Santa Barbara, CA), a hollow brass body with water–air ports, and a pressure transducer (26PCCFA2G Micro Switch; Honeywell, Freeport, IL); except the bottom tensiometer that was connected to a water manometer instead of a transducer. The upper three pressure transducers were monitored with a datalogger (CR10X; Campbell Scientific, Logan, UT) for data acquisition. The tensiometers were attached to the acrylic cylinder support such that the ceramic tip made secure contact with the fiberglass wick, but not enough to compress the wick and thereby disturb the flow. Each pressure transducer was calibrated using hanging water columns. Saturating the column with synthetic pore water solution and then draining the column ensured hydraulic connectivity between wick and tensiometer. The appropriate flow rate for each experimental test case was initiated as the column drained. Before beginning any experiments, the system was allowed to achieve steady state for a period of at least 12 h.

Wick Properties and Preparation

Clean 9.5-mm fiberglass wicks (no. 1380; Pepperell Braiding) were used in each experiment. The fiberglass wicks contain residues left as a result of the manufacturing process. To remove these residues, the wicks were combusted at 400°C, following the recommendations of Knutson et al. (1993). The combustion process removed 1.5% w/w of material, as determined by mass balance before dissolution of post-combustion residues. It has been observed that the combustion process leaves a residue of ash, salts, and polymers (Knutson et al., 1993). Combusted wicks were mounted into the acrylic tube and rinsed with deionized water. The initial pH of the post-combustion effluent when rinsing the wicks was 9.3 to 10.4, and dropped to 8.3 after 48 h. The initial electrical conductivity (EC) of the rinse effluent was 364 $\mu S\ cm^{-1}$, which dropped to 25 $\mu S\ cm^{-1}$ after 20 min. To further remove carbonates and combustion residue, the fiberglass wicks were soaked in a 10 m*M* HNO_3 solution bath, as described by Goyne et al. (2000). Once the pH stabilized at the initial concentration of nitric acid (typically pH of approximately 2), double-deionized water was substituted for the nitric acid bath solution. The double deionized water was replaced daily, until the supernatant solution electrical conductivity fell below 2 $\mu S\ cm^{-1}$.

Measurements of wick contact angle (ProcessorTensiometer K100; Krüss, Hamburg, Germany) were performed with double deionized water on out-of-package wicks, combusted-only wicks, and batch soaked wicks using the Washburn method. These contact angle measurements indicated that the out-of-package wicks, combusted-only wicks, and acid-soaked wicks are all hydrophilic with a contact angle of 0°. Wicks were further characterized by scanning electron microscopy– energy dispersive spectrometry (SEM–EDS; Department of Geosciences, University of Idaho), and Brunauer–Emmett–Teller (BET) surface area analysis (ASAP2010; Micromeritics, Norcross, GA).

The fiberglass wicks were assumed to have a negative surface charge based SEM–EDS analysis that identified the wick material as predominantly silica. The surface charge of silica gel has been documented to be negative in the pH range of 3 to 10 (Langmuir, 1997). This assumption was substantiated in Czigány et al. (2005) for ferrihydrite colloids of different surface charges. In Czigány et al. (2005), positively charged ferrihydrite was nearly 100% removed (attached), while negatively charged ferrihydrite moved without retention through the saturated wick.

Wick Hydraulic Properties

Basic properties of the wick such as, bulk density (ρ_b), porosity (ε), and volumetric water content (θ_v) were determined. The total volume (V_t) for several samples was measured by multiplying the length of 2-cm sections by the area of the cross-section (d = 9.5 mm). The bulk density (ρ_b = 0.34 g cm^{-3}) is an average of multiple air-dried samples and agrees with the bulk density given by Knutson and Selker (1994). The bulk density was used to determine the porosity of the fiberglass wicks, assuming the specific density of the fiberglass wick to be 2.6 g cm^{-3} (Knutson and Selker, 1994).

The volumetric water contents of the fiberglass wicks at various matric potentials were measured to determine the moisture retention curve for the fiberglass wick material. The wet end of the moisture characteristic curve was developed using a hanging water column (Hillel, 1980). Two-centimeter-long sections of the fiberglass wick were placed vertically on a porous plate. Suction was applied by lowering the hanging water column. The samples came to equilibrium soon after the suction was applied. The samples were weighed and oven-dried for at least 24 h and immediately reweighed to determine the gravimetric moisture content. Gravimetric water contents (θ_m) were converted to volumetric water contents using the bulk density. The dry end of the moisture characteristic curve was measured with a Dewpoint PotentiaMeter (WP4; Decagon, Pullman, WA).

The measured data were then analyzed with the van Genuchten model (van Genuchten, 1980):

$$\theta_v = \theta_r + (\theta_s - \theta_r)\left[\frac{1}{1 + (\alpha|\psi|)^n}\right]^{1-\frac{1}{n}} \quad [1]$$

where θ_r is the residual water content $\left(\frac{m^3}{m^3}\right)$; θ_s is the saturated water content $\left(\frac{m^3}{m^3}\right)$; ψ is the matric potential (m); and α (m^{-1}) and n (–) are empirical parameters. Nonlinear regression was used to estimate the model parameters. The model was then used to calculate moisture content from tensiometer data obtained during the experiments.

Silica and Ferrihydrite Colloids

Silica beads were obtained from Bangs Laboratories (Fisher, IN). The beads were spherical with a diameter of 330 nm and specific density of 2.0 g cm^{-3}. Ferrihydrite was synthesized following Schwertmann and Cornell (2000, p. 105–110) with the following modifications: $FeCl_2$ was substituted for $Fe(NO_3)$, and silica was added as Na_2SiO_3. We included silica in the synthesis because Si increases the stability of colloidal ferrihydrite (Anderson and Benjamin, 1985; Mayer and Jarrell, 1996; Schwertmann and Cornell, 2000). The point of zero charge (PZC) was determined by stabilizing the pH of a dilute suspension of the ferrihydrite in the synthetic pore water solution used for the experiments and then measuring the electrophoretic mobility at specific pH values (3 to 12) on a Zetasizer 3000 HSA (Malvern, Worcestershire, UK). The isoelectric point was found to be at pH of approximately 6.3. The published particle density for ferrihydrite is 4 g cm^{-3} (Schwertmann and Cornell, 2000) and the particle diameter was 172 nm, determined by dynamic light scattering (Zetasizer 3000 HSA).

Colloid Transport Experiments

A synthetic pore water solution comprised of 4.45 m*M* $CaCl_2$, 1.4 m*M* $MgCl_2$, 0.7 m*M* NaCl, and 0.4 m*M* KCl in double deionized water was used for all experiments and colloidal suspensions. This solution has an ionic strength of 18 m*M*, consistent with Soil Survey data for a Palouse soil (fine-silty, mixed, superactive, mesic Pachic Ultic Haploxerolls) (USDA Natural Resources Conservation Service, 2001). Palouse soil is a loess silt loam typical of the Palouse region of eastern Washington, with silt fraction composed primarily of quartz and feldspar. Ionic strength in the outflow was monitored for electrical conductivity (Model 250; Denver Instruments, Denver, CO). The input colloidal concentrations were 100 mg L^{-1} for the silica microsphere solutions, and 300 to 600 mg L^{-1} for the ferrihydrite. The pH of the silica microsphere solutions was 6.4 to 6.7 and for the ferrihydrite was 4.0. The pH was adjusted using 1 *M* KOH or 1 *M* HCl.

Nitrate was used as a conservative tracer to make comparisons with the colloid breakthrough curves. Nitrate was quantified spectrophotometrically with absorbance measurement at 206 nm (Model 1601; Shimadzu, Kyoto, Japan). The synthetic pore water solution was used as the carrier solution and 0.2 m*M* $Ca(NO_3)_2$ was added as conservative tracer.

The silica microspheres were used to test the transport of negatively charged colloids moving along a negatively charged

wick, recognizing that surface interactions like London–van der Waals interactions, hydration, steric and/or hydrophobic interactions could result in attachment or exclusion of the colloids. In addition, a reduction of moisture content was expected to cause an increased retention of colloids with the fiberglass wick due to filtering (mechanical straining), thin-film straining, or triple-phase (gas, liquid, solid interface) entrapment (Wan and Tokunaga, 1997; Jin et al., 2000; Lenhart and Saiers, 2002; Crist et al., 2004). To observe whether retention was increased with a reduction in moisture content, three flow rates were chosen for the experiments: a near-saturated flow rate of 6.8 mL min^{-1}, an unsaturated flow rate of 2.5 mL min^{-1}, and an unsaturated flow rate of 0.56 mL min^{-1}. The second two flow rates are reasonable percolation rates in a sandy soil (Boll et al., 1992), and in this system correspond to matric potentials of −10 to −30 cm H_2O, respectively, at the top of the fiberglass wick.

The ferrihydrite experiments were conducted to study qualitatively the electrostatic interactions of the fiberglass wick with a positively charged colloid. Electrostatic attachment was assumed to dominate. The experiments were performed at a flow rate of 2.5 mL min^{-1}.

Three repetitions were performed for each flow rate for silica microspheres, and three repetitions were performed for ferrihydrite. Effluent colloid concentration was measured for every other sample to every fourth sample. The remaining sets of one to three samples were combined to measure the effluent pH and ionic strength.

To compare breakthrough curves, pore volumes ($T = vt/L$), where v is average pore water velocity for each pore reach, and relative concentration (C/C_o) were used to normalize the time and concentration data. Due to the variable water content over the length of the wick, pore water velocity was calculated for each tensiometer location, and then a single average value of pore water velocity was used to calculate an average value of pore volume.

RESULTS

Wick Characterization

The specific surface area for a wick sample was 4752 cm^2 g^{-1} using Brunauer–Emmett–Teller surface area analysis. The SEM–EDS analysis of an acid-soaked fiberglass wick identified the presence of Na, Mg, Al, K, and Ca on the surface (Fig. 2). This corroborates the findings of Goyne et al. (2000) and Brahy and Delvaux (2001) of cations sorbed to the wick surface. The measured and modeled water retention characteristics of the fiberglass wick are shown in Fig. 3. The data show some hysteretic behavior. The van Genuchten relationship fits the data well. Swelling of the wick was observed at near saturated water contents; the saturated volumetric water content was directly measured to be 0.90, although the porosity calculated from bulk density for a dry wick was 0.87.

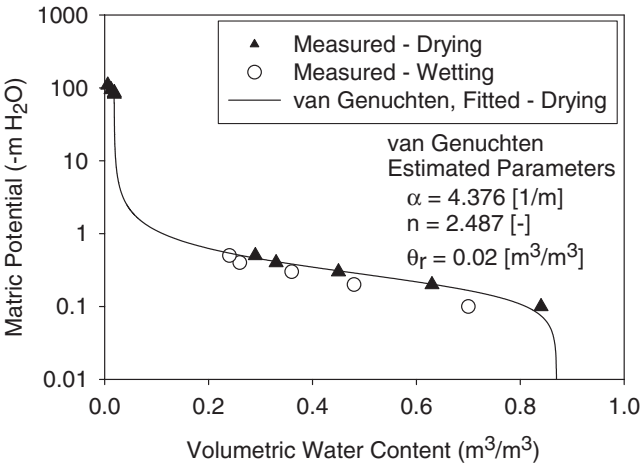

Fig. 3. Liquid retention curve for fiberglass wick. Symbols are measured data, line is fitted van Genuchten relationship. Main hysteresis loop of retention curve is shown for drying limb only.

The practicality of using PCAPS is because their length can be selected to match the matric potential of the porous media while allowing for free drainage at the bottom of the fiberglass wick. A profile of the moisture contents versus wick length as a function of flow rates (Fig. 4) was developed using the liquid retention curve and measured matric potentials. The profile shows that the distribution of moisture is almost uniform at the near-K_s flow rate used in the study (6.8 mL min^{-1}). The difference in moisture content along the length of

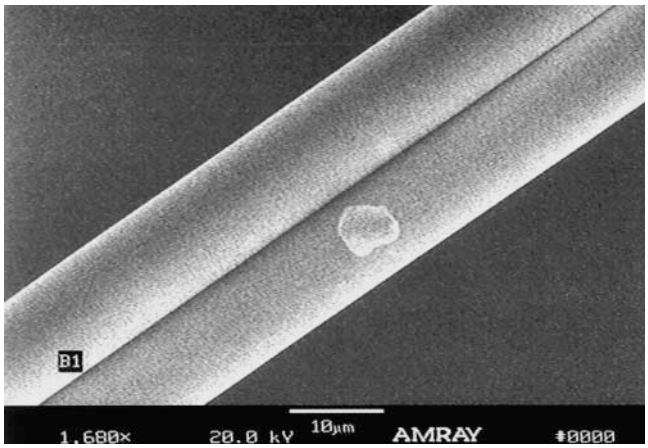

Fig. 2. Scanning electron microscopy (SEM) image of fiberglass wick after cleaning process; notice impurity on one fiber after cleaning, which indicates that the cleaning process is not complete.

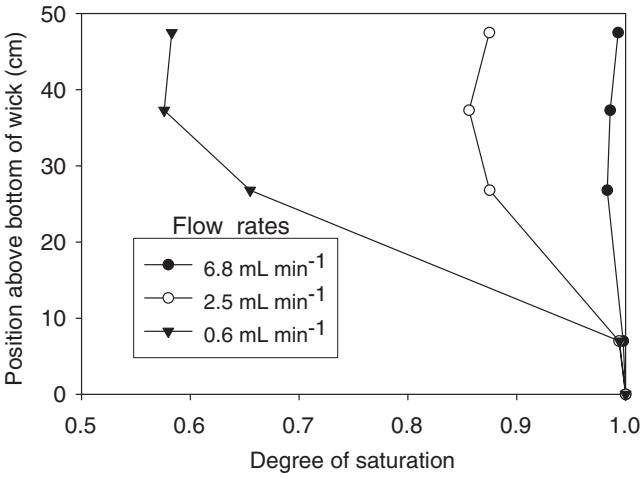

Fig. 4. Vertical moisture profiles in fiberglass wick.

the wick becomes greater as the flux rate and wick top moisture content both decrease.

Nitrate and Colloid Transport Experiments

Nitrate breakthrough curves for different flow rates are shown in Fig. 5. Nitrate transport on the wicks was conservative, yielding C/C_o values of 0.95 to 1.0 and a breakthrough at one pore volume.

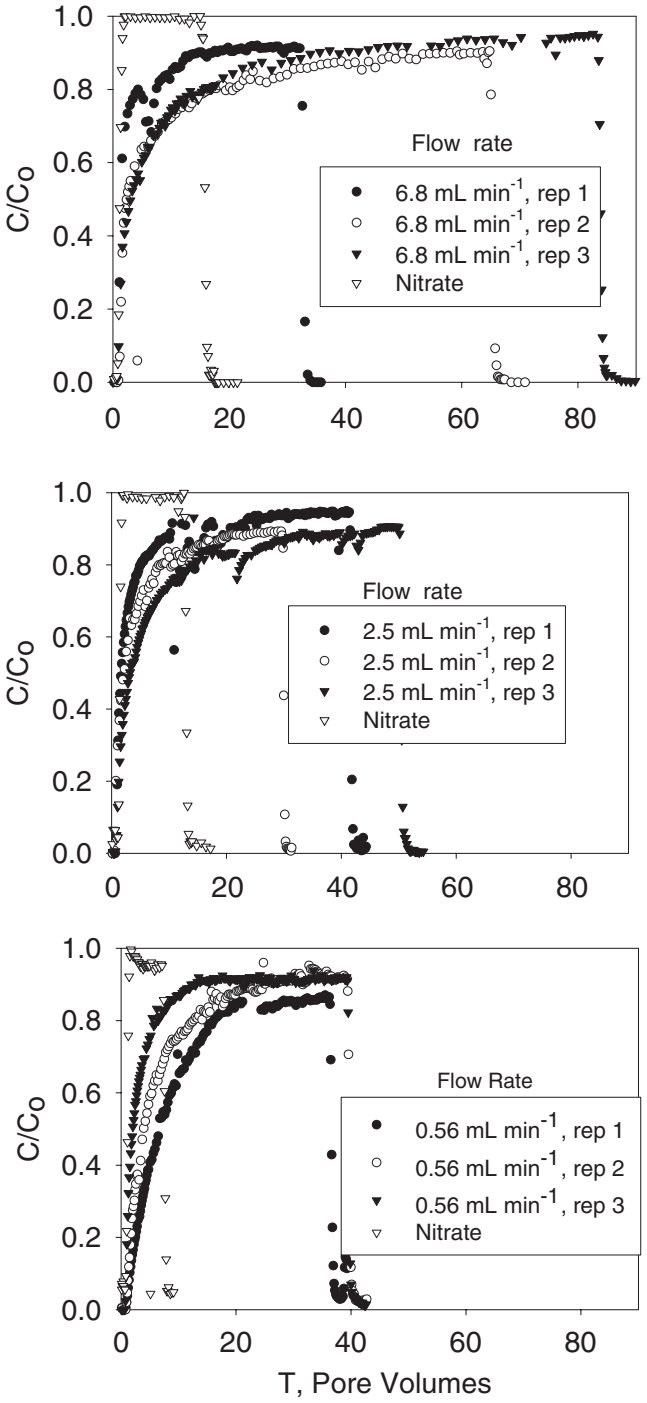

Fig. 5. Breakthrough curves for nitrate and silica microspheres at different flow rates.

We hypothesized that the silica microspheres would behave "conservatively" at a near saturated flow rate, 6.8 mL min^{-1}. From the breakthrough curves it is obvious that the monodispersed silica microspheres in a steady state, synthetic pore water system did not behave conservatively even at near-saturated conditions (Fig. 5). Breakthrough curves indicate that attachment of the microspheres to fiberglass wicks was occurring; transmitted C/C_o values never reached 1.0. Therefore, the first hypothesis was rejected. Retention of silica microspheres did not increase as the flow rate and related moisture content decreased. Therefore, the second hypothesis was also rejected for microspheres, at the flow rates tested in this study. Because there was no change in retention for the silica microspheres as a function of moisture content, attachment is the only likely means of retention. However, straining of natural and modified geologic colloids in fiberglass has been demonstrated to occur at lower moisture contents than tested in this study. Czigány et al. (2005) showed that colloids extracted from calcereous (Hanford) sediments were increasingly strained as moisture content (flow rate) decreased. Straining is discussed in more detail in the section entitled Thin Film Calculation, below.

The breakthrough of positively charge ferrihydrite colloids at pH 4 was strongly retarded (Fig. 6). From the breakthrough curves it is noted that the partitioning of the ferrihydrite is not the same for the three wicks tested. Variability among ferrihydrite breakthrough curves may be due to surface chemical heterogeneity of the fiberglass wicks and/or variations in solution suspension concentration. We note that the increased retention for a positively charged surface supports the interpretation that attachment is an operative mechanism. We make the general observation, however, that if wicks are used to sample positively charged colloids such as ferrihydrite at this pH in soils, adsorption of positive colloids to the fiberglass wick is strong, but may not be complete. Some fraction of the positively charged colloids can be sampled with wicks, depending on the pH. Czigány et al. (2005) observed no breakthrough of ferrihydrite at pH 7, but conservative behavior at pH 10.

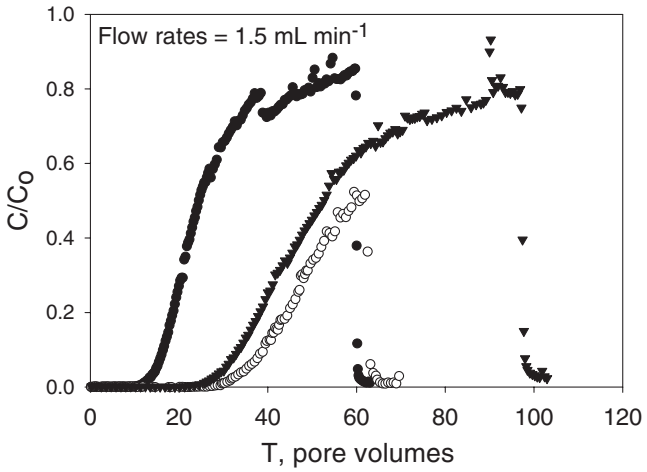

Fig. 6. Breakthrough curves for ferrihydrite colloids at pH 4 (three replicates).

DISCUSSION

Thin Film Calculation

Tuller and Or (2005) introduced an equation where the thickness (h_{est}) of the adsorbed water film can be estimated by dividing the gravimetric water content by the specific surface area and density of water. Applying this relationship to this system, thin-films on the fiberglass wick are expected to range from 5500 nm at a matric potential of −3 cm H_2O to 1700 nm at −50 cm H_2O. This predicts that both the 330-nm silica microspheres and the 172-nm ferrihydrite colloids should be mobile within the adsorbed water film in the range of suctions used in this study. On the basis of these calculations, thin-film straining is not predicted to occur in this wick at these suctions (flow rates). Performing the same calculations for the lowest moisture contents documented in the Czigány et al. (2005) study yields the same conclusion—thin-film straining would not be predicted to occur in that wick for the particle sizes reported there.

Preferential Flow in Wick Center

The weight-averaged moisture contents were not uniform across the cross-section of each bundle of fibers in the wick. This was concluded because orange ferrihydrite staining was more pronounced at the center of each bundle, indicating that the bundle of filaments is more tightly bound near the center than at the periphery. This allows for the center of each filament bundle to hold water at lower flow rates (i.e., more negative pressures). This suggests that at intermediate to low flow rates the radial anisotropy of each twisted bundle of filaments allows for preferential flow through the more tightly bound pore spaces at the center of each bundle (Fig. 7). As moisture content increases, water would spread to the larger pores, moving outward from the center. This suggests that the wick is effectively self-adjusting the portion of area available to flow in response to changing moisture contents (flow rates). It is likely that we did not observe thin-film straining or triple-phase entrapment because as moisture content was lowered, the flux receded to the central core of each bundle. Lower flow rates than those presented here would be needed to ensure that all the pores drain within the twisted bundle of filaments. This is consistent with the finding by Czigány et al. (2005) that at lower moisture contents than those used in this study, a moisture content–dependent straining mechanism does occur.

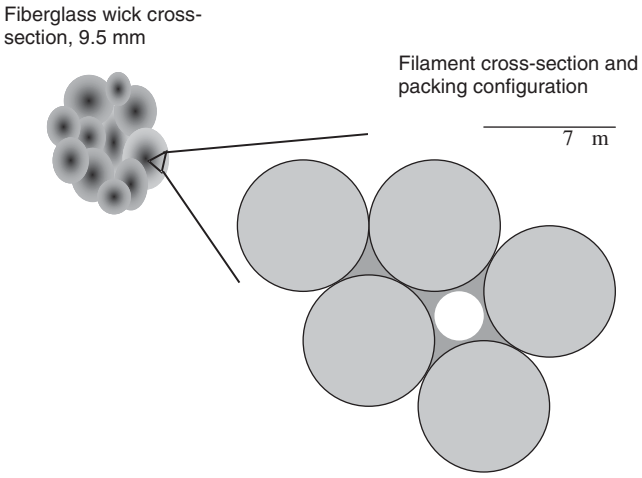

Fig. 7. Conceptual depiction of fiberglass wick pore geometry; shading indicates degree of staining by ferrihydrite. Filament diameter measured with scanning electron microscopy–energy dispersive spectrometry (SEM–EDS).

If the transport of colloids through the fiberglass wick is preferential to the more tightly bound inner filaments of each bundle, allowing for the degree of saturation to vary little over a range of flow rates (by changing the area used for flow), this phenomenon could be important for the successful use of PCAPS for sampling mobile colloids in the vadose zone, by alleviating straining mechanisms due to thin-films and or triple-phase entrapment at intermediate moisture contents (i.e., from 0 to −30 cm of suction). The tight packing of the filaments within the twisted bundles allows for the formation of menisci along the angular pore space. The threshold pressure needed to drain a triangular pore is given by (Tuller et al., 1999):

$$\Psi_1 = -\frac{\gamma}{\rho g L}\left[\frac{2(3+\sqrt[4]{3}\sqrt{\pi})}{\sqrt{3}}\right] \quad [2]$$

where γ is the surface tension of the liquid (g s^{-2}), ρ is the specific density of the liquid (g m^{-3}), g is the acceleration due to gravity (m s^{-2}), and L is the length of the pore side (m). Solving Eq. [2] for emptying of the largest pore space provided by rhombohedral packing geometry of fiberglass filaments with 7-μm diameter (Fig. 7) indicates that a suction greater than −50 cm H_2O of matric potential is needed to drain the pore space. A matric potential of −30 cm H_2O was the highest suction measured in this system; therefore, these pore spaces were never drained. In the Czigány et al. (2005) study, suctions of −50 cm H_2O were probably reached, as described above, which may be why retention increased with decreased moisture contents in that study. When pores snap open to drain, the remaining menisci in the pore corners provide more geometrically confined, wedge-shaped surface areas where corner straining or AWS interface sorption can occur.

A second potentially favorable feature of wicks, in addition to retreat to a smaller wetted cross-section at lower moisture contents, is that the parallel orientation of the filaments to the direction of flow allows for a longitudinal hydraulic connectivity, with fewer pore necks and dead-end pores along the length of the travel path as compared to ceramic or sintered steel sampling devices.

CONCLUSIONS

For sampling 330-nm silica microspheres in a synthetic pore water system with a pH of 6.5 and an ionic strength of 18 mM, approximately 10 pore volumes must pass

through a 47-cm-long wick to obtain a C/C_o greater than 90%. For ferrihydrite, sampled in a pore water system with pH 4 and an ionic strength of approximately 19 m*M*, more than 60 pore volumes must pass through to obtain a C/C_o of 80%. The mechanism of retention is attachment, and not thin-film straining. Based on these findings, the use of PCAPS to measure the concentrations of colloids in vadose zone pore water results in biased (attenuated) output concentrations. Even negatively charged particles are not transported without retention. Transport of colloids along fiberglass wicks is affected by many of the same factors as transport through soil and fractured rock, including attachment, and colloidal stability controls such as pH and ionic strength. These results confirm that although wicks may be used for qualitative identification of colloids in mobile pore water, without specific preparation to reduce attachment or retention, they should not be expected to provide accurate pore water colloid concentration measurements. These findings are consistent with the results of the Czigány et al. (2005) investigation.

Additional evaluation of PCAPS for the purpose of collecting soil-water colloids should include testing other particles with varied size and surface properties [i.e., organic carbon coated ferrihydrite, soil organic matter (SOM), humic acids], and alteration of the pore water solution (i.e., pH, ionic strength, carbonate concentration, and electrolyte species and ratios). Using a different fiber material in the PCAPS system may yield more conservative transport along wicks. To date, fiberglass PCAPS have been used to minimize cost, and no substitute was sought because fiberglass has proven adequate for the sampling of dissolved constituents and measurement of flux. If the conservative transmission of mobile colloids is critical, the use of engineered filaments of an optimized material braided into wicks will likely provide the best results, where charge characteristics, pore geometry, and roughness can be controlled.

ACKNOWLEDGMENTS

The Idaho National Environmental Engineering Laboratory, Grant #00001671005, and the Department of Biological and Agricultural Engineering at the University of Idaho supported this research. We thank Jorge Jerez for synthesizing the ferrihydrite colloids.

REFERENCES

Abdou, H.M., and M. Flury. 2004. Simulation of water flow and solute transport in free-drainage lysimeters and field soils with heterogeneous structures. Eur. J. Soil Sci. 55:229–241.

Anderson, P.R., and M.M. Benjamin. 1985. Effects of silicon on the crystallization and adsorption properties of ferric oxides. Environ. Sci. Technol. 19:1048–1053.

Biddle, D.L., D.J. Chittleborough, and R.W. Fitzpatrick. 1995. Field monitoring of solute and colloid mobility in a gneissic subcatchment, South Australia. Appl. Clay Sci. 9:433–442.

Boll, J., T.S. Steenhuis, and J.S. Selker. 1992. Fiberglass wicks for sampling of water and solutes in the vadose zone. Soil Sci. Soc. Am. J. 56:701–707.

Bradford, S.A., S.R. Yates, M. Bettahar, and J. Simunek. 2002. Physical factors affecting the transport and fate of colloids in saturated porous media. Water Resour. Res. 38, doi:10.1029/2002WR001340.

Brahy, V., and B. Delvaux. 2001. Comments on "Artifacts caused by collection of soil solution with passive capillary samplers". Soil Sci. Soc. Am. J. 65:1571–1573.

Brandi-Dohrn, F.M., R.P. Dick, M. Hess, and J.S. Selker. 1996. Field evaluation of passive capillary samplers. Soil Sci. Soc. Am. J. 60: 1705–1713.

Crist, J.T., J.F. McCarthy, Y. Zevi, P.C. Baveye, J.A. Throop, and T.S. Steenhuis. 2004. Pore-scale visualization of colloid transport and retention in partly saturated porous media. Vadose Zone J. 3:444–450.

Czigány, S., M. Flury, J.B. Harsh, B.C. Williams, and J. Shira. 2005. Suitability of fiberglass wicks to sample colloids from vadose zone pore water. Vadose Zone J. 4:175–183.

Gee, G.W., A.L. Ward, T.G. Caldwell, and J.C. Ritter. 2002. A vadose zone water fluxmeter with divergence control. Water Resour. Res. 38, doi:10.1029/2001WR000816.

Gee, G.W., F. Zhang, and A.L. Ward. 2003. A modified vadose zone fluxmeter with solution collection capability. Vadose Zone J. 2: 627–632.

Goyne, K.W., R.L. Day, and J. Chorover. 2000. Artifacts caused by collection of soil solution with passive capillary samplers. Soil Sci. Soc. Am. J. 64:1330–1336.

Hillel, D. 1980. Applications of soil physics. Academic Press, San Diego, CA.

Holder, M., K.W. Brown, J.C. Thomas, D. Zabcik, and H.E. Murray. 1991. Capillary-wick unsaturated zone soil pore water sampler. Soil Sci. Soc. Am. J. 55:1195–1202.

Jin, Y., Y. Chu, and Y. Li. 2000. Virus removal and transport in saturated and unsaturated sand columns. J. Contam. Hydrol. 43: 111–128.

Knutson, J.H., S.B. Lee, W.Q. Zhang, and J.S. Selker. 1993. Fiberglass wick preparation for use in passive capillary wick soil pore-water samplers. Soil Sci. Soc. Am. J. 57:1474–1476.

Knutson, J.H., and J.S. Selker. 1994. Unsaturated hydraulic conductivities of fiberglass wicks and designing wick pore-water samplers. Soil Sci. Soc. Am. J. 58:721–729.

Landon, M.K., G.N. Delin, S.C. Komor, and C.P. Regan. 1999. Comparison of the stable-isotopic composition of soil water collected from suction lysimeters, wick samplers, and cores in a sandy unsaturated zone. J. Hydrol. 224:45–54.

Langmuir, D. 1997. Aqueous environmental geochemistry. Prentice Hall, Upper Saddle River, NJ.

Lenhart, J.J., and J.E. Saiers. 2002. Transport of silica colloids through unsaturated porous media: Experimental results and model comparison. Environ. Sci. Technol. 36:769–777.

Liu, D., P.R. Johnson, and M. Elimelech. 1995. Colloid deposition dynamics in flow through porous media: Role of electrolyte concentration. Environ. Sci. Technol. 29:2963–2973.

Louie, M.J., P.M. Shelby, J.S. Smesrud, L.O. Gatchell, and J.S. Selker. 2000. Field evaluation of passive capillary samplers for estimating groundwater recharge. Water Resour. Res. 36:2407–2416.

Mayer, T.D., and W.M. Jarrell. 1996. Formation and stability of iron(II) oxidation products under natural concentrations of dissolved silica. Water Res. 30:1208–1214.

McCarthy, J.F., L.D. McKay, and D.D. Bruner. 2002. Influence of ionic strength and cation charge on transport of colloidal particles in fractured shale saprolite. Environ. Sci. Technol. 36: 3735–3743.

McDowell-Boyer, L.M., J.R. Hunt, and N. Sitar. 1986. Particle transport through porous media. Water Resour. Res. 22:1901–1921.

Poletika, N.N., K. Roth, and W.A. Jury. 1992. Interpretation of solute transport data obtained with fiberglass wick soil solution samplers. Soil Sci. Soc. Am. J. 56:1751–1753.

Saiers, J.E., and J.J. Lenhart. 2003. Ionic-strength effects on colloid transport and interfacial reactions in partially saturated porous media. Water Resour. Res. 39, doi:10.1029/2002WR001887.

Schwertmann, U., and R.M. Cornell. 2000. Iron oxides in the laboratory: Preparation and characterization. Wiley-VCH, Toronto.

Sprague, L.A., J.S. Herman, G.M. Hornberger, and A.L. Miller. 2000. Atrazine adsorption and colloid-facilitated transport through the unsaturated zone. J. Environ. Qual. 29:1632–1641.

Tuller, M., and D. Or. 2005. Water films and scaling of soil characteristic curves at low water contents. Water Resour. Res. 41, doi:10.1029/2005WR004142.

Tuller, M., D. Or, and L.M. Dudley. 1999. Adsorption and capillary condensation in porous media: Liquid retention and interfacial configurations in angular pores. Water Resour. Res. 35:1949–1964.

USDA Natural Resources Conservation Service. 2001. National Soil Survey characterization data. Available at http://ssldata.nrcs.usda.gov/ (verified 8 Mar. 2006). USDA-NRCS, Lincoln, NE.

van Genuchten, M.T. 1980. A closed form equation for predicting the hydraulic conductivity of unsaturated soils. Soil Sci. Soc. Am. J. 44: 892–898.

Wan, J., and T.K. Tokunaga. 1997. Film straining of colloids in unsaturated porous media: Conceptual model and experimental testing. Environ. Sci. Technol. 31:2413–2420.

Available online at www.sciencedirect.com
SCIENCE DIRECT®
Microporous and Mesoporous Materials 86 (2005) 277–286
MICROPOROUS AND MESOPOROUS MATERIALS
www.elsevier.com/locate/micromeso

Cesium incorporation and diffusion in cancrinite, sodalite, zeolite, and allophane

Jarai Mon, Youjun Deng, Markus Flury *, James B. Harsh

Department of Crop and Soil Sciences, Center for Multiphase Environmental Research, Washington State University, Pullman, WA 99164, USA

Received 6 May 2005; received in revised form 19 July 2005; accepted 19 July 2005
Available online 8 September 2005

Abstract

At the US Department of Energy's Hanford site, high level nuclear waste has leaked from underground storage tanks. The waste consists of hyperalkaline solutions, which upon contact with the sediments, caused dissolution of silicate minerals and precipitation of new aluminosilicate minerals. Cancrinite, sodalite, LTA zeolite, and allophane have been identified as the new mineral phases in laboratory simulations. Cesium, the major radionuclide in the waste solutions, may be incorporated into the structural framework of the precipitates. The objectives of this study were to determine the resistance of incorporated Cs^+ to ion exchange and the mobility and diffusion coefficient of Cs in the minerals. The minerals were synthesized in solutions mimicking the tank waste and were washed with deionized water. Two sets of experiments were conducted to test the resistance of Cs^+ to ion exchange. In the first set, Cs^+ was exchanged three times at 80 °C by 0.5 N Na^+, K^+, or Ca^{2+}. The Cs remaining in minerals was quantified after acid digestion. In the second set, we studied the Cs^+ desorption kinetics using 0.1 M Na^+ as the ion exchanger. Cesium concentration in the solution phase was measured as a function of time for 23 days. Cesium incorporated in sodalite and cancrinite was far more difficult to replace than that in LTA zeolite or allophane. Most of the incorporated Cs^+ (94–99%) in LTA zeolite and allophane was readily exchangeable with Na^+ or K^+; less than 20% of Cs^+ in sodalite and <55% of Cs^+ in cancrinite could be exchanged. The fraction of desorbed Cs^+ was also affected by the exchanging ions; the ion with lowest dehydration energy (K^+) was the most effective in replacing Cs^+. The ions had to partially dehydrate to access the cages of the minerals. The results of the desorption kinetics experiments showed that Cs^+ desorbed quickly from LTA zeolite and the Cs^+ diffusion coefficient was close to that in solution; i.e., about 10^{-9} m^2/s. Solid-state NMR analysis also provided evidence for the high mobility of Cs^+ in LTA zeolite. Cesium desorption from cancrinite, sodalite, and allophane, however, was slow, suggesting that Cs^+ was trapped in cages and channels of these minerals. Effective diffusion coefficients for Cs^+ in cancrinite and sodalite were near 10^{-14} m^2/s.

Keywords: Cesium; Ion exchange; Desorption; Feldspathoids; Zeolite; Allophane; Intraparticle diffusion

1. Introduction

At the Hanford site, a former plutonium production complex located in southeastern Washington State, USA, millions of gallons of high level nuclear waste solutions have leaked into the subsurface. The waste solutions are highly alkaline (pH ≈ 14), have high ionic strength, high aluminate content, and contain radioactive cesium (^{137}Cs) in concentrations up to 2×10^{10} Bq/L (0.5 Ci/L = 0.04 mmol/L) [1,2]. When the alkaline waste contacts subsurface sediments, minerals such as quartz and phyllosilicates are dissolved and new minerals precipitate [3–6]. These new minerals have been identified as feldspathoids (cancrinite and sodalite) [5–7] and possibly zeolites and allophane [8]. The precipitation of new aluminosilicate minerals may affect the mobility of

* Corresponding author. Tel.: +1 509 335 1719; fax: +1 509 335 8674.
E-mail address: flury@mail.wsu.edu (M. Flury).

1387-1811/$ - see front matter © 2005 Elsevier Inc. All rights reserved.
doi:10.1016/j.micromeso.2005.07.030

^{137}Cs in the subsurface because these minerals are known to have high cation ion exchange capacity [5].

Cancrinite, sodalite, and zeolite are tectosilicates that contain cages and channels in their frameworks. The frameworks are negatively charged because of substitution of Si^{4+} by Al^{3+}. Cations can enter the cages and channels to balance the charge of the structural frameworks. Cancrinite contains small ε-cages made of six-membered rings and wide channels consisting of 12-membered rings (Fig. 1). The wide channels (0.59 nm in diameter) in cancrinite can host both cations and anions, but the ε-cages (aperture diameter of 0.22 nm) can only accommodate cations and/or water molecules [9]. The effective diameter of a water molecule is 0.28 nm [10] and the diameters of selected ions are listed in Table 1. Sodalite contains only β-cages (or "sodalite" cages; aperture diameter of 0.22 nm) made up of six-membered rings. The shape of β-cages is a truncated octahedron [11]. A β-cage of natural sodalite contains four sodium ions tetrahedrally associated with an anion (e.g., Cl^-) at the center of the cages. The cage cations can be exchanged with cations such as Ag and Cu [11]. The LTA zeolite contains α- and β-cages (aperture diameters of 0.42 and 0.22 nm, respectively) (Fig. 1) that can host different cations [12].

During precipitation of the new minerals at the Hanford site, Cs^+ present in the waste solutions can be incorporated into the mineral structure. Chorover et al. [3] suggested that Cs^+ substitutes for Na^+ and serves as a charge-balancing ion during the formation of feldspathoids and zeolites in simulated waste solutions. A series of ions, such as Li^+, Cs^+, CO_3^{2-}, or NO_3^-, can be incorporated into the channels or cages of cancrinite and sodalite [13,14].

In this study, we hypothesized that a fraction of the Cs^+ present in the solutions of Hanford tank waste can be incorporated into, and adsorbed to, the new feldspathoids, zeolite, and allophane. Upon contact with uncontaminated sediments or pure water, we further hypothesize that the incorporated and adsorbed Cs^+ will desorb and diffuse out of the porous mineral structures. Our objectives were (1) to quantify the amount of Cs^+ incorporated into feldspathoids, zeolite, and allophane, (2) to determine the desorption kinetics of Cs^+ from

Table 1
The ionic diameter, hydrated diameter, and hydration energies of exchanging ions

Ion	Ionic diameter[a] (nm)	Hydrated diameter[a] (nm)	Hydration energy[b] (kcal/mol)
Na^+	0.19	0.72	−97
K^+	0.26	0.66	−79
Cs^+	0.33	0.66	−66
Ca^{2+}	0.20	0.83	−373

[a] Ref. [28].
[b] Ref. [29].

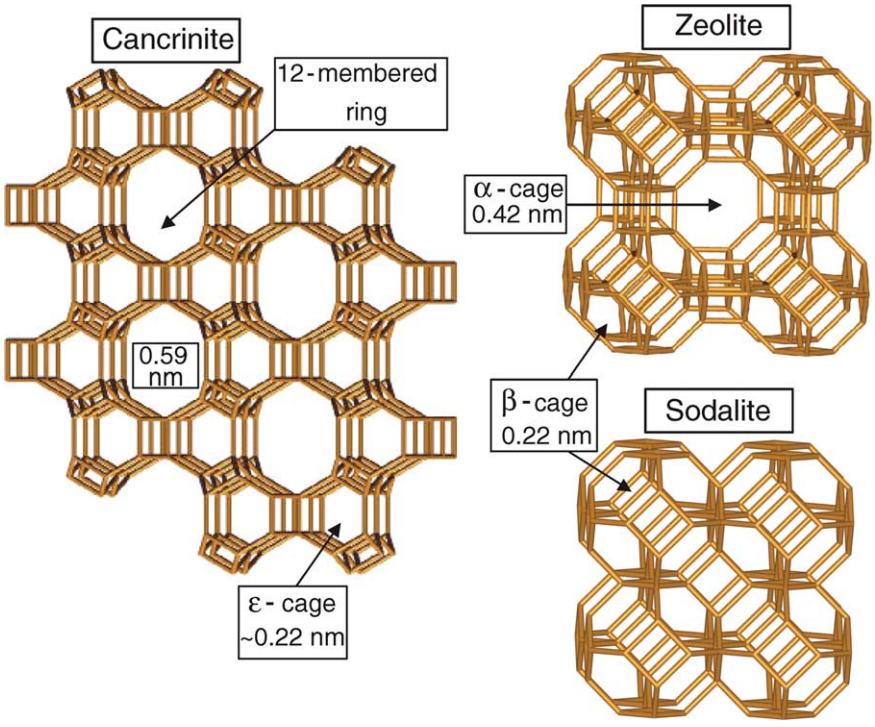

Fig. 1. The structural frameworks of cancrinite, LTA zeolite, and sodalite. The measurements in nanometers are the aperture diameters of respective cages. Structures were generated using data published by the International Zeolite Association and the Weblab ViewerLite software (Accelrys, San Diego, CA).

the minerals, and (3) to estimate the effective diffusion coefficients of Cs^+ inside the porous mineral structures.

2. Materials and methods

2.1. Mineral synthesis and Cs^+ incorporation

We synthesized four minerals in the presence of Cs—cancrinite, sodalite, LTA zeolite, and allophane—by mixing 0.175 M Na_2SiO_3, 0.5 M $NaAlO_2$, and 0.05 M $CsNO_3$ or CsOH with different concentrations of NaOH (1, 4, or 8 M) and $NaNO_3$ (0 or 4 M). The molar Na^+ to Cs^+ ratios in the initial synthesis solutions were 277 for cancrinite, 97 for sodalite, 1.9 for LTA zeolite, and 2.4 for allophane. Varying the molar ratio of Na^+ to Cs^+ changes the mineral formed. Cancrinite, sodalite, and LTA zeolite were synthesized at 80 °C and allophane at room temperature. The precipitates were washed free of salts and residual Cs^+ using deionized water and centrifugation. We denote these washed minerals as "water-washed".

Mineral phases were characterized by X-ray diffraction and electron microscopy. To quantify the amount of Cs^+ associated with the water-washed minerals, 25 mg of air-dry minerals were digested in 1 M HCl. All minerals were readily dissolved by the HCl. Cesium concentrations in digestion solutions were determined with atomic emission spectrometry (AES) (SpectrAA 220, Varian Co., Victoria, Australia).

2.2. Resistance of incorporated Cs^+ to ion exchange

We conducted ion exchange experiments with water-washed minerals to determine the fraction of Cs^+ that is exchangeable with Ca^{2+}, K^+, or Na^+. Specifically, 0.4 g of mineral was equilibrated with 20 mL of 0.5 M Ca^{2+}, K^+, or Na^+ electrolyte solution in a 80 °C oven for 24 h. For the first 8 h, the samples were taken out of the oven every 2 h and shaken on a reciprocal shaker for 20 min. At the end of the 24 h, the samples were centrifuged and the supernatant solution was replaced with 20 mL fresh electrolyte solution. The ion exchange procedure described above was repeated two additional times. At the end, the excess electrolyte in samples were washed with deionized water and the samples were freeze-dried. We denoted these samples as "Ca-, K-, or Na-washed". To determine the amount of Cs^+ remaining in the minerals after ion exchange, they were digested with HCl and Cs^+ was quantified as described above. All experiments were replicated three times.

2.3. Determination of Cs^+ desorption kinetics

We determined the Cs^+ desorption kinetics from "water-washed" minerals using a batch reactor technique. The kinetic ion exchange experiments were conducted with Na^+ electrolyte solutions only. The Na^+ ion had the greatest ability to replace Cs^+ in the batch experiments, and is the most dominant of the cations in the Hanford subsurface below the tanks. The experimental setup consisted of a well-stirred reactor containing Cs-bearing minerals and Na^+ electrolyte solutions, where Cs^+ release into the solution phase was monitored as a function of time. Specifically, minerals (100 mg) were mixed with 200 mL of 0.1 mol/L $NaNO_3$ in polypropylene bottles. The bottles were shaken on a reciprocal shaker at ≈150 rpm. We took an aliquot of 2–4 mL of well-stirred suspension at selected time intervals. The sampling started at 2 min after the beginning of the experiment and the sampling intervals were doubled thereafter ($2, 4, 8, \ldots, 32\,786$ min ≈ 23 days). The aliquots were filtered with 0.2 μm Acrodic Syringe filters (Pall Co., Ann Arbor, MI) and were subsequently centrifuged at $12{,}000 \times g$ for 30 min. Cesium concentration in the supernatant of the aliquots was determined by AES.

These batch reactor experiments were conducted at room temperature (23 ± 2 °C) and 50 ± 6 °C, to examine the effect of temperature on Cs^+ desorption. The high experimental temperature (50 °C) was chosen because the temperature of sediments 40 m beneath the Hanford tanks was reported to be 50 °C and higher [5,15,16], and diffusion-limited desorption would occur faster at 50 °C than at 23 °C. The 50 °C temperature was controlled by a water bath. All experiments were replicated three times.

2.4. Elemental mapping

To check the distribution of cations in minerals during the ion exchange reaction, we mapped the elemental distribution in the minerals with X-ray energy dispersive spectroscopy. Specifically, about 20 mg of powdery mineral were mixed with 1.5 mL of LR White resin (London Resin Company, Ltd., Reading, Berkshire, UK) in a 2 mL centrifuge tube. The tube was shaken overnight and centrifuged. The supernate was replaced with fresh resin. The resin treatment was repeated three times. After the last treatment, the resin with settled minerals was hardened at 60 °C overnight. The resin was then thin-sectioned to 250 nm with a diamond knife on a microtome. Elemental mapping was performed on a LEO982 field emission scanning electron microscope operated at 20 kV.

2.5. Determination of Cs^+ diffusion coefficient

The effective diffusion coefficient of Cs^+ in the minerals was estimated using the following radial diffusion equation, which describes diffusion within porous particles [17]:

$$\frac{\partial C}{\partial t} = \frac{D_{\text{eff}}}{Rr^2}\frac{\partial}{\partial r}\left[r^2\frac{\partial C}{\partial r}\right] \tag{1}$$

where C (mmol/L) is the concentration of Cs^+ in solution, t is the time, D_{eff} is the effective diffusion coefficient, R is the retardation factor, which is given as $R = 1 + \rho\frac{K_d}{\theta}$, where ρ is the particle density, K_d is the distribution coefficient, and θ is the porosity of the particles. The effective diffusion coefficient describes the combined diffusion of Cs^+ and Na^+ inside the porous minerals. We assume that the desorption of Cs^+ to the minerals can be described by a linear isotherm.

Assuming spherical particles of uniform intraparticle porosity, which are initially spiked with Cs^+ and then immersed in a Cs^+ free solution, we can formulate the initial and boundary conditions as follows [18]:

$$C(r, t=0) = \begin{cases} C_0 & \text{for } r < b \\ C_i & \text{for } r = b \end{cases} \tag{2}$$

$$\left.\frac{\partial C(r,t>0)}{\partial t}\right|_{r=b} = -D_{\text{eff}}\theta\left(\frac{4\pi b^2 k}{V_r}\right)\left.\frac{\partial C(r,t>0)}{\partial t}\right|_{r=b} \tag{3}$$

$$\frac{\partial C(r,t>0)}{\partial r} = C_0 \quad \text{for } r = 0 \tag{4}$$

where C_0 is initial Cs^+ concentration inside the particles, C_i is the initial Cs^+ concentration in solution, V_r is the volume of the reservoir, k is the number of particles, θ is the porosity, and b is the radius of the particles.

The analytical solution of the diffusion problem for the Cs^+ concentration outside the particles is given as [17,18]:

$$\frac{C(r,t) - C_i}{C_0 - C_i} = \frac{1}{\alpha+1} - \frac{6\alpha b}{r}\sum_{n=1}^{\infty}\frac{\exp(-D_{\text{eff}}q_n^2\frac{t}{b^2})}{9 + 9\alpha + q_n^2\alpha^2}\frac{\sin(q_n\frac{r}{b})}{\sin(q_n)} \tag{5}$$

where α is

$$\alpha = \frac{3V_r}{4\pi b^3 k\theta R} \tag{6}$$

where V_r is the volume of the reservoir, k is the number of particles, and θ is the porosity; and the q_n are the non-zero roots of $\tan q_n = \frac{3q_n}{3+\alpha q_n^2}$.

The D_{eff} of Cs^+ inside the particles was then estimated from experimental parameters using Eq. (5). The solution of the diffusion problem (Eq. (5)) was fitted to the experimental data by least-square minimization using Powell's method [19]. The effect of temperature on the diffusion coefficient was theoretically estimated based on the Stokes–Einstein relation [18]:

$$D(T) = \frac{(273.15 + T)\mu(T_0)}{(273.15 + T_0)\mu(T)}D(T_0) \tag{7}$$

where $D(T)$ and $D(T_0)$ are diffusion coefficients at temperatures T and T_0 (in °C), respectively, and $\mu(T_0)$ and $\mu(T)$ are dynamic viscosities of water at temperatures T and T_0, respectively. The value of dynamic viscosity for 50 °C was obtained from Lide [20] and for 23 °C from the Andrade equation using tabulated viscosity values [21].

2.6. Solid-state ^{133}MAS NMR

We collected the ^{133}Cs magic-angle spinning nuclear magnetic resonance (MAS-NMR) spectra of the water-washed minerals at room temperature. The NMR peaks (shape, width, symmetry, sidebands) are indicative for Cs^+ mobility inside the minerals. The spectra were collected at 65.608 MHz on a Varian Unity plus 500 NMR spectrometer using a 5-mm HXY MAS probe (Doty Scientific Instruments, Columbia, South Carolina). The samples were spun at 9.0 kHz in silicon nitride rotors. The ^{133}Cs chemical shifts are reported in parts per million (ppm) referenced to 1 M CsCl at 0 ppm.

3. Results and discussion

3.1. Mineral synthesis and Cs^+ incorporation

The X-ray diffraction analysis (data not shown) confirmed that cancrinite, sodalite, LTA zeolite, and allophane formed in the presence of Cs^+; the XRD peak positions matched published ones [9,22,23]. The XRD analysis indicates that sodalite, LTA zeolite, and allophane were pure, but the cancrinite sample contained a trace amount of sodalite. Cancrinite particles were clustered in the form of spherical balls; sodalite was lepispherical; LTA zeolite was cube- to sphere-like; and allophane was grainy (Fig. 2).

There were considerable differences in the amount of Cs^+ associated with the minerals (Fig. 3). The differences are mainly caused by the Na:Cs ratio used in the mineral synthesis and the abilities of the minerals to incorporate Cs^+. Less Cs^+ was incorporated in minerals synthesized at higher Na:Cs ratios (cancrinite and sodalite) than in those at lower Na:Cs ratios (LTA zeolite and allophane).

3.2. Resistance of incorporated Cs^+ to ion exchange

The resistance of incorporated Cs^+ to ion exchange in the minerals increased in the order allophane, LTA zeolite < canrinite < sodalite. Among the cations tested, potassium had the highest efficiency in replacing Cs^+ from the minerals; the efficiencies of Ca^{2+} and Na^+ in replacing Cs^+ varied among the minerals.

A large portion of Cs^+ sorbed to cancrinite and sodalite remained in the minerals after ion exchange with Na^+, K^+, and Ca^{2+} electrolytes (Fig. 3). Less than 20% of the incorporated Cs^+ in sodalite and less than 55% in cancrinite were replaced by Na^+, K^+, or Ca^{2+} at

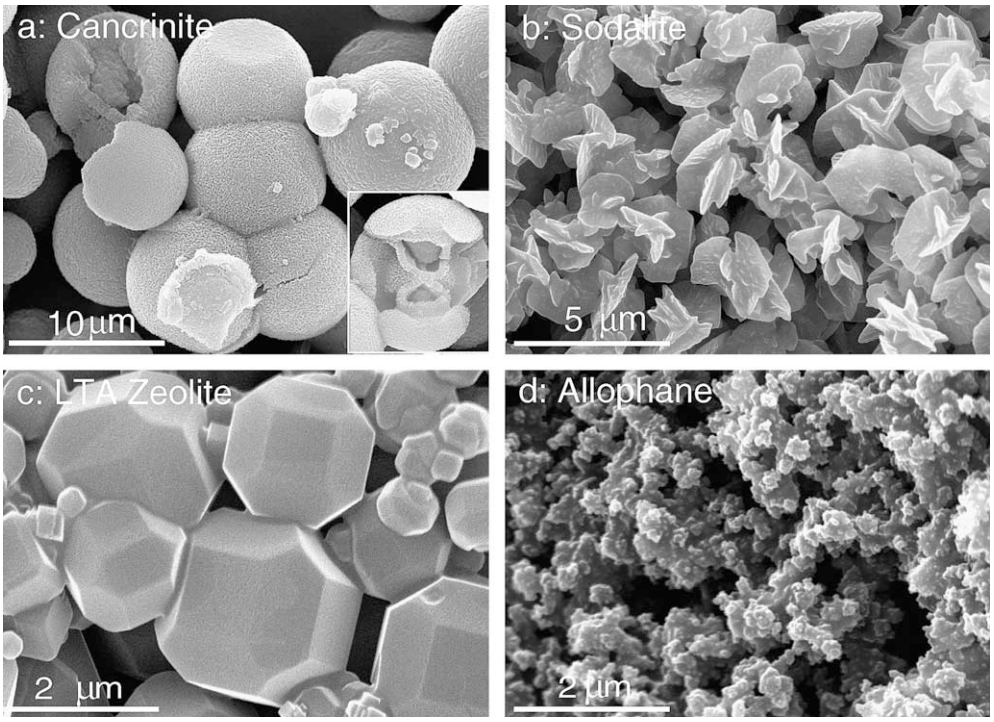

Fig. 2. Scanning electron microscope images of the four minerals studied. The inset in (a) shows the inside of a ball-shaped cancrinite cluster.

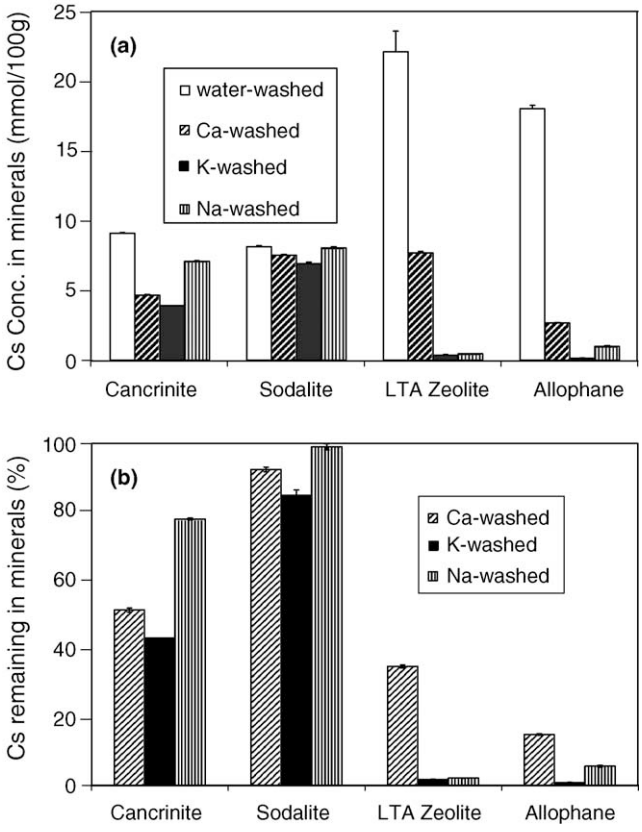

Fig. 3. Amount of total incorporated Cs^+ in the four minerals (water-washed) and Cs^+ remaining in the minerals after ion exchange with Ca^{2+}, K^+, or Na^+. (a) Cs^+ expressed in absolute concentration, (b) Cs^+ expressed relative to water-washed samples. Error bars denote ±one standard deviation.

80 °C. The ability of cations in replacing Cs^+ in cancrinite and sodalite increased in the order $Na^+ < Ca^{2+} < K^+$. Cesium incorporated in LTA zeolite and allophane was readily exchangeable. More than 98% of Cs in LTA zeolite and allophane was replaced by K^+. The abilities of cations in replacing Cs^+ in LTA zeolite and allophane increased in the order $Ca^{2+} < Na^+ < K^+$. These results suggest that cesium was incorporated into the minerals and occupied the internal cages and channels of the minerals. If Cs^+ were sorbed only at the external surfaces, the efficiency of ion exchange should follow the order $Na^+ < K^+ < Ca^{2+}$ [24], and nearly all of the Cs^+ should be replaced by ion exchange.

The resistance of Cs^+ to ion exchange in cancrinite, sodalite, LTA zeolite, and allophane is determined by the accessibility of the exchange sites. The apertures of cages and channels in the minerals are <0.59 nm (Fig. 1), but the diameters of the hydrated ions are >0.66 nm (Table 1). This mismatch between the aperture and the cations suggests that either the cages have to deform or the cations have to be dehydrated when they pass through the apertures. Sodalite has only one type of β-cage with an aperture of 0.22 nm. This aperture is much smaller than a fully dehydrated Cs^+ ion and, therefore, the incorporated Cs^+ in sodalite has the highest resistance to ion exchange. The opening of the α-cage in LTA zeolite is 0.42 nm, which is larger than the diameters of dehydrated Cs^+, Ca^{2+}, K^+, and Na^+. Cations can freely pass through the 8-member rings if the cations are dehydrated. This is likely why Cs^+ in LTA is readily

exchangeable. The 12-membered ring in cancrinite has an aperture of 0.59 nm and cations should pass through the channels the most readily; however, Cs^+ in cancrinite was more resistant to ion exchange than in LTA zeolite. This suggests that non-exchangeable Cs^+ was located in the small ε-cage of cancrinite. Fechtelkord et al. [25] observed that Cs^+ exclusively occupied the ε-cages in Cs–Li cancrinite, likely because Cs^+ expanded the ε-cages and made the mineral framework more stable and less vibrating.

The efficiency of Na^+, K^+, and Ca^{2+} in replacing Cs^+ in the minerals is mainly determined by their dehydration energy. Potassium has the lowest dehydration energy (79 kcal/mol) and, therefore, it has the highest efficiency in replacing Cs^+. Calcium has the highest dehydration energy (373 kcal/mol) and, therefore, has the most difficulty accessing the internal sites of the minerals despite its high tendency to exchange with monovalent cations on available sites. Consequently, Ca^{2+} is less efficient than K^+ in desorbing Cs^+ from the internal sites of the minerals. The differences in dehydration energy also explain why more Cs^+ was desorbed by Na^+ than by Ca^{2+} in LTA zeolite. Allophane formed in alkaline solutions is feldspathoid-like [26]; similar cages to those in feldspathoids may have developed and cannot be accessed by Ca^{2+}; therefore a considerable amount (20%) of Cs^+ could not be exchanged with Ca^{2+} in allophane.

3.3. Site of ion exchange

Elemental mapping indicates that Cs^+ and other cations were homogenously distributed within the mineral particles. It further indicates that the ion exchange reactions occurred both on the external surfaces and inside the minerals. For example, the intensity distribution of Na, Cs, Ca, and other elements in the Ca-washed Cs-sodalite coincide with each other; there was no sign of a site preference (Fig. 4). In a parallel experiment, we examined the distribution of the elements in larger (20 μm) cancrinite and sodalite samples; no site preference was observed there either.

3.4. Cesium desorption kinetics

The relative amount of Cs^+ desorbed by Na^+ exchange in desorption kinetics experiments varied with the minerals. Cancrinite and sodalite released much smaller amounts of Cs^+ than did LTA zeolite or allophane (Fig. 5). Over the duration of the experiments at 23 °C, less than 32% and 3% of incorporated Cs^+ was desorbed from cancrinite and sodalite, respectively; more than 80% of Cs^+ was released from zeolite and allophane (Fig. 5, Table 2). These results were consistent with our equilibrium ion exchange experiments (Fig. 3), i.e., cesium incorporated into cancrinite and sodalite

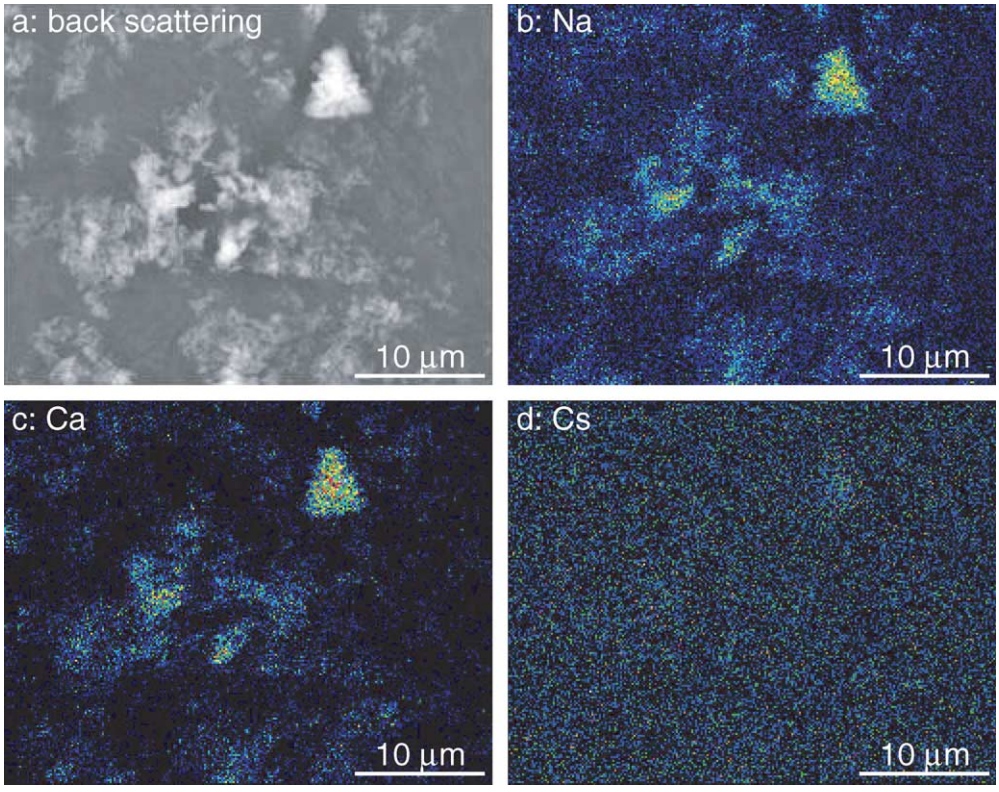

Fig. 4. Elemental mapping of sodalite after washing with $Ca(NO_3)_2$. The distribution of Si and Al (not shown) are nearly identical to that of Na^+. (a) Back scattering showing the location of the minerals, (b) distribution of Na^+, (c) distribution of Ca^{2+}, and (d) distribution of Cs^+.

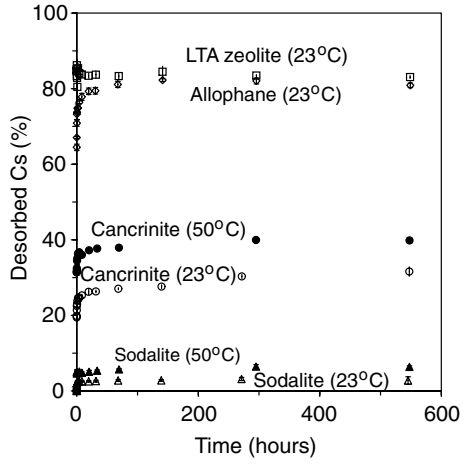

Fig. 5. Desorption of Cs^+ from the four Cs-incorporated minerals: cancrinite, sodalite, LTA zeolite, and allophane. Desorption is expressed as percentage of initial amount of Cs^+ present in minerals (water-washed minerals).

Table 2
The amount of Cs^+ incorporated in the minerals studied and Cs^+ remaining in the minerals after diffusion experiments

Minerals	Cs^+ in water-washed minerals (cmol/kg)	Cs^+ remaining in minerals after 23 days of diffusion			
		23 °C		50 °C	
		(cmol/kg)	(%)	(cmol/kg)	(%)
Cancrinite	9.1 ± 0.03	6.2 ± 0.1	68.4	5.5 ± 0.1	60.2
Sodalite	8.1 ± 0.1	7.9 ± 0.1	97.3	7.6 ± 0.02	93.6
Zeolite	22.1 ± 1.5	3.4 ± 0.1	16.5	na	na
Allophane	18.0 ± 0.2	3.6 ± 0.1	19.1	na	na

na = not applicable.
Errors are ±one standard deviation.

was more resistant to ion exchange, whereas most Cs^+ in allophane and LTA zeolite was readily exchangeable.

The desorption of Cs^+ from cancrinite and sodalite showed an initially fast release of Cs^+, continued by a slow Cs^+ release (Fig. 5). As will be demonstrated later, the fast release of Cs^+ can be fitted to a diffusion model, whereas the slow release (observable after 200 min) is likely caused by mineral dissolution and consequent release of trapped Cs^+. As in most chemical reactions, increasing temperature increased the Cs^+ desorption rate [16]. The percentage of Cs^+ released from cancrinite increased from 31% at 23 °C to 40% at 50 °C (Table 2). Similarly, Cs^+ released from sodalite increased from 2.7% at 23 °C to 6.4% at 50 °C. The small increase suggests that the activation energies for the desorption are high.

The LTA zeolite released most of the Cs^+ immediately upon contact with Na^+ electrolyte solution and Cs^+ concentration remained constant throughout the experiment (Fig. 5). It appears that all the exchangeable Cs^+ was quickly released into the solution and the remaining ≈20% (Table 2) sorbed Cs^+ was at equilibrium with the Cs^+ in solution. One possible explanation for this behavior is that some of the Cs^+ ions inside the β-cages are strongly associated with the framework atoms so that they may be trapped in the cages for a longer time than those in α-cages [12].

In allophane, most of the Cs^+ was released at the beginning of the experiment, but the equilibrium concentration was reached much later compared to the case of zeolite (Fig. 5). The Cs^+ desorption kinetics from allophane was similar to that of cancrinite and sodalite.

3.5. Determination of Cs^+ diffusion coefficient

Ion exchange at mineral surfaces is often an instantaneous process [27]. Ion diffusion can be expected as the controlling step in Cs^+ desorption. To estimate the Cs^+ diffusion coefficient, we assumed that Cs^+ was homogenously distributed inside the minerals, which was confirmed by elemental mapping (e.g., Fig. 4).

All the parameters needed in Eq. (5), except the effective diffusion coefficient D_{eff}, were experimentally determined or taken from the literature, and the values are listed in Table 3. The total Cs^+ released during desorption experiments was estimated from the experimental data (Table 2), and used as input for the modeling. The only parameter fitted was the effective diffusion coefficient D_{eff}.

The analysis of the diffusion problem with Eq. (5) indicates that the characteristic time scale or the intraparticle diffusion was in the order of a few minutes; i.e., the diffusion process was completed within about 10 min. Based on this, we used only the first 64 min of data to estimate the diffusion coefficient. The slow Cs^+ increase observed after this time for cancrinite and sodalite cannot be attributed to diffusion, and is likely caused by slow mineral dissolution.

By and large the diffusion process could be well described with Eq. (5) (Fig. 6a and b). The estimated D_{eff} of Cs^+ in cancrinite and sodalite were in the order of 10^{-14} m^2/s. The diffusion coefficient in sodalite was less than that in cancrinite, likely because the intraparticle porosity of sodalite is less accessible due to the β-cage structure. The D_{eff} of Cs^+ in cancrinite and sodalite increased with increasing temperature. The observed temperature effect on the diffusion coefficient was consistent with what would be expected based on Eq. (7). For cancrinite and sodalite the ratio D_{eff} (50 °C)/D_{eff} (23 °C) was 1.48 and 1.53, respectively, which compares to a ratio of 1.86 calculated from Eq. (7).

In zeolite, we could not estimate D_{eff} because the diffusion process was completed before experimental measurements were taken (Fig. 6c). The model analysis indicates that the D_{eff} of Cs^+ in LTA zeolite is of the magnitude of the free Cs^+ ion diffusion coefficient in solution (2.06×10^{-9} m^2/s at 20 °C) [18]. This suggests

Table 3
Model input parameters needed for Eq. (5)

Minerals	Diameter b (μm)	Porosity θ[a] (cm^3/cm^3)	No. of particles k	Volume of solution V_r (m^3)	K_d (L/kg)	
					23 °C	50 °C
Cancrinite	10	0.4	8.2×10^7	2×10^{-4}	34.3[b]	22.5[b]
Sodalite	4.0	0.35	1.5×10^9	2×10^{-4}	34.3[b]	15.2[b]
Zeolite	1.8	0.47	1.4×10^{10}	2×10^{-4}	36.2[c]	na
Allophane	0.4	0.3	1.3×10^{12}	2×10^{-4}	47.7[c]	na

na = not applicable.
[a] From Ref. [30].
[b] From Ref. [7].
[c] Estimated from the ratio of total amount of Cs desorbed at 23 and 50 °C.

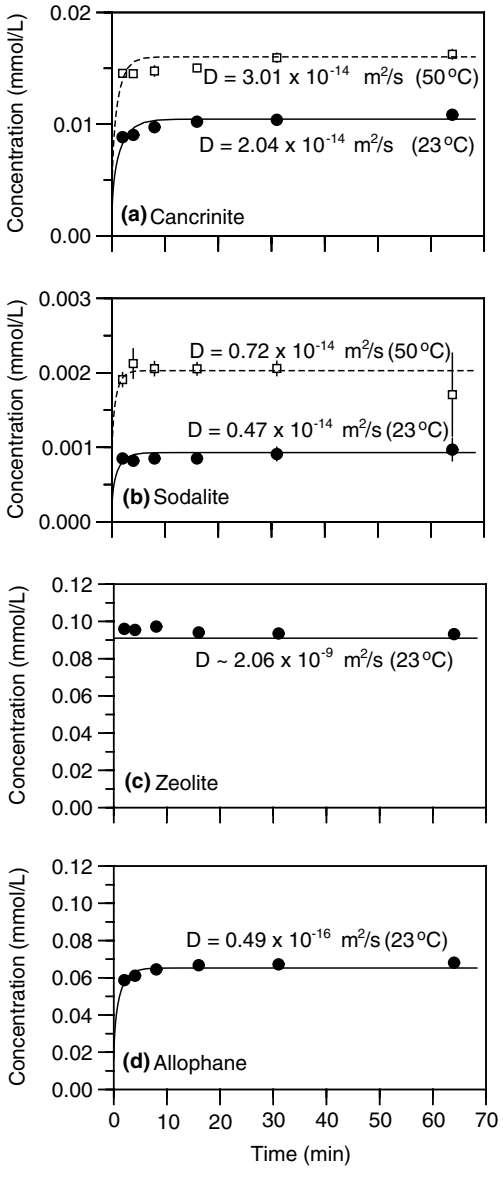

Fig. 6. Desorption of Cs^+ from (a) cancrinite, (b) sodalite, (c) zeolite, and (d) allophane. Symbols represent the experimental data, vertical bars are ±one standard deviation. Solid lines represent solutions of the radial diffusion problem (Eq. (5)).

that Cs^+ and Na^+ ions can easily move in and out of the α-cages, which is indeed possible for the ions in their dehydrated form (Table 1).

The value of D_{eff} of Cs^+ in allophane was estimated to be $\approx10^{-16}$ m^2/s. This suggests that allophane indeed consisted of a porous structure. The modeling results indicate that the diffusion of Cs^+ in cancrinite, sodalite, and allophane is likely a solid-state diffusion, because the estimated diffusion coefficient (10^{-14}–10^{-16} m^2/s) is five to six orders of magnitude smaller than the diffusion coefficient of D_{eff} in aqueous solution ($D = 2.06\times10^{-9}$ m^2/s, [18]). Considering the apertures of ε- or β-cages, it is therefore likely that Cs^+ diffuses out of cancrinite, sodalite, and allophane as it does through a solid matrix.

3.6. Mobility of Cs^+ in cancrinite, sodalite, LTA zeolite and allophane

The solid-state MAS NMR spectra (Fig. 7) suggest that the movement of Cs^+ in LTA zeolite was more

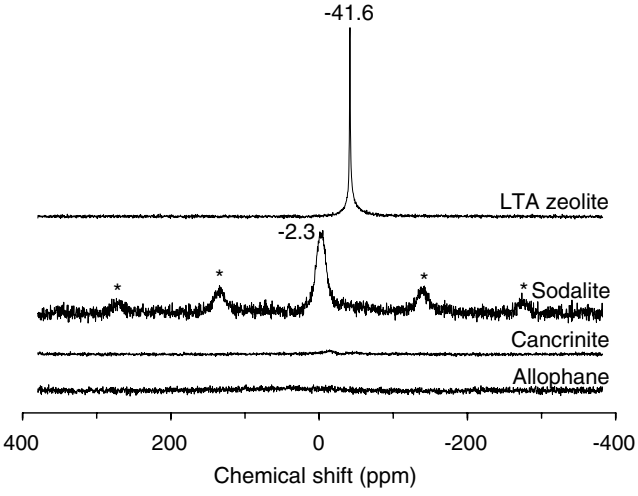

Fig. 7. ^{133}Cs MAS NMR spectra of water-washed LTA zeolite, sodalite, cancrinite, and allophane. The asterisks denote spinning sidebands.

rapid than in other minerals, corroborating the desorption experiments and structural considerations. The peak width at half height of LTA zeolite was 1.4 ppm (91 Hz) and of sodalite was 14.5 ppm (950 Hz). The narrow NMR peak of Cs^+ ions in LTA indicates they had identical chemical environments. This is the result of the averaging effect, which is determined by the high mobility of Cs^+ inside the minerals. The presence of two sidebands on each side of the center peak in sodalite indicates that the movement of Cs^+ in sodalite was slow. Even though the Cs contents in cancrinite and allophane were greater than in sodalite, the NMR peaks of the two samples were too broad to be detected, suggesting that Cs^+ mobility in cancrinite and allophane was too low to average the differences among chemical environments.

4. Conclusions and implications

Cancrinite, sodalite, zeolite, and allophane incorporated Cs in their structural frameworks. Cesium in the cages of cancrinite and sodalite was not easily exchangeable with Na^+, K^+, or Ca^{2+}. The resistance of Cs^+ to ion exchange was determined by the size of the cage apertures as related to the ion radii. Ions had to partially dehydrate to access the cages of the minerals. Only 1–15% of Cs^+ in sodalite and 22–57% of Cs^+ in cancrinite was exchangeable with Na^+, K^+, or Ca^{2+}, while most Cs^+ (94–99%) associated with LTA zeolite and allophane was exchangeable with Na^+ or K^+. The effectiveness of the ions to replace incorporated Cs^+ was mainly determined by their dehydration energy. Among the ions studied, K^+ was the most effective in replacing Cs^+ in all the four minerals. Compared to Na^+ and K^+, Ca^{2+} was less effective in exchanging Cs^+; Ca^{2+} could replace a smaller fraction of Cs^+ (65–85%) in LTA zeolite and allophane; however, Ca^{2+} was more effective than Na^+ in replacing Cs^+ in cancrinite and sodalite. The aperture size of the cages and channels also determined the mobility and diffusion of Cs^+ in the minerals. The mobility and diffusion in LTA zeolite was greater than those in sodalite and cancrinite.

The high resistance of incorporated Cs^+ to desorption in sodalite and cancrinite may have twofold implications to the DOE Hanford site: on one hand, the minerals can immobilize the Cs^+, on the other hand, the minerals can be secondary contaminant sources when they became chemically unstable with respect to the pore water of the sediments.

Acknowledgments

This research was supported by the Office of Science (BER), US Department of Energy, Grant No. DE-FG07-05ER62882. We thank Jeff Boyle (Washington State University) for help with the experiments and Kent Keller (Washington State University) for helping us clarify the diffusion process. We thank the Electron Microscopy Center at Washington State University for the use of SEM. Elemental mapping and NMR analyses were performed in the Environmental Molecular Sciences Laboratory (a national scientific user facility sponsored by the US DOE Office of Biological and Environmental Research) located at Pacific Northwest National Laboratory, operated by Battelle for the DOE.

References

[1] R.J. Serne, J.M. Zachara, D.S. Burke, Chemical Information on Tank Supernatants, Cs Adsorption from Tank Liquids onto Hanford Sediments, and Field Observations of Cs Migration from Past Tank Leaks, Pacific Northwest National Laboratory, PNNL-11495/UC-510, Richland, WA, 1998.
[2] J.P. McKinley, C.J. Zeissler, J.M. Zachara, R.J. Serne, R.M. Lindstrom, H.T. Schaef, R.D. Orr, Environ. Sci. Technol. 35 (2001) 3433–3441.
[3] J. Chorover, S. Choi, M.K. Amistadi, K.G. Karthikeyan, G. Crosson, K.T. Mueller, Environ. Sci. Technol. 37 (2003) 2200–2208.
[4] C. Liu, J.M. Zachara, S.C. Smith, J.P. McKinley, C.C. Ainsworth, Geochim. Cosmochim. Acta 67 (2003) 2893–2912.
[5] N.P. Qafoku, C.C. Ainsworth, J.E. Szecsody, D. Bish, J.S. Young, D.E. McCready, O.S. Qafoku, J. Environ. Qual. 32 (2003) 2364–2372.
[6] K. Mashal, J.B. Harsh, M. Flury, A.R. Felmy, H. Zhao, Environ. Sci. Technol. 38 (2004) 5750–5756.
[7] H. Zhao, Y. Deng, J.B. Harsh, M. Flury, J.S. Boyle, Clays Clay Miner. 52 (2004) 1–13.
[8] K. Mashal, J.B. Harsh, M. Flury, Soil Sci. Soc. Am. J. 69 (2005) 531–538.
[9] J.C. Buhl, F. Stief, M. Fechtelkord, T.M. Gesing, U. Taphorn, C. Taake, J. Alloys Compds. 305 (2000) 93–102.
[10] J. Israelachvili, Intermolecular and Surface Forces, Academic Press, London, 1992.
[11] L. Bernasconi, E. Fois, A. Selloni, J. Chem. Phys. 110 (1999) 9048–9055.
[12] S.H. Lee, G.K. Moon, S.G. Choi, H.S. Kim, J. Phys. Chem. 98 (1994) 1561–1569.
[13] J.C. Buhl, J. Löns, J. Alloys Compds. 235 (1996) 41–47.
[14] M. Fechtelkord, B. Posnatzki, J.-C. Buhl, C.A. Fyfe, L. Groat, M. Raudsepp, Appl. Microbiol. 86 (2001) 881–888.
[15] K. Pruess, S. Yabusaki, C.I. Steefel, P.C. Lichtner, Vadose Zone J. 1 (2002) 68–88.
[16] C. Liu, J.M. Zachara, O. Qafoku, S.C. Smith, Environ. Sci. Technol. 37 (2003) 2640–2645.
[17] J. Crank, The Mathematics of Diffusion, second ed., Clarendon Press, Oxford University Press, Oxford, 1975.
[18] M. Flury, T. Gimmi, in: J.H. Dane, G.C. Topp (Eds.), Methods of Soil Analysis, Part 4, Physical Methods, Soil Science Society of America, Madison, WI, 2002, pp. 1323–1351.
[19] W.H. Press, B.P. Flannery, S.A. Teukolsky, W.T. Vetterling, Numerical Recipes. The Art of Scientific Computing, Cambridge University Press, Cambridge, 1989.
[20] D.R. Lide, CRC Handbook of Chemistry and Physics, 75th ed., CRC Press, Boca Raton, 1994.
[21] R.C. Reid, J.M. Prausnitz, B.E. Poling, The Properties of Liquids and Gases, fourth ed., McGraw-Hill, New York, 1987.

[22] P. Sieger, M. Wiebcke, J. Felsche, J.C. Buhl, Acta Crystallogr., Sect. C: Cryst. Struct. Commun. 47 (1991) 498–501.
[23] R.W.G. Wyckoff, second ed.Crystal Structures: Miscellaneous Inorganic Compounds, Silicates, and Basic Structural Information, vol. 4, John Wiley and Sons, Inc., New York, 1968.
[24] M.B. McBride, Environmental Chemistry of Soils, Oxford University Press, New York, 1994.
[25] M. Fechtelkord, B. Posnatzki, J.-C. Buhl, C.A. Fyfe, L.A. Groat, M. Raudsepp, Am. Miner. 86 (2001) 881–888.
[26] V.C. FarmerThe Infra-Red Spectra of Minerals, vol. 4, Mineralogical Society Monograph, Mineralogical Society, Adlard & Son Ltd., London, 1974.
[27] D.L. Sparks, Kinetics of Soil Chemical Processes, Academic Press, San Diego, 1989.
[28] E.R. Nightingale Jr., J. Phys. Chem. 63 (1959) 1381–1387.
[29] R.-M. Woods, M.E. Gunter, Appl. Microbiol. 86 (2001) 424–430.
[30] F.A. Mumpton, in: F.A. Mumpton (Ed.), Mineralogy and Geology of Natural Zeolites, vol. 4, Mineralogical Society of America, Blacksburg, VA, 1981, pp. 1–17.

Environ. Sci. Technol. **2005**, *39,* 3435−3442

Colloid-Facilitated Transport of Cesium in Variably Saturated Hanford Sediments

GANG CHEN, MARKUS FLURY,* AND JAMES B. HARSH

Department of Crop and Soil Sciences, Center for Multiphase Environmental Research, Washington State University, Pullman, Washington 99164-6420

PETER C. LICHTNER

Earth and Environmental Sciences, Los Alamos National Laboratory, Los Alamos, New Mexico 87545

Radioactive ^{137}Cs has leaked from underground waste tanks into the vadose zone at the Hanford Reservation in south-central Washington State. There is concern that ^{137}Cs, currently located in the vadose zone, can reach the groundwater. In this study, we investigated whether, and to what extent, colloidal particles can facilitate the transport of ^{137}Cs at Hanford. We used colloidal materials isolated from Hanford sediments. Transport experiments were conducted under variably saturated, steady-state flow conditions in repacked, 20 cm long Hanford sediment columns, with effective water saturations ranging from 0.2 to 1.0. Cesium, pre-associated with colloids, was stripped off during transport through the sediments. The higher the flow rates, the less Cs was stripped off, indicating in part that Cs desorption from carrying colloids was a residence-time-dependent process. Depending on the flow rate, up to 70% of the initially sorbed Cs desorbed from colloidal carriers and was captured in the stationary sediments. Less Cs was stripped off colloids under unsaturated than under saturated flow conditions at similar flow rates. This phenomenon was likely due to the reduced availability of sorption sites for Cs on the sediments as the water content decreased and water flow was divided between mobile and immobile regions.

Introduction

Colloid-facilitated transport of radionuclides in porous media has been inferred from various field (*1, 2*) and laboratory experiments (*3*−*5*). Radionuclides susceptible to colloid-facilitated transport are strongly sorbing elements such as Cs, Pu, and Am. As ^{137}Cs constitutes a major portion of the radioactive inventory at the U.S. Department of Energy's (DOE) nuclear facilities, it is important to understand the environmental fate and transport of this radionuclide.

From laboratory experiments, we have evidence that Cs movement can be enhanced by amorphous silica (*5*) and crystalline aluminosilicate colloids (*4, 6*). The extent of the enhancement depends on the porous medium's particle size distribution (*5*), the colloid concentration, and the solution ionic strength (*4, 6*). In most laboratory experiments, the porous matrix consisted of glass beads and silica sand, which have a low sorption affinity for Cs. In natural porous media, however, the stationary solid phase can effectively compete with colloids for Cs sorption (*7*). Cs sorption is an ion exchange process and, therefore, is controlled by the relative sorption affinity of colloids and the stationary phase.

Cesium attaches to colloids usually via ion-exchange. Consequently, Cs can adsorb to colloidal particles in contaminated subsurface regions but may desorb when Cs-containing colloids move through a yet uncontaminated zone (*8*). If the porous medium has a high sorption affinity for Cs, Cs may be effectively stripped off the colloidal carrier (*7*). Such desorption from colloids and adsorption to the stationary solid phase will counteract the colloid-facilitated movement of Cs. On the other hand, if Cs adsorption occurs within the interlayer of colloidal illite, Cs may not easily desorb from carrying colloids.

At the U.S. DOE's Hanford site in south-central Washington State, ^{137}Cs has leaked from underground waste tanks (*9*). The leaking tank waste consists of solutions of high alkalinity and ionic strength, main constituents of which are Na, OH, NO_3, NO_2, and Al (*10*). ^{137}Cs sorption to subsurface sediments is usually strong (*11*) but can be reduced under conditions of high ionic strength (*6, 12, 13*). The current depth distribution of ^{137}Cs below the SX tanks at Hanford can be explained by chromatographic tranport and ion exchange (*12, 14, 15*). As the contaminated plumes move downward through the vadose zone driven by gravity, the ionic strength of the plumes decreases due to dispersion and dilution with pore water (*16, 17*).

It has been demonstrated that colloids from the Hanford sediments can be mobilized when high ionic strength tank liquors are diluted by low ionic strength pore water (*18*). If such colloids contain Cs, either by sorption or coprecipitation, they also will facilitate the movement of Cs (*18*). Unknown, however, is the degree of colloid-facilitated transport. It has been suggested that, under natural subsurface conditions, colloid-facilitated radionuclide transport in general will not be very substantial because mobile colloidal concentrations in natural subsurface media are small (*19*). Moreover, under unsaturated conditions, laboratory column experiments have repeatedly shown that colloid transport is less pronounced than under saturated conditions (*20*−*25*).

The objective of this study was to quantitatively investigate transport of Cs through variably saturated Hanford sediments, as facilitated by colloids representative for Hanford leaking tank conditions. We hypothesize that Cs will desorb from Cs-carrying colloids as the colloids move through uncontaminated sediments, thereby counteracting the colloid-enhanced transport mechanism. We further hypothesize that the sediments' water saturation will affect Cs desorption from colloids, whereby less Cs desorbs from colloids as the water saturation decreases.

Materials and Methods

Artificial Pore Water. The artificial pore water (APW) for the column transport experiments consisted of 1.67 mM $NaHCO_3$ and 1.67 mM Na_2CO_3 (ionic strength $I = 6.67$ mM, pH 10). The artificial pore water was filtered with a 0.1 μm nylon membrane filter and degassed by helium bubbling. The APW offers a stable chemistry and prevents dissolution of carbonates present in the sediments. As APW is pH buffered, the degassing process has no or minimal impact on pH. This APW has a much lower ionic strength than the contaminant plumes below the Hanford waste tanks; however, the plumes become diluted with uncontaminated low ionic strength pore water and infiltrating meteoric water as the plumes move

* Corresponding author phone: (509)335-1719; fax: (509)335-8674; e-mail: flury@mail.wsu.edu.

10.1021/es048978+ CCC: $30.25
Published on Web 04/06/2005

TABLE 1. Selected Colloid and Sediment Characteristics

material	particle diameter[a] (nm)	electrophoretic mobility[a] (μm s^{-1})/(V cm^{-1})	surface area[b] (m^2/g)	mineralogy[c]
native colloids	393 ± 8	−3.5 ± 0.1	78.8 ± 0.3	chlorite, smectite, kaolinite, illite, quartz
modified colloids	407 ± 10	−3.6 ± 0.1	60.5 ± 0.8	cancrinite, sodalite, chlorite, smectite, illite, quartz
Hanford sediment	1.37 × 10^6	na[d]	3.63 ± 0.02	feldspar, mica, pyroxene, chlorite, smectite, illite, quartz

[a] Colloids: *Z*-averaged hydrodynamic diameter determined by dynamic light scattering in pH 10 $NaHCO_3/Na_2CO_3$ buffer solution (I = 6.67mM) (Zetasizer 3000HSA with a Helium−Neon laser of 633 nm wavelength, Malvern Instruments Ltd., Malvern, UK). Sediment: median diameter of weight-based particle size distribution. [b] Surface area measured with N_2 adsorption (ASAP 2010, Micromeritics Corporation, Norcross, GA). [c] Determined by X-ray diffraction with Cu Kα radiation (Philips XRG 3100, Philips Analytical Inc., Mahwah NJ) or petrographic thin sections. [d] na, not available

downward (*16*, *17*). At the low ionic strength of our APW colloid transport is favored; therefore, our experiments constitute a scenario where colloid-facilitated Cs transport is optimal at the Hanford site.

Porous Medium and Colloids. Sediments and colloids used in this study were similar to the ones used in a previous study (*25*). We briefly summarize the procedures here. Hanford sediments were sieved through a 2-mm sieve and extensively flushed with 1 M NaCl buffered at pH 10 with 1.67 mM $NaHCO_3$/1.67 mM Na_2CO_3 to saturate the exchange sites with Na, followed by a flush with APW. Particles with diameter <2 μm were fractionated from the sediments using gravity sedimentation to obtain a porous medium with particle size ranging from 2 to 2000 μm in diameter. The particles <2 μm were used as the colloidal source materials for the colloid-facilitated transport experiments.

The colloidal source materials were further fractionated by gravity settling for 2 weeks in APW. Suspended colloids were decanted and used for the transport experiments. We denote these colloids as "native colloids". To produce colloidal materials representative for a Hanford tank leak, Hanford sediments were reacted with a caustic solution (*26*). The colloidal materials were fractionated from the reacted sediments as described for the unreacted sediments. We denote those latter colloids as "modified" as opposed to "native". Both types of colloids were washed with deionized water to remove entrained salts. Selected colloidal characteristics are listed in Table 1. Particle diameters and electrophoretic mobility differ somewhat from the values reported in Cherrey et al. (*25*), and we attribute these differences to natural variability in the sedimental source material used.

While the packed columns do not represent the undisturbed sediments at Hanford, the pretreatment of the sediments was necessary to prevent in situ colloid mobilization. Consequently, our columns do not exactly mimic conditions at Hanford, but they allow us to conduct colloid transport experiments under well-controlled conditions.

Cesium. We used ^{137}Cs (specific activity 4.9 Ci/g or 1.81 × 10^{11} Bq/g; Isotope Products Laboratories, Valencia, CA) in the form of CsCl. Concentrations of ^{137}Cs were determined using a liquid scintillation analyzer (1900 TR, Packard Instrument Company, Meriden, CT) against external standards of ^{133}Ba (18.8 ± 0.2 mCi).

Cesium Sorption Isotherms. Batch sorption isotherms were used to determine the sorption of ^{137}Cs on colloids and sediments in the APW solution. A series of 250-mL Erlenmeyer flasks containing ^{137}Cs at concentrations ranging from 0 to 28.4 nM (687 Bq/mL) in 100 mL of native colloid suspension at a colloid concentration of about 10 mg/L were placed on a stir plate and mixed gently with a stir bar. ^{137}Cs concentrations ranging from 0 to 30.0 nM (726 Bq/mL) were used for modified colloids. For sediment sorption isotherms, 1.0 g of sediment and 100 mL of solution were used. Initial ^{137}Cs concentrations ranged from 0 to 68.8 nM (1665 Bq/mL). After 24 h, the suspensions were centrifuged at 16100*g* for 15 min. On the basis of Stokes' law, particles greater than 60 nm equivalent diameter should be centrifuged out. ^{137}Cs concentrations in the supernatant were measured, and the ^{137}Cs sorbed on colloids was calculated based on mass balance. All experiments were performed in triplicate.

Column Experiments. Column transport experiments were conducted using an acrylic column with 5.0 cm i.d. × 20.0 cm length. A detailed description and a schematic of the experimental apparatus are given elsewhere (*25*). Hanford sediments, which had particles less than 2 μm removed, were incrementally packed into the column and had a porosity of ≈0.4, a bulk density of 1.54 g/cm^3, and a pore volume of 152.3 cm^3. All experiments were conducted with one single column.

Colloids suspended in APW were fed into the column using a sprinkler head. The boundary condition at the bottom was controlled by a porous plate and a hanging water column. Column transport experiments were performed under steady-state flow conditions at effective water saturations varying from S_e = 0.2−1.0. Effective water saturation is defined as $S_e = (\theta - \theta_r)/(\theta_s - \theta_r)$, where θ is the volumetric water content, θ_s = 0.394 cm^3/cm^3 is the saturated water content, and θ_r = 0.074 cm^3/cm^3 is the residual water content. Volumetric water contents and matric potentials were maintained steady and uniform for each run by balancing the inflow rate and the hanging water column.

Colloid suspensions (≈10 mg/L) were equilibrated with known amounts of ^{137}Cs for 24 h before being introduced into the column. From the Cs sorption isotherm experiments, equilibrium was found to be reached within at least 24 h. Outflow colloid concentrations were measured using an in-line spectrophotometer (LC95 UV/VIS, Perkin-Elmer, Norwalk, CT) at a wavelength of 300 nm. Outflow suspensions were collected using a fraction collector and divided into two aliquots. One of these aliquots was measured for ^{137}Cs directly using the liquid scintillation analyzer, and the other aliquot was centrifuged at 16100*g* for 15 min. The supernatant was measured for ^{137}Cs. The first aliquot yields total ^{137}Cs concentrations, the second aliquot yields dissolved ^{137}Cs concentrations, and Cs concentrations on the colloids were calculated by mass balance.

Under water-saturated conditions, we conducted a series of experiments with different Cs loadings on the colloids at the same pore water velocity (10 cm/min). We used ^{137}Cs at concentrations of 5.63 nM (136 Bq/mL), 10.1 nM (244 Bq/mL), 16.1 nM (390 Bq/mL) and 28.4 nM (687 Bq/mL) preequilibrated with native colloids for 24 h as the injectant. ^{137}Cs at concentrations of 7.59 nM (184 Bq/mL), 12.6 nM (305 Bq/mL), 23.8 nM (576 Bq/mL), and 30.0 nM (726 Bq/mL) were used for modified colloids. To investigate the effect of pore water velocity on Cs transport, native colloids preequilibrated with 27.4 nM (663 Bq/mL) and modified colloids preequilibrated with 32.5 nM (786 Bq/mL) were introduced into the column at pore water velocities of ≈1 cm/min to 10 cm/min. To check whether the retained Cs within the column from previous runs may interfere with the results of the following Cs breakthrough experiments,

we repeated some of the Cs transport experiments after completion of the full sequence of water-saturated breakthrough experiments.

Under water-unsaturated conditions, the Cs loading on the colloids was kept constant, but we varied the effective water saturation S_e in increments of 0.1 by decreasing effective water content from 1.0 to 0.2. We used ^{137}Cs at a concentration of 8.76 nM (212 Bq/mL) preequilibrated with both native and modified colloids for 24 h as the injectant. Each set of colloid breakthroughs was preceded by a nitrate (0.2 mM $NaNO_3$) breakthrough experiment to determine the hydrodynamics of the column. Nitrate was measured with the spectrophotometer at 204 nm wavelength. All experiments were conducted at 20−22 °C.

Modeling of Colloid Breakthrough Curves. We describe colloid transport through the Hanford sediment columns with the two-region transport model (*27*). From our previous (*25*) and current experimental observations, we have evidence that there is no colloid deposition at the liquid−solid interface. We believe that retained colloids in the column are either captured at the liquid−gas interface by film-straining (*21*, *23*) or captured at the solid−liquid−gas three-phase interface due to physical constraint (*21*, *28*). These colloid-capturing actions most likely occur from the mobile region. Thus, we assume that colloids are only deposited within the mobile region only:

$$\frac{\partial(\theta_m c_m)}{\partial t} + \frac{\partial(\theta_{im} c_{im})}{\partial t} = \frac{\partial}{\partial z}\left(\theta_m D_m \frac{\partial c_m}{\partial z}\right) - \frac{\partial(q_m c_m)}{\partial z} - \theta_m \lambda_m c_m \quad (1)$$

$$\frac{\partial(\theta_{im} c_{im})}{\partial t} = \alpha(c_m - c_{im}) \quad (2)$$

where c_m and c_{im} refer to the colloid concentrations in the mobile and immobile phases, respectively; θ_m and θ_{im} refer to the mobile and immobile water, respectively; q_m denotes the Darcy velocity of the mobile water; λ_m is the colloid deposition coefficient from the mobile water phase; D_m is the colloid dispersion coefficient in the mobile phase; and α is the colloid transfer coefficient between mobile and immobile water. Taking the water content constant and using dimensionless variables, we can write eqs 1 and 2 as

$$\beta\frac{\partial C_m}{\partial T} + (1-\beta)\frac{\partial C_{im}}{\partial T} = \frac{1}{Pe}\frac{\partial^2 C_m}{\partial Z^2} - \frac{\partial C_m}{\partial Z} - \mu_m C_m \quad (3)$$

$$(1-\beta)\frac{\partial C_{im}}{\partial T} = \omega(C_m - C_{im}) \quad (4)$$

where C denotes dimensionless colloid concentrations ($C_m = c_m/c_0$ and $C_{im} = c_{im}/c_0$) with c_0 being the colloid concentration in the inflow. The dimensionless time is defined as $T = vt/L$, and the space is defined as $Z = z/L$, where L is the length of the column. The dimensionless parameters are defined as

$$\beta = \frac{\theta_m}{\theta} \quad \text{(fraction of mobile water)} \quad (5)$$

$$Pe = \frac{vL}{\beta D_m} \quad \text{(Peclet number)} \quad (6)$$

$$w = \frac{\alpha L}{\theta v} \quad \text{(mass transfer coefficient)} \quad (7)$$

$$\mu_m = \frac{\beta\lambda_m L}{v} = \frac{\lambda_m L}{v_m} \quad \text{(deposition coefficient)} \quad (8)$$

where $v = q_m/\theta$ is the pore water velocity, $\theta = \theta_m + \theta_{im}$, and $v_m = v/\beta$. An analytical solution of eqs 3 and 4 with Dirichlet boundary conditions was fitted to experimental colloid breakthrough curves using CXTFIT (*29*).

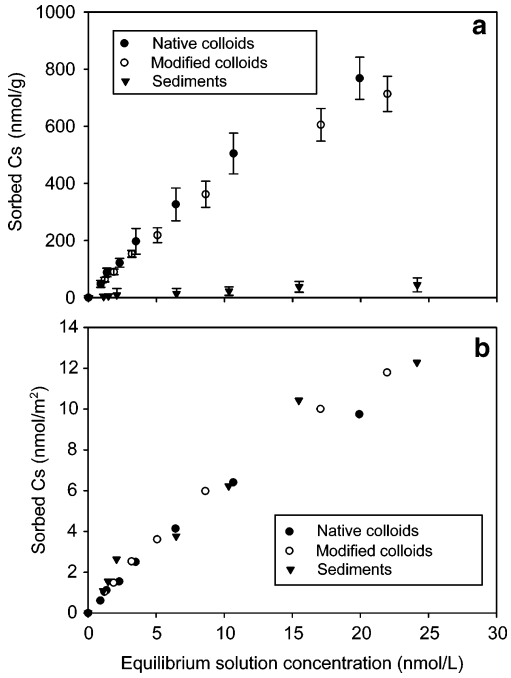

FIGURE 1. Cs sorption isotherms for Hanford native and modified colloids and Hanford sediments. Symbols are averaged sorbed Cs concentrations with respect to aqueous concentrations. Error bars denote ± one standard error. Sorbed Cs concentrations are expressed in terms of mass (a) and surface area (b).

Results and Discussion

Cesium Sorption on Colloids and Sediments. Native colloids had a higher sorption affinity for Cs than the modified colloids, although the differences were not pronounced (Figure 1a). The Cs sorption affinity to the Hanford sediments was considerably less than for the colloids. We related the amount of Cs sorbed on the solids (nmol/g) to the amount of Cs sorbed per surface area of the solids (nmol/m^2) by dividing the former by the specific surface area of the solids shown in Table 1. Cs sorption is an ion exchange reaction that is related to particle surface area. When the Cs sorption was normalized by the surface area of the solids, the sorption isotherms were superimposed (Figure 1b). This indicates that the sorption affinity of Cs to colloids and sediment surfaces was similar. Colloids were derived from the sediments, and apparently the sorption expressed in terms of surface area was similar between colloids and sediments. Such a case was denoted by Honeyman and Ranville (*19*) as a symmetrical system.

Column Water Contents and Water Potentials. Steady-state flow experiments, with uniform unit-gradient conditions, were attempted at effective saturations $S_e = 0.1, ..., 1.0$ in 0.1 increments. However, $S_e = 0.9$ was not possible due to flow restrictions in the porous plate and outflow tubing, and $S_e = 0.1$ was not possible because no stable background colloid concentration after colloid breakthrough could be obtained. The remaining saturations were achieved with steady-state and uniform unit-gradient conditions for most of the column, except for the top and bottom 2.5 cm. The top of the column was dryer (more negative matric potential readings), and the bottom of the column was wetter (less negative matric potential readings) than the middle. The results were similar to the ones reported by Cherrey et al. (*25*), to which we refer for details on tensiometer and water content readings.

TABLE 2. Hanford Native and Modified Colloid Transport Parameters Using the Two-Region Transport Model[a]

measured parameters			fitted parameters[b]					
effective water saturation (−)	gravimetric water content (kg/kg)	v^c (cm/min)	v^d (cm/min)	D (cm²/min)	β (−)	ω (−)	μ_m (−)	R^2 (−)
				Native Colloids				
1.0	0.25	10.03	12.89	26 ± 3				0.9940
0.80	0.23	9.50	10.32	17 ± 2			0.21 ± 0.01	0.9927
0.70	0.21	7.71	6.99	23 ± 6	0.86 ± 0.10	0.25 ± 0.23	0.26 ± 0.01	0.9950
0.60	0.19	7.00	6.10	26 ± 5	0.79 ± 0.08	0.68 ± 0.45	0.21 ± 0.01	0.9953
0.50	0.17	6.85	5.93	17 ± 3	0.41 ± 0.06	2.20 ± 0.51	0.33 ± 0.01	0.9952
0.40	0.15	6.62	5.34	25 ± 2	0.74 ± 0.05	0.76 ± 0.27	0.46 ± 0.01	0.9966
0.30	0.12	6.17	5.30	9 ± 1	0.50 ± 0.01	1.07 ± 0.04	0.65 ± 0.01	0.9993
0.20	0.08	6.13	5.10	6 ± 1	0.44 ± 0.01	1.0 ± 0.05	0.98 ± 0.01	0.9979
				Modified Colloids				
1.0	0.25	10.10	12.89	32 ± 4				0.9893
0.80	0.23	9.94	10.32	12 ± 1			0.02 ± 0.01	0.9968
0.70	0.21	8.25	6.99	16 ± 1	0.81 ± 0.01	0.03 ± 0.01	0.06 ± 0.01	0.9987
0.60	0.19	6.58	6.10	14 ± 2	0.79 ± 0.03	0.29 ± 0.06	0.16 ± 0.01	0.9991
0.50	0.17	5.65	5.93	21 ± 2	0.38 ± 0.04	1.71 ± 0.17	0.23 ± 0.01	0.9956
0.40	0.15	5.12	5.34	35 ± 1	0.41 ± 0.03	1.42 ± 0.10	0.40 ± 0.01	0.9972
0.30	0.12	5.00	5.30	nf	nf	nf	nf	nf
0.20	0.08	4.87	5.10	nf	nf	nf	nf	nf

[a] v, pore water velocity; D, hydrodynamic dispersion; β, fraction of mobile water; ω, mass transfer coefficient; μ_m, rate coefficient for colloid deposition; R^2, coefficient of determination; nf, fit not possible due to high parameter correlations. [b] Values are fitted parameters ± one standard error. [c] Calculated from measured water flux J_w and effective water saturation S_e as $v = J_w/(S_e\theta_s)$. [d] Fitted from nitrate breakthrough curves.

Nitrate and Colloid Transport. The nitrate and colloid data could be well-described with the two-region model, and the results suggest a significant fraction of immobile water when the effective water saturation dropped below 0.8 (Table 2). Under water saturated conditions, both native and modified colloids were quantitatively recovered, and no colloids were deposited inside the column. When the column became unsaturated, colloids began to be retained in the sediment. At an effective water saturation of 0.2, ≈60% of colloids was retained within the column. These colloids were mostly likely retained near the liquid−gas−solid three-phase interface (*30*).

Colloid mass transfer coefficients (ω) did not show a trend as function of water saturation, and the estimated values were associated with large errors (Table 2). Colloid deposition coefficients (μ_m) increased with decreasing system saturation. Both the dimensionless and the dimensional deposition coefficients (μ_m and λ_m, respectively) showed a pronounced dependence on water saturation (Figure 2). The fraction of mobile water (β) decreases with decreasing water saturation (Table 2).

Colloid-Facilitated Cesium Transport under Saturated Conditions. Dissolved Cs could not breakthrough Hanford sediments at either a concentration of 7.66 nM (185 Bq/mL) or 30.6 nM (760 Bq/mL) for a 3 pore volume pulse injectant. In our experiments, where the total time allowed to develop the breakthrough curves was about 8 pore volume, Cs breakthrough only occurred in the presence of colloids. We therefore conclude that cesium could move substantial distances only when associated with colloids. Also, from our previous research, we have evidence that Cs cannot breakthrough the column in the presence of 1 mM NaCl until 950 pore volume have passed (*18*). However, Cs concentrations on the colloids in the effluent were smaller than in the influent, indicating that Cs desorbed from the colloids during the transport through the column.

Cs breakthrough curves, with the same pore velocity, expressed in relation to the total Cs concentration in the inflow are illustrated in Figure 3a. The ratio on the y-axis is defined as $C_{Cs}C_{colloid}/C_{0T}$, where C_{0T} is the sum of sorbed and solution-phase Cs concentration in the inflow; C_{Cs} is the Cs concentration on the colloids in the outflow; and $C_{colloid}$ is the colloid concentration in the outflow. This ratio is the amount of Cs sorbed on colloids in the outflow divided by the total amount of Cs (sorbed and in solution) in the inflow. Figure 3a indicates that the higher the input Cs concentration, the lower the $C_{Cs}C_{colloid}/C_{0T}$ value. This phenomenon, which was more pronounced for native than modified colloids, was likely caused by the nonlinearity of the Cs sorption isotherms. Under water-saturated conditions, only about 8−16% of the total Cs infused in the column could be recovered in the outflow (Table 3).

It is possible that the retained Cs within the column from previous runs may interfere with the results of the following

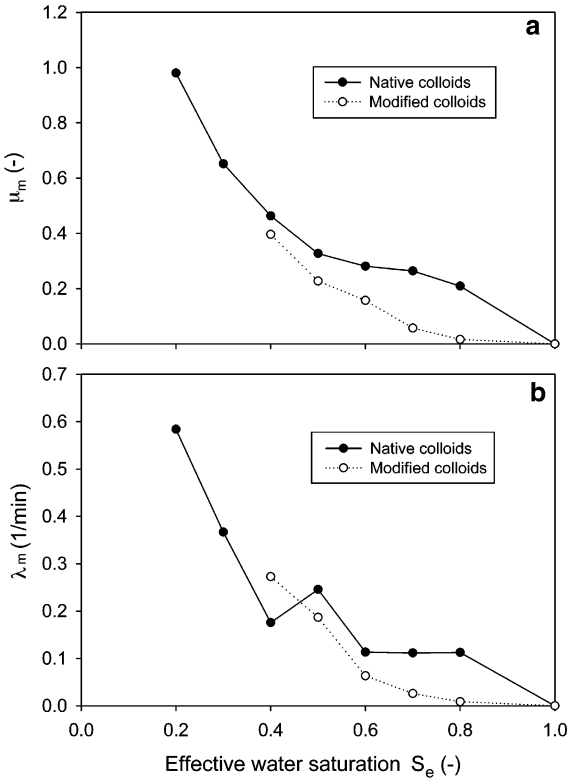

FIGURE 2. Colloid deposition coefficients μ_m (a) and λ_m (b) as function of water saturation.

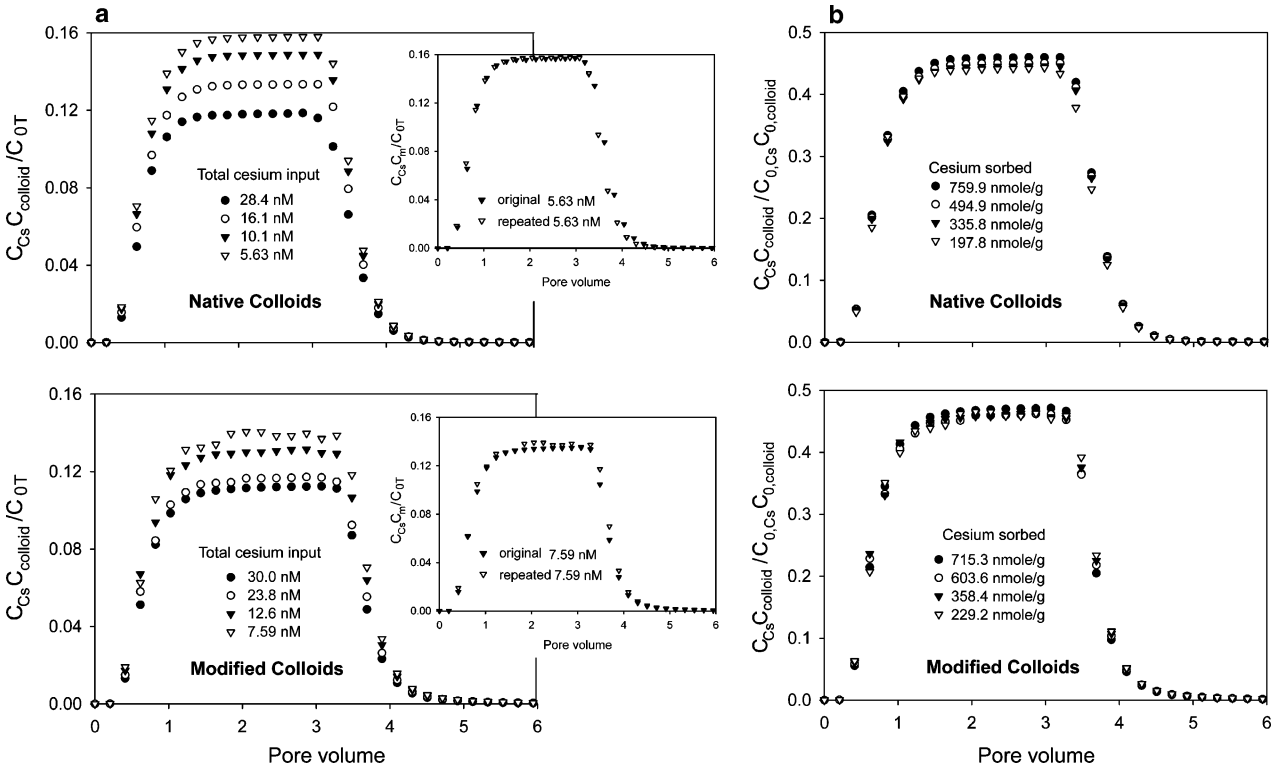

FIGURE 3. Cesium breakthrough data (a) with regard to total amount of Cs in inflow and (b) with regard to initially sorbed Cs on colloids under water-saturated flow conditions. Insets show comparison between Cs breakthrough curves at the beginning and at the end of the experimental sequence.

TABLE 3. Colloid and Cesium Mass Recovery in Column Outflow

		colloid recovery		Cs loading on colloids[a]		Cs mass recovery[b]		Cs stripped off colloids[c]	
effective water saturation (−)	pore water velocity (native/modified) (cm/min)	native colloids (%)	modified colloids (%)	native colloids (nmol/g)	modified colloids (nmol/g)	native colloids (%)	modified colloids (%)	native colloids (%)	modified colloids (%)
				Saturated Flow Experiments					
1.0	10.0/10.1	96.3	100.5	760	715	11.8	11.3	58.6	52.7
1.0	10.0/10.1	93.7	98.4	495	604	13.4	11.8	58.1	50.7
1.0	10.0/10.1	93.3	98.1	336	358	14.9	13.4	56.9	51.0
1.0	10.0/10.1	97.9	100.6	198	230	15.9	14.2	55.6	50.4
1.0	10.5/10.4	99.4	97.4	763	726	11.5	9.64	54.4	53.9
1.0	8.21/7.87	98.7	98.6	790	751	10.1	8.45	62.4	62.2
1.0	6.62/5.47	97.8	99.5	808	771	8.38	8.01	70.1	66.5
1.0	5.41/4.61	100.6	102.1	823	790	8.82	8.05	70.6	67.1
1.0	1.01/0.94	98.6	101.9	780	741	9.29	8.28	72.4	70.0
				Unsaturated Flow Experiments					
0.8	9.50/9.94	83.9	98.7	429	364	24.6	29.6	40.0	27.6
0.7	7.71/8.25	77.9	93.6	432	389	22.9	28.1	40.5	32.2
0.6	7.0/6.58	77.0	87.2	446	417	22.5	26.4	42.4	36.5
0.5	6.85/5.65	73.4	81.4	457	429	21.5	24.6	43.7	38.3
0.4	6.63/5.13	65.5	69.4	474	436	19.3	20.9	45.6	39.4
0.3	6.17/5.0	54.3	59.5	488	452	15.9	17.9	47.3	41.5
0.2	6.13/4.88	40.1	44.9	497	467	11.8	13.5	48.2	43.4

[a] Cs concentration on colloids in column inflow. [b] Total amount of Cs recovered in outflow related to the total amount of Cs in inflow. [c] Amount of Cs on colloids in outflow related to the amount of Cs on colloids in inflow.

Cs breakthrough experiments. Due to the low Cs concentrations, however, the interference should be small. To test for possible interferences, we repeated some of the Cs transport experiments after completion of the full sequence of breakthrough experiments. Representative Cs breakthrough curves of these repetitions are shown in the insets of Figure 3. The Cs breakthrough curves were reproducible, precluding the possible history effect.

Figure 3b shows the Cs breakthrough curves at the same pore velocity but with different Cs loadings expressed in relation to the Cs concentration on the colloids. This ratio on the y-axis is defined as $C_{Cs}C_{colloid}/(C_{0,Cs}C_{0,colloid})$, where $C_{0,Cs}$ and C_{Cs} are the Cs concentrations on the colloids (nmol/g) in inflow and outflow, respectively, and $C_{0,colloid}$ and $C_{colloid}$ are the colloid concentrations (mg/L) in inflow and outflow, respectively. This ratio is the amount of Cs sorbed on colloids in the outflow divided by the amount of Cs sorbed on colloids in the inflow. When related to the colloid-sorbed Cs concentration in the inflow (Figure 3b), a constant fraction of Cs desorbed from the colloids, irrespective of the amount

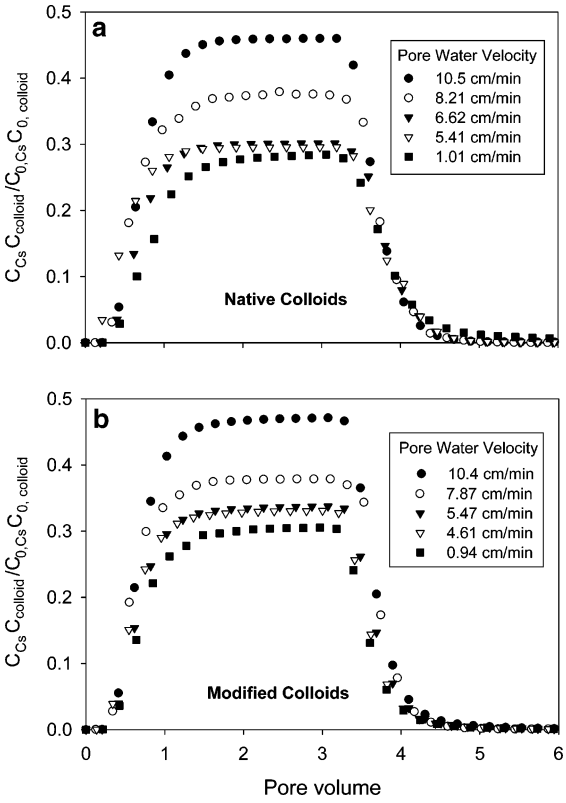

FIGURE 4. Cesium breakthrough data at different pore water velocities under water-saturated flow conditions. Symbols are experimental data. Cs concentrations are expressed relative to Cs sorbed on colloids in the inflow.

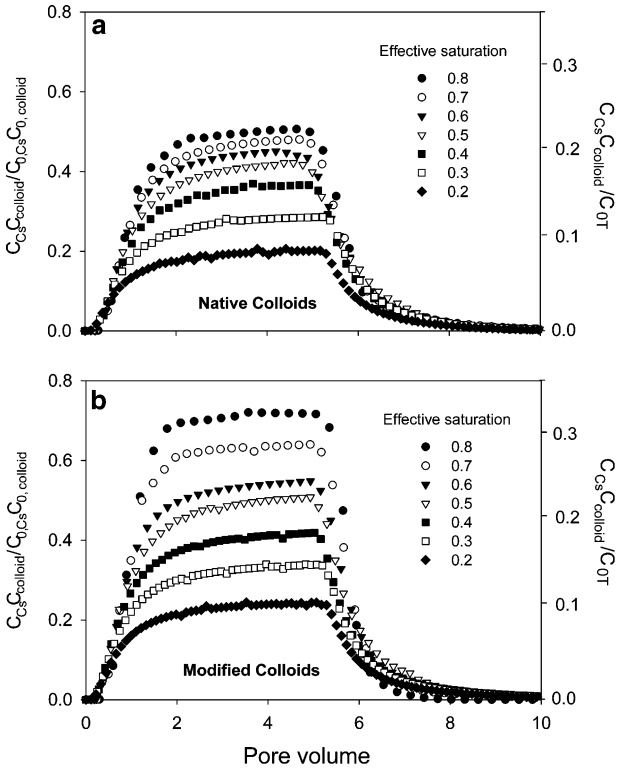

FIGURE 5. Cesium breakthrough data under unsaturated conditions. Cesium concentrations are related to initially sorbed Cs on colloids ($C_{Cs}C_{colloid}/C_{0,Cs}C_{0,colloid}$) and total amount of Cs in inflow ($C_{Cs}C_{colloid}/C_{0T}$).

of Cs initially sorbed on the colloids. The figure also shows that more than 50% of the Cs initially sorbed on the colloids was stripped off the colloids during transport. The greater the amount of initially colloid-sorbed Cs, the greater the absolute amount of Cs desorbed from the colloids during transport.

Colloid-facilitated cesium transport was impeded with decreasing pore velocity (Figure 4), suggesting that Cs desorption from colloids was, in part, a residence-time-dependent process. The Cs desorption from colloids was apparenty not a "pure" ion exchange equilibrium process. As the flow rate decreased, more Cs desorbed from colloids during transport. At the smallest pore water velocity (≈1 cm/min), 70−72% of the initially sorbed Cs was desorbed from the colloids during transport through the column.

Colloid-Facilitated Cs Transport under Unsaturated Conditions. Only a single Cs loading was used for the unsaturated colloid-facilitated Cs transport experiments. Consequently, Cs breakthrough curves expressed relative to colloidal Cs concentrations and relative to total Cs concentrations have the same shape and can be plotted in one graph with different concentration axes (Figure 5). As the water content of the porous medium decreased, colloid transport became less effective, and the fraction of Cs desorbed from the colloids increased (Table 3). This was likely due to the decrease of the water velocity with decreasing water saturation, which allows more time for Cs to desorb from colloids. As was the case under saturated flow conditions, less Cs was stripped off modified colloids than native colloids (Table 3). We attribute this to the different mineralogy of the colloids (i.e., the presence of the feldspathoids cancrinite and sodalite in the modified colloids). The feldspathoids cancrinite and sodalite contain cages and channels in which Cs can sorb (*31*). We believe that desorption from these cages and channels is diffusion-controlled and as such dependent on the residence time of the colloids inside the column.

Compared with water-saturated conditions, less Cs desorbed from colloids under unsaturated conditions. The percentage of Cs desorbed from the colloids under unsaturated conditions increased slightly with decreasing water content for native colloids but moderately for modified colloids (Table 3). Under unsaturated flow, a considerable amount of colloids was retained inside the column, and as we ran the unsaturated experiments in sequence of decreasing water contents, we expect that retained colloids will not be released in subsequent runs. The mass balance calculations shown in Table 3 are based on the amounts of Cs in the inflow and outflow and are therefore likely not biased by release of deposited colloids.

Assuming an equilibrium sorption process, we can calculate the ratio of Cs sorbed to colloids with respect to total Cs within the system. This ratio is given as (*19*)

$$\kappa = \frac{\text{amount of Cs on colloids}}{\text{total amount of Cs}} = \frac{q_{\text{colloid}} C_{\text{colloid}} S_{\text{e}}}{C_{\text{Cs}} S_e + q_{\text{colloid}} C_{\text{colloid}} S_{\text{e}} + q_{\text{sediment}} \rho_{\text{b}}/\epsilon} \quad (9)$$

where C_{Cs} and C_{colloid} are the solution-phase Cs and colloid concentrations, respectively; q is the sorbed-phase Cs concentration on colloids or sediments; ρ_{b} is the bulk density; and ϵ is the porosity. The three terms in the denominator of eq 9 represent, respectively, the solution-phase, the colloid-phase, and the sediment-phase Cs concentrations. On the basis of the sorption isotherms, we calculated the Cs concentrations associated with the different phases. Solution- and colloid-phase Cs concentrations were 4 orders of magnitude smaller than the sediment-phase concentrations,

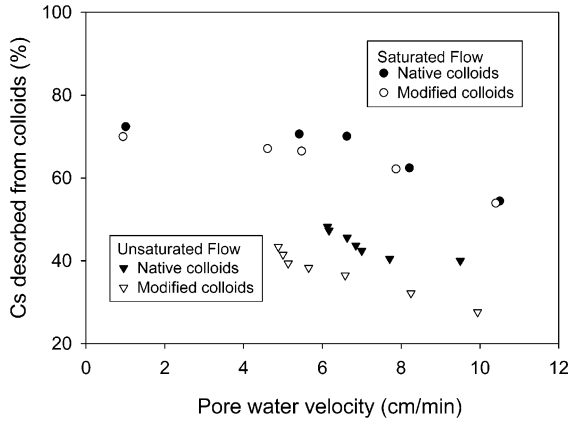

FIGURE 6. Cesium desorbed from colloids during transport through sediment column as a function of the measured pore water velocity $v = q_m/\theta$.

and we can therefore simplify eq 9 to

$$\kappa = \frac{q_{\text{colloid}} C_{\text{colloid}} S_e}{q_{\text{sediment}} \rho_b / \epsilon} = \frac{K_{\text{colloid}} A_{\text{colloid}} C_{\text{colloid}} S_e}{K_{\text{sediment}} A_{\text{sediment}} \rho_b / \epsilon} \quad (10)$$

where K denotes the sorption coefficient (mL/m^2) for colloids or sediments, and A denotes the specific surface area (m^2/g) for colloids and sediments. For a symmetrical system (*19*) as in our case, $K_{\text{colloid}} = K_{\text{sediment}}$, and eq 10 reduces to

$$\kappa = \frac{A_{\text{colloid}} C_{\text{colloid}} S_e}{A_{\text{sediment}} \rho_b / \epsilon} \quad (11)$$

On the basis of eq 11, only a small fraction of Cs would associate with the colloids: the fraction κ ranges from $\kappa = 1 \times 10^{-5}$ at effective saturation of $S_e = 0.2$ to $\kappa = 5 \times 10^{-5}$ at effective saturation of $S_e = 1.0$. On the contrary, our experimental Cs breakthrough curves show that a much larger fraction of Cs was transported by colloids than what would be expected based on the equilibrium sorption assumption. Our data suggest that a portion of the Cs sorbed to colloids could not readily be desorbed and contributed to the increased degree of colloid-facilitated Cs transport.

There was a general trend that less Cs desorbed from colloids during transport as water flow rates increased (Figure 6), likely because of the smaller residence times at higher flow rates. However, under similar flow rates, less Cs desorbed from colloids during unsaturated flow than during saturated flow. We think that during unsaturated flow, less Cs sorption sites on the sediments are available to strip off the Cs from colloids because less sediment surface area is in contact with the mobile flow regions. Furthermore, as the water content decreased, the immobile water fraction increased, indicating that colloids moved through a smaller effective cross-section of the porous medium. That would further decrease the amount of sediment sorption sites available to strip Cs from the colloids.

Implications for Colloid-Facilitated Cs Transport at the Hanford Site. At the Hanford site, an important question is whether Cs that has leaked into the vadose zone can reach the underlying groundwater. From core sampling in the S-SX tank farm, we know that peak concentrations of ^{137}Cs are located at 25−26 m depth below ground, with traces of ^{137}Cs found up to 38 m below ground (*16*, *32*). Based on the results of our laboratory study, it is unlikely that colloids were responsible for the movement of the Cs to these depths. If Cs is reversibly attached to to colloids by ion exchange, Cs would likely be stripped off the colloids as the colloids move through uncontaminated sediments. The sediments underlying Hanford waste tanks sorb Cs with high affinity (*12*, *33*), and this would provide an effective means of opposing colloid-facilitated Cs transport. Other studies have indeed shown that the current location of Cs under Hanford SX waste tanks can be explained by chromatographic solution-phase transport in a high electrolyte waste solution (*14*, *15*, *17*).

In addition, colloid transport itself is restricted in the vadose zone, and with decreasing moisture content, the restriction becomes more obvious. In this study, we show that ≈55−60% of initially present colloids are retained in the column at an effective water saturation of 0.2. At the Hanford site, gravimetric water saturations in sediments of the Hanford formation underlying the S-SX waste tanks range from 0.04 to 0.17 kg/kg (*16*), and the thickness of the vadose zone varies from 40 to 100 m (*33*, *34*). We conducted our column experiments with gravimetric water contents in the ranged of 0.08−0.25 kg/kg (Table 2) and in a column of 20 cm length. The possibility of colloids to be transported from the soil surface to the groundwater at the Hanford tank farms appears minimal, unless water contents and flow rates are locally and temporally increased by snowmelt events or artifical infiltration caused by past waste management practices.

Acknowledgments

This research was supported by the Office of Science (BER), U.S. Department of Energy, Grant DE-FG07-05ER62882. We thank John Zachara and Jeff Serne (Pacific Northwest National Laboratory) for providing us with the Hanford sediments, Hongting Zhao for synthesis of the modified colloids, and Jeff Smith (USDA-ARS Pullman) for allowing us to use his liquid scintillation analyzer.

Literature Cited

(1) Ryan, J. N.; Illangasekare, T. H.; Litaor, M. I.; Shannon, R. Particle and plutonium mobilization in macroporous soils during rainfall simulations. *Environ. Sci. Technol.* **1998**, *32*, 476−482.
(2) Kersting, A. B.; Efurd, D. W.; Finnegan, D. L.; Rokop, D. J.; Smith, D. K.; Thompson, J. L. Migration of plutonium in ground water at the Nevada Test Site. *Nature* **1999**, *397*, 56−59.
(3) Grolimund, D.; Borkovec, M.; Barmettler, K.; Sticher, H. Colloid-facilitated transport of strongly sorbing contaminants in natural porous media: a laboratory column study. *Environ. Sci. Technol.* **1996**, *30*, 3118−3123.
(4) Saiers, J. E.; Hornberger, G. M. The role of colloidal kaolinite in the transport of cesium through laboratory sand columns. *Water Resour. Res.* **1996**, *32*, 33−41.
(5) Noell, A. L.; Thompson, J. L.; Corapcioglu, M. Y.; Triay, I. R. The role of silica colloids on facilitated cesium transport through glass bead columns and modeling. *J. Contam. Hydrol.* **1998**, *31*, 23−56.
(6) Saiers, J. E.; Hornberger, G. M. The influence of ionic strength on the facilitated transport of cesium by kaolinite colloids. *Water Resour. Res.* **1999**, *35*, 1713−1727.
(7) Zhuang, J.; Flury, M.; Jin, Y. Colloid-facilitated Cs transport through water-saturated Hanford sediment and Ottawa sand. *Environ. Sci. Technol.* **2003**, *37*, 4905−4911.
(8) Aharoni, C.; Pasricha, N. S.; Sparks, D. L. Adsorption and desorption kinetics of cesium in an organic matter rich soil saturated with different cations. *Soil Sci.* **1992**, *156*, 233−239.
(9) Gephart, R. E.; Lundgren, R. E. *Hanford Tank Cleanup: A Guide to Understanding the Technical Issues*, 4th ed.; Battelle Press: Columbus, OH, 1998.
(10) Serne, R. J.; Zachara, J. M.; Burke, D. S. *Chemical Information on Tank Supernatants, Cs Adsorption from Tank Liquids onto Hanford Sediments, and Field Observations of Cs Migration from Past Tank Leaks*; Pacific Northwest National Laboratory,: Richland, WA, 1998; PNNL-11495/UC-510.
(11) Cornell, R. M. Adsorption of cesium on minerals: a review. *J. Radioanal. Nucl. Chem.* **1993**, *171*, 483−500.
(12) Zachara, J. M.; Smith, S. C.; Liu, C.; McKinley, J. P.; Serne, R. J.; Gassman, P. L. Sorption of Cs^+ to micaceous subsurface sediments from the Hanford Site, USA. *Geochim. Cosmochim. Acta* **2002**, *66*, 193-211.
(13) Flury, M.; Czigany, S.; Chen, G.; Harsh, J. B. Cesium migration in saturated silica sand and Hanford sediments as impacted by ionic strength. *J. Contam. Hydrol.* **2004**, *71*, 111−126.

(14) Knepp, A. J. *Field Investigation Report for Waste Management Area S-SX*; RPP-7884, Rev. 0, CH2M HILL Hanford Group, Inc.: Richland, WA, 2002.
(15) Steefel, C. I.; Carroll, S.; Zhao, P.; Roberts, S. Cesium migration in Hanford sediment: a multisite cation exchange model based on laboratory transport experiments. *J. Contam. Hydrol.* **2003**, *67*, 219−246.
(16) Serne, R. J.; Clayton, R. E.; Kutnyakov, I. V.; Last, G. V.; LeGore, V. L.; Wilson, T. C.; Schaef, H. T.; O'Hara, M. J.; Wagnon, K. B.; Lanigan, D. C.; Brown, C. F.; Williams, B. A.; Lindenmeier, C. W.; Orr, R. D.; Burke, D. S.; Ainsworth, C. C. *Characterization of Vadose Zone Sediment: Borehole 41-09-39 in the S-SX Waste Management Area*; Pacific Northwest National Laboratory, U.S. Department of Energy: Richland, WA, 2002; PNNL-13757-3.
(17) Lichtner, P. C.; Yabusaki, S.; Pruess, K.; Steefel, C. I. Role of competitive cation exchange on chromatographic displacement of cesium in the vadose zone beneath the Hanford S/SX tank farm. *Vadose Zone J.* **2004**, *3*, 203−219.
(18) Flury, M.; Mathison, J. B.; Harsh, J. B. In situ mobilization of colloids and transport of cesium in Hanford sediments. *Environ. Sci. Technol.* **2002**, *36*, 5335−5341.
(19) Honeyman, B. D.; Ranville, J. F. Colloid properties and their effects on radionuclide transport through soils and groundwater. In *Geochemistry of Soil Radionuclides*; Zhang, P.-C., Brady, P. V., Eds.; SSSA Special Publication 59; Soil Science Society of America: Madison, WI, 2002; pp 131−163.
(20) Wan, J. M.; Wilson, J. L. Colloid transport in unsaturated porous media. *Water Resour. Res.* **1994**, *30*, 857−864.
(21) Wan, J. M.; Tokunaga, T. K. Film straining of colloids in unsaturated porous media: conceptual model and experimental testing. *Environ. Sci. Technol.* **1997**, *31*, 2413−2420.
(22) Schäfer, A.; Ustohal, P.; Harms, H.; Stauffer, F.; Dracos, T.; Zehnder, A. J. B. Transport of bacteria in unsaturated porous media. *J. Contam. Hydrol.* **1998**, *33*, 149−169.
(23) Lenhart, J. J.; Saiers, J. E. Transport of silica colloids through unsaturated porous media: experimental results and model comparisons. *Environ. Sci. Technol.* **2002**, *36*, 769−777.
(24) Jewett, D. G.; Logan, B. E.; Arnold, R. G.; Bales, R. C. Transport of *Pseudomonas fluorescences* strain P17 through quartz sand columns as a function of water content. *J. Contam. Hydrol.* **1999**, *36*, 73−89.
(25) Cherrey, K. D.; Flury, M.; Harsh, J. B. Nitrate and colloid transport through coarse Hanford sediments under steady state, variably saturated flow. *Water Resour. Res.* **2003**, *39*, 1165, doi: 10.1029/2002WR001944.
(26) Mashal, K.; Harsh, J. B.; Flury, M.; Felmy, A. R.; Zhao, H. Colloid formation in Hanford sediments reacted with simulated tank waste. *Environ. Sci. Technol.* **2004**, *38*, 5750−5756.
(27) van Genuchten, M. T.; Wagenet, R. J. Two-site/two-region models for pesticide transport and degradation: theoretical development and analytical solutions. *Soil Sci. Soc. Am. J.* **1989**, *53*, 1303−1310.
(28) Crist, J. T.; McCarthy, J. F.; Zevi, Y.; Baveye, P. C.; Troop, J. A.; Steenhuis, T. S. Pore-scale visualization of colloid transport and retention in partially saturated porous media. *Vadose Zone J.* **2004**, *3*, 444−450.
(29) Toride, N.; Leij, F. J.; van Genuchten, M. T. *The CXTFIT Code for Estimating Transport Parameters from Laboratory or Field Experiments*, Version 2.1; Research Report 137; U.S. Salinity Laboratory: Riverside, CA, 1995.
(30) Chen, G.; Flury, M. Retention of mineral colloids in unsaturated porous media as related to their surface properties. *Colloids Surf. Physicochem. Eng. Aspects* **2005**, *256*, 207−216.
(31) Zhao, H.; Deng, Y.; Harsh, J. B.; Flury, M.; Boyle, J. S. Alteration of kaolinite to cancrinite and sodalite by simulated Hanford tank wastes and its impact on cesium retention. *Clays Clay Miner.* **2004**, *52*, 1−13.
(32) Serne, R. J.; Clayton, R. E.; Kutnyakov, I. V.; Last, G. V.; LeGore, V. L.; Wilson, T. C.; Schaef, H. T.; O'Hara, M. J.; Wagnon, K. B.; Lanigan, D. C.; Brown, C. F.; Williams, B. A.; Lindenmeier, C. W.; Orr, R. D.; Burke, D. S.; Ainsworth, C. C. *Characterization of Vadose Zone Sediment: Slant Borehole SX-108 in the S-SX Waste Management Area*; Pacific Northwest National Laboratory, U.S. Department of Energy: Richland, WA, 2002; PNNL-13757-4.
(33) McKinley, J. P.; Zeissler, C. J.; Zachara, J. M.; Serne, R. J.; Lindstrom, R. M.; Schaef, H. T.; Orr, R. D. Distribution and retention of Cs-137 in sediments at the Hanford site, Washington. *Environ. Sci. Technol.* **2001**, *35*, 3433−3441.
(34) Gee, G. W.; Heller, P. R. *Unsaturated Water Flow at the Hanford Site: A Review of Literature and Annotated Bibliography*; Pacific Northwest National Laboratory: Richland, WA, 1985.

Received for review July 3, 2004. Revised manuscript received March 4, 2005. Accepted March 7, 2005.

ES048978+

ELSEVIER

Colloids and Surfaces A: Physicochem. Eng. Aspects 256 (2005) 207–216

COLLOIDS AND SURFACES A

www.elsevier.com/locate/colsurfa

Retention of mineral colloids in unsaturated porous media as related to their surface properties

Gang Chen, Markus Flury *

Department of Crop and Soil Sciences, Center for Multiphase Environmental Research, Washington State University, Pullman, WA 99164, USA

Received 19 May 2004; accepted 11 January 2005

Abstract

We investigated the transport of mineral colloids through variably saturated Hanford sediments. Column experiments were conducted under steady-state water flow conditions with effective water saturations ranging from 0.56 to 1.0. Four types of colloidal particles were used: native Hanford colloids, Hanford colloids reacted with waste tank solutions, pure kaolinite, and pure Na-montmorillonite. Colloid transport was described by the mobile–immobile region model accounting for first-order colloid removal from the mobile region. Under saturated conditions, no colloids were removed from the liquid phase during transport, while under unsaturated conditions colloids were removed from the mobile water region. Colloid removal increased with decreasing system saturation. Under constant chemical conditions, colloids captured within the column could quantitatively be recovered in the column outflow by re-saturating the column after each unsaturated-flow breakthrough. Through microscopic observations in a glass micromodel containing suspended air bubbles, we found that colloids did not adhere to the liquid–gas interface. Using the extended DLVO theory, free energies of Lifshitz–van der Waals, electrostatic and Lewis acid/base interactions between colloids, sediments and the liquid–gas interface were calculated based on their independently determined surface thermodynamic properties. Experimental results and surface thermodynamic calculations support the hypothesis that colloids were retained near thin water films of thickness comparable to the colloid diameters.

Keywords: Mineral colloids; Transport; Free energy; Unsaturated flow; Liquid–gas interface

1. Introduction

Colloid transport in the saturated subsurface is often described by the filtration theory, where removal of colloidal particles from the fluid phase is governed by physicochemical deposition [1,2]. Key factors that influence colloid deposition include pore water chemistry, i.e., ionic strength and pH, and colloid size and concentration [3]. Factors that influence colloid transport in saturated porous media have been extensively studied. Generally, the amount of colloids transported through porous media decreases with an increase of ionic strength [4–6]. Colloid size influences transport in two different ways: first, larger colloids experience stronger pore size exclusion and travel with higher velocity in single tubes than smaller size colloids [7]; and second, larger size colloids are more efficiently removed from the fluid due to enhanced deposition and interception compared to smaller colloids [2,8]. It is often assumed that colloid deposition at the solid–liquid interface, under conditions identical to those at deposition, is irreversible [4].

In unsaturated porous media, colloids cannot only attach the solid–liquid interface, but also to the liquid–gas interface [9]. In addition, colloids are subject to straining in thin water films when the water saturation of the medium becomes small [10,11]. Film straining becomes effective when the diameter of the colloids is larger than the thickness of the water film and when water pathways become discontinuous [10]. Besides film straining, colloid transport is also subject to physical constraint, i.e., colloid physical entrapment in pore throats that are too small to allow colloids to pass through [12]. Physical constraint is greatly affected by

* Corresponding author. Tel.: +1 509 335 1719; fax: +1 509 335 8674.
E-mail address: flury@mail.wsu.edu (M. Flury).

0927-7757/$ – see front matter © 2005 Elsevier B.V. All rights reserved.
doi:10.1016/j.colsurfa.2005.01.021

colloid size and grain size distribution of the porous media [13].

Liquid–gas interfacial interactions of colloidal particles in porous media have been investigated by microscopy [9,14], bubbling techniques [15] and analysis of column breakthrough curves [11,16]. The liquid–gas interfacial interactions are commonly described by semi-empirical first- or second-order reactions [10,11]. The liquid gas interface can act as barrier for colloid movement when water films become thinner than colloidal diameters, leading to straining or trapping of colloids [10]. It has also been observed that colloids are retained at the menisci of pendular rings of the liquid-gas-solid interface instead of the liquid–gas interface [17].

Colloidal particles approach the solid–liquid interface and the liquid–gas interface through bulk fluid transport and random diffusion. For negatively charged colloids, colloids first encounter repulsive long-range, non-specific electrostatic interactions with negatively charged sediments and negatively charged liquid–gas interfaces [18]. Hydrodynamic forces may overcome the repulsive electrostatic interaction barrier and allow colloids to get close to the sediment surface and liquid–gas interface. Under these conditions, Lifshitz–van der Waals and Lewis acid/base interactions, which are dependent upon surface thermodynamic properties of the colloids, sediments, and the liquid–gas interface as well as the intervening medium, begin to act.

The objective of this study was to investigate colloid retention mechanisms during transport in unsaturated porous media as related to colloid surface thermodynamic properties. We compared transport of four types of colloids with different surface thermodynamic properties in columns at variable effective water saturations $S_e = (\theta_v - \theta_r)/(\theta_s - \theta_r)$ of 0.56, 0.61, 0.70, 0.81 and 1.0, where θ_v, θ_r, and θ_s are the volumetric, residual, and saturated water contents, respectively. Colloid transport was described by a mobile–immobile region model accounting for first-order colloid removal from the mobile region. Colloid attachment to the liquid–gas interface was investigated using a glass micromodel with an optical microscope. Finally, colloidal interaction free energies within the column were calculated according to the traditional and extended Derjaguin–Landau–Verwey–Overbeek (DLVO) theory based on their independently determined surface thermodynamic properties.

2. Materials and methods

2.1. Colloidal materials

We used colloids extracted from Hanford sediments and pure clay minerals. The first type of colloids was fractionated from original Hanford sediments. Hanford sediments were first dispersed in pH 10 buffered water (1.67 mM $NaHCO_3$ + 1.67 mM Na_2CO_3) and agitated and sonicated for at least 5 min. The suspension was decanted to fractionate colloids. These colloids were suspended in the buffer solution for two weeks and supernatants that were dynamically stable were decanted and used for column experiments. We denote these colloids as “native colloids”. The second type of colloids was obtained by reacting the Hanford sediments with a caustic solution [19]. During the caustic reaction, native mineral phases, like kaolinite and quartz, were partially or completely dissolved, and new mineral phases, cancrinite and sodalite, were formed [19]. These colloids were then fractionated following the same procedure as used for native colloids. We denote these latter colloids as “modified colloids”. These types of colloids are expected to form under a Hanford tank leak scenario [19,20]. Pure clay minerals used in this research were kaolinite (KGa1, well crystallized) and Na-montmorillonite (SWy-2), obtained from the Clay Minerals Society (Columbia, MO). Clay mineral suspensions were prepared following the method described by Wan and Tokunaga [21]. Briefly, 50 g clay minerals were suspended in 1 liter pH 10 buffered water. After settling for 24 h, supernatants were decanted and used for the column experiments. *Z*-averaged hydrodynamic diameters of these four colloids were determined by dynamic light scattering using a Zetasizer 3000HAS (Malvern Instruments Ltd., Malvern, UK) with a Helium-Neon laser at a wavelength of 633 nm. Specific surface areas were determined by N2 absorption based on BET isotherms using a surface area analyzer (ASAP 2010, Micromeritics, Norcross, GA). Mineralogy was analyzed by X-ray diffraction with Cu-Kα radiation (Philips XRG 3100, Philips Analytical Inc., Mahwah, NJ).

2.2. Porous medium

We carried out transport experiments with sediment materials obtained from the Hanford formation in southeastern Washington State (Submarine Site 218-E-12B at the U.S. Department of Energy Hanford Reservation). These sediments were pretreated as described by Cherrey et al. [22]. Briefly, the sediments were first screened to remove coarse particles greater than 2 mm in diameter and colloidal particles smaller than 2 μm in diameter. The sediments were then packed in a column of 5 cm diameter and 19 cm length and flushed with 300 pore volumes of pH 10 buffered water (1.67 mM $NaHCO_3$ + 1.67 mM Na_2CO_3) to further remove colloidal materials. The original sediments were the same as the ones used for extraction of “native” colloids.

2.3. Column transport experiments

Column experiments were conducted using the same apparatus as described by Cherrey et al. [22]. Inflow was introduced to the vertically oriented column from the top using a peristaltic pump and a sprinkler head, and outflow from the bottom was connected to a hanging water column. An in-line spectrophotometer (Perkin-Elmer LC95 UV/VIS) was used to monitor colloid and nitrate (tracer) concentrations at wavelengths of 300 and 204 nm, respectively. Variations in

water potentials were monitored by five ceramic tensiometers mounted along the length of the column. An average column water content was measured by continuously weighing the column with a load cell.

Experiments were performed under steady-state flow conditions at effective water saturations of 0.56, 0.61, 0.70, 0.81 and 1.0. Water contents were adjusted from the main drainage loop of the moisture characteristics, i.e., starting with the saturated column and then incrementally lowering the water content. Volumetric water contents and matric potentials were maintained steady and uniform for each run by balancing the column inflow and outflow rate. Time-averaged readings from the five tensiometers were averaged and reported as matric potentials for each run. At each water content, the water flow was first assessed with a conservative nitrate tracer (0.2 mM $NaNO_3$). The nitrate breakthrough was followed by runs of Hanford and clay mineral colloids suspended in the 1.67 mM $NaHCO_3$/1.67 mM Na_2CO_3 (pH 10) solution. After each colloid breakthrough, the column was re-saturated from the bottom upwards with colloid-free pH 10 buffered water to remobilize colloids captured within the column. For this purpose, an end-piece was mounted to the top of the column. This flush was proceeded until background spectrophotometer signal was detected. Between each breakthrough curves, the column was pre-conditioned with sprinkling from the top with colloid-free pH 10 buffered water for the next experiment. All breakthrough curves were run in duplicate in the same column. All experiments in this study were conducted at room temperature, $22 \pm 2\,^{\circ}C$, unless noted otherwise.

2.4. Visualization of colloid capturing at the liquid–gas interface

The micromodel was manufactured by chemical etching of glass microscopy slides using a procedure similar to that described in Wan et al. [14]. The structure etched into the glass plates consisted of cylindrical pillars of 100 μm diameter and pores formed by interstitial spaces. The pillars were arranged in a rectangular structure with a distance between pillar center to pillar center of 170 μm. The micromodel was manufactured at the Microfabrication Laboratory at the University of Washington. Water flow through the micromodel was established by gravity-driven flow, using a constant potential difference between inflow and outflow. Air bubbles were introduced into the micromodel by injecting air into the inflow tube using a syringe. The size of the air bubbles could be controlled by changing the position of the outflow tube, i.e., controlling the tension inside the micromodel.

We selected a single air bubble centered between four glass pillars for the observation of colloid–gas bubble interactions. The size of the air bubble was controlled to be smaller than the width of the micromodel to ensure that the air bubble was completely suspended in the aqueous phase and did not contact the glass. At a constant tension, the air bubble decreased over time because air dissolved in the water. Colloids were introduced into the micromodel by switching the inflow to a colloid suspension. The solution chemistry was the same as in the column experiments. Transport of colloids around the air bubble was established at a flow rate of ≈1.5 ml/h corresponding to a pore water velocity of ≈8.5 cm/s. After stable water flow was established, transport behavior of colloids to the liquid–gas interface was examined for 10 min using an optical light microscope (Nikon Digital Eclipse C1, magnification of objective lense = 100×, numerical aperture of condensor NA_{cond} = 1.4, numerical aperture of objective lense NA_{obj} = 1.25). The spatial resolution of the light microscope was calculated by $d = 1.22\lambda/(NA_{cond} + NA_{obj})$, where λ is the average wavelength of dim light (505 nm) and bright light (555 nm) [23]. For our microscope, we found d = 244 nm. At this resolution, we can distinguish objects that are farther than 244 nm apart, and we can see individual particles of 244 nm diameter or even somewhat smaller particles [23]. When particles are moving, however, it is more difficult to see them, and the resolution of our microscope barely allowed us to trace colloidal particles.

2.5. Colloid surface thermodynamic property estimations

ζ-Potentials of colloids were determined from their electrophoretic mobility based on the Smoluchowski equation [24]:

$$\zeta = \frac{\xi\eta}{\epsilon\epsilon_0} \tag{1}$$

where ζ is the zeta potential measured at the slipping plate (V); ξ, the electrophoretic mobility (m/s)/(V/m); η, the dynamic viscosity of the liquid (N s/m^2); ϵ and ϵ_0, the relative dielectric permittivity of water (78.55 for water at 25 °C) and permittivity under vacuum [8.854×10^{-12} C/(V m)], respectively. Electrophoretic mobility of the colloids was measured in pH 10 buffered water by dynamic light scattering (Zetasizer 3000HAS, Malvern Instruments Ltd., Malvern, UK). Electrophoretic mobility of the sediments could not be measured by dynamic light scattering directly. We assume that the sediments have a similar electrophoretic mobility as the colloids that were extracted from the sediments.

The work of adhesion of a liquid to a solid can be expressed by the Young–Dupré equation [25]:

$$-\Delta G_{SL} = (1 + \cos\theta)_{\gamma_L} \tag{2}$$

where ΔG_{SL} is the adhesion free energy of the liquid to the solid (J/m^2); γ_L, the liquid surface tension (J/m^2); and θ, the solid–liquid contact angle (°). Surface thermodynamic properties of the solid and the liquid are related to each other through the liquid–solid contact angle according to the van Oss–Chaudhury–Good equation [25]:

$$(1 + \cos\theta)\gamma_L = 2\left(\sqrt{\gamma_S^{LW}\gamma_L^{LW}} + \sqrt{\gamma_S^{+}\gamma_L^{-}} + \sqrt{\gamma_S^{-}\gamma_L^{+}}\right) \tag{3}$$

where γ^{LW} is the Lifshitz–van der Waals component of the surface tension (J/m^2) with subscript "S" denoting solid and

"L" denoting liquid; γ^+, the electron-acceptor parameter and γ^- is the electron-donor parameter of the Lewis acid/base component of the surface tension (J/m^2). γ_L, γ_L^{LW}, γ_L^+ and γ_L^- have the following relationship [25]:

$$\gamma_L = \gamma_L^{LW} + 2\sqrt{\gamma_L^- \gamma_L^+} \quad (4)$$

We used three test liquids, diiodomethane, formamide, and water, whose γ_L^{LW}, γ_L^+ and γ_L^- values are known [25], to estimate the unknown solid surface thermodynamic parameters γ_S^{LW}, γ_S^+, and γ_S^-.

Colloid–liquid contact angles were measured using the wicking method and the Washburn equation [26]:

$$h^2 = \frac{R_e t \gamma_L \cos\theta}{2\eta} \quad (5)$$

where h is the height (m) of capillary rise of the wicking liquid at time t (s) and R_e is the average interstitial pore radius (m). As the capillary rise of the wicking liquid is proportional to the mass of the wicking liquid, we can use the following modified form of the Washburn equation:

$$\cos\theta = \frac{m^2\eta}{t\rho^2\gamma_L C} \quad (6)$$

where m is the mass of the wicking liquid sucked into the solid (g); ρ, the density of the wicking liquid (g/m^3); and C, the material constant that is dependent on the porous architecture of the solid (–). The colloidal particles were packed into a Krüss powder sample holder and the measurements were conducted using a tensiometer (K100, Krüss GmbH, Hamburg, Germany). By using a liquid with low surface tension, such as hexane (γ_L = 18.4 mJ/m^2), the material constant C can be obtained from Eq. (6) since hexane is expected to spread over the solid surface during the wicking measurement, resulting in $\cos\theta = 1$. Once C was determined, the measurements were repeated with diiodomethane, formamide, and water to estimate colloid–liquid contact angles. Contact angle measurements were repeated three times and average results were reported. During contact angle measurements, the temperature was held constant at 20.0 °C by circulating thermostated water through a jacketed vessel containing the sample.

3. Theory

3.1. Colloid transport model

Colloid transport through unsaturated Hanford sediments was described by the mobile–immobile region model [27] with the assumption that colloids were deposited from the mobile region only. We also assume that colloids not recovered in the column outflow are either deposited at the solid–liquid interface by physico-chemical deposition, or captured due to the presence of the liquid–gas interface. The dimensionless first-order colloid retention rate coefficient μ was estimated as described in Cherrey et al. [22]. The dimensional colloid retention rate coefficient ϑ can be calculated from $\vartheta = \mu v_m / L$, where v_m is the mobile-phase pore water velocity and L is the length of the column.

3.2. Interaction free energy calculations

The electrostatic interaction free energy ΔG_{132}^{EL} (J) between a spherical colloid, 1, and a flat plate sediment grain or the liquid–gas interface, 2, in the medium of water, 3, can be evaluated for constant surface potential by [28]:

$$\Delta G(y)_{132}^{EL} = \pi R \epsilon\epsilon_0 \left\{ 2\psi_{01}\psi_{02} \log\left(\frac{1+\exp(-\kappa y)}{1-\exp(-\kappa y)}\right) + (\psi_{01}^2 + \psi_{02}^2)\log[1-\exp(-2\kappa y)] \right\} \quad (7)$$

where R is the radius of the colloids (m); $1/\kappa$, the Debye–Hückel length; y, the separation distance between the colloid and the sediment grain or the liquid–gas interface (m); and ψ_{01} and ψ_{02}, surface potentials of the colloids and the sediments or the liquid–gas interface (V), respectively, which can be calculated by:

$$\psi_0 = \zeta\left(1 + \frac{z}{R}\right)\exp(\kappa z) \quad (8)$$

where z is the distance from the colloid surface to the slipping plate (m). The distance z is usually taken as ≈0.3–0.5 nm [25,29] and we take it here as 0.5 nm. The value of κ can be obtained by [24]:

$$\kappa = \sqrt{4\pi e^2 \sum_i \frac{\upsilon_i^2 n_i^2}{\epsilon\epsilon_0 kT}} \quad (9)$$

where e is the charge of the electron (1.6×10^{-19} C); υ_i, the valence of each ionic species (−); n_i, the number concentration of ions of each species in the bulk liquid (number/m^3); k, the Boltzmann constant (1.38×10^{-23} J/K); and T, the absolute temperature (K).

Eq. (7) is only valid for the interaction of a uniformly charged, spherical particle with a uniformly charged, flat surface. Although our colloids are more platy than spherical, we approximate them by a spherical shape. We estimated the surface potential of our colloids with Eq. (8) using the measured electrophoretic mobility, which gives us an overall measure of surface potential.

Electrostatic repulsion prevents colloids from getting close to the sediments and the liquid–gas interface as the colloids, sediments, and the liquid–gas interface are negatively charged. The ζ-potential of gas bubbles in deionized water has been reported as −60 mV [18] and in 1 mM NaCl solution as −65 mV [30]. We take −65 mV as the ζ-potential of the liquid–gas interface and calculated the repulsive electrostatic interactions that operate in the range of several tens of nanometers [25]. Once colloids overcome the repulsive barrier and get close to the sediments or the liquid–gas interface with the help of hydrodynamic forces, Lifshitz–van

Table 1
Characteristics of colloids and sediments at 20 °C

Property	Native colloids	Modified colloids	Kaolinite	Na-montmorillonite	Hanford sediments
Particle diameter	348 ± 14 nm	368 ± 16 nm	332 ± 12 nm	324 ± 17 nm	1.37 mm[a]
Electrophoretic mobility[b] ($\mu m\,s^{-1}$)/(V cm^{-1})	−3.18 ± 0.07	−3.23 ± 0.06	−3.03 ± 0.14	−2.95 ± 0.05	−3.18 ± 0.07[c]
ζ-Potential (mV)	−40.1 ± 0.9	−40.8 ± 0.8	−38.2 ± 1.8	−37.2 ± 0.6	−40.1 ± 0.9[c]
Specific surface area (m^2/g)	78.3 ± 0.3	60.5 ± 0.8	1.6 ± 0.5	30.9 ± 0.6	3.63 ± 0.01
Diiodomethane contact angle (°)	35.7 ± 5.1	36.4 ± 3.7	36.6 ± 4.7	35.3 ± 3.9	N/A
Water contact angle (°)	25.9 ± 2.5	40.4 ± 4.9	52.1 ± 4.3	56.1 ± 0.9	N/A
Formamide contact angle (°)	15.1 ± 6.5	32.7 ± 3.8	47.1 ± 6.0	48.2 ± 3.7	N/A
γ_S^{LW} (mJ/m^2)	41.7	41.4	41.3	41.9	41.7[c]
γ_S^- (mJ/m^2)	44.5	37.4	32.4	27.5	44.5[c]
γ_S^+ (mJ/m^2)	1.1	0.4	0	0	1.1[c]
Mineralogy	Chlorite, smectite, kaolinite, illite, and quartz	Cancrinite, sodalite, chlorite, smectite, illite, and quartz			Quartz, feldspar, mica, magnetite, pyroxene, hornblende, kaolinite, illite, and smectite

'±' Denotes 1 S.D.
[a] Median of diameter.
[b] At pH 10 and 1.67 mM $NaHCO_3$ + 1.67 mM Na_2CO_3 electrolyte background.
[c] Assumed to be identical to native colloids.

der Waals and Lewis acid/base interactions begin to dominate. These separation-distance dependent Lifshitz–van der Waals and Lewis acid/base interaction free energies (J) can be calculated by [25,29]:

$$\Delta G(y)_{132}^{LW} = -4\pi\frac{y_0^2}{y}\chi(\sqrt{\gamma_3^{LW}}-\sqrt{\gamma_2^{LW}})(\sqrt{\gamma_3^{LW}}-\sqrt{\gamma_1^{LW}}) \quad (10)$$

$$\Delta G(y)_{132}^{AB} = -4\pi y_0\chi\exp\left(\frac{y_0-y}{\chi}\right)[\sqrt{\gamma_3^+}(\sqrt{\gamma_1^-}+\sqrt{\gamma_2^-}-\sqrt{\gamma_3^-})+(\sqrt{\gamma_3^-}(\sqrt{\gamma_1^+}+\sqrt{\gamma_2^+}-\sqrt{\gamma_3^+})-\sqrt{\gamma_1^+\gamma_2^-}-\sqrt{\gamma_1^-\gamma_2^+}] \quad (11)$$

where y_0 is the equilibrium distance of 1.57 Å where physical contact occurs and χ is the water decay length of 0.6 nm [25]. The total interaction free energy between colloids and a surface with respect to the separation distance is the sum of electrostatic, Lifshitz–van der Waals and Lewis acid/base interaction free energies:

$$\Delta G(y)_{132}^{TOT} = \Delta G(y)_{132}^{EL} + \Delta G(y)_{132}^{LW} + \Delta G(y)_{132}^{AB} \quad (12)$$

4. Results and discussion

4.1. Colloid and sediment properties

Measured properties of colloids and sediments are summarized in Table 1. All colloids had a negative electrophoretic mobility. Natural colloids (Hanford native and modified colloids) and clay minerals (kaolinite and Na-montmorillonite) had a similar Lifshitz–van der Waals component of surface tension (≈41 mJ/m^2). The electron-donor parameter of Lewis acid/base component surface tension γ_S^- was at least one order in magnitude greater than the electron-acceptor parameter of Lewis acid/base component surface tension γ_S^+ for all the colloids used in this study, suggesting that the colloids had a monopolar surface [25]. The γ_S^- value is closely related to the hydrophilicity or hydrophobicity of a surface, and it plays the most important role in determining colloid stability [25,31]. Hanford native colloids had the greatest γ_S^- (44.5 mJ/m^2), followed by modified colloids (37.4 mJ/m^2), kaolinite (32.4 mJ/m^2), and Na-montmorrillonite (27.5 mJ/m^2). We compared the surface thermodynamic properties of kaolin-

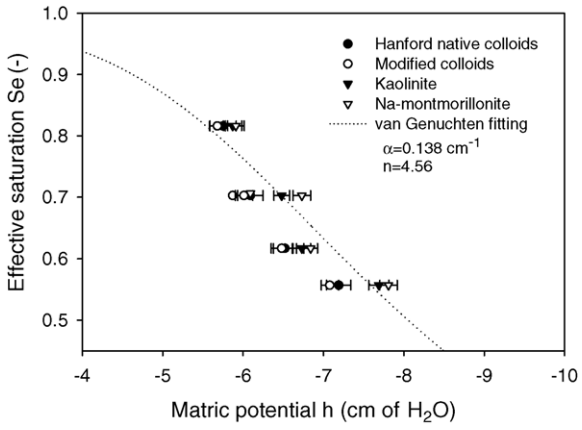

Fig. 1. Effective saturation vs. matric potential for Hanford sediments. The dotted line is the van Genuchten relationship $S_e = [1 + (\alpha h)^n]^{(1/n-1)}$ [32] (with h being the matric potential and the parameters α und n shown in the plot) fitted to hanging water column data (from Cherrey et al. [22]). Symbols are averaged values obtained from the five tensiometers for the different colloid breakthrough curves. Error bars denote ±1 S.D.

ite we obtained with those reported by Wu [31] and found similar results (41.3, 32.4 and 0 mJ/m^2 for γ_S^{LW}, γ_S^- and γ_S^+ in this study and 41.0, 30.0 and 0.7 mJ/m^2 by Wu [31]). For Na-montmorillonite, we determined 41.9, 27.5 and 0 mJ/m^2 for γ_S^{LW}, γ_S^- and γ_S^+, respectively, as compared with 40.9, 44.6 and 0.4 mJ/m^2 reported by Wu [31].

4.2. Matric potentials and volumetric water contents

The average matric potentials measured with the five tensiometers during the column experiments matched the moisture characteristics obtained with the hanging water column technique very closely (Fig. 1). The coarse sediments started to desaturate at potentials of about −4 cm-H_2O and reached S_e = 0.56 at potentials of around −8 cm-H_2O. Volumetric water contents measured for this research (S_e = 0.56–1.0) ranged from 0.25 to 0.40 cm^3/cm^3. The uniformity of water contents could be well maintained in the center of the column, but the top 3 cm was drier and the bottom 2 cm was wetter than the rest of the column.

4.3. Transport of conservative tracer and colloidal particles

Colloid transport could be well described by the mobile/immobile region model (Fig. 2). Analysis of breakthrough curves from saturated columns indicated that colloids did not attach to the solid–liquid interface and

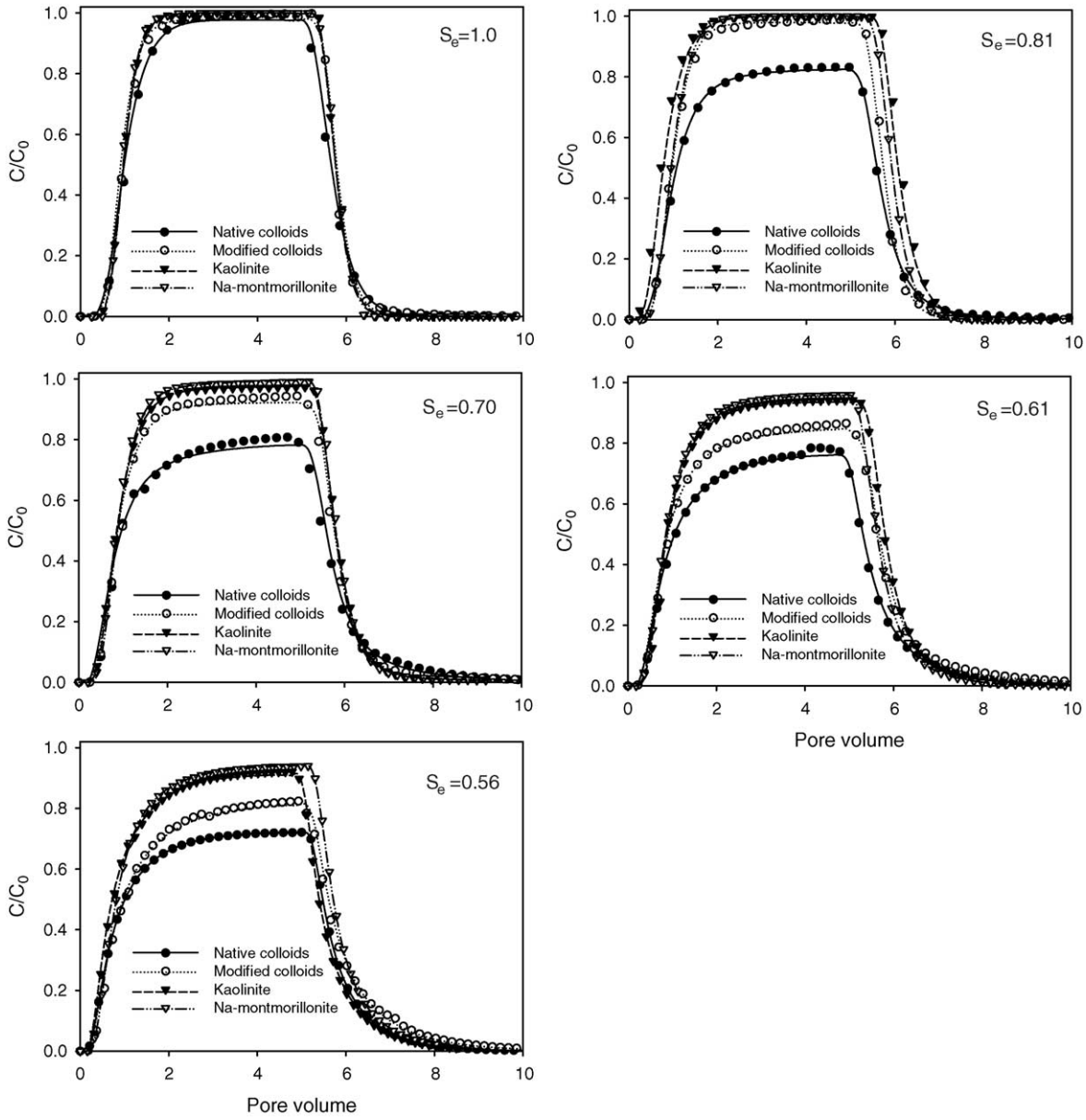

Fig. 2. Breakthrough curves of colloids at effective saturations S_e of 1.0, 0.81, 0.70, 0.61 and 0.56. Symbols are measured data, lines are mobile/immobile region model fits. Only every sixth measured datapoint is shown.

Table 2
Colloid retention coefficients and colloid recovery for variably saturated transport and for subsequent re-saturation of sediments

Effective saturation (–)	Total colloid input (mg)	Colloid recovery breakthrough (mg (%))	Retention coefficient, μ (–)	Retention coefficient, ϑ (min^{-1})	Colloid recovery re-saturation (mg (%))	Total recovery (mg (%))
Native colloids						
1.0	4.81	4.71 (97.9)	0.023 ± 0.006	0.013	0.04 (0.8)	4.75 (98.7)
0.81	4.41	3.87 (87.8)	0.193 ± 0.003	0.111	0.49 (11.1)	4.36 (98.9)
0.70	4.56	3.75 (82.2)	0.244 ± 0.010	0.096	0.72 (15.8)	4.47 (98.0)
0.61	4.52	3.55 (78.5)	0.278 ± 0.005	0.105	0.87 (19.2)	4.42 (97.8)
0.56	4.56	3.45 (75.7)	0.348 ± 0.000	0.122	0.95 (20.8)	4.40 (96.5)
Modified colloids						
1.0	4.62	4.64 (100.4)	0.023 ± 0.006	0.011	0 (0)	4.64 (100.4)
0.81	4.26	4.26 (100)	0.021 ± 0.004	0.010	0 (0)	4.26 (100)
0.70	4.56	4.35 (95.4)	0.068 ± 0.010	0.026	0.13 (2.8)	4.48 (98.2)
0.61	4.56	4.02 (88.2)	0.150 ± 0.006	0.052	0.43 (9.4)	4.45 (97.6)
0.56	4.56	3.80 (83.3)	0.209 ± 0.005	0.062	0.61 (13.4)	4.41 (96.7)
Kaolinite						
1.0	0.376	0.361 (96.0)	0	0	0.002 (0.5)	0.363 (96.5)
0.81	0.379	0.362 (95.5)	0	0	0 (0)	0.362 (95.5)
0.70	0.379	0.366 (96.5)	0.018 ± 0.003	0.007	0.003 (0.8)	0.369 (97.4)
0.61	0.377	0.349 (92.5)	0.066 ± 0.004	0.024	0.017 (4.5)	0.366 (97.1)
0.56	0.378	0.328 (86.7)	0.092 ± 0.003	0.028	0.036 (9.5)	0.364 (96.3)
Na-montmorillonite						
1.0	0.0304	0.0290 (95.4)	0	0	0 (0)	0.0290 (95.4)
0.81	0.0294	0.0300 (102.0)	0	0	0 (0)	0.0300 (102.0)
0.70	0.0294	0.0298 (101.3)	0	0	0 (0)	0.0298 (101.3)
0.61	0.0304	0.0278 (91.4)	0.044 ± 0.002	0.015	0.015 (6.3)	0.0297 (97.7)
0.56	0.0307	0.0282 (91.8)	0.055 ± 0.001	0.017	0.017 (5.5)	0.0299 (97.3)

'±' Denotes 1 S.E.

minimal amounts of colloids were retained inside the column (dimensionless colloid retention coefficient, $\mu < 0.025$) (Table 2).

Under water unsaturated conditions, natural and clay mineral particles were retained within the system, and the retention increased with the decrease of effective water saturation. Native colloids were retained the most, followed by modified colloids, kaolinite, and Na-montmorillonite (Table 2). We hypothesize that the presence of the liquid–gas interface was the dominant factor of unsaturated colloid retention. Most of the retained particles were recovered when the column was re-saturated. Experimental mass balances based on numerical integration of the breakthrough curves and measurements of amounts of colloids eluted after re-saturation suggested that nearly all the colloids retained within the column could be recovered (Table 2). Mass recoveries became smaller with decreasing water saturation, possibly due to incomplete re-saturation of the columns because of hysteresis.

4.4. Visualization of colloid attachment to the liquid–gas interface

We first suspected that colloid retention within the column was due to their attachment to the liquid–gas interface. To test this hypothesis, we suspended an air bubble in the micromodel.

We controlled the air bubble to be smaller than the diameter of the pores in the micromodel and ensured that the air bubble was completely suspended and did not contact the glass. Thus, there was no solid–liquid–gas three-phase interface within the micromodel. We visualized colloid migration in the micromodel and could not see any evidence that colloidal particles adhered to the liquid–gas interface. Fig. 3 is the image of native colloid migrating in the micromodel. We made similar observations for other colloids. In all cases, colloids moved with the flow, avoiding interception with the air bubble.

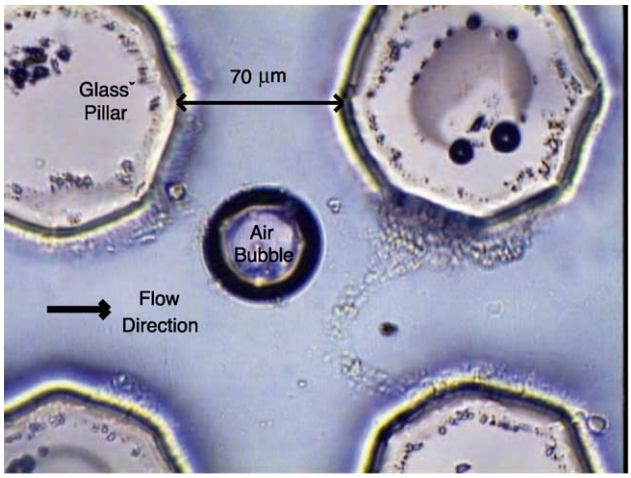

Fig. 3. Native colloid transport in glass micromodel observed with a light microscope. A single air bubble was suspended between four glass pillars in the micromodel.

The moving colloids were barely visible with the microscope, but we did not see any evidence that colloids would intercept and attach to the liquid–gas interface. These observations are only qualitative, but provide supporting evidence that colloids did likely not preferentially attach to the liquid–gas interface.

We did not perform micromodel experiments where the liquid–gas–solid three-phase interface was present. The glass surface properties are different from those of the sediments used in our column experiments, and consequently liquid–gas–solid interactions observed in the micromodel would not necessarily be representative for the column system. In addition, it was difficult to distinguish between the liquid–gas–solid interface and liquid–gas interface within the micromodel.

4.5. Colloid retention mechanisms in water unsaturated systems

To investigate the mechanisms of colloid retention under water unsaturated conditions, we examined interaction free energies of colloidal particles with the sediments and the liquid–gas interface based on their surface thermodynamic properties.

Under water saturated conditions, colloids first had repulsive interactions with the sediments during transport within the column. If the repulsive electrostatic interaction barrier could be overcome and colloids get close to the sediments, colloids had attractive Lifshitz–van der Waals and Lewis acid/base interactions with the sediments. The electrostatic, Lifshitz–van der Waals and Lewis acid/base interaction free energies between colloids and the sediments were calculated based on Eqs. (7)–(12). Total interaction free energies between colloids and the sediments were positive (repulsive) except when the colloids were close to the sediments at the equilibrium distance (Fig. 4a). The maximum electrostatic interaction free energies were several hundreds of kT, which indicates that colloids could not overcome the repulsive electrostatic interaction barrier, and therefore, did not attach to the sediments when transported in the column. This was supported by our experimental observations that colloid retention in water saturated columns was minimal.

Under water unsaturated conditions, colloids also interact with the liquid–gas interface. The colloids had repulsive electrostatic, Lifshitz–van der Waals and Lewis acid/base interactions with the liquid–gas interface for all separation distances because total free energies between colloids and the liquid–gas interface were positive for all separation distances (Fig. 4b). Thus, when colloids were introduced to water unsaturated systems, colloids were repelled from the liquid–gas interface and no colloids would attach to the liquid–gas interface. This was consistent with what we observed with the glass micromodel.

Nonetheless, our experimental data showed that colloids were retained in the column when the system became water unsaturated. We believe that, under water unsaturated conditions, colloid were retained near the region where the water films become similar in thickness as the colloidal diameters by physical constraint, like trapping by thin water films [10,17]. When water films are comparable in thickness to colloidal diameters, repulsive interactions between colloids and the liquid–gas interface aided colloids to overcome the repulsive electrostatic interaction barrier with the sediments and allowed the colloids to get close to the sediment surfaces (Fig. 5). Once colloids overcame the electrostatic repulsive barrier, colloids established attractive Lifshitz–van der Waals and Lewis acid/base interactions. At the equilibrium distance where physical contact between colloids and the sediments occurred, electrostatic interactions dropped significantly owing to the superposition of double layers. Thus, the total interaction free energies between colloids and the sediments at the equilibrium distance were negative (attractive), which in combination with the physical constraint at the liquid–gas–solid interface, accounted for the consequent colloidal retention.

On the contrary, colloids had repulsive van der Waals and Lewis acid/base interactions with the liquid–gas interface, which increased with decreasing separation distance. Thus, even when the electrostatic repulsive barrier was overcome, the repulsive van der Waals and Lewis acid/base interactions

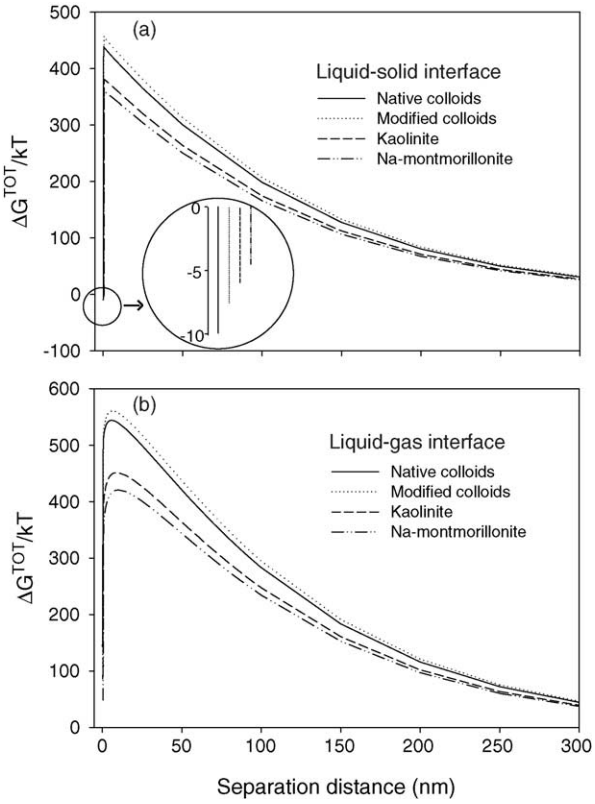

Fig. 4. Total interaction free energies between (a) colloids and sediments and (b) colloids and the liquid–gas interface. Curves were calculated with Eqs. (7)–(12). Interaction energies are normalized by kT at 25 °C. Inset shows a magnification of the liquid–solid interfacial interactions at close separation distance.

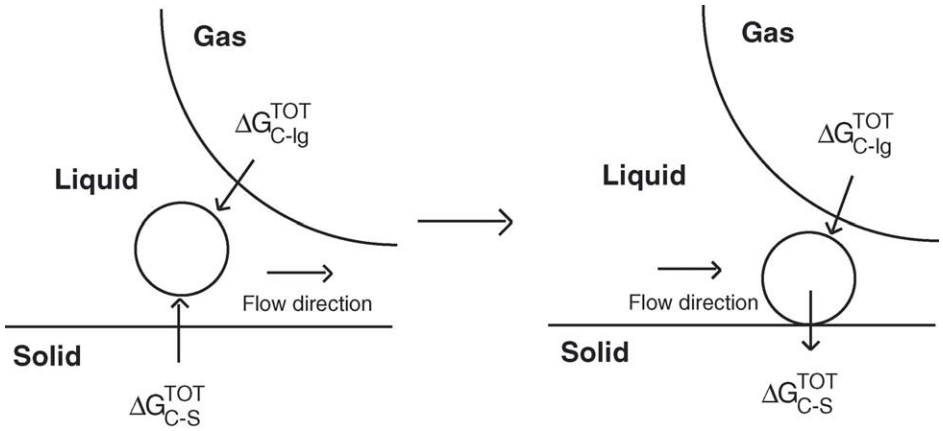

Fig. 5. Schematic illustration of colloid retention near thin water films. Repulsive interactions between colloids and the liquid–gas interface allowed colloids to overcome the repulsive interaction barrier between colloids and the sediments. Once getting close to the sediments, colloids established attractive interactions with the sediments.

would prevent the attachment of colloids to the liquid–gas interface.

The attractive interactions between colloids and the sediments were not very strong (ΔG^{TOT}_{C-S} was −9.9, −7.5, −5.9, and −4.5 kT for native colloids, modified colloids, kaolinite, and Na-montmorillonite, respectively). When the column was re-saturated, the liquid–gas interface was removed from the system, and the retained colloids were mobilized in the absence of the physical constraint because the attractive energies were small. Analysis of the results revealed that colloid retention inside the column was related to Δ^{TOT}_{C-S}, the total interaction free energy between colloids and the sediments, evaluated at the equilibrium distance (Fig. 6). Greater colloid retention coincided with a negatively greater ΔG^{TOT}_{C-S}. Native colloids were retained most as they had the most attractive interaction free energies, followed by modified colloids, kaolinite, and Na-montmorrillonite. This corroborates the hypothesis that colloids were retained at the solid–liquid interface near water films which have similar thickness as the colloidal diameters.

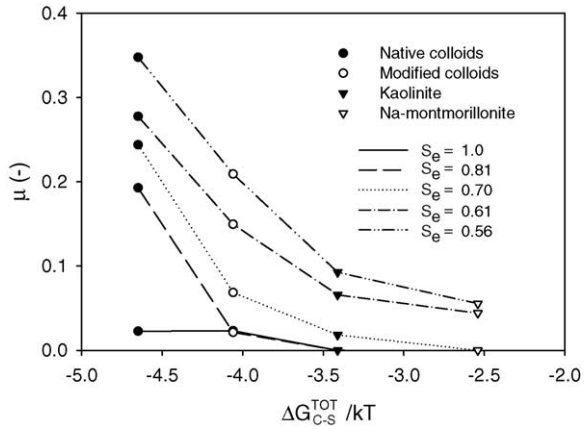

Fig. 6. Colloid retention rate coefficient μ vs. total interaction free energies between colloids and the sediments. Interaction energies are normalized by kT at 25 °C.

5. Conclusions

Previous studies have attributed colloid retention in water unsaturated porous media to deposition on solid surfaces [12], attachment to the liquid–gas interface [9], and straining in thin water films [10,11]. In this research, based on surface thermodynamic considerations and column and micromodel observations, we concluded that colloids were most likely to be retained by attachment to the sediments caused by repulsive interactions exerted by the liquid–gas interface. Surface thermodynamic considerations helped to explain qualitatively the differences in transport among the different colloids.

References

[1] R. Rajagopalan, C. Tien, AIChE J. 22 (1976) 523.
[2] C. Tien, Granular Filtration of Aerosols and Hydrosols, Butterworths, Boston, 1989.
[3] J.N. Ryan, M. Elimelech, Colloids Surf. Physicochem. Eng. Aspects 107 (1996) 1.
[4] R. Kretzschmar, M. Borkovec, D. Grolimund, M. Elimelech, Adv. Agron. 66 (1999) 121.
[5] J.E. Saiers, G.M. Hornberger, Water Resour. Res. 35 (1999) 1713.
[6] A.P. Gamerdinger, D.I. Kaplan, Environ. Sci. Technol. 35 (2001) 3326.
[7] H. Small, J. Colloid Interface Sci. 48 (1974) 147.
[8] D. Liu, P.R. Johnson, M. Elimelech, Environ. Sci. Technol. 29 (1995) 2963.
[9] J.M. Wan, J.L. Wilson, Water Resour. Res. 30 (1994) 857.
[10] J.M. Wan, T.K. Tokunaga, Environ. Sci. Technol. 31 (1997) 2413.
[11] J.J. Lenhart, J.E. Saiers, Environ. Sci. Technol. 36 (2002) 769.
[12] L.M. McDowell-Boyer, J.R. Hunt, N. Sitar, Water Resour. Res. 22 (1986) 1901.
[13] S.A. Bradford, S.R. Yates, M. Bettahar, J. Simunek, Water Resour. Res. 38 (2002) 1327.
[14] J.M. Wan, J.L. Wilson, T.L. Kieft, Appl. Environ. Microbiol. 60 (1994) 509.
[15] J. Wan, T.K. Tokunaga, Environ. Sci. Technol. 32 (1998) 3293.

[16] Y. Chu, Y. Jin, M. Flury, M.V. Yates, Water Resour. Res. 37 (2001) 253.
[17] J.T. Crist, J.F. McCarthy, Y. Zevi, P.C. Baveye, J.A. Troop, T.S. Steenhuis, Vadose Zone J. 3 (2004) 444.
[18] A. Graciaa, G. Morel, P. Saulnier, J. Lachaise, R. Schechter, J. Colloid Interface Sci. 172 (1995) 131.
[19] K. Mashal, J.B. Harsh, M. Flury, A.R. Felmy, H. Zhao, Environ. Sci. Technol. 38 (2004) 5750.
[20] B.R. Bickmore, K.L. Nagy, J.S. Young, J.W. Drexler, Environ. Sci. Technol. 35 (2001) 4481.
[21] J. Wan, T. Tokunaga, J. Colloid Interface Sci. 247 (2002) 54.
[22] K.D. Cherrey, M. Flury, J.B. Harsh, Water Resour. Res. 39 (2003) 1165.
[23] D.B. Murphy, Fundamentals of Light Microscopy and Electronic Imaging, John Wiley & Sons, New York, 2001.
[24] J.T.G. Overbeek, Electrokinetics, in: H. Kruyt (Ed.), Colloid Science, Elsevier, Amsterdam, Netherlands, 1952, pp. 194–244.
[25] C.J. van Oss, Interfacial Forces in Aqueous Media, Marcel Dekker, New York, 1994.
[26] E.W. Washburn, Phys. Rev. 17 (1921) 273.
[27] M.T. van Genuchten, R.J. Wagenet, Soil Sci. Soc. Am. J. 53 (1989) 1303.
[28] R. Hogg, T.W. Healy, D.W. Fuerstenau, Trans. Faraday Soc. 62 (1966) 1638.
[29] H. Dong, T.C. Onstott, C. Ko, A.D. Hollingsworth, D.G. Brown, B.J. Mailloux, Colloids Surf. B 24 (2002) 229.
[30] P. Saulnier, J. Lachaise, G. Morel, A. Graciaa, J. Colloid Interface Sci. 182 (1996) 395.
[31] W. Wu, Clays Clay Miner. 49 (2001) 446.
[32] M.T. van Genuchten, Soil Sci. Soc. Am. J. 44 (1980) 892.

Available online at www.sciencedirect.com
ScienceDirect
Colloids and Surfaces A: Physicochem. Eng. Aspects 289 (2006) 254–255
COLLOIDS AND SURFACES A
www.elsevier.com/locate/colsurfa

Erratum

Erratum to "Retention of mineral colloids in unsaturated porous media as related to their surface properties" (Coll. Surf. Physicochem. Eng. Aspects 256 (2005) 207–216)

Gang Chen, Markus Flury *

Department of Crop and Soil Sciences, Center for Multiphase Environmental Research, Washington State University, Pullman, WA 99164, USA

Received 25 May 2006; received in revised form 13 June 2006; accepted 27 June 2006
Available online 1 July 2006

In the paper by Chen and Flury [1], Eqs. (9)–(11) were incorrectly reported. The correct equations should read:

$$\kappa = \sqrt{e^2 \sum_i \frac{v_i^2 n_i}{\varepsilon \varepsilon_0 kT}} \tag{9}$$

where $1/\kappa$ is the Debye-Hückel length (m), e the charge of the electron (1.6×10^{-19} C), v_i the valence of each ionic species (−), n_i the number concentration of ions of each species in the bulk liquid (number/m^3), ε and ε_0 are the relative dielectric permittivity of water (78.55 for water at 25 °C) and permittivity under vacuum [8.854×10^{-12} C/(Vm)], respectively; k the Boltzmann constant (1.38×10^{-23} J/K), and T the absolute temperature (K).

$$\Delta G(y)_{132}^{\mathrm{LW}} = -4\pi \frac{y_0^2}{y} R \left(\sqrt{\gamma_3^{\mathrm{LW}}} - \sqrt{\gamma_2^{\mathrm{LW}}}\right) \times \left(\sqrt{\gamma_3^{\mathrm{LW}}} - \sqrt{\gamma_1^{\mathrm{LW}}}\right) \tag{10}$$

$$\Delta G(y)_{132}^{\mathrm{AB}} = -4\pi y_0 R \exp\left(\frac{y_0 - y}{\chi}\right) \times \left[\sqrt{\gamma_3^+}\left(\sqrt{\gamma_1^-} + \sqrt{\gamma_2^-} - \sqrt{\gamma_3^-}\right) + \sqrt{\gamma_3^-}\left(\sqrt{\gamma_1^+} + \sqrt{\gamma_2^+} - \sqrt{\gamma_3^+}\right) - \sqrt{\gamma_1^+ \gamma_2^-} - \sqrt{\gamma_1^- \gamma_2^+}\right] \tag{11}$$

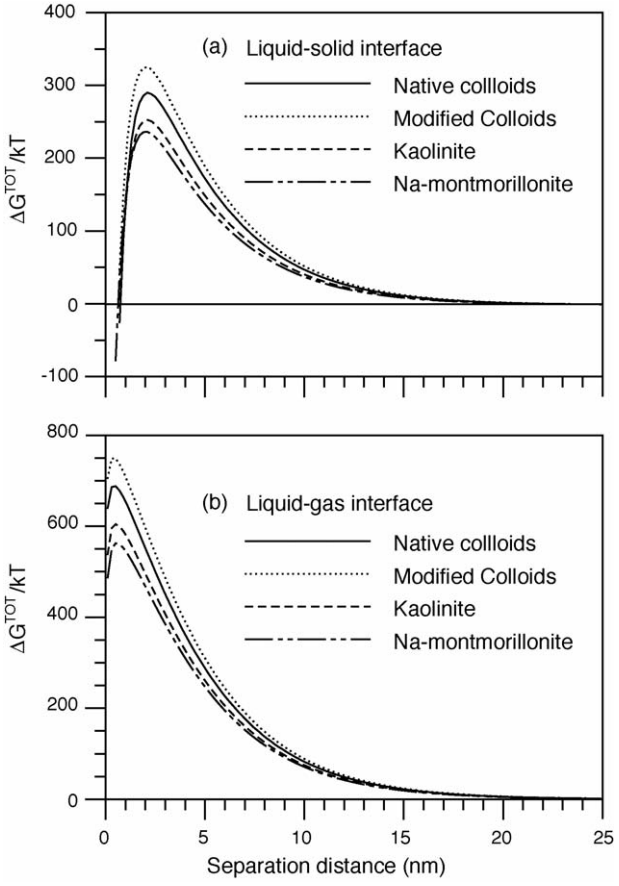

Fig. 4. Total interaction free energies between (a) colloids and sediments and (b) colloids and the liquid–gas interface. Interaction energies are normalized by kT at 25 °C.

DOI of original article:10.1016/j.colsurfa.2005.01.021.
* Corresponding author.
E-mail address: flury@mail.wsu.edu (M. Flury).

doi:10.1016/j.colsurfa.2006.06.029

where $G(y)_{132}^{LW}$ is the Lifshitz-van der Waals interaction free energy (J), $\Delta G(y)_{132}^{AB}$ the Lewis acid/base interaction free energy (J), y_0 the equilibrium distance of 0.157×10^{-9} m where physical contact occurs, R the radius of the spherical colloid (m), χ the water decay length of 0.6×10^{-9} m, y the separation distance (m), γ^{LW} the Lifshitz-van der Waals component of the surface tension (J/m^2), γ^+ the electron-acceptor parameter and γ^- the electron-donor parameter of the Lewis acid/base component of the surface tension (J/m^2), with subscripts denoting colloid, 1, a flat sediment or the liquid–gas interface, 2, in the medium of water, 3.

Fig. 4 of the paper was based on the wrong equations and consequently incorrect. The correct Fig. 4 is reproduced here. The discussion and conclusions of the paper are not affected by the incorrect equations and the incorrect Fig. 4.

Acknowledgement

We thank Christiane Shani (Ben-Gurion University of the Negev) for pointing out the error in Eq. (9).

Reference

[1] G. Chen, M. Flury, Retention of mineral colloids in unsaturated porous media as related to their surface properties, Coll. Surf. Physicochem. Eng. Aspects 256 (2005) 207–216.

Environ. Sci. Technol. **2005**, *39,* 1506−1512

Colloid Stability in Vadose Zone Hanford Sediments

SZABOLCS CZIGÁNY, MARKUS FLURY,* AND JAMES B. HARSH

Department of Crop and Soil Sciences, Center for Multiphase Environmental Research, Washington State University, Pullman, Washington 99164

We experimentally determined colloid stability of natural colloids extracted from vadose zone sediments from the U.S. Department of Energy's Hanford Reservation. We also used reference minerals, kaolinite, montmorillonite, and silica, for comparative purposes. Colloid stability was assessed with two different methods: the batch turbidity method and dynamic light scattering. Critical coagulation concentrations (CCCs) were determined for pure Na and pure Ca electrolyte solutions, as well for mimicked Hanford vadose zone pore waters with varying sodium adsorption ratios (SARs). Critical coagulation concentrations obtained from the batch turbidity method were sensitive to initial colloid mass concentrations, settling time, and CCC criteria. The lower the initial colloid concentration and the shorter the settling times were, the larger was the CCC. The CCCs determined from the dynamic light scattering, where diluted colloidal suspensions are used, were not dependent on settling time and arbitrary CCC criteria, so dynamic light scattering is therefore the preferred method to determine colloid stability. The CCC values determined from dynamic light scattering ranged from 90 to 200 mmol/L for Na systems and 1.7 to 3.8 mmol/L for Ca systems. The stability of natural colloids was intermediate between that of pure kaolinite and montmorillonite. The results indicate that colloids in the Hanford vadose zone form stable suspensions, i.e., are in the slow aggregation regime. Nonetheless, due to the long travel times in the vadose zone, nearly all colloids will aggregate and be removed from the water column before reaching groundwater levels.

Introduction

Colloid-facilitated radionuclide transport is a major concern at nuclear facilities, such as the Hanford Reservation, the Yucca Mountain high-level waste repository, and the Nevada Test Site (*1*, *2*). A prerequisite for colloid-facilitated transport is that colloids, present in the subsurface, form stable colloid suspensions. Colloid suspensions are thermodynamically unstable, and the term "stable" therefore refers to a suspension that is sustained over a specific time period of interest. For subsurface processes, the time period of interest can range from hours to hundreds of years.

A formalized description of colloid stability is given by the DLVO theory, which accounts for attractive and repulsive interactions between individual particles (*3*). The critical coagulation concentration (CCC) is the electrolyte concentration at which the repulsive interaction energy diminishes below the kinetic energy of an individual particle, and colloids aggregate. Critical coagulation concentrations for subsurface colloids have been reported for various clay minerals, and the experimental data demonstrate the dependence of CCC on pH and sodium adsorption ratio (SAR) (*4*−*8*).

The batch turbidity method is a common technique to study colloid stability. This method consists of clay dispersion in a series of vials containing different concentrations of electrolytes. After a predetermined time, the turbidity is measured and the CCC is taken at the electrolyte concentration where the turbidity of the suspension decreases considerably. The CCC value determined in such a way will depend on initial colloid concentration, the time allowed for coagulation, and the criteria used to determine when coagulation has occurred (*4*). In most batch turbidity coagulation studies, high initial colloid concentrations have been used, in the order of ≈100−1000 mg/L (*4*, *5*, *9*). Different authors have used different settling times which range from 3 h (*9*, *10*) to 7 days (*4*) and even 15 months (*6*). Coagulation criteria used by different authors differ as well, and range between 50% and 95% drop in colloid concentrations (*5*, *9*, *11*).

A second common method to determine the CCC is based on the dynamics of aggregate formation in suspension (*12*−*14*). Aggregate size is usually measured by light scattering, and, consequently, low initial colloid concentrations are employed for these measurements (*3*). The determination of colloid stability by light scattering, however, is based on the assumption of monodisperse, spherical particles, and caution should be applied when particles are polydisperse and nonspherical (*15*).

To assess the role of colloids on the migration of radionuclides at nuclear waste sites, one needs to determine the site-specific stability of subsurface colloids. In this study, we focus on the subsurface chemical conditions affecting colloidal stability at the U.S. Department of Energy's (DOE) Hanford Reservation, one of the most contaminated sites in the United States. This site, located in southcentral Washington State, is characterized by an arid climate, and sediments have a pH of 7 or higher (*16*). Previous observations on colloid stability using the batch turbidity method indicated that natural colloids likely will not form stable suspensions in Hanford groundwaters (*17*). However, as CCC determinations with the batch turbidity method depend on the specific experimental protocol, no firm conclusions can be made regarding the colloid stability at the Hanford site from the data currently available.

The objectives of this study were to compare different experimental methods to determine CCCs and to quantify colloid stability in Hanford vadose zone pore water. Specifically, we determined CCCs of colloid suspensions from Hanford sediments as affected by ionic strength, electrolyte type, SAR, pH, suspended particle concentration, and time. We also determined CCCs for reference clay minerals (kaolinite and montmorillonite) for comparative purposes.

Materials and Methods

Colloid Material and Fractionation. We used three different types of colloids: colloids from sediments at the Hanford site, aluminosilicate source clays (Clay Minerals Repository, Columbia, MO), and pure silica beads (Bangs Laboratories, Fishers, IN). The source clays were used as standards to compare our results with literature data. Silica was used only in the light scattering studies to represent a monodisperse, spherical colloid system. All experiments were carried out at 22 ± 1 °C.

* Corresponding author phone: 1-509-335-1719; fax: 1-509-335-8674; e-mail: flury@mail.wsu.edu.

10.1021/es048714n CCC: $30.25
Published on Web 02/03/2005

Two types of Hanford sediments were obtained from the submarine pit (218-E-12B) at the Hanford site in spring 2001: a coarse and a fine sand. Extensive characterization of the sediments is given elsewhere (*16*). The coarse and fine sands are the two characteristic sediment layers of the Hanford formation and represent the majority of the Hanford vadose zone (*18*). Sediments were air-dried and sieved through a 2-mm square screen. Two types of clay mineral standards, montmorillonite (SWy-2) and kaolinite (KGa-1), were used as received.

We saturated the cation exchange sites of sediments and source clay minerals with either Na or Ca. The sediments were wet-packed into 2.5-cm-diameter acrylic columns and flushed with at least 40 pore volumes of either 1 M NaCl or $CaCl_2$ buffered at pH 10 with 1.67 mM Na_2CO_3/$NaHCO_3$. The sediments were then dialyzed against deionized water. The clay mineral standards and silica beads were washed with either 1 M NaCl or 1 M $CaCl_2$ by shaking clay dispersions on a reciprocal shaker. Samples were then centrifuged and the supernatant was decanted. This procedure was repeated three times and the samples were dialyzed against deionized water.

Sediments and clay mineral standards were transferred as dilute suspensions to 1-L volumetric cylinders, which were filled with either 1.67 mM Na_2CO_3/$NaHCO_3$ buffer for the Na-saturated systems or deionized water for the Ca-saturated systems. Suspensions were sonicated for 10 min. Colloids, operationally defined as material with equivalent diameter of $<2\ \mu$m, were fractionated by gravity sedimentation based on Stokes' law, assuming a specific gravity of 2.65. Colloids were always kept in suspension and used within 7 days after fractionation. The total amount of colloids in the sediments was quantified by static light scattering (MasterSizer S, Malvern Instruments Ltd., Malvern, U.K.). Hanford colloids were characterized by scanning electron microscopy and X-ray diffraction with Cu Kα radiation.

Colloid Stability Experiments. *Electrolyte Solutions and Hanford Pore Water Composition.* Pure NaCl and $CaCl_2$ solutions were used to determine colloid stability for 1:1 and 2:1 electrolytes. The effect of the SAR was studied in solutions containing different proportions of Na and Ca. Synthetic Hanford pore water was used to mimic conditions of the Hanford vadose zone. All solutions were adjusted to pH 10 with 1.67 mM Na_2CO_3/$NaHCO_3$ for the Na systems and with CaOH for the Ca systems to prevent dissolution of carbonates in the Hanford sediments. Chemical composition and initial colloid concentrations of the different suspensions are listed in Table A of the Supporting Information.

To determine the pore water composition of the vadose zone sediments used in this study, we extracted pore water from coarse Hanford sediments using 1:1 (w/w) sediment-to-water extracts (*19*). Sodium, Ca, K, and Mg were measured with ICP-AES. Calculations of ideal pore water concentrations were performed with Visual MINTEQ 2.15 (Jon Peter Gustaffson, KTH, Dep. of Land and Water Resources Eng., Stockholm, Sweden; *20*) for solutions in equilibrium with different carbonaceous solids at 0.00035 atm CO_2 pressure and 25 °C.

Batch Turbidity Experiments. Critical coagulation concentrations were determined with the test tube method (*10*) using 30-mL glass vials and initial colloid concentrations of 30−55 mg/L. Electrolyte solutions were either NaCl, $CaCl_2$, or a simulated Hanford pore water composition with various SARs (with the unit of $\sqrt{\text{mmol}_c/\text{L}}$). Vials were capped, shaken by hand end-over-end for about one minute, and then placed in a rack for 19 ± 1 h. We then took 3.8 mL of suspension with a pipet from a depth of 5 cm from each vial (the total suspension height was 12.5 cm), and measured turbidity by spectrophotometry.

To study the effect of colloid concentration on CCC, we tested suspensions of different initial colloid concentrations ranging from 10 to 400 mg/L using the same procedure as described above. To study the effect of time on CCC, we measured turbidity in the suspensions after 3, 6, 9, 18, and 36 h following preparation. We used initial colloid concentrations of about 10, 50, and 100 mg/L for these tests. For these experiments (effect of time and colloid concentration) we used NaCl electrolyte and Hanford sediments only.

We studied the effect of Hanford porewater composition on colloid stability using solutions containing different electrolytes (Na^+, K^+, Ca^{2+}, Mg^{2+}) in concentrations typical for vadose zone Hanford sediments. We varied the SAR by changing the Ca^{2+} concentration.

A long-term stability experiment was conducted by using 1-L volumetric cylinders. Colloids were suspended in 1 L of 1.67 mM Na_2CO_3/$NaHCO_3$ buffer solutions (pH 10). Colloids were left to settle for three months, and samples were periodically taken to determine colloid concentration in the supernatant. Each time, a 10-mL sample was taken with a pipet at 15-cm depth.

All batch colloid stability experiments were performed in triplicate, except for the study of the effect of colloid concentration, which was done in duplicate. For the determination of the colloid stability, we define the CCC operationally as the electrolyte concentration at which the turbidity of the suspension fell below 20% of the mass concentration of a noncoagulating suspension (*9*). Colloid concentrations were determined with turbidity measurements at a wavelength of 300 nm using a spectrophotometer (HP 8452A, Hewlett-Packard).

Dynamic Light Scattering. We used dynamic light scattering to determine the rate of colloid aggregation. Hydrodynamic *Z*-averaged diameters were measured with a helium−neon laser of 633 nm wavelength and fixed scattering angle of 90° (ZetaSizer 3000 HSA, Malvern Instruments Ltd., Malvern, UK) at 20 °C. The colloid concentrations were 10−25 mg/L. The colloid suspension was adjusted to the desired electrolyte concentration and immediately analyzed with light scattering. The cuvette was thoroughly cleaned both inside and outside between individual measurements with Nanopure water and 2-propanol. The auto-correlation function was accumulated for 50 s, and was repeated up to a total duration of 70 min.

The stability ratio W is defined as the ratio of fast to slow aggregation rates (*13*)

$$W = \frac{k_{a,\text{fast}}}{k_a} \tag{1}$$

where $k_{a,\text{fast}}$ and k_a are the fast and slow aggregation rates, respectively. It is convenient to use the inverse of the stability ratio, as W^{-1} is equivalent to the collision efficiency in colloid deposition (*21*). The W^{-1} can be calculated as (*13*, *14*)

$$\frac{1}{W} = \frac{n_{\text{fast}}}{n} \frac{\dfrac{d\ \ln R_h}{dt}}{\left(\dfrac{d\ \ln R_h}{dt}\right)_{\text{fast}}} \tag{2}$$

where n_{fast} and n are the initial particle number concentration in the fast and slow aggregation regimes, respectively, and R_h is the hydrodynamic radius measured by light scattering.

The CCC is obtained when fast and slow aggregation rates are equal, i.e., when the stability ratio $W \approx 1$ (*3*). Grolimund et al. (*21*) proposed an empirical equation to determine the CCC from stability ratio data

$$\frac{1}{W} = \frac{1}{1 + \left(\dfrac{CCC}{C_s}\right)^{\beta}} \tag{3}$$

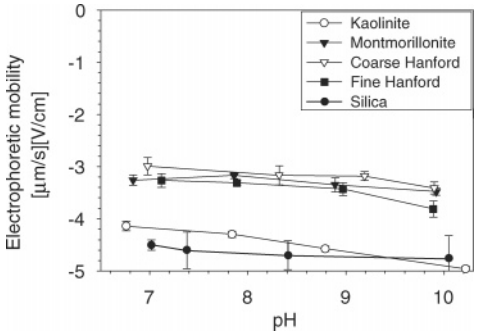

FIGURE 1. Electrophoretic mobility between pH 7 and 10 for the colloids used in this study. Error bars denote ± one standard deviation. Electrophoretic mobilities were determined in 0.01 M NaCl with dynamic light scattering.

where C_s is the molar electrolyte concentration, and β is the slope $d\ln(1/W)/d\ln(C_s)$ for slow aggregation.

A linear (for slow aggregation) and a third-order polynomial (for fast aggregation) were fitted to the experimental data to obtain the slope $d\ln R_h/dt$ needed in equation 2. The slope for fast aggregation was obtained when the aggregation rate $k_{a,\text{fast}}$ was independent of the electrolyte concentration (*13*). The initial particle concentrations n and n_{fast} were calculated from the colloid mass concentration and the initial average hydrodynamic diameter. The inverse stability ratio W^{-1} was then plotted as a function of electrolyte concentration C_s in a double logarithmic fashion, and these data were used to fit equation 3 to obtain the CCC and the slope β.

Results and Discussion

Colloid Characterization and Hanford Pore Water Composition. Scanning electron micrographs of the Hanford colloids show predominantly particles with a platy morphology, characteristic of 1:1 and 2:1 layered aluminosilicate clays. According to the XRD analysis, the Hanford colloids consist dominantly of quartz, illite, smectite, chlorite, kaolinite, and albite. The colloids from the coarse sediments were richer in mafic minerals than those from the fine sediments. Coarse Hanford colloids also contained the mafic minerals ilmenite, magnetite, and Ca-plagioclase. The coarse sediments contained ≈1.5% colloids by weight, and the fine sediments contained ≈3%. All colloids used in this study had a net negative charge in the pH range of 6.6 to 10, indicated by the negative electrophoretic mobility (Figure 1). The electrophoretic mobility did not change much between pH 6.5 and 10 for any of the colloids. Colloid diameters ranged from 490 to 590 nm (Table B, Supporting Information).

Cation compositions of the pore water in the Hanford sediments determined with different methods are shown in Table 1. Our measured cation concentrations generally agree with data from Serne et al. (*16*), except for the Na concentrations, which were much higher for our samples. Consequently, the SAR values for our samples were larger than those from Serne at al. (*16*). With respect to the equilibrium concentrations of the bivalent cations, calculated with MINTEQ, the experimentally measured Ca was oversaturated with respect to calcite and the experimentally measured Mg was undersaturated with respect to calcite and magnesite.

Colloid Stability. *Batch Turbidity Experiments.* The stability of the colloid suspensions differed among the minerals and sediments used. For Na systems (SAR = ∞), the montmorillonite suspension was the least stable and the kaolinite suspension was the most stable system (Figure 2a). The colloids from coarse Hanford sediments appear to be somewhat more stable than those from fine Hanford sediments (Figure 2) and the CCC values were higher for coarse than for fine Hanford sediments (Table 2). The Hanford colloids were more stable than the pure montmorillonite for Na (SAR = ∞), but equally or less stable than montmorillonite for Ca (SAR = 0) systems. We did not determine the stability of kaolinite in pure Ca-systems (SAR = 0), because without the presence of Na, no stable kaolinite suspensions could be obtained. According to the Schulze−Hardy rule for symmetric electrolytes (*22*, *23*) the CCC ratio for NaCl to $CaCl_2$ is 42. The observed deviations of the CCC ratio from the theoretical value (Table 2) can be explained by particle polydispersity, surface charge heterogeneity, and surface morphology (*21*).

Colloid stability as a function of SAR is depicted in Figure 3. As the SAR increased, the colloid concentration versus cation concentration curves became less steep, which makes the CCC determination less accurate. The CCC values show that for SAR = 0 to 60 mmol_c/L, coarse and fine Hanford colloids have the same CCCs, but at SAR > 60 mmol_c/L, the coarse Hanford colloids were more stable than the fine Hanford colloids.

Initial colloid concentration affected the colloid stability, with the colloid suspensions becoming more stable as the initial colloid concentrations decreased (Figure 4). The CCC clearly increased as colloid concentration decreased. A sharp concentration decline is observed for initial concentrations of 100−270 mg/L, and the corresponding CCCs are well defined. At colloid concentration less than 50 mg/L, the relative colloid concentrations decrease gradually over a large range of electrolyte concentrations. For 10 and 25 mg/L initial colloid concentrations, the CCC was not reached in our experiments (Figure 4).

The results of the batch turbidity experiments highlight that, in case of polydisperse, natural colloids, colloid stability determinations depend on initial colloid concentrations and the duration of the experiment. The higher the initial colloid concentrations and the longer the duration of the settling period, the smaller will be the experimentally determined CCC (Figure A, Supporting Information). Critical coagulation concentrations from batch experiments therefore need to be evaluated based on the specific experimental conditions used, e.g., initial colloid concentration and duration of the experiment. Critical coagulation concentrations reported in the literature are difficult to compare with our measurements, because most investigators used much higher colloid concentrations. Corroborating our observation of a lower CCC at higher colloid concentration, reported kaolinite CCCs for Na (at pH 9 to 10 and 10 000 mg/L colloid concentrations) are between 10 and 40 mmol_c/L (*8*), as compared to >100 mmol_c/L in our experiments.

The stability of the colloids in synthetic Hanford pore water is illustrated in Figure 5. We plot colloid stability versus the sum of Ca and Mg concentrations for a given concentration of Na in the system. The Na and Ca concentrations cover the range of concentrations observed in the vadose zone Hanford sediments (Table 1). The results illustrate that both SAR and the absolute values of Na and Ca concentrations determine the colloid stability. The higher the Na concentration, the higher will be the SAR where colloids become unstable. In Figure 5, we also plot the approximate pore water composition of vadose zone Hanford sediments as determined from boreholes at the Hanford site (Table 1, (*16*)). These results suggest that conditions in Hanford sediments are such that colloids can likely form stable suspensions, as most of the measured pore waters lie in the stable regime.

The long-term colloid stability experiment in low ionic strength Na systems (7 mmol_c/L Na) indicates that a considerable amount of colloids can remain in suspension for an extensive period of time (Figure 6). After 113 days, most of the colloids had settled out from the suspension, but a measurable fraction remained suspended. Although this suspended fraction was less than our experimental quan-

TABLE 1. Electrolyte Composition of Porewater of Vadose Zone Hanford Sediments at 20 °C

solid phase	Na ($mmol_c/L$)	K ($mmol_c/L$)	Ca ($mmol_c/L$)	Mg ($mmol_c/L$)	pH (1:1 w/w H_2O)	SAR ($\sqrt{mmol_c/L}$)
1:1 Solution Extracts						
coarse Hanford sediment	5.38	0.30	0.63	0.22	7.8−8.2	8.25
fine Hanford sediment	6.38	0.32	0.89	0.37	8.2−8.3	8.04
RCRA borehole, 299-W22-48[a]	0.62−1.26	0.07−0.12	0.30−0.54	0.09−0.29	7.2−8.0	1.07−2.63
RCRA borehole, 299-W22-50[a]	0.48−1.22	0.07−0.26	0.26−0.96	0.00−0.35	7.0−10.3	1.02−1.91
MINTEQ Simulations[b]						
calcite	0	0	0.234	0	9.9	na[c]
calcite and magnesite	0	0	0.057	0.596	10.2	na
calcite and kaolinite	0	0	0.270	0	9.7	na
calcite, magnesite, and kaolinite	0	0	0.063	0.662	10.1	na
calcite, magnesite, and gypsum	0	0	9.64	101	9.0	na
calcite, magnesite, kaolinite, and gypsum	0	0	9.64	101	8.9	na

[a] Resource Conservation and Recovery Act borehole, Hanford formation sediments, data are from Serne et al. (*16*). [b] Pore water concentrations in equilibrium with the solid phase at 0.00035 atm CO_2. [c] na: not applicable.

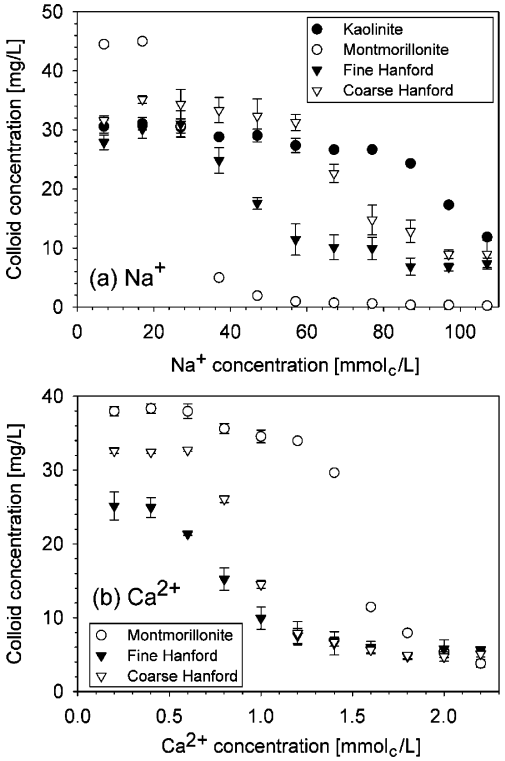

FIGURE 2. Colloid stability at pH 10 as a function of (a) Na concentrations (SAR = ∞) and (b) Ca concentrations (SAR = 0). Settling time was 19 h. Error bars denote ± one standard deviation.

TABLE 2. Critical Coagulation Concentrations (CCC) for the Different Colloids Using the Batch Turbidity Method

colloid type	CCC_{NaCl} ($mmol_c/L$)	CCC_{CaCl_2} ($mmol_c/L$)	CCC_{NaCl}/CCC_{CaCl_2}
kaolinite	>100	na[a]	na
montmorillonite	35	1.8	19
coarse Hanford	100	1.4	71
fine Hanford	70	1.8	39

[a] na: not available.

tification limit, we still could detect the presence of these colloids. The long-term experiment suggests that the "shelf life" of the colloids was in the order of several weeks (at pH 10 and 7 $mmol_c$/L Na, which represents an optimal solution chemistry for colloid stability).

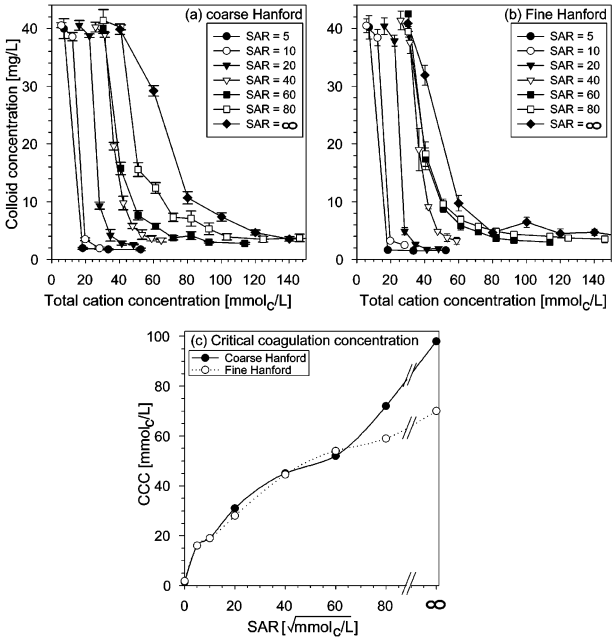

FIGURE 3. Effect of sodium adsorption ratio (SAR) on colloid stability of Hanford colloids at pH 10. (a) Coarse Hanford colloids, (b) fine Hanford colloids, and (c) critical coagulation concentrations (CCC) as a function of SAR. Settling time was 19 h. Error bars denote ± one standard deviation.

We fitted the data with a second-order aggregation model (*24*)

$$\frac{dn}{dt} = -kn^2 \tag{4}$$

where n is the colloid number concentration, and k is the aggregation rate coefficient. The model fit the data closely (Figure 6). For spherical, monodisperse particles, the rate constant k is related to the collision efficiency α by (*24*)

$$k = \alpha\frac{4k_BT}{3\eta} \tag{5}$$

where k_B is the Boltzmann constant, T is absolute temperature, and η is dynamic viscosity. The rate coefficient and collision efficiencies (Table 3) indicate that the colloidal suspensions were stable, i.e., in the slow aggregation regime. Nonetheless, after several weeks of aggregation, most of the colloids were aggregated and settled out from the suspension.

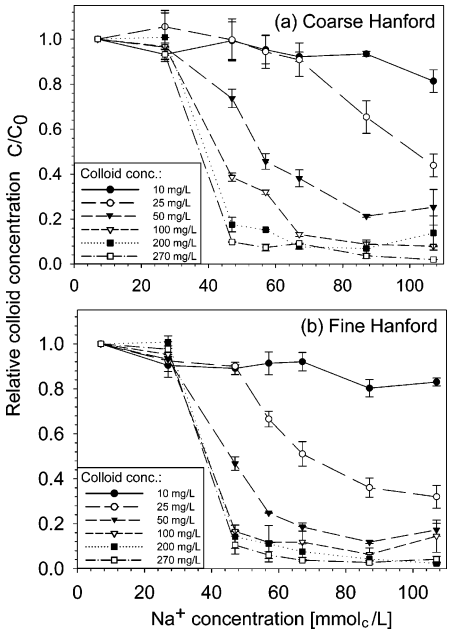

FIGURE 4. Effect of initial colloid concentration on colloid stability in Na electrolyte solutions (SAR = ∞) at pH 10 for (a) coarse and (b) fine Hanford colloids. Colloid concentrations are normalized with the initial colloid concentration in each experiment. Settling time was 19 h. Error bars denote ± one standard deviation.

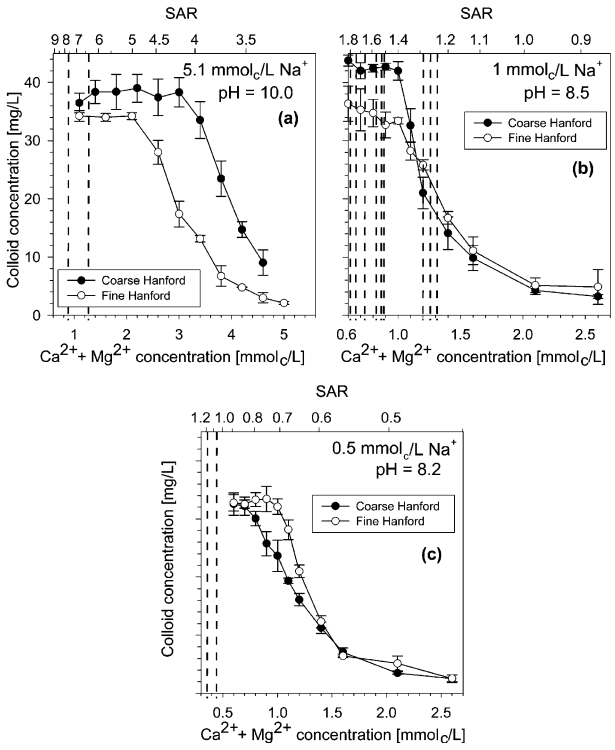

FIGURE 5. Colloid stability in mimicked Hanford pore waters for different Ca concentrations at three constant Na concentrations: (a) 5.1 mmol$_c$/L, (b) 1 mmol$_c$/L, and (c) 0.5 mmol$_c$/L. Settling time was 19 h. Concentrations of K and Mg were kept constant at 0.2 mmol$_c$/L K and 0.6 mmol$_c$/L Mg. Dashed lines indicate Ca and Mg concentrations in vadose zone Hanford sediments measured by Serne et al. (*16*), and represent in situ pore water chemistry from several boreholes (Table 1).

Dynamic Light Scattering. The results of the dynamic light scattering experiments are summarized in Figure 7. At small electrolyte concentrations, where the inverse stability ratio increases monotonically, aggregation occurs slowly. At larger

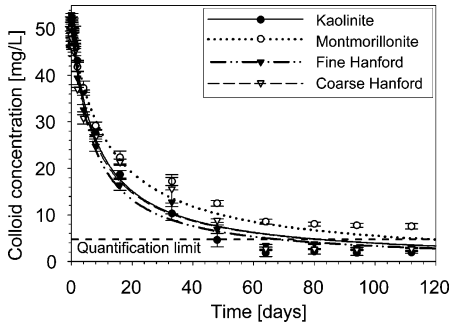

FIGURE 6. Colloid suspension concentration as a function of time in the long-term batch experiments in a pH 10 buffered 1.67 mM Na_2CO_3/$NaHCO_3$ solution. Symbols are experimental data and lines are fitted second-order aggregation model. Error bars denote ± one standard deviation.

electrolyte concentrations, aggregation is fast, and the stability ratio becomes independent of electrolyte concentration. The stability plots indicate that the silica beads were the most stable colloidal system, and the montmorillonite was the least stable in both the Na and Ca electrolytes. Silica beads and kaolinite had the most negative electrophoretic mobility of all colloids used (Figure 1). Less negative electrophoretic mobility, heterogeneous charge distribution, and polydispersity are likely reasons for the lower stability of the montmorillonite. The coarse and fine Hanford colloids had similar stabilities, and their stability was intermediate between the silica and the montmorillonite. This intermediate stability is likely because the Hanford colloids are a mixture of quartz, aluminosilicates, and other minerals.

Equation 3 fitted the experimental data well (Figure 7), and the fitted CCC and β values are listed in Table 3. The ratios of the Na- to Ca-CCC were between 50 and 54, which is somewhat higher than the theoretical value of 42 (*22*, *23*). Grolimund et al. (*21*) determined a ratio of 40 for colloids from a noncalcareous forest soil, but large deviations from the theoretical values are not uncommon (*25*).

The CCCs (at pH 5.7) of the noncalcareous colloids reported by Grolimund et al. (*21*) were similar but slightly higher for both Na and Ca (i.e., 155 and 3.2 mmol/L, respectively) than our values for the calcareous Hanford colloids (Table 3). Dynamic light scattering studies with pure minerals have been reported by others (*15*, *26*), but electrolytes different from NaCl and $CaCl_2$ were used, so that direct comparisons with our data are difficult. Kretzschmar et al. (*15*) demonstrated the strong dependence of kaolinite stability on pH and organic coatings.

The slopes β of the stability curves (Table 3) were considerably steeper than the slopes reported by Grolimund et al. (*21*), who reported slopes of 3.8 for NaCl and 2.3 for $CaCl_2$. In our experiments, the ratio of the NaCl to $CaCl_2$ slopes was about 0.5, which is much less than the ratio of 1.6 reported by Grolimund et al. (*21*). It is theoretically expected that the slopes for Na systems are steeper than those for Ca systems (*21*, *25*), but our measurements showed the opposite result.

The theory of light scattering assumes that colloids and aggregates are spherical and monodisperse. These assumptions are not met in experiments with natural colloids. Consequently, light scattering data will not yield accurate coagulation rates and have to be interpreted with caution. Aggregation further increases polydispersity and makes light scattering data less reliable. This can be a reason for the difference in slopes observed in our experiments. The observed deviation of the CCC ratio for NaCl and $CaCl_2$ from the theoretical value, however, cannot be solely attributed to polydispersity and nonsphericity. The monodisperse,

TABLE 3. Rate Coefficients (k) and Collision Efficiencies (α) of Second-Order Aggregation Model (Eqs 4 and 5), and Critical Coagulation Concentrations (CCC) and Slope (β) of the Stability Curves for the Different Colloids Using the Light Scattering Method (Eq 3)

colloid type	k (m^3/s)	α	CCC_{NaCl} (mmol/L)	CCC_{CaCl_2} (mmol/L)	CCC_{NaCl}/CCC_{CaCl_2}	β_{NaCl}	β_{CaCl_2}	$\beta_{NaCl}/\beta_{CaCl_2}$
silica	na	na	203	3.8	53	6.1	9.6	0.6
kaolinite	1.63×10^{-17}	8.26×10^{-4}	188	na[a]	na	4.0	na	na
montmorillonite	0.99×10^{-17}	5.02×10^{-4}	92	1.7	54	3.5	6.6	0.5
coarse Hanford	2.81×10^{-17}	1.42×10^{-3}	139	2.8	50	4.4	8.2	0.5
fine Hanford	2.79×10^{-17}	1.41×10^{-3}	148	2.8	53	4.7	9.2	0.5

[a] na: not available.

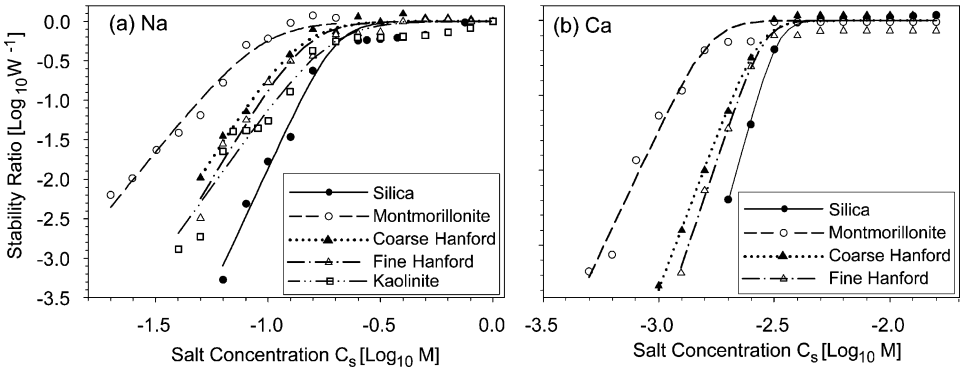

FIGURE 7. Inverse stability ratio W^{-1} at pH 10 as a function of (a) Na and (b) Ca concentration. The symbols indicate the experimentally determined values (eq 2), and the lines are best fits of eq 3.

spherical silica in our experiments did not show a CCC ratio closer to the expected value than the clay mineral colloids (Table 3).

Comparison of Methods to Determine Critical Coagulation Concentrations. The comparison of the CCCs determined by batch turbidity and light scattering methods indicates the arbitrariness of the batch turbidity method (Tables 2 and 3). The CCC determined with the batch turbidity method very much depended on the CCC criteria used. The dynamic light scattering CCCs were considerably greater than the batch turbidity CCCs for the 80% removal criteria. The light scattering measurements yielded more consistent CCC_{NaCl}/CCC_{CaCl_2} ratios than the batch turbidity method, and the ratios were closer to the theoretically expected value of 42 (*22*). As the light scattering method does not depend on specific experimental conditions, this method is the preferred technique to determine CCCs.

According to both the batch turbidity and the dynamic light scattering results, the CCC of natural Hanford colloids was intermediate between that of the kaolinite and montmorillonite clay mineral standards. This suggests that the clay mineral standards can be used to bracket the behavior of natural Hanford colloids. In contrast to the batch studies, the light scattering studies did not reveal differences in colloidal stability between coarse and fine Hanford colloids.

Implications

Many of the radioactive contaminants sorb strongly to subsurface minerals and are therefore considered fairly immobile. Colloids can potentially facilitate the movement of such contaminants, provided colloids are present, sorb contaminants strongly, form stable suspensions, and are mobile in the subsurface. All of these conditions must be met if colloid-facilitated transport is a relevant transport mechanism.

The results of our colloid stability experiments and the measured pore water compositions in vadose zone Hanford sediments indicate that colloids likely form stable suspensions in vadose zone Hanford sediments. However, the colloidal stability, as defined by the CCC, does not necessarily imply that colloids stay suspended for sufficiently long times to play a relevant role for contaminant transport. Long-term stability experiments indeed indicated that colloids from the Hanford sediments will form stable suspensions for several weeks, but over longer time periods, colloids will settle out from suspension. After about 16 weeks, on average 90% of the colloidal mass settled out from suspension.

Measured recharge rates at Hanford range from near 0 to more than 100 mm/year, depending on variation in precipitation, soil type, and vegetation cover (*27*). One of the most contaminated locations at Hanford, the waste tank area, has some of the highest recharge rates, because of the coarse-textured sediment used for backfill and the absence of vegetation. In addition, the "umbrella effect", i.e., the runoff and redirection of water due to the presence of the tanks, enhances the local recharge rates. The thickness of the Hanford vadose zone where the waste tanks are located varies from 40 to 100 m (*28*, *29*). Assuming the worst-case scenario of a shallow vadose zone (40-m thickness), a high recharge rate (100 mm/year), and an average volumetric water content of 10%, the travel time of the recharge water is 40 years. Over this time period, colloidal suspensions at the Hanford site will not be stable. Estimations based on measured aggregation rates show that after 40 years only up to 0.08% of the initially suspended colloids remain in suspension.

Under natural conditions, the potential for colloid mobilization and stable colloid suspensions is greatest during infiltration events, when low ionic strength rainwater increases soil moisture. As the water drains to deeper depths, the changes in moisture dampen and the ionic strength increases due to equilibration with soil mineral phases. Our experiments and conclusions regarding colloidal stability were based on these equilibrium ionic strengths, and are therefore representative for the deeper vadose zone at Hanford. In addition to colloid aggregation and sedimentation in suspension, colloids will also be removed from the solution phase by filtration mechanisms in the sediments. As we have shown in previous experiments (*30*), colloids will

be retained considerably during transport in water-unsaturated Hanford sediments. Taken together, colloid aggregation and filtration seem to be favored at Hanford.

Nonetheless, aggregated colloids can be remobilized when the ionic strength decreases (*31*) or when flow rates increase. At certain locations at the Hanford site, the natural recharge has been disturbed considerably. For instance, at the tank farms, water leaks and fluids from the tanks themselves, in addition to the "umbrella effect", have increased infiltration rates and provided an enhanced water flux (*32*) and possibly preferential flow. Under such conditions, travel times in the vadose zone are considerably reduced, and the potential for colloid movement is enhanced.

Acknowledgments

We thank Glendon Gee for helpful comments, and Jeff Boyle, Jon Mathison, and Ron Bolton for help with the experiments. This research was supported by the Office of Science (BER), U.S. Department of Energy, Grant DE-FG07-05ER62882, and by the Inland Northwest Research Alliance.

Supporting Information Available

Experimental electrolyte concentrations, selected colloidal properties, and a figure showing the effect of settling time on colloid stability in batch experiments are available as supporting information (pdf). This material is available free of charge via the Internet at http://pubs.acs.org.

Literature Cited

(1) National Research Council. *Science and Technology for Environmental Cleanup at Hanford*; National Academy Press: Washington DC, 2001.

(2) Kersting, A. B.; Efurd, D. W.; Finnegan, D. L.; Rokop, D. J.; Smith, D. K.; Thompson, J. L. Migration of plutonium in groundwater at the Nevada Test Site. *Nature* **1999**, *397*, 56−59.

(3) Hiemenz, P. C.; Rajagopalan, R. *Principles of Colloid and Surface Chemistry*, 3rd ed.; Marcel-Dekker: New York, 1997.

(4) Keren, R.; Shainberg, I.; Klein, E. Settling and flocculation value of sodium-montmorillonite particles in aqueous media. *Soil Sci. Soc. Am. J.* **1988**, *52*, 76−80.

(5) Miller, W. P.; Frenkel, H.; Newman, K. D. Flocculation concentration and sodium/calcium exchange of kaolinitic soil clays. *Soil Sci. Soc. Am. J.* **1990**, *54*, 346−351.

(6) Permien, T.; Lagaly, G. The rheological and colloidal properties of bentonite dispersions in the presence of organic compounds. III. The effect of alcohols on the coagulation of sodium montmorillonite. *Colloid Polym. Sci.* **1994**, *272*, 1306−1312.

(7) Swartzen-Allen, S. L.; Matejevic, E. Colloid and surface properties of clay suspensions. III. Stability of montmorillonite and kaolinite. *J. Colloid Interface Sci.* **1976**, *56*, 159−167.

(8) Goldberg, S.; Forster, H. S.; Heick, E. L. Flocculation of illite/kaolinite and illite/montmorillonite mixtures as affected by sodium adsorption ratio and pH. *Clays Clay Miner.* **1991**, *39*, 375−380.

(9) Goldberg, S.; Forster, H. S. Flocculation of reference clays and arid-zone soil clays. *Soil Sci. Soc. Am. J.* **1991**, *54*, 714−718.

(10) van Olphen, H. *An Introduction to Clay Colloid Chemistry*, 2nd ed.; John Wiley: New York, 1977.

(11) Kretzschmar, R.; Robarge, W. P.; Weed, S. B. Flocculation of kaolinitic soil clays—effects of humic substances and iron oxides. *Soil Sci. Soc. Am. J.* **1993**, *57*, 1277−1283.

(12) Virden, J. W.; Berg, J. C. The use of photon correlation spectroscopy for estimating the rate constant for doublet formation in an aggregating colloidal dispersion. *J. Colloid Interface Sci.* **1992**, *149*, 528−535.

(13) Holthoff, H.; Egelhaaf, S. U.; Borkovec, M.; Schurtenberger, P.; Sticher, H. Coagulation rate measurement of colloidal particles by simultaneous static and dynamic light scattering. *Langmuir* **1996**, *12*, 5541−5549.

(14) Behrens, S. H.; Christl, D. I.; Emmerzael, R.; Schurtenberger, P.; Borkovec, M. Charging and aggregation properties of carboxyl latex particles: Experiments versus DLVO theory. *Langmuir* **2000**, *16*, 2566−2575.

(15) Kretzschmar, R.; Holthoff, H.; Sticher, H. Influence of pH and humic acid on coagulation kinetics of kaolinite: A dynamic light scattering study. *J. Colloid Interface Sci.* **1998**, *202*, 95−103.

(16) Serne, R. J.; Bjornstad, B. N.; Schaef, H. T.; Williams, B. A.; Lanigan, D. C.; Horton, D. G.; Clayton, R. E.; Mitroshkov, A. V.; LeGore, V. L.; O'Hara, M. J.; Brown, C. F.; Parker, K. E.; Kutnyakov, I. V.; Serne, J. N.; Last, G. V.; Smith, S. C.; Lindenmeier, C. W.; Zachara, J. M.; Burke, D. S. *Characterization of Vadose Zone Sediment: Uncontaminated RCRA Borehole Core Samples and Composite Samples*; Pacific Northwest National Laboratory, U.S. Department of Energy, PNNL-13757-1; Richland, WA, 2002.

(17) McGraw, M. A.; Kaplan, D. I. *Colloid Suspension Stability and Transport through Unsaturated Porous Media*; Pacific Northwest National Laboratory, PNNL-11565; Richland, WA, 1997.

(18) Deju, R. A.; Fecht, K. R. *Preliminary Description of Hydrologic Characteristics and Contminant Transport Potential of Rocks in the Pasco basin—South-Central Washington*; RHO-BW1-LD-20; Rockwell Hanford Operations: Richland, WA, 1973.

(19) Rhoades, J. D. Salinity: Electrical conductivity and total dissolved solids. In *Methods of Soil Analysis. Part 3. Chemical Methods*, 3rd ed.; Klute, A., Ed.; American Society of Agronomy: Madison, WI, 1996; pp 417−435.

(20) Allison, J.; Brown, D.; Novo-Gradac, K. *MINTEQA2/PRODEFA2. A Geochemical Assessment Model for Environmental Systems, v. 3.0 User's Manual*; U.S. EPA: Athens, GA, 1991.

(21) Grolimund, D.; Elimelech, M.; Borkovec, M. Aggregation and deposition kinetics of mobile colloidal particles in natural porous media. *Colloids Surf. Physicochem. Eng. Aspects* **2001**, *191*, 179−188.

(22) Hsu, J.-P.; Kuo, Y.-C. An extension of the Schulze-Hardy rule to asymmetric electrolytes. *J. Colloid Interface Sci.* **1995**, *171*, 254−255.

(23) Hsu, J.-P.; Kuo, Y.-C. The critical coagulation concentration of counterions: Spherical particles in asymmetric electrolyte solutions. *J. Colloid Interface Sci.* **1997**, *185*, 530−537.

(24) Stumm, W.; Morgan, J. J. *Aquatic Chemistry*, 2nd ed.; John Wiley & Sons: New York, 1981.

(25) Elimelech, M.; Gregory, J.; Jia, X.; Williams, R. A. *Particle Deposition and Aggregation: Measurement, Modelling, and Simulation*; Butterworth-Heinemann: Oxford, 1995.

(26) Novich, B. E.; Ring, T. A. Colloid stability of clays using photon correlation spectroscopy. *Clays Clay Miner.* **1984**, *32*, 400−406.

(27) Gee, G. W.; Fayer, M. J.; Rockhold, M. L.; Campbell, M. D. Variations in recharge at the Hanford site. *Northwest Sci.* **1992**, *66*, 237−250.

(28) Gee, G. W.; Heller, P. R. *Unsaturated Water Flow at the Hanford Site: A Review of Literature and Annotated Bibliography*; Pacific Northwest National Laboratory: Richland, WA, 1985.

(29) McKinley, J. P.; Zeissler, C. J.; Zachara, J. M.; Serne, R. J.; Lindstrom, R. M.; Schaef, H. T.; Orr, R. D. Distribution and retention of Cs-137 in sediments at the Hanford Site, Washington. *Environ. Sci. Technol.* **2001**, *35*, 3433−3441.

(30) Cherrey, K. D.; Flury, M.; Harsh, J. B. Nitrate and colloid transport through coarse Hanford sediments under steady-state, variably-saturated flow. *Water Resour. Res.* **2003**, *39*, 1165. doi:10.1029/2002WR001944.

(31) Flury, M.; Mathison, J. B.; Harsh, J. B. In situ mobilization of colloids and transport of cesium in Hanford sediments. *Environ. Sci. Technol.* **2002**, *36*, 5335−5341.

(32) Lichtner, P. C.; Yabusaki, S.; Pruess, K.; Steefel, C. I. Role of competitive cation exchange on chromatographic displacement of cesium in the vadose zone beneath the Hanford S/SX tank farm. *Vadose Zone J.* **2004**, *3*, 203−219.

Received for review August 17, 2004. Revised manuscript received December 4, 2004. Accepted December 13, 2004.

ES048714N

Suitability of Fiberglass Wicks to Sample Colloids from Vadose Zone Pore Water

Szabolcs Czigány, Markus Flury,* James B. Harsh, Barbara C. Williams, and Jason M. Shira

ABSTRACT

Fiberglass wicks are frequently used to sample pore water and determine water fluxes in soils. In this study we evaluated the performance of fiberglass wicks to sample colloids. Different colloids were used for the wick testing: feldspathoids, ferrihydrite, montmorillonite, kaolinite, and a mixture of mineral colloids extracted from a coarse calcareous sediment. The colloids were dispersed in either a buffered Na_2CO_3–$NaHCO_3$ solution (ionic strength 6.7 m*M*, pH 10) or deionized water. Colloid breakthrough curves through 77-cm-long fiberglass wicks were determined for three different flow rates. Flow rate, pH, and colloid type affected colloid breakthrough. Colloid recovery in the effluent was higher at pH 10 than at pH 7, and increased with increasing flow rate. The mixture of mineral colloids extracted from sediment moved almost conservatively through the wicks; the colloid recoveries ranged from 88 to about 100% for pH 7 and 10, respectively. Ferrihydrite at pH 10 moved conservatively, with recoveries ranging from 95 to about 100%. All other colloids, however, showed lower mass recoveries. At pH 10, colloid recovery ranged from 55% for montmorillonite to about 100% for ferrihydrite and the mixture of mineral colloids, whereas at pH 7, the recovery ranged from <5% for kaolinite and ferrihydrite to approximately 100% for the mixture of mineral colloids. These results suggest that for certain conditions and colloid types, fiberglass wicks can be an acceptable tool for colloid sampling in the vadose zone. However, under many conditions studied here colloids were significantly retained inside the wicks, and consequently, the use of wicks for colloid sampling in the vadose zone must be considered with caution.

DIFFERENT TECHNIQUES are used to sample pore water in the vadose zone, such as free-drainage lysimeters, suction cups or porous plates, and fiberglass wicks or rockwool samplers. Each of these devices has advantages and disadvantages. Free-drainage lysimeters only operate when the soil becomes saturated, and thereby cause hydrodynamic artifacts (Abdou and Flury, 2004). These artifacts are eliminated when using a porous material on which a suction is pulled to remove the pore water from the soil. Different types of porous materials have been used for that purpose, including ceramic materials, stainless steel, Teflon, or fiberglass.

Fiberglass wicks are attractive because no external vacuum device is needed to extract pore water. They were introduced as pore water samplers by Brown et al. (1986) and have been used since in numerous studies (Gee and Campbell, 1990; Boll et al., 1992; Brandi-Dohrn et al., 1996; Louie et al., 2000; Brahy et al., 2002; Cox et al., 2002). The volume of the soil sampled by the wicks can be closely estimated (Boll et al., 1991). Wick lysimeters are relatively inexpensive and easy to maintain. The length of the hanging wick determines the suction exerted on the soil above, and it needs to be matched with the soil type and the particular experiment (Rimmer et al., 1995). Wick lysimeters can collect pore water samples from soils with a wide range of structure (Holder et al., 1991).

Fiberglass wicks need to be cleaned before their use for sampling, as they may contain organic residues (Knutson et al., 1993). Knutson et al. (1993) recommended combustion at 400°C for 3 h to remove impurities, unless the wicks contain more than 3.5% (w/w) impurities, for which higher temperature and longer combustion time may be needed. Additional treatments, such as an acid wash in 10-m*M* HNO_3, may be required if wicks are used to determine pore water composition (Goyne et al., 2000). Brahy and Delvaux (2001) suggested that, besides acid treatment, the wicks should be soaked in deionized water until the electrical conductivity of the water falls below 2 $\mu S\ cm^{-1}$.

Wicks have been tested extensively in terms of water and solute collection efficiency (Boll et al., 1991; Steenhuis et al., 1995; Zhu et al., 2002). Experimental and numerical studies indicate that wicks are useful in determining water fluxes in the vadose zone (Louie et al., 2000; Gee et al., 2002, 2003). Solute transport characteristics of wicks were assessed with anions and organic dyes, and it is generally reported that dispersion and retardation is much smaller in wicks than in soils (Boll et al., 1992; Poletika et al., 1992; Knutson and Selker, 1996). Only a few studies are available on colloid transport in fiberglass wicks. The results of these studies are inconsistent in terms of the usefulness of wicks for colloid sampling. Poletika et al. (1992) reported that only 28.8 to 52% of an MS-2 virus was recovered in wick outflow. Biddle et al. (1995) found that colloids of particle diameters between 0.45 and 2 μm were not retained in the wicks, and colloid mineral composition in the effluent did not differ from that of the bulk soil. It remains to be shown whether fiberglass wicks are useful to sample colloids.

The objective of this study was to systematically test fiberglass wicks for their suitability to sample vadose zone colloids. We conducted transport experiments with five types of colloids: kaolinite, montmorillonite, ferrihydrite, feldspathoids, and colloids extracted from a calcareous sediment. Colloids were directly applied to the top of the wicks, and breakthrough curves determined in the outflow. Solution pH was either 7 or 10, and three different flow rates were used.

MATERIALS AND METHODS

Colloidal Material and Fractionation

We used different types of colloids in this study: colloids extracted from sediments (mixture of minerals) and mineralogi-

S. Czigány, M. Flury, and J.B. Harsh, Department of Crop and Soil Sciences, Center for Multiphase Environmental Research, Washington State University, Pullman, WA 99164; B.C. Williams and J.M. Shira, Department of Biological and Agricultural Engineering, University of Idaho, Moscow, ID 83844. Received 11 May 2004. Original Research Paper. *Corresponding author (flury@mail.wsu.edu).

Published in Vadose Zone Journal 4:175–183 (2005).

677 S. Segoe Rd., Madison, WI 53711 USA

Abbreviations: SEM, scanning electron microscopy.

cally homogeneous colloids (montmorillonite, kaolinite, and ferrihydrite). The sediments used as colloidal source material were gravelly-sandy, very coarse Hanford sediments obtained from the submarine pit (218-E-12B) at the Hanford Site, WA in January 2000. Serne et al. (2002) provided a detailed description of the Hanford formation sediments. The mineralogy of the sediments is dominated by quartz, phyllosilicates (primarily micas, illites, and smectites), and feldspars. Plastic buckets were used to collect and store the sediments. The sediments were air-dried and sieved through a 2-mm square screen. This material served as the source for the "native colloids." An aliquot of the sediments was treated with an alkaline solution, which caused quartz and kaolinite to dissolve and the feldspathoids, cancrinite and sodalite, to precipitate (Zhao et al., 2004). These treated sediments served as a source for the "modified colloids." Pure clay mineral standards, Na-montmorillonite (SWy-2) and Na-kaolinite (KGa-1), were obtained from the Clay Minerals Repository (Columbia, MO). Two-line ferrihydrite was synthesized according to Schwertmann and Cornell (2000, p. 105–111), whereby 10 mmol L^{-1} Si was used in the synthesis procedure to stabilize the mineral and prevent mineral transformations. The ferrihydrite was stored in suspension at pH 2 in a Nalgene bottle until it was used. We used X-ray diffraction (Philips XRG 3100, Philips Analytical Inc., Mahwah, NJ) to verify whether the ferrihydrite was mineralogically stable during the experiments. The shape of ferrihydrite particles was examined by Transmission Electron Microscopy (JEOL 1200EX, JEOL, Peabody, MA) and found to be roughly spherical.

To fractionate the colloidal fraction, about 1 kg of Hanford sediments or 200 to 250 mg of clay mineral standards were dispersed in 1-L glass cylinders. We used two different solutions to disperse the solids: (i) deionized water and (ii) a 1.67-m*M* Na_2CO_3/$NaHCO_3$ solution (pH 10). Dispersions were stirred with a rod, sonicated for 10 min, and briefly shaken end-over-end by hand. Colloids, operationally defined as material with an equivalent diameter of <2 μm, were fractionated by decantation based on Stokes' sedimentation law. The mineralogy of the fractionated "native colloids" was dominated by chlorite, smectite, vermiculite, kaolinite, and quartz (Cherrey et al., 2003), and the "modified colloids" were dominated by cancrinite, sodalite, chlorite, smectite, and vermiculite. Ferrihydrite was not fractionated because its particle size was much less than 2 μm.

The colloid suspensions were diluted to a particle concentration of about 50 mg L^{-1} and used for the wick experiments described below. Colloid suspensions were sonicated for 30 min before the start of the wick experiments. Colloids were used within at most 7 d after fractionation. Average hydrodynamic diameter and electrophoretic mobility of the colloids were measured by dynamic light scattering (ZetaSizer 3000HSa, Malvern Instruments Ltd., Malvern, UK) in a weak electrolyte solution (1.67-m*M* $NaHCO_3$/1.67 m*M* Na_2CO_3, pH 10).

Wick Treatment and Characterization

Fiberglass wicks of 12.5-mm diameter were obtained from Pepperell Braiding Co. (catalog no. 1381, Pepperell, MA). We treated the wick with a procedure described by Goyne et al. (2000). The wicks were first cut into 77-cm-long pieces, weighed, and rinsed extensively with deionized water and combusted in a kiln at 400°C for 4 h. The wicks were weighed after combustion to determine the weight loss. Then, they were soaked in deionized water (EC = 3.8 μS cm^{-1}) in a 17-L Tupperware plastic container. Six wicks were treated simultaneously. We measured pH and electrical conductivity daily. Water was replaced with clean deionized water each day until pH and conductivity were constant. It took 5 to 6 d to reach constant pH and electrical conductivity. The equilibrated wicks were then soaked in a 10-m*M* HNO_3 solution in the same container. The solution was replaced daily for 7 d. After the acid treatment, wicks were soaked again in deionized water for 7 d. It took 4 to 6 d to reach a constant pH and EC.

Treated and untreated (as shipped from supplier) wicks were characterized by scanning electron microscopy (SEM) and specific surface area determination. The SEM images were taken on gold-coated samples with a Hitachi S-570 SEM. We also took SEM images of wicks after they were used for colloid transport experiments to check for colloid deposition. For N_2 BET surface area determination, about 5 g of wick material was used (ASAP 2010, Micromeritics Inc., Norcross, GA). The specific density of wicks was measured on individual wick braids with a Le Chatelier pycnometer (ASTM, 2000). The bulk density was approximated by weighing oven-dried pieces of wicks and estimating the volume using a circular wick cross section. The porosity was then calculated from these measurements. Quantitative measurements were made with three replicates.

Experimental Setup for Breakthrough Curves

The wick was mounted into an acrylic tube (18.5-mm i.d., 68.5-cm length) topped by a Plexiglas disk 9 cm in diameter (Fig. 1). The top 4.5 cm of the wick was unwoven, and the individual braids were spread and tightened to the disk with a Plexiglas ring and binder clips. A steady-state flow rate was established by dripping solution onto the center of the wick from a point dripper. The flow rate was controlled with a peristaltic pump (Ismatec IP4, Glattburg, Switzerland). The top of the wick was covered with a plastic beaker and a wrap to minimize evaporation.

Nitrate and Colloid Breakthrough Curves

Nitrate and colloid breakthrough curves were performed at three different flow rates: 5, 10, and 55 mL h^{-1}. First, the wick was equilibrated with at least 12 pore volumes at a flow rate of 55 mL h^{-1}, and the flow rate was then adjusted to the desired value. A new wick was used for each experiment to avoid contamination between experiments. Consequently, the wick pore volume differed slightly from run to run. We ran some experiments with the same wick to check for "history" effects in the wick. All experiments were performed at a room temperature of 22 ± 1°C.

Nitrate was used as a conservative tracer. A pulse of about three pore volumes of 0.2-m*M* $NaNO_3$ was injected into the wicks. Effluent NO_3^- concentrations were determined with a UV-VIS spectrophotometer (Hewlett-Packard HP8452A) at 214-nm wavelength. The pH of the solutions for these experiments was between 6.5 and 7.5.

For the colloid breakthrough experiments, the wicks were first equilibrated for at least 12 pore volumes with the desired solution, either deionized water (pH ≈6.5) or a buffered 1.67-m*M* $NaHCO_3$/1.67-m*M* Na_2CO_3 solution (pH 10). The inflow solution was then switched to an approximately 50 mg L^{-1} colloid suspension for two to four pore volumes. Effluent pH was determined with a pH meter, and colloid concentrations were determined spectrophotometrically at 300-nm wavelength, except the ferrihydrite, which was measured at 214 nm. Before the measurements, individual vials were vigorously shaken by hand to resuspend any sedimented particles. The effluent flow rate was determined by weighing every sixth vial. After each breakthrough experiment, the overall water content of the wicks was determined gravimetrically by drying at 105°C for 24 h. This water content was used to estimate pore volumes for the breakthrough experiments. Some experiments were repeated to test reproducibility of the results.

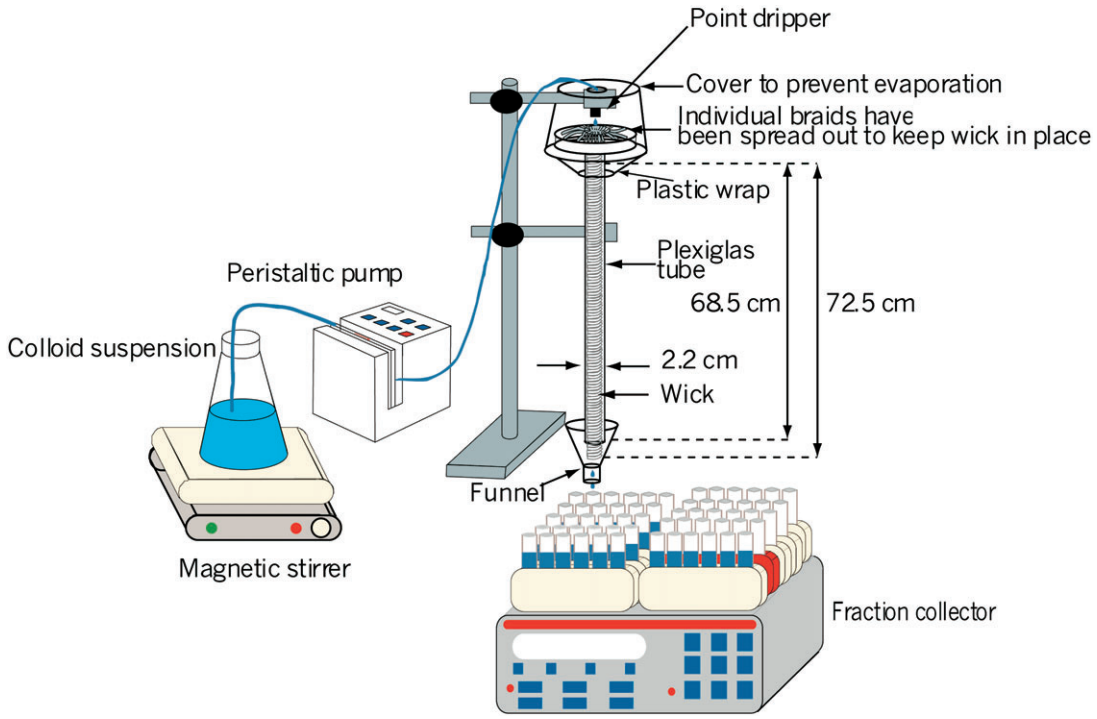

Fig. 1. Experimental setup for the wick experiments.

To obtain more detailed information about the water content distribution in the wicks, we equilibrated clean wicks with colloid-free buffered solution at the three flow rates used for the colloid transport experiments. The wicks were then cut into 11-cm-long pieces, which were oven-dried to determine the water content.

RESULTS AND DISCUSSION

Colloid Properties

The hydrodynamic diameters of the colloids are summarized in Table 1. The hydrodynamic diameters of the colloids ranged from 475 to 620 nm, except for the ferrihydrite, which was smaller (175 nm). The electrophoretic mobilities as a function of pH are shown in Fig. 2. The values depicted in Fig. 2 are in the range typical for soil minerals (Wu, 2001). The kaolinite particles had the most negative electrophoretic mobilities at both pH 7 and 10. At pH 7, the ferrihydrite particles had the least negative electrophoretic mobilities of all colloids. The isoelectric point for ferrihydrite was at pH ≈6.2. Ferrihydrite remained mineralogically stable during the experiments; the X-ray diffraction patterns indicated no mineral transformations.

Table 1. *Z*-averaged hydrodynamic diameters of the colloids used in this study.

Colloid type	*Z*-averaged hydrodynamic diameter†
	mm
Native colloids	497 ± 38
Modified colloids	621 ± 84
Montmorillonite	493 ± 25
Kaolinite	475 ± 44
Ferrihydrite	175 ± 32

† Measured in 1.67-m*M* Na_2CO_3/$NaHCO_3$ at pH 10.

Wick Treatment and Characterization

The weight loss of the wicks during combustion ranged from 0.5 to 1.5% by weight, which is in the lower range reported by Knutson et al. (1993). When the wicks were soaked in deionized water after combustion, the pH of the water increased from 5.7 to 9.2 within the first 24 h. After 4 to 6 d the pH remained constant. The pH of the HNO_3 solution remained fairly constant during soaking. The SEM micrographs show some impurities on the surface of the nontreated wicks (Fig. 3a). The combustion and washing removed these impurities to a large degree, but not completely (Fig. 3b). Some dark spots, likely caused by combustion, could be observed on the treated wicks. The specific surface areas were 0.48 ±

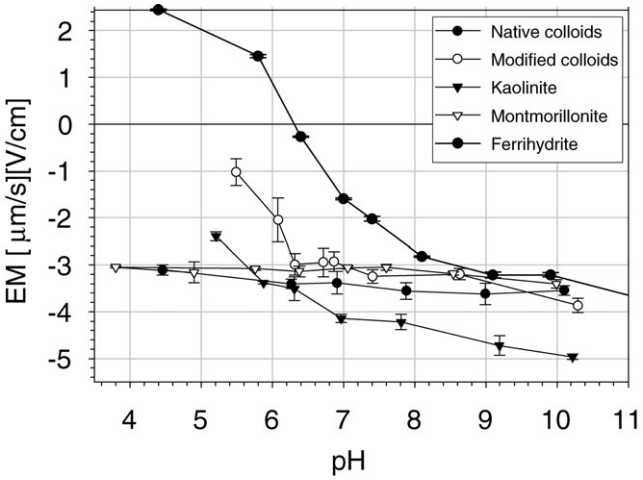

Fig. 2. Electrophoretic mobility of the colloids as a function of pH, measured in a 1.67-m*M* Na_2CO_3/$NaHCO_3$ solution. Error bars denote ± one standard deviation.

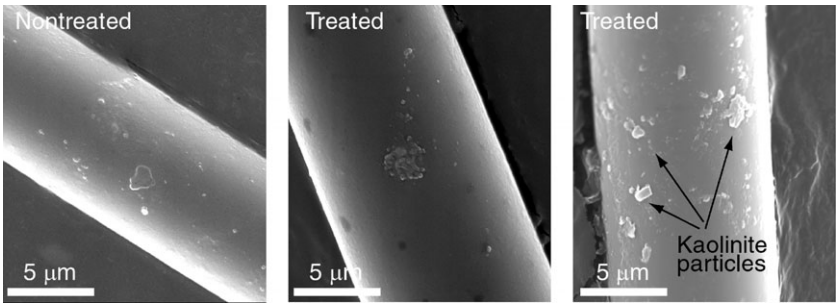

Fig. 3. Scanning electron micrographs of (a) nontreated wick fiber (as received from supplier), (b) treated wick fiber (combusted and washed), and (c) treated wick fiber covered with kaolinite particles (after kaolinite breakthrough experiment).

0.02 $m^2\ g^{-1}$ for the nontreated wicks and 0.46 ± 0.02 $m^2\ g^{-1}$ for the treated wicks. The specific density of the wick material was 2.10 ± 0.08 g cm^{-3}, and the bulk density was 0.29 ± 0.01 g cm^{-3}. The corresponding porosity was 0.86 ± 0.01 $cm^3\ cm^{-3}$.

Nitrate Breakthrough Curves

The overall water content of the wicks increased with increasing flow rate. At flow rates of 5, 10, and 55 mL h^{-1}, the overall gravimetric water contents of the wick material were 1.54 ± 0.10, 1.63 ± 0.06, and 1.78 ± 0.06 g g^{-1}, respectively. Exact values varied somewhat between different wick pieces. These water contents were used to estimate approximate pore volumes for the breakthrough experiments. We tested the water balance during the breakthrough experiments gravimetrically. For the 55 mL h^{-1} flow rate, about 3% of the inflow water was lost by evaporation.

The detailed measurements of the water content distribution showed that the top of the wick was considerably drier than the bottom (Fig. 4). No significant differences were observed in the water content distribution among the different flow rates.

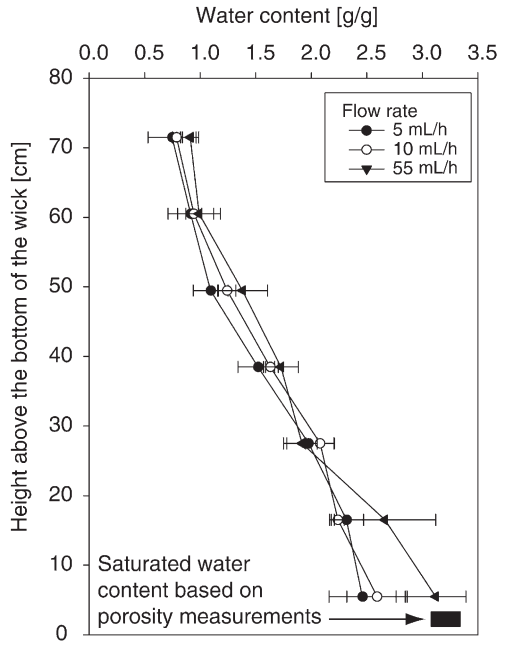

Fig. 4. Distribution of water content as a function of height above the bottom of the wick for different water flow rates. Error bars denote ± one standard deviation (n = 3).

The NO_3 breakthrough curves indicate that NO_3 moved like a conservative tracer through the wicks. Nitrate broke through the wicks after about one pore volume and the breakthrough curves had no tailing (Fig. 5). The shape of the NO_3 breakthroughs was not affected by flow rate. The variability of the breakthrough curves within the same wick at different flow rates was small (Fig. 5a). The variability among different wick pieces at the same flow rates was small as well (Fig. 5b, 5c), indicating that different wick pieces behaved similarly in terms of NO_3 transport.

Colloid Breakthrough Curves

The results of the colloid breakthrough curves are shown in Fig. 6 and 7. While there was no effect of flow rate on NO_3 transport, the flow rate did affect colloid transport. Generally, as flow rate decreased, fewer colloids were recovered in the effluent. The magnitude of the flow rate effect depended on colloid type, as the different colloids have different deposition rate coefficients. For native colloids and ferrihydrite, the flow rate effect was less pronounced than for modified colloids, montmorillonite, and kaolinite.

For the deionized water experiments, the pH of the effluent was between 6.5 and 7.5, and we denote the pH of these experiments as pH ≈7. For the Na_2CO_3/$NaHCO_3$ solution experiments, the pH of the effluent was generally 0.5 to 1.0 pH units less than the pH of the influent, with a smaller pH drop when the flow rate was high. We denote the pH of these experiments as pH ≈10.

Generally, colloid recovery was less at pH ≈7 than at pH ≈10. This can be explained by the increased electrostatic repulsion of colloids in the wicks. The surfaces of the wick silica fibers are negatively charged at the pH values of our experiments (point of zero net proton charge of amorphous silica is pH 3.5 to 3.9 (Langmuir, 1997, p. 351). At pH 7 and 10, all colloids used in our experiments had a net negative surface charge, as indicated by the negative electrophoretic mobility (Fig. 2). For native, modified, and montmorillonite colloids the electrophoretic mobility did not change much from pH 7 to 10, suggesting that the transport of these colloids should not be different between these two pH values.

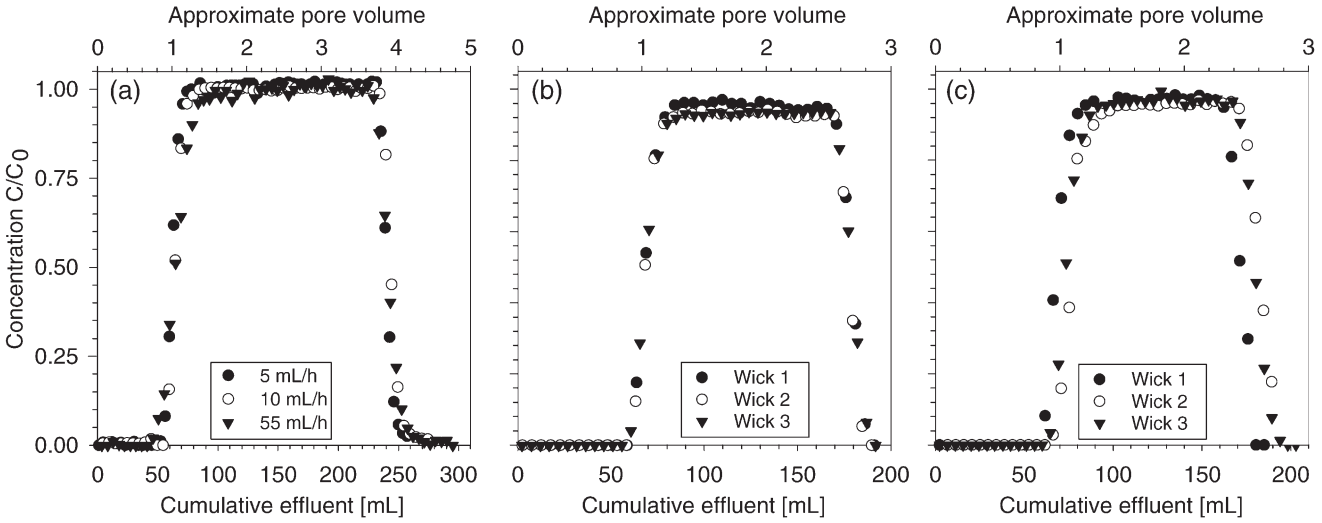

Fig. 5. Nitrate breakthrough curves at pH ≈7 (a) for different flow rates in the same wick, (b) for 10 mL h^{-1} flow rate in three different wicks, and (c) for 55 mL h^{-1} flow rate in three different wicks.

Indeed, the breakthrough curves for these colloids support this hypothesis (Fig. 6, 7a, 7b).

Compared with all colloids used, native colloids and ferrihydrite had the greatest recovery in the effluent at pH ≈10 (Fig. 6b and 7f). The colloid breakthrough curves were fairly consistent among repetitive runs (Fig. 6a, 6b). The modified colloids had smaller relative effluent concentration than the native colloids, as a result of the

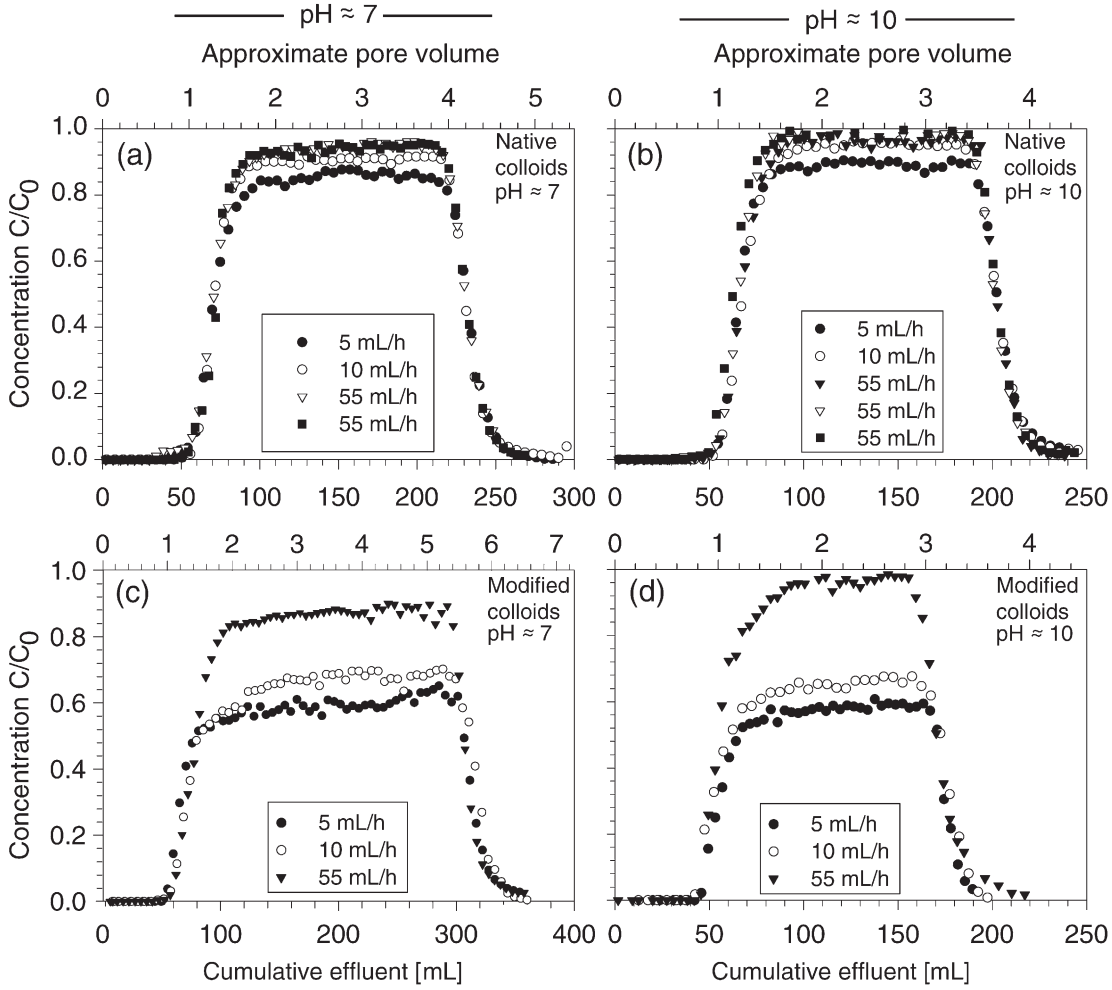

Fig. 6. Breakthrough curves of native and modified Hanford colloids at different flow rates and pH. Breakthrough curves at the same flow rate within one plot are repetitions with different wicks.

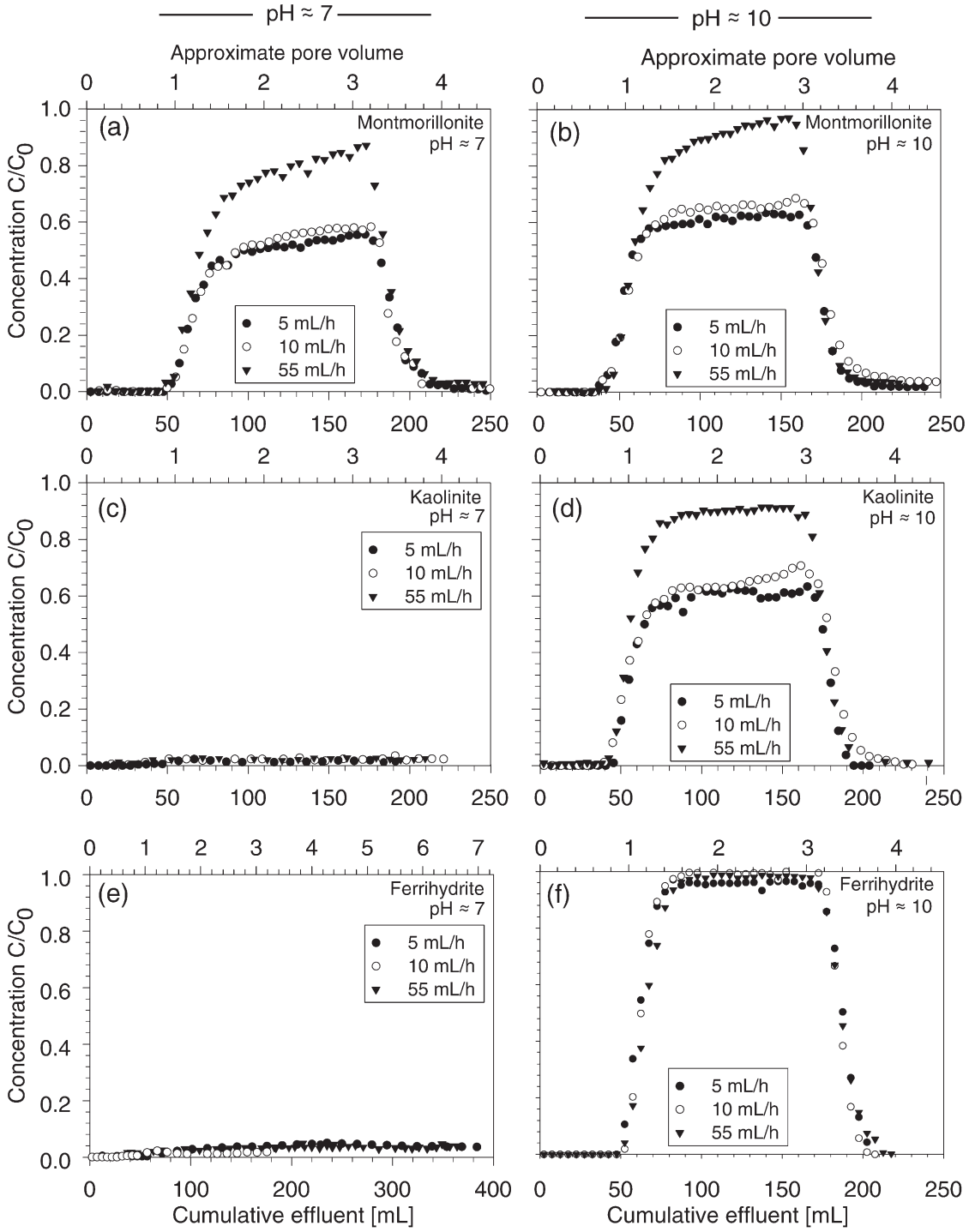

Fig. 7. Breakthrough curves of pure mineral colloids at different flow rates and pH.

larger particle size of the modified colloids and their less negative electrophoretic mobility (Fig. 2). The pure mineral colloids had lower recovery than the native colloids, except for ferrihydrite at pH ≈10, for which case an almost complete recovery was observed. The observation that native colloids moved with less restriction than the pure minerals through the wick can be attributed to several factors. Compared with montmorillonite, native colloids had a somewhat more negative electrophoretic mobility at pH ≈7, making the native colloids more mobile. At pH ≈10, the differences between native colloids and montmorillonite were not as pronounced as at pH ≈7, but still, the native colloids showed a higher recovery. This is likely due to differences in the mineralogical compositions. Native Hanford colloids are composed of a mixture of aluminosilicates and quartz. Colloidal stability experiments performed in our laboratory showed that montmorillonite was less stable than "native colloids" at pH 7 and 10 (data not shown), suggesting that the montmorillonite is more susceptible to aggregation and filtration inside the wicks.

No kaolinite and ferrihydrite moved through the wicks

Table 2. Experimental mass recovery of colloid breakthrough curves at different flow rates.

	Mass recovery					
	pH ≈7			pH ≈10		
Colloid type	5 mL h^{-1}	10 mL h^{-1}	55 mL h^{-1}	5 mL h^{-1}	10 mL h^{-1}	55 mL h^{-1}
	%					
Native colloids	88	93	97–99†	92	94	98–103†
Modified colloids	66	70	80	59	66	97
Montmorillonite	49	53	78	55	61	90
Kaolinite	<5‡	<5	<5	56	61	89
Ferrihydrite	<5	<5	<5	93–95†	97–99†	101–103†

† Range of mass recovery in repeated breakthrough curves.
‡ Measured values were below analytical detection limit.

at pH ≈7 (Fig. 7c, 7e). The ferrihydrite has little net surface charge at pH 7 and is efficiently removed by aggregation and physicochemical filtration inside the wick. The kaolinite has a pronounced net negative charge at pH 7; however, it also has protonated aluminol groups at this pH (White and Dixon, 2002), making the particles susceptible to filtration inside the wicks. Breakthrough curves of ferrihydrite at pH ≈10 showed that the iron oxide moved without retention through the wicks. In addition, there was little effect of flow rate on the breakthrough curves; almost complete recovery was observed for all three flow rates (Fig. 7f).

In many cases, colloids were deposited on the wick fibers (Fig. 3c). The mass recovery for the different breakthrough curves ranged from <5% for kaolinite and ferrihydrite at pH ≈7 to about 100% for native colloids and ferrihydrite at pH ≈10 (Table 2). The varying mass recoveries suggest that the suitability of wicks for colloid sampling depends on flow rates and colloid types, although for some cases (native colloids and ferrihydrite at pH ≈10) the wicks were well suited for colloid sampling.

We tested the differences between repeated colloid breakthrough curves performed in the same wick (in-wick variability) and among different wicks (among-wick variability) (Fig. 8). We only used the native colloids at pH ≈10 because the wicks could be cleaned fairly readily by flushing the wicks extensively with the background solution between consecutive breakthrough curves. We did not observe pronounced differences in the subsequent runs.

Colloid removal by the wicks can be explained by two phenomena: (i) physicochemical effects (electrostatic and van der Waals interactions) between the particles and the wick and (ii) physical straining. Electrostatic interactions dominated removal when particles with less negative surface charge were transported through the wick. Nonetheless, we observed approximately 100% removal in the case of the kaolinite, which had the most negative charge of all colloids at pH 7. Positive edge charges were likely responsible for strong particle deposition.

Physical straining can play an important role if the water film on the surface of the wicks is sufficiently thin. On the basis of the water content distributions along the wick, we can estimate the water film thicknesses by dividing water contents by specific surface areas. The estimated film thicknesses ranged from 1.6 to 2.0 μm at the top to 5.4 to 6.8 μm at the bottom, depending on the flow rate. Because these film thicknesses are all much larger than the particle diameters, it is unlikely that particles were removed by straining in water films. Because the water contents in the wicks were similar for the different flow rates used, we do not attribute the observed dependence of colloid transport on flow rate to physical straining, but rather to physicochemical interactions.

Alternative Wick Materials

Our experiments indicate that fiberglass wicks can impede the movement of colloids and that the colloid

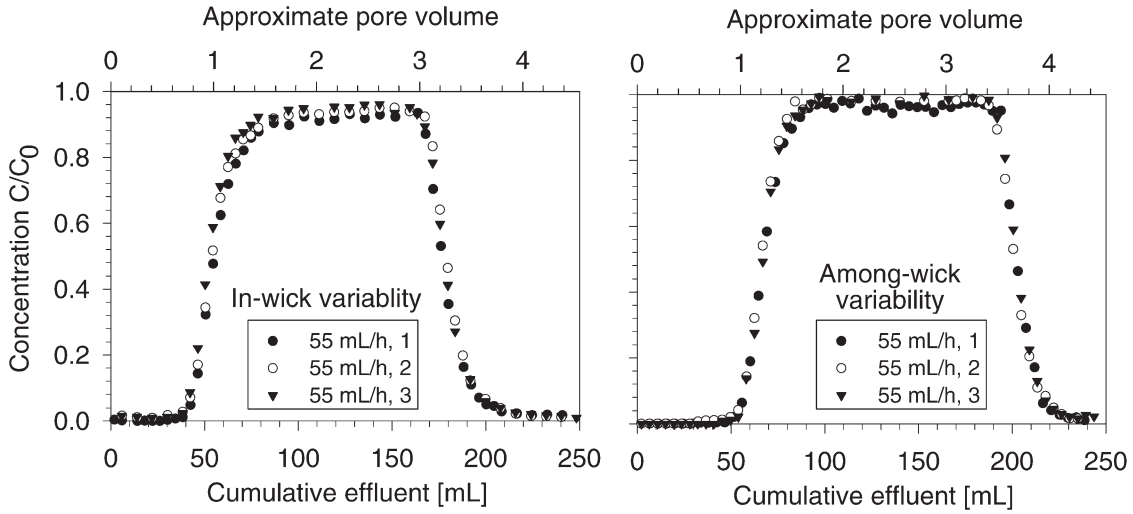

Fig. 8. In-wick and among-wick variability for three repeated breakthrough curves using native colloids at pH ≈10.

recovery often depended on the flow rate through the wicks. It would therefore be useful to test materials other than glass fibers for their suitability for colloid sampling. Wicks are made of fibers with diameters of dozens of micrometers, and these fibers can be composed of different types of materials. Alternative candidates for wick fibers are polymers, graphite, or ceramic. The most suitable materials for colloid sampling in the vadose zone (in temperate climate and pH conditions where most colloids are net-negatively charged) should be negatively charged to overcome the attractive van der Waals interactions between colloids and wick surfaces. Noncharged polymers are therefore unlikely to be good candidates for wick materials because there will be no electrostatic repulsion between colloids and wick fibers. Negatively charged polymers may be suitable materials. Systematic experimental tests would be required to determine the most suitable material for use in wicks.

CONCLUSIONS

Flow rate, pH, and colloid type affected colloid breakthrough. Only two of the five colloids (native colloids and ferrihydrite) showed complete breakthrough through the wicks at pH ≈10; all other colloids were retained to some degree inside the wicks. Generally, colloid recovery was less at pH ≈7 than at pH ≈10. The mechanism of colloid retention in the wicks was due to physicochemical deposition rather than straining in water films because the estimated water film thicknesses were much larger than the colloid diameters.

Colloid recovery in the wick was very variable. Greatest recovery was observed for the mineral mixture extracted from sediments, 88 to about 100% of the colloid mass was recovered in the wick outflow at pH ≈7 and ≈10. Almost complete recovery was observed for ferrihydrite at pH ≈10. In two cases, kaolinite and ferrihydrite at pH ≈7, no colloids moved through the wicks. For other cases, colloid recovery varied from 50 to about 100%. Feldspathoids (modified colloids) and montmorillonite showed considerable retention inside the wicks. This inconsistency in colloid recovery limits the use of fiberglass wicks for colloid sampling. The results of this study suggest that fiberglass wicks may be suitable for sampling colloids from vadose zone pore water under certain conditions, particularly at high pH; however, the wicks may retain a considerable fraction of colloidal material.

ACKNOWLEDGMENTS

This research was supported by the Office of Science (BER), U.S. Department of Energy, Grant no. DE-FG07-99ER62882, and the Inland Northwest Research Alliance. We thank Jorge Jerez for his help synthesizing the ferrihydrite colloids, Glendon Gee (Pacific Northwest National Laboratory) and anonymous reviewers for helpful comments, and the Electron Microscopy Center at Washington State University for use of their facility.

REFERENCES

Abdou, H.M., and M. Flury. 2004. Simulation of water flow and solute transport in free-drainage lysimeters and field soils with heterogeneous structures. Eur. J. Soil Sci. 55:229–241.

American Society for Testing and Materials. 2000. Standard test method for density of hydraulic cement, C 188-95. p. 177–178. Annual Book of ASTM Standards, Section 4: Construction. Vol. 04.01. ASTM, West Conshohocken, PA.

Biddle, D.L., D.J. Chittleborough, and R.W. Fitzpatrick. 1995. Field monitoring of solute and colloid mobility in a gneissic sub-catchment, South Australia. Appl. Clay Sci. 9:433–442.

Boll, J., J.S. Selker, B.M. Nijssen, T.S. Steenhuis, J.V. Winkle, and E. Jolles. 1991. Water quality sampling under preferential flow conditions. p. 290–298. *In* R.G. Allen (ed.) Lysimeters for evapotranspiration and environmental measurement. Proc. ASCE Int. Symp. Lysimetry, Honolulu, HI. 23–25 July 1991. ASCE, New York.

Boll, J., T.S. Steenhuis, and J.S. Selker. 1992. Fiberglass wicks for sampling of water and solutes in the vadose zone. Soil Sci. Soc. Am. J. 56:701–707.

Brahy, V., and B. Delvaux. 2001. Comments on "Artifacts caused by collection of soil solution with passive capillary samplers." Soil Sci. Soc. Am. J. 65:1571–1572.

Brahy, V., M.-C. Henao-Toro, F. Goor, J.-F. Ledent, and B. Delvaux. 2002. Assessing passive capillary-wick samplers for monitoring resident nitrate concentration in real field. Soil Use Manage. 18:18–25.

Brandi-Dohrn, F.M., R.P. Dick, M. Hess, and J.S. Selker. 1996. Field evaluation of passive capillary samplers. Soil Sci. Soc. Am. J. 60: 1705–1713.

Brown, K.W., J.C. Thomas, and M.W. Holder. 1986. Development of a capillary wick unsaturated zone pore water sampler. USEPA Tech. Rep. USEPA Environ. Monit. Syst. Lab., Las Vegas, NV.

Cherrey, K.D., M. Flury, and J.B. Harsh. 2003. Nitrate and colloid transport through coarse Hanford sediments under steady-state, variably-saturated flow. Water Resour. Res. 39:1165. doi:10.1029/2002WR001944.

Cox, J.W., D.J. Chittleborough, H.J. Brown, A. Pitman, and J.C.R. Varcoe. 2002. Seasonal changes in hydrochemistry along a toposequence of texture-contrast soils. Aust. J. Soil Res. 40:581–604.

Gee, G.W., and M.D. Campbell. 1990. A wick tensiometer to measure low tensions in coarse soils. Soil Sci. Soc. Am. J. 54:1498–1500.

Gee, G.W., A.L. Ward, T.G. Caldwell, and J.C. Ritter. 2002. A vadose zone water fluxmeter with divergence control. Water Resour. Res. 38(8):1141. doi:10.1029/2001WR000816.

Gee, G.W., F. Zhang, and A.L. Ward. 2003. A modified vadose zone fluxmeter with solution collection capability. Available at www.vadosezonejournal.org. Vadose Zone J. 2:627–632.

Goyne, K.W., R.L. Day, and J. Chorover. 2000. Artifacts caused by collection of soil solution with passive capillary samplers. Soil Sci. Soc. Am. J. 64:1330–1336.

Holder, M., K.W. Brown, J.C. Thomas, D. Zabcik, and H.E. Murray. 1991. Capillary-wick unsaturated zone soil pore water sampler. Soil Sci. Soc. Am. J. 55:1195–1202.

Knutson, J.H., S.B. Lee, W.Q. Zhang, and J.S. Selker. 1993. Fiberglass wick preparation for use in passive capillary wick soil pore-water samplers. Soil Sci. Soc. Am. J. 57:1474–1476.

Knutson, J., and J.S. Selker. 1996. Fiberglass wick sampler effects on measurements of solute transport in the vadose zone. Soil Sci. Soc. Am. J. 60:420–424.

Langmuir, D. 1997. Aqueous environmental chemistry. Prentice Hall, Upper Saddle River, NJ.

Louie, M.J., P.M. Shelby, J.S. Smesrud, L.O. Gatchell, and J.S. Selker. 2000. Field evaluation of passive capillary samplers for estimating groundwater recharge. Water Resour. Res. 36:2407–2416.

Poletika, N.N., K. Roth, and W.A. Jury. 1992. Interpretation of solute transport data obtained with fiberglass wick soil solution samplers. Soil Sci. Soc. Am. J. 56:1751–1753.

Rimmer, A., T.S. Steenhuis, and J.S. Selker. 1995. One-dimensional model to evaluate the performance of wick samplers in soils. Soil Sci. Soc. Am. J. 59:88–92.

Schwertmann, U., and R.M. Cornell. 2000. Iron oxides in the laboratory: Preparation and characterization. 2nd ed. Wiley-VCH, Weinheim, Germany.

Serne, R.J., B.N. Bjornstad, H.T. Schaef, B.A. Williams, D.C. Lanigan, D.G. Horton, R.E. Clayton, A.V. Mitroshkov, V.L. LeGore, M.J. O'Hara, C.F. Brown, K.E. Parker, I.V. Kutnyakov, J.N. Serne, G.V. Last, S.C. Smith, C.W. Lindenmeier, J.M. Zachara, and D.S. Burke. 2002. Characterization of vadose zone sediment: Uncontaminated RCRA borehole core samples and composite sam-

ples. PNNL-13757-1. USDOE. Pacific Northwest Natl. Lab., Richland, WA.
Steenhuis, T.S., J. Boll, E. Jolles, and J.S. Selker. 1995. Field evaluation of wick and gravity pan samplers. p. 629–638. *In* L.G. Wilson et al. (ed.) Handbook of vadose zone characterization and monitoring. Lewis Publ., Boca Raton, FL.
White, G.N., and J.B. Dixon. 2002. Kaolin-serpentine minerals. p. 389–414. *In* J.B. Dixon and D.G. Schulze (ed.) Soil mineralogy with environmental applications. SSSA Book Ser. 7. SSSA, Madison, WI.
Wu, W. 2001. Baseline studies of the Clay Minerals Society source clays: Colloid and surface phenomena. Clays Clay Miner. 49:446–452.
Zhao, H., Y. Deng, J.B. Harsh, M. Flury, and J. Boyle. 2004. Alteration of kaolinite to cancrinite and sodalite by simulated Hanford Tank Wastes and its impact on cesium retention. Clays Clay Miner. 52: 1–13.
Zhu, Y., R.H. Fox, and J.D. Toth. 2002. Leachate collection efficiency of zero-tension pan and passive capillary fiberglass wick lysimeters. Soil Sci. Soc. Am. J. 66:37–43.

Available online at www.sciencedirect.com
SCIENCE DIRECT®
Applied Geochemistry 20 (2005) 1357–1367
Applied Geochemistry
www.elsevier.com/locate/apgeochem

Analysis of precipitates from reactions of hyperalkaline solutions with soluble silica

Kholoud Mashal [a], James B. Harsh [a], Markus Flury [a,*], Andrew R. Felmy [b]

[a] *Department of Crop and Soil Sciences, Center for Multiphase Environmental Research, Washington State University, Pullman, WA 99164, USA*
[b] *Pacific Northwest National Laboratory, Environmental Molecular Science Laboratory, Richland, WA 99352, USA*

Received 11 August 2004; accepted 31 January 2005
Editorial handling by J.-C. Petit
Available online 13 June 2005

Abstract

Cancrinite, sodalite, and zeolite A have been found to form upon contacting hyperalkaline simulated tank waste (STW) with vadose zone sediments from the Hanford Reservation. Here, soluble silica and STW are used to study mineral formation and transformation. Two Hanford sediment fractions (diameters <50 and >50 μm instead of soluble silica) are also used as silica sources for comparison. A series of batch experiments at 50 °C and 25 days duration were conducted by reacting 0.026 mol/kg soluble Si with 6 different STW solutions. The STW solutions differed in NaOH and Al concentrations. Cancrinite, sodalite, and zeolite A formed when soluble Si was used as the Si source. The minerals were characterized by X-ray diffraction (XRD), scanning electron microscopy (SEM), Fourier transform infrared spectroscopy (FT-IR), and ^{27}Al and ^{29}Si magic-angle spinning nuclear magnetic resonance (MAS-NMR). Larger NaOH and Al concentrations favored formation of the more compact structures of cancrinite and sodalite. At larger NaOH concentration more Al for Si substitution occurred in the tetrahedral sites. A greater Al(4)/Al(6) ratio in the solids was found for the higher Si/Al ratio solutions based on NMR results. Mixtures of cancrinite and sodalite were characterized by particles with lepispheric morphology. At low Al concentration, increasing NaOH resulted in distinct hexagonal, prismatic particles common to crystalline cancrinite. At low Al/Si ratio, the characteristic cubic morphology of zeolite was observed in addition to cancrinite and sodalite.

1. Introduction

The Hanford site served as a Pu production facility for nuclear weapons from 1944 to the end of the Cold War era. A total of 177 underground tanks were used to store waste fluid. Many of the single shell tanks leaked and released waste fluids into the vadose zone. These fluids contain high concentrations of Al, OH, and Na and react with vadose zone sediments to release Si and other soluble elements (Kaplan et al., 1998; Qafoku et al., 2003a). Previous studies showed that Si released from Hanford sediments reacts with Al, OH and NO_3 from simulated tank wastes (STW) to form the feldspathoids, cancrinite and sodalite (Qafoku et al., 2003b; Mashal et al., 2004). Similar minerals formed when STW was reacted with pure clay mineral systems (Bickmore et al., 2001; Chorover et al., 2003; Zhao et al., 2004).

* Corresponding author. Fax: +1 509 335 8674.
E-mail address: flury@mail.wsu.edu (M. Flury).

0883-2927/$ - see front matter © 2005 Elsevier Ltd. All rights reserved.
doi:10.1016/j.apgeochem.2005.01.015

Because of the structural similarity among zeolites and feldspathoids, those minerals can coexist and the dominant phase depends on the conditions of formation. Cancrinite, sodalite, and Linde type A zeolite have been synthesized from a variety of Si–Al–Na–OH solutions under highly alkaline conditions and in the presence of natural clay minerals (Buhl, 1991; Hackbarth et al., 1999; Buhl et al., 2000; Armstrong and Dann, 2000). When bauxite ores are digested with concentrated NaOH, 3 aluminosilicate phases, respectively, cancrinite, sodalite and Linde A zeolite, have been observed to coexist at elevated temperature and the relative abundance of these phases depended on the temperature, solution composition, NaOH concentration, and length of aging (Gerson and Zheng, 1997; Barnes et al., 1999). For example, a high concentration of $NaCO_3$ in the Bayer process caused a decrease in the rate and extent of cancrinite formation (Zheng et al., 1997).

The composition of the initial solid material is also an important factor in the formation of zeolitic materials. Basic sodalite (OH-sodalite) was formed from reacting kaolinite at high NaOH concentration (8 M) at different temperatures (353 and 473 K) (Buhl et al., 1997); whereas, nitrate sodalite (NO_3-sodalite) was formed from reacting zeolite A with 8 M NaOH and sodium nitrate (Buhl, 1991). Nitrate cancrinite formed when zeolite X or a mixture of sodium aluminate and sodium silicate was the starting material (Buhl et al., 2000). Under high pH conditions (0.1–4 mol kg^{-1} KOH), kaolinite transformed in sequence to: illite, K1-zeolite, phillipsite, and K-feldspar, and the transformation rates depended on solution composition, temperature, and reaction time (Bauer et al., 1998). Carbonate cancrinite was formed from reaction of kaolinite with NaOH concentration ($\leqslant$8 M) at high temperature (>80 °C); whereas OH-sodalite formed at higher NaOH concentration (>8 M) at the same temperature (Hackbarth et al., 1998).

The formation of zeolitic phases in the Hanford vadose zone is of considerable interest because of the potential for the products to interact with radionuclides, metals, and ligands. Some researchers found that the altered sediments or clay minerals adsorb more Cs than the original materials (Chorover et al., 2003; Zhao et al., 2004). Zeolitic and feldspathoid materials, which are likely to form under the hyperalkaline conditions of a Hanford tank leak, have a large intraparticle porosity consisting of cages and channels, which possibly can trap radionuclides (Qafoku et al., 2003b).

Previous studies showed that the formation of cancrinite and sodalite in Hanford sediments depends on reaction time, NaOH, and Al concentrations (Qafoku et al., 2003a,b; Mashal et al., 2004). To examine the influence of these variables more systematically, we conducted similar experiments with simulated tank waste solutions to which soluble silica was added. In this way, we avoided the complexity introduced by the heterogeneity of the sediment matrix and variable Si release rates was avoided. The overall objective was to investigate mineral formations when simulated Hanford waste tank solutions leak into the subsurface. Specifically, we characterized: (1) the precipitation products under different NaOH, Al, and Si concentrations, (2) the order of formation of the precipitates, and (3) the mineral transformations occurring in two different particle size fractions of Hanford sediments.

2. Materials and methods

2.1. Synthesis solutions

The sediments used in this study were collected from the submarine pit (218-E-12B) at the Hanford site in January 2000 and have been described previously (Serne et al., 2002). The sediments were air dried and the fractions with equivalent diameters <50 μm and 50 μm to 2 mm were separated using gravity sedimentation.

Tetraethyl orthosilicate from Aldrich was used to prepare soluble Si. The initial Si concentration was 0.013 mol kg^{-1}, based on the highest concentration of Si observed in Hanford sediments in contact with simulated tank waste at 50 °C (data not shown). The tank waste composition at Hanford varies among tanks (Serne et al., 1998); therefore, 6 different STWs were used to determine how varying NaOH concentrations and Al/Si ratios affect mineral formation. The STW1, 2, 3 and 4 were high in Al concentration (high Al/Si ratio), whereas STW5 and STW6 were low in Al concentration (low Al/Si ratio) (Table 1).

2.2. Batch reaction experiments

Two batch experiments were conducted. In the first set, an aqueous solution with dissolved Si, Al, Na, OH and NO_3 was used (Table 1). To initiate the reactions, soluble Si solutions (0.013 mol kg^{-1}) were mixed with STW at 40 mL:40 mL (1:1 v/v) ratios. In the second set of experiments, Hanford sediments (particle diameters either <50 μm or between 50 and 2000 μm) were reacted with STW1 solution at 50 g:50 mL (1:1 w/v). All reactions were carried out in 125 ml polyethylene bottles, closed with a screw cap and stored at 50 °C for 25 days. Bottles were shaken by hand once a day to ensure good mixing, but to minimize abrasion. After the 25 days reaction time, the solid materials were separated from the liquids by centrifugation. The supernatant solution was kept at 50 °C until analyzed.

For the experiments involving Hanford sediments, colloids (particles with diameters <2 μm) were separated from the sediments after the batch reactions by gravity sedimentation, assuming a particle density of 2.65 g cm^{-3}. These colloids were then used for the

Table 1
Initial solution compositions and experimental conditions of batch experiments at 50 °C for 25 days in simulated tank waste (STW) with tetraethyl orthosilicate solutions (0.013 mol Si kg^{-1})

Solution	NaOH (mol kg^{-1})	$NaAlO_2$ (mol kg^{-1})	$NaNO_3$ (mol kg^{-1})	$14 + \log_{10}(NCA)$[a] (mol kg^{-1})	N_{Al}/N_{Si} (mol mol^{-1})	Solution density (kg L^{-1})
STW1	0.7	0.0625	1.5	14.2	5:1	1.2
STW2	1.4	0.0625	1.5	14.5	5:1	1.4
STW3	0.7	0.125	1.5	14.2	10:1	1.3
STW4	1.4	0.125	1.5	14.5	10:1	1.4
STW5	0.7	0.0065	1.5	14.2	1:2	1.4
STW6	0.7	0.026	1.5	14.2	2:1	1.4

[a] "pH", determined by titration; NCA is non-carbonate alkalinity.

characterization work. The colloidal material is of particular concern because colloids potentially can facilitate the movement of radionuclides at the Hanford site (Flury et al., 2002).

The separated solids from both the pure solution and the Hanford sediment experiments were dialyzed until the electric conductivity of the dialysate was less than 0.8 mS/m. The solids were then kept at 50 °C for further analysis.

2.3. Supernatant solution composition and colloid characterization

Supernatant concentrations of Al, Si, Fe, K, Ca, and Mg were determined by ICP-AES (Thermo Jarrell Ash IRIS ICP-AES), and Na concentration by atomic absorption spectrophotometry (Varian 220 Flame Atomic Absorption Spectrometer, Varian Ltd., Mulgrave, Australia). Non-carbonate alkalinity (NCA) and CO_3 were determined by titration (Jenkins et al., 1976). Nitrate was measured with an ion-selective electrode. Samples often had to be diluted for analytical measurements.

The X-ray diffraction (XRD) was performed on randomly oriented colloidal material (Na-saturated) on a glass slide using Cu Kα radiation (Philips XRG 3100, Philips Analytical Inc., Mahwah NJ) at a scanning rate of $2\theta = 0.02°$. The FT-IR spectra were obtained on colloidal material pressed into KBr pellets (1% w/w) and analyzed using a Perkin–Elmer 2000 FT-IR spectrometer. For scanning electron micrographs (SEM, Hitachi S-570), samples were diluted with deionized water and a drop of suspension was placed on Al or C stubs.

Selected products were investigated by ^{29}Si and ^{27}Al NMR. These included the products of STW5 and STW6 of the soluble Si solutions and the colloidal products of the <50 and >50 μm sediment fractions reacted with STW1. The NMR spectra were recorded using an Avance 600 spectrometer at 14.09 T. Chemical shifts were expressed relative to the standard samples of tetramethylsilane and $Al(NO_3)_3$ for ^{29}Si and ^{27}Al spectra, respectively. For ^{27}Al NMR pulse duration was 0.75 μs, pulse delay was 6.0 s, and spinning rate was 35 kHz. For ^{29}Si NMR measurements, pulse duration was 5.8 μs, pulse delay was 10.0 s, and spinning rate was 15 kHz. No cross-polarization was used for ^{29}Si NMR.

2.4. Thermodynamic modeling

The GMIN chemical equilibrium model was used to predict the aqueous species and solid phases of Al and Si in equilibrium with the supernatant solutions after reactions with the Si solution (Felmy, 1995). GMIN is based upon the aqueous thermodynamic model of Pitzer and co-workers and is valid to high ionic strength. Its thermodynamic data base comes from the thermodynamic model of Felmy and Weare (1986) and standard chemical potentials and Pitzer ion-interaction parameters for Na, K, Ca, Mg, CO_2, H, and H_2O are taken from Harvie et al. (1987). The Pitzer ion-interaction parameters in the GMIN data base for the important aluminate ($Al(OH)_4^-$) species are from Wesolowski (1992) and for monomeric and polymeric silica species from Felmy et al. (2001). The equilibrium constants for dissolution of sodalite (Park and Englezos, 1999) and two different crystalline phases of nitrate-cancrinite (Bickmore et al., 2001) were used. The equilibrium constants for the nitrate-cancrinite phases were determined only at one temperature (89 °C) (Bickmore et al., 2001). The starting compositions of the STW were entered into GMIN to evaluate the predicted phases that would form from these solutions and to predict the final equilibrium concentrations in solutions. The final equilibrium concentrations were then compared with the experimentally observed values.

3. Results and discussion

3.1. Solution composition

Reaction of the STW with Si in solution resulted in the formation of a white precipitate in all systems. The final solution concentrations were lower in Al, Si, Na, NO_3, and total alkalinity than the starting solutions,

indicating the formation of aluminosilicates containing Na, OH, and NO_3 as structural ions. The percentage reduction in Al, Si, and non-carbonate alkalinity (NCA) show that Si was the limiting element in solid phase formation (Fig. 1). The Si disappeared almost completely from the solution phase; only a few percent of the Si remained in solution after the precipitation reactions.

As NaOH concentration increased, more Al was incorporated into precipitated solids, but the Si remaining in solution was little affected. This could have resulted either from a higher Al/Si ratio in the aluminosilicates formed or from precipitation of a discrete Al-hydroxide phase such as gibbsite. More silica was incorporated into the solid phase at higher initial Al concentration (STW3, STW4). At the same NaOH concentration, an increase in Al concentration resulted in a greater percentage of Al remaining in solution (Fig. 1(a), STW1 vs. STW3 and STW2 vs. STW4), likely because of the Si-limited precipitation reactions. As discussed by Qafoku et al. (2004), Al has a dual effect on the dissolution and precipitation of mineral phases in alkaline solutions: Al decreases the free OH concentrations by forming aluminate ions, and Al may inhibit the base-promoted mineral dissolution. In the experiments, where only precipitation was studied for Al/Si mol ratios of 5:1 and 10:1, Si appeared to be the limiting factor in the mineral precipitation.

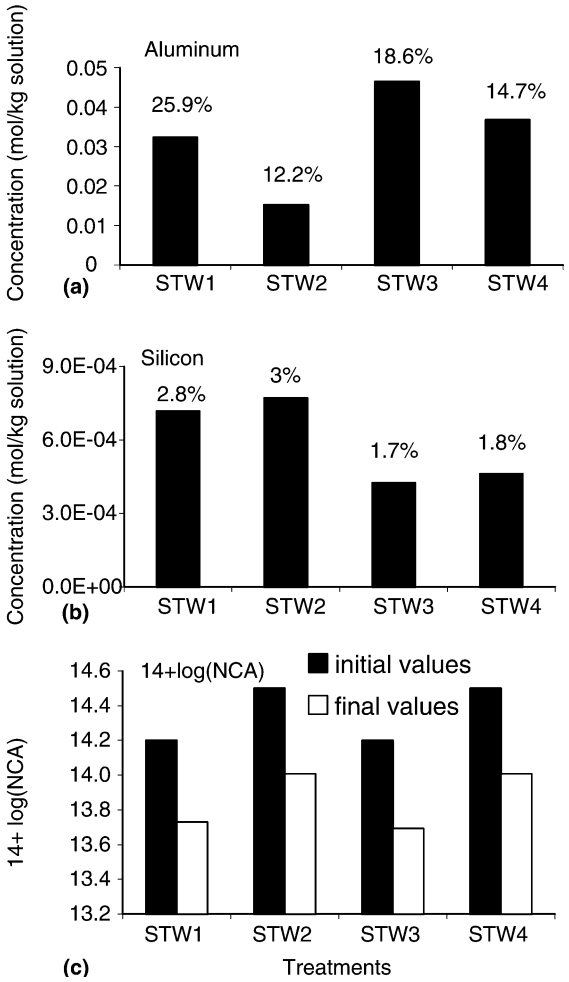

Fig. 1. Supernatant solution characteristics after 25 days at 50 °C. The figures show the concentrations of (a) Al, (b) Si, and (c) $14 + \log_{10}(\mathrm{NCA})$. The percentage above each column denotes the Al and Si remaining in the final solution compared with the initial concentration.

Fig. 1(c) shows that less hydroxide was consumed in the systems (STW2 and STW4) where more precipitation occurred as indicated from the Al concentrations in the final solutions. This implies that precipitation of the new phases generates alkalinity. This is consistent with the formation of zeolites and feldspathoids from solutions containing NaOH, $NaAlO_2$, $NaNO_3$, and Si as shown in the following generic reactions:

$$SiO_2 + 2OH^- \rightleftharpoons H_2SiO_4^{2-}$$

$$6H_2SiO_4^{2-} + 6Al(OH)_4^- + 6Na^+ + 2NaX \rightleftharpoons Na_8[AlSiO_4]_6X_2 \cdot nH_2O_{(s)} + (12-n)H_2O + 12OH^-$$

$$6H_2SiO_4^{2-} + 6Al(OH)_4^- + 6Na^+ \rightleftharpoons Na_6[AlSiO_4]_6.nH_2O_{(s)} + (12-n)H_2O + 12OH^-$$

where X is $\frac{1}{2}CO_3^{2-}$, NO_3^-, or OH^-, and $Na_8[AlSiO_4]_6X_2 \cdot nH_2O$ represents cancrinite and sodalite and $Na_6[AlSiO_4]_6 \cdot nH_2O$ represents zeolite A.

3.2. Thermodynamic modeling

The modeling results indicate that the 4 solutions STW1, 2, 3, and 4 are initially oversaturated with respect to nitrate-cancrinite phases and sodalite (Table 2). This suggests that these solutions, which are not in contact with any solid phase, have the potential to precipitate feldspathoids. Interestingly, all 4 solutions were undersaturated with respect to Al hydroxide phases (e.g., gibbsite). However, owing to the wide range of stability constants reported for cancrinite phases (e.g., the $\log_{10} K$ values for cancrinite range from 30.4 to 36.2 depending upon the specific solution composition) (Bickmore et al., 2001), it is difficult to exactly predict the final dissolved Al or silica concentrations in solution. The unknown rates of precipitation, which could favor one phase over another, even if not the thermodynamically stable material, further complicate the interpretation. Nevertheless, the starting solution compositions was used as input to the geochemical model and final solution compositions were computed under the assumption that different

Table 2
Computed saturation indices for two cancrinites and sodalite with respect to simulated tank waste (STW1, 2, 3, and 4) reacted with soluble Si

Treatment	Low-OH cancrinite	High-OH cancrinite	Sodalite	Most stable phase
STW1	0.13	0.30	0.69	Sodalite
STW2	0.09	0.26	0.67	Sodalite
STW3	0.20	0.37	0.77	Sodalite
STW4	0.15	0.32	0.73	Sodalite

All values are $\log_{10}(IAP/K)/N$, where IAP is the ion activity product, K is the thermodynamic equilibrium constant, and N is the number of ions in the solid phase.

phases were allowed to equilibrate. These results show that the experimentally measured silica concentrations correspond to a solubility product intermediate between the high-OH cancrinite and the low-OH cancrinite (Table 3). Equilibration with a high-OH cancrinite phase resulted in final silica concentrations that are slightly below the experimental values, but equilibration with a low-OH cancrinite results in calculated silica concentrations that are slightly higher than the experimental values. This is expected if cancrinite is the observed solid; however, the silica concentrations would be lower if sodalite were the solid phase. The computed Al concentrations are about 30–50% higher than the experimental values. The experimental values seem inconsistent solely with precipitation of cancrinite or sodalite phases because Si is the limiting element on a mass balance basis. It is possible that an Al hydroxide solid formed in the experiments, although the final solutions were undersaturated with respect to gibbsite.

3.3. Nature and crystallinity of the solids formed

3.3.1. X-ray diffraction

Peaks of the X-ray diffraction patterns were identified and referenced to published data: for cancrinite (Buhl et al., 2000), sodalite (Sieger et al., 1991), and LTA zeolite (Wyckoff, 1968). The XRD peaks were normalized relative to the strong 0.36 nm peak, common to zeolite A,

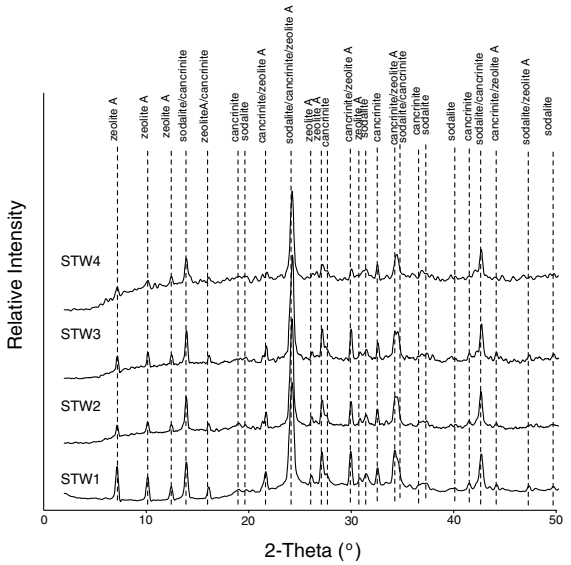

Fig. 2. X-ray diffraction patterns of solid material formed from simulated tank waste (STW1, STW2, STW3 and STW4) reacted with soluble Si.

cancrinite, and sodalite, all of which were formed in each treatment (Fig. 2). There was a decrease in the relative intensity of zeolite A peaks at both NaOH concentrations when Al was increased from 0.625 to 0.25 mol kg^{-1}. The relative size of the zeolite peak also decreased as NaOH was increased at the same Al concentration.

Treatments STW5 and STW6 were done at the same NaOH concentration (1.4 mol kg^{-1}) but different Al/Si ratios. The lower Al/Si ratio of 1:2 of STW5 resulted in strong peaks of zeolite A and relatively weak peaks of cancrinite and sodalite; whereas, STW6 (Al/Si ratio of 2:1) resulted in weak peaks indicative of cancrinite only (Fig. 3(a)).

In general, the zeolite structures that contain high levels of Al are not stable (Healey et al., 2000). This is consistent with the observation that Al–O–Si linkages are generally formed in structures with small cages made up of 4 and 6 membered rings, such as sodalite and cancrinite (Healey et al., 2000; Rayalu et al.,

Table 3
Experimental and calculated Al and silica concentrations in simulated tank waste samples (STW1, 2, 3, and 4) reacted with soluble Si

Treatment	Model predictions						Experiment	
	Al			Si			Al (mol kg^{-1})	Si (mol kg^{-1})
	Sodalite (mol kg^{-1})	High-OH cancrinite (mol kg^{-1})	Low-OH cancrinite (mol kg^{-1})	Sodalite (mol kg^{-1})	High-OH cancrinite (mol kg^{-1})	Low-OH cancrinite (mol kg^{-1})		
STW1	0.0495	0.050	0.053	5.0E − 6	3.4E − 4	0.0031	0.038	8.5E − 4
STW2	0.0495	0.050	0.054	7.5E − 6	5.4E − 4	0.0046	0.031	1.6E − 3
STW3	0.1120	0.112	0.113	2.3E − 6	1.3E − 4	0.0012	0.051	4.7E − 4
STW4	0.1120	0.112	0.114	3.4E − 6	2.4E − 4	0.0022	0.074	9.3E − 4

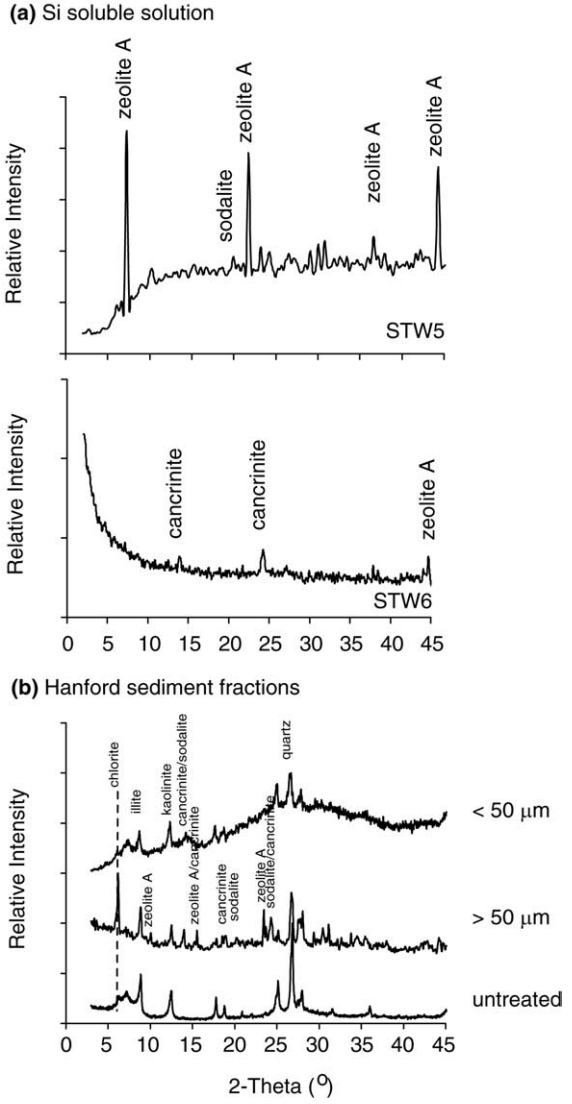

Fig. 3. X-ray diffraction patterns of solid material formed (a) from 1:2 (STW5) and 2:1 Al/Si (STW6) experiments and (b) from Hanford sediment fractions reacted with STW1.

2001). The reduced stability of the hydrated framework of zeolite A, at higher Al/Si ratios, results from the fact that the Al–O–Si linkage is weak compared with the Si–O–Si linkage; whereas, in the dense structure of cancrinite, the strong coordination of non-framework cations helps to stabilize the Al–O–Si linkage (Healey et al., 2000).

The products of the Hanford sediment fractions reacted with STW1 were zeolite A, cancrinite, and sodalite from the >50 μm fraction and only the feldspathoids in the <50 μm fraction (Fig. 3(b)). This suggests that more Si was released relative to Al in the larger particle size fraction allowing zeolite to form. We hypothesize that quartz is the primary Si source in the >50 μm materials, whereas aluminosilicate clays provide relatively more Al in the <50 μm fraction. A likely source of Si in the <50 μm fraction is smectite, which was found to dissolve upon contact with alkaline tank waste solutions (Qafoku et al., 2003b).

3.3.2. Fourier transform infrared spectroscopy

The absorption bands of the STW1 spectrum show the asymmetric and symmetric vibration modes within the "fingerprint" region for cancrinite, sodalite, and zeolite A between 400 and 800 cm^{-1} (Fig. 4) (Barnes et al., 1999; Aronne et al., 2002). The broad absorption region between 1005 and 1108 cm^{-1}, indicating a mixture of tectosilicates, is assigned to the stretching vibrations of Si–O and Al–O bonds belonging to the SiO_4 and AlO_4 tetrahedra (Barnes et al., 1999; Aronne et al., 2002).

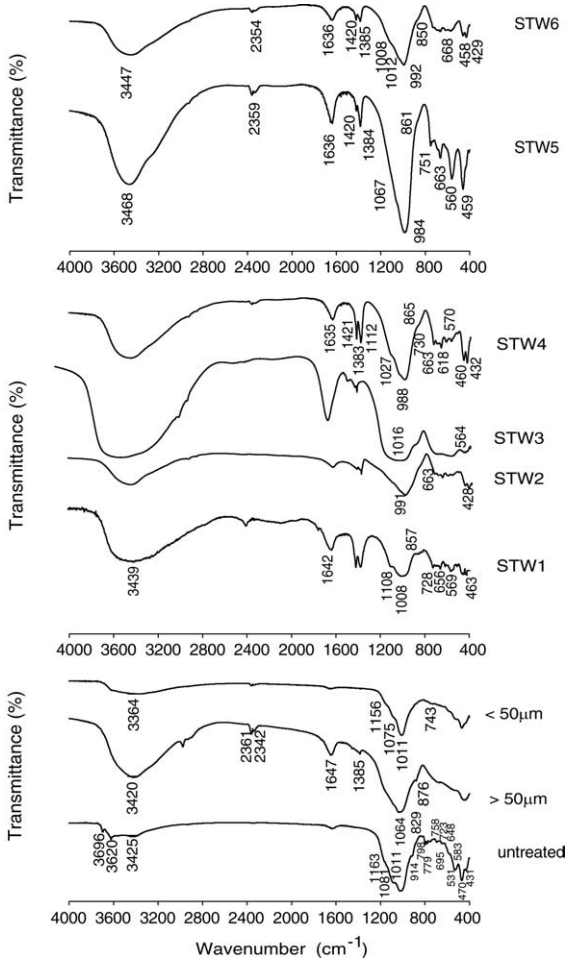

Fig. 4. FT-IR of solid material formed from simulated tank waste (STW1 through STW6) reacted with soluble Si and from Hanford sediment fractions (<50 and >50 μm) reacted with STW1.

Increasing NaOH concentration (STW2) resulted in a shift of absorbance for the asymmetric stretch of the Si–O–Al framework to a lower peak near 991 cm^{-1}. Characteristic peaks in the fingerprint region included two peaks at 663 and 428 cm^{-1}. This shift to lower wavenumbers indicates that there are more Al substitution in tetrahedral sites of the silica framework with NaOH acting as a structure modifier (Aronne et al., 1997, 2002; Park et al., 2000). In general, symmetric and asymmetric stretching of the Si–O–Si bonds of the tetrahedra with n bridging oxygens are IR active in the 800–1300 cm^{-1} range; with $n = 4, 3, 2, 1, 0$, the bands are centered around 1200, 1100, 950 and 850 cm^{-1}, respectively (Aronne et al., 1997). Lower wavenumbers result from replacing Si with Al (Aronne et al., 1997, 2002; Park et al., 2000).

At higher Al and low OH concentrations (STW3), broad peaks at 1016 and 564 cm^{-1} suggest that there was a greater mixture of materials or more disordered structures in this sample. This is not evident in the XRD pattern for STW3. Increasing NaOH concentration (STW4) resulted in well identified peaks for the asymmetric stretch of the Si–O–Al framework at 988 cm^{-1}, and small shoulders at 1027 and 1112 cm^{-1} relative to the other samples. The fingerprint area showed well defined peaks that are characteristic of feldspathoids and zeolite A. These absorptions indicate that there is more structural modification by Al substitution for Si in tetrahedral sites (Aronne et al., 1997, 2002).

The lower Al concentration (STW5, STW6) resulted in better defined structures containing more Al in tetrahedral coordination as indicated by the sharp peak centered near 984 cm^{-1} (Fig. 4). This suggests that when Al concentration was reduced to 6.5×10^{-3} and 0.026 mol/kg, most of the Al was found in tetrahedral coordination. This is consistent with allophane synthesis at lower pH, where lower initial Al/Si ratios increased Al(4) relative to Al(6) in the products (Goodman et al., 1985; Childs et al., 1990; Su et al., 1994).

The results of Hanford sediment fractions spectra provide evidence for alteration of the original clay minerals (Fig. 4). The most important feature is the disappearance of the 914 cm^{-1} band for the <50 μm fraction. Some of the characteristic bands for the pre-existing clay minerals, especially in the fingerprint region, disappeared after reaction with STW1 and the OH-stretching region became broader. The FT-IR peak width is an indication of the level of the crystallinity of the products: the larger the peak width the lower the crystallinity of structure (Barnes et al., 1999). For all treatments a broad absorption at 3450 cm^{-1} can be assigned to hydroxyl groups in the sodalite cages or in the hexagonal prisms of zeolite (Wang et al., 2003).

The absorption bands at 1422 and 1384 cm^{-1} in all STW treatments are assigned to NO_3 in cancrinite (Hackbarth et al., 1999; Buhl et al., 2000) and sodalite (Buhl and Löns, 1996; Fechtelkord et al., 1997; Buhl et al., 1997), respectively. The enclathration of nitrate occured in sodalite when products were formed from Hanford sediments, indicated by the weak peak at 1385 cm^{-1} for the >50 μm fraction (Fig. 4).

3.3.3. NMR spectra

The ^{27}Al NMR spectra of STW5 and STW6 show sharp peaks due to tetrahedrally coordinated Al(4) and a small peak associated with octahedrally coordinated Al(6) (Fig. 5(a)). The small amount of Al(6) may be due to poorly crystalline Al hydroxide or amorphous aluminosilicates (allophane) containing some Al(6) (Huang et al., 2002). The amount of Al(6) was greatest

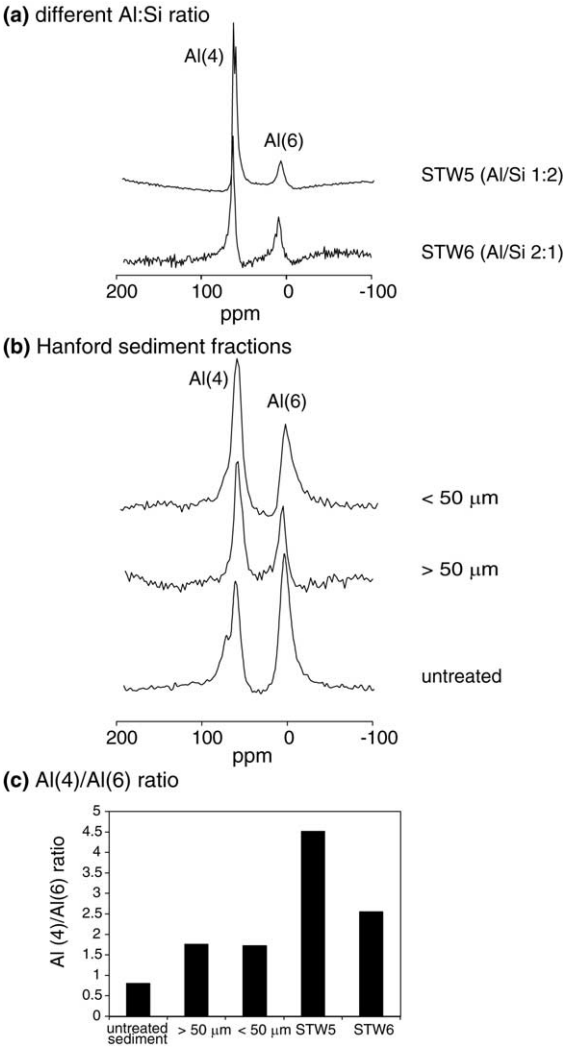

Fig. 5. Results of ^{27}Al NMR for solid material formed: (a) from STW5 and STW6 experiments, (b) from Hanford sediment fractions reacted with STW1, and (c) from Al(4)/Al(6) ratios of ^{27}Al NMR spectra.

Table 4
^{29}Si chemical shifts of solid materials formed from STW5 and STW6 solutions and solid materials formed from reacting Hanford sediment fractions with STW1

Treatment	^{29}Si chemical shifts (ppm)	(ppm)
STW5 (Al/Si 1:2)	−85.9	−88.9
STW6 (Al/Si 2:1)	−88.9	None
Untreated sediment	−91.8	−105.7
STW1 + <50 μm sediment	−89.4	None
STW1 + >50 μm sediment	−94.8	None

in STW6 where the initial Al concentration was larger (Fig. 5(c)). These results corroborate the FT-IR results (Fig. 4).

Hanford sediments showed two peaks consistent with the tetrahedrally coordinated Al of the tectosilicates and octahedrally coordinated Al of aluminosilicate clays (Fig. 5(b)). Reaction of the sediments with STW resulted in a shift of Al from octahedral to tetrahedral coordination (Fig. 5(c)). This is likely due to the dissolution of secondary clay minerals and the concurrent precipitation of tectosilicates.

The ^{29}Si NMR chemical shifts for the same samples are listed in Table 4. Two chemical shifts were observed at −85.9 and −88.9 ppm at the higher Si/Al ratio (STW5), whereas, a sharp peak at −88.9 ppm was observed at higher Al concentration (STW6). We attribute the peak at −85.9 ppm to $Q^3(4)$Al and the small peak at −88.9 ppm to $Q^4(4)$Al (Wilson, 1987). The Q^n notation represents the number of bridging O per Si tetrahedron. These chemical shifts stem from the alternating Si and Al orderings in the tetrahedral frameworks of cancrinite, sodalite, and zeolite A. The presence of these two Si sites at the lower Al/Si ratio indicate imperfect Al/Si ordering in tetrahedral sites. The sharp peak at −88.9 ppm at higher Al/Si results from greater substitution of Al for Si in $Q^4(4)$Al sites. This single peak also indicates an Al/Si ratio of 1:1 for this framework. The ^{29}Si NMR chemical shifts of the <50 μm fraction of Hanford sediments at −89.4 ppm is consistent with alternating Si and Al ordering in the $Q^4(4)$Al of cancrinite and sodalite. In addition, the −94.8 ppm chemical shift in the >50 μm fraction of Hanford sediments can be assigned to the $Q^4(4)(2)$Al in the zeolite A structure (Wilson, 1987).

3.3.4. Morphology of the solids

Characteristic SEM micrographs are shown in Fig. 6; for some treatments two different features were observed and these are shown as separate images. In the STW1 treatment, a lepispheric morphology dominated (Fig. 6(a)). This morphology has been observed in mixtures of cancrinite and sodalite (Deng et al., 2003; Qafoku et al., 2003b). At the same low Al concentration, increasing NaOH (STW1 vs. STW2) resulted in a more crystalline product dominated by a mixture of hexagonal prismatic crystals of cancrinite, similar to those identified by Barnes et al. (1999), and needle-like morphology growing out of small cubes (Fig. 6(b)). These morphological features are consistent with the mixture of cancrinite, sodalite, and zeolite A observed in the XRD patterns of these samples. Agglomerates of different morphologies, including some cubic structures, were observed in the

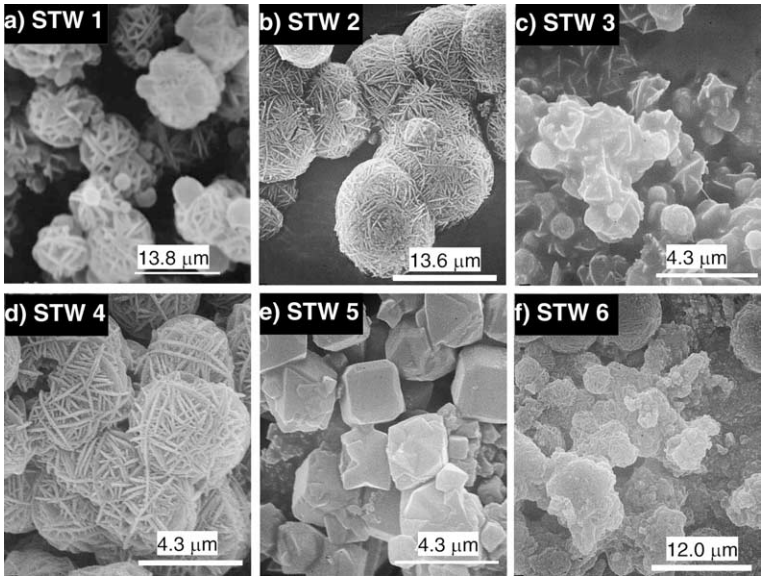

Fig. 6. Scanning electron micrographs of solid material formed from different simulated tank wastes (STW) reacted with soluble Si.

STW3 samples (Fig. 6(c)). Higher Al and NaOH concentrations (STW4) resulted in the formation of a needle-like morphology (Fig. 6(d)). The results of STW5 (Fig. 6(e)) indicate the presence of a separate, more crystalline cubic structure of zeolite A (Barnes et al., 1999) in addition to the needle-like-structure. Sample STW6 was dominated by spherical particles that have been observed in sodalite samples (Barnes et al., 1999) and needle and cubic particles more common to cancrinite and zeolite, respectively (Fig. 6(f)).

The >50 μm Hanford sediment fraction contained a mixture of cubic particles and, to a small degree, needle-like particles along with the original clay particles. These morphological features are consistent with the mixture of cancrinite, sodalite, and zeolite A observed with XRD and FT-IR in these samples. The treated <50 μm fraction contained the same mixture, but with more needle and spherical particles and less cubic particles than the >50 μm fraction. These results suggest that the cubic particles of zeolite A are favored at higher Si:Al ratios, which is consistent with the products of the soluble Si solutions.

4. Conclusions

Cancrinite, sodalite, and zeolite A were formed when soluble Si reacted with different tank waste compositions. Essentially the same products are formed as in experiments where solid phase starting materials are used including Hanford sediments (Mashal et al., 2004; Qafoku et al., 2003b), kaolinite (Zhao et al., 2004), quartz (Bickmore et al., 2001), and bauxite (Gerson and Zheng, 1997). As in the above studies, cancrinite and sodalite appear to be the most likely products from these solutions. Zeolite A, however, is present in significant quantities when Al solution concentration is low. In the presence of Hanford sediments, larger sediment particles appeared to favor zeolite, suggesting that the larger size fraction may have been Al deficient. One difference that is observed in the homogeneous system is that both sodalite and cancrinite are found as products under most treatments. In most of the heterogenous systems mentioned above, there is a tendency for sodalite to transform to cancrinite. The relatively high Al levels used in 4 of the treatments likely inhibit this transformation. In the Hanford sediments, dissolution and precipitation kinetics limit Al concentration (Qafoku et al., 2003b). In the low Al treatments of the study, sodalite is absent or at very low concentration.

The fact that similar products are formed homogeneously to what is found in the heterogeneous cases is important in two respects: (1) solid surfaces need not be present for feldspathoids and zeolites to form below leaking tanks and (2) the same products result without the presence of a melange of elements such as Fe, Mn, Ca, Mg, K, etc., from accessory minerals in the sediments. The first point leaves open the possibility that colloidal materials may form in the mobile solution and transport adsorbed and incorporated radionuclides before sorbing to the sediment matrix. Finally, our results suggest two roles of the sediment matrix when precipitation occurs under extreme conditions such as those under the leaking Hanford tanks. Precipitation at a mineral surface will certainly be influenced by the nature of the surface and the ions present, but also, the composition of the matrix solutions produced by mineral dissolution may, alone, influence the secondary products even when heterogeneous precipitation does not occur.

Acknowledgements

This research was supported by the Office of Science (BER), US Department of Energy, Grant No. DE-FG07-05ER62882. We thank Jeff Boyle (Washington State University, WSU) for help with XRD measurements, the Electron Microscopy Center at WSU for use of their facility, Dan Mitchell (Center for NMR Spectroscopy at WSU) for the NMR work, and Dan Strawn (University of Idaho) for the use of FT-IR equipment. The WSU NMR Center equipment was supported by NIH Grants RR0631401 and RR12948, NSF Grants CHE-9115282 and DBI-9604689 and the Murdock Charitable Trust.

References

Armstrong, J.A., Dann, S., 2000. Investigation of zeolite scales formed in the Bayer process. Micropor. Mesopor. Mater. 41, 89–97.

Aronne, A., Esposito, S., Pernice, P., 1997. FT-IR and DTA study of lanthanum aluminosilicates glasses. Materials Chem. Phys. 51, 163–168.

Aronne, A., Esposito, S., Ferone, C., Pansini, M., Pernice, P., 2002. FT-IR study of the thermal transformation of barium-exchanged zeolite A to celsian. J. Mater. Chem. 12, 3039–3045.

Barnes, M.C., Addai-Mensah, J., Gerson, A.R., 1999. The mechanism of the sodalite-to-cancrinite phase transformation in synthetic spent Bayer liquor. Micropor. Mesopor. Mater. 31, 287–302.

Bauer, A., Velde, B., Berger, G., 1998. Kaolinite transformation in high molar KOH solutions. Appl. Geochem. 13, 619–629.

Bickmore, B.R., Nagy, K.L., Young, J.S., Drexler, J.W., 2001. Nitrate-cancrinite precipitation on quartz sand in simulated Hanford tank solutions. Environ. Sci. Technol. 35, 4481–4486.

Buhl, J.C., 1991. The properties of salt-filled sodalites. Part 2. Synthesis, decomposition reactions and phase transitions of nitrate sodalite, $Na_8[AlSiO_4]_6(NO_3)_2$. Thermochim. Acta 189, 75–82.

Buhl, J.-C., Löns, J., 1996. Synthesis and crystal structure of nitrate enclathrated sodalite $Na_8[AlSiO_4]_8(NO_3)_2$. J. Alloys Compd. 235, 41–47.

Buhl, J.C., Hoffmann, W., Buckermann, W.A., Müller-Warmuth, W., 1997. The crystallization kinetics of sodalites grown by the hydrothermal transformation of kaolinite studied by ^{29}Si MAS NMR. Solid State Nucl. Mag. Reson. 9, 121–128.

Buhl, J.C., Stief, F., Fechtelkord, M., Gesing, T.M., Taphorn, U., Taake, C., 2000. Synthesis, X-ray diffraction and MAS NMR characteristics of nitrate cancrinite $Na_7[AlSiO_4]_6(NO_3)_{1.6}(H_2O)_2$. J. Alloys Compd. 305, 93–102.

Childs, C.W., Parfitt, R.L., Newman, R.H., 1990. Structural studies of silica springs allophane. Clay Miner. 25, 329–341.

Chorover, J., Choi, S., Amistadi, M.K., Karthikeyan, K.G., Crosson, G., Mueller, K.T., 2003. Linking cesium and strontium uptake to kaolinite weathering in simulated tank waste leachate. Environ. Sci. Technol. 37, 2200–2208.

Deng, Y., Harsh, J.B., Flury, M., Young, J., Boyle, J., 2003. Mineral phase transformation in conditions mimic sediment solutions underlying leaked Hanford waste tanks. Abstracts. In: The Clay Minerals Society 40th Annual Meeting; June 7–12, Athens, Georgia pp. 50–51.

Fechtelkord, M., Posnatzki, B., Buhl, J.C., 1997. On the synthesis of nitrate enclathrated sodalite in organic solvents. Zeolites 19, 334–342.

Felmy, A.R., 1995. GMIN, a computerized chemical equilibrium program using a constrained minimization of the Gibbs free energy. Chemical Equilibrium and Reaction Models. Soil Sci. Soc. Am., Spec. Publ. 42, Madison, WI, pp. 377–407.

Felmy, A.R., Weare, J.H., 1986. The prediction of borate mineral equilibria in natural waters: application to Searles Lake, California. Geochim. Cosmochim. Acta 50, 2771–2783.

Felmy, A.R., Cho, H.M., Rustad, J.R., Mason, M.J., 2001. An aqueous thermodynamic model for polymerized silica species to high ionic strength. J. Solution Chem. 30, 509–525.

Flury, M., Mathison, J.B., Harsh, J.B., 2002. In situ mobilization of colloids and transport of cesium in Hanford sediments. Environ. Sci. Technol. 36, 5335–5341.

Gerson, A.R., Zheng, K.L., 1997. Bayer process plant scale: transformation of sodalite to cancrinite. J. Crystal Growth 171, 209–218.

Goodman, B.A., Russel, J.D., Montez, B., Oldfield, E., Kirkpatrick, R.J., 1985. Structural studies of imogolite and allophanes by aluminum-27 and silicon-29 nuclear magnetic resonance spectroscopy. Phys. Chem. Mineral. 12, 342–346.

Hackbarth, K., Fechtelkord, M., Buhl, J.-C., 1998. Crystalization kinetics of $Na_{7.4}[AlSiO_4]_6(CO_3)_{0.7}\cdot 4H_2O$, an intermediate phase between cancrinite and sodalite grown under low temperature hydrothermal conditions. Reaction Kinetics Catalysis Lett. 65, 33–39.

Hackbarth, K., Gesing, T.M., Fechtelkord, M., Stief, F., Buhl, J.C., 1999. Synthesis and crystal structure of carbonate cancrinite $Na_8[AlSiO_4]_6CO_3(H_2O)_{3.4}$ grown under low-temperature hydrothermal conditions. Micropor. Mesopor. Mater. 30, 347–358.

Harvie, C.E., Greenberg, J.P., Weare, S.H., 1987. A chemical equilibrium algorithm for highly non-ideal multiphase systems: free energy minimization. Geochim. Cosmochim. Acta 51, 1045–1057.

Healey, A.M., Henry, P.F., Johnson, G.M., Weller, M.T., Webster, M., Genge, A.J., 2000. The synthesis and characterisation of JBW-type zeolites. Part B: sodium/rubidium aluminogermanate, $Na_2Rb[Al_3Ge_3O_{12}]H_2O$. Micropor. Mesopor. Mater. 37, 165–174.

Huang, P.M., Wang, M.K., Kampf, N., Schulze, D.G., 2002. Aluminum Hydroxides: Soil Mineralogy with Environmental Applications. Soil Science Society of America, Madison, WI, pp. 261–289.

Jenkins, D., Snoeyink, V.L., Ferguson, J.F., Leckie, J.O., 1976. Water Chemistry Laboratory Manual. Association of Environmental Engineering Professors.

Kaplan, D.I., Parker, K.E., Ritter, J.C., 1998. Effects of aging quartz sand and Hanford sediment with sodium hydroxide on radionuclide sorption coefficients and sediment physical and hydrologic properties: final report for Subtask 2a. Pacific Northwest National Laboratory, US Department of Energy, PNNL-11965, Richland, Washington.

Mashal, K., Harsh, J.B., Flury, M., Felmy, A.R., Zhao, H., 2004. Colloid formation in Hanford sediments reacted with simulated tank waste. Environ. Sci. Technol. 38, 5750–5756.

Park, H., Englezos, P., 1999. Thermodynamic modeling of sodium aluminosilicate formation in aqueous alkaline solutions. Industrial Eng. Chem. Resourc. 38, 4959–4965.

Park, M., Choi, C.L., Lim, W.T., Kim, M.C., Choi, J., Heo, N.H., 2000. Molten-salt method for the synthesis of zeolitic materials: I. Zeolite formation in alkaline molten-salt system. Micropor. Mesopor. Mater. 37, 81–89.

Qafoku, N.P., Ainsworth, C.C., Szecsody, J.E., Qafoku, O.S., 2003a. Aluminum effect on dissolution and precipitation under hyperalkaline conditions: I. Liquid phase transformations. J. Environ. Qual. 32, 2354–2363.

Qafoku, N.P., Ainsworth, C.C., Szecsody, J.E., Qafoku, O.S., 2004. Transport-controlled kinetics of dissolution and precipitation in the sediments under alkaline and saline conditions. Geochim. Cosmochim. Acta 68, 2981–2995.

Qafoku, N.P., Ainsworth, C.C., Szecsody, J.E., Bish, D., Young, J.S., McCready, D.E., Qafoku, O.S., 2003b. Aluminum effect on dissolution and precipitation under hyperalkaline conditions: II. Solid phase transformations. J. Environ. Qual. 32, 2364–2372.

Rayalu, S.S., Udhoji, J.S., Munshi, K.N., Hasan, M.Z., 2001. Highly crystalline zeolite-a from flyash of bituminous and lignite coal combustion. J. Hazardous Materials 88, 107–121.

Serne, R.J., Zachara, J.M., Burke, D.S., 1998. Chemical information on tank supernatants, Cs adsorption from tank liquids onto Hanford sediments, and Field observations of Cs migration from past tank leaks. Pacific Northwest National Laboratory, PNNL-11495/UC-510, Richland, WA.

Serne, R.J., Bjornstad, B.N., Schaef, H.T., Williams, B.A., Lanigan, D.C., Horton, D.G., Clayton, R.E., Mitroshkov, A.V., LeGore, V.L., O'Hara, M.J., Brown, C.F.,

Parker, K.E., Kutnyakov, I.V., Serne, J.N., Last, G.V., Smith, S.C., Lindenmeier, C.W., Zachara, J.M., Burke, D.S., 2002. Characterization of vadose zone sediment: uncontaminated RCRA borehole core samples and composite samples. Pacific Northwest National Laboratory, US Department of Energy, PNNL-13757-1, Richland, Washington.

Sieger, P., Wiebcke, M., Felsche, J., Buhl, J.C., 1991. Orientational disorder of the nitrite anion in the sodalite sodium aluminum silicate nitrite ($Na_8[AlSiO_4]_6(NO_2)_2$). Acta Crystallogr., Sect. C 47, 498–501.

Su, C.M., Harsh, J., Bertsch, P.M., 1994. Sodium and chloride sorption by imogolite and allophanes. Clays Clay Miner. 40, 280–286.

Wang, X.X., de Mallmann, A., Bayard, F., Lefebvre, F., Basset, J.M., 2003. Study of the reaction of tetramethyltin with H-faujasite: characterization of the grafted species and thermal stability. Micropor. Mesopor. Mater. 63, 147–161.

Wesolowski, D.J., 1992. Aluminum speciation and equilibria in aqueous solutions: I. The solubility of gibbsite in the system Na–K–Cl–OH–$Al(OH)_4$ from 0 to 1000 °C. Geochim. Cosmochim. Acta 56, 1065–1091.

Wilson, M.A., 1987. NMR Techniques and Applications in Geochemistry and Soil Chemistry. Pergamon Press, Oxford.

Wyckoff, R.W.G., 1968. Crystall structures: miscellaneous inorganic compounds, silicates, and basic structural information, second ed., vol. 4. Wiley, New York.

Zhao, H., Deng, Y., Harsh, J.B., Flury, M., Boyle, J.S., 2004. Alteration of kaolinite to cancrinite and sodalite by simulated Hanford Tank Wastes and its impact on cesium retention. Clays Clay Miner. 52, 1–13.

Zheng, K., Gerson, A.R., Addai-Mensah, J., Smart, R.S.C., 1997. The influence of sodium carbonate on sodium aluminosilicate crystallization and solubility in sodium aluminate solutions. J. Crystal Growth 171, 197–208.

DIVISION S-9—SOIL MINERALOGY

Clay Mineralogical Transformations over Time in Hanford Sediments Reacted with Simulated Tank Waste

Kholoud Mashal, James B. Harsh, and Markus Flury*

ABSTRACT

Buried waste storage tanks at the USDOE Hanford Reservation in Washington State have released solutions containing high concentrations of Na, OH, NO_3, and Al into the vadose zone. When such solutions contact vadose zone sediments, mineral transformations will change the sediment matrix. We hypothesized that Si, dissolved from primary and secondary minerals, will combine with Al from the tank waste to form crystalline or poorly crystalline network silicates such as zeolites and feldspathoids. In this study, we characterized the colloidal (<2 μm equivalent diam.) minerals formed when simulated tank solutions reacted with vadose zone Hanford sediments. Variables studied included simulated tank waste (STW) composition, reaction time, and temperature. Hanford sediments were reacted with a series of simulated tank solutions in batch experiments at 25 and 50°C for 1, 10, 25, 40, and 50 d. The mineralogical, structural, and chemical properties of the resulting colloidal fractions and bulk solutions were determined by x-ray diffraction (XRD), Fourier transform infrared (FTIR), ^{27}Al- and ^{29}Si-magic angle spinning-nuclear magnetic resonance (MAS-NMR), scanning electron microscopy (SEM), energy-dispersive x-ray analysis (EDAX), colorimetry, atomic absorption spectroscopy, and inductively coupled plasma–atomic emission spectroscopy (ICP–AES). Upon contact with STW, Si was released from the sediments and a portion was incorporated into poorly crystalline solids. The amount of poorly crystalline solids increased initially and reached maximum quantities between 0 and 25 d. Lability of minerals in the presence of NaOH followed the order quartz → kaolinite → illite. New secondary minerals, NO_3–cancrinite, NO_3–sodalite, and zeolite A, were formed at the expense of the original clay minerals. Zeolite A was labile and disappeared after about 25 d of reaction time. Cancrinite and sodalite, however, appeared to be stable and increased in abundance with time.

Aqueous high-level radioactive wastes have been produced as a byproduct of Pu production at the Hanford nuclear site in Washington state. The high-level waste was stored in 177 steel-lined underground tanks and has an estimated volume of about 65 million gallons (Gephart and Lundgren, 1998). These wastes are alkaline and high in ionic strength. The composition of the waste includes radionuclides and high concentrations of NaOH, $NaNO_2$, $NaNO_3$, and $NaAlO_2$ (Serne et al., 1998). Following leakage of the tanks, the heat generated by radioactive decay resulted in temperatures beneath the tank in excess of 50°C (Pruess et al., 2002).

When highly alkaline solutions contact clay minerals, mineral dissolution and precipitation may occur. The effect of alkaline solutions on the transformation of clay minerals has been the subject of intensive research (Cuadros and Linares, 1996; Bauer and Berger, 1998; Bauer and Velde, 1999; Taubald et al., 2000). Bauer and coworkers (1998, 1999) studied the reaction of kaolinite in KOH solutions and reported the formation of new solid phases. Buhl et al. (1997) found that kaolinite was transformed to sodalite at pH > 10. Upon the reaction of kaolinite with a NaOH-$NaNO_3$ mixture, the following mineral transformation sequence was found: kaolinite → fly ash → montmorillonite → natural zeolite (Park et al., 2000).

Many studies have been conducted on the transformation of aluminosilicates at high pH, but few reports are available on the type of minerals that could form in situ under the leaking Hanford waste tanks. Hanford sediments consist of primary phases such as quartz and feldspars and secondary phases such as aluminosilicate clays and iron oxides (Serne et al., 2002). Recently, minerals representative of Hanford sediments were subject to mineral transformation studies. For example, when quartz was reacted with STWs, NO_3–cancrinite was found to precipitate on the quartz surface (Bickmore et al., 2001). Chorover et al. (2003) examined the dissolution of kaolinite reacted with STW and reported the formation of network aluminosilicates, including zeolite (chabazite), NO_3–cancrinite, and NO_3–sodalite. Zhao et al. (2004) corroborated these results, finding that both cancrinite and sodalite formed when kaolinite reacted with STWs.

Similar reactions occurred when Hanford sediments reacted with STWs at elevated temperatures (60–90°C) where silicate minerals dissolved and zeolitic phases precipitated (Kaplan et al., 1998; Nyman et al., 2000; Qafoku et al., 2003a, 2004; Mashal et al., 2004). The mineral dissolution rates and the morphology of the secondary precipitates were found to be dependent on Si/Al aqueous molar ratios (Qafoku et al., 2003a). In another study, STWs in contact with Hanford sediments precipitated cancrinite and sodalite in the colloidal size fraction (Mashal et al., 2004).

Here, we want to expand the existing knowledge of colloidal material formed in Hanford sediments reacted with STW. The objective of this work was to investigate and characterize the colloidal materials (<2 μm in

Dep. of Crop and Soil Sciences, Center for Multiphase Environmental Research, Washington State Univ., Pullman, WA 99164-6420. Received 5 July 2004. *Corresponding author (flury@mail.wsu.edu).

Published in Soil Sci. Soc. Am. J. 69:531–538 (2005).

677 S. Segoe Rd., Madison, WI 53711 USA

Abbreviations: AAO, acidic ammonium oxalate; AES, atomic emission spectroscopy; EDAX, energy-dispersive x-ray analysis; FTIR, Fourier transform infrared; ICP, inductively coupled plasma; MAS, magic angle spinning; NCA, noncarbonate alkalinity; SEM, scanning electron microscopy; STW, simulated tank waste; XRD, x-ray diffraction.

diam.) resulting from Hanford sediments reacted with STWs with varying NaOH, $NaNO_3$, and $NaAlO_4$ concentrations and temperatures (25 and 50°C). We focus on colloidal material because of its potential role in the facilitation of contaminant transport.

MATERIALS AND METHODS

Sediments and Simulated Tank Waste Solutions

The sediments used in this study were obtained from the Hanford Reservation, Richland, WA. Sediment characterization is described in detail elsewhere (Serne et al., 2002; Mashal et al., 2004). Uncontaminated sediments were collected from the submarine pit (218-E-12B) at the Hanford site and are considered representative for the material underlying the S-SX (single-shell) tank farm at Hanford (personal communication, September 2001, Bruce N. Bjornstad, Pacific Northwest National Laboratories, Richland, WA). The sediments were air dried and sieved through a 2-mm square screen.

The colloidal fraction (equivalent diam. < 2 μm) of the sediments was separated using gravity sedimentation. For that purpose, sediments were dispersed in a solution containing 0.5 g L^{-1} Na-hexametaphosphate. The suspension was kept in a 1-L volumetric cylinder and the suspension height was 30 cm. The particles were left to settle for 24 h. According to Stokes law, particles with equivalent diam. < 2 μm should remain in suspension after that time. The suspension was then decanted and used for the colloidal material retained for further characterization.

We used different STW solutions to represent leaking Hanford tank waste (Table 1). The composition of the STW solutions was based on data presented by Serne et al. (1998). Hanford tank waste has a very complex chemistry, and only the major chemical constituents were included in our study to keep the experimental system simple. The NaOH concentration was varied in the first two STWs (STW1 and STW2), while the Al concentration was constant. The STW3 solution consisted of a mixture of NaOH and $NaNO_3$, and was most representative of S-SX tank waste. All chemicals used were analytical grade; $NaAlO_2$ was obtained from Strem Chemicals; NaOH and $NaNO_3$ from Fisher Scientific; and $Al(NO_3)_3$ from Aldrich.

Batch Reaction Experiments

Hanford sediments were reacted with STW to mimic a Hanford tank leak. We reacted 100 g of Hanford sediments (<2-mm diam.) with 100 mL STW1 and STW2 in capped 250-mL polyethylene bottles for 1, 10, 25, and 50 d at two different temperatures (25 and 50°C) in a water bath. For STW3, 1 kg of sediment and 1 L of STW3 in capped 2-L polyethylene bottles were place in a 50°C electric oven for 25 and 40 d. To minimize abrasion, bottles were gently mixed by hand in an orbital motion once a day.

After the specified time periods (Table 1), sediments and liquids were separated by centrifugation (27 200 g for 60 min). Supernatant solution was transferred into polypropylene bottles, sealed with a screw cap, and kept at room temperature. The 50°C samples were diluted before cooling to room temperature to prevent precipitation of solids.

The solid materials were washed four times with deionized water and centrifuged. Colloidal particles with equivalent spherical diam. < 2 μm (assuming a 2.65 g cm^{-3} particle density) were fractionated by gravity sedimentation and dialyzed against deionized water until the electric conductivity was <0.01 dS m^{-1}. The suspended colloidal material was stored in polyethylene bottles.

Supernatant and Colloid Characterization

For the first two batch studies (STW1, STW2), Si and Al in the supernatant solutions were measured colorimetrically (Koroleff, 1983; Bertsch and Bloom, 1996). For the STW3 reactions, we measured Al, Si, Fe, K, Ca, and Mg in the supernatant by ICP–AES (Thermo Jarrell Ash IRIS ICP–AES, Thermo Electron Corporation, Waltham, MA) and Na by atomic absorption spectrophotometry (Varian 220 Flame Atomic Absorption Spectrometer, Varian Ltd., Mulgrave, Australia). Noncarbonate alkalinity (NCA) and carbonates were determined by titration (Jenkins et al., 1976). The NCA is reported as "14-pNCA" to use the same scale as pH. Nitrate was measured with an ion-selective electrode.

The colloidal fraction was characterized as follows. X-ray diffraction was performed with randomly oriented colloidal material on a glass XRD slide using Cu-Kα radiation (Philips XRG 3100, Philips Analytical, Inc., Mahwah, NJ) with scanning rates of 0.02° 2θ. The XRD patterns were obtained for Na-saturated samples, K-saturated (25 and 550°C), Mg-saturated, and Mg-glycerol saturated samples. The FTIR analysis was only obtained on the STW3 products. Colloidal material was pressed into KBr pellets (1% w/w) and analyzed using a PerkinElmer 2000 FTIR spectrometer (Wellesley, MA). Solid samples were also examined using SEM (Hitachi S570, Hitachi Limited, Tokyo, Japan) and EDAX. Electron micrographs were scanned optically to ensure representative images. Solid-state MAS-NMR spectra were recorded using an Avance 600 spectrometer (Bruker, Germany) at 14.09 T. Samples were packed into 2.5- and 4.0-mm rotors and measured at 119.217 and 156.375 MHz for ^{27}Al and ^{29}Si, respectively. For ^{27}Al-NMR, pulse duration was 0.75 μs, pulse delay was 6.0 s, and spinning rate was 35 kHz. For ^{29}Si-NMR measurements, pulse duration was 5.8 μs, pulse delay was 10.0 s, and spinning rate was 15 kHz. No cross-polarization was used for ^{29}Si NMR. Chemical shifts were expressed relative to the standard samples of $Al(NO_3)_3$ and tetramethylsilane for ^{27}Al and ^{29}Si, respectively.

The colloidal fraction was further treated with a 0.2 *M* acidic (pH 3) ammonium oxalate (AAO) solution to extract poorly crystalline precipitates (Smith and Mitchell, 1987) and labile aluminosilicates (Chorover et al., 2003). For these extractions,

Table 1. Simulated tank waste (STW) solutions, prepared at room temperature (20 to 22°C), and experimental conditions of batch experiments.

Designation of solution	NaOH	$NaAlO_2$	$Al(NO_3)_3$	$NaNO_3$	pH	Density (20°C)	Temperature†	Time†
	mol kg^{-1}					kg L^{-1}	°C	d
Control‡	0	0	0	0	7.1	0.99	50	25, 40
STW1	0.1	0	3.7×10^{-3}	0	13.0§	0.99	25, 50	1, 10, 25, 50
STW2	0.5	0	3.7×10^{-3}	0	13.7§	1.00	25, 50	1, 10, 25, 50
STW3	1.4	0.125	0	3.7	14.2§	1.20	50	25, 40

† Temperature and duration of batch reactions with sediments.
‡ Distilled water.
§ Determined by titration, which measures noncarbonate alkalinity (NCA), values reported are 14-pNCA [= 14 + $\log_{10}$(NCA)] to retain the same scale as pH.

the colloid suspension was shaken on a reciprocal shaker for 4 h in the dark. The supernatant solution obtained after centrifugation was acidified to pH ≈ 1. Aluminum, Si, and Mg in the supernatant were determined by ICP–AES. The solid material was examined by XRD as described above.

RESULTS AND DISCUSSION

Solution Characterization

Under STW2 (0.5 *M* NaOH), Al and Si concentrations in the supernatant solutions initially increased and reached a maximum between 1 and 25 d of reaction time, after which the concentrations decreased (Fig. 1). Higher reaction temperatures resulted in greater dissolved Al and Si concentrations. The AAO extractions indicate that a portion of the Si, Al, and Mg was incorporated into poorly crystalline or labile solids at both temperatures (25 and 50°C). The amount of labile solids increased initially and reached maximum values within the first 25 d of reaction.

In sediments treated with STW1 (0.1 *M* NaOH), dissolved Al concentrations steadily decreased and Si concentrations were relatively constant and much lower than under 0.5 *M* NaOH, a result similar to that reported by Kaplan et al. (1998). The solution alkalinity (14-pNCA) decreased as the Si concentration increased (Fig. 1), indicating the dissolution of silicate minerals. After the initial drop, the NCA remained constant, likely because of the high NaOH concentration and the buffering effect of Si dissolution and precipitation of new solid phases.

Higher OH and Al concentration (STW3) further increased Si release from the sediments (Table 2). Increased Si release is caused by elevated OH, but not by the elevated Al concentration, because Al decreases free OH concentrations through formation of $Al(OH)_4^-$ and thereby inhibits mineral dissolution (Qafoku et al., 2003b).

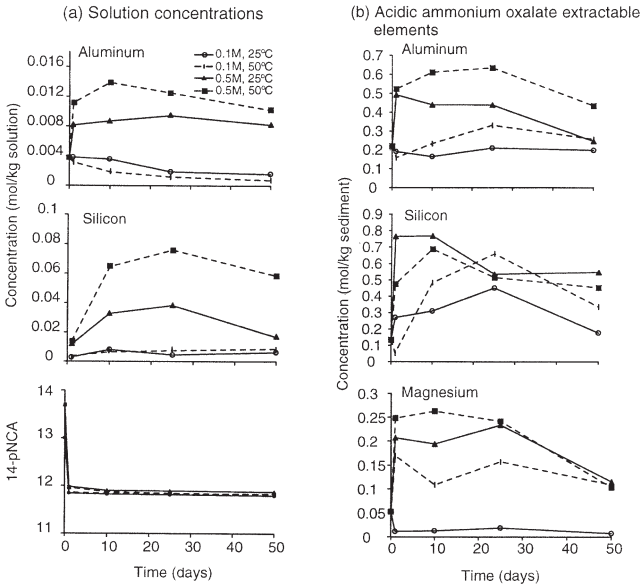

Fig. 1. (a) Chemical composition of the supernatant solution for STW1 (0.1 *M* NaOH) and STW2 (0.5 *M* NaOH) reactions as a function of time, and (b) acidic ammonium oxalate extractable Al, Si, and Mg from colloidal reaction products. 14-pNCA is noncarbonate alkalinity at the same scale as pH.

Silica concentrations in solution decreased slightly between 25 and 40 d of reaction time, similar to the results from the lower OH treatments (Fig. 1 and Table 2). Only a small fraction of the Al initially added to the solutions remained in the supernatant solution (Table 2). The AAO extracts showed no differences in the amount of poorly crystalline solids between 25 and 40 d of reaction time, indicating no obvious change in lability and/or quantity of the solids precipitated during this time interval (data not shown).

The results of our study are similar to the ones reported by Qafoku et al. (2003b), who also observed an initial increase in Si concentration, followed by a decrease after about 3 d of reaction time, when Hanford sediments were contacted with alkaline tank waste simulants. The decrease in Si concentrations was also attributed to precipitation of secondary phases (Qafoku et al., 2003a, 2003b).

Colloid Formation and Characterization

X-Ray Diffraction

The untreated Hanford sediments contain four major layered clay minerals—chlorite, smectite, kaolinite, and illite—and primary minerals mica, quartz, christobalite, albite, and microcline (Fig. 2). Figure 2 also shows the XRD patterns of the colloidal material obtained with 0.1 and 0.5 *M* NaOH solutions at 50°C. No new mineral phases were detected by XRD. We observed that the diffraction peak at *d*-spacing 0.142 nm broadened and shifted to 0.147 nm after 1 d of reaction for both 0.1 and 0.5 *M* NaOH treatments. This peak disappeared following extraction with AAO (Fig. 3), which suggests that the peak is caused by minerals that dissolve in AAO. We believe that the peak is caused by hydroxy-interlayering of Al, Si, and Mg in chlorite and/or smectite. No shift in the 0.142-nm peak occurred in the XRD pattern of colloids from untreated sediment when extracted with AAO, indicating that the interlayered material formed as a result of the STW treatment.

To investigate relative peak differences of the untreated and treated Hanford sediments, we normalized the XRD intensities of kaolinite and illite (Na-saturated) with respect to the intensity of quartz (at 0.34 nm) (Table 3). The ratio of the intensities of kaolinite to quartz was fairly constant across time in the products of the 0.1 and 0.5 *M* NaOH treatments; however, the illite to quartz ratio increased over time. This indicates that the relative abundance of illite compared with quartz and kaolinite increases with time. It seems that quartz and kaolinite are dissolving at a higher rate than illite, leading to a relatively more pronounced illite XRD peak.

As NaOH concentration increased, the relative peak intensities of kaolinite and illite decreased relative to quartz (Table 3) and, at the highest NaOH concentration (1.68 *M*), new peaks characteristic of the feldspathoids NO_3–cancrinite and NO_3–sodalite (Buhl et al., 2000; Buhl, 1991) and zeolite A (Wyckoff, 1968) appeared (Fig. 2c). Zeolite seemed not to be stable in this system and disappeared after 40 d of reaction time (Fig. 3b).

Table 2. Measured chemical composition of the supernatant solution (STW3) at 50°C.

Supernatant	Al	Ca	Fe	K	Mg	Si	Na	NO_3	CO_3	pH
	mol kg^{-1}									
				25 d of reaction time						
Control	0	0.6375	0	0.0001	0.0001	0.001	0	0	0	7.1
STW3	0.0008	0	0.0004	0.028	2.5×10^{-5}	0.301	2.481	1.606	0.0274	13.8†
				40 d of reaction time						
Control	0	0.6329	0	0.0001	0.0001	0.001	0	0	0	7.9
STW3	0.0015	5.3×10^{-5}	0.0035	0.030	8.4×10^{-6}	0.252	2.542	2.064	0.0274	13.8†

† Determined by titration which measures noncarbonate alkalinity (NCA). Values reported are 14 + $\log_{10}$(NCA) to maintain the same scale as pH.

Treatment of the reacted sediments with AAO removed the zeolite peak, and the sodalite and cancrinite peaks weakened. This indicates that these new phases are labile phases in the presence of AAO (pH = 3) (Fig. 3b). The XRD intensities of the new minerals (cancrinite and sodalite) relative to quartz increased with time for STW3 (25 to 40 d), indicating that the new minerals are more stable than quartz (Table 3). At the same time, a decrease in the kaolinite/quartz relative intensity suggests that the formation of zeolite, cancrinite, and sodalite enhanced the dissolution of kaolinite by removing Al from solution.

For all treatments (0.1, 0.5, and 1.68 *M* NaOH), the supernatant compositions and XRD patterns indicate enhanced desilication along with the alteration of preexisting colloidal silicates. Increasing NaOH concentrations resulted in a reduction of the quartz and feldspar peaks along with a relative change in the aluminosilicate mineral peaks. Illite seemed to be more resistant toward alkaline treatment than kaolinite. Kaolinite is known to

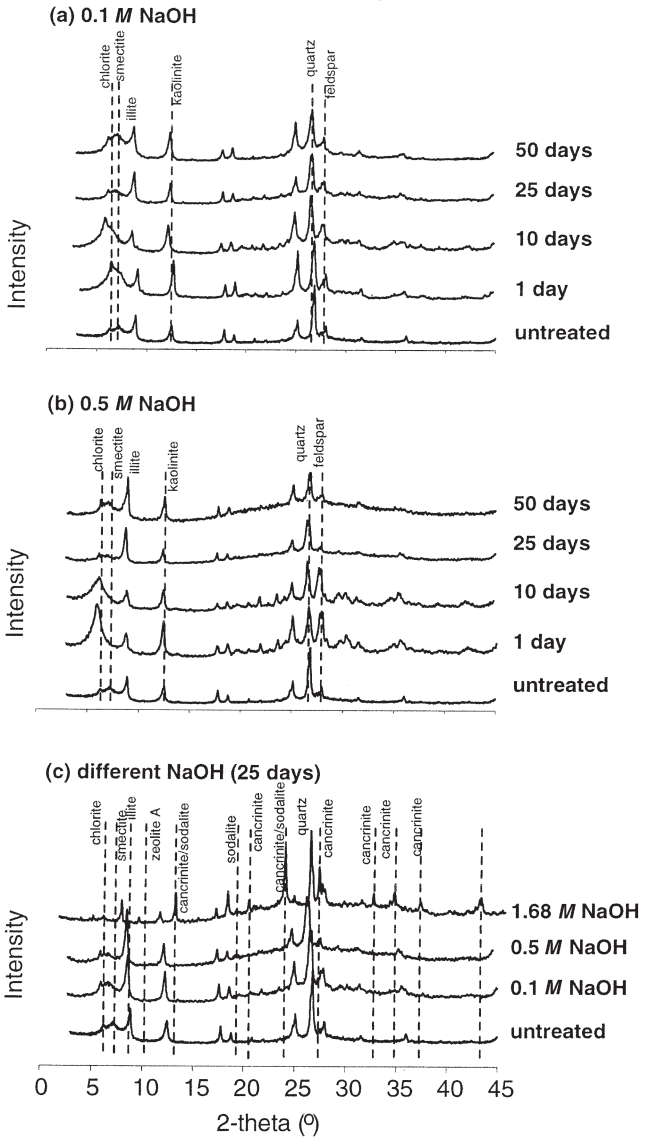

Fig. 2. X-ray diffraction patterns of Na-saturated colloidal material extracted from Hanford sediments reacted with simulated tank waste solutions at 50°C; (a) and (b) show the effect of reaction time on mineral alteration, and (c) shows the effect of NaOH concentrations on mineral alterations.

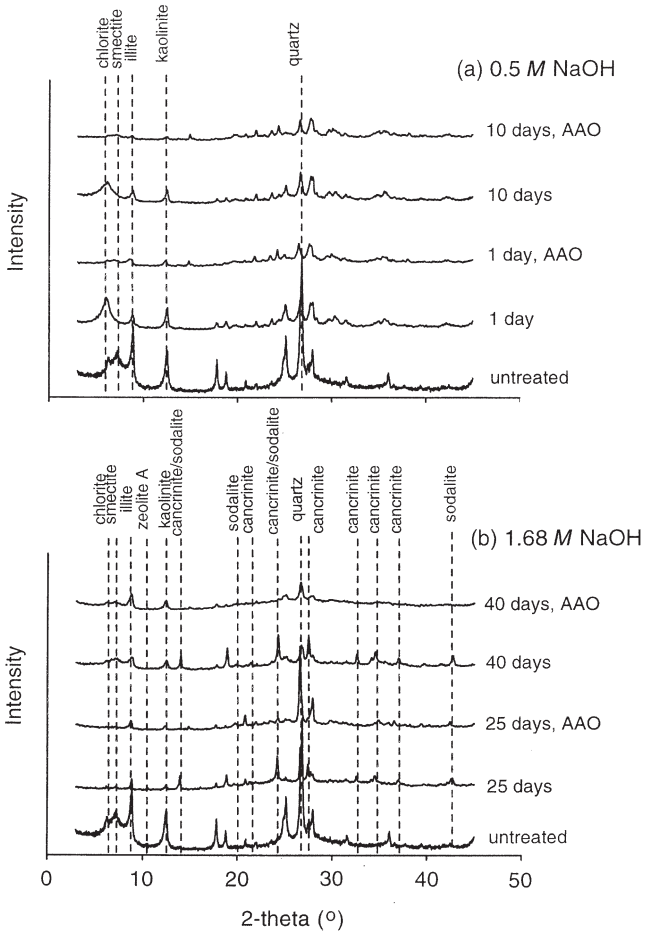

Fig. 3. X-ray diffraction patterns of Na-saturated colloidal material extracted from Hanford sediments reacted with simulated tank waste solutions at 50°C. Patterns are shown for colloids before and after acidic ammonium oxalate (AAO) extraction.

Table 3. Relative XRD intensities of kaolinite (K), illite (I), cancrinite (C), and sodalite (S) with respect to quartz (Q) for simulated tank wastes STW1 (0.1 *M* NaOH), STW2 (0.5 *M* NaOH), and STW3 (1.68 *M* NaOH).

	0.1 *M* NaOH		0.5 *M* NaOH		1.68 *M* NaOH			
Reaction time	K/Q	I/Q	K/Q	I/Q	K/Q	I/Q	C/Q	S/Q
d								
0 (untreated)	0.48	0.32	0.48	0.32	0.48	0.32	0	0
1	0.64	0.49	0.65	0.46	nd†	nd	nd	nd
10	0.48	0.39	0.50	0.45	nd	nd	nd	nd
25	0.45	0.59	0.48	0.68	0.14	0.28	0.63	0.20
50/40	0.56‡	0.66‡	0.57‡	0.64‡	0.31§	0.41§	0.90§	0.23§

† nd, not determined.
‡ 50 d of reaction time.
§ 40 d of reaction time.

be labile in NaOH solutions (e.g., Barrer, 1982; Chorover et al., 2003; Zhao et al., 2004). In contrast to kaolinite, smectite appeared fairly resistant to dissolution by STW solutions. The difference in behavior between the two kinds of minerals (1:1 and 2:1) can be explained by structural differences. For kaolinite, hydrolysis of the tetrahedral and octahedral sheets occurs as simultaneous dissolution reactions, and the rate-limiting step is the dissolution of the octahedral layer. In smectite, dissolution occurs as serial reactions, where dissolution of the tetrahedral layer is the rate-limiting step (Bauer and Berger, 1998). Smectite, however, is still susceptible to dissolution in alkaline Hanford tank waste, and its dissolution contributes to the Si concentration in solution (Qafoku et al., 2003a).

Fourier Transform Infrared Spectra

The FTIR spectra of the products of the 1.4 *M* NaOH treatment substantiate the results obtained from the XRD patterns (Fig. 4). The absorption bands in the midinfrared indicate the alteration of original clay minerals and the formation of new phases. We notice that the intensities of the kaolinite bands at 3696 and 3620 cm^{-1} remain, but relative to the Si–O–Al stretch near 1000 cm^{-1}, these band intensities decreased with time. The absorption bands for the 25-d spectrum show the asymmetric and symmetric vibration modes within the fingerprint area of tectosilicates (400–800 cm^{-1}). The characteristic bands occur for sodalite at ≈668 and 730 cm^{-1}, for cancrinite at ≈512, 571, 619, and 682 cm^{-1} (Barnes et al., 1999), and for zeolite A at ≈668 and 462 cm^{-1} (Aronne et al., 2002). The asymmetric stretching vibrations at 1011, 1081, and 1163 cm^{-1} were shifted to a broad band centered near 999 cm^{-1}. This band supports the presence of tectosilicates containing tetrahedral SiO_4 and AlO_4. Main absorption bands occur at 999 cm^{-1} for zeolite A (Aronne et al., 2002), at 1095, 1035, and 979 cm^{-1} for cancrinite, and at 979 cm^{-1} for sodalite (Zheng et al., 1997). The results after 40 d of reaction time indicate the presence of cancrinite and sodalite, but there is no evidence for zeolite A. The narrowing of the Si–O–Al stretch near 1000 cm^{-1} suggests increasing crystallinity and/or homogeneity of the products, consistent with the XRD patterns and AAO extractions.

For both reaction times (25 and 40 d), the sharp FTIR absorption bands at 1423 and 1383 cm^{-1} indicate the enclathration of nitrate within the cancrinite (Buhl et al., 2000) and sodalite cages (Buhl and Löns, 1996). This nitrate was not sorbed or precipitated at the mineral surface, as we had extensively washed and dialyzed the samples with water. No evidence was found for enclathration of carbonate, which would have characteristic bands at 1410 and 1455 cm^{-1} (Hackbarth et al., 1999; Barnes et al., 1999).

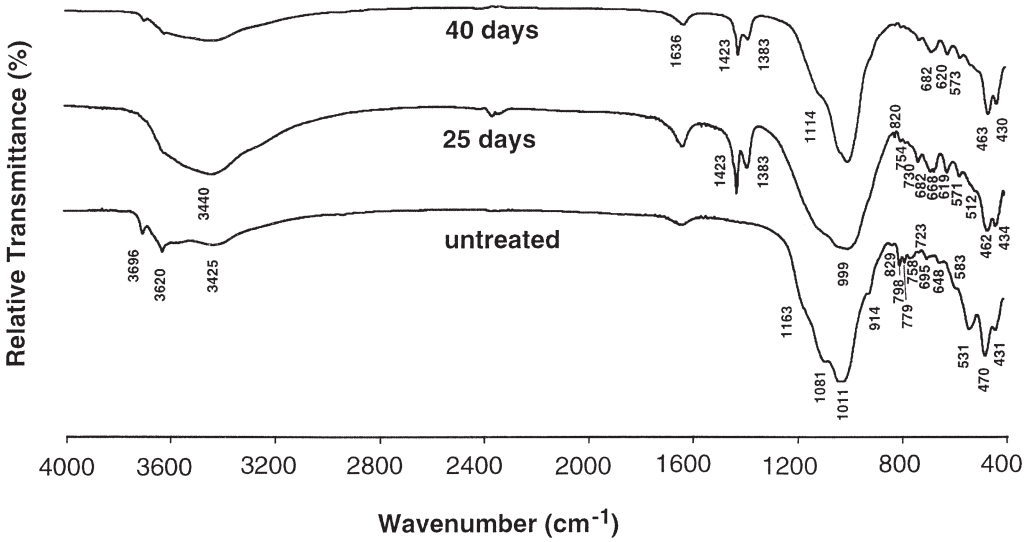

Fig. 4. Fourier transform infrared spectra of Hanford sediments reacted with simulated tank waste (STW3, 1.68 *M* NaOH) at 50°C.

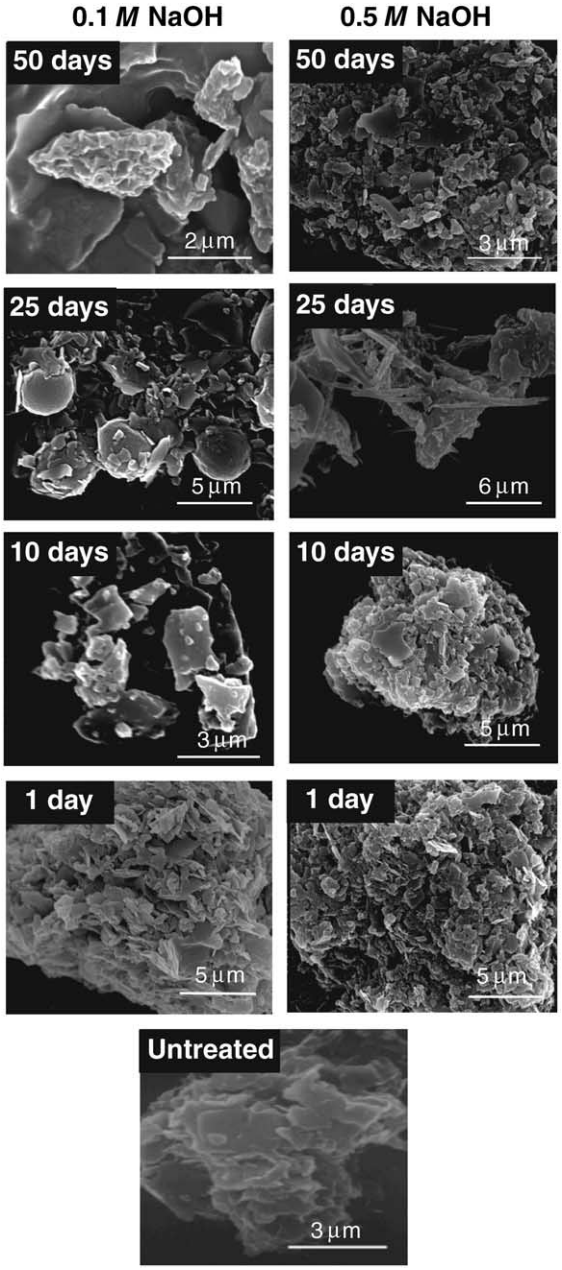

Fig. 5. Scanning electron micrographs of Hanford sediments reacted with simulated tank waste STW1 (0.1 *M* NaOH) and STW2 (0.5 *M* NaOH) at 50°C.

The characteristic peak at 1636 cm^{-1} for the water bending vibration became less pronounced relative to the Si–O–Al stretch with increasing reaction time (Fig. 4). This implies an increase of bonded OH^- in the crystal structure. Parallel to the increased amount of OH^-, the amount of NO_3^- inside the structure decreased with time. The intensity of the two nitrate absorption bands (1423 and 1383 cm^{-1}) also decreased with time, indicating the loss of NO_3^- from the framework. Within the same time interval, we observed an increase in NO_3^- in the solution phase (Table 2).

The XRD, FTIR, and AAO extracts indicate that there was an increase in the crystallinity of the new solid phases, sodalite and cancrinite, between 25 and 40 d. The simultaneous loss of nitrate from the solid phases indicates that these more crystalline phases enclathrate less nitrate into their structures. Cancrinite has both cages and channels (Gerson and Zheng, 1997), whereas sodalite (Gerson and Zheng, 1997) and zeolite A (Aronne et al., 2002) have a series of interlocking cages. The wide channel in the cancrinite is filled with cations and intracrystalline anions such as CO_3 or NO_3, whereas the small cages contain only cations and water molecules (Hackbarth et al., 1999; Buhl et al., 2000). Bickmore et al. (2001) suggested that defects in the cancrinite structure could close channel access to the bathing solution. Such defects could account for more trapped nitrate in the less-crystalline phases formed at 25 d.

Colloid Morphology

The distinct morphology of the native clay minerals, illite, smectite, and kaolinite can be seen in the colloidal fraction of the untreated Hanford sediment (Fig. 5). The sediments treated with 0.1 and 0.5 *M* NaOH show alteration of the native clay minerals as a result of mineral dissolution. The most pronounced change occurred after 25 d, when spherical particles appeared in the 0.1 *M* NaOH treatment and rod-shaped particles in the 0.5 *M* NaOH treatment. The EDAX results showed that the spherical particles consisted dominantly of Fe, whereas the rod-shaped particles contained Al, Si, Mg, and Fe. Both particle types were labile (or metastable) and disappeared after 50 d of reaction time. Iron-rich precipitates were also observed by others when Hanford sediments were contacted with 1 mol L^{-1} NaOH solutions (Qafoku et al., 2003a). The SEM photographs for STW3 showed a pronounced change in the morphology of the original clay minerals: spherical, cauliflower-like, and rod-shaped particles with surface features common to sodalite and cancrinite appeared. These morphological changes indicate the formation of neophases at the expense of the original clay minerals as a result of secondary nucleation.

Structural Characterization with ^{27}Al and ^{29}Si NMR

The ^{27}Al-NMR spectra of the untreated colloidal materials have two intense peaks at chemical shifts of 59.7 and 4.1 ppm (Fig. 6), representing four and six-coordinated Al, respectively (Wilson, 1987). Little change was observed in the NMR spectrum of 0.1 *M* NaOH samples compared with untreated sediment. For the 0.5 *M* NaOH treatment, the intensity of the Al(4) peak increased relative to the Al(6) peak at the beginning then decreased after 10 d. We interpret the initial decrease in the Al(6)/Al(4) ratio as due to dissolution of clay minerals, primarily kaolinite. The subsequent increase in this ratio probably reflects the rates of quartz and feldspar dissolution relative to kaolinite dissolution (Fig. 2 and Table 3) and to precipitation of poorly crystalline aluminosilicates as indicated by the increase in AAO-extractable Al in Fig. 1. At a higher NaOH concentration (1.68 *M*), the Al coordination changed from octahedral to tetrahedral (Fig. 6c), again consistent with the formation of tectosilicate minerals.

Untreated Hanford sediments showed a major ^{29}Si NMR resonance at −91.8 ppm and a minor resonance at −105.7 ppm (Fig. 7). Kaolinite has a resonance at −92.1 ppm, illite at −91.0 ppm (Kinsey et al., 1985), and crystalline SiO_2 at −105.7 ppm (Wilson, 1987). The chemical shift for Si becomes less negative when Si is shielded by increasing Al(4) concentration in the structure (Kinsey et al., 1985). In both the 0.1 and 0.5 *M* NaOH treatments, the resonance near −91.8 ppm shifts toward −92.6 ppm, indicating increased Si polymerization and Al-shielding as network aluminosilicates begin to form and phyllosilicates are dissolved. Neither of these treatments resulted in obvious changes in the ^{27}Al-NMR spectra or XRD diffractograms; ^{29}Si-NMR is evidently more sensitive to changes occurring at lower NaOH concentration. Increasing the alkalinity to 1.68 *M* NaOH resulted in a more pronounced chemical shift of the −91.8 ppm peak to −87.3 ppm characteristic of Si(4Al) units in cancrinite and sodalite (Buhl, 1991; Buhl et al., 2000).

The NMR results provide further evidence that native minerals (octahedral Al) are dissolved and zeolite and feldspathoids (tetrahedral Al and increasing Al/Si disorder) are forming. The NMR results corroborate the results obtained by XRD and FTIR, and provide semiquantitative information regarding the relative abundance of Al(4) and Al(6). Furthermore, the chemical shifts indicate changes in short range ordered minerals and are more sensitive to the overall Si and Al transformations than XRD or FTIR.

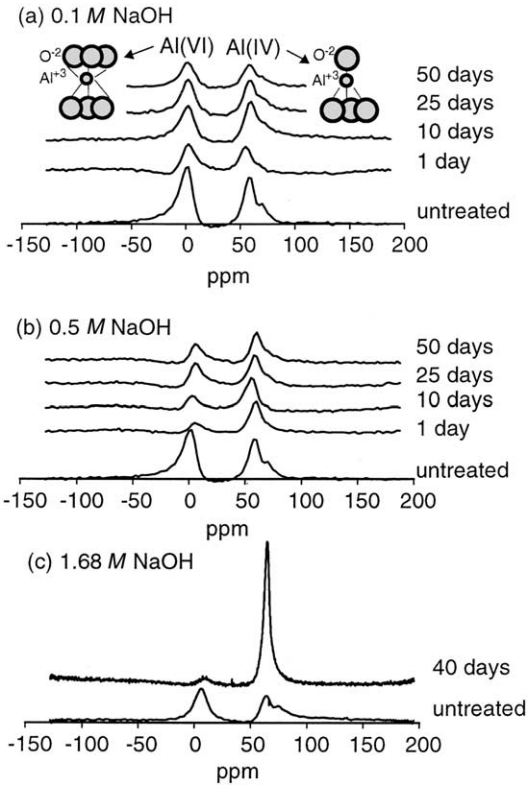

Fig. 6. ^{27}Al NMR of unreacted and reacted Hanford sediments at 50°C. (a) NMR spectra for 0.1 *M* NaOH, (b) NMR spectra for 0.5 *M* NaOH, and (c) NMR spectra for 1.68 *M* NaOH.

CONCLUSIONS

Leaking tank solutions at the Hanford Reservation can alter the mineralogical composition of vadose zone sediments. First, Si is released from the native minerals and second, new minerals precipitate. Both processes are enhanced as temperature and NaOH concentration are increased. At high NaOH concentration (1.68 *M* NaOH), we observed the formation of three new minerals: NO_3–cancrinite, NO_3–sodalite, and zeolite A. Zeolite A was less stable than cancrinite and sodalite. The dissolution and precipitation reactions occurred during time scales of several days, with dissolution of kaolinite dominating initially and precipitation of feldspathoids dominating in the later stages. At lower alkalinity (<0.5 *M* NaOH), there is evidence that poorly crystalline materials precipitated, likely hydroxy-interlayer Mg, Al, and Si in the existing 2:1 layered clay minerals. Portions of the dissolved Si, Al, and Mg were incorporated into poorly crystalline solids. Kaolinite and quartz were both more labile relative to illite during 40 to 50 d of reaction time.

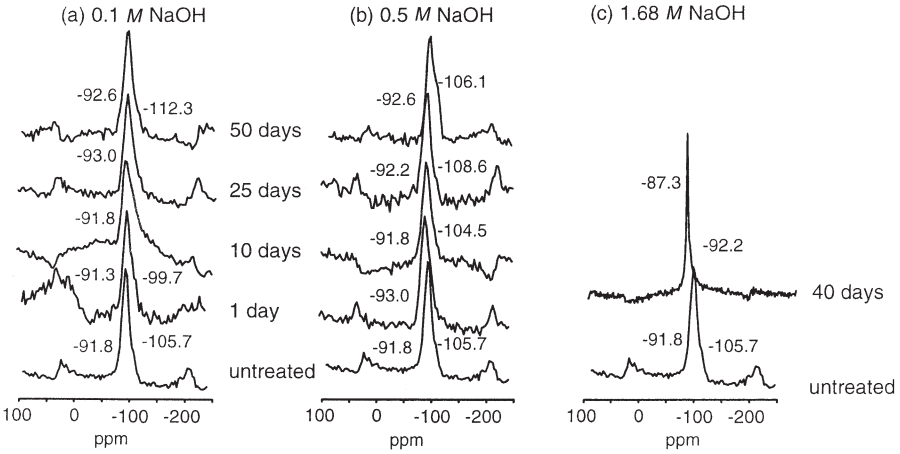

Fig. 7. ^{29}Si NMR of unreacted and reacted Hanford sediments at 50°C. (a) 0.1 *M* NaOH, (b) 0.5 *M* NaOH, and (c) 1.68 *M* NaOH. Numbers indicate major chemical shifts with respect to tetramethylsilane.

ACKNOWLEDGMENTS

This research was supported by the Office of Science (BER), U.S. Department of Energy, Grant No. DE-FG07-99ER62882. We thank Jeff Boyle and Hongting Zhao for help with the experiments, the Electron Microscopy Center at WSU for use of their facility, Dan Mitchell (Center for NMR Spectroscopy at WSU) for the NMR work, Dan Strawn (University of Idaho) for the use of FTIR equipment, and John Zachara and Jeff Serne (Pacific Northwest National Laboratory) for providing us with the Hanford sediments. The WSU NMR Center equipment was supported by NIH grants RR0631401 and RR12948, NSF grants CHE-9115282 and DBI-9604689 and the Murdock Charitable Trust.

REFERENCES

Aronne, A., S. Esposito, C. Ferone, M. Pansini, and P. Pernice. 2002. FTIR study of the thermal transformation of barium-exchanged zeolite A to celsian. J. Mater. Chem. 12:3039–3045.

Barnes, M.C., J. Addai-Mensah, and A.R. Gerson. 1999. The mechanism of the sodalite-to-cancrinite phase transformation in synthetic spent Bayer liquor. Microporous Mesoporous Mater. 31:287–302.

Barrer, R.M. 1982. Hydrothermal chemistry of zeolites. Academic Press, London.

Bauer, A., and G. Berger. 1998. Kaolinite and smectite dissolution rate in high molar KOH solutions at 35° and 80°C. Appl. Geochem. 13:905–916.

Bauer, A., and B. Velde. 1999. Smectite transformation in high molar KOH solutions. Clay Miner. 34:259–273.

Bertsch, P.M., and P.R. Bloom. 1996. Aluminum. p. 517–550. *In* D.L. Sparks (ed.) Methods of soil analysis: Part 3—Chemical methods. SSSA Book Ser. No. 5. SSSA and ASA, Madison, WI.

Bickmore, B.R., K.L. Nagy, J.S. Young, and J.W. Drexler. 2001. Nitrate-cancrinite precipitation on quartz sand in simulated Hanford tank solutions. Environ. Sci. Technol. 35:4481–4486.

Buhl, J.C. 1991. The properties of salt-filled sodalites. Part 2. Synthesis, decomposition reactions and phase transitions of nitrate sodalite, $Na_8[AlSiO_4]_6(NO_3)_2$. Thermochim. Acta 189:75–82.

Buhl, J.C., W. Hoffmann, W.A. Buckermann, and W. Müller-Warmuth. 1997. The crystallization kinetics of sodalites grown by the hydrothermal transformation of kaolinite studied by ^{29}Si MAS NMR. Solid State Nucl. Magn. Reson. 9:121–128.

Buhl, J.-C., and J. Löns. 1996. Synthesis and crystal structure of nitrate enclathrated sodalite $Na_8[AlSiO_4]_8(NO_3)_2$. J. Alloys Comp. 235:41–47.

Buhl, J.C., F. Stief, M. Fechtelkord, T.M. Gesing, U. Taphorn, and C. Taake. 2000. Synthesis, x-ray diffraction and MAS NMR characteristics of nitrate cancrinite $Na_7[AlSiO_4]_6(NO_3)_{1.6}(H_2O)_2$. J. Alloys Comp. 305:93–102.

Chorover, J., S. Choi, M.K. Amistadi, K.G. Karthikeyan, G. Crosson, and K.T. Mueller. 2003. Linking cesium and strontium uptake to kaolinite weathering in simulated tank waste leachate. Environ. Sci. Technol. 37:2200–2208.

Cuadros, J., and J. Linares. 1996. Experimental kinetic study of the smectite-to-illite transformation. Geochim. Cosmochim. Acta 60: 439–453.

Gephart, R.E., and R.E. Lundgren. 1998. Hanford tank cleanup: A guide to understanding the technical issues. 4th ed. Battelle Press, Columbus.

Gerson, A.R., and K. L. Zheng. 1997. Bayer process plant scale: Transformation of sodalite to cancrinite. J. Crystal Growth 171:209–218.

Hackbarth, K., T.M. Gesing, M. Fechtelkord, F. Stief, and J.C. Buhl. 1999. Synthesis and crystal structure of carbonate cancrinite $Na_8[AlSiO_4]_6CO_3(H_2O)_{3.4}$ grown under low-temperature hydrothermal conditions. Microporous Mesoporous Mater. 30:347–358.

Jenkins, D., V.L. Snoeyink, J.F. Ferguson, and J.O. Leckie. 1976. Water chemistry laboratory manual. Association of Environmental Engineering Professors.

Kaplan, D.I., K.E. Parker, and J.C. Ritter. 1998. Effects of aging quartz sand and Hanford sediment with sodium hydroxide on radionuclide sorption coefficients and sediment physical and hydrologic properties: Final report for Subtask 2a. Pacific Northwest National Laboratory, USDOE, Richland, WA.

Kinsey, R.A., R.J. Kirkpatrick, J. Hower, K.A. Smith, and E. Oldfield. 1985. High resolution aluminum-27 and silicon-29 magnetic resonance spectroscopic study of layer silicates, including clay minerals. Am. Mineral. 70:537–548.

Koroleff, F. 1983. Determination of silicon. p. 174–183. *In* K. Grasshoff et al. (ed.) Methods of seawater analysis. Verlag Chemie, Weinheim.

Mashal, K., J.B. Harsh, M. Flury, A.R. Felmy, and H. Zhao. 2004. Colloid formation in Hanford sediments reacted with simulated tank waste. Environ. Sci. Technol. 38:5750–5756.

Nyman, M., J.L. Krumhansl, P. Zhang, H. Anderson, and T.M. Nenoff. 2000. Chemical evolution of leaked high-level liquid wastes in Hanford soils. Mater. Res. Soc. Symp. Proc. 600:225–230.

Park, M., C.L. Choi, W.T. Lim, M.C. Kim, J. Choi, and N.H. Heo. 2000. Molten-salt method for the synthesis of zeolitic materials: I. Zeolite formation in alkaline molten-salt system. Microporous Mesoporous Mater. 37:81–89.

Pruess, K., S. Yabusaki, C.I. Steefel, and P.C. Lichtner. 2002. Fluid flow, heat transfer, and solute transport at nuclear waste storage tanks in the Hanford vadose zone. Available at www.vadosezonejournal.org. Vadose Zone J. 1:68–88.

Qafoku, N.P., C.C. Ainsworth, J.E. Szecsody, D. Bish, J.S. Young, D.E. McCready, and O.S. Qafoku. 2003a. Aluminum effect on dissolution and precipitation under hyperalkaline conditions: II. Solid phase transformations. J. Environ. Qual. 32:2364–2372.

Qafoku, N.P., C.C. Ainsworth, J.E. Szecsody, and O.S. Qafoku. 2003b. Aluminum effect on dissolution and precipitation under hyperalkaline conditions: I. Liquid phase transformations. J. Environ. Qual. 32:2354–2363.

Qafoku, N.P., C.C. Ainsworth, J.E. Szecsody, and O.S. Qafoku. 2004. Transport-controlled kinetics of dissolution and precipitation in the sediments under alkaline and saline conditions. Geochim. Cosmochim. Acta 68:2981–2995.

Serne, R.J., R.E. Clayton, I.V. Kutnyakov, G.V. Last, V.L. LeGore, T.C. Wilson, H.T. Schaef, M.J. O'Hara, K.B. Wagnon, D.C. Lanigan, C.F. Brown, B.A. Williams, C.W. Lindenmeier, R.D. Orr, D.S. Burke, and C.C. Ainsworth. 2002. Characterization of vadose zone sediment: Borehole 41–09–39 in the S-SX Waste Management Area. No. PNNL-13757-3. Pacific Northwest National Laboratory, USDOE, Richland, WA.

Serne, R.J., J.M. Zachara, and D.S. Burke. 1998. Chemical information on tank supernatants, Cs adsorption from tank liquids onto Hanford sediments, and field observations of Cs migration from past tank leaks. No. PNNL-11495. Pacific Northwest National Laboratory, Richland, WA.

Smith, B.F.L., and B.D. Mitchell. 1987. Characterization of poorly ordered minerals by selective chemical methods. p. 275–299. *In* M.J. Wilson (ed.) A handbook of determinative methods in clay mineralogy. Chapman and Hall, New York.

Taubald, H., A. Bauer, T. Schäfer, M. Satir, and J.I. Kim. 2000. Experimental investigation of the effect of high-pH solutions on the Opalinus shale and the Hammerschmiede smectite. Clay Miner. 35:515–524.

Wilson, M.A. 1987. NMR techniques and applications in geochemistry and soil chemistry. Pergamon Press, Oxford.

Wyckoff, R.W.G. 1968. Crystall structures: Miscellaneous inorganic compounds, silicates, and basic structural information. Vol. 4. 2nd ed. John Wiley & Sons, New York.

Zhao, H., Y. Deng, J.B. Harsh, M. Flury, and J. Boyle. 2004. Alteration of kaolinite to cancrinite and sodalite by simulated Hanford tank wastes and its impact on cesium retention. Clays Clay Miner. 52: 1–13.

Zheng, K., A.R. Gerson, J. Addai-Mensah, and R.S.C. Smart. 1997. The influence of sodium carbonate on sodium aluminosilicate crystallization and solubility in sodium aluminate solutions. J. Crystal Growth 171:197–208.

Environ. Sci. Technol. **2004**, *38,* 5750−5756

Colloid Formation in Hanford Sediments Reacted with Simulated Tank Waste

KHOLOUD MASHAL,[†] JAMES B. HARSH,[†] MARKUS FLURY,*[,†] ANDREW R. FELMY,[‡] AND HONGTING ZHAO[†,§]

Department of Crop and Soil Sciences, Center for Multiphase Environmental Research, Washington State University, Pullman, Washington 99164-6420, and Pacific Northwest National Laboratory, Richland, Washington 99352

Solutions of high pH, ionic strength, and aluminum concentration have leaked into the subsurface from underground waste storage tanks at the Hanford Reservation in Washington State. Here, we test the hypothesis that these waste solutions alter and dissolve the native minerals present in the sediments and that colloidal (diameter < 2 μm) feldspathoids form. We reacted Hanford sediments with simulated solutions representative of Hanford waste tanks. The solutions consisted of 1.4 or 2.8 mol/kg NaOH, 0.125 or 0.25 mol/kg $NaAlO_4$, and 3.7 mol/kg $NaNO_3$ and were contacted with the sediments for a period of 25 or 40 days at 50 °C. The colloidal size fraction was separated from the sediments and characterized in terms of mineralogy, morphology, chemical composition, and electrophoretic mobility. Upon reaction with tank waste solutions, native minerals released Si and other elements into the solution phase. This Si precipitated with the Al present in the waste solutions to form secondary minerals, identified as the feldspathoids cancrinite and sodalite. The solution phase was modeled with the chemical equilibrium model GMIN for solution speciation and saturation indices with respect to sodalite and cancrinite. The amount of colloidal material in the sediments increased upon reaction with waste solutions. At the natural pH found in Hanford sediments (pH 8) the newly formed minerals are negatively charged, similar to the unreacted colloidal material present in the sediments. The formation of colloidal material in Hanford sediments upon reaction with tank waste solutions is an important aspect to consider in the characterization of Hanford tank leaks and may affect the fate of hazardous radionuclides present in the tank waste.

Introduction

Hazardous waste containing radionuclides, such as ^{137}Cs and ^{90}Sr, stored in the underground tanks at the Hanford site (Washington State, U.S.A.) has leaked into the vadose zone. Hanford tank waste consists of supernatant liquids, slurries, sludges, and salt cakes (*1*). It is estimated that more than a million gallons of supernatant fluids have leaked into the subsurface, containing, at the time when the leaks occurred, 3.7×10^{16} to 7.4×10^{16} Bq (1 to 2 million Ci) of radiation, mainly from ^{137}Cs (*1*). The radioactive cesium is currently located in the vadose zone below the tanks with the majority of the activity concentrated between 20.1 and 25.6 m below ground surface with a leading edge perhaps reaching 40 m (*2, 3*). It is likely that Cs has moved to the observed depths by chromatographic transport within a high ionic strength liquor (*4*−*6*).

The composition of the tank waste at Hanford varies considerably, and there is a large uncertainty about concentrations and composition, but in general the supernatants show high pH, high aluminate concentrations, and high ionic strength, mainly contributed by NaOH, $NaNO_3$, and $NaNO_2$ (*7*). In some of the tanks, like the SX-108 and SX-109 tanks, it is estimated that concentrations of NaOH, $NaNO_3$, and $NaNO_2$ can reach 5 molar or higher (*7, 8*). When such concentrated liquors contact subsurface sediments, natural minerals are partially dissolved by the high alkaline waste solutions. Most Al and Si oxides show elevated solubility under high pH conditions; for instance, the solubility of silica compounds above pH 12.8 is greater than 0.1 mol/L (*9*). Dissolution rates of many aluminosilicates above pH 12 are similar to those below pH 3 (*9*).

At Hanford, leaking waste solutions are released to the sediments of the Hanford formation. These sediments are cataclysmic flood deposits and contain various mineral phases, including unstable primary minerals (e.g., feldspars and micas) and stable minerals (e.g., quartz, aluminosilicate clays, and sesquioxides) (*2*). Preliminary studies showed that considerable amounts of Si and Al are released from mineral phases when Hanford sediments were contacted with high pH solutions consisting of 1 M NaOH (*10*). As concentrations of Si and Al in the solution phase increase, secondary mineral phases can precipitate.

Different types of minerals may form under the conditions of extreme pH, ionic strength, and aluminum concentration as found at a Hanford leak situation. It is likely that amorphous and poorly crystalline aluminosilicates will form rapidly. As pH increases beyond mildly alkaline conditions, certain minerals, such as montmorillonite, are no longer stable and are transformed to tectosilicates, such as zeolites (*11*). Other minerals, such as kaolinite, have been found to transform to feldspathoids, i.e., sodalite and cancrinite, when reacted with NaOH at temperatures of 80 to 140 °C (*11*). From studies involving the Bayer process, where liquors of high NaOH concentration are reacted with bauxite ores, it has been reported that at high aqueous SiO_2 concentrations the mineral transformations follow a specific sequence, i.e., amorphous aluminosilicates → zeolite (Linde A) → sodalite → cancrinite (*12*). In experiments representing Hanford site conditions, where quartz was reacted with caustic $NaNO_3$ solutions containing dissolved Al, nitrate cancrinite precipitated on the quartz surface (*13*), and in an experiment with kaolinite, neoformation of the zeolite chabazite and the feldspathoids cancrinite and sodalite was observed (*14*).

Based on these studies of mineral transformations, we expect that, under conditions of a Hanford tank leak, native primary and secondary minerals will dissolve and transform to feldspathoid- and zeolite-type minerals. These newly formed minerals have a negative charge under alkaline conditions and contain both cations and anions in their framework. Consequently, contaminant cations present in the tank supernatants, such as ^{137}Cs, can adsorb to or

* Corresponding author phone: (509)335-1719; fax: (509)335-8674; e-mail: flury@mail.wsu.edu.
[†] Washington State University.
[‡] Pacific Northwest National Laboratory.
[§] Present address: Sandia National Laboratories, Albuquerque, NM 8718.

10.1021/es0349709 CCC: $27.50

Published on Web 09/29/2004

TABLE 1. Composition of Simulated Tank Waste (STW), Prepared at Room Temperature (20 to 22 °C), and Experimental Conditions of Batch Experiments

designation of solution	NaOH (mol/kg)	$NaAlO_4$ (mol/kg)	$NaNO_3$ (mol/kg)	pH	density (20 °C) (kg/L)	temp[a] (°C)	time[a] (days)	designation of colloids formed
control[b]	0	0	0	7.1[b]	0.99	50	40	colloid 0
STW1	1.4	0.125	3.7	14.2[c]	1.20	50	25, 40	colloid 1
STW2	2.8	0.125	3.7	14.5[c]	1.40	50	40	colloid 2
STW3	1.4	0.25	3.7	14.2[c]	1.30	50	40	colloid 3
STW4	2.8	0.25	3.7	14.5[c]	1.40	50	40	colloid 4

[a] Temperature and duration of batch reactions with sediments. [b] Distilled water. [c] Determined by titration which measures non-carbonate alkalinity (NCA), values reported are $14 + \log_{10}$ (NCA).

coprecipitate with them. If the new minerals occur in the colloidal size fraction, then there exists the possibility for colloid-facilitated transport of ^{137}Cs in the Hanford vadose zone.

We hypothesize that the elevated hydroxide concentrations of leaking Hanford tank waste cause native minerals to dissolve, thereby releasing Si from the mineral lattices. The increased Si concentrations, together with high Al concentrations originating from the tank waste itself, will lead to the precipitation of feldspathoid- and zeolite-type minerals, which are in the colloidal size fraction (operationally defined in this work as $< 2\ \mu$m in diameter).

Based on this hypothesis, the objectives of this work were to (1) determine the chemical, physical, and mineralogical characteristics of colloids formed by reacting Hanford sediments with simulated tank waste and (2) determine how colloid formation changes with tank waste composition.

Materials and Methods

Sediments and Sediment Characterization. Sediments used in this study were collected from the submarine pit (218-E-12B) at the Hanford site in January 2000. These sediments are representative, both in texture and mineralogy, of the material underlying the immediate vicinity of the S-SX (single-shell) tank farm at Hanford (personal communication, Bruce N. Bjornstad, September 2001, Pacific Northwest National Laboratories, Richland, WA). Detailed characterization data are given elsewhere (*15*). The sediments collected were uncontaminated and consisted of pebbly coarse sand belonging to the Hanford Formation. The sediments were air-dried and sieved through a 2 mm square screen. The sieved sediments were characterized in terms of pH (in 1:1 w/w water extract), organic carbon, EC, "free" Fe, cation exchange capacity, and particle size distribution. Particle size distribution was analyzed by wet sieving and static light-scattering with a Helium−Neon laser of 633 nm wavelength and reverse Fourier optics (MasterSizer S, Malvern Instruments Ltd., Malvern, U.K.). For particle size analysis, organic matter and calcium carbonate were removed with 30% w/w H_2O_2 and 0.5 M Na-acetate. The mineralogy of the sand and silt fraction of the sediments was determined by preparing thin-sections and examination with a petrographic microscope (*16*). The colloidal fraction (diameter $< 2\ \mu$m) of the sediments was characterized for a series of properties as described below.

Simulated Tank Waste Solutions. As there exists considerable uncertainty about, and variability in, the composition of Hanford tank waste (*7*, *10*), we used four different simulated tank waste (STW) solutions (Table 1). The solutions were prepared by incrementally dissolving various salts in deionized water, and the final solutions differed in NaOH and Al concentrations while NO_3^- concentration was kept constant (Table 1). The composition of the STW solutions was chosen to represent conditions found in the Hanford waste tanks (*7*). The waste solutions were always freshly prepared for each batch reaction experiment.

Batch Reaction Experiments. We reacted the Hanford sediments with the STW solutions in a series of batch experiments. One kilogram of sediment (<2 mm) and 1 L of STW (STW1, STW2, STW3, STW4) were placed into airtight capped 2 L polyethylene bottles. Temperature was controlled at 50 °C by an electric oven, and the reaction times were 25 and 40 days. Bottles were shaken by hand in an orbital motion once a day. The control treatment consisted of sediments with distilled water only.

A temperature of 50 °C was chosen based on ambient temperatures measured below Hanford waste tanks (*17*). Model simulations indicate that temperatures below SX-108 waste tanks at the time of leaks ranged from 30 up to 100 °C (*18*). Measured temperatures below the SX-108 waste tank in August 2000 were reported to be up to 55 °C and possibly even higher (*17*). The reaction times of 25 and 40 days were chosen based on the results of a preliminary study (data not shown), which showed that Si dissolution increased for the first 25 days of reaction time and then decreased, indicating both dissolution and precipitation processes.

After the specified time periods, sediments and liquids were transferred to polyethylene centrifuge bottles and centrifuged at 27 200 rgf for 60 min. The supernatant solution was decanted and stored at room temperature in polypropylene bottles sealed with a screw cap. The solid materials were washed with deionized water and centrifuged as specified above. This washing procedure was repeated four times. Solids were then transferred into a polyethylene graduated cylinder and dispersed in deionized water by sonication, and the fraction with diameter $< 2\ \mu$m was separated by gravity sedimentation. This fraction was then dialyzed with deionized water until the electrical conductivity of the dialysate fell below 0.01 dS/m. The dialyzed colloidal material, suspended in the dialysis solution, was stored in polyethylene bottles. An aliquot of the suspension was air-dried to determine colloid yield.

Solution Characterization. We measured Al, Si, Fe, K, Ca, and Mg in the supernatant solution by ICP-AES (Thermo Jarrell Ash IRIS ICP-AES) and Na by atomic absorption spectroscopy (Varian 220 Flame Atomic Absorption Spectrometer, Varian Ltd., Mulgrave, Australia). The pH and CO_3^{2-} were determined by titration. Nitrate was measured with an ion-selective electrode (Orion, 93 Series). Analytical equipment was calibrated with standard procedures. An aliquot of the supernatant was titrated with 0.53 M HCl to pH 8 and aged for one week. The precipitated solids were dried at 105 °C at atmospheric pressure for 24 h and weighed to measure solid yield.

Colloid Characterization. The colloidal fraction (diameter $< 2\ \mu$m) was characterized in terms of mineralogy, morphology, and surface characteristics. Mineralogy was determined by X-ray diffraction (XRD) with Cu−Kα radiation (Philips XRG 3100, Philips Analytical Inc., Mahwah NJ) with scanning

rates of 0.02 degrees 2-θ/s. The scans were collected using Datascan and processed with Jade (Materials Data, Inc.). The samples for XRD analysis were prepared by placing a small amount of colloidal material, suspended in deionized water, on a glass XRD slide, and letting the water evaporate at room temperature. We obtained FTIR spectra using KBr pellets (1% w/w) and a Perkin-Elmer 2000 IR spectrometer. The analyses were carried out in transmission mode between 400 and 4000 cm^{-1}. The resolution was 1.0 cm^{-1} with 64 scans. For scanning electron microscopy (SEM), the samples were diluted with deionized water and sonicated for 1 h, and a drop of suspension was placed on aluminum or carbon stubs. After air-drying, the samples were sputter-coated with gold or carbon and examined with an SEM Hitachi S-570. Carbon-coated samples were used for energy-dispersive X-ray analysis (EDAX) with a Kevex Micro-X7000 unit coupled with SEM. Mineralogical and microscopic methods were used in a qualitative mode, no quantitative analyses were attempted.

Electrophoretic mobilities were determined by dynamic light scattering using a ZetaSizer 3000 HSA with a Helium−Neon laser of 633-nm wavelength (Malvern Instruments Ltd., Malvern, U.K.) in a background electrolyte concentration of 10 mM $NaNO_3$ and a particle concentration of about 50 mg/L. The pH of the suspensions was adjusted between pH 4 and 11 with HNO_3 or NaOH. After pH adjustment, the solutions were gently agitated on a reciprocal shaker overnight. A final pH reading was taken immediately prior to the electrophoretic mobility measurement. Instrument performance was checked with standards of known electrophoretic mobility.

Thermodynamic Modeling. The GMIN chemical equilibrium model (*19*) was used in this study to predict the aqueous species and solid phases of Al and Si in equilibrium with the supernatant solutions after reactions with the sediments. GMIN is based upon the aqueous thermodynamic model of Pitzer and co-workers and is valid to high ionic strength. The Pitzer ion-interaction parameters in the GMIN database for aluminate ($Al(OH)_4^-$) are from ref *20* and for monomeric and polymeric silica species from ref *21*. The equilibrium constants for dissolution of sodalite (*22*) and two different crystalline phases of nitrate-cancrinite (*13*) were added to the thermodynamic database. The equilibrium constants calculated for the nitrate-cancrinite phases were determined only at one temperature (i.e. 89 °C), and since no information was available to correct these results to other temperatures, the 89 °C values were used for all temperatures.

Results and Discussion

Sediment and Supernatant Characterization. Unreacted sieved sediments were very coarse, consisting mainly of material between 50 and 2000 μm. Selected properties of the sediments are shown in Table 2.

After 40 days reaction time with STW1, STW2, STW3, and STW4, the Al concentration in the supernatant solution was lower than its initial concentration in the simulated tank solution (Figure 1). Only a small fraction (up to 2%) of the Al added to the solution remained in the supernatant. The fraction of Al remaining in solution was higher for the low initial Al concentrations (STW1 and STW2) than for the high initial Al concentrations (STW3 and STW4). A considerable amount of Si was released from the sediments (Figure 1). High NaOH concentrations produced higher Si concentrations after 40 days. The pH (non-carbonate alkalinity) dropped consistently relative to the initial pH, indicating the consumption of OH^- during dissolution of the minerals. The high pH treatments (STW2, STW4) resulted in a greater pH decrease, corresponding to the high dissolved Si concentration in the solution. The control solution (Hanford sediments reacted with deionized water, pH 7.1) had insignificant amounts of soluble Si in solution (0.001 mol/kg) and Al (0 mol/kg). The pH of the solution increased from pH 7.1 to 7.9 after 40 days, indicating a small amount H^+ consumption in these samples (Tables 1 and 3).

The composition of the solution after 40 days reflects the initial composition, OH^- attack of the sediment minerals, and precipitation of secondary phases (Table 3). Sodium and NO_3^- concentrations have been reduced as a result of the formation of cancrinite and sodalite, each of which contain these ions in their framework. Potassium and Fe are released from dissolution of native mineral sediments, including feldspars, micas, and magnetite (Table 2).

TABLE 2. Selected Properties of Hanford Sediments (Diameter < 2 mm)

attribute	value
particle diameter (% wt)	
< 2 μm	1
2−50 μm	3.8
50−2000 μm	95.2
median diameter[a] (μm)	1369
"free" Fe[b] (mg/kg)	2307.6
organic carbon[c] (g/kg)	2.19
pH (1:1 w/w H_2O)	7.8
EC (dS/m)	0.24
clay mineralogy	kaolinite, illite, chlorite, smectite
primary minerals	quartz, christobalite, amphibole, plagioclase, feldspar, mica, magnetite, microcline, albite

[a] By weight. [b] Citrate-bicarbonate-dithionite method (*33*). [c] Dry combustion using a LECO CNS 2000 Analyzer, St. Joseph, MI.

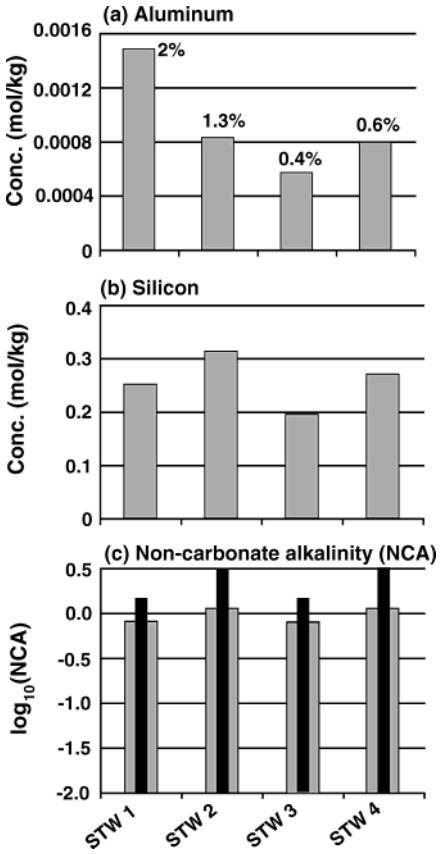

FIGURE 1. Measured concentrations of (a) Al and (b) Si and (c) non-carbonate alkalinity in solutions from batch reactions of Hanford sediments with simulated tank waste after 40-days reaction time at 50 °C. The percentages shown for Al are percentages of Al remaining from the initial solutions; the inner bars for the alkalinity show the initial alkalinity of the solutions.

TABLE 3. Measured Chemical Composition of the Solution Following Reaction of Simulated Tank Wastes (STWs) with Hanford Sediments at 50 °C for 40 Days

designation	Al (mol/kg)	Ca (mol/kg)	Fe (mol/kg)	K (mol/kg)	Mg (mol/kg)	Si (mol/kg)	Na (mol/kg)	NO_3 (mol/kg)	CO_3 (mol/kg)	NCA[a] (mol/kg)	pH[b] (mol/kg)
control	0	3.9×10^{-4}	0	7×10^{-5}	1.3×10^{-4}	0.0010	4.2×10^{-4}	0	0	7.1×10^{-7}	7.9
STW 1	0.0015	5.3×10^{-5}	0.0035	0.030	8.4×10^{-6}	0.2516	2.542	2.0642	0.0274	0.6254	13.8
STW 2	0.0008	1.1×10^{-5}	0.0021	0.031	8.1×10^{-5}	0.3129	2.669	1.6276	0.0427	1.1682	14.1
STW 3	0.0006	2.3×10^{-5}	0.0018	0.027	3.6×10^{-5}	0.1948	2.326	2.0096	0.0299	0.6026	13.8
STW 4	0.0008	2.1×10^{-5}	0.0018	0.033	6.0×10^{-5}	0.2704	2.691	1.8323	0.0320	1.0871	14.0

[a] NCA: non-carbonate alkalinity. [b] pH calculated from NCA by $pH = 14 + \log_{10}(NCA)$.

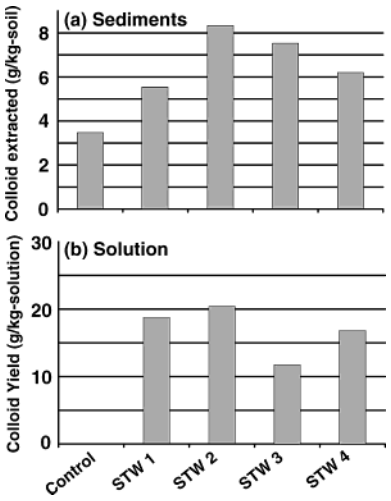

FIGURE 2. Amount of colloids (diameter < 2 μm) present after 40-days reaction time at 50 °C in (a) reacted Hanford sediments and (b) from solution after titration to pH 8.

Colloid Formation and Characterization. After treatment of the sediments with simulated tank wastes, the mass of colloidal particles in the sediments increased considerably (Figure 2a), indicating formation of secondary solids in the colloidal size range. In addition, the supernatant solution contained high amounts of dissolved silica, which upon titration to pH 8, precipitated as colloidal silica gel (Figure 2b), as confirmed by EDAX. The high amount of Si remaining in solution while most Al was precipitated (Figure 1a,b) indicates that Al was limiting colloid formation. Colloid yield from precipitating soluble material (mostly Si) from the supernatant solution at pH 8 was consistent with an Al limiting reaction. More Si was available for precipitation as gel at the higher NaOH concentrations (STW2 vs STW1 and STW4 vs STW3) but was lowered by increasing Al concentration (STW3 vs STW1 and STW4 vs STW2) (Figure 2b).

The X-ray diffraction pattern of the untreated Hanford sediments indicates that the < 2 μm fraction consisted of four major layered aluminosilicates, chlorite, smectite, kaolinite, and illite, and primary minerals, including quartz, christobalite, albite, and microcline (Figure 3). Upon reaction with STW, the diffraction peaks of the aluminosilicate clays became less pronounced, indicating alteration or dissolution of the clays. Under the high pH treatments (STW 2 and 4), chlorite, smectite, and kaolinite peaks almost disappeared. Illite appeared to be more resistant against STW treatment than the other aluminosilicate clays. The illite peak is stronger than the kaolinite, smectite, and chlorite peaks at the higher NaOH and Al concentrations. The quartz peak declined relative to the illite peak, indicating that colloidal quartz along with the aluminosilicate clays, was a significant source of Si in the sediments. It is also apparent that the high NaOH and low Al treatment of STW2 led to a large poorly crystalline component. Secondary minerals were formed upon reaction with STW and were identified as nitrate-cancrinite and sodalite, both feldspathoids. Nitrate-cancrinite dominated the diffraction patterns for all STW treatments, indicating an abundance of this mineral. Sodalite was present, but less abundant than cancrinite, as evidenced by the small peak at 20° 2θ, which is representative of sodalite alone.

The FTIR spectra corroborate the results from the XRD patterns. The unreacted sediments exhibit vibrational spectra typical of the same aluminosilicate and primary minerals indicated by XRD, namely kaolinite, smectite, chlorite, illite, quartz, and feldspars (Figure 4). We recognize the sharp OH doublet of kaolinite at 3696 and 3620 cm^{-1}. The absorption bands at 829 and 758 cm^{-1} and the slight broadening under the 3620 cm^{-1} band are indicative of illite, kaolinite, and smectite. The OH-stretching at 3425 cm^{-1} and the absorbance at 758 cm^{-1} are indicative of chlorite. The Al−OH stretching frequency band at 3620 cm^{-1} and the deformation band at 914 cm^{-1} are characteristic of dioctahedral smectites (*23*). The 1163, 1081, 798, 779, and 695 cm^{-1} bands indicate the presence of quartz. Albite can be identified at 531 and 470 cm^{-1} and microcline at 583 and 431 cm^{-1}.

The spectra of the reacted sediments provide evidence for the alteration of preexisting clay minerals and the formation of new minerals. The characteristic peaks for the preexisting aluminosilicates became less pronounced in some regions. The disappearance of the band at 914 cm^{-1} indicates that significant aluminum has been removed from octahedral environments. We also notice a decrease in intensity of the quartz bands and the appearance of new absorption bands. Strong peaks occurred at 682, 620, 573, 501, 463, and 430 cm^{-1}, which are characteristic for nitrate-cancrinite (*24*−*26*). There is evidence for the enclathration of nitrate groups in the cancrinite regardless of the STW composition. The peak at 1421 cm^{-1} is interpreted as NO_3^- inside the cancrinite structure, while the peak at 1382 cm^{-1} is attributed to small amounts of precipitated $NaNO_3$ on the outer surface of the crystal (*26*). These two peaks became sharper going from STW 1 to 4. The broad asymmetric Al−O−Si stretch at 1081 and 1011 cm^{-1} for the unreacted sediments shifted to 1032 and 993 cm^{-1}, consistent with the formation of feldspathoids (*27, 28*), at the expense of quartz (1081 cm^{-1}) and layer aluminosilicate clays (1011 cm^{-1}).

The electron micrograph of the untreated sample (colloid 0) shows the distinct morphology of the clay minerals present (Figure 5). Kaolinite, illite, and chlorite are platy in morphology, and the hexagonal structures are likely kaolinites, whereas the veil-like structures are smectites (*29*). After reaction with STW, we still see distinct platelike features of the original clay minerals, but, in addition, there occur spherical structures (Figure 5). This new morphology is typical for sodalite and cancrinite minerals (*12, 13*). These new minerals seem to nucleate and grow out of the platy structures of the original clay minerals, although it is also likely that particles have aggregated when colloidal suspensions dried on the electron microscopy stubs. There appears to be no significant morphological differences among the different tank waste compositions.

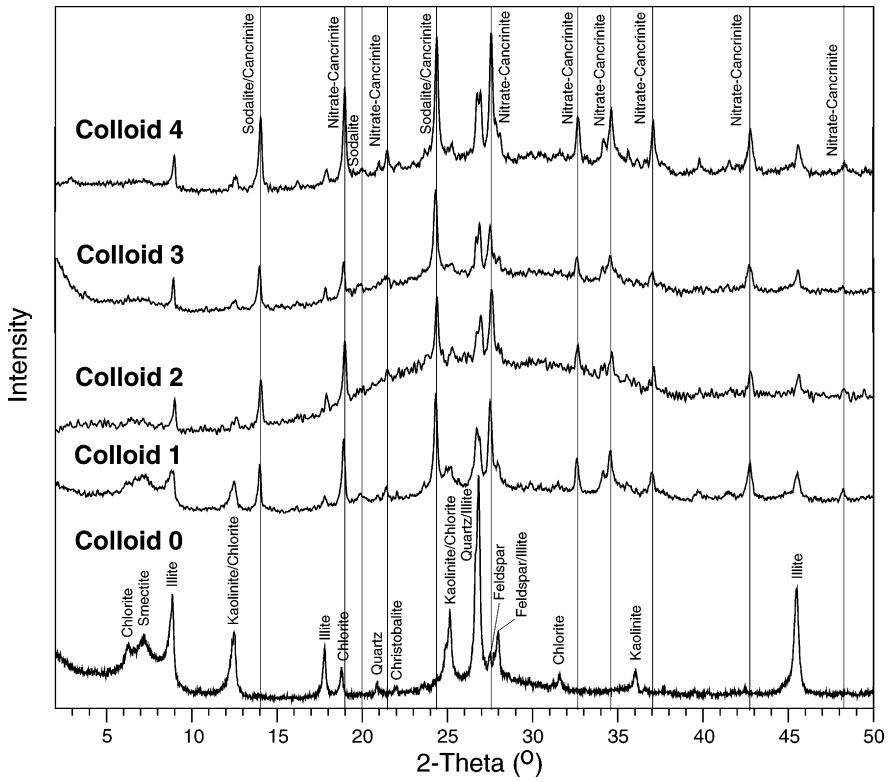

FIGURE 3. XRD patterns of unreacted (colloid 0) and reacted (colloids 1 to 4) Hanford sediments at 50 °C after 40-days reaction time. Vertical lines are characteristic spacings for nitrate-cancrinite and sodalite.

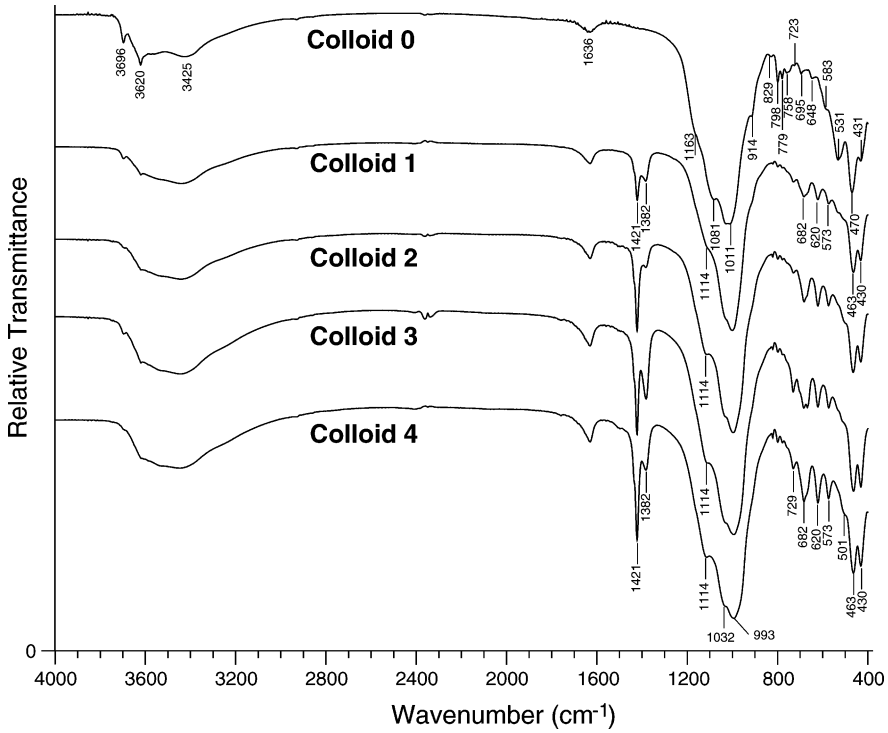

FIGURE 4. FTIR spectra of unreacted (colloid 0) and reacted (colloids 1 to 4) Hanford sediments at 50 °C after 40-days reaction time.

Electron micrographs of colloids formed from sediment after 25 days of reaction time with STW1 illustrate how the secondary minerals are formed (Figure 6a−d). The spherical structures, associated with sodalite and cancrinite, clearly grow out of the platelike structures of the original clay minerals (Figure 6b). This indicates that sodalite and cancrinite are the product of secondary nucleation and not the result of a direct solid-state transformation (*12*). A similar observation has been reported from reactions of simulated tank liquors with pure quartz (*13*). Some particles occur as single particles (Figure 6a,b) or appear to be aggregated (Figure 6d). The new ball-shaped structures contain mainly Si and Al, with smaller amounts of K, Ca, Fe, and Na, as identified by EDAX.

The electrophoretic mobility of the colloidal particles changed considerably after reaction with STW (Figure 7).

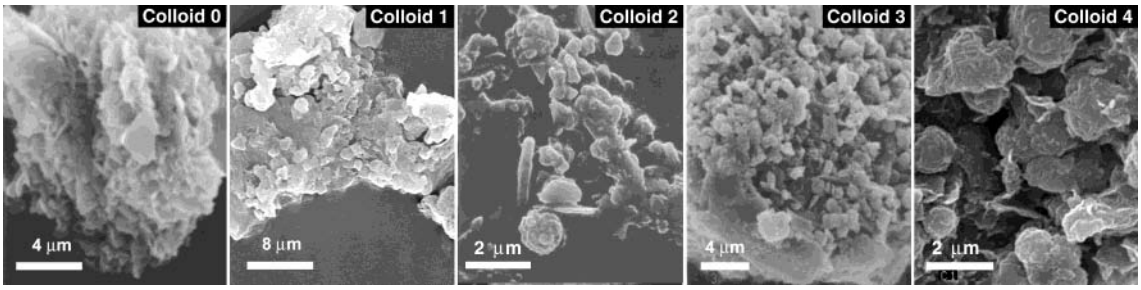

FIGURE 5. Scanning electron images of colloidal material in unreacted (colloid 0) and reacted (colloids 1 to 4) Hanford sediments following 40-days reaction time at 50 °C. Images were taken at 20 kV.

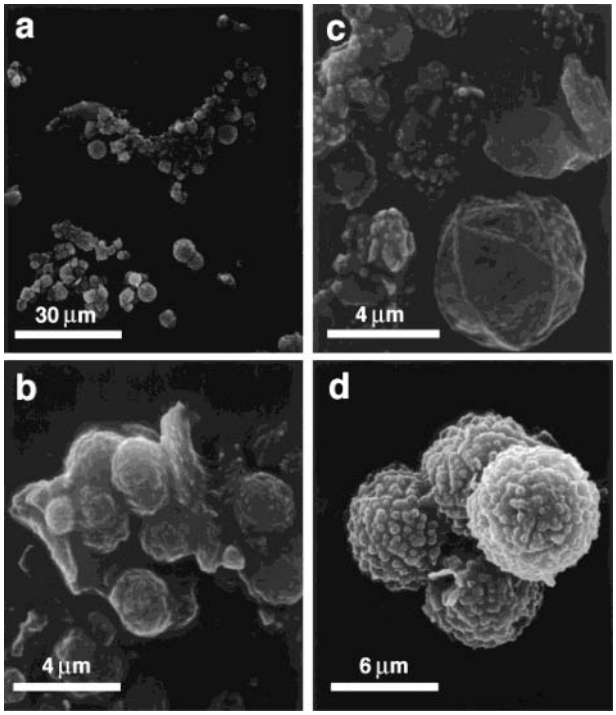

FIGURE 6. Scanning electron images of colloidal material in reacted Hanford sediments with simulated tank waste STW1 following 25-days reaction time at 50 °C. Images were taken at 20 kV.

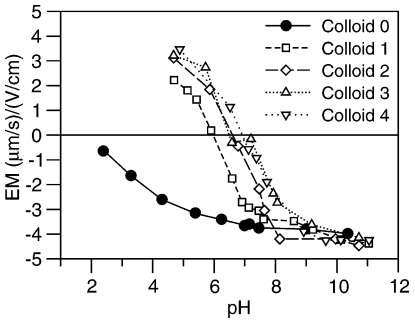

FIGURE 7. Electrophoretic mobility of colloidal material in unreacted (colloid 0) and reacted (colloids 1 to 4) Hanford sediments following 40-days reaction time at 50 °C. Measurements were made in 10 mM $NaNO_3$ electrolyte. Standard deviations of the measurements are smaller than twice the symbol size and are not shown.

The unreacted colloids have a negative electrophoretic mobility for pH values ranging from 2.5 to 11, typical for aluminosilicate clays, like smectite, illite, and chlorite (*30*). The mobility of these minerals becomes less negative at low pH due to protonation of edge sites or dissolution-exchange reactions with Al (*31*). The reacted colloids show a different behavior, and a charge reversal was observed between pH 6 and 8. The charge reversal is probably due to an artifact resulting from dissolution of the feldspathoids and formation of poorly crystalline aluminosilicates (allophane) and/or aluminum hydroxide at lower pH values. We have observed the loss of feldspathoids formed from kaolinite when pH becomes acidic (*32*). This suggests that the feldspathoids are not stable at acidic to neutral pH.

At higher pH, the reacted particles remain negatively charged and have a similar electrophoretic mobility to the unreacted colloids, although slightly more negative. Based on the results from XRD, FTIR, and electron microscopy, we know that the reacted colloids are a composite of unreacted, native minerals, altered native minerals, and secondary mineral phases. The electrophoretic mobility measured is an average of these composite samples and does not represent the mobility of any individual mineral phase.

The negative charge on the reacted colloids at pH values typical for the vadose zone at Hanford (pH > 7.5) suggests that the colloids (*1*) are likely to form relatively stable suspensions (*2*) and are not electrostatically attracted to the predominantly negatively charged surfaces of Hanford sediments, and (*3*) cations such as Cs^+ and Sr^{2+} will be electrostatically attracted to the colloids.

Thermodynamic Modeling. The results of the thermodynamic modeling showed that, despite the very high dissolved silica concentrations after reactions of simulated tank solutions with sediments, the dominant aqueous species in solution were monomeric (i.e., the $H_2SiO_4^{2-}$ species). Monomeric species accounted for 75 to 85% of the total silica species in solution. The most important polysilicate species were the linear and cyclic trimers (*21*). The high base concentration (0.3 to 0.8 M) enhanced the formation of $H_2SiO_4^{2-}$ from the polysilicates via reactions such as

$$Si_3O_6(OH)_3^{3-}(\text{cyclic}) + 3OH^- = 3H_2SiO_4^{2-}$$

The calculations also indicated that both forms of nitrate-cancrinite and sodalite were close to equilibrium, but all of the solutions were slightly oversaturated with respect to these minerals (Table 4). In the case of nitrate-cancrinite the calculated oversaturation could result from the use of a solubility product for these phases determined at 89 °C rather than the experimental temperature of 50 °C. It could also result from differences in the nature of the solids in this study. In any event, the thermodynamic modeling results indicate that precipitation of sodium aluminum silicate phases is indicated for these solutions, in agreement with the experimental observations.

Implications for Hanford Tank Leaks. When highly alkaline solutions, such as those from Hanford tank waste, leak into the subsurface, native minerals can be partially dissolved, releasing Si into the solution phase, and secondary mineral phases—cancrinite and sodalite—can form. In addition, we observed in our experiments that upon titration of the high pH supernatants, which result from the sediment-waste interactions, silica gel precipitated. This is likely to happen under natural conditions as well when tank leak

TABLE 4. Calculated Saturation Indices for Sodium Aluminosilicates[c]

	saturation index[a]		
solution	low OH cancrinite[b]	high OH cancrinite[b]	sodalite
STW 1	0.26	0.43	0.79
STW 2	0.12	0.29	0.65
STW 3	0.15	0.32	0.65
STW 4	0.14	0.29	0.65

[a] The saturation index is defined as $(\log_{10} \mathrm{IAP}/K)/N$, where IAP is the ion activity product, K is the thermodynamic equilibrium constant, and N is the number of ions in the dissolution reaction. [b] Based on equilibrium constants from ref *13* for solutions of 0.1 *m* OH^- (log $K_{eq} = 30.4$) and 1.0 *m* OH^- (log $K_{eq} = 36.2$). [c] Solution compositions are given in Table 3.

solutions are neutralized by dilution and chemical reactions. The newly formed minerals were in the colloidal size range and carried a negative net charge within the pH range found in natural Hanford sediments. Contaminant cations, such as ^{137}Cs, are likely to sorb to the newly formed minerals. Dissolution and precipitation of minerals due to the extreme chemical nature of the waste tank solutions should be considered in the characterization and interpretation of Hanford tank leaks.

Acknowledgments

This research was supported by the Office of Science (BER), U.S. Department of Energy, Grant No. DE-FG07-99ER62882. We thank Jeff Boyle and Youjun Deng (Washington State University, WSU) for help with XRD and cesium measurements, the Electron Microscopy Center at WSU for use of their facility, Dan Strawn for the use of FTIR, and John Zachara and Jeff Serne (Pacific Northwest National Laboratory) for providing us with the Hanford sediments.

Literature Cited

(1) Gephart, R. E.; Lundgren, R. E. *Hanford Tank Cleanup: A Guide to Understanding the Technical Issues*, 4th ed.; Battelle Press: Columbus, 1998.

(2) Serne, R. J.; Clayton, R. E.; Kutnyakov, I. V.; Last, G. V.; LeGore, V. L.; Wilson, T. C.; Schaef, H. T.; O'Hara, M. J.; Wagnon, K. B.; Lanigan, D. C.; Brown, C. F.; Williams, B. A.; Lindenmeier, C. W.; Orr, R. D.; Burke, D. S.; Ainsworth, C. C. *Characterization of Vadose Zone Sediment: Borehole 41-09-39 in the S-SX Waste Management Area*; PNNL-13757-3; Pacific Northwest National Laboratory, U.S. Department of Energy: Richland, Washington, 2002.

(3) Serne, R. J.; Clayton, R. E.; Kutnyakov, I. V.; Last, G. V.; LeGore, V. L.; Wilson, T. C.; Schaef, H. T.; O'Hara, M. J.; Wagnon, K. B.; Lanigan, D. C.; Brown, C. F.; Williams, B. A.; Lindenmeier, C. W.; Orr, R. D.; Burke, D. S.; Ainsworth, C. C. *Characterization of Vadose Zone Sediment: Slant Borehole SX-108 in the S-SX Waste Management Area*; PNNL-13757-4; Pacific Northwest National Laboratory, U.S. Department of Energy: Richland, Washington, 2002.

(4) Zachara, J. M.; Smith, S. C.; Liu, C.; McKinley, J. P.; Serne, R. J.; Gassman, P. L. *Geochim. Cosmochim. Acta* **2002**, *66*, 193-211.

(5) Steefel, C. I.; Carroll, S.; Zhao, P.; Roberts, S. *J. Contam. Hydrol.* **2003**, *67*, 219−246.

(6) Lichtner, P. C.; Yabusaki, S.; Pruess, K.; Steefel, C. I. *Vadose Zone J.* **2004**, *3*, 203−219.

(7) Serne, R. J.; Zachara, J. M.; Burke, D. S. *Chemical Information on Tank Supernatants, Cs Adsorption from Tank Liquids onto Hanford Sediments, and Field Observations of Cs Migration from Past Tank Leaks*; PNNL-11495/UC-510; Pacific Northwest National Laboratory: Richland, WA, 1998.

(8) Lichtner, P.; Felmy, A. *Comput. Geosci.* **2003**, *29*, 371−383.

(9) Brady, P. V.; Walter, J. V. *Geochim. Cosmochim. Acta* **1989**, *53*, 2823−2830.

(10) Kaplan, D. I.; Parker, K. E.; Ritter, J. C. *Effects of Aging Quartz Sand and Hanford Sediment with Sodium Hydroxide on Radionuclide Sorption Coefficients and Sediment Physical and Hydrologic Properties: Final Report for Subtask 2a*; PNNL-11965; Pacific Northwest National Laboratory, U.S. Department of Energy: Richland, Washington, 1998.

(11) Barrer, R. M. *Hydrothermal Chemistry of Zeolites*; Academic Press: London, 1982.

(12) Barnes, M. C.; Addai-Mensah, J.; Gerson, A. R. *Microporous Mesoporous Mater.* **1999**, *31*, 287−302.

(13) Bickmore, B. R.; Nagy, K. L.; Young, J. S.; Drexler, J. W. *Environ. Sci. Technol.* **2001**, *35*, 4481−4486.

(14) Chorover, J.; Choi, S.; Amistadi, M. K.; Karthikeyan, K. G.; Crosson, G.; Mueller, K. T. *Environ. Sci. Technol.* **2003**, *37*, 2200−2208.

(15) Serne, R. J.; Bjornstad, B. N.; Schaef, H. T.; Williams, B. A.; Lanigan, D. C.; Horton, D. G.; Clayton, R. E.; Mitroshkov, A. V.; LeGore, V. L.; O'Hara, M. J.; Brown, C. F.; Parker, K. E.; Kutnyakov, I. V.; Serne, J. N.; Last, G. V.; Smith, S. C.; Lindenmeier, C. W.; Zachara, J. M.; Burke, D. S. *Characterization of Vadose Zone Sediment: Uncontaminated RCRA Borehole Core Samples and Composite Samples*; PNNL-13757-1; Pacific Northwest National Laboratory, U.S. Department of Energy: Richland, Washington, 2002.

(16) Cady, J. G.; Wilding, L. P.; Drees, L. R. In *Methods of Soil Analysis. Part 1. Physical and Mineralogical Methods*, 2nd ed.; Klute, A., Ed.; American Society of Agronomy: Madison, Wisconsin, 1986; pp 185−218.

(17) Gardner, M. G.; Reynolds, K. D. *SX-108 Slant Borehole Completion Report*; Report No. RPP-6917, Rev. 0; prepared for CH2M HILL Hanford Group, Inc., Single Shell Tank Farms Vadose Zone Program by Waste Management Technical Services: Richland, WA, 2000.

(18) Pruess, K.; Yabusaki, S.; Steefel, C. I.; Lichtner, P. C. *Vadose Zone J.* **2002**, *1*, 68−88.

(19) Felmy, A. R. In *Chemical Equilibrium and Reaction Models*; Special Publication 42, Soil Science Society of America: Madison, WI, 1995; pp 377-407.

(20) Wesolowski, D. J. *Geochim. Cosmochim. Acta* **1992**, *56*, 1065−1091.

(21) Felmy, A. R.; Cho, H. M.; Rustad, J. R.; Mason, M. J. *J. Solution Chem.* **2001**, *30*, 509−525.

(22) Park, H.; Englezos, P. *Ind. Eng. Chemical Resourc.* **1999**, *38*, 4959−4965.

(23) Borchardt, G. In *Minerals in the Soil Environment*; Dixon, J. B., Weed, S. B., Eds.; Soil Science Society of America: Madison, WI, 1989; pp 675−727.

(24) Barrer, R. M.; Cole, J. F.; Villiger, H. *J. Chem. Soc. A* **1970**, 1523−1531.

(25) Moenke, H. H. In *The Infrared Spectra of Minerals*; Farmer, V. C., Ed.; Mineralogical Society: London, 1974; pp 365−382.

(26) Buhl, J. C.; Stief, F.; Fechtelkord, M.; Gesing, T. M.; Taphorn, U.; Taake, C. *J. Alloys Compds.* **2000**, *305*, 93−102.

(27) Farmer, V. C.; McHardy, W. J.; Palmieri, F.; Violante, A.; Violante, P. *Soil Sci. Soc. Am. J.* **1991**, *55*, 1162−1166.

(28) Whittington, B. I.; Fletcher, B. L.; Talbot, C. *Hydrometallurgy* **1998**, *49*, 1−22.

(29) McHardy, W. J.; Birnie, A. C. In *A Handbook of Determinative Methods in Clay Mineralogy*; Wilson, M. J., Ed.; Chapman and Hall: New York, 1987; pp 174−208.

(30) McBride, M. B. In *Minerals in the Soil Environment*; Dixon, J. B., Weed, S. B., Eds.; Soil Science Society of America: Madison, WI, 1989; pp 35−88.

(31) Swartzen-Allen, S. L.; Matijevic, E. *Chem. Rev.* **1974**, *74*, 385−400.

(32) Zhao, H.; Deng, Y.; Harsh, J. B.; Flury, M.; Boyle, J. *Clays Clay Miner.* **2004**, *52*, 1−13.

(33) Loeppert, R. H.; Inskeep, W. P. In *Methods of Soil Analysis. Part 3. Chemical Methods*; Sparks, D. L., Ed.; American Society of Agronomy: Madison, Wisconsin, 1996; pp 639−664.

Received for review September 4, 2003. Revised manuscript received August 16, 2004. Accepted August 17, 2004.

ES0349709

Colloid Transport in the Subsurface: Past, Present, and Future Challenges

John F. McCarthy* and Larry D. McKay

ABSTRACT

This paper attempts to introduce the work described in this special section on colloid transport within a more general perspective of the evolution of our understanding of the importance of colloids in subsurface systems. The focus will be on the transport of colloidal particles in natural (i.e., chemically and physically heterogeneous) geological settings because the complexity imposed by these situations represents the greatest challenge to current and future understanding. Great progress has been made in addressing many of the key questions related to colloid transport. However, as in most areas of science, increased knowledge also serves to reveal new and more complex challenges that must be addressed.

In evaluating progress in this area, it is worth recalling that the nature of our interests in particle transport in the subsurface has changed dramatically in the past few decades. Initial interest focused on microbial contaminants in aquifers, then expanded to include the influence of colloids on soil development, permeability of oil and gas reservoirs, transport of contaminants attached to colloids, and introduction of microorganisms for remediation of contaminated subsurface materials. Our understanding of even the most basic issues, such as the appropriate methods for obtaining a representative sample of groundwater that includes mobile colloids while avoiding colloidal artifacts, has changed substantially. Progress was quickly made in some areas, such as the development of a sense of the distribution of subsurface colloids and the processes that controlled their nature and abundance. However, even as understanding of groundwater colloids progressed, it became clear that theoretical understanding was not always successful in describing behavior in natural systems. While most work to date has focused on colloid transport in saturated systems, increased attention is being directed at problems in vadose transport. The vadose zone represents the critical connection between shallow contaminant sources and migrating groundwater. The complexities related to dealing with water, solute, and colloid transport in partially saturated systems is a challenge that will lead us well into the future.

RECOGNIZING THE PROBLEMS

Interest in colloid behavior in porous media is not new. Early studies on colloid mobilization and transport focused on microbial contamination of aquifers and water supply wells. Many of the approaches for dealing with microbial contamination, such as establishing minimum setback distances between wells and septic fields (onsite wastewater disposal systems) for individual homes, were based on empirical evidence of contaminant filtration and are still in use today (TDEC, 2002). Other studies focused on the role of clay migration from surface to deeper horizons in soil diagenesis (Jenny and Smith, 1935; Thorp et al., 1957). Mechanistic studies of colloid transport originally focused on issues of wastewater filtration and controlling aquifer permeability. Yao et al. (1971) described colloid removal for water filtration in terms of two rate-limiting steps: (i) the physical processes of diffusion, interception, and gravitation settling that result in collisions between colloids and grains and (ii) the chemical factors controlling the interaction forces that result in attachment of the colloid to the grain surface. Many early studies on colloid behavior in geological media focused on the effects of aqueous chemical conditions on colloid dispersion and the permeability of geological formations in an effort to improve oil and gas recovery (Khilar and Fogler, 1984; Cerda 1987; Kia et al., 1987). An early field-scale manipulation of colloid dispersion resulted from concern about drinking water supply at an artificial recharge site in California. High turbidity in the groundwater was attributed to the low ionic strength recharge water, and application of gypsum (calcium sulfate) at the recharge area prevented release of clays and alleviated problems with groundwater turbidity (Nightingale and Bianchi, 1977).

Recognition that colloids might be important in facilitating transport of other contaminants arose from studies demonstrating that strongly sorbing contaminants could travel much further and faster than would be anticipated from traditional solute transport models based on batch sorption data. For example, at the Nevada Test Site, surface-reactive radionuclides were observed in groundwater outside nuclear detonation cavities (Coles and Ramspott, 1982; Buddemeier and Hunt, 1988; Kersting et al., 1999). Likewise, enhanced transport of radionuclides at Chalk River Nuclear Laboratories in Canada (Walton and Merritt, 1980; Champ et al., 1984), Oak Ridge National Laboratory in Tennessee (McCarthy et al., 1998a, 1998b), and a U deposit in Australia (Short et al., 1988) were attributed to association of the contaminants with a mobile colloidal phase.

McDowell-Boyer et al. (1986) reviewed particle transport in porous media and pointed out that in addition to its importance in sanitary and geological engineering applications, groundwater colloids appeared capable of enhancing transport of contaminants that had a high affinity for sorbing to aquifer solids. A review by McCarthy and Zachara (1989) focused attention on colloid-

J.F. McCarthy and L.D. McKay, Department of Earth and Planetary Sciences, 306 Earth and Planetary Sciences Bldg., University of Tennessee, Knoxville, TN 37996-1410. Received 5 Aug. 2003. Special Section: Colloids and Colloid-Facilitated Transport of Contaminants in Soils. *Corresponding author (jmccart1@utk.edu).

Published in Vadose Zone Journal 3:326–337 (2004).

677 S. Segoe Rd., Madison, WI 53711 USA

Abbreviations: AW, air–water [interface]; CEC, cation exchange capacity; SW, solid–water [interface].

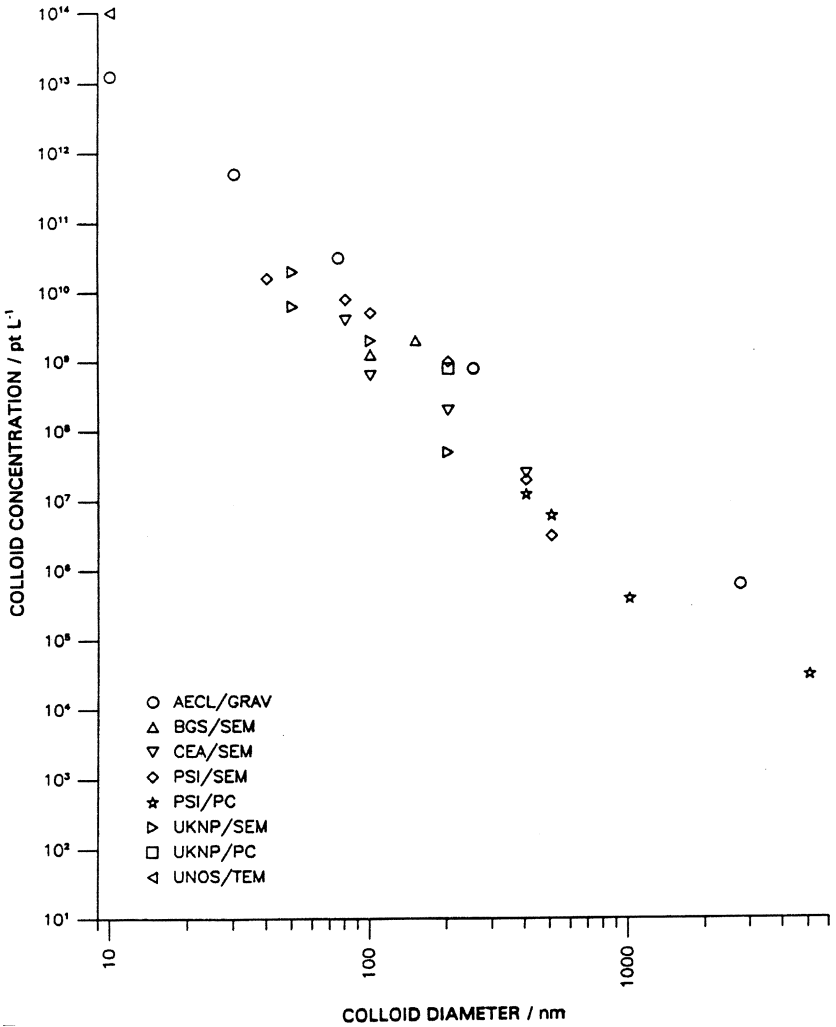

Fig. 1. The main result of the Grimsel Colloid Exercise interlaboratory comparison of the cumulative size distribution of colloidal particles recovered at the Grimsel Test Site. Laboratories that contributed to this exercise included: Atomic Energy of Canada, Limited (AECL); British Geological Survey (BGS); Commissariat de l'Energie Atomique (CEA); Paul Scherrer Institute (PSI); Harwell Laboratory Nuclear Physics Division (UKNP); and the University of Norway (UNOS). Techniques used to characterize colloids includes gravimetry (GRAV), scanning electron microscopy (SEM), single-particle counting (PC), and transmission electron microscopy (TEM). The cumulative contribution of different sized particles to the total colloid concentration in Grimsel groundwater (particles [pt] L^{-1}) is indicated. The cumulative size distribution follows Pareto's power law: $\log C_n = 15.8(\pm 0.4) - 3.2(\pm 0.2) \log(d)$, where C_n is the cumulative particle concentration for sizes ranging from 25 000 nm to d (Degueldre et al., 1989).

facilitated contaminant transport. Subsequent reviews of the subject have highlighted the growing body of literature on colloid transport (Ryan and Elimelech, 1996; Kretzschmar et al., 1999). Much of the progress in understanding groundwater colloids can be attributed to coordinated and interdisciplinary research programs at the national and international level. For example, the Commission of European Countries' program on performance assessment of nuclear waste repositories included a subgroup (dubbed the Co-Co Club), which focused on the role of colloids and complexants on radionuclide transport. This group organized the first systematic study of colloids in the subsurface. The Grimsel colloid exercise (Degueldre et al., 1989) examined colloids in a series of sites within crystalline rock in the Swiss Alps. The study mobilized a dozen research groups using multiple methods to characterize the nature and abundance of colloids (Fig. 1). They demonstrated the polydispersity of groundwater colloids, but found that the particle size distribution of colloids conformed to a power law. Other funding agencies, such as the USDOE's Subsurface Science Program, also organized multidisciplinary groups to examine colloid transport in groundwater. Subsequently, a large number of national and international workshops and symposia have been organized to share new results and help promote cooperation among colloid researchers. The workshop in Tjele, Denmark that has resulted in this special section is the latest effort in this direction and has the distinction of focusing attention on colloid transport in the vadose zone.

COLLOID TYPES AND CHARACTERISTICS

A variety of inorganic and organic materials exist as colloids and small particles in groundwater, including mineral precipitates (notably iron, aluminum, calcium,

and manganese oxides, hydroxides, carbonates, silicates and phosphates, but also including oxides and hydroxides of actinide elements such as U, Np, and Am), rock and mineral fragments (including layer silicates, oxides, and other weathering products of mineral phases), biocolloids (including viruses, bacteria, and protozoans), microemulsions of nonaqueous phase liquids, and macromolecular components of natural organic matter (including some components of humic substances and other polymers such as exocellular biopolymeric material secreted by microorganisms). This paper will focus primarily on inorganic colloids and biocolloids.

Considering this diversity of materials, it is worth noting that much of our understanding of colloid transport is based on studies of model colloids, which are not necessarily representative of the complex shapes and surface characteristics of natural environmental colloids. For example, even in model systems of latex particles and glass beads, particle deposition has frequently been observed to be greater than that theoretically predicted, and surface roughness has been considered a possible cause (Tobiason, 1989; Elimelech and O'Melia, 1990). This association is consistent with theoretical and experimental results by Suresh and Walz (1996, 1997), who demonstrated that surface roughness on latex microspheres reduced electrostatic repulsion. In their model system, roughness of only tens of nanometers resulted in the lower repulsive barrier, suggesting that roughness could have a significant impact on transport of irregularly shaped natural colloids. Spatial heterogeneity in surface chemistry is another characteristic of natural systems, and the impact of patch-wise heterogeneity of surface properties of colloids transport will be discussed below.

Bacterial transport is of interest as both a pathogen risk and a remedial strategy to degrade or immobilize contaminants in groundwater. However, the bacterial cell wall is structurally and chemically more complex and heterogeneous than the surfaces of inorganic colloidal particles. The cell surface is highly dynamic, responding to a variety of environmental changes. For example, cell size, hydrophobicity, exopolymer production, and other factors that affect transport can change in response to starvation (Heise and Gust, 1999). From an electrostatic perspective, bacteria must be viewed as soft particles in which ions can penetrate through the thickness of the surface appendages on the cells, and thus require a fundamentally different description of surface interaction forces than for ion-impenetrable inorganic colloids (Poortinga et al., 2002). Exocellular polysaccharides can promote attachment by bridging between the bacteria and aquifer surface, or inhibit it by preventing the bacteria from getting close to the surface. The role of these forces will vary, depending on the aqueous chemistry of the groundwater (Rijnaarts et al., 1999). Furthermore, individual cells within a bacterial population express different surface properties (Simoni et al., 1998), and surface charges and attachment probabilities can vary even within a single monoclonal bacterial population (Dong, 2002).

SAMPLING GROUNDWATER COLLOIDS

As the role of colloids in contaminant migration began to be recognized, it became quickly obvious that meaningful and accurate descriptions of subsurface colloids required a reevaluation and modification of groundwater sampling techniques typically accepted at the time. Groundwater samples are routinely obtained by pumping from wells. However, drilling, well construction, and pumping can greatly disturb the groundwater system. Drilling redistributes materials, creates fine particles, and provides a conduit for air to contact groundwater. Interaction between groundwater and the well screen, sand-pack, or casing can cause chemical changes. Sampling procedures can introduce artifacts, including the shearing of attached colloids at high pumping rates (Puls and Powell, 1992) and creation of colloids by alteration in chemical and physical conditions, such as alterations of O_2 and CO_2 content, temperature, pH, and redox potential. For example, introduction of O_2 into Fe(II)-rich groundwater can lead to production of Fe(III) oxides colloids (Liang et al., 1993).

New protocols were formulated to address these concerns (Backhus et al., 1993; McCarthy and Degueldre, 1993). Gentle sampling at low purging and pumping rates was advocated to minimize shear forces at or near the well screen. The criteria for selecting pumping rates for a given well was to minimize draw-down of the water elevation in the well, so that the pumping rate was matched to the rate of natural recharge into the well. Furthermore, rather than purging a fixed number of well volumes to remove stagnant water in the well casing, the criteria for adequate purging became stabilization of water quality parameters, such as pH, O_2, specific conductance, redox potential, and turbidity. Exclusion of atmospheric O_2 during sampling is also important for anaerobic samples.

While these precautions have been broadly implemented for sampling of colloids in saturated groundwater systems, the concept of a representative colloidal sample is still problematic because the nature and abundance of colloids can be influenced by seasonal or storm-related variations in flow and chemistry, especially in unconfined aquifers or in fast-flow karst systems. Sampling and analysis of microorganisms in groundwater are especially problematic because traditional analytical methods (APHA, 1995) are based on culturing of viable cells and many pathogens of interest are not readily cultureable in the laboratory (Maier et al., 2000). This problem has been partly alleviated by the development of nucleic acid-based analyses, which can detect both viable and nonviable microorganisms (Abbadaszadegan et al., 1993, 1999a; Josephson et al., 1993).

The situation for colloid sampling in the vadose zone is even more uncertain because there have been few, if any, comparable studies on appropriate and effective techniques for sampling colloids in the vadose zone. This remains a critical challenge.

COLLOID TRANSPORT IN SATURATED SYSTEMS: THE PROBLEM OF HETEROGENEITY

While a theoretical framework exists for describing colloid formation, stability, and transport in model systems, the principal scientific issue that limits prediction is understanding of how colloids behave in natural subsurface systems. Natural systems have complex solution chemistry and include mixed colloidal phases (e.g., layer silicates, Fe-, Al-, and Si-(hydr)oxides and natural organic matter). The kinetics of colloid formation and dissolution, and the crystallinity, surface characteristics, and colloidal stability of mineral oxides are affected by the presence of specific solutes and other colloids. Furthermore, chemical and physical heterogeneity affects colloid behavior at a range of spatial and temporal scales. At the microscopic scale, detachment and mobilization rates are affected by factors such as the arrangement and nature of surface functional groups, surface hydrophobicity, and surface roughness, as well as by the physical arrangement of the colloidal phases relative to the larger grains and pore spaces. Colloid transport at the field scale will be affected by the spatial distribution of physical and chemical features along a flow path in an aquifer. Some examples of these issues are discussed below.

Heterogeneity in Surface Charge

Filtration theory (Yao et al., 1971) has proven effective in predicting colloid attachment under conditions where colloid–grain interactions are attractive, but subsurface environments most often involve conditions unfavorable to colloid deposition due to electrostatic repulsion between the generally negatively charged media and colloids. The extent of colloid transport is generally described in terms of the magnitude of the surface charge on the colloids and aquifer surfaces. However, spatial heterogeneity in surface charge can render the average surface charge of the grains (as measured by the zeta (ζ) potential) irrelevant to transport predictions. This was very effectively illustrated by Elimelech et al. (2000), who created patchwise heterogeneity by treating quartz grains with aminosilane, which reversed the surface charge from negative to positive. Mixing the aminosilane-modified and unaltered quartz grains in varying proportions created chemically heterogeneous porous media. The measured ζ potential increased with the increasing abundance of aminosilane-modified grains in the media (Fig. 2a). Conversely, the breakthrough of negatively charged 0.3-μm silica colloids was reduced as the proportion of the positively charged aminosilane-modified grains increased (Fig. 2b). However, these results differed substantially from those that would have been predicted based on the average ζ potential of the media. Theoretical collision efficiencies calculated for the measured ζ potential of porous media containing 0 to 50% aminosilane-modified grains predicted essentially complete breakthrough of the colloids ($C/C_0 \approx 1$). At the pH of the experiments, the ζ potential of the media containing 75 or 100% of the aminosilane-modified grains was positive, so all of the colloids should have been retained ($C/C_0 \approx 0$). Thus, the theoretical prediction of a dichotomous result of either complete breakthrough or complete retention is clearly at odds with the observed breakthrough curves (Fig. 2b). Colloid retention was controlled by attachment of individual aminosilane-modified grains, regardless of the average surface properties of the media. The results demonstrated the insignificance of the average ζ potential of chemically heterogeneous porous media. Although the extent of patchwise heterogeneity to colloid transport is clearly established in this study, characterization of

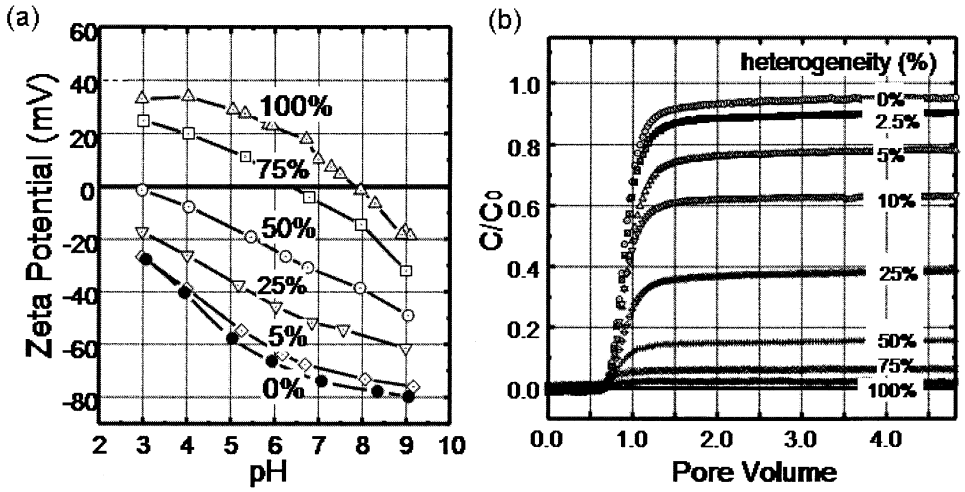

Fig. 2. Influence of patchwise heterogeneity on colloid transport. (a) Zeta potential as a function of solution pH for clean sand grains (filled circles), aminosilane-modified sand grains (filled triangles), and various mixtures of aminosilane-modified and clean sand grains (open symbols). Zeta potentials were calculated from measured streaming potentials. Experiments were conducted with 10^{-3} *M* NaCl as a background electrolyte at a temperature of 21°C. (b) Colloid transport in chemically heterogeneous granular porous medium at pH 5.6 to 5.8 and solution ionic strength of 10^{-3} *M*. Colloid breakthrough curves are expressed as normalized colloid concentration at the column effluent as a function of pore volume for various mixtures of aminosilane-modified and clean sand grains (ranging from clean sand, 0%, for the top curve to 100% for the bottom curve) (Elimelech et al., 2000).

the chemical heterogeneity is difficult even in laboratory-scale studies, and impractical in field studies.

Colloid Transport and Aqueous Chemistry

The importance of ionic strength and composition on colloid transport is well established. The expected effect—increased deposition at higher ionic strengths, and much greater retention in the presence of divalent, compared with monovalent, cations of comparable ionic strengths—is attributed to screening of repulsive surface interaction energies between colloids and grain surfaces. These relationships have been extensively demonstrated in laboratory studies, including in experiments with natural soil material (Grolimund et al., 1998). Particle deposition rates with solutions of Ca^{2+} were shown to be higher than with Na^{1+}, and the critical deposition concentrations with Na^{1+} were greater than those with Ca^{2+}. Although Grolimund et al. (1998) used natural soil, the columns were constructed using repacked, 2-mm soil particles. The aqueous chemistry within the column was controlled during the experiments, a precaution that was facilitated by the noncalcareous nature of the soil and its low cation exchange capacity (CEC).

While aqueous chemistry may control the interactions between colloids and geological media, chemical and physical properties of natural geological materials may in some cases control the aqueous chemistry, and thus the extent of colloid transport. The role of pore structure and geochemical processes was illustrated in a study of microsphere transport in intact monoliths of saprolite, which is a highly weathered, decomposed material that retains the fabric of the parent rock (McCarthy et al., 2002). As was found by Grolimund et al. (1998), recovery of the microspheres consistently decreased with ionic strength, but a much greater concentration of Na^{+1} in the influent solution was required to result in a similar reduction in colloid recovery as compared with Ca^{+2} (Fig. 3a).

Interpretation of those data was complicated, however, because the composition of the effluent solution was significantly altered along the flow path through the monolith (Fig. 3b). The change in aqueous chemistry was attributed in part to the significant CEC of the saprolite (140 mmol kg^{-1}), although the inputs of the monovalent influent solution before the introduction of the colloid injections greatly exceeded the total 1800 mmol of charge in the monolith. Of greater importance was the influence of the pore structure on the kinetics of solute interactions. While the total porosity of the saprolite was 49%, advective flow was primarily through the fractures, which constituted only about 3% of the porosity. Thus, failure to achieve a monocationic system during experiments with Na^{+1} input solutions (Fig. 3b) was attributed to slow diffusive exchange between the pore water in the fractures and in the fine-grained, Ca- and Mg-rich matrix. Divalent cations were released at concentrations sufficiently high that surface potentials would be determined solely by the divalent cation concentration, even during inputs of the Na solutions. The dominance of the divalent cations in colloid transport is

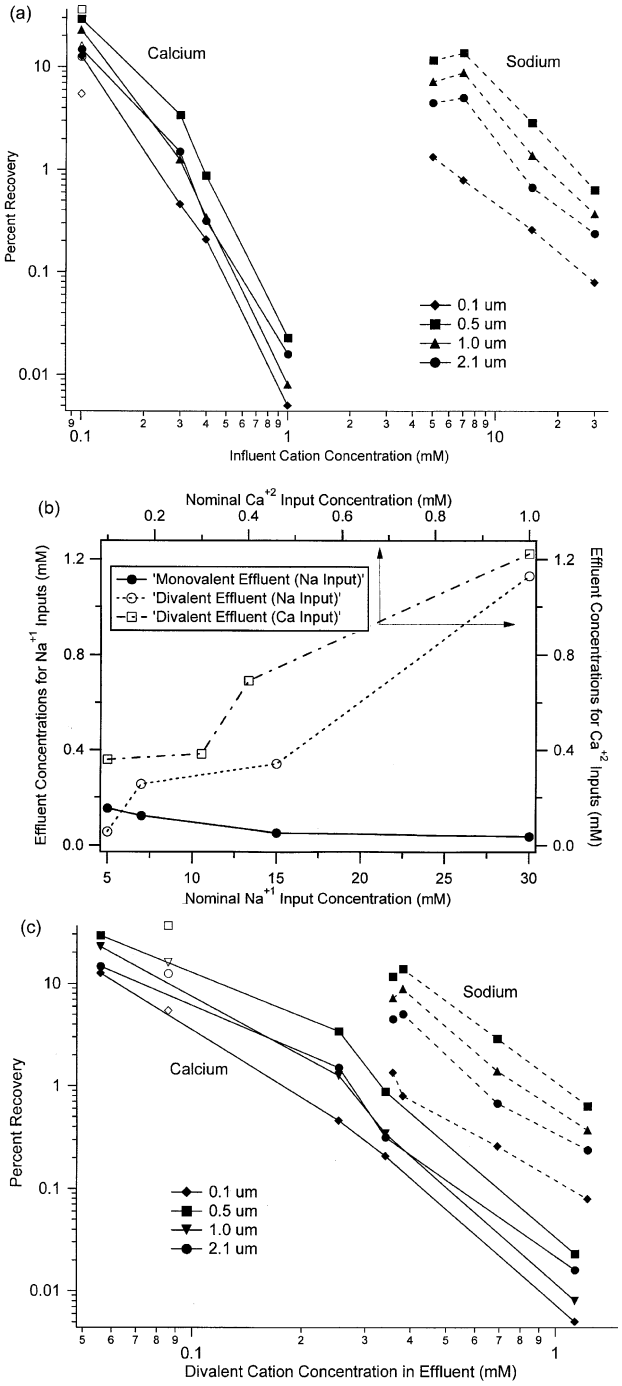

Fig. 3. Transport of four sizes of colloids through a saprolite monolith using input solutions of varying cation charge and ionic strengths. (a) The recovery of different sized microspheres is plotted as a function of the concentration of Na^{1+} (dotted lines) or Ca^{2+} (solid lines) in the influent tracer solution. The open symbols represent the percentage of recovery of microspheres in a replicate experiment conducted at the end of the series of injection experiments. (b) The concentration of monovalent (Na and K) and divalent (Ca and Mg) cations in the effluent of the monolith is plotted as a function of the concentration of Na^{+1} (bottom axis) or Ca^{+2} (top axis). The effluent concentrations of mono- and divalent cations during the experiments with Na^{+1} input solutions is shown on the left axis, while the effluent concentration of divalent cations during the experiments with Ca^{+2} input solutions is shown on the right axis. (c) The recovery of microspheres is plotted as a function of the concentration of divalent cations (sum of Ca^{2+} and Mg^{2+}) in the column effluent (McCarthy et al., 2002).

illustrated by the similarity in the slopes of the colloid stability curves (Fig. 3c). The greater recoveries of colloids in the Na experiments is likely related to the creation of a gradient of Na- to Ca-dominated chemistry along the flow path, resulting in shorter effective travel distances for colloids with a Ca-dominated solution chemistry.

Colloid Transport in Fractures and Karst

In addition to the effects described above of pore-scale exchange on colloid transport within dual-porosity systems, larger-scale structural heterogeneities, such as fractured or karstic formations, can function as superhighways for rapid transport of colloids. Karst aquifers, which typically occur in carbonate rocks, contain solution-enlarged fractures or conduits and often experience very rapid flow (kilometers per day) during and after heavy rains (White, 1988). Under these conditions large amounts of colloids and sediments can be suspended and rapidly transported. Studies of spring discharge in the marble karst of the Colonnata basin in Italy indicate annual sediment yields in the order of 100 t km^{-2} (Drysdale et al., 2001). Karst systems can transport a wide range of particle sizes and types (Atteia and Kozel, 1997), which can include pathogenic microorganisms as well as contaminants such as metals, that are attached to the suspended particles (Vesper and White, 2003). These systems are highly dynamic, with changes in suspended load a function of both physical factors such as flow rate and conduit size and chemical factors such as the pH of the infiltrating water (Shevenell and McCarthy, 2002). Understanding these processes and making even the most simple predictions of their behavior is still a major challenge.

Rapid transport of colloids can also occur in fractured materials, even those that are typically considered aquitards, rather than aquifers. This was demonstrated by a series of solute and colloid field tracer experiments that were performed in fractured, fine-grained glacial tills in Canada (McKay et al., 1993) and Denmark (McKay et al., 1999), and in a highly weathered shale saprolite in Tennessee (McKay et al., 2000). All of the materials had low to moderate hydraulic conductivity values (geometric mean of approximately 10^{-7} m s^{-1}) and flow was dominated by the fracture systems (Fig. 4). Solute and colloid tracers were introduced under conditions simulating natural flow. First arrival of the colloidal tracers (latex microspheres and bacteriophage) in the samplers occurred at rates of 2 to 5 m d^{-1} over a distance of 4 m in the Canadian till, and 1 to 6 m d^{-1} over a distance of 1.4 to 3.4 m in the Danish till. In the saprolite experiment, first arrival rates for the colloidal tracers ranged from 5 to 200 m d^{-1}, over distances of 2 to 35 m. In all cases the colloidal tracers arrived much earlier than the nonreactive solute tracers (bromide, chloride, or fluorescent dye), typically by factors of 10 to 100. This was largely due to diffusion of the solutes, but not the colloids, into the fine pore structure. These experiments demonstrate that colloid transport can occur very rapidly in a wide range of types of fractured materials and suggests the need for research on colloid entrainment and retention processes under these conditions.

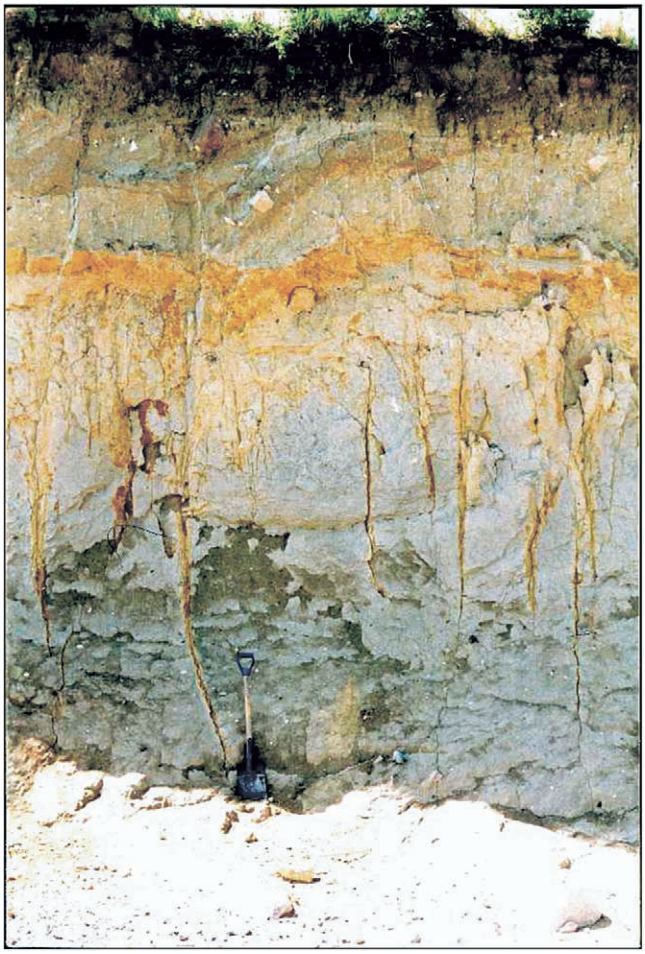

Fig. 4. Photograph of an exposure of a typical clay till overlying the Danien limestone in Denmark. The yellow staining results from infiltration along fractures through the till to the aquifer. For scale, the shovel at the bottom of the profile is 1.2 m long (source: Knud Erik Klint, Danish Geological Survey, GEUS).

COLLOID TRANSPORT IN THE VADOSE ZONE

Understanding colloid transport in partially saturated porous media is a major challenge that is only beginning to be addressed. In addition to all the difficulties posed by chemical and physical heterogeneity in water-saturated systems, predictions of colloid and pathogen transport in the vadose zone are further complicated by the presence of an air phase in addition to the solid and water phases present in saturated media. Challenges exist at a range of spatial scales, from the microscopic (interactions of colloids with the air-, water-, and solid interfaces) to the macroscopic (preferential flow and fingering), and include kinetic considerations on the resupply of colloids following transient infiltration events. In spite of the relevance of colloids to many environmental problems in the vadose zone, there has not been a strong focus on this topic by research groups or funding agencies. For example, colloids were barely mentioned

in a recent workshop and subsequent National Research Council Report on conceptual models of flow and transport in the fractured vadose zone (NRC, 2001).

Many of these issues are addressed in papers of this special issue, and will be addressed only briefly to place the results of specific studies in broader perspective.

Colloids and the Air, Water, Solid Interfaces

The interaction of colloids with the air–water (AW) interface has been invoked as a dominant process in colloid retention (Wan and Wilson, 1994a). Wan and Tokunaga (1997) also proposed an additional colloid retention mechanism, film straining, which hypothesizes that transport of suspended colloids can be retarded due to physical restrictions imposed when the thickness of water films falls below the diameter of the colloids.

Most subsequent studies of colloid transport under conditions of partial saturation have been based on mass balance of colloid breakthrough in packed sand columns (Wan and Wilson, 1994b; Schafer et al., 1998; Jewett et al., 1999; Jin et al., 2000; Lenhart and Saiers, 2002), rather than direct visualization. Reduced colloid transport at lower water contents (and presumably greater areas of AW interfaces) was attributed to sorption at the AW interface and film straining (Corapcioglu and Choi, 1996; Lenhart and Saiers 2002). However, recent studies suggest that the assumed dominant roles of the AW interface and film straining should be reevaluated.

It has been generally assumed, based on visualization studies of Wan and Wilson (1994a), that retention at the AW interface was relevant to a wide variety of colloids, including hydrophilic and hydrophobic latex microspheres, clay particles, and bacteria and viruses (Wan and Wilson, 1994b; Corapcioglu and Choi, 1996; Schafer et al., 1998; Lenhart and Saiers, 2002; Gamerdinger and Kaplan, 2001; Sirivithayapakorn and Keller, 2003). More recently, Wan and Tokunaga (2002) demonstrated in bubble column experiments that only positive charged particles attached to the negatively charged AW interface, suggesting that immobilization at the AW interface would be limited to a smaller subset of environmental colloids. Wan and Tokunaga (1997) conceptualized film straining as a colloid retention process within thin films of water flowing from one pendular ring to the next. However, Lenhart and Saiers (2002), noting that calculated water film thicknesses were 20-fold smaller than their 0.4-μm colloids, concluded that the relevant immobilization process was the degree of pendular ring discontinuity, rather than immobilization in thin water film.

Crist et al. (2004) reported a real-time, pore-scale, three-dimensional visualization technique to examine colloid movement through a packed sand column. They observed that hydrophilic, negatively charged latex colloids were not retained at either the AW or the solid–water (SW) interfaces. Instead, the colloids concentrated at the edge of pendular rings, that is, within but not attached to the thin film of water between the AW interface and the surface of the sand grain. Although the importance of distinguishing between colloid attachment at the AW interface and colloid immobilization near the air–water–solid interface has not been examined, there may be implications for remobilization of colloids. Air–water interfaces would be swept away by infiltrating water, thus favoring remobilization of colloids attached to that interface. In contrast, as was observed by Crist et al. (2004), colloids retained very near the grain surfaces, under laminar flow conditions characteristic of water movement in porous media, would be subject to very slow flow velocities, and thus could remain near the grain surfaces even without firm attachment.

Kinetic Constraints on Colloid Mobilization

Water movement in natural soils is dominated by transient infiltration events rather than steady-state unsaturated flow. Infiltration of water through intact macroporous soil was shown to result in mobilization and transport of previously deposited, in situ colloids (Jacobsen et al., 1997; de Jonge et al., 1998; Schelde et al., 2002). Furthermore, subsequent irrigation events could leach more colloids, although the amount of colloids mobilized in the subsequent wetting was dependent on the length of the flow delay. The amount of colloids leached appeared unrelated to the irrigation rate, suggesting that hydrodynamic shear was not involved.

The data demonstrate that irrigation can result in rapid mobilization and transport of an initial peak of colloids. As infiltration continues, the supply of readily mobilized colloids in the soil macropores is depleted. Between irrigation events, a time-dependent process replenishes the supply of readily mobilized colloids. Schelde et al. (2002) developed an equivalent macropore model that hypothesized that the resupply of colloids was a diffusion-limited process governed by two processes, one involving time-dependent release of colloids from the soil matrix to the crust at the macropore wall, followed by diffusion of those colloids through a layer of immobile water adjacent to the crust. The magnitudes of the mass transfer coefficients reported in these studies raise some question as to true origin of the time-dependent process(es). However, the work clearly highlights the need for additional experimental and theoretical studies to resolve the mechanistic basis for the time-dependent resupply of mobile colloids. Kjaergaard et al. (2004) examined the effect of clay content and soil water potential on colloid mobilization. Their results make clear that understanding of colloid mobilization in natural structured soil will be a complex challenge that must encompass both intrinsic soil properties and dynamic processes controlling soil aggregate structure and stability, macropore development, and colloid dispersion.

Episodic Flow, Preferential Flow, and Fingering

Most current models of water, solute, and colloid movement in partially saturated media are based on the traditional Richards equation without hysteresis in the soil water characteristic curve, which is based on uniform flow in a continuum (Milly, 1988). However, infil-

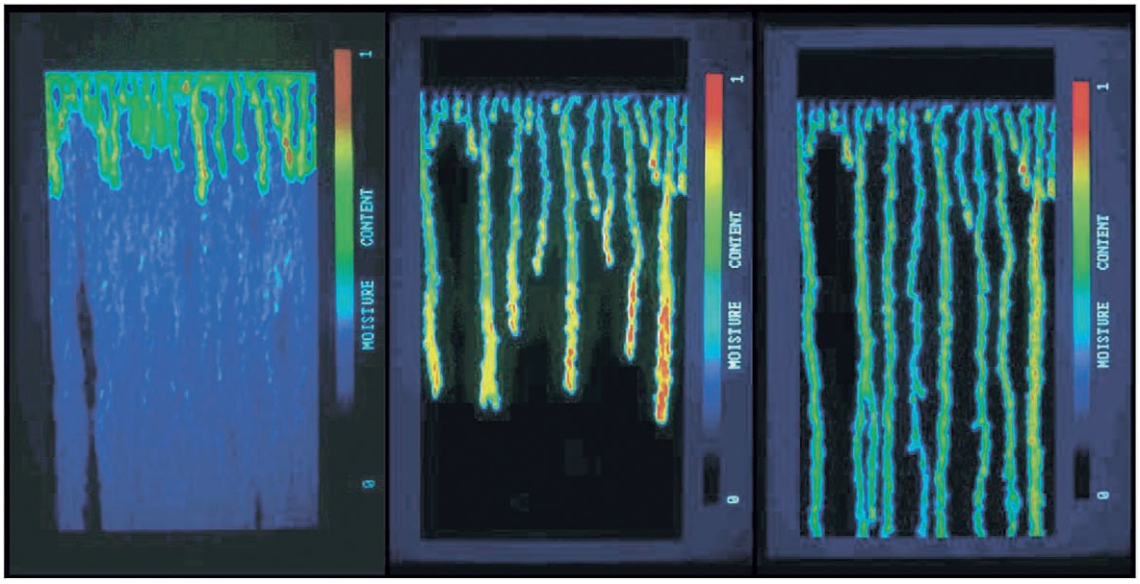

Fig. 5. Moisture content visualization of finger formation and persistence in a sand slab (Glass et al., 1989).

tration at the soil surface is often highly episodic, which can lead to large changes in the water table elevation or even development of perched water tables (i.e., transient saturated conditions underlain by unsaturated materials). This is especially common in fractured or macropore-dominated materials, where filling and drainage occur much more rapidly in the fractures and macropores than in the fine-grained soil matrix (NRC, 2001). As a result, flow rates and shear stresses, which can mobilize colloids, tend to vary over a much wider range in the vadose zone than in the saturated zone.

Rapid infiltration, especially in materials that initially have a relatively low degree of saturation, can also induce flow instabilities or fingers (Fig. 5). Development of fingering can result in rapid downward flow and the efficient transport of colloids through the vadose zone, even under bulk moisture conditions where traditional theory (uniform flow) would predict very slow migration. Also, when the bulk moisture content (outside the fingered flow paths) is below the critical moisture content for interconnected water films, much thicker water films along grain surfaces or more hydraulically conductive fingers (DiCarlo et al., 1999) are postulated to exist within the flow paths.

Layered structural interfaces can also initiate development of fingered flow paths by creating capillary fringes when a fine layer overlies the coarse-grained layer (Kung, 1990a, 1990b; Steenhuis et al., 1991). Likewise, macropores and structural cracks will transport water to deeper depths with locally high moisture contents (Andreini and Steenhuis, 1990; Flury 1996). Episodic infiltration, preferential flow, and transient saturation at fingertips are important topics of research that could significantly alter predictions of the rate and extent of colloid transport through the vadose zone.

Microbial Transport

Understanding the transport behavior of microorganisms is particularly important in the vadose zone because the majority of pathogens found in drinking water supply wells likely originated from sources such as septic fields, land application of sewage sludge or animal waste, or leaking sewer lines. Although there is a substantial body of published research on microbial transport in the subsurface, much of it focuses on transport in the saturated zone (e.g., Keswick et al., 1982; Bales et al., 1989; Fontes et al., 1991; Hornberger et al., 1992; McKay et al., 1993; Pieper et al., 1997; Harvey, 1997; Chu et al., 2000; Ginn et al., 2002), rather than on transport in the vadose zone (e.g., Lance and Gerba, 1984; Powelson et al., 1990; Schafer et al., 1998; Jin et al., 2000; Chu et al., 2001). The vast majority of the published studies are based on laboratory experiments or modeling studies, with very few based on actual field investigations of microbial transport in the vadose zone.

In addition to the uncertainties concerning scaling of findings from the lab scale to the field scale, there are a number of other basic research issues relevant to both the saturated and vadose zones that still need to be addressed. One such issue is the influence of microbial shape, size, and surface characteristics on transport. Microbial surfaces are often very complex, with cell walls ranging from loosely held slime layers to rigid capsules, frequently with protrusions such as spikes, fimbria, and flagella (Maier et al., 2000). The protrusions can play an especially important role in attachment to soil particles. Poortinga et al. (2002) argued that this is one of the reasons that DLVO-based descriptions often fail to describe microbial adhesion. Even within monoclonal populations, the size and surface characteristics of bacteria can vary widely, affecting transport behavior (Heise and Gust, 1999; Simoni et al., 1998; Dong, 2002). Another problem is that there is very little information on the actual occurrence of pathogens in soils or groundwater. Instead, most environmental monitoring of microorganisms is based on indicator bacteria, such *Escherichia coli* and fecal coliforms (USEPA, 1986; Maier et al., 2000). Not only are many strains of these indicator organisms

nonpathogenic to humans, they may not be good indicators for the occurrence of other types of pathogens, such as protozoa and viruses. Only recently have there been any studies of the actual occurrence of pathogenic viruses in groundwater (Abbadaszadegan et al., 1999b; Azadpour-Keeley et al., 2003). Research on microbial transport also tends to focus on a just a few types of nonhazardous microbial or nonmicrobial tracers, such as bacteriophage PRD1 and MS2, *E. coli*, *Pseudemonas syringae*, indigenous bacterial strains, and various yeast cells or fluorescent microspheres (Keswick et al., 1982; Harvey, 1997). As a result, in many cases it isn't clear how widely applicable the results of these studies are to transport of actual microorganisms of environmental interest, such as specific pathogenic strains, or bacteria added to soils to increase contaminant degradation.

Other issues that need to be addressed include transport and survival of pathogens at large spatial and temporal scales. For example, performance of wastewater infiltration systems or land application of sewage sludge is likely to be influenced by the physical scale of the operation, the magnitude of water fluxes through the system, and the duration of operation. Intensive application of wastes has the potential to substantially change the physical, chemical, and biological properties of the vadose zone, and hence change its ability to filter out pathogens.

SUMMARY AND CONCLUSIONS

This introductory paper has presented a general, and admittedly subjective, perspective on some of the key challenges in colloid transport that have been, or need to be, addressed. These are summarized in Tables 1 and 2.

Two general topics were highlighted. First, the problem of chemical and physical heterogeneity in natural systems remains a key challenge in describing colloid transport and retention in saturated groundwater systems. Although the effect of individual factors, such as the surface charge of porous media, solution chemistry, or flow regime, can be fairly well described, these factors are seldom uniform and unchanging across spatial and temporal scales that are relevant to environmental processes. Practical methods do not currently exist for characterizing the distribution of those factors in natural systems, making it difficult to develop robust descriptions of behavior in natural systems. However, even given these limitations, it is important to recognize that research in complex systems is needed to at least help us to understand what we do not understand. For example, insights into the irrelevance of ζ potential in predicting colloid behavior in patchwise heterogeneous media (Elimelech et al., 2000) is critical to avoiding fallacious predictions. Likewise, it is important to realize that geochemical and pore-scale structural properties of a formation can have complex, and sometimes nonintuitive effects on colloid behavior. Slow diffusive exchange processes can strongly buffer against any effort to manipulate colloid behavior through imposed changes in solution chemistry (McCarthy et al., 2002). However, exchange of meteoric water and solutes in fine pores during storm events can also create rapid changes in solution chemistry that can result in short-term pulses of colloid mobilization and transport (Shevenell and McCarthy, 2002). New modeling approaches may be successful in addressing some of these problems. For example, inverse modeling theory may help identify the key processes controlling colloid transport in heterogeneous porous media. The technique has been used extensively in groundwater flow and solute transport. Comprehensive reviews have been provided by Yeh (1986), Kuiper (1986), Carrera (1998), Ginn and Cushman (1990), Sun (1999), and McLaughlin and Townley (1996). Using colloid arrival breakthrough curves, a forward colloid transport model can be used to solve a generalized inverse problem by identifying and prioritizing the subset of potential geologic and geochemical parameters and parameter structure needed to construct an accurate realization of colloid transport, and thus determine the most probable parameters and processes that are needed to accurately predict colloid transport (Sun, 1999; Sun et al., 2001; Tsai et al., 2003).

The second category of challenges, and the one that is the focus of this special issue, is colloid transport in the vadose zone. In many ways, it is fair to say that, with respect to the vadose zone, we don't really even know all the questions, let alone understand the an-

Table 1. Key challenges in saturated groundwater.

Issue	Implementation	Status
	Sampling	
Mobilization of colloids during sampling	Broad application	Well recognized
	Surface properties	
Patch-wise Heterogeneity	Lab and models Field application	Some success Largely ignored
	Solution chemistry	
Electrostatics	Lab and models Field application	Some success Limited, qualitative
Geochemical or structural	Lab and field	Generally ignored
	Structural heterogeneity	
Fracture flow	Intact monoliths, field scale	Descriptive at best

Table 2. Key challenges in the vadose zone.

Issue	Implementation	Status
	Sampling	
Distinguishing entrained- and retained colloids	Limited	Generally ignored
Temporal variations	Not well understood	Generally ignored
	Interfaces	
Air–water interface	Micromodels, columns	Accepted mechanism
Air–water–solid interface	New concept	Is it real? Implications?
	Kinetics and Flow	
Diffusive limitations	Macroporous soil	Needs broader investigation
Preferential flow	Heterogeneous and structured media	Unexplored for colloid transport

swers. Where are colloids retained? How are they mobilized? Even more fundamentally, how do we sample colloids in the vadose zone? The problem of heterogeneity is much more complex in the vadose zone and must account for additional features such as the spatial and temporal distribution of water content, water films, and matric potential. These complexities are exacerbated by the influence of transient recharge events that result in large and rapid excursions in water content and water chemistry. These challenges need to be addressed because mobile colloid transport can have a significant impact in terms of human risk from infiltrating pathogens, and environmental and ecological hazards from transport of contaminants to groundwater.

Rather than being discouraged by these difficulties, the work presented in this special issue clearly documents that current research is recognizing and systematically addressing these issues. The number of young and talented researchers focusing their careers on these challenges makes it difficult to be anything but optimistic about future progress in this field.

ACKNOWLEDGMENTS

We thank R.W. Gentry for reviewing the manuscript and valuable discussion, and the Center for Environmental Biotechnology of the University of Tennessee for partial support of this effort. We also thank M. Flury and two anonymous reviewers for comments that improved the manuscript.

REFERENCES

Abbadaszadegan, M., M.S. Huber, C.P. Gerba, and L.I. Pepper. 1993. Detection of enteroviruses in groundwater with the polymerase chain reaction. Appl. Environ. Microbiol. 59:1318–1324.

Abbadaszadegan, M.P., W. Stewart, M.W. LeChevallier, J.S. Rosen, and C.P. Gerba. 1999a. A strategy for detection of viruses in groundwater by PCR. Appl. Environ. Microbiol. 65:444–449.

Abbadaszadegan, M.P., W. Stewart, M.W. LeChevallier, J.S. Rosen, and C.P. Gerba. 1999b. Occurrence of viruses in groundwater in the United States. AWWARF, Denver, CO.

American Public Health Association. 1995. Standard methods for the examination of water and wastewater. 19th ed. APHA, Washington, DC.

Andreini, M.S., and T.S. Steenhuis. 1990. Preferential paths of flow under conventional and conservation tillage. Geoderma 46:85–102.

Atteia, O., and R. Kozel. 1997. Particle size distributions in waters from a karstic aquifer: From particles to colloids. J. Hydrol. 201: 102–119.

Azadpour-Keeley, A., B.R. Faulkner, and J.-S. Chen. 2003. Movement and longevity of viruses in the subsurface. EPA/540/S-03/500. USEPA, Washington, DC.

Backhus, D.A., J.N. Ryan, D.M. Groher, J.K. MacFarlane, and P.M. Gschwend. 1993. Sampling colloids and colloid-associated contaminants in groundwater. Ground Water 31:467–479.

Bales, R.C., C.P. Gerba, G.H. Grondin, and S.L. Jensen. 1989. Bacteriophage transport in sandy soil and fractured tuff. Appl. Environ. Microbiol. 55:2061–2067.

Buddemeier, R.W., and J.R. Hunt. 1988. transport of colloidal contaminants in groundwater: Radionuclide migration at the Nevada Test Site. Appl. Geochem. 3:535–548.

Carrera, J. 1998. State of the art of the inverse problem applied to the flow and solute transport problems. p. 549–585. *In* Groundwater flow and quality modeling. NATO ASI Ser. C. Kluwer, Dordrecht, The Netherlands.

Cerda, C.M. 1987. Mobilization of kaolinite fines in porous media. Colloids Surf. 27:219–241.

Champ, D.R., J.L. Young, D.E. Robertson, and K.H. Abel. 1984. Chemical speciation of long-lived radionuclides in a shallow groundwater flow system. Water Pollut. Res. J. Can. 19(2):35–54.

Chu, J., Y. Jin, M. Flury, and M.V. Yates. 2001. Mechanisms of virus removal during transport in unsaturated porous media. Water Resour. Res. 37:253–263.

Chu, J., Y. Jin, and M.V. Yates. 2000. Virus transport through saturated sand columns as affected by different buffer solutions. J. Environ. Qual. 29:1103–1110.

Coles, D.G., and L.D. Ramspott. 1982. Migration of ruthenium-106 in a Nevada Test Site aquifer: Discrepancy between field and laboratory results. Science 215:1235–1237.

Corapcioglu, M.Y., and H. Choi. 1996. Modeling colloid transport in unsaturated porous media and validation with laboratory column data. Water Resour. Res. 32:3437–3449.

Crist, J.T., J.F. McCarthy, Y. Zevi, P.C. Baveye, J.A. Throop, and T.S. Steenhuis. 2004. Pore-scale visualization of colloid transport and retention in partly saturated porous media. Available at www.vadosezonejournal.org. Vadose Zone J. 3:444–450 (this issue).

Degueldre, C., G. Longworth, V. Moulin, P. Vilks, C. Ross, G. Bidoglio, A. Cremers, J. Kim, J. Pieri, J. Ramsay, B. Salbu, and U. Vuorinen. 1989. Grimsel colloid exercise: An international intercomparison exercise on the sampling and characterization of groundwater colloids. Rep. TM-36. Paul Scherrer Institute, Würenlingen and Villigen, Switzerland.

de Jonge, H., O.H. Jacobsen, L.W. de Jonge, and P. Moldrup. 1998. Particle-facilitated transport of prochloraz in undisturbed sandy loam soil columns. J. Environ. Qual. 27:1495–1503.

Di Carlo, D.A., T.W.J. Bauters, C.J.G. Darnault, T.S. Steenhuis, and J.-Y. Parlange. 1999. Lateral expansion of preferential flow paths in sands. Water Resour. Res. 35:427–434.

Dong, H. 2002. Significance of electrophoretic mobility distribution to bacterial transport in granular porous media. J. Microbiol. Methods 51:83–93.

Drysdale, R., L. Pierotti, L. Piccini, and F. Baldacci. 2001. Suspended sediments in karst spring waters near Massa (Tuscany), Italy. Environ. Geol. 40:1037–1050.

Elimelech, M., and C.R. O'Melia. 1990. Effect of electrolyte type on the electrophoretic mobility of polystyrene latex colloids. Colloid Interface Sci. 44:165–178.

Elimelech, M., M. Nagai, C.H. Ko, and J.N. Ryan. 2000. Relative insignificance of mineral grain zeta potential to colloid transport in geochemically heterogeneous porous media. Environ. Sci. Technol. 34:2143–2148.

Flury, M. 1996. Experimental evidence of transport of pesticides through field soils—A review. J. Environ. Qual. 25:25–45.

Fontes, D.E., A.L. Mills, G.M. Hornberger, and J.S. Herman. 1991. Physical and chemical factors influencing transport of microorganisms through porous media. Appl. Environ. Microbiol. 57:2473–2481.

Gamerdinger, A.P., and D.I. Kaplan. 2001. Physical and chemical determinants of colloid transport and deposition in water-unsaturated sand and Yucca Mountain tuff material. Environ. Sci. Technol. 35:2497–2504.

Ginn, T.R., and J.H. Cushman. 1990. Inverse methods for subsurface flow: A critical review of stochastic techniques. Stochastic Hydrol. Hydraul. 4:1–26.

Ginn, T.R., B.D. Wood, K.E. Nelson, T.D. Scheibe, E.M. Murphy, and T.P. Clement. 2002. Processes in microbial transport in the natural subsurface. Adv. Water Resour. 25:1017–1042.

Glass, R.J., T.S. Steenhuis, and J.-Y. Parlange. 1989. Wetting front instability. 2. Experimental determination of relationships between system parameters and two-dimensional unstable flow field behavior in initially dry porous media. Water Resour. Res. 25:1195–1207.

Grolimund, D., M. Elimelech, M. Borkovec, K. Barmettler, R. Kretzschmar, and H. Sticher. 1998. Transport of in situ mobilized colloidal particles in packed soil columns. Environ. Sci. Technol. 32:3562–3569.

Harvey, R.W. 1997. Microorganisms as tracers in groundwater injection and recovery experiments: A review. FEMS Microbiol. Rev. 20:461–472.

Heise, S., and G. Gust. 1999. Influence of the physiological status of bacteria on their transport into permeable sediments. Mar. Ecol. Prog. Ser. 190:141–153.

Hornberger, G.M., A.L. Mills, and J.S. Herman. 1992. Bacterial trans-

port in porous media: Evaluation of a model using laboratory observations. Water Resour. Res. 28:915–938.
Jacobsen, O.H., P. Moldrup, C. Larsen, L. Konnerup, and L.W. Petersen. 1997. Particle transport in macropores of undisturbed soil columns. J. Hydrol. 196:185–203.
Jenny, H., and G.D. Smith. 1935. Colloid transport aspects of clay pan formation in soil profiles. Soil Sci. 39:377–379.
Jewett, D.G., B.E. Logan, R.G. Arnold, and R.C. Bales. 1999. Transport of Pseudomonas fluorescens strain P17 through quartz sand columns as a function of water content. J. Contam. Hydrol. 36 (1–2):73–89.
Jin, Y., Y. Chu, and Y. Li. 2000. Virus removal and transport in saturated and unsaturated sand columns. J. Contam. Hydrol. 43: 111–128.
Josephson, K.L., C.P. Gerba, and L.I. Pepper. 1993. Polymerase chain reaction detection of nonviable bacterial pathogens. Appl. Environ. Microbiol. 59:3513–3515.
Kersting, A.B., D.W. Efurd, D.L. Finnegan, D.J. Rokop, D.K. Smith, and J.L. Thompson. 1999. Migration of plutonium in ground water at the Nevada Test Site. Nature 397:56–59.
Keswick, B.H., D. Wang, and C.P. Gerba. 1982. The use of microorganisms as ground-water tracers: A review. Ground Water 20:142–149.
Khilar, K.C., and H.S. Fogler. 1984. The existence of a critical salt concentration for particle release. J. Colloid Interface Sci. 101:214–224.
Kia, S.F., H.S. Fogler, and M.G. Reed. 1987. Effect of pH on colloidally induced fines migration. J. Colloid Interface Sci. 118:158–168.
Kjaergaard, C., L.W. de Jonge, P. Moldrup, and P. Schjønning. 2004. Water dispersible colloids: Effects of measurement method, clay content, initial soil matric potential and wetting rate. Available at www.vadosezonejournal.org. Vadose Zone J. 3:403–412 (this issue).
Kretzschmar, R., M. Borkovec, D. Grolimund, and M. Elimelech. 1999. Mobile subsurface colloids and their role in contaminant transport. Adv. Agron. 66:121–193.
Kuiper, L. 1986. A comparison of several methods for the solution of the inverse problem in two-dimensional steady state groundwater flow modeling. Water Resour. Res. 22:705–714.
Kung, K.-J.S. 1990b. Preferential flow in a sandy vadose soil: 2. Mechanism and implications. Geoderma 46:59–71.
Kung, K.-J.S. 1990a. Preferential flow in a sandy vadose soil: 1. Field observations. Geoderma 46:51–58.
Lance, J.C., and C.P. Gerba. 1984. Virus movement in soil during saturated and unsaturated flow. Appl. Environ. Microbiol. 47:335–337.
Lenhart, J.J., and J.E. Saiers. 2002. Transport of silica colloids through unsaturated porous media: Experimental results and model comparisons. Environ. Sci. Technol. 36:769–777.
Liang, L., J.F. McCarthy, L.W. Jolley, J.A. McNabb, and T.W. Mehlhorn. 1993. Iron dynamics: Transformation of Fe(II)/Fe(III) during injection of natural organic matter in a sandy aquifer. Geochim. Cosmochim. Acta 57:1987–1999.
Maier, R.M., I.L. Pepper, and C.P. Gerba. 2000. Environmental microbiology. Academic Press, San Diego, CA.
McCarthy, J.F., and C. Degueldre. 1993. Sampling and characterization of groundwater colloids for studying their role in the subsurface transport of contaminants. p. 247–315. *In* J. Buffle and H. van Leeuwen (ed.) Environmental particles. Vol. II. Lewis Publ., Chelsea, MI.
McCarthy, J.F., and J.M. Zachara. 1989. Subsurface transport of contaminants: Binding to mobile and immobile phases in groundwater aquifers. Environ. Sci. Technol. 23:496–504.
McCarthy, J.F., K.R. Czerwinski, W.E. Sanford, P.M. Jardine, and J.D. Marsh. 1998a. Mobilization of transuranic radionuclides from disposal trenches by natural organic matter. J. Contam. Hydrol. 30:49–77.
McCarthy, J.F., L.D. McKay, and D.D. Bruner. 2002. Influence of ionic strength and cation charge on transport of colloidal particles in fractured shale saprolite. Environ. Sci. Technol. 36:3735–3743.
McCarthy, J.F., W.E. Sanford, and P.L. Stafford. 1998b. Lanthanide field tracers demonstrate enhanced transport of transuranic radionuclides by natural organic matter. Environ. Sci. Technol. 32:3901–3906.
McDowell-Boyer, L.M., J.R. Hunt, and N. Sitar. 1986. Particle transport through porous media. Water Resour. Res. 22:1901–1921.
McKay, L.D., J.A. Cherry, R.C. Bales, M.T. Yahya, and C.P. Gerba. 1993. A field example of bacteriophage as tracers of fracture flow. Environ. Sci. Technol. 27:1075–1079.
McKay, L.D., J. Fredericia, M. Lenczewski, J. Morthorst, and K.E. Klint. 1999. Spatial variability on contaminant transport in a fractured till, Avedore Denmark. Nord. Hydrol. 30:333–360.
McKay, L.D., W.E. Sanford, and J.M. Strong. 2000. Field-scale migration of colloidal tracers in a fractured shale saprolite. Ground Water 38:139–147.
McLaughlin, D., and L.R. Townley. 1996. A reassessment of the groundwater inverse problem. Water Resour. Res. 32:1131–1161.
Milly, P.C.D. 1988. Advances in modeling of water in the unsaturated zone. Transp. Porous Media 3:491–514.
National Research Council. 2001. Conceptual models of flow and transport in the fractured vadose zone. National Academy Press, Washington, DC.
Nightingale, H.I., and W.C. Bianchi. 1977. Ground-water turbidity resulting from artificial recharge. Ground Water 15:146–152.
Pieper, A.P., J.N. Ryan, R.W. Harvey, G.L. Amy, T.H. Illangasekare, and D.W. Metge. 1997. Transport and recovery of bacteriophage PRD1 in a sand and gravel aquifer: Effect of sewage-derived organic matter. Environ. Sci. Technol. 31:1163–1170.
Poortinga, A.T., R. Bos, W. Norde, and H.J. Busscher. 2002. Electric double layer interactions in bacterial adhesion to surfaces. Surf. Sci. Rep. 47:3–32.
Powelson, D.K., J.R. Simpson, and C.P. Gerba. 1990. Virus transport and survival in saturated and unsaturated flow through soil columns. J. Environ. Qual. 19:396–401.
Puls, R.W., and R.M. Powell. 1992. Acquisition of representative ground water quality samples for metals. Ground Water Monit. Rev. 12:167–176.
Rijnaarts, H.H.M., W. Norde, J. Lyklema, and A.B. Zehnder. 1999. DLVO and steric contributions to bacterial deposition in media of different ionic strengths. Colloids Surf. B 14:179–195.
Ryan, J.N., and M. Elimelech. 1996. Colloid mobilization and transport in groundwater. Colloids Surf. A 107:1–56.
Schafer, A., P. Ustohal, H. Harms, F. Stauffer, T. Dracos, and A.J.B. Zehnder. 1998. Transport of bacteria in unsaturated porous media. J. Contam. Hydrol. 33:149–169.
Schelde, K., P. Moldrup, O.H. Jacobsen, H. de Jonge, L.W. de Jonge, and T. Komatsu. 2002. Diffusion-limited mobilization and transport of natural colloids in macroporous soil. Available at www.vadosezonejournal.org. Vadose Zone J. 1:125–136.
Shevenell, L., and J.F. McCarthy. 2002. Effects of precipitation events on colloids in a karst aquifer. J. Hydrol. 255:50–68.
Short, S.A., R.T. Lowson, and J. Ellis. 1988. $^{234}U/^{238}U$ and $^{230}Th/^{234}U$ activity ratios in the colloidal phases of aquifers in lateritic weathered zones. Geochim. Cosmochim. Acta 52:2555–2563.
Simoni, S.F., H. Harms, T.N.P. Bosma, and A.B. Zehnder. 1998. Population heterogeneity affects transport of bacteria through sand columns at low flow rates. Environ. Sci. Technol. 32:2100–2105.
Sirivithayapakorn, S., and. A. Keller. 2003. Transport of colloids in unsaturated porous media: A pore-scale observation of processes during dissolution of air–water interface. Water Resources Res. 39(12) 1346. DOI: 10.1029/2003WR002487
Steenhuis, T.S., J.-Y. Parlange, and K.-J.S. Kung. 1991. Comment on the diversion capacity of capillary barriers, by B. Ross. Water Resources Res. 27:2155–2156.
Sun, N., N.-Z. Sun, M. Elimelech, and J.N. Ryan. 2001. Sensitivity analysis and parameter identifiability for colloid transport in geochemically heterogeneous porous media. Water Resour. Res. 37: 209–222.
Sun, N.-Z. 1999. Inverse problems in groundwater modeling. Kluwer Acad., Dordrecht, The Netherlands.
Suresh, L., and J.Y. Walz. 1996. Effect of surface roughness on interaction energy between a colloidal sphere and a flat plate. J. Colloid Interface Sci. 183:199–213.
Suresh, L., and J.Y. Walz. 1997. Direct measurement of the effect of surface roughness on the colloidal forces between a particle and flat plate. J. Colloid Interface Sci. 196:177–190.
Tennessee Department of Environment and Conservation. 2002. Rules for public water systems. Chapter 1200-5-1. TDEC, Nashville, TN.

Thorp, J., L.E. Strong, and E. Gamble. 1957. Experiments in soil genesis–The role of leaching. Soil Sci. Soc. Am. J. 21:99–102.
Tobiason, J.E. 1989. Chemical effects on the deposition of non-brownian particles. Colloids Surf. 39:53–77.
Tsai, F.T.-C., N.-Z. Sun, and W.W.-G. Yeh. 2003. Global-local optimization for parameter structure identification in three-dimensional groundwater modeling. Water Resour. Res. 39(2):1043 DOI: 10.1029/2001WR001135.
USEPA. 1986. Ambient water quality. Criteria-1986. EPA440/5-84-002. EPA, Washington, DC.
Vesper, D.J., and W.B. White. 2003. Metal transport to karst springs during storm flow: An example from Fort Campbell, Kentucky/Tennessee, USA. J. Hydrol. 276:20–36.
Walton, F.B., and W.F. Merritt. 1980. Long-term extrapolation of laboratory glass leaching data for the prediction of fission product release under actual groundwater conditions. p. 155–166. *In* Scientific basis for nuclear waste management. Vol. 2. Plenum Press, New York.
Wan, J., and J.L. Wilson. 1994a. Visualization of the role of the gas–water interface on the fate and transport of colloids in porous-media. Water Resources Res. 30:11–23.
Wan, J., and J.L. Wilson. 1994b. Colloid transport in unsaturated porous media. Water Resour. Res. 30:857–864.
Wan, J., and T.K. Tokunaga. 1997. Film straining of colloids in unsaturated porous media: Conceptual model and experimental testing. Environ. Sci. Technol. 31:2413–2420.
Wan, J.M., and T.K. Tokunaga. 2002. Partitioning of clay colloids at air–water interfaces. J. Colloid Interface Sci. 247:54–61.
White, W.B. 1988. Geomorphology and hydrology of karst terrains. Oxford Univ. Press, Oxford, UK.
Yao, K.-M., M.T. Habibian, and C.R. O'Melia. 1971. Water and waste water filtration: Concepts and applications. Environ. Sci. Technol. 5:1105–1106.
Yeh, W.W.-G. 1986. Review of parameter identification procedures in groundwater hydrology: The inverse problem. Water Resour. Res. 22:95–108.

Pore-Scale Visualization of Colloid Transport and Retention in Partly Saturated Porous Media

John T. Crist, John F. McCarthy, Yuniati Zevi, Philippe Baveye, James A. Throop, and Tammo S. Steenhuis*

ABSTRACT

In unsaturated porous media, sorption of colloids at the air–water (AW) interface is accepted as a mechanism for controlling colloid retention and mobilization. However, limited actual pore-scale observations of colloid attachment to the AW interface have been made. To further investigate these processes, a real-time pore-scale visualization method was developed. The method builds on the light transmission technique for fingered flow studies in packed-sand infiltration chambers and combines it with high-resolution, electro-optical hardware and public domain imaging software. Infiltration and drainage of suspensions of hydrophilic negatively charged carboxylated latex microspheres provides compelling visual evidence that colloid retention in sandy porous media occurs via trapping in the thin film of water where the AW interface and the solid interface meet, the air–water–solid (AWS) interface. With this modified theory of trapped colloids at the AWS interface, we are able to explain the apparent discrepancy between previous experimental evidence of hydrophilic colloids seemingly partitioning to the AW interface and more recent findings that suggest this type of colloid does not adsorb at the AW interface.

Typically defined as suspended particulate matter with diameters <10 μm (Stumm, 1977), colloids exist as organic and inorganic materials such as microorganisms, humic substances, clay minerals, and metal oxides (McCarthy and Zachara, 1989). Scientific reviews emphasize the need for more research on the mechanisms controlling transport and retention of colloids in the unsaturated zone (Ouyang et al., 1996; Kretzschmar et al., 1999; McCarthy, 2003). While colloid transport in saturated porous media is dominated by colloid interactions at water–solid interfaces, the presence of a third phase, air, introduces additional retention mechanisms for colloid transport in partially saturated porous media. Based on the pioneering work of Wan and Wilson (1994a), the interaction of colloids with the AW interface has been invoked as a dominant process in colloid retention. Wan and Tokunaga (1997) also introduced an additional mode of colloid retention. Invoking a concept of film straining, they proposed that transport of suspended colloids could be retarded due to physical restrictions imposed when the thickness of water films fell below the diameter of the colloids.

Other than the pioneering visualization studies of Wan and Wilson (1994a), colloid transport experiments with porous media have been based on mass balance of breakthrough colloid concentrations in packed-sand columns (Wan and Wilson, 1994b; Schafer et al., 1998; Jewett et al., 1999; Jin et al., 2000; Lenhart and Saiers, 2002). On the basis of analyses of outflow concentrations of colloid particles, these authors found that more particles were retained in the column at lower water contents (or under conditions where there were higher percentages of trapped air). Retention, measured as reduced colloid concentrations in the column outflow, was attributed to sorption at the AW interface and film straining. In one case retention of bacteriophages in a batch system was ascribed to the presence of a dynamic AWS interface (Thompson et al., 1998; Thompson and Yates, 1999). New data suggest, however, that conceptual models of colloid transport in unsaturated media need to be reexamined. It has been generally assumed, based on visualization studies using etched-glass micromodels (Wan and Wilson, 1994a), that retention at the AW interface was relevant to a wide variety of colloids, including hydrophilic and hydrophobic latex microspheres, clay particles, and bacteria. In contrast, Wan and Tokunaga (2002) demonstrated in bubble column experiments that only positively charged particles attached to the negatively charged AW interface, suggesting that immobilization at the AW interface would be limited to a smaller subset of environmental colloids. Wan and Tokunaga (1997) conceptualized film straining as a colloid retention process within thin films of water flowing from one pendular ring to the next. However, Lenhart and Saiers (2002), noting that calculated water film thicknesses were 20-fold smaller than their 0.4-μm colloids, concluded that the relevant immobilization process was the degree of pendular ring discontinuity, rather than immobilization in thin water film.

Therefore, it is appropriate to consider alternate explanations for the observed retention of colloids in unsaturated transport studies. In this paper, we describe a novel pore-scale visualization technique. In contrast to two-dimensional micromodel visualization studies, this new method is adapted to the three-dimensional, sandy soil matrix with flowing water through a complete infiltration and drainage cycle (Wan and Wilson, 1994a, 1994b; Wan et al., 1994). The results help to reconcile some inconsistencies among earlier studies.

MATERIAL AND METHODS

The principal components of the experimental setup were the infiltration chamber, mounting assembly, light source, electro-optical equipment (lens, camera, and computer sys-

J.T. Crist, Y. Zevi, J.A. Throop, T.S. Steenhuis, Dep. of Biological and Environmental Engineering, Riley-Robb Hall, Cornell University, Ithaca, NY 14853; J.F. McCarthy, Dep. of Geological Sciences, Univ. of Tennessee, Knoxville, TN 37996; P. Baveye, Dep. of Crop and Soil Sciences, Cornell Univ., Ithaca, NY 14853. Received 6 June 2003. Special Section: Colloids and Colloid-Facilitated Transport of Contaminants in Soils. *Corresponding author (tss1@cornell.edu).

Published in Vadose Zone Journal 3:444–450 (2004).

677 S. Segoe Rd., Madison, WI 53711 USA

Abbreviations: AW, air–water; AWS, air–water–solid; PV, pore volume.

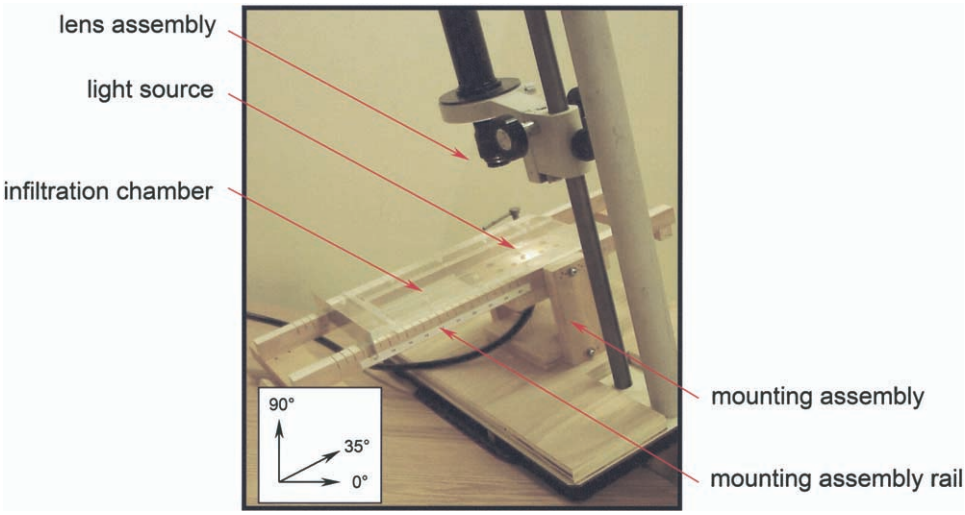

Fig. 1. Principal components of the experimental setup. Not shown are the CDC camera and the computer system.

tem), and imaging software (Fig. 1). The infiltration chamber was constructed from 0.5-cm-thick, clear acrylic sheets. The chamber's interior was 26.0 cm high, 4.8 cm wide, and 0.5 cm deep. Channels were machined into the lower section of the chamber to facilitate water drainage, and the openings were covered with a stainless-steel wire mesh.

The infiltration chamber was supported on a mounting assembly at an incline of 35° from horizontal and perpendicular to the focus of the camera. The viewing area was adjusted across the camera by sliding the chamber along rails on the mounting assembly. Alignment slots on the rails, separated at 1-cm intervals, allowed for consistent placement to record images at each height of the chamber. The viewing area was illuminated using a variable intensity, 150-W tungsten-halogen lamp with a fiber optics cable (D.O. Industries, Inc., Rochester, NY). The electro-optical equipment included a Zoom 6000 II lens assembly with 1X adaptor (D.O. Industries, Inc.) and a color charged-coupled device camera (Cohu, Inc., Poway, CA). An IBM-compatible computer, monitor, frame-grabber card (Scion Corp., Frederick, MD), and Scion Image software were used for image processing and display. Maximum image resolution for the complete system was 212 000 square pixels mm^{-2}. In addition to capturing still digital images with Scion Image, a videocassette recorder and monitor were used to gather continuous real-time images for subsequent review and analysis.

The infiltration experiments depended on detection of micrometer- and submicrometer-sized particles on silica sand grains and on the menisci connecting sand grains. Fluorescent and nonfluorescent dyed polystyrene latex microspheres (Magsphere Inc., Pasadena, CA) of different sizes and surface characteristics were evaluated as surrogates for natural colloids. In trial studies, analysis of spectral output or transmitted light using a fiber optic spectrophotometer (Ocean Optics, Inc., Dunedin, FL) revealed no significant wavelength peaks for characterizing fluorescent colloid distribution in packed sand. More encouraging results were found with the nonfluorescent dyed particles in various colors such as red, bright green, and blue. Through visual inspection, it was determined that microspheres dyed blue provided excellent color contrast against the yellowish-white and grayish-white (acid-washed) sand grains.

Quartz sand (Unimin Corp., NJ), with grain diameters between 0.43 and 0.60 mm, was chosen as the porous media because of its semitranslucent quality, well-established characterization (Schroth et al., 1996), and successful application in light transmission studies (Darnault et al., 1998). Inorganic and organic impurities on the sand surface were removed using concentrated hydrochloric and chromic acids, following procedures outlined by Litton and Olson (1993). The chamber was assembled, placed in a vertical position, and filled with sand to a height of 20 cm. Bulk densities were between 1.66 and 1.70 g cm^{-3}, and porosities ranged from 0.36 to 0.37 cm^3 cm^{-3}.

The chamber was laid flat after packing with dry sand, and the front panel was removed to avoid light reflections that obscured the view and, thus, exposed one side of the packed-sand column to air. One pore volume (PV, ≈18 mL) of distilled, deionized water was delivered through the drainage channels at an inlet flow rate of 2 mL min^{-1} at the flat position. The one-PV injection completely saturated the pore space in the packed-sand column. The infiltration chamber was then placed at a 35° incline to maximize gravitational effects on flow while preventing erosion of the packed-sand layers during infiltration and drainage. Images of water distribution in the packed-sand column were captured at 1-cm intervals from depths of 1 to 18 cm. Image recordings were continued every hour for the next 6 h as the wetted sand was allowed to drain. A gradient in water content developed during the 6-h drainage period, simulating various saturation values, from unsaturated near the surface of the soil to completely saturated at the bottom of the chamber. Six hours after prewetting the packed-sand layers, microspheres dispersed in a low ionic strength solution (0.1 m*M* $CaCl_2$ and pH 5.6) were applied as a point source over the top layer (0-cm depth) of the packed sand using a peristaltic pump. One PV of colloidal suspension was delivered at a flow rate of 1.3 mL min^{-1}, after which the column was allowed to drain.

Digital still images were captured before and immediately following application of the colloidal suspension, and every hour thereafter for the next 2 h. Images were recorded at 1-cm intervals from depths of 1 to 18 cm, yielding over 160 still images at the end of each experiment. The chamber was laid flat after the additional 2-h drainage period and was sectioned at 1-cm intervals for oven drying and gravimetric water content determination.

Several experiments were completed to demonstrate the practicality of the new visualization method and to examine the distribution of colloids on silica sand. We will report on three of these experiments conducted with negatively charged hydrophilic (carboxylated) microspheres. Variations in microsphere diameters and concentrations were evaluated in these experiments. Microspheres (Magsphere, Inc., Pasadena,

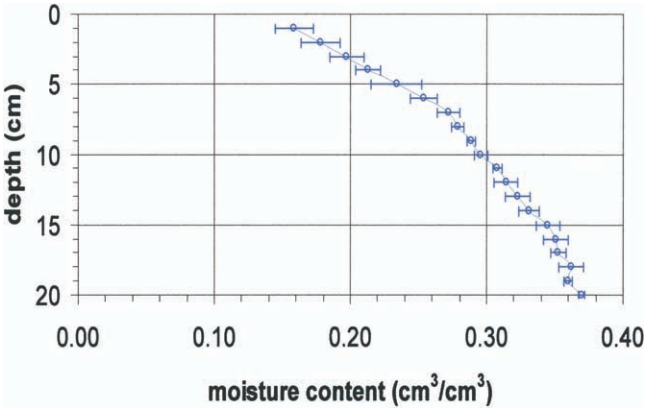

Fig. 2. Moisture content of packed-sand layers 2 h after application of the colloidal suspension. Values reflect the average of five experiments; error bars shown are one standard deviation.

CA) were chosen with mean diameters of 0.3 and 0.8 μm, and prepared in two different concentrations of approximately 3×10^7 and 6×10^7 particles mL^{-1}, respectively. These experiments were performed in duplicate, and consistent results were obtained between replicates. Picture clarity between the experimental results was variable and only the best visualizations are shown.

RESULTS

Regardless of the colloid concentrations, the size of the colloids had a large effect on our ability to visually detect the particles. The 0.8-μm hydrophilic colloids were easily visible from the background environment with this experimental setup. However, the 0.3-μm hydrophilic colloids were only faintly visible. Consequently, experimental results relating to colloids in this size range are not presented.

After 2 h of drainage, moisture contents in the chamber ranged from 0.37 $cm^3\ cm^{-3}$ saturation at the bottom to 0.16 $cm^3\ cm^{-3}$ near the top (Fig. 2). The moisture content did not vary significantly thereafter, as the drainage from the bottom of the column was minimal to undetectable. A similar gradient of moisture distribution was present before and after application of the colloidal suspension, thus providing uniform initial conditions for all experiments. Recorded images (Fig. 3) clearly show the presence of menisci or AW interfaces connecting sand grains.

Direct observations of microspheres during infiltration convincingly showed the dynamic nature of colloid transport. Even though it is impossible to completely convey this dynamic behavior through still photographs, captured images indicate that not all pore spaces carry the same amount of flow during infiltration and that distinct paths are followed. In the example depicted in Fig. 4, the pores with the menisci or AW interfaces connecting wetted sand grains before inputs of the colloidal suspension (Fig. 4a) were filled with water after the infiltration front of the colloidal suspension advanced past a depth of 9 cm (Fig. 4b). It should be noted that the blue rings on the surface of the grains resulted from removal of the front panel of the chamber, creating an additional interface with the air. These rings form

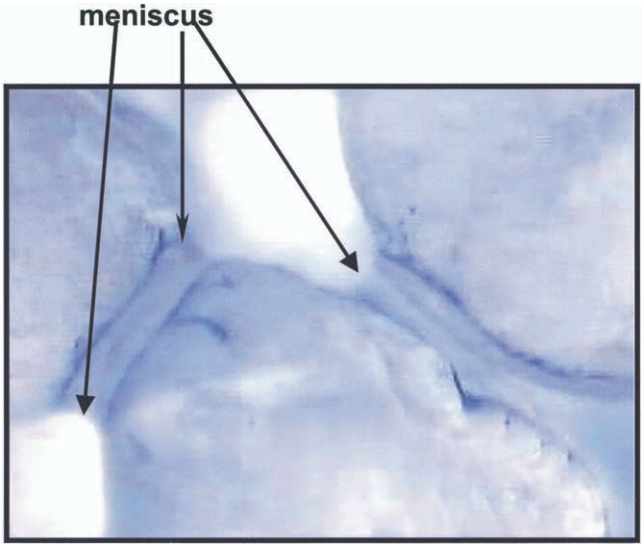

Fig. 3. Menisci or air–water interfaces connecting sand grains after application.

at the edges of the menisci at locations where the sand grains stick out of the water. We fully recognize that these rings may not occur in infiltration experiments using vertical sand columns. Nevertheless, our experimental setup provided ample opportunities to investigate our area of interest—the interface region centered about the meniscus—over a broader range.

In Fig. 5, photographs of the 0.8-μm colloids are shown at depths of 2 to 18 cm below the top of the column immediately after the application of colloids was stopped and colloids had infiltrated to the bottom of the chamber. We first consider observations on the distribution of water along the column, and will then discuss the distribution of colloids. The sand at the bottom of the column (18 cm below the top) was a fully saturated horizon. Moving up the column along the gradient of water content from 12 to 4 cm below the top of the column, the pores below the upper surface of the sand are filled with water. The presence of nearly saturated pores is in agreement with earlier findings on unstable wetting front flow experiments. Water was found to flow as saturated columns through the sand, and not through films, even at low flow rates (Lu et al., 1994). At a depth of 2 cm from the top of the column, the water had drained sufficiently that isolated pendular rings are observed.

The distribution of the colloids can be observed as blue bands. In the fully saturated horizon (18 cm), the suspended colloids could not be distinguished as anything more than a faint blue cast to the water, and there is no evidence of colloid deposition at the solid–water interface of the grains. Moving up the column, drainage exposes more of the AW interface at the upper surface of the column. At depths from 4 to 12 cm, blue bands form where the grains stick out of the water and are seen as partial rings in the photographs in Fig. 5. Although the AW interface is difficult to capture on the photographic film, computer monitor images clearly show that bands form at positions where the meniscus appears to be

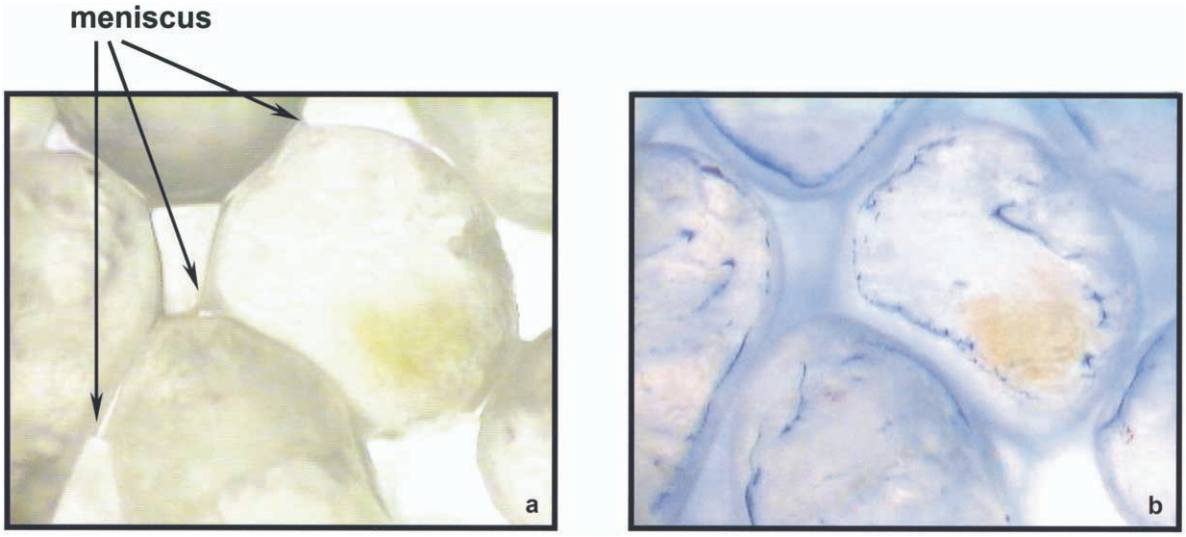

Fig. 4. (a) Menisci or air–water interfaces after 6 h of drainage; (b) colloid–water distribution after application of the colloidal suspension. Rewetting of the sand eliminated the static air–water interfaces.

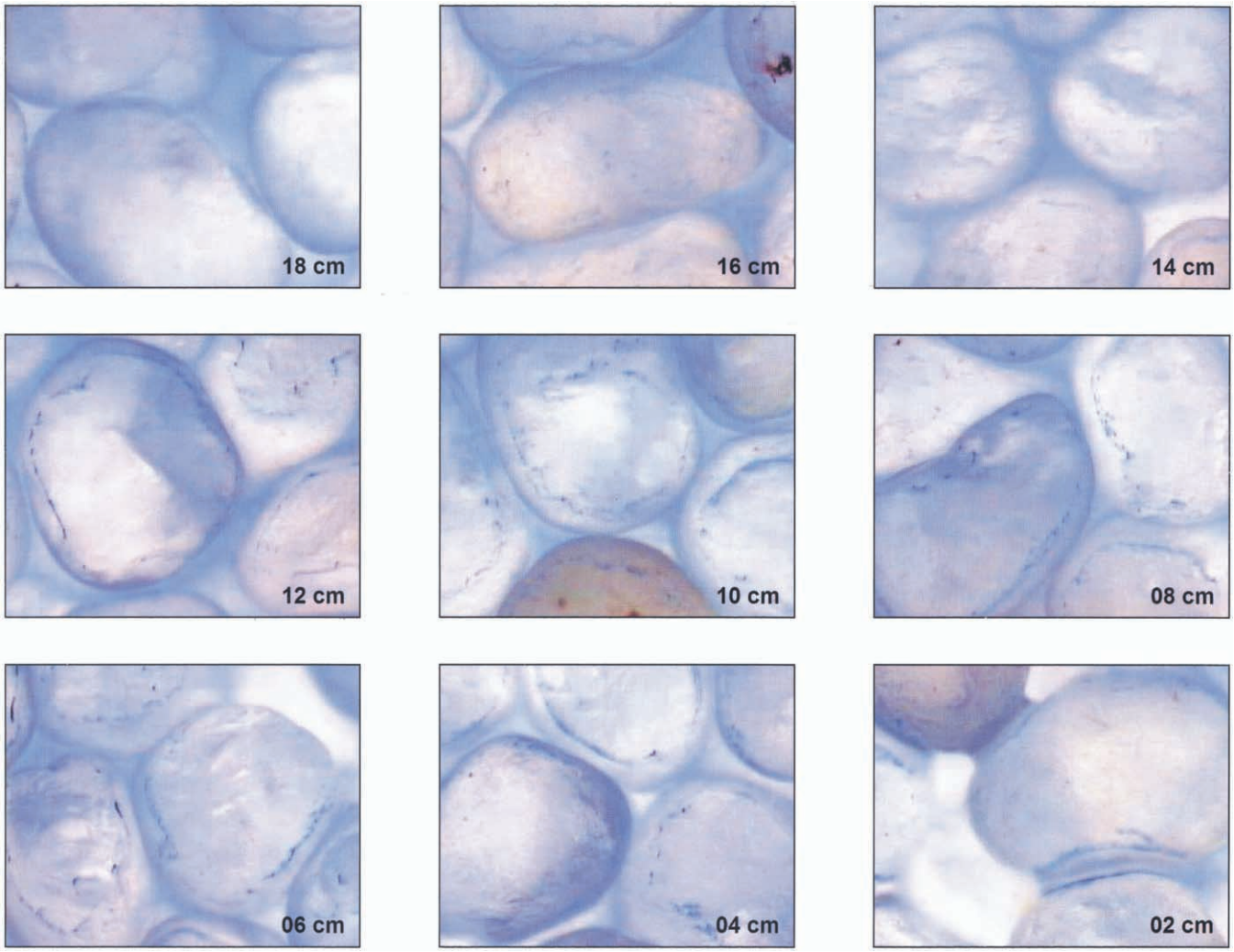

Fig. 5. Distribution of 0.8-μm hydrophilic colloids (≈3 × 10^7 particles mL^{-1}) after application of the colloidal suspension. Values shown are depths below the top layer of the sand column.

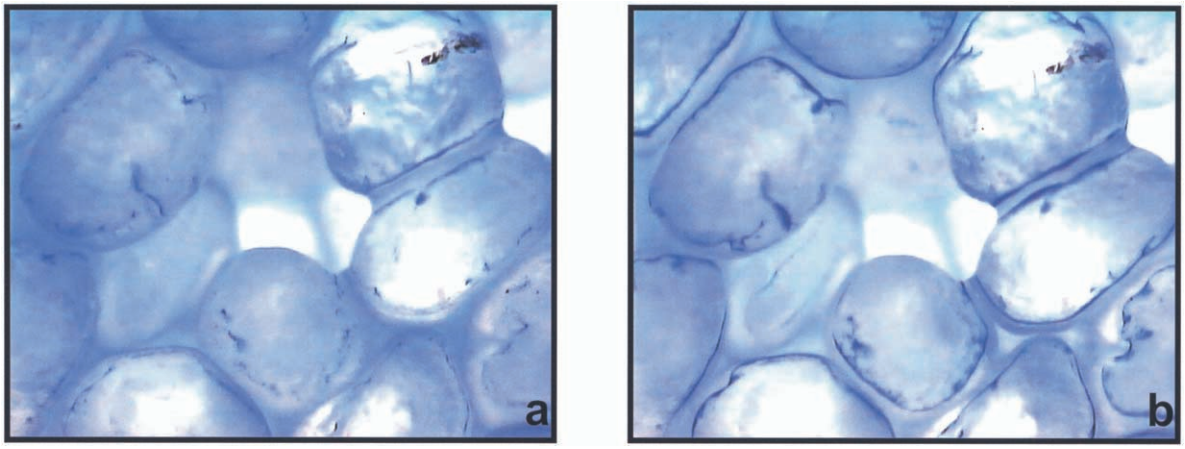

Fig. 6. (a) Blue banding patterns of 0.8-μm hydrophilic colloids (≈3 × 10^7 particles mL^{-1}) after application of the colloidal suspension; (b) 1 h later. With time and continued drainage, the banding patterns widened and darkened to a deeper blue hue.

attaching to the sand grains. We refer to this as the AWS interface or water thin film. Visual inspection and analysis of the timed videotape recordings suggest that the bands formed within 30 to 60 s after passage of the colloid solution. The photographs taken near the bottom of the column at depths of 14 to 18 cm show that when the grains are submerged, the characteristic blue rings do not form. Pendular rings with intense blue bands at the edges of the menisci are visible at 2 cm from the surface (see also Fig. 3).

Figure 5 shows that not all of the colloids are captured at the AWS interface. Some are also deposited at other locations on the sand grains, especially in parts where there are imperfections in the grains (see, e.g., photographs at the 6- and 8-cm depths in Fig. 5). Figure 5 shows again that the colloids flow in preferential paths between the grains. This is well illustrated at the depth of 12 cm, where most of the colloids are flowing in the upper and right half of the photograph, as indicated by the diffuse dark blue color in the fluid-filled pores. The videotape clearly showed that there was little movement of the colloidal suspension in the lower left-hand corner.

With time and continued drainage, the banding patterns widened and darkened to a more intense blue as the meniscus retreated and the circumference of the AWS interface decreased (Fig. 6). Similar distribution patterns developed on the sand grains, including the pendular rings, for all experiments.

DISCUSSION

Many experimental studies in the literature use breakthrough curves of colloids and their mathematical simulation to infer the mechanisms of colloid transport in partially saturated porous media. These studies have attributed the decreased concentration of colloids in the outflow water to mechanisms such as deposition on solid surfaces, sorption to stagnant AW interfaces, and film straining at low moisture contents (McDowell-Boyer et al., 1986; Wan and Tokunaga, 1997). The novel experimental setup described here can be used to directly investigate the relative importance of the first two processes. The third process, however, could not be examined because moisture contents throughout the chamber were too high for significant film straining to occur as described by Wan and Tokunaga (1997). In our study, the only thin water film occurred at the edge of the menisci, as is visible in Fig. 7.

The data from experiments with unsaturated colloid transport in both natural soils and model systems (Wan and Wilson, 1994b; Jewett et al., 1999; Jin et al., 2000) clearly demonstrate that retention of colloids does occur, and it occurs to a significant extent in some cases. Nonetheless, the question of what actually controls the fate of colloids in the unsaturated subsurface environment is still largely unanswered. Results of this investigation suggest that more serious consideration should be given to colloid interactions at or near the AWS interface. In all cases in our experiments, colloids were retained near the AWS interface, as demonstrated by the blue banding pattern at the edge of the menisci as soon as colloid suspension drained to create an air interface (Fig. 3, 4, and 5). The intensity of the blue bands increased as the water level subsided from individual grains (Fig. 5 and 6). It appeared that colloids initially collected at the AWS interface when the water first fell below the level of the tops of the grains (e.g., faint blue line in Fig. 5, 12 cm), were "trapped" at the interface as the perimeter of the meniscus decreased with continued drainage (Fig. 6). There is likely an additional capture of colloids as the AWS interface recedes. The end result is a widening and darkening of the blue

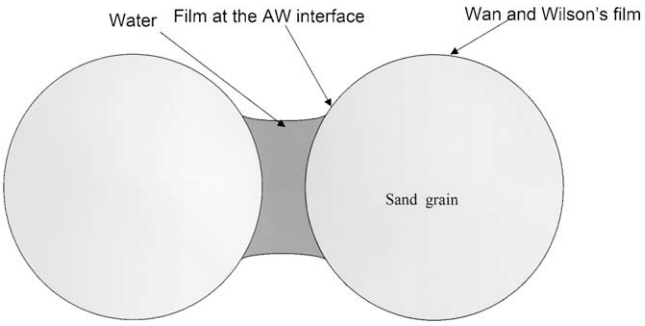

Fig. 7. Water films at cross section of two grains with pendular ring.

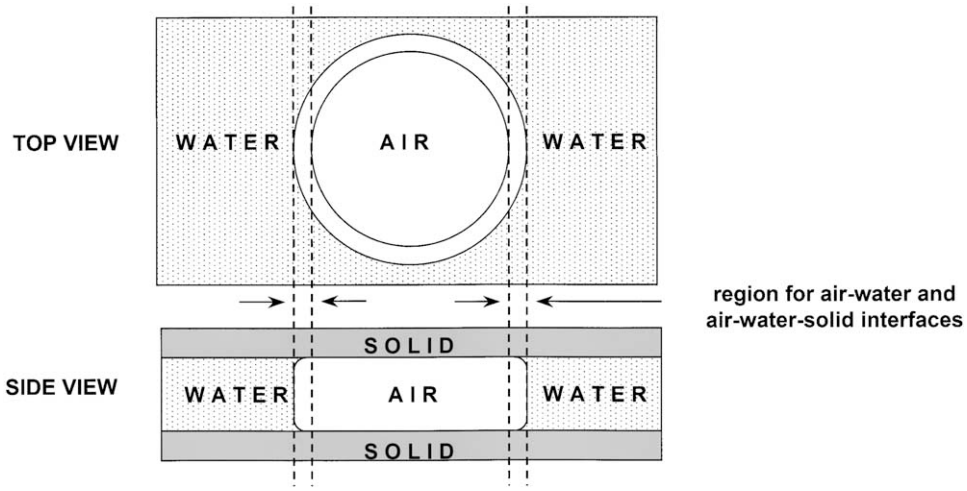

Fig. 8. Trapped air bubble between narrowly separated, hydrophilic solid surfaces.

banding patterns or rings on the grains reflecting immobilization of the colloids.

The occurrence of AW interfaces in unsaturated porous media increases with decreasing moisture content, and, correspondingly, the number of AWS interfaces also increases at lower saturation levels. Uncovering the front panel of the infiltration chamber considerably increased the prevalence of AW as well as AWS interfaces, extending the possibilities of capturing colloid retention at these two interfaces. However, there was clearly no retention of the negatively charged colloids with the AW interface, which is consistent with recent studies using a bubble column (Wan and Tokunaga, 2002).

It is not clear from our experiments why the negatively charged colloids move to the AWS interface. Once there, thin films that exist at that location appear to prevent further movement. But, rather than being trapped by receding water films as suggested by film straining (Wan and Tokunaga, 1997), the colloids moved with the contracting AWS interface during drainage. Thus, it appears that the colloids were not attached to either the AW interface or the solid–water interface, but rather were trapped near the edges of the meniscus near the AWS interface. Colloid retention at the AWS interface is also consistent with the batch experiments of Thompson et al. (1998) and Thompson and Yates (1999).

Because of the apparent discrepancy between descriptions of colloid retention at the AW vs. AWS interface, it is worth reexamining Wan and Wilson's (1994a) micromodel images. In these images, the critical region for attachment at the AW interface is at the outside edge of the darkened ring on the stationary air bubble. In an air bubble trapped between narrowly separated, hydrophilic glass plates, the distinction between the AW and AWS interfaces is difficult to distinguish on the basis of transmission-based images alone (Fig. 8). In other words, it is likely that colloids at the AWS interface were interpreted as being at the AW interface.

But, is the distinction between the AWS and AW interfaces important? After all, the AWS interface is part of the AW interface. However, for unsaturated colloid transport experiments, the distinction between the assumptions may be far from inconsequential. In most cases, water movement in column transport experiments occurs via laminar flow. Under laminar flow theory, for pores that carry flow, the velocity at the surface of a solid is zero, while it is positive anywhere else, including the AW interface away from the solid. For pores that do not participate in the flow process, the AW interface would have a zero velocity, but these AW interfaces are not likely to contain any colloids because they are not connected to the flow paths with colloids. Our observations are, therefore, a refinement on the results of Lenhart and Saiers (2002) who attributed colloid retention to the formation of pendular rings. However, our results suggest that these pendular rings are part of the flow network and not disconnected.

In summary, the laminar flow theory would not explain very well the retention of colloids at the AW interface unless we conceptualize that the medium has a significant number of stationary bubbles. Our visualizations did not reveal many such bubbles. Therefore, the retention of colloids in the thin film of water located at the triple point where the AW and solid–water interfaces meet is much more straightforward to explain colloid retention, and is in agreement with our experimental observations.

REFERENCES

Darnault, C.J.G., J.A. Throop, D.A. DiCarlo, A. Rimmer, T.S. Steenhuis, and J.-Y. Parlange. 1998. Visualization by light transmission of oil and water contents in transient two-phase flow fields. J. Contam. Hydrol. 31:337–348.

Jewett, D.G., B.E. Logan, R.G. Arnold, and R.C. Bales. 1999. Transport of *Pseudomonas fluorescens* strain P17 through quartz sand columns as a function of water content. J. Contam. Hydrol. 36: 73–89.

Jin, Y., Y.J. Chu, and Y.S. Li. 2000. Virus removal and transport in saturated and unsaturated sand columns. J. Contam. Hydrol. 43: 111–128.

Kretzschmar, R., M. Borkovec, D. Grolimund, and M. Elimelech. 1999. Mobile surface colloids and their role in contaminant transport. Adv. Agron. 66:121–193.

Lenhart, J.J., and J.E. Saiers. 2002. Transport of silica colloids through

unsaturated porous media: Experimental results and model comparisons. Environ. Sci. Technol. 36:769–777.
Litton, G.M., and T.M. Olson. 1993. Colloid deposition rates on silica bed media and artifacts related to collector surface preparation methods. Environ. Sci. Technol. 27:185–193.
Lu, T.X., J.W. Biggar, and D.R. Nielsen. 1994. Water movement in glass bead porous media. 2. Experiments of infiltration and finger flow. Water Resour. Res. 30:3283–3290.
McCarthy, J.F. 2003. Colloid-facilitated transport: Past, present, and future concerns. Available at www.vadosezonejournal.org. Vadose Zone J. 3:xxx–xxx (this issue).
McCarthy, J.F., and J.M. Zachara. 1989. Subsurface transport of contaminants—Mobile colloids in the subsurface environment may alter the transport of contaminants. Environ. Sci. Technol. 23: 496–502.
McDowell-Boyer, L.M., J.R. Hunt, and N. Sitar. 1986. Particle transport in porous media. Water Resour. Res. 22:1901–1921.
Ouyang, Y., D. Shinde, R.S. Mansell, and W. Harris. 1996. Colloid-enhanced transport of chemicals in subsurface environments: A review. Crit. Rev. Environ. Sci. Technol. 26:189–204.
Schafer, A., P. Ustohal, H. Harms, F. Stauffer, T. Dracos, and A.J.B. Zehnder. 1998. Transport of bacteria in unsaturated porous media. J. Contam. Hydrol. 33:149–169.
Schroth, M.H., S.J. Ahearn, J.S. Selker, and J.D. Istok. 1996. Characterization of Miller-similar silica sands for laboratory hydrologic studies. Soil Sci. Soc. Am. J. 60:1331–1339.
Stumm, W. 1977. Chemical interaction in particle separation. Environ. Sci. Technol. 11:1066–1070.
Thompson, S.S., and M.V. Yates. 1999. Bacteriophage inactivation at the air–water–solid interface in dynamic batch systems. Appl. Environ. Microbiol. 65:1186–1190.
Thompson, S.S., M. Flury, M.V. Yates, and W.A. Jury. 1998. Role of the air–water–solid interface in bacteriophage sorption experiments. Appl. Environ. Microbiol. 64:304–309.
Wan, J.M., and T.K. Tokunaga. 1997. Film straining of colloids in unsaturated porous media: Conceptual model and experimental testing. Environ. Sci. Technol. 31:2413–2420.
Wan, J.M., and T.K. Tokunaga. 2002. Partitioning of clay colloids at air–water interfaces. J. Colloid Interface Sci. 247:54–61.
Wan, J.M., and J.L. Wilson. 1994a. Visualization of the role of the gas–water interface on the fate and transport of colloids in porous media. Water Resour. Res. 30:11–23.
Wan, J.M., and J.L. Wilson. 1994b. Colloid transport in unsaturated porous media. Water Resour. Res. 30:857–864.
Wan, J.M., J.L. Wilson, and T.L. Kieft. 1994. Influence of the gas-water interface on transport of microorganisms through unsaturated porous media. Appl. Environ. Microbiol. 60:509–516.

Available online at www.sciencedirect.com
SCIENCE DIRECT®
Journal of Contaminant Hydrology 71 (2004) 111–126
JOURNAL OF Contaminant Hydrology
www.elsevier.com/locate/jconhyd

Cesium migration in saturated silica sand and Hanford sediments as impacted by ionic strength

Markus Flury*, Szabolcs Czigány, Gang Chen, James B. Harsh

Department of Crop and Soil Sciences, Center for Multiphase Environmental Research, Washington State University, Pullman, WA 99164, USA

Received 3 September 2002; received in revised form 18 September 2003; accepted 26 September 2003

Abstract

Large amounts of ^{137}Cs have been accidentally released to the subsurface from the Hanford nuclear site in the state of Washington, USA. The cesium-containing liquids varied in ionic strengths, and often had high electrolyte contents, mainly in the form of $NaNO_3$ and NaOH, reaching concentrations up to several moles per liter. In this study, we investigated the effect of ionic strengths on Cs migration through two types of porous media: silica sand and Hanford sediments. Cesium sorption and transport was studied in 1, 10, 100, and 1000 mM NaCl electrolyte solutions at pH 10. Sorption isotherms were constructed from batch equilibrium experiments and the batch-derived sorption parameters were compared with column breakthrough curves. Column transport experiments were analyzed with a two-site equilibrium–nonequilibrium model. Cesium sorption to the silica sand in batch experiments showed a linear sorption isotherm for all ionic strengths, which matched well with the results from the column experiments at 100 and 1000 mM ionic strength; however, the column experiments at 1 and 10 mM ionic strength indicated a nonlinear sorption behavior of Cs to the silica sand. Transport through silica sand occurred under one-site sorption and equilibrium conditions. Cesium sorption to Hanford sediments in both batch and column experiments was best described with a nonlinear Freundlich isotherm. The column experiments indicated that Cs transport in Hanford sediments occurred under two-site equilibrium and nonequilibrium sorption. The effect of ionic strength on Cs transport was much more pronounced in Hanford sediments than in silica sands. Effective retardation factors of Cs during transport through Hanford sediments were reduced by a factor of 10 when the ionic strength increased from 100 to 1000 mM; for silica sand, the effective retardation was reduced by a factor of 10 when ionic strength increased from 1 to 1000 mM. A two order of magnitude change in ionic

* Corresponding author. Tel.: +509-335-1719; fax: +509-335-8674.
E-mail address: flury@mail.wsu.edu (M. Flury).

0169-7722/$ - see front matter
doi:10.1016/j.jconhyd.2003.09.005

strength was needed in the silica sand to observe the same change in Cs retardation as in Hanford sediments.

Keywords: Cesium migration; Equilibrium; Kinetic sorption; Ionic strength; Silica sand; Hanford sediments

1. Introduction

The Hanford Reservation in southcentral Washington State, USA, was the major production facility of weapons grade plutonium in the United States. Radioactive byproducts from the Pu production process were disposed of directly to the subsurface or, in the case of high-level waste, stored in underground tanks. Over the last 40 years, it was suspected that as many as 67 tanks of the 149 single-shell tanks at Hanford had leaked into the subsurface (Gephart and Lundgren, 1998). A major radioactive element in these tanks is ^{137}Cs, which, decay-corrected as of 1996, contributes 24% of the total radioactivity of the waste (Gephart and Lundgren, 1998). It is estimated that more than 1 million curies of radioactivity may have been released into the subsurface due to the leaking of ^{137}Cs (U.S. DOE, 1998; McKinley et al., 2001).

It is difficult to assess the spatial distribution of ^{137}Cs below the tanks, but core sampling has indicated that ^{137}Cs has moved considerable distances through the subsurface (Serne et al., 2002b; McKinley et al., 2001). Peak concentrations of ^{137}Cs below the SX-tank farm have been found at 25- to 26-m depth, with traces of ^{137}Cs up to 38 m (Serne et al., 2002b; 2002c). The waste tanks contain solutions of high ionic strength (>1 mol/l), consisting, in part, of large amounts of NaOH and $NaNO_3$ (Serne et al., 1998). These high ionic strength solutions, in particular the high Na concentrations, have been shown to reduce Cs sorption to Hanford sediments (Zachara et al., 2002). Hanford sediments contain both nonexpandable (biotite, muscovite) and expandable (vermiculite, smectite) phyllosilicates. Under normal (low ionic strength) environmental conditions, phyllosilicates sorb Cs strongly and selectively (Tamura and Jacobs, 1960; Sawhney, 1970, 1972; Cornell, 1993). Two major types of Cs sorption have been proposed: (1) ion-exchange with hydrated cations on planar sites of expandable phyllosilicates, and (2) selective sorption to the frayed edge sites of nonexpandable phyllosilicates (micas) and interlayer sites of vermiculites (Francis and Brinkley, 1976; Cornell, 1993). Sodium at high concentrations has been found to effectively compete with Cs for planar as well as frayed edge sites (Zachara et al., 2002) and, consequently, Cs migration in sediments below the Hanford tanks has likely occurred with little retardation, at least initially, when ionic strengths of the leaking solutions were high and not yet diluted by dispersion and mixing with soil water.

The distinct sorption properties of Cs on phyllosilicates has been represented mathematically by using multiple sorption sites with different sorption characteristics. Most commonly, a two-site sorption model, one site with high affinity and one site with low affinity, for Cs sorption was used. On an empirical basis, the two sorption sites were modeled as equilibrium and kinetically controlled reaction sites (Fukui, 1978; Fujikawa and Fukui, 1991; Comans and Hockley, 1992). This two-site equilibrium–nonequilibrium approach, in combination with a Freundlich isotherm representing the sorption equilibrium

has been applied to silica sands (Fukui, 1978), illite (Comans and Hockley, 1992), and different types of rock materials (Fujikawa and Fukui, 1991). A similar two-site (equilibrium and nonequilibrium) kinetic sorption model, but using a Langmuir instead of a Freundlich-type isotherm, was used to describe Cs sorption to silica sands in transport experiments under ionic strengths varying from 0.002 to 0.1 M (Saiers and Hornberger, 1996). A two-site equilibrium ion-exchange model was found to best describe Cs sorption to micaceous subsurface sediments (Zachara et al., 2002), and was later extended to a three-site ion-exchange model (Steefel et al., 2003).

Cesium transport in natural porous media has not been studied extensively. Most transport experiments were conducted in silica sands (Fukui, 1978; Saiers and Hornberger, 1996; Sätmark et al., 1996) or glass beads (Noell et al., 1998). Few reports are available on Cs distribution and transport in field soils (Cheshire and Shand, 1991) and sites associated with US nuclear weapons production facilities (Garten et al., 2000). Laboratory experiments on Cs transport through natural sediments were reported by Reynolds et al. (1982), who used sandy aquifer material, and by Steefel et al. (2003), who used micaceous vadose zone sediments.

Given that large amounts of Cs, dissolved in high ionic strength solutions, have leaked from underground Hanford waste tanks, there is a need to understand Cs fate and transport in natural sediments under conditions of varying ionic strengths ranging from millimolar to molar concentrations. It was demonstrated that high electrolyte concentrations reduced Cs sorption to Hanford sediments, and the competitive sorption process in electrolyte solutions varying from 0.01 to 5 mol/l $NaNO_3$ was best described with a two-site (high- and low-affinity) equilibrium ion-exchange model (Zacha et al., 2002). Using batch sorption from Zachara et al. (2002) and Steefel et al. (2003) showed that a three-site ion-exchange model was necessary to describe Cs transport through Hanford sediments. The use of a two-site model and binary batch experiments alone tended to underpredict Cs retardation in the columns (Steefel et al., 2003). Based on these results, it is anticipated that Cs migration in Hanford sediments has been significantly affected by the high ionic strength solutions of the Hanford waste tanks. Indeed, depth profiles of Cs obtained from cores drilled beneath the Hanford tanks have provided evidence for reduced Cs sorption (McKinley et al., 2001; Serne et al., 2002b).

The goal of this study was to investigate the influence of solution ionic strengths, i.e., Na concentrations, on cesium migration through subsurface sediments. Our specific objectives were (1) to compare Cs sorption to the silica sand and Hanford sediments in batch and column transport experiments, and (2) to elucidate the impact of ionic strengths, i.e., Na concentrations, on Cs migration through silica sand and Hanford sediments. A nonlinear two-site (equilibrium and nonequilibrium) model was used to analyze the experimental data.

2. Materials and methods

2.1. Artificial pore water and Cs analysis

To mimic the conditions under leaking Hanford tanks, artificial pore water used in our experiments was adjusted to concentrations of 1, 10, 100, and 1000 mM NaCl.

The pH of the solution was buffered at pH 10 with equimolar 0.1 mM $NaHCO_3$/Na_2CO_3. The solutions were filtered through a 0.1 μm Millipore filter and degassed before use.

Cesium-133 solutions were made from $CsNO_3$ (VWR, West Chester, PA) at a concentration of 0.1 mM for the column experiments, and at various concentrations up to 0.5 mM for the batch sorption experiments. Concentrations of up to 0.1 mM Cs are representative for ^{137}Cs in Hanford waste tank solutions (Serne et al., 1998). Cesium concentrations were determined with atomic emission spectrometry (AES) at a wavelength of 852.1 nm using a Varian 220 Flame Atomic Absorption Spectrometer (AAS) (Varian, Mulgrave, Australia). The detection limit for Cs was 0.38 μmol/l. To suppress ionization, both standards and samples were spiked with 2 M KCl solution to reach a final concentration of 1000 mg/l K in solution before analysis.

2.2. Silica sand and Hanford sediments

Two types of materials were used for the experiments: a commercially available silica sand and Hanford sediments. The silica sand (Lot Nr. L11623, J.T. Baker, Phillipsburg, NJ) was first rinsed with deionized water 12 times and decanted through a 53 μm sieve. An aliquot of the sand was further treated to remove carbonates and "free" iron oxides. Carbonates were removed by washing the sand with 0.5 M Na-acetate solution and centrifugation until the supernatant was clear (Gee and Bauder, 1986). "Free" iron oxides were removed following the citrate–bicarbonate–dithionite method (Loeppert and Inskeep, 1996, pp. 647–648), which involves reductive dissolution of Fe with Na-dithionite and chelation of dissolved Fe^{2+} with citrate. The two different treatments of the silica sand are denoted as "water-washed" and "iron-removed".

Hanford sediments were obtained from the U.S. Department of Energy's Hanford Reservation (Submarine Site, 218-E-12B). The material stems from the cataclysmic events of the Missoula floods and belongs to the Hanford Formation. The sediments were taken from a trench wall in January 2000, air-dried, dry-sieved through a 2-mm square screen, and stored in 5-gal plastic buckets. The pH, measured in a 1:1 w/w water extract, was 8.0. After sieving, the particles had the following size distribution: 89% of the mass was larger than 0.5 mm and only 1% smaller than 2 μm. The sand and silt fractions were dominated by quartz, amphibole, plagioclase, K-feldspar, mica, and magnetite. Among the micas, both muscovite and biotite were common. The clay-size fraction consisted mainly of chlorite, smectite, vermiculite, kaolinite, illite, and quartz (Flury et al., 2002). Carbonate and Fe removal with the citrate–bicarbonate–dithionite method was attempted, but was not successful due to the large Fe content of the sediments.

Although not directly taken from beneath the Hanford waste tanks, the sediments used in this study are representative for the material underlying the S-SX tank farm (personal communication, Bruce N. Bjornstad, September 2001, Pacic Northwest National Laboratories, Richland, WA). Hanford formation sediments consist of alternating fine and coarse sands, and we used the coarse sand material. More detailed characterization data of the sediments used in this study are summarized by Serne et al. (2002a).

Total content of "free" iron oxides in the "water-washed", "iron-removed" silica sand, and the Hanford sediments was determined using the citrate–bicarbonate–dithionite

method (Loeppert and Inskeep, 1996) with Fe measured by atomic absorption spectrometry. The dithionite treatment resulted in a complete removal of Fe from the silica sand. Cation exchange capacity was determined with the compulsive exchange method using Ba and Mg (Sumner and Miller, 1996). Selected properties of the porous materials used are listed in Table 1.

2.3. Batch sorption experiments

Batch sorption experiments were carried out in 50 ml polypropylene centrifuge tubes (Nalgene tubes, Nalge, Rochester, NY) containing $CsNO_3$ at concentrations ranging from 0.025 to 0.2 mM for the silica sand and from 0.025 to 0.5 mM for the Hanford sediments. The solid-to-liquid mass ratios were 1:1.7 to 1:5 for silica sand and 1:8.3 for Hanford sediments. Solid-to-liquid mass ratios were varied for the silica sand to improve analytical accuracy, and initial tests showed that the solid-to-liquid ratio did not affect the isotherm determinations. Batch experiments were carried out in 1, 10, 100, and 1000 mM NaCl background electrolyte buffered at pH 10 with equimolar 0.1 mM $NaHCO_3/Na_2CO_3$. Centrifuge tubes were sealed with Teflon-lined screw caps and agitated on a reciprocal shaker for 24 h. Initial test showed that the amount of Cs sorbed changed less than 1% after 2 h of shaking. The solution was then centrifuged at 48,800 × g for 20 min, and cesium concentrations in the supernatant were analyzed with AAS. Batch experiments were performed in triplicate and included two blank treatments, one without solids and one without Cs. Amount of Cs sorbed was calculated based on mass balance considerations. Experiments were carried out at room temperature (20–22 °C).

2.4. Column transport experiments

The columns used for the transport experiments consisted of glass cylinders with 1.0-cm i.d. and 7.2-cm length, equipped with Teflon end pieces and 25 μm pore size frits (Omnit, Cambridge, UK). All tubing at in- and outflow was of Teflon. Flow was controlled with a peristaltic pump (Ismatec, Glattbrugg, Switzerland). Outflow was collected with a fraction collector. The media used for the column experiments, the silica sands and Hanford sediments, were filled into the columns by incrementally packing 1 cm sediment under a CO_2 atmosphere and saturating with a 1 M NaCl electrolyte solution to prevent dispersion of fine particles from the Hanford sediments. The columns were then preconditioned with 30 pore volumes of 1 M NaCl followed by 30 pore volumes of the artificial pore water with the appropriate ionic strength. By the end of the preconditioning, the pH of the effluent was

Table 1
Selected properties of porous materials

Material	Particle size distribution (% mass)			Median diameter (μm)	"Free" Fe (mg/kg)	CEC ($mmol_c/kg$)
	<2 μm	2–50 μm	50–2000 μm			
Water-washed silica sand	0	0	100	704	27.3	12.38
Fe-removed silica sand	0	0	100	704	0	11.88
Hanford sediments	1	3.8	95.2	1369	2307.6	21.58

Table 2
Column parameters and operating conditions

Parameters	Silica sand[a]	Hanford sediment
Length and diameter (cm)	$L = 7.2$, i.d. = 1.0	$L = 7.2$, i.d. = 1.0
Bulk density (g/cm^3)	1.70	1.54
Saturated water content (cm^3/cm^3)	0.37	0.45
Pore volume (cm^3)	2.09	2.54
Flow rate Q (cm^3/h)	11.8	22.74
Water flux J (cm/h)	15.02	28.95
Pore water velocity V (cm/h)	40.6	64.33
Temperature (°C)	20–22	20–22
Eluent Solutions		
pH buffer	0.1 mM $NaHCO_3/Na_2CO_3$, pH 10	0.1 mM $NaHCO_3/Na_2CO_3$, pH 10
Ionic strength	1, 10, 100 and 1000 mM NaCl	100 and 1000 mM NaCl
Column Peclet numbers[b] ($Pe = VL/D$)	30.3 (water-washed) 21.2 (iron-removed)	12.63

[a] Operating conditions were the same for "water-washed" and "iron-removed" silica sand, except when noted.

[b] Peclet numbers determined from nitrate breakthrough curves (V: pore water velocity, L: column length, D: hydrodynamic dispersion coefficient).

consistent with the influent pH. Most of the exchangeable K, Ca, and Mg have likely been replaced with Na after this preconditioning (Steefel et al., 2003). A pulse of a conservative tracer (nitrate in form of 0.1 mM $NaNO_3$) was introduced to determine the hydrodynamics of the column system. Nitrate was analyzed using a UV/VIS Spectrophotometer (HP 8452A, Hewlett Packard) at a wavelength of 202 nm. After the NO_3^- had eluted from the columns, we introduced a pulse of Cs. In total, 10 different Cs transport experiments were conducted: four in each "water-washed" and "iron-removed"' silica sand (1, 10, 100, 1000 mM NaCl), and two in Hanford sediments (100 and 1000 mM NaCl); only the higher ionic strength solutions were run for the Hanford sediments because colloidal material dispersed in the pore water and eluted from the column in the 1 and 10 mM NaCl electrolyte solutions, and consequently the matrix was not stable at these ionic strengths. Experiments were carried out in duplicate at room temperature (20–22 °C). Operating conditions and column parameters are summarized in Table 2.

3. Theory

We represent the migration of Cs through the homogeneously packed columns by the one-dimensional advection–dispersion equation (ADE)

$$\theta \frac{\partial C}{\partial t} + \rho \frac{\partial S}{\partial t} = \theta D \frac{\partial^2 C}{\partial z^2} - \theta V \frac{\partial C}{\partial z} \tag{1}$$

where C is the solution-phase concentration (flux concentration), S is the sorbed-phase concentration, t is time, z is distance, θ is the volumetric water content, ρ is the bulk density, D is the dispersion coefficient, and V is the pore water velocity. We describe the

sorption reactions of Cs by a two-site (equilibrium and nonequilibrium) model, combined with an appropriate sorption isotherm model. This approach has been successfully used to describe Cs transport through silica sands using a Langmuir isotherm (Saiers and Hornberger,1996). Based on the batch sorption data, we found a linear and nonlinear Freundlich isotherm to be best suited for the concentration range in our experiments. The two-site model can then be written as (Selim et al., 1976; Rao et al., 1979)

$$S = S_1 + S_2 \tag{2}$$

$$S_1 = fKC^n \tag{3}$$

$$\frac{\partial S_2}{\partial t} = \alpha[(1-f)KC^n - S_2] \tag{4}$$

where S_1 and S_2 are the sorbed-phase concentrations for equilibrium and nonequilibrium sorption sites, K is the sorption coefficient, n is the Freundlich exponent, f is the fraction of equilibrium sorption sites, and α is the sorption rate coefficient. Eqs. 1 and 2 in combination with a Dirichlet boundary condition at the top and a Neumann condition at the bottom were solved numerically with the Hydrus code (Šimůnek et al., 1998). The Hydrus code simulates water flow and solute transport in variably saturated porous media (Šimůnek et al., 1998). In this study, we used the code to simulate solute transport for water-saturated conditions.

Model parameters were either measured or obtained by nonlinear least-square optimization using the Levenberg–Marquardt algorithm (Marquardt, 1963), as implemented in Hydrus. The pore water velocity V was calculated from the measured water flux as J_w/θ and the dispersion coefficient D was obtained by fitting the ADE to the conservative nitrate tracer breakthrough. The dispersion coefficients obtained from the nitrate breakthrough curves were then used for the analysis of the Cs breakthrough data. We estimated the sorption parameters by least square optimization from batch and column experiments.

The two-site model, Eqs. (2) to (4), includes as special cases simpler models, such as the one-site, linear equilibrium model ($f=1$, $n=1$), the one-site nonlinear equilibrium model ($f=1$, $n\neq 1$), and the two-site, linear sorption model ($f\neq 1$, $n=1$). We fitted the experimental data with all these models, and then compared model performance with an extra sum of squares analysis to test whether the inclusion of new model parameters led to a significant improvement of the model fit (Bates and Watts, 1988).

4. Results

4.1. Batch sorption experiments

Batch sorption data indicated that Cs sorption to the silica sand could be described with a linear isotherm, whereas the sorption to Hanford sediments was best described with a nonlinear Freundlich isotherm (Fig. 1, Table 3). The Fe-removal on the silica sand reduced the Cs sorption only slightly but significantly. Cesium sorption to the silica sand is usually weak (Cornell, 1993), whereby cesium exchanges with the protons of the Si–OH groups

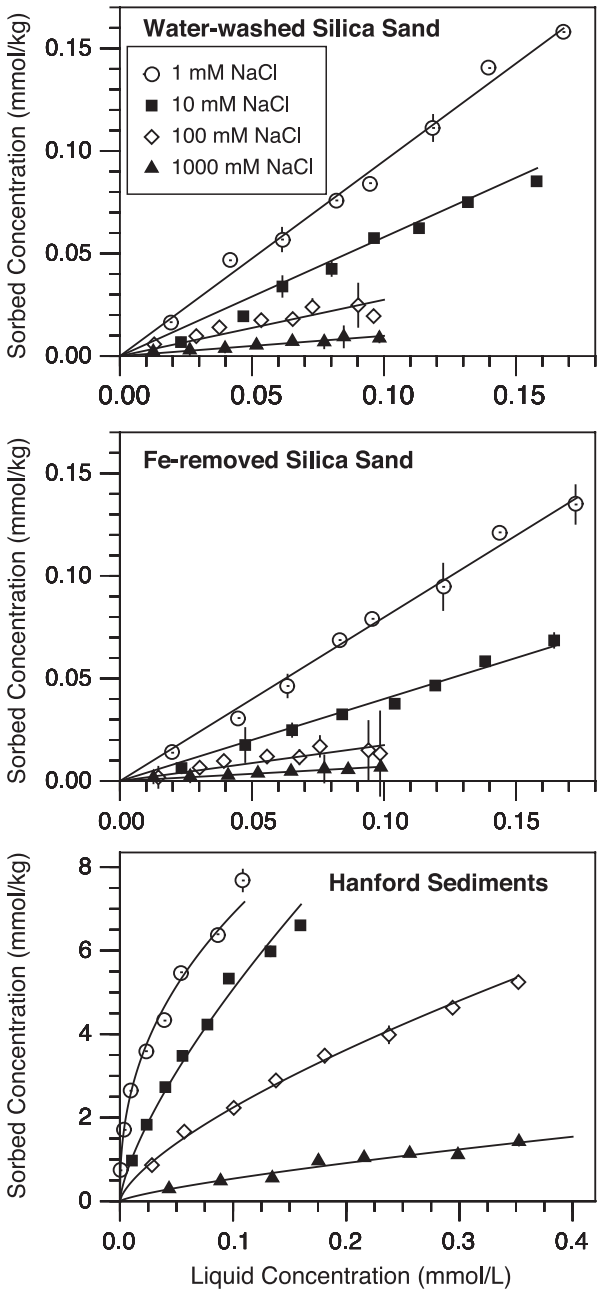

Fig. 1. Cesium sorption isotherms obtained from batch experiments with different NaCl solutions for water-washed silica sand, Fe-removed silica sand, and Hanford sediments. Vertical bars represent ± 1 standard deviation. Solid lines are fitted linear (silica sand) and nonlinear (Hanford sediments) isotherms.

Table 3
Comparison between batch and column sorption parameters and effective retardation factors

Ionic strength	Batch		Column		Retardation factor[a]
	K (ml/g)	n	K (ml/g)	n	R (−)
Water-washed silica sand					
1 mM	0.951 ± 016[b]	1.0	0.359 ± 0.012	0.69 ± 0.02	5.0
10 mM	0.550 ± 0.014	1.0	0.260 ± 0.010	0.71 ± 0.01	2.9
100 mM	0.274 ± 0.020	1.0	0.308 ± 0.018	1.0	1.7
1000 mM	0.098 ± 0.004	1.0	0.061 ± 0.010	1.0	0.6
Fe-removed silica sand					
1 mM	0.798 ± 0.014	1.0	0.440 ± 0.018	0.72 ± 0.02	5.0
10 mM	0.400 ± 0.009	1.0	0.368 ± 0.014	0.95 ± 0.01	2.2
100 mM	0.175 ± 0.014	1.0	0.201 ± 0.086	1.0	0.8
1000 mM	0.070 ± 0.002	1.0	0.028 ± 0.031	1.0	0.6
Hanford sediments					
1 mM	18.04 ± 1.47	0.418 ± 0.025	na[c]	na	na
10 mM	26.30 ± 1.85	0.714 ± 0.035	na	na	na
100 mM	11.07 ± 0.31	0.693 ± 0.019	31.71 ± 1.02	0.81 ± 0.015	289
1000 mM	3.093 ± 0.341	0.759 ± 0.047	3.14 ± 0.042	0.76 ± 0.001	31

[a] Retardation factors calculated from experimental breakthrough curves with Eq. (5).
[b] Values after the ± signs represent 1 standard error. Values without standard errors were not fitted.
[c] na: not applicable.

of SiO_2. At alkaline pH, hydrous Fe-oxides have a higher Cs sorption capacity than quartz (Cornell, 1993, Ferris, et al., 2000), and it consequently can be expected that Fe-coated silica sand retards the movement of Cs more as compared with Fe-removed silica sand. Cesium sorption to the silica sands was reduced by one order of magnitude when ionic strengths increased from 1 to 1000 mM.

There was considerable sorption of Cs to the Hanford sediments, and for all ionic strengths tested, the sorption isotherm was nonlinear. The pronounced nonlinearity of Cs sorption to similar Hanford sediments has also been reported by others (Zachara et al., 2002; Liu et al., 2003). From the sorption isotherms, we calculated single point K_d values ($K_d = S/C$, where S is sorbed concentration and C is liquid concentration) for each isotherm point. These K_d values are plotted in Fig. 2 together with data from Zachara et al. (2002). Our K_d values are smaller than those reported by Zachara et al. (2002), but follow a similar trend. Differences between the sorption parameters between the two studies can be attributed to different pretreatment of sediments and different sampling location of the sediments. Zachara et al. (2002) obtained their sediments from a monitoring well near the SX tank farm and treated their sediments with sodium acetate to remove carbonates and soluble salts.

4.2. Nitrate transport experiments

Nitrate breakthrough curves could be well described with the ADE (Eq. (1)) and the fitted Peclet numbers are shown in Table 2. Column Peclet numbers were about twice as

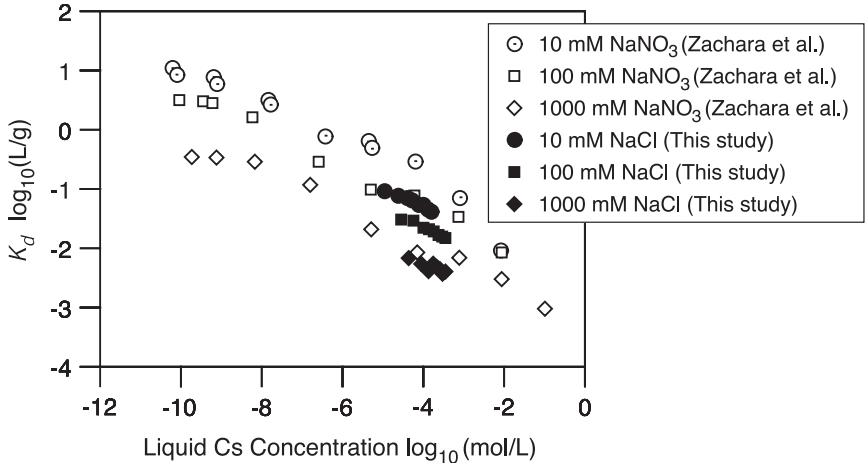

Fig. 2. Cesium distribution coefficients (K_d) for Hanford sediments. Open symbols are data from Zachara et al. (2002), solid symbols are from our study.

large for the Hanford columns than for the silica sand, caused by the coarser grain sizes of the Hanford sediments. The good fit of the ADE to nitrate breakthrough curves indicates that there was no immobile water present in the columns.

4.3. Cs transport experiments

In silica sand, little or no tailing of Cs breakthrough curves was observed at high ionic strengths (100 and 1000 mM NaCl), but pronounced tailing occurred at low ionic strength (1 and 10 mM NaCl) (Fig. 3). We used the batch-derived sorption parameters in combination with a one-site equilibrium model to predict the Cs migration through the silica sands, and the results are shown as dashed lines in Fig. 3. Close agreement between experimental observations and independent model predictions was obtained at 100 and 1000 mM, but not at 1 and 10 mM ionic strengths. Best model fits to the experimental data are shown as solid lines in Fig. 3, and model parameters are listed in Table 4. While the one-site linear, equilibrium assumption was appropriate for 100 and 1000 mM ionic strengths, a one-site nonlinear, equilibrium model was best suited for the 1 and 10 mM ionic strengths. The pronounced tailing of the experimental data at low ionic strengths, however, could not fully be reproduced by the model.

Cesium transport through Hanford sediments could only be measured at 100 and 1000 mM ionic strengths; at 1 and 10 mM NaCl artificial pore water, colloidal material was mobilized and eluted from the columns (as indicated by visual observation of turbidity), and no stable column system could be achieved. No turbidity of column outflow was detected visually for 100 and 1000 mM NaCl. The one-site equilibrium model predictions using the sorption parameters from the batch experiments failed to reproduce the experimental Cs breakthrough curves, at both the breakthrough and the elution portions (dashed lines in Fig. 4). The least-square model optimization indicated that the two site,

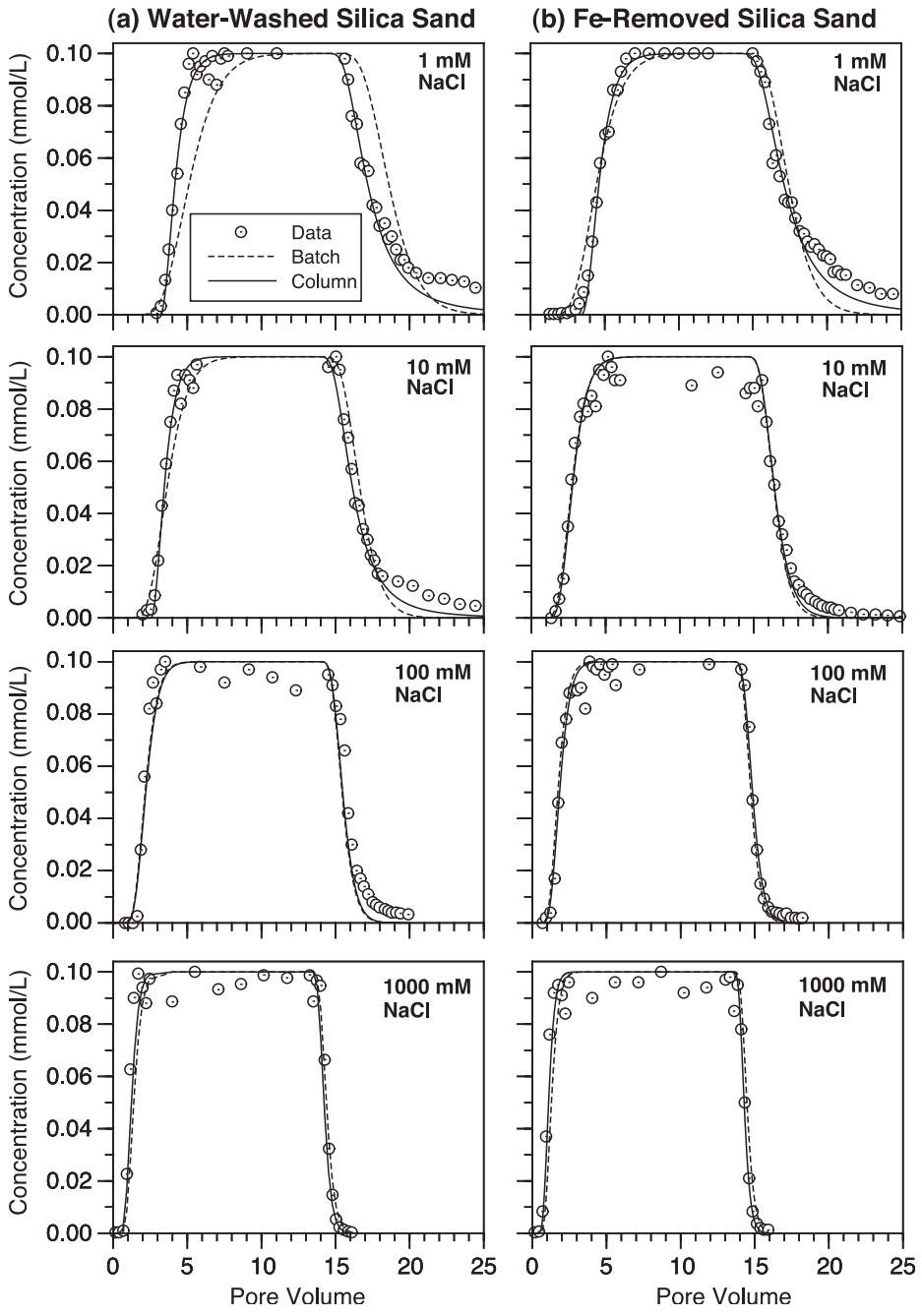

Fig. 3. Cesium breakthrough curves (0.1 mM Cs inflow) in (a) water-washed and (b) Fe-removed silica sand for different ionic strength NaCl solutions. Lines represent model calculations: dashed line is model prediction based on batch isotherm data, solid line is best model fit.

Table 4
Parameters of linear equilibrium and nonlinear equilibrium transport models

Ionic Strength	K (ml/g)	n	f	α (1/h)	SSQ[a] ($\times 10^{-1}$)
Water-washed silica sand					
1 mM	0.359 ± 0.012[b]	0.69 ± 0.02	na[c]	na	0.23
10 mM	0.260 ± 0.010	0.71 ± 0.01	na	na	0.19
100 mM	0.308 ± 0.018	na	na	na	0.51
1000 mM	0.061 ± 0.010	na	na	na	0.24
Fe-removed silica sand					
1 mM	0.440 ± 0.018	0.72 ± 0.02	na	na	0.19
10 mM	0.368 ± 0.014	0.95 ± 0.01	na	na	0.25
100 mM	0.201 ± 0.086	na	na	na	0.12
1000 mM	0.028 ± 0.031	na	na	na	0.27
Hanford sediments					
100 mM	31.71 ± 1.02	0.81 ± 0.015	0.339 ± 0.023	0.163 ± 0.011	0.02
1000 mM	3.14 ± 0.042	0.76 ± 0.001	0.324 ± 0.001	0.115 ± 0.001	0.43

[a] SSQ: sum of squares, given in units of mM^2.
[b] Values after the $\pm$ signs represent 1 standard error.
[c] na: not applicable.

nonequilibrium model, including a nonlinear sorption isotherm, was best for describing Cs breakthrough in the Hanford sediments (solid lines in Fig. 4). The experimental breakthrough curves were well represented by the model. The model parameters showed that the equilibrium sorption sites comprised an equilibrium fraction f of about 0.3 at the two ionic strengths (Table 4). The sorption rate coefficient α, however, was affected by the ionic strength, with α being smaller at 1000 mM than at 100 mM ionic strength. The slower sorption rate at high ionic strength could be related to the stronger competition of Na with Cs for the nonequilibrium sorption sites. The slower sorption rate might also be due to increased flocculation and quasicrystal formation of clay minerals at the higher

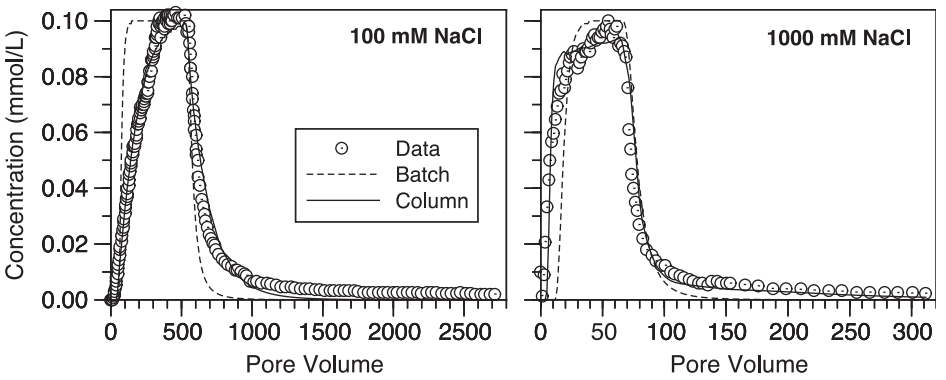

Fig. 4. Cesium breakthrough curves (0.1 mM Cs inflow) in Hanford sediments for different ionic strength NaCl solutions. Lines represent model calculations: dashed line is model prediction based on batch isotherm data, solid line is best model fit.

ionic strength, which may slow diffusion into and out of sites. The optimized Freundlich parameters showed a one order of magnitude difference of the *K*-value between the two ionic strengths. Consequently, the equilibrium sorption of Cs at the maximum fluid concentration of 0.1 mM on Hanford sediments decreased by a factor of 10 with the increase of ionic strength from 100 to 1000 mM. Compared to the Hanford sediments, the impact of ionic strength on Cs sorption was less significant for both water-washed and Fe-removed silica sands, which experienced a five- and seven-fold decrease, respectively. Another comparison can be made using the retardation of cesium relative to the speed of water. We can define an effective retardation factor using the first temporal moment of the cesium breakthrough curves (e.g., Dohse and Lion, 1994)

$$R = \frac{\int_0^\infty C(\vartheta)\vartheta \, d\vartheta}{\int_0^\infty C(\vartheta) \, d\vartheta} - \frac{\vartheta_p}{2} \tag{5}$$

where ϑ is the pore volume and ϑ_p is the pulse length of the cesium input. The calculated retardation at 1000 mM ($R = 31$) is about 10 times less than at 100 mM ($R = 289$) (Table 3). A similar reduction in retardation was observed for the silica sand.

4.4. Comparison between batch and column Cs experiments

The batch and column derived sorption parameters for silica sand displayed fairly good agreement at high ionic strengths when the sorption isotherm was linear (Table 3, Fig. 5). At high ionic strengths, batch sorption data could well predict cesium breakthrough through the silica sand. Less agreement was observed at low ionic strengths where batch data indicated a linear isotherm, but column data indicated a nonlinear isotherm. The approximate shape of the cesium breakthrough curves could be predicted from the batch experiments, but the steepening of the breakthrough front and the tailing of the elution part, caused by the nonlinear sorption isotherm, are not reproduced.

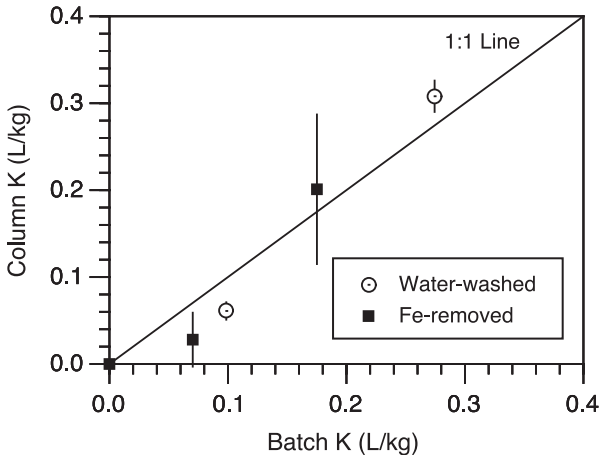

Fig. 5. Comparison of sorption coefficients in silica sand determined from batch sorption and column transport experiments at 100 and 1000 mM ionic strength. Vertical bars represent ± 1 standard error.

In contrast to the silica sand, transport of cesium in the Hanford sediments occurred under nonequilibrium conditions, so that the batch sorption data, which were obtained under equilibrium conditions, were not sufficient to predict cesium breakthroughs in the columns. While the approximate shape of the breakthrough curves could be reproduced, the early breakthrough and pronounced tailing, caused by the sorption nonequilibrium, could not be captured by the batch predictions (Fig. 4). Nonequilibrium for Cs sorption could be explained by diffusion of Cs into interlayer sites in illites and micas (Comans et al., 1991; Smith and Comans, 1996; Steefel et al., 2003).

5. Discussion

Our results indicate that Cs sorption was at equilibrium during transport through the silica sand, but not during transport through the Hanford sediments. Hanford sediments consist of various minerals, including micas and their weathering products, both of which are known to consist of high and low affinity sorption sites for Cs. These two types of sorption sites are also known to sorb Cs at different rates (Comans and Hockley, 1992). Silica sands have also been reported to possess both equilibrium and nonequilibrium sorption sites during transport of Cs (Fukui, 1978; Saiers and Hornberger, 1996); however, the mechanistic interpretation of the nonequilibrium sorption in silica sands is less straightforward than for phyllosilicates. Variations in surface composition and differences between smooth and rough surfaces on silica grains have been considered to cause different sorption rates (Saiers and Hornberger, 1996). The lack of nonequilibrium found in our experiments is likely due to the small Cs sorption affinity of our silica sand. The maximal amount of Cs sorbed to the silica sand in the column experiments was about two orders of magnitude smaller than the CEC of the sand.

In our experiments, we used a higher flow rate for the Cs transport in the Hanford sediments than in the silica sand, which could induce the observed nonequilibrium in the Hanford sediments. We repeated some of the silica sand experiments with the same flow rates as used in the Hanford sediments and did not see a difference in the Cs breakthrough curves (data not shown). Even at the higher flow rates, Cs transport through the silica sand remained at equilibrium. In contrast, Cs transport in the Hanford sediments was strongly affected by sorption nonequilibria. Consequently, batch sorption parameters determined under equilibrium conditions could not accurately reproduce Cs breakthrough curves in the column experiments. Effective retardation of Cs transport in Hanford sediments was reduced by a factor of 10 when the ionic strength increased from 100 to 1000 mM, clearly demonstrating the important effect of Na competition for Cs transport under Hanford tank leaking conditions.

Acknowledgements

This work was supported by the Environmental Management Science Program, U.S. Department of Energy under contract DE-FG07-99ER62882. We thank Jeff Boyle and Jon

Mathison (Washington State University, WSU) for their help with cesium measurements, and John Zachara and Jeff Serne (Pacific Northwest National Laboratory) for providing us with the Hanford sediments.

References

Bates, D.M., Watts, D.G., 1988. Nonlinear Regression Analysis and its Applications. Wiley, New York.

Cheshire, M.V., Shand, C., 1991. Translocation and plant availability of radio caesium in an organic soil. Plant Soil 134, 287–296.

Comans, R.N.J., Hockley, D.E., 1992. Kinetics of cesium sorption on illite. Geochim. Cosmochim. Acta 56, 1157–1164.

Comans, R.N.J., Haller, M., de Preter, P., 1991. Sorption of cesium on illite: non-equilibrium behaviour and reversibility. Geochim. Cosmochim. Acta 55, 433–440.

Cornell, R.M., 1993. Adsorption of cesium on minerals: a review. J. Radioanal. Nucl. Chem. 171, 483–500.

Dohse, D.M., Lion, L.W., 1994. Effect of microbial polymers on the sorption and transport of phenanthrene in a low-carbon sand. Environ. Sci. Technol. 28, 541–548.

Ferris, F.G., Hallberg, R.O., Lyvén, B., Pedersen, K., 2000. Retention of strontium, cesium, lead, and uranium by bacterial iron oxides from a subterranean environment. Appl. Geochem. 15, 1035–1042.

Flury, M., Mathison, J.B., Harsh, J.B., 2002. In situ mobilization of colloids and transport of cesium in Hanford sediments. Environ. Sci. Technol. 36, 5335–5341.

Francis, C.W., Brinkley, F.S., 1976. Preferential adsorption of ^{137}Cs to micaceous minerals in contaminated freshwater sediments. Nature 260, 511–513.

Fujikawa, Y., Fukui, M., 1991. Analysis of radioactive cesium and cobalt adsorption to rocks using the two-site kinetic model equations. J. Contam. Hydrol. 8, 43–69.

Fukui, M., 1978. Evaluation of a combined sorption model for describing cesium transport in a soil. Health Phys. 35, 555–562.

Garten Jr., C.T., Hamby, D.M., Schreckhise, R.G., 2000. Radiocesium discharges and subsequent environmental transport at the major us weapons production facilities. Sci. Total Environ. 255, 55–73.

Gee, G.W., Bauder, J.W., 1986. Particle-size analysis. In: Klute, A. (Ed.), Methods of Soil Analysis: Part 1. Physical and Mineralogical Methods, 2nd ed. American Society of Agronomy, Madison, WI, pp. 383–411.

Gephart, R.E., Lundgren, R.E., 1998. Hanford Tank Cleanup: A Guide to Understanding the Technical Issues, 4th ed. Battelle Press, Columbus.

Liu, C., Zachara, J.M., Qafoku, O., Smith, S.C., 2003. Effect of temperature on Cs^+ sorption and desorption in subsurface sediments at the Hanford site, USA. Environ. Sci. Technol. 37, 2640–2645.

Loeppert, R.H., Inskeep, W.P., 1996. Iron. In: Sparks, D.L. (Ed.), Methods of Soil Analysis: Part 3. Chemical Methods. American Society of Agronomy, Madison, WI, pp. 639–664.

Marquardt, D.W., 1963. An algorithm for least-squares estimation of non-linear parameters. J. Soc. Ind. Appl. Math. 11, 431–441.

McKinley, J.P., Zeissler, C.J., Zachara, J.M., Serne, R.J., Lindstrom, R.M., Schaef, H.T., Orr, R.D., 2001. Distribution and retention of Cs-137 in sediments at the Hanford Site, Washington. Environ. Sci. Technol. 35, 3433–3441.

Noell, A.L., Thompson, J.L., Corapgioglu, M.Y., Triay, I.R., 1998. The role of silica colloids on facilitated cesium transport through glass bead columns and modeling. J. Contam. Hydrol. 31, 23–56.

Rao, P.S.C., Davidson, J.M., Jessup, R.E., Selim, H.M., 1979. Evaluation of conceptual models for describing nonequilibrium adsorption–desorption of pesticides during steady-flow in soils. Soil Sci. Soc. Am. J. 43, 22–28.

Reynolds, W.D., Gillham, R.W., Cherry, J.A., 1982. Evaluation of distribution coefficients for the prediction of strontium and cesium migration in a uniform sand. Can. Geotech. J. 19, 92–107.

Saiers, J.E., Hornberger, G.M., 1996. Migration of ^{137}Cs quartz sand: experimental results and modeling approaches. J. Contam. Hydrol. 22, 255–270.

Sätmark, B., Albinsson, Y., Liang, L., 1996. Chemical effects of goethite colloid on the transport of radionuclides through a quartz-packed column. J. Contam. Hydrol. 21, 231–241.

Sawhney, B.L., 1970. Potassium and cesium ion selectivity in relation to clay mineral structure. Clays Clay Miner. 18, 47–52.

Sawhney, B.L., 1972. Selective sorption and fixation of cations by clay minerals. Clays Clay Miner. 20, 93–100.

Selim, H.M., Davidson, J.M., Mansell, R.S., 1976. Evaluation of a two-site adsorption–desorption model for describing solute transport in soils. Summer Computer Simulation Conference, Washington, DC. Simulation Councils, La Jolla, CA, pp. 444–448.

Serne, R.J., Zachara, J.M., Burke, D.S., 1998. Chemical Information on Tank Supernatants, Cs Adsorption from Tank Liquids onto Hanford Sediments, and Field Observations of Cs Migration from Past Tank Leaks. Pacific Northwest National Laboratory, Richland, WA. PNNL-11495/UC-510.

Serne, R.J., Bjornstad, B.N., Schaef, H.T., Williams, B.A., Lanigan, D.C., Horton, D.G., Clayton, R.E., Mitroshkov, A.V., LeGore, V.L., O'Hara, M.J., Brown, C.F., Parker, K.E., Kutnyakov, I.V., Serne, J.N., Last, G.V., Smith, S.C., Lindenmeier, C.W., Zachara, J.M., Burke, D.S., 2002a. Characterization of Vadose Zone Sediment: Uncontaminated RCRA Borehole Core Samples and Composite Samples. Pacific Northwest National Laboratory, US Department of Energy, Richland, Washington. PNNL-13757-1.

Serne, R.J., Clayton, R.E., Kutnyakov, I.V., Last, G.V., LeGore, V.L., Wilson, T.C., Schaef, H.T., O'Hara, M.J., Wagnon, K.B., Lanigan, D.C., Brown, C.F., Williams, B.A., Lindenmeier, C.W., Orr, R.D., Burke, D.S., Ainsworth, C.C., 2002b. Characterization of Vadose Zone Sediment: Borehole 41-09-39 in the S-SX Waste Management Area. Pacific Northwest National Laboratory, US Department of Energy, Richland, Washington. PNNL-13757-3.

Serne, R.J., Clayton, R.E., Kutnyakov, I.V., Last, G.V., LeGore, V.L., Wilson, T.C., Schaef, H.T., O'Hara, M.J., Wagnon, K.B., Lanigan, D.C., Brown, C.F., Williams, B.A., Lindenmeier, C.W., Orr, R.D., Burke, D.S., Ainsworth, C.C., 2002c. Characterization of Vadose Zone Sediment: Slant Borehole SX-108 in the S-SX Waste Management Area. Pacific Northwest National Laboratory, US Department of Energy, Richland, Washington. PNNL-13757-4.

Smith, J.T., Comans, R.N.J., 1996. Modeling the diffusive transport and remobilization of ^{137}Cs in sediments: the effects of sorption kinetics and reversibility. Geochim. Cosmochim. Acta 60, 995–1004.

Steefel, C.I., Carroll, S., Zhao, P., Roberts, S., 2003. Cesium migration in Hanford sediment: a multisite cation exchange model based on laboratory experiments. J. Contam. Hydrol. 67, 219–246.

Sumner, M.E., Miller, W.P., 1996. Cation exchange capacity and exchange coefficients. In: Sparks, D.L. (Ed.), Methods of Soil Analysis: Part 3. Chemical Methods. American Society of Agronomy, Madison, WI, pp. 1201–1229.

Tamura, T., Jacobs, D.G., 1960. Structural implication in cesium sorption. Health Phys. 2, 391–398.

U.S. DOE, 1998. Groundwater/vadose zone integration project specification. DOE/RL-98-48, Draft C, United States Department of Energy, Richland, WA.

Šimůnek, J., Šejna, M., van Genuchten, M.T., 1998. The HYDRUS-1D Software Package for Simulating the One-Dimensional Movement of Water, Heat and Multiple Solutes in Variably-Saturated Media. U.S. Salinity Laboratory, Agricultural Research Service, U.S. Department of Agriculture, Riverside, CA.

Zachara, J.M., Smith, S.C., Liu, C., McKinley, J.P., Serne, R.J., Gassman, P.L., 2002. Sorption of Cs^+ to micaceous subsurface sediments from the Hanford Site, USA. Geochim. Cosmochim. Acta 66, 193–211.

Comparison of Hanford Colloids and Kaolinite Transport in Porous Media

Jie Zhuang, Yan Jin,* and Markus Flury

ABSTRACT

Understanding colloid transport at the Hanford site in Washington State is critical in assessing migration of radionuclides because colloid transport is a potential means for facilitated off-site migration of radioactive wastes. In this study, eight saturated column experiments were conducted to investigate transport of Hanford colloids and a model colloid (kaolinite) through two types of porous media (Hanford sediments characteristic of 2:1 clay minerals and silica Accusand). Experiments were conducted at a pH value of 10 to mimic the conditions at the Hanford site. The Hanford colloids used were obtained by reacting Hanford sediments with simulated tank waste solutions. The results show that factors influencing transport of Hanford colloids and kaolinite include flow velocity, solution ionic strength, medium type, and colloid properties. Hanford colloids exhibited higher deposition rates than kaolinite in both Hanford sediments and Accusand. Likewise, Hanford sediments retained more colloids than did the silica Accusand. Comparison of transport behaviors of the two colloids through two sands supports the assumption that chemical heterogeneity is important in controlling particle–particle and particle–collector interactions in colloid retention and transport.

Colloids are ubiquitously present in subsurface formations and are formed in situ through geochemical alterations of primary minerals (McCarthy and Zachara, 1989). Colloid transport and its potential to enhance subsurface contaminant transport have been well documented (Mills et al., 1991; Ryan and Elimelech, 1996; Kretzschmar et al., 1999; Ryan et al., 2000; McGechan and Lewis, 2002). Colloid-facilitated transport has been recognized as an important mechanism controlling migration of strongly sorbing contaminants in subsurface environments (Ramsay, 1988; Grolimund et al., 1996; Saiers and Hornberger, 1996; Zhuang et al., 2003).

Colloid deposition kinetics in natural and model porous media have been studied as a function of colloid size, colloid type, surface properties, flow velocity, water content, pore size, and solution chemistry (Goldenberg et al., 1989; Elimelech and O'Melia, 1990a, 1990b; McDowell-Boyer, 1992; Wan and Tokunaga, 1997; James and Chrysikopoulos, 2000; Gamerdinger and Kaplan, 2001; Lenhart and Saiers, 2002). Although great advancements have been made in the study of colloid reaction and transport in porous media, both theoretically and experimentally, our understanding of colloid–soil interactions and our ability to predict transport of colloids in natural subsurface media are limited. In many of the studies conducted to date, model colloids (latex microspheres, silica and pure mineral colloids) and model porous media have been used to study colloid or colloid-facilitated contaminant transport (Kretzschmar et al., 1999). These colloids, however, are not necessarily good surrogates for colloids that are found in the natural environment (Grolimund et al., 1998) because the surface properties of model colloids are different from colloids that are heterogeneous in composition and properties.

The objective of this study was to examine how transport of Hanford colloids, which are heterogeneous in nature, is influenced by flow velocity, solution ionic strength, and matrix properties. We also included kaolinite in the study to provide a systematic comparison on transport behavior between chemically heterogeneous Hanford colloids and a relatively homogenous mineral colloid kaolinite.

THEORY

Calculation of Colloid Attachment Efficiency (α) and Travel Distance (L_T)

Colloid deposition in porous media can be described by the following equation (Yao et al., 1971; O'Melia, 1990):

$$\frac{dC}{dx} = \frac{3}{2}\alpha\eta\frac{(1-\epsilon)}{d_g}C \qquad [1]$$

where C is colloid concentration (mg L^{-1}), d_g the diameter of collectors (sand grains) (m), ε the porosity of porous medium (m^3 m^{-3}), η the collector efficiency, and α the attachment efficiency, both of which are dimensionless.

The collector efficiency (η) describes the approach of colloids to the collector surface. It can be determined from (Rajagopalan and Tien, 1976; Logan et al., 1995)

$$\eta = 4A_s^{1/3}N_{Pe}^{-2/3} + A_s N_{Lo}^{1/8} N_R^{15/8} + 0.00338A_s N_G^{1.2} N_R^{-0.4} \qquad [2]$$

where A_s is Happel's porosity-dependent parameter, accounting for the influence of neighboring collectors on the flow, and N_{Pe}, N_{Lo}, N_R, and N_G are dimensionless parameters accounting for colloid-collector collisions due to diffusion, London–van der Waals interactions, interception, and sedimentation, respectively. A_s can be calculated by $A_s = 2(1-\gamma^5)/(2-3\gamma+3\gamma^5-2\gamma^6)$, where $\gamma = (1-\varepsilon)^3$. The diffusion term is given by the Peclet number, $N_{Pe} = qd_g/D_p$, where q is the water flux (m s^{-1}) defined as $q = v\varepsilon$ with v being the pore water velocity, and D_p is the aqueous diffusion coefficient of colloidal particles. The diffusion coefficient D_p can be calculated from the Stokes–Einstein equation $D_p = B_z T/(3\pi\mu d_c)$, where B_z is the Boltzmann constant (1.38×10^{-23} J K^{-1}), T is the absolute temperature (K), d_c is the diameter (m) of colloidal particles, and μ is the dynamic viscosity (1.025×10^{-3} kg (m s)$^{-1}$ at 20°C) The interception and sedimentation terms are defined as $N_R = d_c/d_g$, and $N_G = g(\rho_c - \rho_f)/(18\mu d_c^2 q)$, respectively, where ρ_c is the colloid density (kg m^{-3}), ρ_f is the

J. Zhuang and Y. Jin, Department of Plant and Soil Sciences, University of Delaware, Newark, DE 19717; M. Flury, Department of Crop and Soil Sciences, Center of Multiphase Environmental Research, Washington State University, Pullman, WA 99164. Received 17 July 2003. Special Section: Colloids and Colloid-Facilitated Transport of Contaminants in Soils. *Corresponding author (yjin@udel.edu).

Published in Vadose Zone Journal 3:395–402 (2004).

677 S. Segoe Rd., Madison, WI 53711 USA

Table 1. Some basic properties of the experimental porous media and colloids.†

Materials	CEC	Fe_0	OM	d_g, d_c	Mineralogy
	cmol kg^{-1}	mg kg^{-1}	g kg^{-1}	mm	
Hanford sand	6.6	6 461	1.0	1.02	mica, illite, smectite, vermiculite, quartz, feldpars, pyroxene
Accusand	0.6	28.7	0.4	0.44	quartz
Hanford colloid	6.7	56 709	–	6.27×10^{-4}	mica, illite, smectite, vermiculite, quartz, cancrinite, sodalite
Kaolinite	2.0	1 300	–	1.92×10^{-3}	kaolinite

† CEC, cation exchange capacity; Fe_0, free Fe oxide; OM, organic matter; d_g, geometric diameter of sand grains; d_c, Z-averaged hydrodynamic diameter of the colloidal particles measured in 2 m*M* $NaNO_3$ by dynamic light scattering with a Malvern Zetasizer 3000HSA (Malvern Instruments Ltd., Malvern, UK). Mineralogical composition was analyzed with X-ray diffraction.

fluid density (kg m^{-3}), and g is acceleration due to gravity. The term accounting for London–van der Waals interactions is given as $N_{Lo} = 4H/(9\pi\mu q d_c^2)$, where H is the Hamaker constant. For both Hanford sand and Accusand, we used the same Hamaker constant of 1.6×10^{-21} J, which is the measured Hamaker constant (in water) for quartz (Ackler et al., 1996), because H does not vary very much for different materials and we do not know the value for Hanford sand.

The attachment efficiency (α) describes the attachment of colloids to collector surfaces by accounting for electrostatic interactions between colloids and the porous medium. It is the ratio of the number of colloids approaching the collector surface to the number of colloids attached on that surface, and can be calculated by (Yao et al., 1971)

$$\alpha = \frac{2}{3}\frac{d_g}{(1-\varepsilon)}\frac{K_a}{v\eta} \quad [3]$$

where K_a is the deposition rate, defined as $K_a = -(v/L)\ln(C_e/C_0)$, where C_e represents the stable effluent concentration of the colloid (g m^{-3}), C_0 the influent colloid concentration (g m^{-3}), and L the column length (m).

Integrating Eq. [1] with the boundary conditions of $C = C_0$ at $x = 0$ and $C = C_L$ at $x = L$ yields (Yao et al., 1971)

$$\ln\left(\frac{C_L}{C_0}\right) = -\left[\frac{3(1-\varepsilon)\alpha\eta L}{2d_g}\right] \quad [4]$$

This equation can be rearranged in terms of column length L and can be used to calculate how far a certain fraction of colloids will move in a porous medium. For this study, we define the distance (L_T) at which 99.9% of colloids ($C_L/C_0 = 0.001$) are removed as the maximum travel distance for the colloids.

Calculation of Fractional Surface Coverage (θ)

The dynamics of colloid deposition in porous media can be illustrated by the temporal change of fractional surface coverage of sediment grains. For irreversible colloid deposition on spherical collectors, the dimensionless collector surface coverage (θ) can be estimated as a function of time from experimental results of colloid breakthrough from the porous media according to (Song and Elimelech, 1993a):

$$\theta = \frac{q d_g C_0 \int_0^t (1 - C/C_0)\,dt}{4\rho d_c L(1-\varepsilon)} \quad [5]$$

where ρ is the specific density of the colloids (taken as 2650 kg m^{-3}), t is time, and we have assumed that the colloidal particles in our experiments are spherical.

It should be noted that filtration theory in its present form is only applicable to ideal systems where colloids are spherical and monodisperse, which is not the case in our experimental systems, especially with the Hanford colloids. Therefore, the calculated parameters presented in this paper allow only qualitative comparisons between the experiments and should not be used for prediction. Absolute values calculated in this study should be considered with caution.

MATERIALS AND METHODS

Porous Materials and Colloids

Two types of porous materials, Hanford sediments and Accusand, were used in this study. Coarse Hanford sediments, representative of the material underlying the Hanford waste tanks, were obtained from the Submarine Pit (218-E-12B) at the Hanford Site in Washington, USA. The sediments came from the same site as the ones used by Zhuang et al. (2003), but from a different layer of the Hanford formation. The sediments had the same mineralogical composition as the ones used by Zhuang et al. (2003), but a different particle size distribution (Table 1). Detailed characterization of the sediments is given in Serne et al. (2002). The sediments were dry sieved and the fraction between 0.053 and 2-mm grains (particle size distribution by weight: 0.65% of 0.053–0.3 mm, 4.58% of 0.3–0.5 mm, and 94.77% of 0.5–2.0 mm) was used in the experiments. Accusand, a typical silica sand, was purchased from Unimin Corporation (Le Sueur, MN). Its particle size distribution was 9% 0.1 to 0.25 mm, 69.8% 0.25 to 0.5 mm, and 21.2% 0.5 to 1.0 mm. The two sands were rinsed with deionized water, until there were no particles suspended in the liquid phase as verified by turbidity measurement, and dried at 60°C.

The Hanford colloids used in this study were specially prepared to mimic vadose zone conditions after a waste tank leak, and they are considered to represent colloidal material in Hanford sediments after a tank leak occurred (Zhao et al., 2002, 2004). Hanford colloids were obtained by reacting Hanford sediments with a solution simulating that in the waste storage tanks at the Hanford site (Zhao et al., 2002). The procedure is briefly described as follows. First, 1 L of the simulated tank solution (2.8 mol kg^{-1} NaOH, 0.125 mol kg^{-1} $NaAlO_4$, and 3.7 mol kg^{-1} $NaNO_3$) was added to 1 kg of the Hanford sediment of sizes smaller than 2 mm. The mixture was kept at 50°C and shaken periodically for 40 d. Then, colloidal particles (diameter <2 μm) were separated by gravity sedimentation. The colloidal particles were equilibrated with 1 *M* $NaNO_3$ for 24 h, centrifuged, washed, and dialyzed against deionized water until the conductivity was <0.01 dS m^{-1}. By tank solution treatment, some of the native colloidal particles (e.g., quartz and kaolinite) partially dissolved, and new minerals (e.g., cancrinite and sodalite) formed. About 20 g of colloidal material was obtained from 1 kg of Hanford sediment.

The kaolinite particles (diameter <2 μm) were extracted by gravity sedimentation in deionized water from well-crystalline kaolin (KGa-1, Source Clay Minerals Repository, University of Missouri, Columbia, MO). Some basic properties of the materials are provided in Table 1.

Transport Experiments

A series of saturated column experiments were performed to investigate effects of flow velocity, solution ionic strength,

Table 2. Experimental conditions and parameters.†

Column Exp.	Sand	Colloid	ε	v	I	D_p	N_{Pe}	K_a	η	α	L_T
				cm h^{-1}	mM	10^{-13} m^2 s^{-1}		h^{-1}			m
1	Hanford	Hanford	0.38	2.13	1	6.72	3 412	0.20	0.36	0.03	0.74
2	Hanford	Hanford	0.37	4.54	1	6.72	7 081	0.35	0.17	0.05	0.89
3	Hanford	Kaolinite	0.41	2.17	1	2.19	11 485	0.14	2.07	0.004	1.09
4	Hanford	Kaolinite	0.37	4.54	1	2.19	21 684	0.23	1.25	0.004	1.35
5	Hanford	Hanford	0.37	4.54	10	6.72	7 081	7.00	0.17	1.00	0.04
6	Hanford	Kaolinite	0.37	4.45	10	2.19	21 254	0.72	1.28	0.01	0.43
7	Accusand	Hanford	0.33	5.03	1	6.72	3 018	0.29	0.20	0.01	1.19
8	Accusand	Kaolinite	0.32	4.88	1	2.19	8 696	0.13	1.39	0.001	2.52

† ε, porosity; v, pore water velocity; I, ionic strength; D_p, colloid diffusion coefficient; N_{Pe}, colloid Peclet number; K_a, deposition rate; η, collector efficiency; α, attachment efficiency; L_T, travel distance.

matrix properties, and colloid types on colloid deposition and transport (Table 2). The column system used in the study was similar to that illustrated in Jin et al. (2000). The column was made of acrylate, with an inner diameter of 5.1 cm and height of 10.0 cm. In the experiments, a stainless-steel screen (0.3-mm mesh size) was placed on the bottom plate for mechanical support. Teflon tubing was used throughout the system except for a portion of tygon tubing used in the peristaltic pump. When the column was packed, a deaerated $NaNO_3$ background solution (pH = 10, either 1 mM, buffered with 0.024 mM mixture of Na_2CO_3 and $NaHCO_3$ or 10 mM, buffered with 0.24 mM mixture of Na_2CO_3 and $NaHCO_3$) was preintroduced into the column from its bottom to a certain height. Then the sand was slowly poured into the column in 1-cm increments while it was stirred with a plastic rod to ensure packing uniformity and to avoid air entrapment in the column.

Before each experiment was run, the deaerated $NaNO_3$ background solution was flushed through the column overnight (at least 15 pore volumes) to precondition the columns for the transport experiments. The flushing removed residual colloids present in the columns, established a steady-state flow, and standardized background ionic strength and pH. The background solution was adjusted to pH 10 to mimic the high pH condition in the pore water at the Hanford site and to avoid dissolution of carbonates from the sediments during the experiments. The input solution, composed of the $NaNO_3$ background solution along with the experimental colloid (50 mg L^{-1}) and a Cl^- tracer (0.68 mM in NaCl), was then pumped into the column at a constant flow rate. For experiments that involved different ionic strengths, we adjusted the concentrations of $NaNO_3$ and the carbonate buffer. The influent reservoir was stirred during the entire experiment. Colloids were infused for 6 to 10 pore volumes. Then we applied a colloid-free $NaNO_3$ buffer solution until effluent colloid returned to a baseline level that was determined at the beginning of each experiment. During the course of the experiments, effluent samples were collected from the top of the column into 15-mL polypropylene centrifuge tubes in regular time intervals using a fraction collector. The Cl^- tracer was analyzed using ion chromatography (Dionex Corporation, Sunnyvale, CA). We determined the colloid concentration from predetermined calibration curves by turbidity measurements at 350 nm (Zhuang et al., 2003) using a UV-VIS spectrophotometer (DU Series 640, Beckman Instruments, Inc., Fullerton, CA). During the experiments room temperature was 22 ± 1°C.

RESULTS AND DISCUSSION

Effect of Flow Velocity

Figure 1 illustrates the effect of flow velocity on the transport of both Hanford colloids and kaolinite through Hanford sediments. Colloid breakthrough occurred at about one pore volume, and reached a plateau at 1.4 to 2 pore volumes (Fig. 1a and 1b). The shape of the breakthrough curves indicates that the initial attachment of colloidal particles on the sand and elution process by colloid-free background solution were insensitive to the change of flow velocity. However, the steady-state breakthrough concentrations (C/C_0) of the two colloids at high velocity were higher than at low velocity, suggesting that a hydrodynamic effect occurred for the colloid attachment. This result agrees with previous studies performed with various colloids and porous media (Goldenberg et al., 1989; Kretzschmar et al., 1997; Compere et al., 2001). A possible mechanism is that high velocity decreased thickness of shear interface of immobile–mobile phase on the sand, and helped the colloids remain in streamlines because of fluid-particle phase stresses, hydrodynamic drag, and lift forces. Consequently, high velocity decreased colloid deposition on the sediment surfaces. The absence of tailing of the breakthrough curves indicates an irreversible sorption of the particles on the sand.

The dynamics of surface coverage (θ) (calculated using Eq. [5]) and the relationship between θ and attachment efficiency (α) (calculated using Eq. [3]) are determined for the breakthrough experiments. Figures 1c and 1d show that the values of θ of both Hanford colloids and kaolinite in the early stage of transport were not affected by flow velocity, indicating that chemical interactions likely dominated the initial sorption process. As shown in Table 2, the colloid Peclet number ($N_{Pe} = qd_g/D_p$), which represents influence of hydrodynamic interaction, is about three times larger for the larger kaolinite particles than for Hanford colloids. This suggests that influence of the hydrodynamic interactions is more pronounced for larger particles (Ko et al., 2000).

The θ–α relationship shows how retained particles affect the retention of the subsequent particles approaching the collector surface. Figures 1e and 1f indicate that the retained particles blocked attachment of the subsequent particles. For Hanford colloids, at the same fractional surface coverage, their attachment efficiency of colloids was higher at higher flow velocity. This effect of flow velocity agrees with the experimental results of Kretzschmar et al. (1997), who used latex colloids, and the theoretical predictions by Song and Elimelech (1993b) of colloid deposition rate under unfavorable particle–surface interaction conditions. At higher flow velocity, more colloids can stay in the streamlines

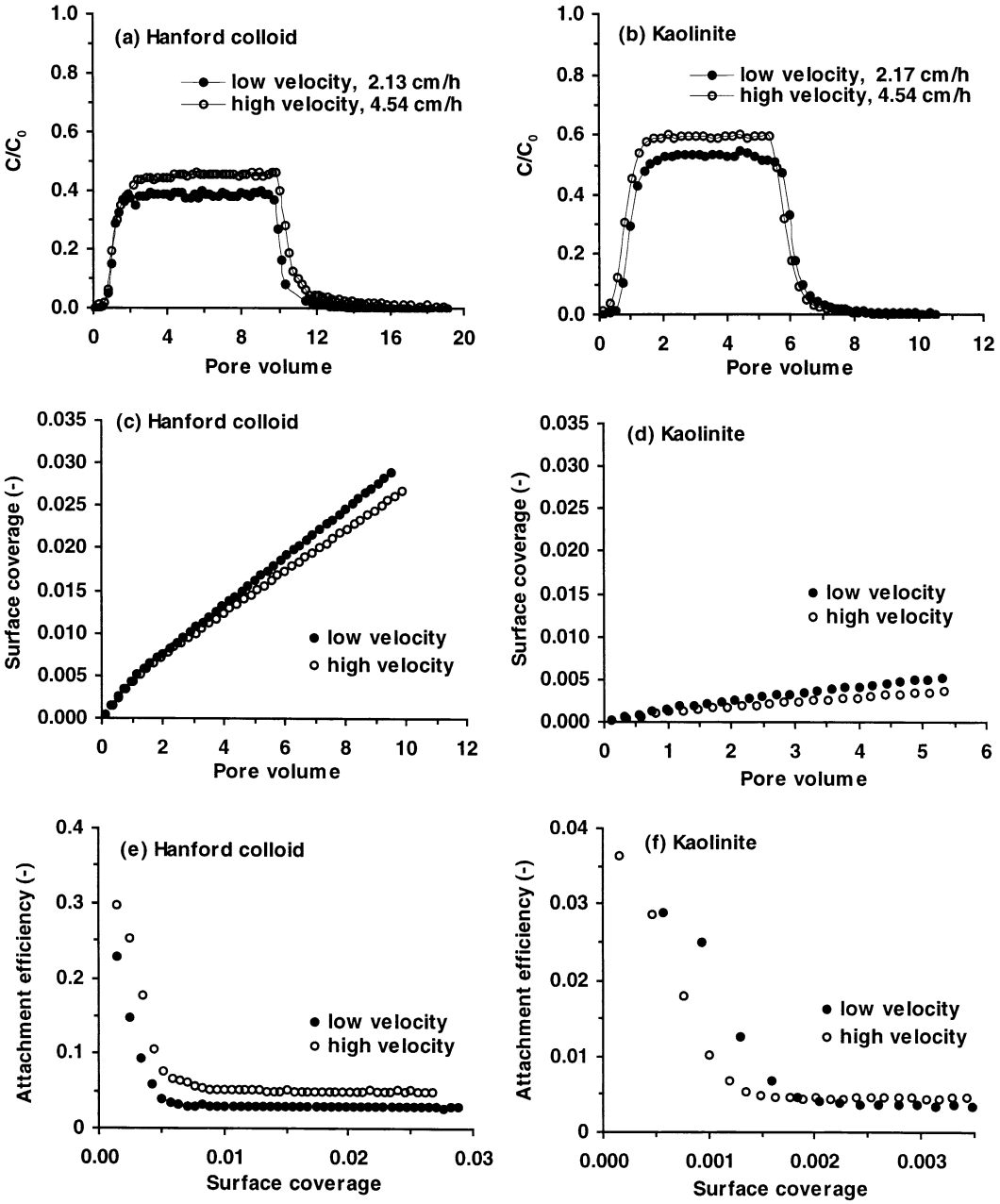

Fig. 1. Effect of flow velocity on transport of Hanford colloids and kaolinite through Hanford sand-packed columns in $NaNO_3$ solution (1 m*M*, pH = 10).

of flow. Consequently the number of colloids approaching the collector surface was reduced, as indicated by the calculated collector efficiency (η) (Table 2). In contrast, kaolinite, with larger sizes than the Hanford colloids, behaved differently. The attachment efficiency (α) of kaolinite decreased as the flow velocity increased during the early stage of transport but was not affected by flow velocity at the plateau stage (Table 2, Fig. 1f). The deposition rate (K_a) increased for both Hanford and kaolinite colloids as the flow rate increased (Table 2). Song and Elimelech (1993b) concluded that at low to moderate flow velocities (10^{-6} to 10 m s^{-1}) the deposition rate of colloids is controlled by both flow intensity and particle–surface interaction and the effects of fluid convection and colloidal interaction cannot be separated.

Effect of Solution Ionic Strength

Solution ionic strength influences particle–surface and particle–particle electrostatic interactions through a charge screening effect. Transport of Hanford colloids and kaolinite through Hanford sediments at two ionic strengths (1 and 10 m*M*) is compared in Fig. 2a and 2b. No Hanford colloids broke through the Hanford sand column in 10 m*M* solution, whereas kaolinite particles exhibited a steady-state breakthrough rate of 0.2 C/C_0 under the same experimental conditions. In 1 m*M* solution, the maximum effluent concentrations reached

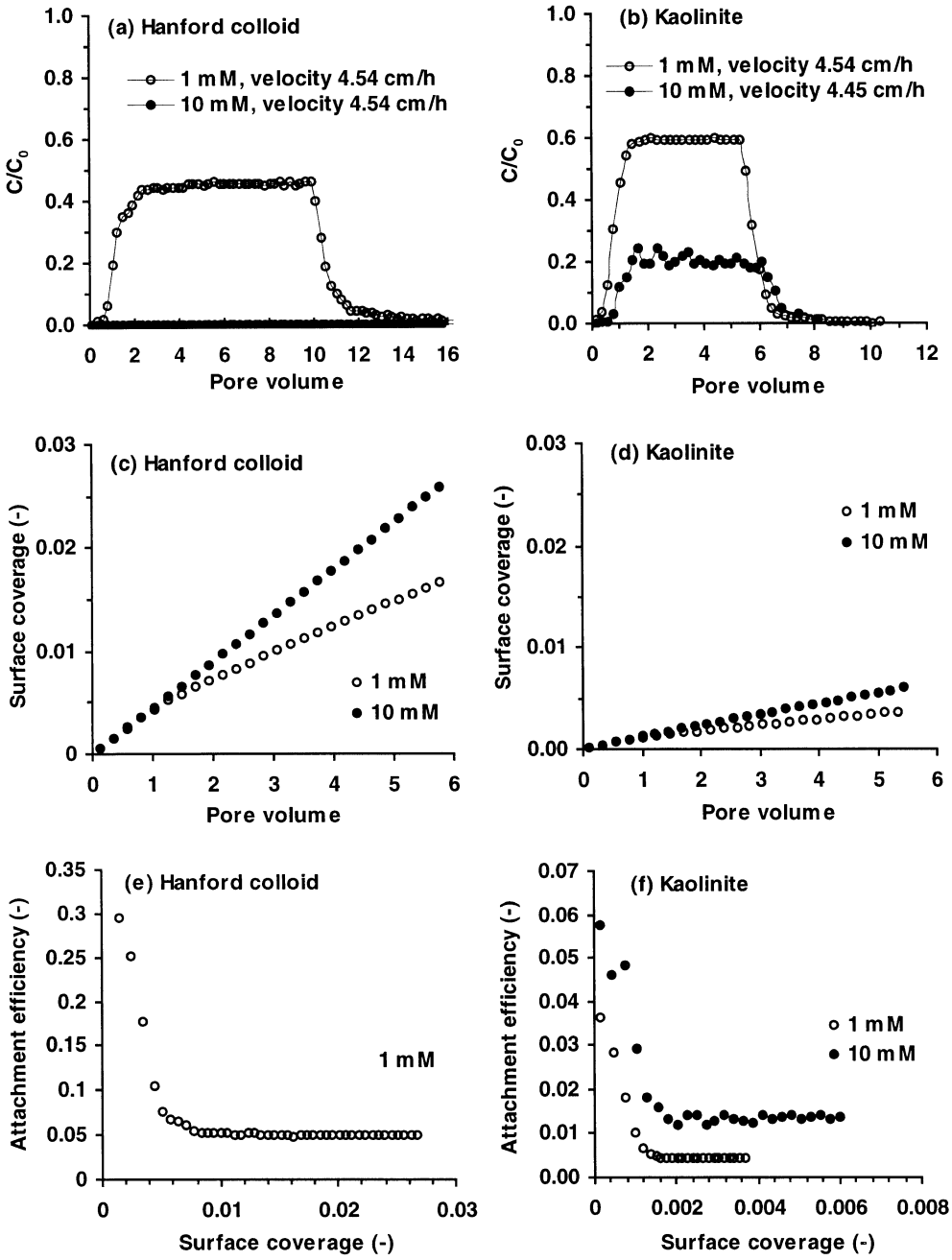

Fig. 2. Effect of ionic strength on transport of Hanford colloids and kaolinite through Hanford sand-packed columns in $NaNO_3$ solution (pH = 10).

about 0.6 C/C_0 for kaolinite particles and about 0.45 C/C_0 for Hanford colloids. Evidently, kaolinite was less filtered than Hanford colloids during the transport, regardless of the larger size of the kaolinite particles. This effect of ionic strength on the transport of both colloids is expected (Elimelich and O'Melia, 1990a). The dynamics of θ (Fig. 2c and 2d) indicate that increasing ionic strength did not cause a significant change in colloid deposition in the early transport stage. However, in the plateau stage, high ionic strength increased surface coverage by Hanford colloids, but had a minimum effect on kaolinite coverage on the sand. This implies that electrostatic interactions were more dominant for the attachment of Hanford colloids than kaolinite particles.

Figure 2f shows that the attachment efficiency of kaolinite increased as solution ionic strength rose. For Hanford colloids at 10 m*M* ionic strength, the value of α was equal to one, since screening of surface charge resulted in attachment for every collision. The strong nonlinear relationship of θ–α suggests the involvement of different retention mechanisms at different transport stages.

The influence of ionic strength on colloid mobility can be further illustrated by calculating colloid travel distances using Eq. [4]. Table 2 shows that Hanford colloids can travel 0.9 m in 1 m*M* $NaNO_3$ in Hanford sediments, while kaolinite particles move about 1.4 m before 99.9% of the colloids are captured by the porous media.

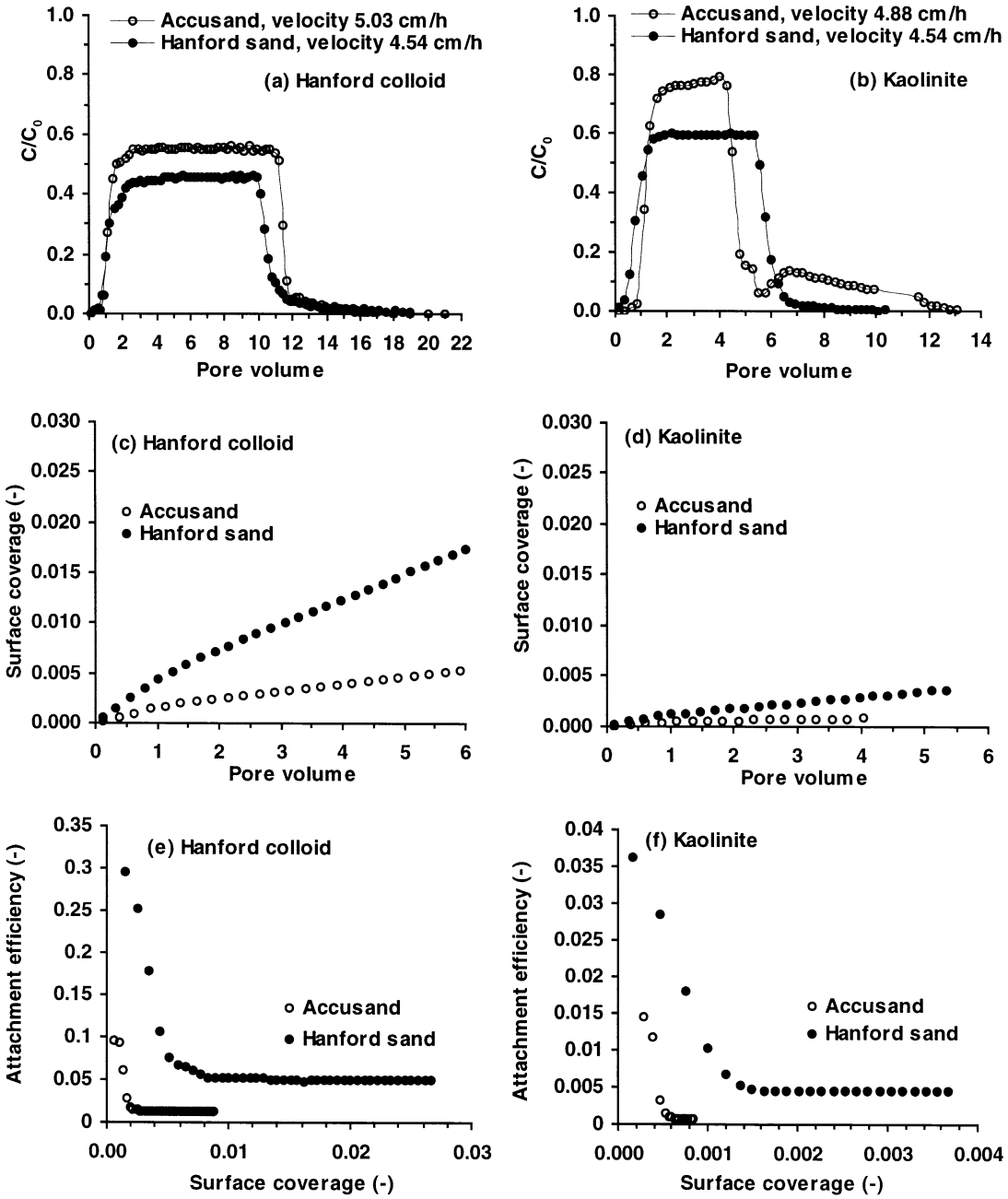

Fig. 3. Transport of Hanford colloids and kaolinite through Hanford sand and Accusand in $NaNO_3$ solution (1 m*M*, pH = 10).

Effect of Medium Surface Properties

Breakthrough results of kaolinite and Hanford colloids in two types of sands are plotted in Fig. 3a and 3b. Different column packing and the use of a peristaltic pump that only could be adjusted incrementally caused the slightly different flow rates between the experiments. The differences in flow rates were small, so they were unlikely to have caused any of the effects discussed below.

Both colloids showed a higher breakthrough from Accusand than from Hanford sand. The steady-state effluent concentration increased by approximately 0.1 and 0.2 C/C_0 for Hanford colloid and kaolinite, respectively. A second peak is observed for the colloid breakthrough in Accusand, and we attribute this peak to an experimental artifact. The dynamics of θ, as depicted in Fig. 3c and 3d, reveal that deposition of both colloids resulted in higher coverages on Hanford sand than on Accusand. In addition, the fractional surface coverages by Hanford colloids on both types of sands were one order of magnitude larger than those of kaolinite. This was likely caused by the more chemical heterogeneous nature of the natural Hanford colloids than the model kaolinite colloids. The slope of the α–θ relationship curves reduced to a constant value at one pore volume (Fig. 3e and 3f). This indicates a critical point of attachment efficiency (α), at which the decreasing deposition rate stabilized at a constant value. The attachment effi-

ciency of Hanford colloids leveled off at a larger surface coverage compared with kaolinite. Taking the constant attachment efficiency at the flat portion in Fig. 3e and 3f as the particle–particle collision efficiency, we see that Hanford colloids stick more easily than kaolinite particles under the same experimental conditions.

Johnson et al. (1996) suggested that geochemical heterogeneity has a profound impact on colloid transport. Capacity of attachment-favorable sites of a collector determines the amount of colloidal particles directly attached on the matrix, and this further influences how many subsequent colloidal particles can be removed from the liquid flowing through the column. Commonly, heterogeneous surfaces possess more favorable settings than relatively uniform surfaces for colloid attachment (Song and Elimelech, 1993a; Johnson and Elimelech, 1995; Johnson et al., 1996; Ren et al., 2000). Hanford sediments have more heterogeneous surfaces, both physically and chemically, than the relatively uniform silica Accusand (Serne et al., 2002; Zhuang et al., 2003). The different types of minerals contained in Hanford sediments, differently exposed crystallographic faces, and irregular surface coatings or cracks have been reported (McKinley et al., 2001; Zachara et al., 2002). Therefore, Hanford sediments likely provided more settings favorable for colloid deposition than the Accusand.

CONCLUSION

Comparison of the transport of Hanford colloids and kaolinite through chemically heterogeneous Hanford sand and chemically homogeneous silica sand generated several interesting results. Increased water flow velocity caused more colloids to break through the Hanford sand and Accusand, and the colloid deposition rate increased as the flow velocity increased. Chemical heterogeneity associated with the Hanford colloids caused stronger particle–particle and particle–matrix interactions than was the case for the more homogeneous kaolinite colloids. Hanford colloids also had higher deposition rates than kaolinite, again due to pronounced chemical heterogeneity. While both hydrodynamic interaction (due to variation of flow velocity) and electrostatic interaction (due to chemical heterogeneity) were involved in the attachment of Hanford colloids, chemical interaction was relatively weak and hydrodynamic interaction probably dominated the attachment of kaolinite particles. Therefore, solution chemistry had more significant effects on the transport of Hanford colloids than kaolinite. The same trend was found on the natural Hanford sand and the model Accusand. This study indicates that several interaction mechanisms might be involved simultaneously during colloid transport, but their relative importance in the overall transport depends on the chemical and physical properties of colloids and transport media as well as the environmental conditions.

ACKNOWLEDGMENTS

This work was supported by the Environmental Management Science Program, U.S. Department of Energy under Grant no. DE-FG07-99ER62882.

REFERENCES

Ackler, H., R.H. French, and Y. Chiang. 1996. Comparisons of Hamaker constants for ceramic systems with intervening vacuum or water: From force laws and physical properties. J. Colloid Interface Sci. 179:460–469.

Compere, F., G. Porel, and F. Delay. 2001. Transport and retention of clay particles in saturated porous media: Influence of ionic strength and pore velocity. J. Contam. Hydrol. 49:1–21.

Elimelech, M., and C.R. O'Melia. 1990a. Kinetics of deposition of colloidal particles in porous-media. Environ. Sci. Technol. 24:1528–1536.

Elimelech, M., and C.R. O'Melia. 1990b. Effect of particle-size on collision efficiency in the deposition of Brownian particles with electrostatic energy barriers. Langmuir 6:1153–1163.

Gamerdinger, A.P., and D.I. Kaplan. 2001. Colloid transport and deposition in water-saturated Yucca Mountain tuff as determined by ionic strength. Environ. Sci. Technol. 35:3326–3331.

Goldenberg, L.C., I. Hutcheon, and N. Wardlaw. 1989. Experiments on transport of hydrophobic particles and gas-bubbles in porous-media. Transp. Porous Media 4:129–145.

Grolimund, D., M. Borkovec, K. Barmettler, and H. Sticher. 1996. Colloid-facilitated transport of strongly sorbing contaminants in natural porous media: A laboratory column study. Environ. Sci. Technol. 30:3118–3123.

Grolimund, D., M. Elimelech, M. Borkovec, K. Barmettler, R. Kretzschmar, and H. Sticher. 1998. Transport of in situ mobilized colloidal particles in packed soil columns. Environ. Sci. Technol. 32:3562–3569.

James, S.C., and C.V. Chrysikopoulos. 2000. Transport of polydisperse colloids in a saturated fracture with spatially variable aperture. Water Res. Resour. 36:1457–1465.

Jin, Y., Y. Chu, and Y. Li. 2000. Virus removal and transport in saturated and unsaturated sand columns. J. Contam. Hydrol. 43: 111–128.

Johnson, P.R., and M. Elimelech. 1995. Dynamics of colloid deposition in porous media: Blocking based on random sequential adsorption. Langmuir 11:801–812.

Johnson, P.R., N. Sun, and M. Elimelech. 1996. Colloid transport in geochemically heterogeneous porous media: Modeling and measurements. Environ. Sci. Technol. 30:3284–3293.

Ko, C.H., S. Bhattacharjee, and M. Elimelech. 2000. Coupled influence of colloidal and hydrodynamic interactions on the RSA dynamic blocking function for particle deposition onto packed spherical collectors. J. Colloid Interface Sci. 229:554–567.

Kretzschmar, R., K. Barmettler, D. Grolimund, Y.D. Yan, M. Borkovec, and H. Sticher. 1997. Experimental determination of colloid deposition rates and collision efficiencies in natural porous media. Water Resour. Res. 33:1129–1137.

Kretzschmar, R., M. Borkovec, D. Grolimund, and M. Elimelech. 1999. Mobile subsurface colloids and their role in contaminant transport. Adv. Agron. 66:121–193.

Lenhart, J.J., and J.E. Saiers. 2002. Transport of silica colloids through unsaturated porous media: Experimental results and model comparisons. Environ. Sci. Technol. 36:769–777.

Logan, B.E., D.G. Jewett, R.G. Arnold, E.J. Bouwer, and C.R. O'Melia. 1995. Clarification of clean-bed filtration models. J. Environ. Eng. 121:869–873.

McCarthy, J.F., and J.M. Zachara. 1989. Subsurface transport of contaminants-mobile colloids in the subsurface environment may alter the transport of contaminants. Environ. Sci. Technol. 23:496–502.

McDowell-Boyer, L.M. 1992. Chemical mobilization of micro-sized particles in saturated porous media under steady flow conditions. Environ. Sci. Technol. 26:586–593.

McDowell-Boyer, L.M., J.R. Hunt, and N. Sitar. 1986. Particle-transport through porous-media. Water Resour. Res. 22:1901–1921.

McGechan, M.B., and D.R. Lewis. 2002. Transport of particulate and colloid-sorbed contaminants through soil. Part 1. General principles. Biosyst. Eng. 83:255–273.

McKinley, J.P., C.J. Zeissler, J.M. Zachara, R.J. Serne, R.M. Lindstrom, H.T. Schaef, and R.D. Orr. 2001. Distribution and retention of ^{137}Cs in sediments at the Hanford site, Washington. Environ. Sci. Technol. 35:3433–3441.

Mills, W.B., S. Liu, and F.K. Fong. 1991. Literature review and model

(COMET) for colloid/metals transport in porous media. Ground Water 29:199–208.
O'Melia, C.R. 1990. Kinetics of colloidal chemical processes in aquatic systems. p. 447–474. *In* W. Stumm (ed.) Aquatic chemical kinetics: Reaction rates of processes in natural water. Wiley-Interscience, New York.
Rajagopalan, R., and C. Tien. 1976. Trajectory analysis of deep-bed filtration with the sphere-in-cell porous media model. AIChE J. 22:523–533.
Ramsay, J.D.F. 1988. The role of colloids in the release of radionuclides from nuclear waste. Radiochim. Acta 44/45:165–170.
Ren, J.H., A.I. Packman, and C. Welty. 2000. Correlation of colloid collision efficiency with hydraulic conductivity of silica sands. Water Resour. Res. 36:2493–2500.
Ryan, J.N., and M. Elimelech. 1996. Colloid mobilization and transport in groundwater. Colloid Surf. A 107:1–56.
Ryan, J.N., M. Elimelech, J.L. Baeseman, and R.D. Magelky. 2000. Silica-coated titania and zirconia colloids for subsurface transport field experiments. Environ. Sci. Technol. 34:2000–2005.
Saiers, J.E., and G.M. Hornberger. 1996. The role of colloidal kaolinite in the transport of cesium through laboratory sand columns. Water Resourc. Res. 32:33–41.
Serne, R.J., B.N. Bjornstad, H.T. Schaef, B.A. Williams, D.C. Lanigan, D.G. Horton, R.E. Clayton, A.V. Mitroshkov, V.L. LeGore, M.J. O'Hara, C.F. Brown, K.E. Parker, I.V. Kutnyakov, J.N. Serne, G.V. Last, S.C. Smith, C.W. Lindenmeier, J.M. Zachara, and D.S. Burke. 2002. Characterization of vadose zone sediment: Uncontaminated RCRA borehole core samples and composite samples. PNNL-13757-1. USDOE, Pacific Northwest National Laboratory, Richland, WA.
Song, L.F., and M. Elimelech. 1993a. Dynamics of colloid deposition in porous-media-Modeling the role of retained particles. Colloid Surf. A 73:49–63.
Song, L.F., and M. Elimelech. 1993b. Calculation of particle deposition rate under unfavorable particle-surface interactions. J. Chem. Soc. Faraday Trans. 89:3443–3452.
Wan, J., and T. Tokunaga. 1997. Film straining of colloids in unsaturated porous media: Conceptual model and experimental testing. Environ. Sci. Technol. 31:2413–2420.
Yao, K.M., M.T. Habibian, and C.R. O'Melia. 1971. Water and wastewater filtration: Concepts and applications. Environ. Sci. Technol. 5:1105–1112.
Zachara, J.M., S.C. Smith, C.X. Liu, J.P. McKinley, R.J. Serne, and P.L. Gassman. 2002. Sorption of Cs^+ to micaceous subsurface sediments from the Hanford site, USA. Geochim. Cosmochim. Acta 66:193–211.
Zhao, H., Y. Deng, J.B. Harsh, M. Flury, and J. Boyle. 2004. Alteration of kaolinite to cancrinite and sodalite by simulated Hanford Tank Wastes and its impact on cesium retention. Clay Clay Miner. 52:1–13.
Zhao, H., J.B. Harsh, M. Flury, and K. Mashal. 2002. Alteration of mineralogical and surface properties of Hanford sediments contaminated with tank waste *In* Geochemistry Division Abstracts, 222nd ACS National Meeting, Chicago, IL. 26–30 Aug. 2002. ACS, Washington, DC.
Zhuang, J., M. Flury, and Y. Jin. 2003. Colloid-facilitated cesium transport through water-saturated Hanford sediments and Ottawa sand. Environ. Sci. Technol. 37:4905–4911.

Clays and Clay Minerals, Vol. 52, No. 1, 1–13, 2004.

ALTERATION OF KAOLINITE TO CANCRINITE AND SODALITE BY SIMULATED HANFORD TANK WASTE AND ITS IMPACT ON CESIUM RETENTION

HONGTING ZHAO, YOUJUN DENG, JAMES B. HARSH, MARKUS FLURY* AND JEFFREY S. BOYLE

Department of Crop and Soil Sciences, Center for Multiphase Environmental Research, Washington State University, Pullman, WA 99164, USA

Abstract—Caustic nuclear wastes have leaked from tanks at the US Department of Energy's Hanford site in Washington State (USA) causing hundreds of thousands of gallons of waste fluids to migrate into the underlying sediments. In this study, four simulant tank waste (STW) solutions, which are high in NaOH (1.4 and 2.8 mol/kg), $NaNO_3$ (3.7 mol/kg) and $NaAlO_2$ (0.125 and 0.25 mol/kg), were prepared and reacted with reference kaolinite KGa-1 and KGa-2 at 50 and 80ºC for up to 2 months. The structure and morphology of the resulting products were characterized using X-ray diffraction, scanning electron microscopy, and Fourier transform infrared spectroscopy. The products were also examined for cation exchange and Cs^+ sorption as a function of ionic strength and types of cations in the background solutions. Cancrinite and sodalite were the only new minerals observed in all of the conditions tested in this experiment. Two major chemical processes were involved in the reactions: dissolution of kaolinite and precipitation of cancrinite and sodalite. Increasing NaOH concentration and temperature, and decreasing $NaAlO_2$ concentration increased the transformation rate. Both cancrinite and sodalite appeared stable thermodynamically under the experimental conditions. The newly formed feldspathoids were vulnerable to acid attack and pronounced dissolution occurred at pH below 5.5. Cancrinite and sodalite can incorporate $NaNO_3$ ion pairs in their cages or channels. Sodium in cancrinite and sodalite was readily exchangeable by K^+, but less easily by Cs^+ or Ca^{2+}. The feldspathoid products sorb nearly an order of magnitude more Cs^+ than the unaltered kaolinite. The Cs adsorption is reduced by competing cations in the background solutions. At low ionic strength (0.01 M $NaNO_3$ or 0.005 M $Ca(NO_3)_2$), Ca^{2+} was more competitive than Na^+. When the concentration of the background solution was increased 10 times, Na^+ was more competitive than Ca^{2+}.

Key Words—Cancrinite, Cation Exchange, Cesium Sorption, Feldspathoid, Hanford Waste Tanks, Kaolinite, Mineral Stability, Mineral Transformation, Sodalite.

INTRODUCTION

Many single-shell tanks of the 177 nuclear waste tanks located at the US Department of Energy's Hanford Reservation near Richland, WA (USA) have leaked, allowing 0.6–1.4 million gallons of high-level nuclear waste fluids to migrate into the underlying coarse-textured, relatively unweathered sediments (Hanlon, 1996; Gephart and Lundgren, 1998). Tank sludge, arising from the Pu production and extraction procedures at the Hanford site, is chemically very complex and of extreme chemical conditions. In most cases, tank sludge has very high $NaNO_3$ (up to ~8 M), NaOH (pH >13), and aluminate concentrations (>0.1 M) (Serne *et al.*, 1998). The temperature in several tanks rose to >100ºC during storage and was reported as high as 160ºC in one tank (Pruess *et al.*, 2002). The temperature in the immediate neighborhood sediments was estimated as high as 120ºC, and in the sediments 20 m below the tanks could be as high as 70ºC (Pruess *et al.*, 2002).

Reaction of the leaked waste solution with the underlying soil and sedimentary matrix will potentially result in dissolution of native minerals and subsequent formation of new secondary mineral phases. These chemical reactions can alter mineral surface properties, as well as the porosity and flow paths of the surrounding porous media. The physicochemical and mineralogical alterations of the sediment matrix could together lead to significant changes in the fate and transport of tank contaminants. Recent studies have shown that cancrinite, a feldspathoid, was formed after reacting Hanford sediments or quartz with tank simulant solutions at 60–90ºC (Nyman *et al.*, 2000; Bickmore *et al.*, 2001). We have found another feldspathoid, sodalite, in addition to cancrinite, which formed upon reacting the Hanford sediments with tank simulant for five weeks at 68ºC (our unpublished data). To the best of our knowledge, the retention properties of these materials for radionuclides have not yet been addressed. Quartz, feldspar, hornblende, mica, chlorite, illite, kaolinite, smectite and calcite are the most common minerals in Hanford sediments (Serne *et al.*, 1998). We found that these minerals have different reactivities toward the simulant solutions (our unpublished data). Even though kaolinite is not the most abundant clay mineral in Hanford sediments, here we report kaolinite alteration results because this mineral had shown the fastest alteration rate and the final precipitates are common products in the reactions with Hanford sediments.

* E-mail address of corresponding author:
flury@mail.wsu.edu
DOI: 10.1346/CCMN.2004.0520101

Kaolinite reactions give a high yield of the new mineral phases and the simplest mineral composition to study the retention behavior of radioactive nuclides on the new minerals.

It is known that kaolinite is not stable under highly alkaline conditions and various zeolite and feldspathoids can form (Breck, 1974). For instance, at high molarity of KOH (0.1 to 4.0 M) and temperatures of 35 and 80ºC, kaolinite transformed, in sequence, to illite, KI-zeolite, phillipsite, and finally, K-feldspar (Bauer *et al.*, 1998). Kaolinite has been used as the Al and Si sources for zeolite synthesis. Linde Type A, X and Y zeolites, cancrinite, sodalite, faujasite, and several other types of zeolites have been synthesized from kaolinite (Dudzik and Kowalak, 1974; Buhl, 1991; Alberti *et al.*, 1994; Gualtieri *et al.*, 1997). For zeolite synthesis, most of the experiments were carried out at high temperatures (*e.g.* 220ºC) and high pressures in autoclaves. These conditions are not likely to occur in the sediments underlying the tanks at the Hanford site. In addition, the presence of high concentrations of electrolytes such as $NaNO_3$ in the leaked waste solution may alter the reaction path.

The objectives of this study were to study: (1) the mineral alteration of kaolinite after contacting simulant Hanford tank solutions; (2) the stability and ion-exchange properties of resulting precipitates; and (3) the sorption behavior of Cs, a common radioactive element of Hanford nuclear wastes, on the newly formed precipitates. We hypothesized that kaolinite, with a low Cs^+ sorption capacity, would be transformed to feldspathoids under conditions designed to mimic those under leaking high-level waste tanks. Such a transformation should enhance the sorption of Cs^+.

MATERIAL AND METHODS

Kaolinite samples and their reaction with simulant solutions

Two kaolinite samples, a highly crystalline KGa-1 kaolinite and a poorly crystalline KGa-2 kaolinite, were used as received from the Clay Minerals Society (CMS) Source Clay Repository (Columbia, Missouri). Four simulant tank waste solutions (STWs) were prepared. The concentration of each component was within the range reported in Hanford waste process fluids (Serne *et al.*, 1998). Sodium hydroxide, sodium aluminate and sodium nitrate were divided into portions and added incrementally to make the four solutions (Table 1). 10 g of KGa-1 or KGa-2 powder were mixed with STWs at a solid/solution ratio of 1/10 (w/v) in 250 mL Nalgene polypropylene centrifuge tubes. The tubes were capped and stored in an 80ºC oven for various time periods (1, 2, 4 and 8 weeks). The tubes were shaken for 5 min each day on a reciprocal shaker. One set of parallel reactions between KGa-1 and STWs was performed at 50ºC for 2 months. After incubation for the designed time, the solids in the tubes were separated by centrifugation and dialyzed with 12,000–14,000 Dalton MWCO dialysis tubing against deionized water until the electrical conductivity was <10 μS/cm. The untreated KGa-1 kaolinite was dialyzed for the Cs adsorption experiment. The samples were dried at 40ºC and ground gently to break apart aggregates. The samples reacted at 80ºC were coded according to kaolinite sources, simulant solutions and reaction time. For example, code 'KGa-1-STW1-4-weeks' denotes the resulting solid sample of KGa-1 reacted with STW1 for 4 weeks at 80ºC. The sodium aluminate used in this experiment was of technical grade supplied by Strem Chemicals (Newburyport, Massachusetts, USA). Other chemicals used were of analytical grade obtained from Fisher Scientific or Aldrich.

Characterization of new mineral phases

X-ray diffraction (XRD) analyses were performed on a Philips diffractometer with CuKα radiation (Philips XRG 3100, Philips Analytical Inc., Mahwah, New Jersey, USA) operated at 35 kV and 30 mA. Step-scan mode was used during the XRD analysis with a step size of 0.05º2θ and a dwell time of 5 s at each step. The initial kaolinite samples were powder mounted on aluminum frames. The altered mineral suspensions were quickly dried on glass slides under a heating lamp. Infrared (IR) spectra were recorded with a Perkin Elmer Spectrum GX FTIR System spectrometer. Samples KGa-1-STW1-8-weeks and KGa-1-STW3-8-weeks were pressed into KBr pellets (<1% w/w) and heated at 150ºC or 350ºC overnight before IR analysis. The IR instrument was purged with dry and low-CO_2 air produced by a Whatman Lab Gas Generator (Haverhill, MA). Electron micrographs were obtained with a Hitachi S-570 scanning electron microscope (SEM) operated at 25 kV. Powder samples were mounted directly on carbon conductive tabs, and sputter coated with gold before SEM analysis.

Stability of cancrinite and sodalite in acidic conditions

A series of 0.05 g samples of KGa-1-STW3-8-weeks were mixed with 20 mL solutions containing different amounts of HCl in 40 mL Nalgene centrifuge tubes. The tubes were shaken overnight at room temperature and centrifuged. The supernatant solutions were collected for pH, Na^+ and Al^{3+} analyses. The released Na^+ and Al^{3+} were quantified with a Varian 220 Flame Atomic

Table 1. Chemical compositions of simulated tank waste (STW) solutions.

Simulant solutions	NaOH (mol/kg)	$NaAlO_2$ (mol/kg)	$NaNO_3$ (mol/kg)
STW1	1.4	0.125	3.7
STW2	2.8	0.125	3.7
STW3	1.4	0.250	3.7
STW4	2.8	0.250	3.7

Absorption Spectrometer (Varian Ltd., Mulgrave, Australia) at 589 and 309 nm, respectively. The remaining solids were washed with distilled water and oven dried at 50ºC before weighing and XRD analysis.

Cesium sorption isotherms

Cesium sorption isotherms were determined using the batch equilibration method using samples of KGa-1 reacted with STW1 and STW3 at 80ºC. 120 mg of powder samples were weighed into 40 mL polycarbonate Nalgene centrifuge tubes. 25 mL of 0.01 or 0.1 M $NaNO_3$, or 0.005 or 0.05 M $Ca(NO_3)_2$ background solution were added to each tube. An appropriate amount of $CsNO_3$ stock solution, prepared in the corresponding matrix solution, was spiked into the tubes. The initial Cs^+ concentrations ranged from 0 to 0.4 mmol/L. The tubes were shaken on a reciprocal shaker at ambient condition (~22ºC) for 24 h. Initial trials showed that the amount of Cs^+ sorbed changed by <1% after 2 h of reaction. The tubes were centrifuged for 30 min at 12,060 g. An aliquot of the supernatant solution was sampled for Cs quantification with the atomic absorption spectrometer at a wavelength of 852.1 nm. To suppress ionization, both standards and samples were spiked with 2 M KCl solution to reach a final concentration of 1000 mg/L K in solution before analysis. The pH values of the supernatant solutions at the end of the sorption experiments were between 8.2 and 8.9. Sorption isotherms were constructed by plotting amounts sorbed, *i.e.* the difference between the quantity of Cs^+ added and the quantity in the final solution, *vs.* concentrations remaining in solution.

Accessibility of internal sites in cancrinite/sodalite

Sodalite and cancrinite are not considered as typical zeolite minerals because of the difficulty of molecular diffusion in their frameworks (Coombs *et al.*, 1997). To test if the internal sites in cancrinite and sodalite are accessible by inorganic ions, 0.05 g of sample KGa-1–STW3-8-weeks were mixed with 15 mL of 0.5 M KNO_3, $CsNO_3$ or 0.25 M $Ca(NO_3)_2$ solutions in a 40 mL Nalgene centrifuge tube. The tubes were kept in an oven at 80ºC for 24 h. During the day time of the 24 h storage, the tubes were shaken for 20 min every 2 h. At the end of the 24 h treatment, the tubes were centrifuged, and ~15 mL of supernatant solution from each tube were collected for Na^+ quantification with the atomic absorption spectrometer. An additional 15 mL of the corresponding KNO_3, $CsNO_3$ or $Ca(NO_3)_2$ solutions were added to the tubes. The tubes were stored, shaken and centrifuged as in the first washing. The washing process was repeated six times in total. After the sixth washing with the electrolyte solutions, the solids in the tubes were washed three times with deionized water; 15 mL of water were used in each washing. All these experiments were duplicated. The solids were mounted on glass slides for XRD analysis.

RESULTS

Mineralogical phase transformation in KGa-1 at 80ºC

The major mineral in the KGa-1 sample is kaolinite as indicated by its characteristic X-ray diffraction peaks at 0.71 nm (001) and 0.356 nm (002) (Figure 1, bottom pattern). It also contains a minor amount of anatase (TiO_2) (101 diffraction at 0.351 nm) and mica. When KGa-1 reacted with the simulant solution STW1, the most distinct changes reflected on the XRD patterns are the reduction in intensity of the kaolinite peaks and the appearance of cancrinite and sodalite peaks. The intensity of the kaolinite peaks reduced progressively with time during the 8 weeks of monitoring period, with cancrinite and sodalite peaks enhanced accordingly (Figure 1). The kaolinite peaks are negligible after 8 weeks of reaction. Cancrinite and sodalite have several common peaks located at 0.632, 0.365, 0.259 and 0.211 nm on their XRD patterns, yet cancrinite can be identified by its characteristic diffraction peaks at 0.324 nm (121), 0.274 nm (400), 0.469 nm (101) and 0.415 nm (210). Sodalite has a unique peak at 0.284 nm (310) which can be used to differentiate it from other minerals. Other characteristic peaks of sodalite at 0.446 and 0.400 nm were too weak. The relative height of the 310 diffraction peak of sodalite at 0.284 nm to the nearby 400 peak of cancrinite at 0.274 nm appeared to be constant after 1–8 weeks of reaction, indicating that both sodalite and cancrinite were thermodynamically stable under the experimental conditions.

The 101 peak of anatase at 0.351 nm remained on all of the XRD patterns during the 8 week monitoring period, indicating its stability in the caustic simulant solutions. Weak mica peaks (1.0 nm) were present in the patterns of the samples reacted for 1 and 2 weeks.

Morphology of KGa-1 and new minerals under SEM

Kaolinite particles in KGa-1 showed platy structure with hexagonal outlines even though there were discontinuities observed on certain edges (Figure 2a). Some plates stack together forming a vermicular structure. All of these morphologies are typical of kaolinite. The new cancrinite/sodalite precipitates formed after contacting the simulant solutions showed very different morphology from kaolinite. The sizes of most of the individual new grains are a few tenths of a μm or even less (Figure 2b). Some of the grains developed along two dimensions forming platy structures with diameters of ~0.5 μm (Figure 2,c,d). The new type of plate does not have the abrupt edges or flat surfaces of the kaolinite plates. Moreover, one very common feature formed by the new plates is their intergrowth by which open spheres, lepispheres, formed (Figure 2c,d). Another type of morphology, thin flakes with larger diameters, were occasionally observed in the reacted samples (*e.g.* a flake at the upper left corner of Figure 2c). The flakes were very often curled and they are believed to be mica.

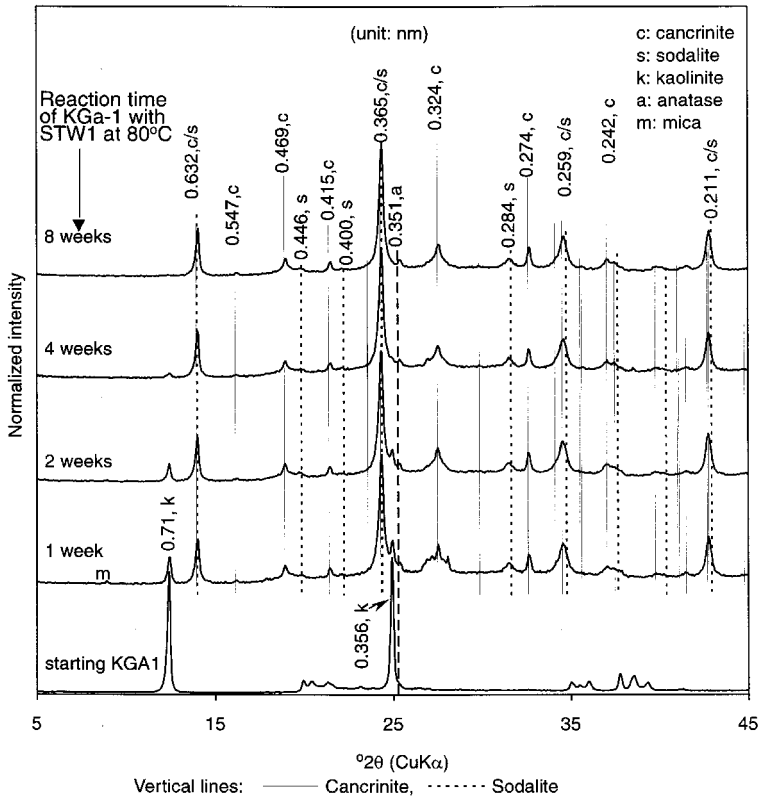

Figure 1. Normalized XRD patterns of KGa-1 kaolinite and the solid phases formed at different times following reaction with STW1 at 80°C. The vertical solid lines indicate the peak positions of cancrinite as published by Buhl *et al.* (2000). The vertical dotted lines indicate sodalite as published by Sieger *et al.* (1991). The dashed line is for anatase.

Effect of aluminate concentration on mineral transformation rate

When aluminate concentration was doubled to 0.25 M as in the simulant solution STW3, similar mineral phase transformations occurred in the kaolinite samples. The small lepispheric morphology as in Figure 2b,c was observed. The mineral transformation rate in STW3, however, appeared slower than that in STW1. More kaolinite remained in STW3 than in STW1 after the same reaction time (Figure 3). Kaolinite peaks are still visible on the XRD pattern of the sample reacted for 8 weeks with STW3. The slower transformation observed in STW3 compared to STW1 suggests that lower aluminate concentration in the simulant solution favors the dissolution of kaolinite and the formation of cancrinite and sodalite. Similar to the nearly constant cancrinite/sodalite ratio during the 8 weeks of reaction in STW1, the relative intensity of the 0.284 nm peak of sodalite to the 0.274 nm of cancrinite in STW3 did not show any obvious changes during the 8 weeks. Yet the 0.274, 0.324 and 0.469 nm peaks of cancrinite in the samples formed in STW3 are stronger than the corresponding peaks of cancrinite formed in STW1. This might be an indication of more cancrinite formed after reacting with STW3. We have also observed that the intensities of these peaks are strongly correlated to the crystallinity of cancrinite. The more crystalline cancrinite produced stronger diffraction peaks at these three positions (data not shown).

Incorporation of nitrate in cancrinite/sodalite

There were several distinct changes on the Fourier transform infrared (FTIR) spectra (Figure 4) when KGa-1 reacted with the simulated solutions. The characteristic OH-stretching vibrations of kaolinite at 3695, 3669, 3652 and 3620 cm^{-1} disappeared or weakened after reacting with the simulated solutions. Other kaolinite bands at 938 cm^{-1} (surface OH bending), and 914 cm^{-1}(inner OH bending) were also weakened. The reduction of the kaolinite bands in the solid phase formed in STW1 was more extensive than that in STW3. Weak kaolinite bands at 3695cm^{-1} (surface OH) and 3620 cm^{-1} were still visible in sample KGa-1-STW3-8-weeks. Coincident with the reduction or disappearance of kaolinite, cancrinite and sodalite bands appeared on the IR spectra, including the asymmetric Al–O stretch of cancrinite and sodalite located in the range 980–1120 cm^{-1}, and the symmetric Al–O stretch the minerals located in the range 660–770 cm^{-1}. The bands in the range 560–630 cm^{-1} arose from the parallel 4- or 6-membered double rings of cancrinite and sodalite. The bands with wavenumbers <500 cm^{-1} arose from the

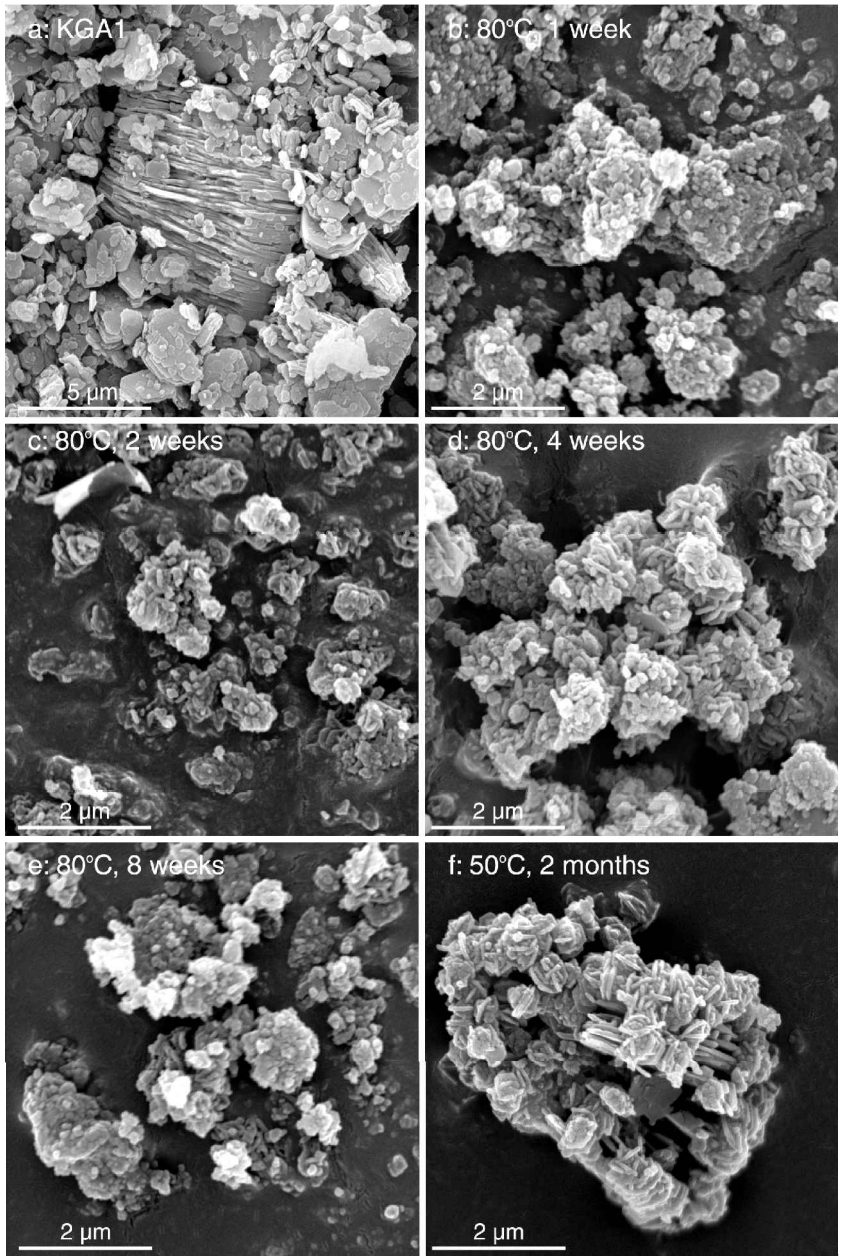

Figure 2. Mineral morphology change of KGa-1-kaolinite after reacting with STW1 for different times; (a) starting KGa-1 kaolinite with vermiform structure; (b–e) after 1, 2, 4, 8 weeks of reaction at 80ºC, respectively; (f) after 2 months of reaction at 50ºC.

bending vibrations of Si–O and Al–O of the tetrahedra of the feldspathoids. The detailed IR assignments for cancrinite and sodalite were summarized by Barnes *et al.* (1999b). Based on our pure mineral analyses (data not shown), the characteristic bands of cancrinite are located at 1113, 1032, 821, 618, 571 and 503 cm^{-1}. Sodalite can be distinguished by its bands at 733 and 707 cm^{-1}. The band positions shown in Figure 4 are slightly different from the bands observed in pure minerals, presumably due to crystallinity differences between the samples in this experiment and the synthetic pure minerals.

The FTIR spectra indicate that NO_3^- was incorporated in the precipitates, the 1422 and 1384 cm^{-1} bands being attributed to the NO_3^- group. Our IR analysis of pure minerals showed that nitrate-cancrinite has only one NO_3^- band at 1422 cm^{-1}. The 1384 cm^{-1} band arose from either sodalite or $NaNO_3$ residue. Pure $NaNO_3$ salt alone has a band at 1384 cm^{-1}. It has been observed that pure nitrate-sodalite has a distinct NO_3^- band at 1380 cm^{-1} (Buhl and Loens, 1996). It is likely that the 1384 cm^{-1} band belonged to the nitrate group in sodalite, because free $NaNO_3$ should have been removed

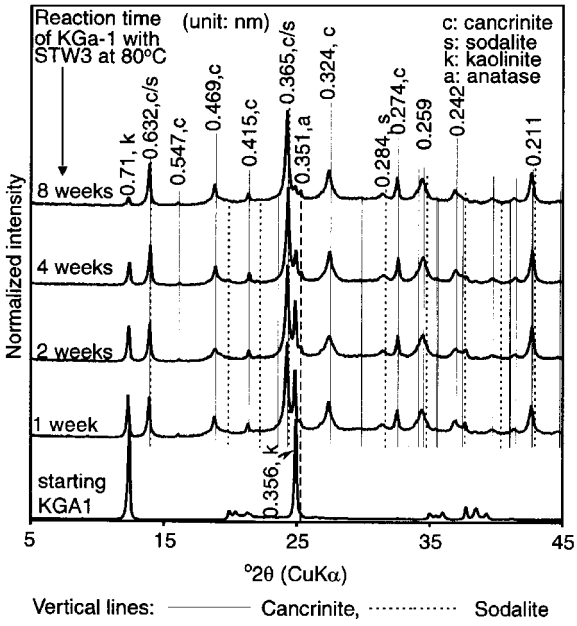

Figure 3. Normalized XRD patterns of KGa-1 kaolinite and the solid phases reacted for different times with STW3 at 80ºC.

after extensive dialysis against deionized water. When the samples were heated at 350ºC overnight, an additional band appeared at 1351 cm^{-1} in both the KGa-1-STW1-8-weeks and KGa-1-STW3-8-weeks samples, and the 1422 cm^{-1} band was weakened. It is likely that the 1351 cm^{-1} band arose from the dehydrated nitrate group. The broad bands around 3500 cm^{-1} indicate that water remained in the feldspathoids even after heating overnight at 150ºC. Heating the samples at 350ºC reduced the moisture content as reflected by the near disappearance of the broad band around 3500 cm^{-1}.

The FTIR spectra also indicate that NaOH was not incorporated to a significant extent in the cancrinite or sodalite lepispheres formed under the experimental conditions even though 1.4 M NaOH was used in the simulant solutions. There is no sharp NaOH band in the typical OH-stretching band range (3000–4000 cm^{-1}) after the samples were heated at 350ºC. In a highly crystalline sodalite formed in 16 M NaOH, we found a sharp band at 3640 cm^{-1} that was attributed to the incorporated NaOH (data not shown). The lack of NaOH bands in cancrinite/sodalite lepispheres in this experiment indicate that cancrinite and sodalite prefer nitrate groups to hydroxide groups in their cages or channels under the conditions used.

Mineral transformation at lower temperature (50ºC)

When KGa-1 reacted with the simulant solutions at 50ºC, mineral transformation appeared to be similar to the transformation at 80ºC but with a slower reaction rate. Contrary to the near complete dissolution of kaolinite at 80ºC, kaolinite was still dominant after 2 months of reaction at 50ºC (Figure 5). The area of the 001 peak of kaolinite at 0.71 nm and the common 110 peaks of cancrinite and sodalite at 0.632 nm were used to estimate roughly the quantity of undissolved kaolinite based on the percentage of each peak area. Calculation indicated 65–75% of the solids was undissolved kaolinite. The total percentage of cancrinite and sodalite increased from 28% to 34% when NaOH concentration was raised from 1.4 to 2.8 mol/kg at 0.125 mol/kg $NaAlO_2$ level, and from 22% to 25% at 0.25 mol/kg

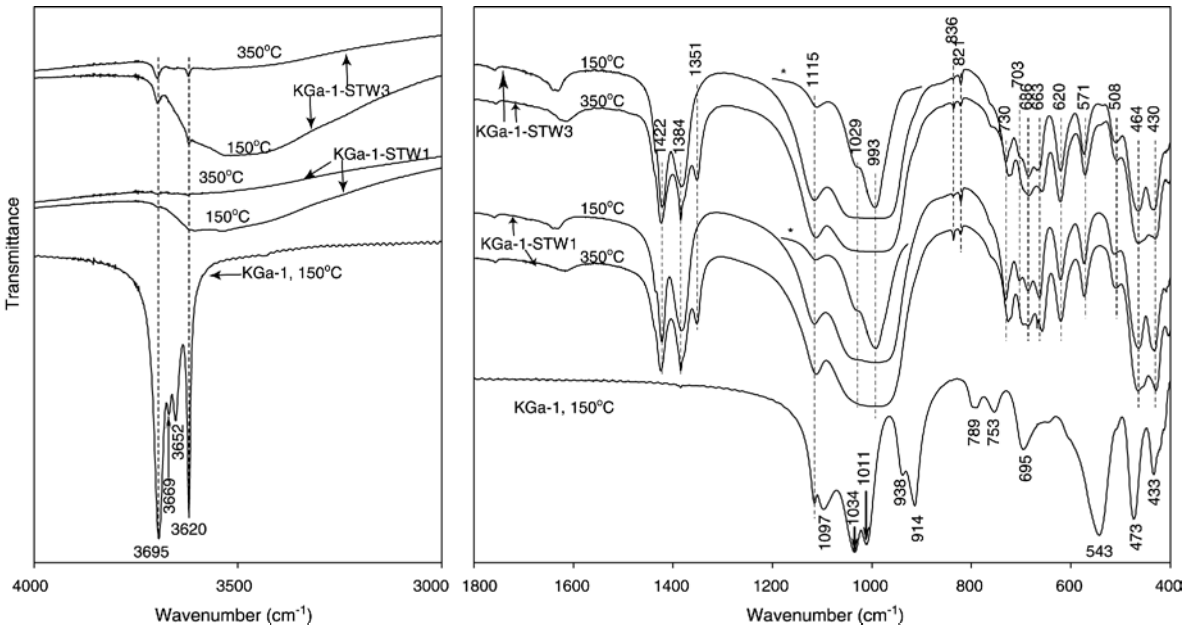

Figure 4. FTIR spectra of KGa-1 and samples KGa-1-STW1-8-weeks and KGa-1-STW3-8-weeks. The pellets were heated overnight at 150ºC and 350ºC, respectively. The asterisk-marked spectra were recorded with less concentrated unheated samples.

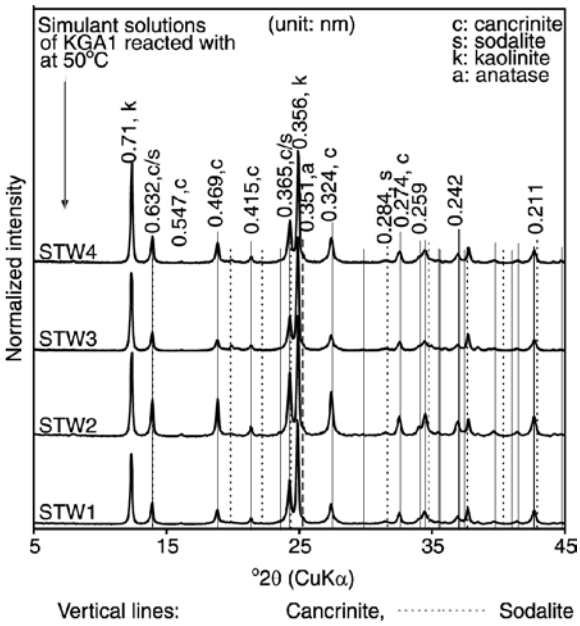

Figure 5. Normalized XRD patterns of KGa-1 reacted with four simulant solutions for 2 months at 50ºC.

$NaAlO_2$ level. These data also suggest that the cancrinite and sodalite yield was reduced when aluminate concentration was doubled at the same NaOH concentration level. Cancrinite and sodalite formed at 50ºC also showed the lepispheric structure (Figure 2f). Combining the information from Figures 1, 3 and 5, we conclude that increasing temperature, increasing NaOH concentration, and decreasing aluminate concentration facilitate the transformation of kaolinite to cancrinite and sodalite.

Effect of kaolinite crystallinity on the transformation

The mineral transformation of the poorly crystalline KGa-2 in the simulant solutions was similar to that of KGa-1. The XRD patterns of the resulting solids of KGa-2 after reacting with the simulant solutions were very similar to those in Figures 1, 3 and 5, and therefore are not shown here. No obvious morphology differences have been observed on the new mineral phases that formed from KGa-1 and KGa-2 kaolinites. The lack of a difference in the products formed from KGa-1 and KGa-2 kaolinites indicates that the reactant crystallinity is not an important factor in determining the mineral phases in alkaline solutions.

Stability of cancrinite and sodalite under acidic conditions

Cancrinite and sodalite were vulnerable to acid attack. When sample KGa-1-STW3-8-weeks was treated with HCl, the amount of Na^+ and Al^{3+} released to the solution increased with increasing HCl concentration (Figure 6a). When the pH of the suspension was reduced to 5.5 by adding 0.24 mmol of HCl, 0.25 mmol of Na^+, nearly 90% of the total Na^+ in the sample, and 0.09 mmol of Al^{3+} were released to the solution. The mass of solid was reduced by nearly 50%. The release of Na^+ and Al^{3+} and the loss of the solid mass indicate pronounced dissolution of cancrinite and sodalite at pH 5.5. The released Al^{3+} concentration did not increase in synchrony with that of Na^+. The lag of Al^{3+} release to the solution indicates that there are other forms of Al-containing solids formed in weak acidic conditions. X-ray diffraction analysis indicates that only residual kaolinite, mica and anatase remained as the crystalline phases in the solid after treating with a large amount of acid (Figure 6b). Between pH 5.5 and 3.65, the diffraction patterns were noisy and broad humps occurred around 30º2θ, indicating poorly diffracting materials in the samples. When the pH was reduced from 3.65 to 1.4, the diffraction of residual kaolinite and mica enhanced progressively, indicating the loss of the amorphous phase. The XRD patterns also suggest that more anatase dissolved in the lower pH conditions as reflected by its reduced 101 diffraction at 0.351 nm relative to the kaolinite peak.

Cs^+ adsorption

Most Cs isotherm curves showed L-type adsorption on samples KGa-1-STW1 and KGa-1-STW3 (see Figures 7 and 8). The L-type isotherms were fitted with the Langmuir equation:

$$q = q_{max}\,KC/(1 + KC) \quad (1)$$

Where q is the amount adsorbed, q_{max} is the maximum adsorption capacity of the solid phase, K is the Langmuir constant, and C is the final Cs aqueous concentration. The Langmuir parameters (Table 2) were determined by the normal nonlinear least-square method as recommended by Schulthess and Dey (1996). The newly formed cancrinite and sodalite showed much greater adsorption for Cs than kaolinite given the same Cs solution concentration. Generally, there was a 4–6 times increase in Kq_{max} for Cs adsorption on the new minerals compared to KGa-1. Adsorption did not reach plateaux in the Cs solution concentration range tested. The ideal maximum adsorption should be equal to the CEC of each sample. Based on the formula $Na_6Al_6Si_6O_{24}{\cdot}2NaX$ of cancrinite and sodalite, the theoretical CEC of the fully dehydrated minerals should be in the range of 704–879 cmol/kg depending on the incorporated anion X, assuming that all of the Na^+ cations are exchangeable. The maximum adsorption capacities estimated from the sorption isotherms (Table 2) were far below the theoretical CEC of the feldspathoids; this is probably the result of the strong competition from the cations in the background solutions. The calculated maximum adsorption q_{max} in 0.01 M $NaNO_3$ was nearly 9–12 times higher after reacting with the simulant solutions. The new solids formed in STW1 after 1, 2, 4 and 8 weeks displayed very

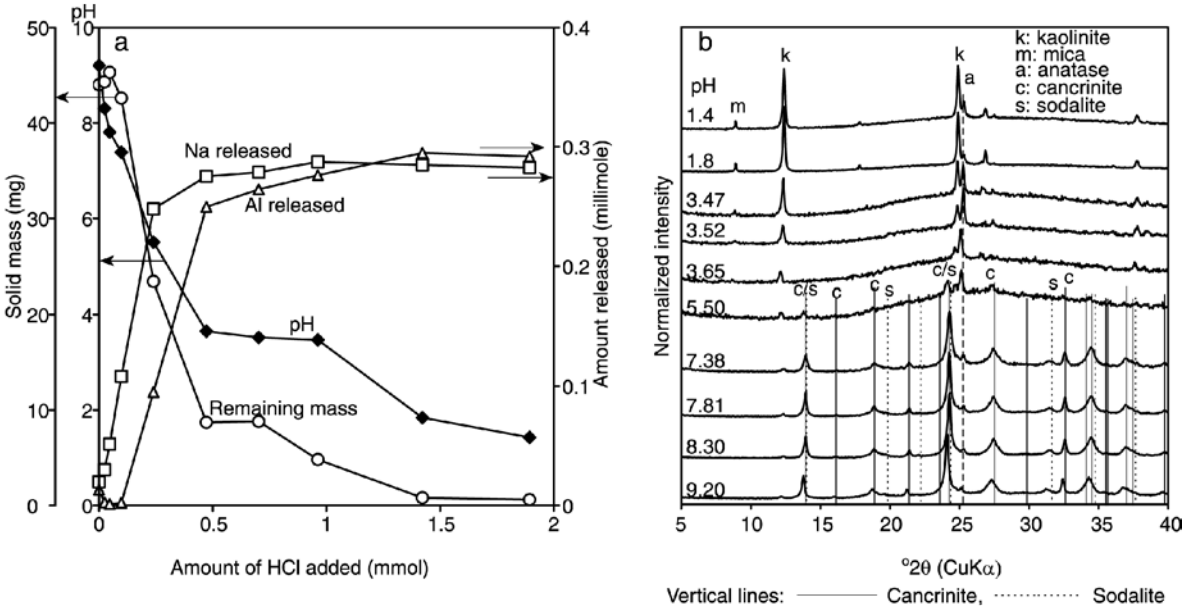

Figure 6. Acid attack on sample KGa-1-STW3-8-weeks, (a) remaining solid mass, released Na^+ and Al^{3+}, and suspension pH, and (b) XRD patterns of residue.

similar adsorption isotherms indicating that the mineral composition of the solid phase was fairly constant over the 8 week period. The precipitates formed in STW3 showed higher Cs adsorption than the corresponding precipitates formed in STW1, and the STW3 solids showed higher Cs^+ sorption with increasing reaction time (Figure 7). Since there is more kaolinite remaining after reacting with STW3, the difference observed on Cs^+ sorption is more likely to be caused by the relative amount of cancrinite to sodalite in the samples. It appears that cancrinite has a greater adsorption capacity than sodalite. The XRD peaks of cancrinite in KGa1-STW3-8-weeks were stronger than in KGA1-STW1-8-weeks as shown in Figures 1 and 3.

Cation competition in Cs^+ adsorption

Cations in the background electrolyte solutions compete for sorption sites on cancrinite and sodalite. Samples KGa1-STW1-8-weeks and KGa1-STW3-8-weeks had very similar responses to the concentration change of the background electrolytes (Figure 8). When the background electrolyte concentration was increased, Cs adsorption decreased. Yet, the cations with different valence in the background electrolytes had different

Table 2. Langmuir parameters for Cs^+ sorption calculated with nonlinear regression analysis.

Sample	Background electrolyte	q_{max} (cmol/kg)	K (L/mmol)	Initial slope (L/kg)	Correlation coefficient † n^{*2}
KGa-1-STW1, 1 week	0.01 M $NaNO_3$	6.70	2.94	197.3	0.997
KGa-1-STW1, 2 weeks	0.01 M $NaNO_3$	5.31	4.53	241.1	0.997
KGa-1-STW1, 4 weeks	0.01 M $NaNO_3$	5.61	4.05	226.7	0.999
KGa-1-STW1, 8 weeks	0.01 M $NaNO_3$	4.65	6.23	289.8	0.999
KGa-1-STW3, 1 week	0.01 M $NaNO_3$	5.39	5.38	289.9	0.999
KGa-1-STW3, 2 weeks	0.01 M $NaNO_3$	5.83	5.22	304.6	0.999
KGa-1-STW3, 4 weeks	0.01 M $NaNO_3$	5.73	5.58	319.5	0.999
KGa-1-STW3, 8 weeks	0.01 M $NaNO_3$	6.14	6.40	393.1	0.999
KGa-1-STW1, 8 weeks	0.1 M $NaNO_3$	0.93	2.85	26.5	0.932
KGa-1-STW3, 8 weeks	0.1 M $NaNO_3$	5.79	0.59	34.3	0.995
KGa-1-STW1, 8 weeks	0.005 M $Ca(NO_3)_2$	4.12	2.83	116.8	0.990
KGa-1-STW3, 8 weeks	0.005 M $Ca(NO_3)_2$	6.54	2.65	173.4	0.996
KGa-1-STW1, 8 weeks	0.05 M $Ca(NO_3)_2$	2.04	3.46	70.6	0.988
KGa-1-STW3, 8 weeks	0.05 M $Ca(NO_3)_2$	4.41	2.33	102.7	0.996
KGa-1	0.01 M $NaNO_3$	0.54	11.41	61.8	0.995
KGa-1	0.1 M $NaNO_3$	0.92	1.01	9.3	0.948

† n^{*2} assumes that a normal minimum correlates best (Schulthess and Dey, 1996)

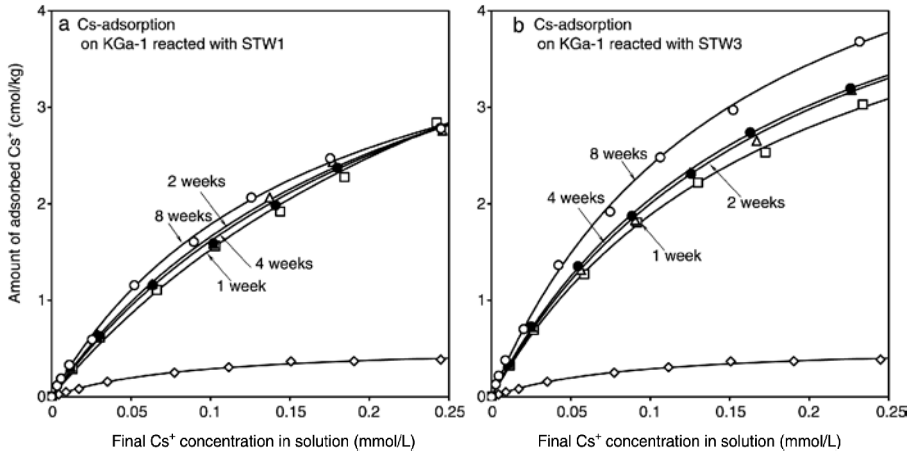

Figure 7. Cesium adsorption isotherms and fitted Langmuir curves of KGa-1 and the solid phases after reacting with (a) STW1 and (b) STW3 for 1, 2, 4 and 8 weeks at 80ºC. The background electrolyte was 0.01 M $NaNO_3$, and the pH of the final solutions was in the range 8.2–8.9.

competition capacities. At low ionic strength, *e.g.* 0.01 M $NaNO_3$ or 0.005 M $Ca(NO_3)_2$, the Cs adsorption in the 0.005 M $Ca(NO_3)_2$ was much lower than that in 0.01 M $NaNO_3$, indicating stronger competition from Ca^{2+} than from Na^+. When the concentration of the two background electrolytes was increased by 10 times, the reduction in $NaNO_3$ solution was more extensive than that in $Ca(NO_3)_2$ solution. Indeed, Cs adsorption in 0.05 M $Ca(NO_3)_2$ solution was greater than that in 0.1 M $NaNO_3$ solution even though the Ca^{2+} and Na^+ still had the same charge concentration. The lower adsorption of Cs^+ in the presence of a high concentration of Na^+ compared to the same charge concentration of Ca^{2+} runs counter to what is expected for exchange between divalent and monovalent cations on phyllosilicate clay minerals and soils (McBride, 1994). The ability of 0.1 M Na^+ to compete more effectively with Cs^+ than the 0.05 M Ca^{2+} suggests that there are some sites that are accessible to Na^+ and Cs^+ but not to Ca^{2+}.

Accessibility of internal sites in cancrinite/sodalite

When the KGa-1-STW3-8-weeks sample was washed with pure $CsNO_3$, $Ca(NO_3)_2$ or KNO_3 solutions containing 0.5 M NO_3^-, a large amount of Na^+ was released in the first 24 h washing at 80ºC (Figure 9), indicating that Na^+ in the cages of cancrinite and sodalite was exchangeable. Twice the amount of Na^+ was released by the first KNO_3 washing as by $CsNO_3$ or $Ca(NO_3)_2$, indicating that K^+ is the most efficient cation in the ion-exchange reaction. Substantial amounts of Na^+ are still released from the third through the sixth washings with $CsNO_3$. The different amounts of Na^+ released from the sequential washings indicate that Na^+ ions can readily migrate out of or into the cages and channels of cancrinite and sodalite. Other cations, such as Cs^+, K^+ and Ca^{2+} can access the internal part of the minerals, yet they had different abilities to access those sites. Potassium ions can easily diffuse into the minerals, whereas Cs^+ ions take longer to reach the same sites,

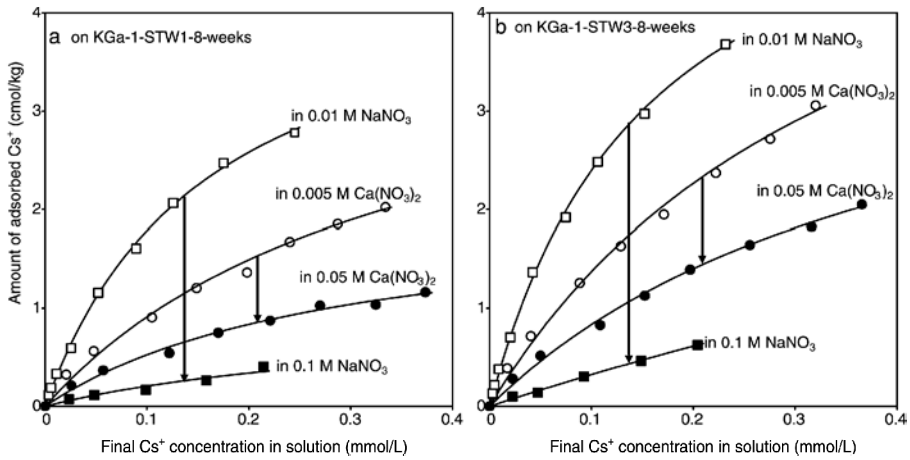

Figure 8. Cesium adsorption isotherms and fitted Langmuir curves of samples (a) KGa-1-STW1-8-weeks and (b) KGa-1-STW3-8-weeks. Background electrolytes are marked on the curves, and the pH of final solutions was in the range 8.2–8.9.

presumably due to slower diffusion of the large Cs^+ ion. Calcium cations appeared to have the most difficulty in fully replacing the Na^+ even though the ionic radii of Ca^{2+} and Na^+ are about the same (0.099 and 0.097 nm, respectively). That Cs^+ more easily accesses some sites occupied by Na^+ than does Ca^{2+} explains the lower adsorption of Cs^+ in the 0.1 M Na^+ system relative to 0.05 M Ca^{2+}. Na^+ displaces Cs^+ on internal sites of cancrinite and sodalite which Ca^{2+} cannot easily access.

The XRD patterns of the $CsNO_3$, $Ca(NO_3)_2$ and KNO_3 washed samples (Figure 10) indicate that KNO_3 washing expanded the minerals. For example, the common peak of cancrinite and sodalite at 0.632 nm was expanded to 0.656 nm, the 0.365 nm peak was expanded to 0.379 nm after KNO_3 washing. Similarly, the d_{101} of cancrinite was expanded from 0.469 nm to 0.486 nm, the d_{400} of 0.274 nm was expanded to 0.284 nm, the d_{310} of sodalite was expanded from 0.284 nm to 0.293 nm. There was little, if any, expansion or shrinkage caused by Ca exchange. The $CsNO_3$ washing did not shift the diffraction peak positions, but weakened the diffraction at 0.632, 0.365 and 0.284 nm. The XRD diffraction intensity changes imply that the structure became more disordered when Cs^+ replaced the Na^+ in cancrinite and sodalite.

DISCUSSION

Thermodynamic stability of cancrinite and sodalite

The mineral phase transformation of kaolinite after contacting the simulated tank solutions indicates that there are two major processes involved in the reactions: dissolution of kaolinite releasing Si and Al (equation 2), and precipitation of the feldspathoids cancrinite and sodalite (equation 3).

$$Al_2Si_2O_5(OH)_4 + 6OH^- + H_2O = 2Al(OH)_4^- + 2H_2SiO_4^{2-} \quad (2)$$

$$6Al(OH)_4^- + 6H_2SiO_4^{2-} + 8\ Na^+ + 2X^- = Na_6Si_6Al_6O_{24}\cdot 2NaX + 12OH^- + 12\ H_2O \quad (3)$$

where X^- represents NO_3^-, OH^- or $0.5CO_3^{2-}$.

Equation 2 suggests that the dissolution of kaolinite is favored at high NaOH concentrations, which is probably the reason why more kaolinite converted to cancrinite and sodalite in the 2.8 mol/kg NaOH solutions than in 1.4 mol/kg NaOH. Theoretically, kaolinite [$Al_2Si_2O_5(OH)_4$] dissolution releases Si and Al at a 1:1 ratio, and the formation of ideal cancrinite and sodalite also requires a 1:1 of Si to Al ratio. The presence of excess aluminate or silicate in the starting solution will drive the reaction to the left in equation 2. This is probably why doubling aluminate concentration in the simulant solutions resulted in more unaltered kaolinite. Equation 3 implies that high silicate and aluminate concentration will favor the formation of cancrinite or sodalite thermodynamically, and increased NaOH will inhibit the formation of the feldspathoids. The kaolinite to cancrinite and sodalite ratios reflected in Figures 1, 3 and 5 imply that the dissolution of kaolinite (equation 2) is the rate-determining step in the overall reaction.

The formation of cancrinite and sodalite has also been observed under similar experimental conditions. When synthetic Bayer liquors containing 3.9–5.4 M NaOH, 0.38 M Na_2CO_3, 1.6–2.33 M $Al(OH)_3$ and 0.1 M SiO_2 were heated to 250ºC in an autoclave, Linde type A zeolite, sodalite and cancrinite formed, and

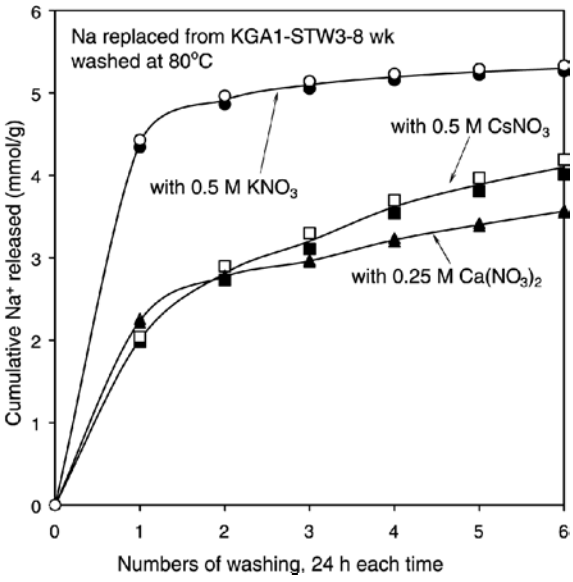

Figure 9. Released Na^+ from sample KGa-1-STW3-8-weeks. The sample was washed at 80ºC with 0.5 M $CsNO_3$, 0.25 M $Ca(NO_3)_2$ or 0.5 M KNO_3, respectively.

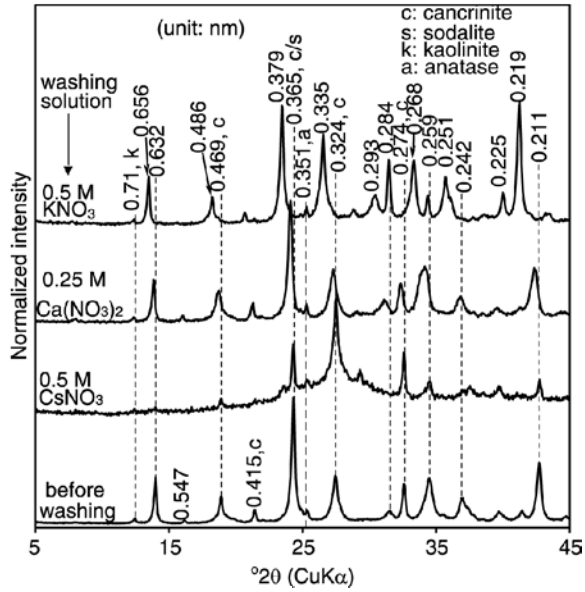

Figure 10. XRD patterns of sample KGa-1-STW3-8-weeks before and after six washings with $CsNO_3$, $Ca(NO_3)_2$ or KNO_3 solutions at 80ºC.

cancrinite appeared more stable than sodalite (Barnes *et al.*, 1999a). It was proposed that the cancrinite would be the final product, whereas amorphous material, Linde type A zeolite and sodalite would be the transition phases (Barnes *et al.*, 1999a). The presence of a high concentration (*e.g.* 0.38 M) of sodium carbonate decreased the rate of cancrinite formation (Gerson and Zheng, 1997; Zheng *et al.*, 1997, 1998). Fetchtelkord *et al.* (2001) argued that sodalite is the thermodynamically more stable phase and cancrinite formation is kinetically favored at lower NaOH concentrations (<5 M) based on a series of tests in mixed solvents of butanediol and water. Combining these observations and our experimental results, it appears that the relative stability of sodalite and cancrinite depends on the initial chemical composition of the alkaline solutions. At high $NaNO_3$ concentration, such as the Hanford tank waste solutions, both cancrinite and sodalite are stable at NaOH concentration of 1.4 M. The consistent mineral phases observed at different temperatures, different NaOH or $NaAlO_2$ concentrations, and with different kaolinite sources are probably caused by the presence of high concentration of $NaNO_3$ in the experiment.

Incorporation of ion pairs in cancrinite and sodalite

The stoichiometry of cancrinite and sodalite has been reported as $Na_6Al_6Si_6O_{24}{\cdot}2NaX$, where X is $1/2CO_3^{2-}$, $1/2SO_4^{2-}$, Cl^-, OH^- or NO_3^- (Barnes *et al.*, 1999a, 1999b). The crystal structure of cancrinite is similar to those of the zeolites, with a three-dimensional aluminosilicate host framework in which Na^+ and Ca^{2+} cations, inorganic anions and water molecules exist as the guest components (Gerson and Zheng, 1997). The hexagonal cancrinite framework contains two main structural features: the ε-cages and the large 12-membered ring channel along the crystallographic *c* axis (Figure 11a), which can accommodate cations such as Na^+, K^+ and Ca^{2+}, as well as anions such as CO_3^{2-}, OH^- and NO_3^- (Barrer, 1978; Hund, 1984). The cubic sodalite structure can be described by the space-filling array of a $[4^66^8]$-truncated octahedron known as the sodalite- or β-cage (Figure 11b). Like cancrinite, each cage contains constituents of four water molecules or cation/anion pairs (Gerson and Zheng, 1997). The fundamental reason for the ability of cancrinite and sodalite to incorporate cation/anion pairs in their cages is their stability requirement. The Al/Si substitution in the sodalite framework requires three alkali metal cations within each β-cage to balance the charge of the AlO_4^- unit on the framework. This requirement means that the three alkali cations will face each other directly in each cage and their repulsion makes the arrangement unstable. Incorporating a cation/anion ion pair inside the cage will compensate the direct cation-cation repulsion. The incorporated anion will be in the center of the β-cage, and a monovalent anion will tetrahedrally coordinate to the four alkali cations (Rabo, 1976). It has also been suggested that the ion pairs serve as a template during the formation of cancrinite and can stabilize the one-dimensional channel as a 'backbone' (Fechtelkord *et al.*, 2001).

Due to the high NO_3^- concentration and high pH of the STWs, and the possibility of sorbing CO_2 from the atmosphere, the potential anions for the cancrinite/sodalite in our experiments are NO_3^-, CO_3^{2-} and OH^-. Analysis by FTIR indicates that NO_3^- is the major anion in the incorporated form. Carbonate or OH^- did not incorporate to a detectable extent. Incorporated CO_3^{2-} had two IR bands at 1410 and 1455 cm^{-1} (Hackbarth *et al.*, 1999). The IR band of incorporated CO_3^{2-} in sodalite synthesized in an autoclave has been reported at 1470 cm^{-1}(Barnes *et al.*, 1999c). No obvious bands near 1455 or 1470 cm^{-1} on the FTIR spectra of the precipitates formed in our experiment. The two NO_3^- bands at 1422 and 1384 cm^{-1} which we observed suggested that both cancrinite and sodalite can incorporate NO_3^- in the structure. Since Na^+ was the only cation in the system, the $NaNO_3$ ion pairs are expected to occur in the cages and channels of the feldspathoids.

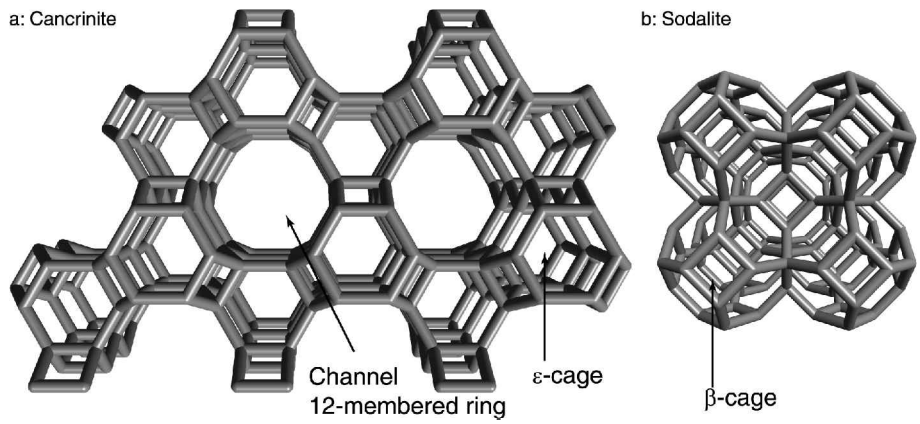

Figure 11. The 12-membered channel, ε-cage in cancrinite and the β-cage in sodalite frameworks. Images were generated with WebLab ViewerLite software (Accelrys, San Diego, California, USA) according to structural data published by the International Zeolite Association (www.iza-structure.org, accessed March 2003).

Accessibility of interior sites of cancrinite and sodalite

The accessibility of cations to the interior of cancrinite and sodalite is dependent on the feldspathoid structure, and the size and valence of the cations. The 12-membered channel in cancrinite might be easier to access than the ε-cage. Access to the cages of cancrinite and sodalite requires that the cations be smaller than the aperture afforded by the 6-member rings. The free aperture size of hydrated sodalite is estimated as 0.22 nm (Breck, 1974), meaning that the cations must be dehydrated when they pass through the 6-member ring. The size limitation may explain why Cs^+ replaces Na^+ more slowly than does K^+. Divalent Ca has nearly the same ion radius as Na^+. It appears that Ca^{2+} can migrate into the channels of the cancrinite, but not into the cages. One possible reason is the difficulty of Ca^{2+} dehydration. The dehydration energy of Ca^{2+} is 1650 kJ/mol, which is nearly three times as high as that of Na^+. Another possible reason is that it would be less favorable electrostatically to distribute two Ca^{2+} cations as opposed to four Na^+ in the cages when the negative charges on the framework are strictly localized. It has been proposed that stacking faults in cancrinite could block channels and limit exchange and sorption (Bickmore *et al.*, 2001). The intergrowth of the plates observed in the cancrinite/sodalite lepispheres (Figure 2) implied that a joint interface of the two plates may cause a discontinuity in cancrinite channels; yet, 5.3 mmol/g or 530 cmol/kg of Na^+ released by KNO_3 washing (Figure 9) indicates that the internal Na^+ of sodalite and cancrinite are readily exchangeable.

CONCLUSIONS

There were two major chemical processes involved in the reaction when kaolinite contacted the caustic simulant tank solutions: dissolution of kaolinite and formation of the feldspathoids cancrinite and sodalite. Kaolinite dissolution appeared to be the controlling step in the transformation. At the NaOH concentrations tested, cancrinite and sodalite particles have diameters of a few tenths of a μm or less. The new minerals form lepispheres by the intergrowth of their plates. Increasing NaOH concentration and temperature, and decreasing aluminate concentration in the initial solutions favor the dissolution of kaolinite and formation of cancrinite and sodalite. Both cancrinite and sodalite appeared stable under the experimental conditions, presumably because of the presence of a high concentration of $NaNO_3$ (3.7 M). Cancrinite and sodalite can incorporate $NaNO_3$ in their cages or channels. Little or no NaOH or Na_2CO_3 was incorporated under the experimental conditions. Cancrinite and sodalite are not stable under acidic conditions and pronounced dissolution occurred below pH 5.5. Cancrinite and sodalite have much higher Cs sorption capacities than kaolinite. This is because of the high degree of Al for Si substitution in the cancrinite and sodalite framework, whereas kaolinite has little or no Al for Si substitution. Cation exchange reactions indicate that Na^+ and K^+ can readily diffuse in cancrinite and sodalite, whereas Cs diffusion appeared relatively slow, presumably due to its large ionic radius. The frameworks of cancrinite and sodalite can be expanded by K^+ or become disordered by Cs^+. It is more difficult for Ca^{2+} to access the internal sites of the minerals making Ca^{2+} less competitive than Na^+ for Cs^+ sorption sites at high ionic strength.

ACKNOWLEDGMENTS

This work was supported by the Environmental Management Science Program, US Department of Energy under contract DE-FG07-99ER62882. We thank the Electron Microscopy Center and the Department of Geology at Washington State University for the use of the SEM and FTIR equipment. Dr Daniel Strawn at the University of Idaho allowed us to use his FTIR spectrometer. We also thank three reviewers and the Associate Editor for their constructive comments.

REFERENCES

Alberti, A., Colella, C., Oggiano, G., Pansini, M. and Vezzalini, G. (1994) Zeolite production from waste kaolin-containing materials. *Materials Engineering (Modena, Italy)*, **5**, 145–158.

Barnes, M.C., Addai-Mensah, J. and Gerson, A.R. (1999a) The mechanism of the sodalite-to-cancrinite phase transformation in synthetic spent Bayer liquor. *Microporous Mesoporous Materials*, **31**, 287–302.

Barnes, M.C., Addai-Mensah, J. and Gerson, A.R. (1999b) A methodology for quantifying sodalite and cancrinite phase mixtures and the kinetics of the sodalite to cancrinite phase transformation. *Microporous Mesoporous Materials*, **31**, 303–319.

Barnes, M.C., Addai-Mensah, J. and Gerson, A.R. (1999c) The solubility of sodalite and cancrinite in synthetic spent Bayer liquor. *Colloids and Surfaces A, Physicochemical and Engineering Aspects*, **157**, 106–116.

Barrer, R.M. (1978) *Zeolites and Clay Minerals as Sorbents and Molecular Sieves*. Academic Press, London, 496 pp.

Bauer, A., Velde, B. and Berger, G. (1998) Kaolinite transformation in high molar KOH solutions. *Applied Geochemistry*, **13**, 619–629.

Bickmore, B.R., Nagy, K.L., Young, J.S. and Drexler, J.W. (2001) Nitrate-cancrinite precipitation on quartz sand in simulated Hanford tank solutions. *Environmental Science and Technology*, **35**, 4481–4486.

Breck, D.W. (1974) *Zeolite Molecular Sieves: Structure, Chemistry, and Use*. John Wiley, New York, 752 pp.

Buhl, J.-c. (1991) Synthesis and characterization of the basic and non-basic members of the cancrinite-natrodavyne family. *Thermochimica Acta*, **178**, 19–31.

Buhl, J.-c. and Loens, J. (1996) Synthesis and crystal structure of nitrate enclathrated sodalite $Na_8[AlSiO_4]_6(NO_3)_2$. *Journal of Alloys and Compounds*, **235**, 41–47.

Buhl, J.-c., Stief, F., Fechtelkord, M., Gesing, T.M., Taphorn, U. and Taake, C. (2000) Synthesis, X-ray diffraction and MAS NMR characteristics of nitrate cancrinite $Na_{7.6}[AlSiO_4]_6(NO_3)_{1.6}(H_2O)_2$. *Journal of Alloys and Compounds*, **305**, 93–102.

Coombs, D.S., Alberti, A., Armbruster, T., Artioli, G., Colella, C. and Galli, E. *et al.* (1997) Recommended nomenclature

for zeolite minerals: report of the subcommittee on zeolites for the Internaltional Mineralogical Association, Commission on New Minerals and Mineral Names. *The Canadian Mineralogist*, **35**, 1571–1606.

Dudzik, Z. and Kowalak, S. (1974) Preparation of zeolites of faujasite type from kaolinite. *Przemyśl Chemiczny*, **53**, 616–618.

Fechtelkord, M., Posnatzki, B. and Buhl, J.-c. (2001) Synthesis of basic cancrinite in a butanediol-water system. *Chemistry of Materials*, **13**, 1967–1975.

Gephart, R.E. and Lundgren, R.E. (1998) *Hanford Tank Cleanup: A Guide to Understanding the Technical Issues*. 4th edition, Battelle Press, Columbus, Ohio.

Gerson, A.R. and Zheng, K. (1997) Bayer process plant scale: transformation of sodalite to cancrinite. *Journal of Crystal Growth*, **171**, 209–218.

Gualtieri, A., Norby, P., Artioli, G. and Hanson, J. (1997) Kinetic study of hydroxysodalite formation from natural kaolinites by time-resolved synchrotron powder diffraction. *Microporous Materials*, **9**, 189–201.

Hackbarth, K., Gesing, T.M., Fechtelkord, M., Stief, F. and Buhl, J.-c. (1999) Synthesis and crystal structure of carbonate cancrinite $Na_8[AlSiO_4]_6CO_3(H_2O)_{3.4}$, grown under low-temperature hydrothermal conditions. *Microporous Mesoporous Materials*, **30**, 347–358.

Hanlon, B.M. (1996) Waste tank summary report for month ending January 31, 1996 WHC-EP-0182-94. Westinghouse Hanford Company, Richland, WA.

Hund, F. (1984) Nitrate-, thiosulfate-, sulfate- and sulfide cancrinite. *Zeitschrift für Anorganische und Allgemeine Chemie*, **509**, 153–160.

McBride, M. (1994) *Environmental Chemistry of Soils*. Oxford University Press, New York, 406 pp.

Nyman, M., Krumhansl, J.L., Zhang, P., Anderson, H. and Nenoff, T.M. (2000) Chemical evolution of leaked high-level liquid wastes in Hanford soils. *Materials Research Society Symposium Proceedings*, **608**, 225–230.

Pruess, K., Yabusaki, S., Steefel, C. and Lichtner, P. (2002) Fluid flow, heat transfer, and solute transport at nuclear waste storage tanks in the Hanford vadose zone. *Vadose Zone Journal*, **1**, 68–88.

Rabo, J.A. (1976) Salt occlusion in zeolite crystals. Pp. 332–349 in: *Zeolite Chemistry and Catalysis* (J.A. Rabo, editor). ACS monograph **171**, American Chemical Society, Washington, D.C.

Schulthess, C.P. and Dey, D.K. (1996) Estimation of Langmuir constants using linear and nonlinear least squares regression analyses. *Soil Science Society of America Journal*, **60**, 433–442.

Serne, R.J., Zachara, J.M. and Burke, D.S. (1998) *Chemical information on tank supernatants, Cs adsorption from tank liquids onto Hanford sediments, and field observations of Cs migration from past tank leaks*. PNNL-11498/UC-510, Pacific Northwest National Laboratory, Richland, Washington.

Sieger, P., Wiebcke, M., Felsche, J. and Buhl, J.-c. (1991) Orientational disorder of the nitrite anion in the sodalite sodium aluminum silicate nitrite $(Na_8[AlSiO_4]_6(NO_2)_2)$. *Acta Crystallographica, Section C: Crystal Structure Communications*, **C47**, 498–501.

Zheng, K., Gerson, A.R., Addai-Mensah, J. and Smart, R.S.C. (1997) The influence of sodium carbonate on sodium aluminosilicate crystallization and solubility in sodium aluminate solutions. *Journal of Crystal Growth*, **171**, 197–208.

Zheng, K., Smart, R.S.C., Addai-Mensah, J. and Gerson, A. (1998) Solubility of sodium aluminosilicates in synthetic Bayer liquor. *Journal of Chemical and Engineering Data*, **43**, 312–317.

(*Received 26 April 2002; revised 27 August 2003; Ms. 651; A.E. James E. Amonette*)

Miscible displacement of salinity fronts: Implications for colloid mobilization

Markus Flury, James B. Harsh, and Jon B. Mathison

Department of Crop and Soil Sciences, Center for Multiphase Environmental Research, Washington State University, Pullman, Washington, USA

Received 15 July 2003; revised 28 October 2003; accepted 5 November 2003; published 31 December 2003.

[1] Colloids can be mobilized in the subsurface when low ionic strength pore water displaces high ionic strength pore water. Various experiments in saturated porous media, where such a change in ionic strength was used to mobilize colloids, have been reported in the literature. Here we experimentally test the effect of the flow direction on the hydrodynamic stability of the salinity displacement front. A series of experiments was conducted in packed columns where a solution of 1000 mM NaCl was displaced by 1 mM $NaNO_3$ in a saturated porous medium. The flow direction was vertically downward, horizontal, or vertically upward. Nitrate breakthrough curves were determined at the column outflow. Results show that for downward flow of a salinity front the displacement fronts were hydrodynamically stable, but breakthrough curves showed less dispersion than in the case of equimolar miscible displacement. For upward flow of the salinity front the displacement was unstable. Breakthrough curves were not reproducible, and a family of breakthrough curves was observed for repeated experiments. This was caused by the development of distinct fingers at the displacement front. For horizontal flow of the salinity front the displacement was unstable. Repeated breakthrough curves were reproducible, but there was more dispersion than under equimolar displacement, which we attribute to some instability in the displacement front. Front instability inferred from breakthrough curves was consistent with theoretical expectations for miscible displacement. *INDEX TERMS:* 1829 Hydrology: Groundwater hydrology; 1832 Hydrology: Groundwater transport; 1831 Hydrology: Groundwater quality; *KEYWORDS:* colloids, instability, miscible displacement, mobilization, salinity

Citation: Flury, M., J. B. Harsh, and J. B. Mathison, Miscible displacement of salinity fronts: Implications for colloid mobilization, *Water Resour. Res.*, *39*(12), XXXX, doi:10.1029/2003WR002491, 2003.

1. Introduction

[2] Colloid and colloid-facilitated contaminant transport have received increased scientific and public attention in recent years [*Honeyman*, 1999; *Kretzschmar et al.*, 1999; *Honeyman and Ranville*, 2002]. Colloids are suspected and in some cases have been shown to facilitate the movement of strongly sorbing contaminants [*Kersting et al.*, 1999]. A prerequisite for colloid-facilitated transport is the presence of suspended colloids in the pore water. Colloids can be mobilized in situ by a change of ionic strength of pore water, a scenario occurring at various waste sites when clean, low ionic strength meteoric water displaces high ionic strength contaminant plumes [*Grolimund et al.*, 1996; *Roy and Dzombak*, 1996; *Flury et al.*, 2002].

[3] Displacement of high ionic strength solutions with low ionic strength solutions is also common during groundwater recharge [*Nightingale and Bianchi*, 1977], and in the petroleum industry when low salinity water is used to displace brine [*Vaidya and Fogler*, 1990]. In both cases, colloid mobilization can result in undesired effects, such as diminishing groundwater quality or reduction of hydraulic permeability. The reduction of hydraulic permeability via mobilized and redeposited colloids is often referred to as formation damage [*Vaidya and Fogler*, 1990].

[4] When a solution of low ionic strength displaces a solution of high ionic strength, the displacement interface may become hydrodynamically unstable. This instability is caused by viscosity and density differences between the displaced and displacing fluids, and is known as viscous fingering [*Homsy*, 1987]. An unstable front displacement causes an overall non-Fickian behavior at the displacement front, resulting in the occurrence of earlier breakthrough of the salinity front and prolonged tailing as a consequence of finger formation. As colloids can be mobilized when the ionic strength of pore water decreases, colloid breakthrough curves will be affected by the viscous fingering phenomenon. The stability of the displacement front is determined by viscous and gravitational forces, and depending on flow direction, gravity can be a stabilizing or destabilizing force [*Homsy*, 1987]. It is therefore important to consider the direction of flow during colloid mobilization experiments when salinity changes are used to induce colloid release. Various salinity-induced colloid mobilization experiments have been reported in the literature, some of which used upward flow [*Roy and Dzombak*, 1996; *Grolimund and Borkovec*, 1999], some used downward flow [*Flury et al.*, 2002], and some horizontal flow [*Vaidya and Fogler*, 1990;

0043-1397/03/2003WR002491$09.00

Seaman et al., 1995, 1997]. Depending on electrolyte concentrations, flow velocity, and flow directions, the salinity displacement front may be hydrodynamically unstable and result in the formation of fingers.

[5] The objective of this study was to test experimentally the effect of the flow direction on miscible displacement of solutions of differing salinity in porous media. Breakthrough curves of an inert solute (NO_3) were determined for a sequence of displacements of high with low ionic strength solutions, for horizontal flow and vertical upward and downward flow.

2. Theoretical Considerations

[6] In absence of surface tension and dispersion, the interface between a fluid 1 displacing a fluid 2 in a porous medium becomes unstable if [*Chuoke et al.*, 1959; *Homsy*, 1987]

$$(\mu_2 - \mu_1)U/K + (\rho_1 - \rho_2)g\sin\beta > 0 \quad (1)$$

where μ is the dynamic viscosity, ρ the density, U the displacement or Darcy velocity, K the permeability of the porous medium, g the acceleration due to gravity, β the angle between the interface plane and gravity, and the indices denote fluid 1 or 2, respectively. Equation (1), which is the general instability criterion in absence of surface tension and dispersion [*Homsy*, 1987; *Rogerson and Meiburg*, 1993], shows that the instability is caused by viscous or gravitational forces.

[7] The stability criterion (1) can be modified to account for the effects of surface tension, in the case of immiscible displacement, and dispersion, in the case of miscible displacement [*Homsy*, 1987]. Both surface tension and dispersion tend to have a stabilizing effect on the flow. Stability criteria for immiscible [*Chuoke et al.*, 1959] and miscible displacement [*Tan and Homsy*, 1986; *Rogerson and Meiburg*, 1993] have been developed.

[8] In the context of colloid mobilization due to changes in ionic strength, we are mainly interested in miscible displacement. In the case of miscible displacement, the stability analysis requires knowledge of the functional dependence of viscosity and density on the concentration c of a chemical causing the viscosity and density differences, because the concentration across the interface changes with time due to dispersion. For exponential relationships between viscosity μ and concentration c, $\mu(c) = \exp(Rc)$, and between density ρ and concentration, and $\rho(c) = \exp(Sc)$, with $R = \ln(\mu_2/\mu_1)$ and $S = \ln(\rho_2/\rho_1)$, the instability criterion is [*Rogerson and Meiburg*, 1993]

$$(\mu_1 + \mu_2)(\ln\mu_2 - \ln\mu_1)U/K - (\rho_1 + \rho_2)(\ln\rho_2 - \ln\rho_1)g\sin\beta > 0, \quad (2)$$

where subscript 1 refers to the displacing fluid and subscript 2 refers to the displaced fluid. However, as we do not have information on the functional dependence of viscosity on concentration for the electrolyte solutions used in our experiments, we use the stability criterion given in (1).

[9] The three cases of interest in colloid mobilization are displacement of a high ionic strength solution (fluid 2) with a low ionic strength solution (fluid 1) for $\beta = 0$ (horizontal flow), $\beta = \pi/2$ (vertical downward flow), and $\beta = -\pi/2$ (vertical upward flow). As the viscosity of an electrolyte solution increases as electrolyte concentrations increase, the displacement front in these three cases will always be viscously unstable. The stability criterion (1) shows that for horizontal flow, the displacement interface will be unstable for any velocity U. For vertical downward flow, gravity is a stabilizing force, and the interface becomes unstable if the displacement velocity U exceeds the critical velocity [*Homsy*, 1987]

$$U_c = (\rho_1 - \rho_2)gK/(\mu_1 - \mu_2). \quad (3)$$

For upward flow, gravity is destabilizing, and as viscosity is also destabilizing, the displacement is unstable for any velocity U.

3. Materials and Methods

3.1. Column Experiments

[10] We conducted a series of miscible displacement experiments using a column of 2.5-cm diameter and 21.4-cm length (Omnifit, Cambridge, UK). The column itself was made of glass and the end pieces were Teflon with 60 μm frits at both ends to support the porous material. The column was filled with a coarse, pebbly Hanford sediment that has previously been used in a colloid mobilization experiment [*Flury et al.*, 2002]. During this previous experiment, the sediment has been flushed extensively with a high ionic strength electrolyte solution (1000 mM NaCl) followed by a low ionic strength electrolyte solution (1 mM NaCl and $NaNO_3$) to remove the colloidal fraction. The column was filled under a CO_2 atmosphere by incrementally packing sediment and saturating the sediment with a 1000 mM NaCl solution from the bottom. The bulk density of the packed column was 1.68 g/cm^3 and the pore volume of the saturated column was 38.5 cm^3. A steady state flow with a rate Q of 24 cm^3/h, corresponding to a water flux or Darcy velocity of U = 4.9 cm/h (=1.5 $\times$ 10^{-5} m/s), was established with a peristaltic pump. The column outflow was led through two flow-cells, one connected to a spectrophotometer and the other one to a pH electrode. All experiments were done at a laboratory temperature of 22 $\pm$ 1°C.

[11] We used two different electrolytes, NaCl and $NaNO_3$. It is assumed that Cl and NO_3 behave identically in terms of transport in our column system. The concentrations of the electrolyte solutions were either 1 mM or 1000 mM. The solutions were degassed by He bubbling and buffered at pH 10 with equimolar 0.1 mM $Na_2CO_3/NaHCO_3$.

[12] A series of experiments was conducted by displacing a NaCl solution with a $NaNO_3$ solution (Table 1). In between experiments, the column was flushed with at least 100 pore volumes of the initial NaCl electrolyte solution to equilibrate the column for the next displacement experiment. The experiments were repeated several times. The flow direction was changed by rotating the column end-over by angles of $\pi/2$ or π. Nitrate, measured by UV/VIS absorption at 220 nm wavelength, and pH were recorded at 2 minute intervals. Two nitrate calibration curves were constructed for the concentration range used in the experiments (0 to 1 mM and 0 to 1000 mM). The pH electrode was calibrated before each displacement experiment and the calibration was checked after the displacement experiment with a pH 10 standard. The pH reading drifted by up to 0.3 pH units during an experiment, and we corrected for this drift by linear interpolation in time.

Table 1. Summary of Experimental Conditions in Columns

Experiment	Flow Direction	Angle β	Initial Solution (NaCl)	Displacement Solution ($NaNO_3$)	Expected Interface Stability Based on Equation (1)
1	downward	π/2	1 mM	1 mM	stable
2	upward	−π/2	1 mM	1 mM	stable
3	horizontal	0	1 mM	1 mM	stable
4	downward	π/2	1000 mM	1 mM	stable
5	upward	−π/2	1000 mM	1 mM	unstable
6	horizontal	0	1000 mM	1 mM	unstable

[13] Saturated hydraulic conductivity K_s of the porous medium was measured at the end of the displacement experiments with a 1 mM NaCl solution using the constant-head method [*Hillel*, 1998]. The measured saturated conductivity was 4.5×10^{-4} m/s, and the calculated permeability $K = K_s\rho g/\mu$ for pure water at 22°C was $K = 4.4 \times 10^{-11}$ m^2.

3.2. Fluid Properties

[14] Properties of the two electrolyte solutions are shown Table 2. Densities at 22°C were measured using 250-mL volumetric Pyrex flasks. Viscosities at 25°C were calculated using equation 11.34 from *Robinson and Stokes* [1959, p. 305], which is based on viscosity increase due to electrolytes considered as rigid spheres. For this calculation, we assumed identical parameters for NaCl and $NaNO_3$. Viscosity values were then corrected for the experimental temperature of 22°C using the Andrade equation [*Reid et al.*, 1987, p. 439] using tabulated viscosity data of water at 20 and 25°C [*Robinson and Stokes*, 1959, p. 457]. For the latter calculation, we assumed that the relative viscosity changes due to temperature are the same for pure water and the electrolyte solutions.

3.3. Data Analysis

[15] The dimensionless form of the advection-dispersion equation was fitted to the experimental breakthrough curves to determine the Peclet number, Pe, using nonlinear least squares [*Press et al.*, 1992]. The Peclet number is defined here as $\mathrm{Pe} = UL/(\epsilon D)$, where U is the Darcy velocity, L is the length of the column, D is the hydrodynamic dispersion coefficient, and ϵ is the porosity. Mean and standard deviation of the Peclet numbers were calculated based on the replicated breakthrough curves. Equation (3), together with the fluid properties listed in Table 2, was used to calculate the critical velocity, U_c, above which the interface for the downward displacement experiments becomes unstable.

4. Results and Discussion

4.1. Expected Front Instability

[16] On the basis of the stability criterion and the experimental conditions used, we expect all but two experimental scenarios to have a stable front displacement (Table 1). The displacement of equimolar solutions is stable as there are no significant viscosity and density differences across the displacement interface. The downward displacement ($\beta = \pi/2$) of 1000 mM NaCl by 1 mM $NaNO_3$ is stable according to (3) because the critical velocity $U_c = 1.9 \times 10^{-4}$ m/s is larger than the experimental velocity $U = 1.4 \times 10^{-5}$ m/s. The upward displacement ($\beta = -\pi/2$) of 1000 mM NaCl by 1 mM $NaNO_3$ is unstable as both viscosity and gravity cause instability. The horizontal displacement ($\beta = 0$) of 1000 mM NaCl by 1 mM $NaNO_3$ is unstable as viscosity causes instability.

[17] For the experimental conditions used in this study, the ratio of gravitational to viscous forces in equation (1) was about 12:1, indicating that gravity has a more pronounced effect on the instability than has viscosity. We consequently expect the horizontal flow, where gravitational forces are absent, to develop less pronounced fingers than the upward flow.

4.2. Nitrate Breakthrough Curves and Front Instability

[18] The experimental results of the displacement experiments are graphically summarized in Figure 1. Repeated experiments indicated that experiments 1, 2, 3, 4, and 6 were reproducible, whereas experiment 5 resulted in a family of different breakthrough curves.

[19] Displacing 1 mM NaCl solution with 1 mM $NaNO_3$ resulted in identical breakthrough curves, independent of the flow direction (Figures 1a, 1b, and 1c). The Peclet numbers of the breakthrough curves were very similar for upward, downward, and horizontal flow. This result is expected as we are displacing Cl by NO_3 at the same concentration. The displacement front is governed by advection and dispersion.

[20] The introduction of a salinity change during displacement resulted in a pronounced change of the breakthrough curves. For the displacement in direction of gravity, the breakthrough curves became steeper as compared to the case without salinity gradient (Figure 1d). This increased steepness is clearly reflected by an increase of the Peclet number $\mathrm{Pe} = UL/(\epsilon D) = 177$. The hydrodynamic dispersion D is the sum of a dispersive and diffusive (molecular diffusion) component. The molecular diffusion coefficient should be unaffected by the salinity gradient, but the dispersive component appears to decrease for downward flow. There is less dispersion occurring at the displacement front of the two fluids under the salinity gradient than for equal molarity displacement. Gravity seems to decrease dispersion under the gravitationally stable displacement.

Table 2. Properties of Electrolyte Solutions

Fluid	Electrolyte	Concentration (22°C), mmol/L	Density (22°C),[a] kg/m^3	Dynamic Viscosity (25°C),[b] Pa s	Dynamic Viscosity (22°C),[c] Pa s
Fluid 1	$NaCl/NaNO_3$	1	997.0	0.890×10^{-3}	0.956×10^{-3}
Fluid 2	NaCl	1000	1037.0	0.977×10^{-3}	1.049×10^{-3}

[a]Densities measured with an accuracy of about 0.3% as determined from pure water measurement.
[b]Calculated from *Robinson and Stokes* [1959, p. 305].
[c]Calculated from viscosity at 25°C using the Andrade equation [*Reid et al.*, 1987, p. 439].

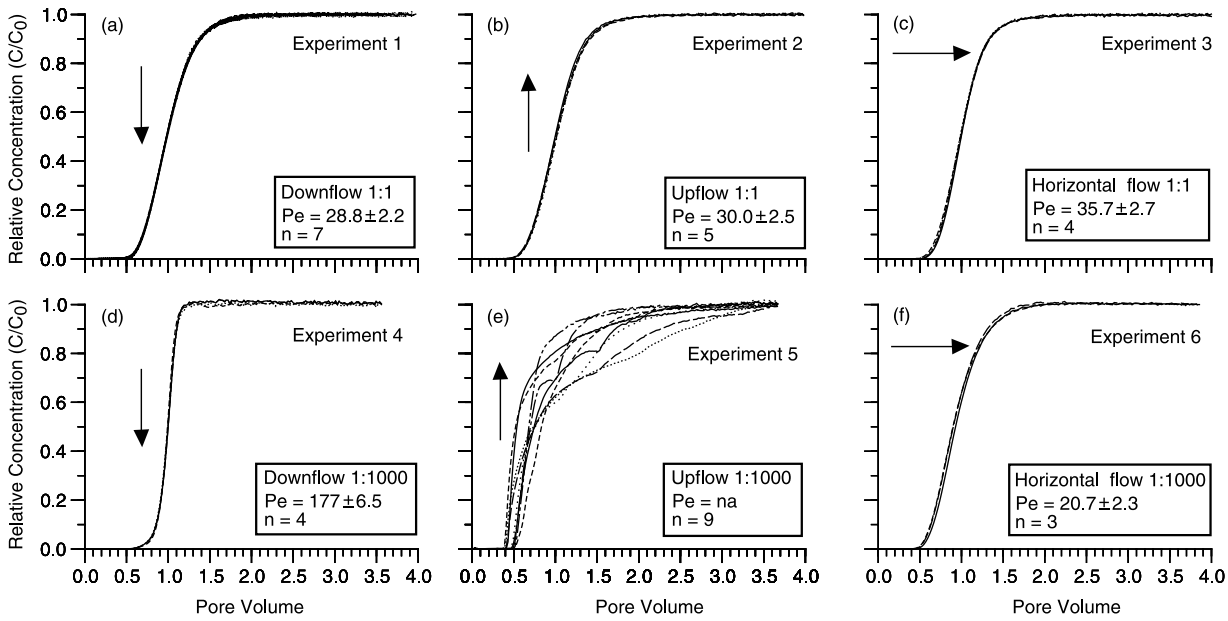

Figure 1. Breakthrough curves of nitrate during displacement of (a, b, and c) 1 mM NaCl by 1 mM $NaNO_3$ and (d, e, and f) 1000 mM NaCl by 1 mM $NaNO_3$. Arrows indicate the flow direction. Peclet numbers Pe represent mean and standard deviation of *n* duplicated experiments. No Peclet numbers were determined for experiment 5.

[21] When the flow is upward against gravity, the salinity change caused the displacement front to become unstable, as indicated by the unreproducibility of the breakthrough curves (Figure 1e). None of the experiments in this case could be reproduced. The breakthrough curves do not show the sigmoidal shape typical for advective-dispersive behavior, and often show early initial NO_3 breakthrough, followed by a slow approach to the inflow concentration. Inflow concentrations were reached after about four pore volumes of through flow. Some breakthrough curves are smooth, monotonous functions, others have one or several humps. We attribute the humps to the breakthrough of distinct viscous fingers. The main features of the breakthrough curves, early breakthrough, humps, and slow approach of inflow concentration caused by flow instability, have been reported previously for miscible displacement experiments in porous media using fluids of different viscosity [*Brigham et al.*, 1961].

[22] Horizontal displacement of the high ionic strength solution by the low ionic strength solution also resulted in an unstable front, but the effect was not very pronounced in our experiments (Figure 1f). The breakthrough curves were smooth and could be described by advective-dispersive behavior; however, the Peclet numbers indicate that breakthrough occurred earlier and with more spreading than in the case of equal molarity displacements. We interpret this as an indication of displacement instability, and the earlier breakthrough was likely caused by viscous fingers preceding the main displacement front. The finger development, as expected based on the instability criterion (1), however, is much less pronounced than for the upward flow case. This is expected from the dominance of gravity in the instability criterion for our specific experimental conditions.

[23] The breakthrough curves for stable displacements could be well fitted by the ADE. As an example, we show the results of the stable displacement fronts for downward movement (Figure 2).

4.3. The pH Breakthrough Curves

[24] The pH remained stable during displacement of equimolar electrolyte solutions, no matter in which direction the flow (Figures 3a, 3b, and 3c). This behavior is expected

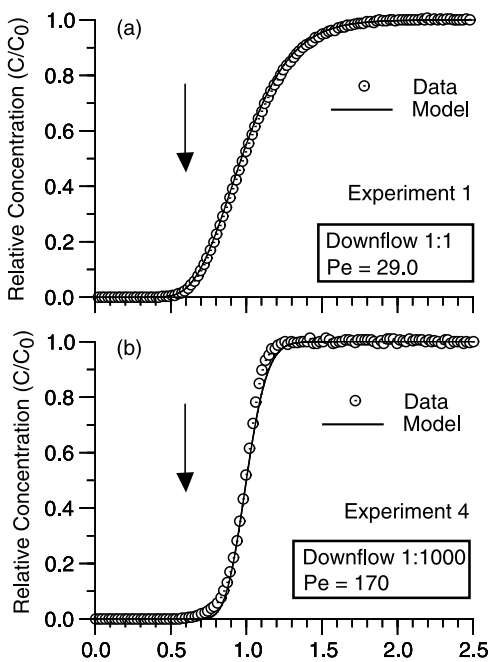

Figure 2. Modeling of nitrate breakthrough during displacement of (a) 1 mM NaCl by 1 mM $NaNO_3$ and (b) 1000 mM NaCl by 1 mM $NaNO_3$. Solid lines are advection-dispersion equation fitted to the data. Arrows indicate the flow direction.

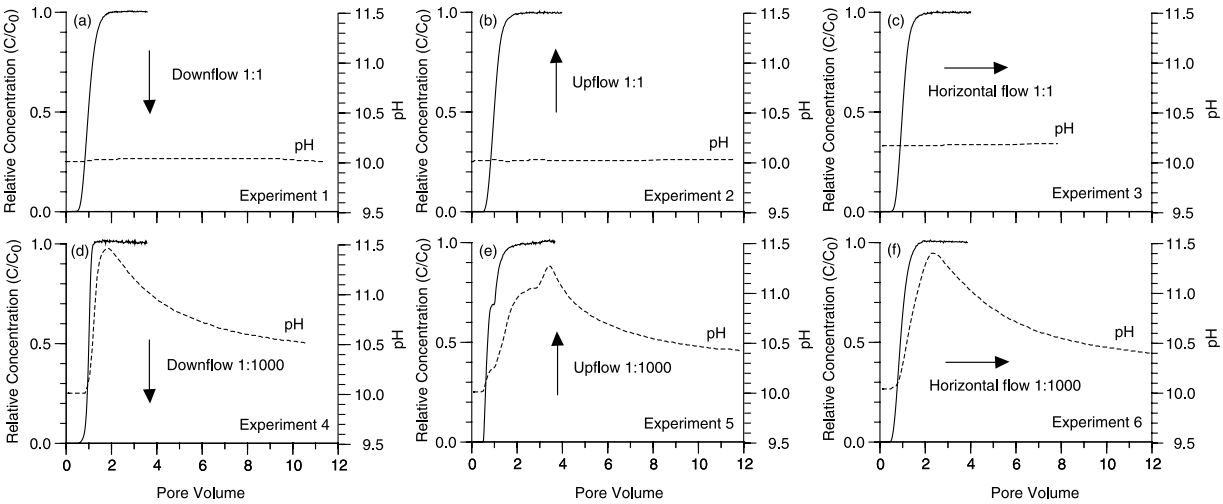

Figure 3. Nitrate breakthrough curves and pH in effluent during displacement of (a, b, and c) 1 mM NaCl by 1 mM $NaNO_3$ and (d, e, and f) 1000 mM NaCl by 1 mM $NaNO_3$. Arrows indicate the flow direction.

as during equimolar displacement no protons are expected to be involved in cation exchange reactions at the solid surfaces. A salinity change induced a change in pH (Figures 3d, 3e, and 3f). The displacement of a high with a low concentration electrolyte solution causes cation exchange according to the mass action

$$NaX + H \rightleftharpoons HX + Na \quad (4)$$

where Na is sodium, H is a proton, and X the sorbent. This ion exchange consumes H, and causes pH fronts to develop [*Schweich et al.*, 1993b; *Scheidegger et al.*, 1994].

[25] In the hydrodynamically stable case (Figure 3d), we can distinguish two pH fronts, a nonretarded front (pH increase) at about one pore volume and a retarded front (pH decrease). The nonretarded pH front is sharp and coincides with the salinity front. The second, retarded front is diffuse and has a pronounced tailing. The shape of the pH fronts is determined by the acidity isotherms [*Scheidegger et al.*, 1994]. In the case of the hydrodynamically unstable salinity front displacement, the nonretarded pH front shows several humps (Figure 4). These humps appear to correspond with humps in the salinity breakthrough. We therefore associate these humps in the pH front to the breakthrough of distinct viscous fingers.

5. Implications

[26] Colloid mobilization in the subsurface is often triggered by a change of the salinity of the pore water. When a higher ionic strength pore water solution is displaced by a lower ionic strength solution, colloids may be mobilized and transported with the water flow. During such a displacement, a salinity front develops, which depending on the flow direction and flow velocity, may be hydrodynamically stable or unstable. In the unstable case, the salinity front breaks up into distinct viscous fingers.

[27] Under conditions of horizontal flow, the salinity displacement front is unstable for any Darcy velocity U, but as the viscosity differences between displacing and displaced fluids are usually small, the finger development is not very pronounced. Under upward flow, both gravity and viscosity are destabilizing forces, and distinct fingers will develop. Under vertical downward flow, viscosity is a destabilizing force and gravity is a stabilizing force, and the development of instability for two given fluids depends on the Darcy velocity. For typical Darcy velocities U in the subsurface ($U < 1 \times 10^{-4}$ m/s [*Domenico and Schwartz*, 1998]) and ionic strength changes expected at waste sites, the displacement during vertical downward flow is likely stable.

[28] It is therefore expected that in most field situations (horizontal or downward flow), where a higher ionic strength solution is displaced by a lower ionic strength solution, colloid mobilization occurs in association with a hydrodynamically stable front displacement. The salinity displacement front for downward flow tends to be less dispersive than during equimolar displacement, causing a sharpening of the breakthrough curves of mobilized colloid. Upward flow, however, would result in an earlier breakthrough and a pronounced tailing of colloid breakthrough curves, caused by the viscous fingering.

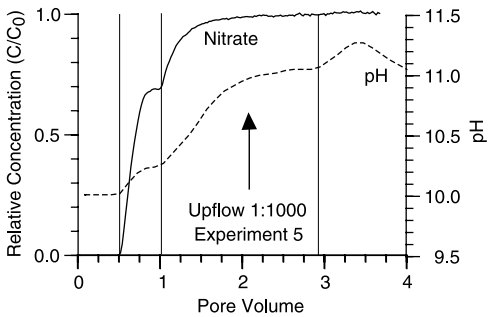

Figure 4. Nitrate breakthrough curves and pH in effluent during displacement of 1000 mM NaCl by 1 mM $NaNO_3$. Arrow indicates the flow direction. Vertical lines indicate distinct humps in outflow pH.

[29] **Acknowledgments.** This work was supported by the Environmental Management Science Program, U.S. Department of Energy under contract DE-FG07-99ER62882.

References

Brigham W. E., P. W. Reed, and J. N. Dew, Experiments on mixing during miscible displacement in porous media, *Soc. Petrol. Eng. J.*, *1*, 1–8, 1961.

Chuoke, R. L., P. van Meurs, and C. van der Poel, The instability of slow, immiscible, viscous liquid-liquid displacements in permeable media, *Trans. Am. Inst. Min. Metall. Pet. Eng.*, *216*, 188–194, 1959.

Domenico, P. A., and F. W. Schwartz, *Physical and Chemical Hydrogeology*, 2nd ed., John Wiley, Hoboken, N. J., 1998.

Flury, M., J. B. Mathison, and J. B. Harsh, In situ mobilization of colloids and transport of cesium in Hanford sediments, *Environ. Sci. Technol.*, *36*, 5335–5341, 2002.

Grolimund, D., and M. Borkovec, Long-term release kinetics of colloidal particles from natural porous media, *Environ. Sci. Technol.*, *33*, 4054–4060, 1999.

Grolimund, D., M. Borkovec, K. Barmettler, and H. Sticher, Colloid-facilitated transport of strongly sorbing contaminants in natural porous media: A laboratory column study, *Environ. Sci. Technol.*, *30*, 3118–3123, 1996.

Hillel, D., *Environmental Soil Physics*, Academic, San Diego, Calif., 1998.

Homsy, G. M., Viscous fingering in porous media, *Annu. Rev. Fluid Mech.*, *19*, 271–311, 1987.

Honeyman, B. D., Colloidal culprits in contamination, *Nature*, *397*, 23–24, 1999.

Honeyman, B.D., and J.F. Ranville, Colloid properties and their effects on radionuclide transport through soils and groundwater, in *Geochemistry of Soil Radionuclides*, edited by P.-C. Zhang and P. V. Brady, *Spec. Publ. Soil Sci. Soc. Am.*, *59*, 131–163, 2002.

Kersting, A. B., D. W. Efurd, D. L. Finnegan, D. J. Rokop, D. K. Smith, and J. L. Thompson, Migration of plutonium in ground water at the Nevada Test Site, *Nature*, *397*, 56–59, 1999.

Kretzschmar, R., M. Borkovec, D. Grolimund, and M. Elimelech, Mobile subsurface colloids and their role in contaminant transport, *Adv. Agron.*, *66*, 121–193, 1999.

Nightingale, H. I., and W. C. Bianchi, Ground-water turbidity resulting from artificial recharge, *Ground Water*, *15*, 146–152, 1977.

Press, W. H., S. A. Teukolsky, W. T. Vetterling, and B. P. Flannery, *Numerical Recipes: The Art of Scientific Computing*, 2nd ed., Cambridge Univ. Press, New York, 1992.

Reid, R. C., J. M. Prausnitz, and B. E. Poling, *The Properties of Liquids and Gases*, 4th ed., McGraw-Hill, New York, 1987.

Robinson, R. A., and R. H. Stokes, *Electrolyte Solutions*, 2nd ed., Academic, San Diego, Calif., 1959.

Rogerson, A., and E. Meiburg, Shear stabilization of miscible displacement processes in porous media, *Phys. Fluids A*, *5*, 1344–1355, 1993.

Roy, S. B., and D. A. Dzombak, Colloid release and transport processes in natural and model porous media, *Colloids Surf. Physicochem. Eng. Aspects*, *107*, 245–262, 1996.

Scheidegger, A., C. S. Bürgisser, M. Borkovec, H. Sticher, H. Meeussen, and W. van Riemsdijk, Convective transport of acids and bases in porous media, *Water Resour. Res.*, *30*, 2937–2944, 1994.

Schweich, D., M. Sardin, and M. Jauzein, Properties of concentration waves in presence of nonlinear sorption, precipitation/dissolution, and homogeneous reactions: 2. Illustrative examples, *Water Resour. Res.*, *29*, 735–741, 1993.

Seaman, J. C., P. M. Bertsch, and W. P. Miller, Chemical controls on colloid generation and transport in a sandy aquifer, *Environ. Sci. Technol.*, *29*, 1808–1815, 1995.

Seaman, J. C., P. M. Bertsch, and R. N. Strom, Characterization of colloids mobilized from southeastern coastal plain sediments, *Environ. Sci. Technol.*, *31*, 2782–2790, 1997.

Tan, C. T., and G. M. Homsy, Stability of miscible displacements in porous media: Rectilinear flow, *Phys. Fluids*, *29*, 3549–3556, 1986.

Vaidya, R. N., and H. S. Fogler, Formation damage due to colloidally induced fines migration, *Colloids Surf. Physicochem. Eng. Aspects*, *50*, 215–229, 1990.

M. Flury, J. B. Harsh, and J. B. Mathison, Department of Crop and Soil Sciences, Center for Multiphase Environmental Research, Washington State University, Pullman, WA 99164, USA. (flury@mail.wsu.edu)

Environ. Sci. Technol. **2003**, *37,* 4905−4911

Colloid-Facilitated Cs Transport through Water-Saturated Hanford Sediment and Ottawa Sand

JIE ZHUANG,[†] MARKUS FLURY,[‡] AND YAN JIN*,[†]

Department of Plant and Soil Sciences, University of Delaware, Newark, Delaware 19717, and Department of Crop and Soil Sciences, Center for Multiphase Environmental Research, Washington State University, Pullman, Washington 99164

In this study, a series of saturated column experiments were conducted to investigate effects of colloids on Cs transport in two types of porous media (Hanford sediment characteristic of 2:1 clay minerals and silica Ottawa sand). The colloids used were obtained by reacting Hanford sediment with simulated tank waste solutions. Because of the highly nonlinear nature of Cs sorption found in batch experiments, we used two different concentrations of Cs (7.5×10^{-5} M and 1.4×10^{-8} M) for the transport experiments. The presence of colloids facilitated the transport of Cs through both Hanford sediment and Ottawa sand via association of Cs with mobile colloidal particles. Due to the nonlinearity of the Cs sorption, the colloid-facilitated Cs transport was more pronounced at the low Cs concentration (1.4×10^{-8} M) than at the high concentration (7.5×10^{-5} M) when expressed relative to the inflow Cs concentration. In the absence of colloids, no Cs moved through the 10-cm long columns during the experiment within about 20 pore volumes, except for the high Cs concentration in the Ottawa sand where a complete Cs breakthrough was obtained. Also, it was found that colloid-associated Cs could be partially stripped off from colloids during the transport. The stripping effect was controlled by both Cs concentration and sorption capacity of the transport matrix.

Introduction

In the waste tanks at the former plutonium production site at Hanford in eastern Washington State, U.S.A., a major portion of the radioactivity is contributed by the radionuclides ^{137}Cs and ^{90}Sr. It is reported that 67 of the 177 single-shell tanks have leaked, discharging ~3800 m^3 (more than 1 million gallons) of mixed wastes and $\sim 4 \times 10^{16}$ Bq (1 million Ci) of ^{137}Cs to the vadose zone (*1*). The directly measured activity from the contaminated sediments under Hanford tanks was as high as 10^5 Bq/g, and indirect field estimates were as high as 10^8 Bq/g (*2*).

The fate and transport of Cs in natural systems depend, to a large degree, on its partitioning behavior between aqueous and immobile solid phases and the factors affecting the partitioning (*3, 4*). Many studies conducted during the past decades indicate that Cs is preferentially sorbed by phyllosilicate minerals, e.g., expansible layer silicates such as smectite and vermiculite, and nonexpansible micas, such as biotite and muscovite (*5*−*12*). In particular, Cs sorbs in a highly selective fashion to wedge or frayed edge sites (FES) that develop along the weathered periphery of micas (e.g., biotite and muscovite) and their immediate weathering products (hydrous-mica and illite) (*13*). Therefore, the materials containing these 2:1 layer-silicates have generally been chosen as candidates for radioactive waste depositories (*14*−*16*). In contrast, Cs sorption onto quartz, apatite, calcite, or iron oxides is low (K_d < 5 L/kg), due to low ion exchange capacity of the minerals (*17, 18*).

At the Hanford site, the sediments are coarse-textured, and micaeous 2:1 phyllosilicates play a significant role in sorbing radiocesium and limiting its vertical migration to groundwater (*2, 12, 19*). The radiocesium at the SX Tank Farm has reached depths of 20−25 m below surface, with maximum depths possibly reaching 38 m (*20, 21*). Modeling results using cesium sorption parameters measured in Hanford sediments indicate that the current depth distribution of cesium at Hanford can be explained by chromatographic solute transport in high electrolyte solutions and that cesium movement is slowed considerably at present due to strong sorption to micaeous minerals and decreased ionic strength of the pore water (*22*).

While solution phase cesium movement at present and in the future appears unlikely at Hanford (*22*), cesium can potentially move facilitated by colloidal particles. At the Hanford tank farms, alkaline tank waste that has leaked into the subsurface can dissolve native minerals to form colloidal-sized new mineral phases (feldspathoids and zeolites) (*23, 24*). These new mineral phases can sorb and coprecipitate with Cs (*23*). If these minerals are mobile in the subsurface, there exists a risk for enhanced movement of Cs.

Colloid-facilitated transport of radionuclides has been reported from several field sites (*25*−*27*). In laboratory column studies, Cs transport in the presence and absence of mobile colloidal particles was investigated (*28*−*30*). Colloidal kaolinite was found to increase Cs migration velocity in a packed sand column by a factor of 2 when kaolinite concentration in the influent was increased from 0 to 200 mg/L (*30*). Noell et al. (*31*) studied the role of an amorphous silica colloid on facilitating Cs transport through glass bead columns. They found that when Cs was injected into columns with a constant flux of colloids, the retardation of Cs was reduced by 14−32% and 38−51% when the sizes of glass beads were 150−210 μm and 355−420 μm, respectively. Faure et al. (*32*) conducted packed-column experiments with sand mixed with 5% bentonite clay to study colloid and radionuclide transport induced by a salinity gradient. The results indicate that when the salt concentration decreased below a critical threshold of 0.16 M (NaCl), colloidal particles started to be mobilized and colloid-facilitated transport of ^{137}Cs was observed.

Chemical sorption experiments of Cs and other radionuclides have been performed using Hanford site materials (*2, 12, 22, 33*). However, little is known about Cs transport in Hanford sediments characteristic of 2:1 clay minerals. Most of the previous studies have focused on Cs transport in silica-type sand and facilitated transport by colloids such as silica and kaolinite that have a lower sorption capacity for Cs than the 2:1 clays. Therefore, it is important to examine the role of micaeous colloids and their alteration products, which can form in situ under a Hanford Tank leak situation, in facilitating Cs transport through Hanford sediments.

The major objectives of this study were to investigate (i) Cs transport in two types of materials (Hanford sediment

* Corresponding author phone: (302)831-6962; fax: (302)831-0605; e-mail: yjin@udel.edu.
[†] University of Delaware.
[‡] Washington State University.

10.1021/es0264504 CCC: $25.00
Published on Web 10/07/2003

TABLE 1. Selected Properties of the Hanford Sediment, Ottawa Sand, and Colloids

materials	CEC[a] ($cmol_c/kg$)	SA[b] (m^2/g)	Fe_0[c] (mg/kg)	Al_0[c] (mg/kg)	OM[d] (g/kg)	D_g[e] (mm)	mineralogy
Hanford sediment	6.6	12.22	6461	3220	1.0	0.52	mica, smectite, illite, vermiculite, kaolinite, quartz
Ottawa sand	0.6	0.07	28.7	18.4	0.4	0.44	quartz
Hanford colloid	6.7	39.43	56709	51722	na[f]	6.27×10^{-4}	mica, illite, smectite, vermiculite, quartz, cancrinite, sodalite

[a] Cation exchange capacity. [b] Specific surface area (BET N_2 absorption measurements with ASAP2010, Micromeritics, Inc.). [c] 6 M HNO_3 dissolved Fe and Al, respectively. [d] Organic matter content. [e] Geometric diameter of sand grains or Z-averaged hydrodynamic diameter of colloidal particles, measured in 0.002 M $NaNO_3$ (pH 10 buffered with 2.4×10^{-5} M Na_2CO_3 and $NaHCO_3$) with a Zetasizer 3000HSA (Malvern Instruments, Ltd., England). [f] Not measured.

and Ottawa sand) and the facilitated migration by colloids formed by reacting Hanford sediment with simulated tank waste solutions and (ii) how Cs loading affects the facilitation efficiency of the colloids with respect to Cs transport. The conditions used in our study promoted colloid transport in porous media, i.e., we used low ionic strength pore water, saturated flow, and a colloid-free (prewashed) porous medium. While these conditions are not exactly transferable to the situation below Hanford waste tanks, they provide a worst-case scenario for colloid and colloid-facilitated cesium transport.

Materials and Methods

Porous Materials and Colloids. Two types of porous materials, Hanford sediment and Ottawa sand, were used in this study. Uncontaminated Hanford sediments, representative of the material underlying the Hanford waste tanks, were obtained from the Submarine Pit (218-E-12B) at the Hanford site. Detailed characterization data are given elsewhere (*34*). The sediment was dry-sieved through a 2-mm square grid and the material >2 mm was discarded. Ottawa sand, a typical silica sand, was obtained by mixing four sizes of the sands (C-190, C-109, 40/60, and 30/40), which were purchased from Unimin Corporation (Le Sueur, Minnesota, U.S.A.). Before the batch sorption and column experiments, both sediment and sand were washed in tap water until the rinse water was free of suspended impurities, followed by rinsing with deionized water and oven-drying at 105 °C. The rinsing of the Hanford sediment removed the fine fraction of sediments but was necessary to obtain a stable porous medium that does not contribute to in situ colloid mobilization during the transport experiments. Some properties of the materials are provided in Table 1.

The colloids used in this study (referred to as Hanford colloids) were synthesized under conditions similar to those of a leak of the waste tanks at the Hanford site, following the procedure described here. One liter of a simulated tank solution (2.8 M NaOH, 0.125 M $NaAlO_4$, and 3.7 M $NaNO_3$) was added to 1 kg of the <2 mm Hanford sediment. The mixture was kept at 50 °C and shaken periodically for 40 d. Then, the supernatant was decanted, and the sediment was washed with 1 M $NaNO_3$ by centrifugation. This process was repeated several times, and the suspension was dialyzed against deionized water until the electrical conductivity was smaller than 0.01 dS/m. Colloidal particles (<2 μm) were separated from the sediment by gravity settling, air-dried, and stored in a polyethylene bottle. X-ray diffraction (XRD) analyses, carried out using a Philips diffractometer with Cu−K radiation, showed that the colloids had similar mineralogical composition as the parent sediment material and contained newly formed mineral phases, cancrinite and sodalite (*23*). Colloidal suspensions were prepared by redispersing the air-dried colloids in artificial pore water and sonication for 20 min.

Artificial Pore Water. We used an artificial pore water consisting of 0.002 M $NaNO_3$, with its pH adjusted to 10 using 2.1×10^{-4} M $NaHCO_3$ and Na_2CO_3 at a CO_3^{2-} to HCO_3^- ratio of 0.562. This solution was chosen to maximize colloid stability and transport in the porous media. In addition, a chloride tracer (8.5×10^{-4} M NaCl) was used in the transport experiment. The high pH ensured that no carbonates were dissolved from the sediment during the experiments. The pore water composition at the Hanford site has higher ionic strength (*34*); consequently our experiments do not mimic Hanford conditions but rather are a worst-case scenario for colloid mobility.

Sorption of Cs on Colloids, Hanford Sediment, and Ottawa Sand. Sorption experiments were performed in duplicates at room temperature (22 ± 1 °C) in 50-mL Teflon centrifuge tubes using the artificial pore water as a background solution. The equilibrium suspension in the tubes consisted of 20-mL background solution, the synthesized colloids (0.1 g/L) or Na-saturated Hanford sediment, or Ottawa sand (40 g/L) and Cs with concentrations ranging from 2×10^{-10} to 2×10^{-4} M. In each tube a predetermined amount of ^{137}Cs was added for radioactive labeling and complemented with ^{133}Cs to achieve the desired Cs concentrations. The higher concentration generally matches the higher Cs concentrations reported in Hanford SX tank supernatant solutions (*19*). The samples were equilibrated by rotating the tubes end-over-end for 24 h. We chose the 24-h equilibration time based on preliminary kinetic studies, which showed that more than 95% of Cs sorption occurred in less than 4 h. After equilibration, the samples were centrifuged at 18 000 g for 15 min, and the activity of ^{137}Cs in the equilibrium aqueous phase was determined using a liquid scintillation analyzer Tri-Carb 2900TR (Packard Instrument Company, CT). ScintiSafe Econo 1 cocktail liquid (Fisher Scientific, NJ) was used as the scintillation solution for ^{137}Cs concentration measurements. Total cesium sorption was calculated assuming that stable ^{133}Cs and radioactive ^{137}Cs behaved identically in terms of sorption. UV/vis spectroscopic measurements of the supernatant after centrifugation showed no significant above-background turbidity, indicating that no colloids remained in suspension after centrifugation. The amount of Cs sorbed onto the solids was determined by the difference between the initial Cs concentration added and the equilibrium Cs concentration in the aqueous phase after centrifugation. Sorbent-free controls with initial ^{137}Cs concentration of 1×10^{-8} M showed that the loss of Cs to Teflon tubes was negligible. Values reported are means of the duplicates.

Column Transport Experiments. Nine breakthrough experiments of Cs in the presence and absence of Hanford colloids were performed under saturated flow conditions (Table 2) at room temperature (22 ± 1 °C). The column system used in the study was the same as that in Jin et al. (*35*). The column was made of acrylate, with an inside diameter of 5.1

TABLE 2. Conditions and Parameters of the Column Experiments

expt no.	matrix	colloid concn (mg/L)	Cs concn (mol/L)	ρ_b[a] (Mg/m^3)	ϕ[b]	V[c] (cm/h)	D[d] (cm^2/h)	Pe[e]
1	Hanford sediment	0	7.5×10^{-5}	1.45	0.45	10.0	0.86	116.3
2	Hanford sediment	50	7.5×10^{-5}	1.48	0.44	10.7	0.58	184.5
3	Hanford sediment	100	7.5×10^{-5}	1.47	0.45	9.9	0.85	116.5
4	Hanford sediment	37	1.4×10^{-8}	1.49	0.44	9.7	1.05	92.4
5	Hanford sediment	79	1.4×10^{-8}	1.47	0.45	8.7	1.23	70.7
6	Ottawa sand	0	7.5×10^{-5}	1.73	0.36	8.6	1.23	69.9
7	Ottawa sand	45	7.5×10^{-5}	1.78	0.34	8.8	0.96	91.7
8	Ottawa sand	0	1.3×10^{-8}	1.77	0.34	9.6	0.68	141.2
9	Ottawa sand	35	1.3×10^{-8}	1.73	0.36	9.9	0.64	154.7

[a] Bulk density. [b] Porosity. [c] Pore water velocity. [d] Hydrodynamic dispersion coefficient, determined from Cl data using CXTFIT. [e] Peclet number Pe = VL/D, where L is the column length.

cm and a length of 10.0 cm, and consisted of a top and a bottom plate and sealed by an O-ring on each end. The O-ring had no contact with the inside of the column. A stainless steel screen (0.3 mm pore size) was placed on the column end pieces for mechanical support. Teflon tubing was used throughout the system except for a portion of Tygon tubing in the peristaltic pump. When the column was packed, deaerated artificial pore water solution was preintroduced into the column from the bottom to a certain height, and then porous materials were slowly poured into the solution as 1-cm increments. During packing, the content in the column was continuously stirred with a plastic rod to ensure uniformity of packing and to avoid air entrapment in the column.

For each experiment, the column was flushed with the deaerated artificial pore water to establish a steady-state flow and to standardize the chemical conditions of the experimental system. Once the pH value of the effluent became the same as that of the influent (after roughly 15 pore volumes), the input solution containing either Cs or a preequilibrated Cs-colloid mixture was introduced into the column upward at a constant flow rate. The input solution was prepared in several steps. First, a mixture of ^{137}Cs and ^{133}Cs as well as chloride tracer (8.5×10^{-4} M NaCl) was added to a 1-L plastic bottle that contained artificial pore water. Cesium was added in two different concentrations: 7.5×10^{-5} M (2.19 MBq/mL) and 1.4×10^{-8} M (407 Bq/mL), which correspond to high and low concentrations used in the batch experiments. Then a predetermined amount of sonicated, concentrated Hanford colloidal suspension was added to the bottle while the solution was continuously stirred. The colloidal suspension was stirred slowly and equilibrated for 24 h. Before each experiment, three samples (15 mL for each) were taken from the prepared input solution to determine the total Cs concentration, amount of Cs sorbed on the colloids, and concentrations of colloids as well as chloride. Separation of colloids from solution and Cs quantification was done as described for the batch sorption experiments. Column experiments were not replicated. However, each column was packed carefully following the same procedure to ensure reproducibility between the columns.

During the transport experiments, a continuously stirred suspension of constant colloid concentration was fed to the column. The colloid concentration varied from 35 to 100 mg/L, a range frequently found in natural subsurface environments. Column outflow was collected into 15-mL polypropylene centrifuge tubes in regular time intervals using a fraction collector. Colloid concentrations in the inflow and outflow were measured with UV/vis spectrophotometry (DU Series 640, Beckman Instrument, Inc. MD) at 350 nm. A calibration curve was constructed by dilution of a 0.1 g/L colloid suspension. Colloid concentration versus spectrometer response was linear with a coefficient of determination of $R^2 = 0.9997$ ($n = 8$) between a concentration range of 0−100 mg/L. Wavelengths of 300−350 nm were found to be well suited for colloid quantification (*36*). After a stable colloid concentration in the effluent had been reached for a duration of 10 pore volumes, the input was switched to artificial pore water free of colloids and Cs. The Cs concentration was analyzed as described in the sorption experiments. The chloride tracer, which was used to test the hydrodynamic performance of the column, was analyzed using ion chromatography (Dionex Corporation, Sunnyvale, CA). Based on the tracer concentration data (C) and measured pore water velocity (V), the dispersion coefficient (D) of the porous media was determined by fitting the standard convection-dispersion equation for a conservative solute [$\partial C/\partial t = D(\partial^2 C/\partial x^2) - V(\partial C/\partial x)$] to the chloride breakthrough curves (*37*) using the CXTFIT program. Chloride, colloid, and cesium concentrations in the outflow were related to the concentrations in the inflow and represented as relative concentrations C/C_0.

Results and Discussion

Sorption Isotherms of Cs. Figure 1 illustrates the Cs sorption data on Hanford colloid, Hanford sediment, and Ottawa sand. The overall Cs sorption isotherms are nonlinear and fitted well by the Freundlich model. The fitted equations are $q = 90.5C^{0.71}$ ($R^2 = 0.994$) for Hanford colloid, $q = 58.3C^{0.84}$ ($R^2 = 0.996$) for Hanford sediment, and $q = 0.03C^{0.64}$ ($R^2 = 0.997$) for Ottawa sand, where q is the amount sorbed in mol/kg and C is the equilibrium concentration in mol/L. The observed nonlinear (Freundlich) sorption behavior indicates the presence of multiple types of Cs sorption sites on the colloids and matrices (*39*, *40*). The isotherms can also be approximated by three linear regions, each of them having a different slope (Figure 1). We speculate that three types of sorption sites exist on the heterogeneous surfaces. This concentration-dependent characteristic of Cs sorption agrees well with previous findings (*3*, *12*, *33*, *41*, *42*). Sorption sites may be broadly classified into three categories: sites with high affinity/low capacity, sites with intermediate affinity/low capacity, and sites with low affinity/high capacity. Each linear region of the isotherms is dominated by one type of sites, which possesses relatively uniform binding energy. The entire sorption process may be described as follows. The high affinity sites (frayed-edge sites) are responsible for the uptake of Cs at very low concentrations. As Cs concentration increases the frayed-edge sites are saturated because of their low sorption capacity. Then, the intermediate affinity sites become the major sites for Cs sorption. This type of sites also has a low capacity. Once they are completely occupied after the Cs concentration increases to a certain level, the third type of sites, which is referred to as the "planar sites" and has a lower affinity associated with the structural negative charge on the minerals arising from isomorphous substitution, starts to dominate Cs sorption.

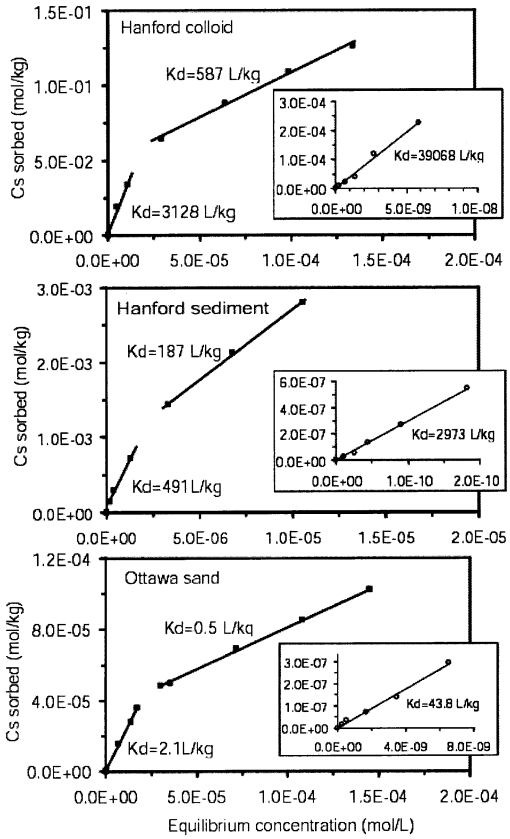

FIGURE 1. Sorption isotherms of Cs on Hanford colloids, Hanford sediment, and Ottawa sand. The inserts show a magnified view of the low concentrations, with the same units of the axes as in the larger plots.

TABLE 3. Single Point K_d Values for Sands and Colloids Measured at Different Cs Concentrations in 0.002 M $NaNO_3$[a] Background Solution

	K_d (L/kg)		
initial Cs concn (M)	Hanford sediment	Ottawa sand	Hanford colloid
2×10^{-10}	2964	70.5	44057
2×10^{-9}	2295	53.0	43468
2×10^{-8}	1625	38.0	32399
2×10^{-7}	937	23.9	20484
2×10^{-6}	527	3.0	4609
2×10^{-5}	117	1.8	2549
2×10^{-4}	na[b]	0.5	490

[a] pH 10 buffered with 2.1×10^{-4} M Na_2CO_3 and $NaHCO_3$. [b] na = not available.

Nonlinear sorption leads to a dependence of the Cs distribution coefficient (K_d) on Cs concentration. Table 3 shows the single-point K_d values calculated for the three materials, which decrease with increasing Cs concentrations. Comparing the K_d values for each material at the same initial concentrations, we found that the values for Hanford colloids were over 10-fold higher than those for Hanford sediment and almost 1000-fold higher than those for Ottawa sand.

Cl Transport in Hanford Sediment and Ottawa Sand. Cl breakthrough curves in Hanford sediment and Ottawa sand were reproducible (see Figures 2 and 3). The analysis of the breakthrough curves showed that the column Peclet numbers were in the order of 70 or higher, indicating a convectively dominated flow regime (Table 2).

Cs and Colloid-Facilitated Cs Transport in Hanford Sediment. At the high Cs input concentration (7.5×10^{-5} M),

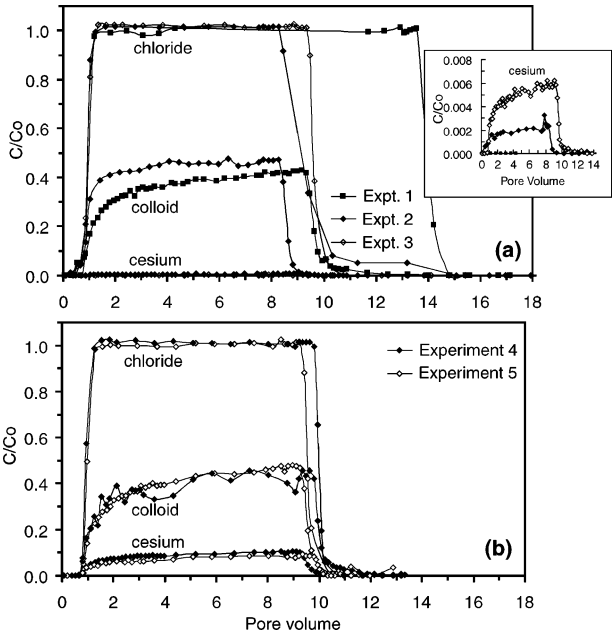

FIGURE 2. Breakthrough curves of Cs, Cl, and colloids in Hanford sediment at various colloid concentrations at (a) high Cs loading (7.5×10^{-5} M) and (b) low Cs loading (1.4×10^{-8} M). The insert shows a magnified view of the Cs breakthrough.

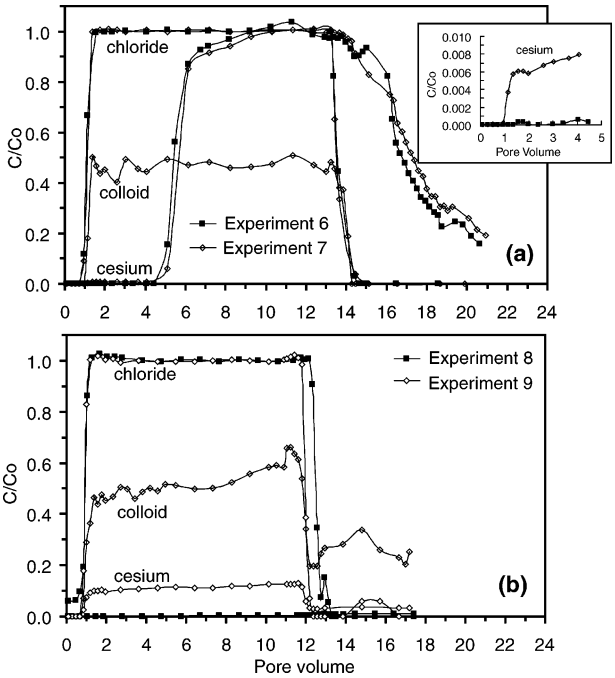

FIGURE 3. Breakthrough curves of Cs, Cl, and colloids in Ottawa sand at various colloid concentrations at (a) high Cs loading (7.5×10^{-5} M) and (b) low Cs loading (1.3×10^{-8} M). The insert shows a magnified view of the Cs breakthrough.

Figure 2a shows that in the absence of colloids (experiment 1), Cs in the aqueous phase was completely sorbed by the Hanford sediment in the column and no Cs breakthrough was observed. This result was expected because the retardation factor ($R = 1 + \rho_b K_d/\phi$) was calculated to be 243 based on the estimated K_d value of 75 L/kg at the Cs concentration of 7.5×10^{-5} M. However, in the presence of Hanford colloids, Cs was detected in the outflow, with relative Cs concentrations (C/C_0) of 0.2−0.3% (experiment 2) and 0.6% (experiment 3) at 50 and 100 mg/L colloid concentrations, respectively.

TABLE 4. Sorption and Desorption of Cs on Colloids in Inflow and Outflow Samples

				inflow			outflow	
				Cs sorbed on colloids				
expt. no.	matrix	colloid concn (mg/L)	Cs concn (mol/L)	(μg/g)[a]	(%)	Cs in solution (%)	Cs sorbed on colloids (μg/g)[a]	Cs desorbed from colloids[b] (%)
2	Hanford sediment	50	7.5×10^{-5}	12007	6.0	94.0	961	92.0
3	Hanford sediment	100	7.5×10^{-5}	12690	12.8	87.2	1269	90.0
4	Hanford sediment	37	1.4×10^{-8}	26	50.6	49.4	12	53.8
5	Hanford sediment	79	1.4×10^{-8}	17	68.2	31.8	5	70.8
7	Ottawa sand	45	7.5×10^{-5}	11569	5.3	94.7	3471	70.0
9	Ottawa sand	35	1.3×10^{-8}	29	53.4	46.6	12	58.6

[a] μg Cs/g colloid. [b] Amount of Cs desorbed from colloids in outflow compared to Cs on colloids in inflow.

Evidently, colloid-facilitated transport was solely responsible for the observed Cs movement.

At the low Cs input concentration (1.4×10^{-8} M), we did not run a Cs experiment in the absence of colloids. No Cs breakthrough was expected because the K_d measured in batch experiments at Cs concentration at 10^{-8} M was greater than that at 10^{-5} M (Table 3). Figure 2b shows that after adding colloids to the input solution at the low concentration of Cs, effluent concentrations of Cs reached ~12% C/C_0 (experiments 4 and 5), indicating a considerable migration of Cs via the colloids.

The efficiency of colloids in binding Cs, and thus facilitating Cs transport, varied with Cs concentration. Cesium association with the colloidal phase in the input solution of each experiment was calculated as percentages and on per gram colloids basis (Table 4). At the high Cs loading, sorption of Cs on unit mass of colloids was similar for both colloid concentrations (50 and 100 mg/L); therefore, the total amount of Cs sorbed in the inflow solutions was doubled when the amount of colloids was doubled. This resulted in an approximately 2-fold increase in outflow Cs concentration (Figure 2a, insert). In contrast, at the low Cs loading, there was minimal difference in Cs effluent concentrations when the colloid concentration increased from 37 to 79 mg/L (Figure 2b). Table 4 indicates that at low colloid concentration (37 mg/L), 26 μg Cs was sorbed on 1 g of the colloids, while at high colloid concentration (79 mg/L), only 17 μg Cs was sorbed on 1 g of colloid.

Cs and Colloid-Facilitated Cs Transport in Ottawa Sand. As shown in Figure 3a, at high Cs concentration (7.5×10^{-5} M) and in the absence of colloids (experiment 6), the initial breakthrough front of Cs occurred at ~5 pore volumes. Following the initial breakthrough front, relative concentrations of Cs in the effluent increased rapidly to 0.9 in one pore volume and then more slowly to reach unity. This different behavior from Hanford sediment was expected because Ottawa sand had considerably lower CEC (Table 1) and a much smaller sorption affinity for Cs (Table 3) as compared with Hanford sediment. In the presence of colloids (experiment 7), an almost identical main breakthrough curve of Cs was observed as in the absence of colloids. However, a small fraction of Cs was detected simultaneously with the detection of colloid breakthrough in the effluent (Figure 3a insert). This additional Cs peak was clearly due to colloid-facilitated transport, although the fraction of Cs transported via colloids was low (~0.8% C/C_0). The magnitude of the colloid-facilitated Cs transport was similar as in the Hanford sediment, corroborating the interpretation of colloid-assisted movement. It is, however, evident that dissolved Cs transport dominated the migration of Cs through Ottawa sand at the high Cs concentration.

At the low Cs concentration (1.3×10^{-8} M, equivalent to 344 Bq/mL), Cs was removed completely by Ottawa sand during transport without colloid involved (experiment 8, Figure 3b). This was expected based on batch sorption results. Addition of 35 mg/L Hanford colloids to the input solution caused 12% of Cs breakthrough (experiment 9). Obviously, at the low Cs concentration movement of the Cs-bearing colloids dominated Cs migration. This result agrees well with that of Saiers and Hornberger (*29*), where they used a similar Cs concentration (365 Bq/mL). They found that within 17 pore volumes Cs injected to the column was completely sorbed by the Ottawa sand, but addition of 50 mg/L kaolinite particles to the input solution caused breakthrough of Cs at about one pore volume.

Desorption of Cs from Colloids during Transport. For each experiment, we calculated the amount of Cs associated with each gram of colloids in the influent by taking the difference between the measured total Cs concentration and Cs concentration in solution after centrifugation. As we did not observe any dissolved Cs transport in the Hanford sediment and the Ottawa sand in the absence of colloids (except for experiment 7), we assume that all the cesium breaking through the columns in the presence of colloids was associated with the colloidal particles. We calculated the percentage of Cs desorption from colloids based on the difference in Cs concentrations sorbed on colloids between the inflow and outflow. Significantly less Cs was recovered on the colloids in the effluent compared with Cs sorption in the influent (Table 4). This suggests that during transport Cs was partially "stripped" off from the colloidal particles to equilibrate with the pore water solution and subsequently sorbed by the transport medium in the column. The results also suggest that the degree of stripping depends on both Cs concentration and the sorption capacity of the transport matrix. In both the Hanford sediment and Ottawa sand columns, the stripping was more pronounced at the higher Cs concentration. We attribute this to the nonlinearity of Cs sorption on the colloids. As discussed earlier, at high Cs loading, more Cs might have been sorbed on the relatively low affinity sites, while at low Cs loading most of the Cs might have been sorbed on high affinity sites. The weakly bound Cs at low affinity sites was more easily desorbed from the colloids than the strongly bound Cs at high affinity sites. Table 4 also indicates that at the same Cs concentration, more Cs was stripped off the colloids traveling through Hanford sediment than through Ottawa sand, likely because of the high sorption capacity of the Hanford sediment.

Effect of Nonlinear Cs Sorption and Sorption Reversibility on the Efficiency of Colloid-Facilitated Cs Transport. The nonlinear feature of Cs sorption resulted in the observation of a series of interesting scenarios of colloid-facilitated Cs transport. At the low Cs loading, a high percentage of Cs was retained on the colloids due to availability of adequate amount of high-affinity sorption sites on the particles. This resulted in relatively effective colloid-facilitated Cs transport (Figure 2b). When Cs concentration increased to a sufficiently high level at which the amount of high-affinity sorption sites on the colloidal particles could be saturated by Cs, colloid concentration became the limiting factor in affecting the

efficiency of colloid-facilitated Cs transport. This was the result we observed from the Hanford sediment column at the high Cs loading (Figure 2a). In this case, because the migration of Cs became more of a function of the behavior of the colloid than of the dissolved Cs, all factors (e.g., flow velocity, solution chemistry, medium and colloid properties) affecting colloid transport would govern the transport of Cs (*43*, *44*). Furthermore, if Cs concentration increased to a level high enough to saturate the high affinity sites of both the collector grains and the colloids, transport of Cs in the dissolved phase would dominate the breakthrough process. When our tests had $> 10^{-5}$ M dissolved Cs, although the amount of Cs transport via colloids accounted for only a small fraction of the total amount of Cs in the effluent, rapid migration of the colloids considerably reduced the breakthrough time of Cs (Figure 3a). This phenomenon should be common for media with low CEC value (e.g., silica sand).

In a strongly sorbing sediment matrix, Cs transport via colloids will be limited due to desorption of Cs from colloids and sorption to the sediment matrix. Such desorption/sorption processes will also affect transport of other radionuclides that undergo reversible sorption on colloidal particles. Under constant geochemical conditions, the degree of desorption of radionuclides from colloids depends on type of radionuclide and colloidal material (*45*, *46*). For instance, sorption reversibility on hematite, montmorillonite, and silica colloids has been observed for ^{239}Pu and ^{243}Am but not for ^{237}Np and ^{238}U (*45*).

We found that the efficiency of colloid-facilitated Cs transport was controlled by the nonlinear nature of Cs sorption by both solid surfaces and colloids. Cesium sorbed onto the colloids was effectively stripped off from the colloids during transport. The extent of the stripping depends on Cs concentration and sediment matrix properties. The results show that colloid-facilitated Cs transport at the Hanford site is likely not an effective mechanism for Cs movement. At Hanford, it can be expected that Cs would be stripped from colloidal carriers as the colloids move through the 27−33 m thick uncontaminated vadose zone and only a very small fraction of initially sorbed Cs would move with mobile colloids. Furthermore, under the conditions at the Hanford site (pore water chemistry, degree of water saturation) colloids are less likely to be stable in suspension than under our experimental conditions, further limiting the possibility for colloid-facilitated transport. Our results can be interpreted as a worst-case scenario for colloid-facilitated Cs transport at the Hanford site, but even in this case, the quantitative amount of Cs that can be cotransported appears to be limited.

Acknowledgments

This work was supported by the Environmental Management Science Program, U.S. Department of Energy under Grant DE-FG07-99ER62882. We thank John Zachara and Jeff Serne (Pacific Northwest National Laboratory) for providing the Hanford sediments. We thank Jeff Serne, Wooyong Um, Eric Pierce, Chris Brown (Pacific Northwest National Laboratory), and an anonymous reviewer for constructive comments on the manuscript.

Literature Cited

(1) U.S. Department of Energy. *Groundwater/Vadose Zone Integration Project Specification, Report DOE/RL-98-48, Draft B, C and D*; 1998.
(2) McKinley, J. P.; Zeissler, C. J.; Zachara, J. M.; Serne, R. J.; Lindstrom, R. M.; Schaef, H. T.; Orr, R. D. *Environ. Sci. Technol.* **2001**, *35*, 3433−3441.
(3) Bradbury, M. H.; Baeyens, B. *J. Contam. Hydrol.* **2000**, *42*, 141−163.
(4) Staunton, S.; Roubaud, M. *Clays Clay Miner.* **1997**, *45*, 251−260.
(5) Anderson, K.; Allard, B. Report No. SKBF-KBS-TR-83-07; Svensk Kärnsbränsteförjning, Stockholm, 1983.
(6) Cremers, A.; Elsen, A.; De Preters, P.; Maes, A. *Nature* **1988**, *335*, 247−249.
(7) De Preter, P.; Van Loon, L.; Maes, A.; Cremers, A. *Radiochim. Acta* **1991**, *52/53*, 299−302.
(8) Adeleye, S. A.; Clay, P. G.; Oladipo, M. O. A. *J. Mater. Sci.* **1994**, *29*, 954−958.
(9) Ohnuki, T.; Kozai, N. *Radiochim Acta*. **1994**, *66/67*, 327−331.
(10) Wauters, J.; Elsen, A.; Cremers, A. *Appl. Geochem*. **1996**, *11*, 601−603.
(11) Bors, J.; Gorny, A.; Dultz, St. *Radiochim. Acta*. **1996**, *74*, 231−234.
(12) Zachara, J. M.; Smith, S. C.; Liu, C.; McKinley, J. P.; Serne, R. J.; Gassman, P. L. *Geochim. Cosmochim. Acta* **2002**, *66*, 193-211.
(13) Francis, C. W.; Brinkley, F. S. *Nature* **1976**, *260*, 511−513.
(14) Gutierrez, M.; Fuentes, H. R. *Appl. Clay Sci.* **1996**, *11*, 11−24.
(15) Krumhansl, J. L.; Brady, P. V.; Anderson, H. L. *J. Contam. Hydrol.* **2001**, *47*, 233−240.
(16) Sawhney, B. L. *Clays Clay Miner.* **1972**, *20*, 93−100.
(17) Cornell, R. M. *J. Radioanal. Nucl. Chem*. **1993**, *171*, 483−500.
(18) Kaplan, D. I.; Serne, R. J. *Radiochim. Acta* **1998**, *81*, 117−124.
(19) Serne, R. J.; Zachara, J. M.; Burke, D. S. *Chemical Information on Tank Supernatants, Cs Adsorption from Tank Liquids onto Hanford Sediments, and Field Observations of Cs Migration from Past Tank Leaks*; Project Report of Pacific Northwest National Laboratory, PNLL-11495; Richland, WA, 1998.
(20) Serne, R. J.; Last, G. V.; Schaef, H. T.; Lanigan, D. C.; Lindenmeier, C. W.; Ainsworth, C. C.; Clayton, R. E.; LeGore, V. L.; O'Hara, M. J.; Brown, C. F.; Orr, R. D.; Kutnyakov, I. V.; Wilson, T. C.; Wagnon, K. B.; Williams, B. A.; Burke, D. S. *Characterization of Vadose Zone Sediment: Borehole 41-09-39 in the S-SX Waste Management Area*; Project Report of Pacific Northwest National Laboratory, PNLL-13757-3; Richland, WA, 2002a.
(21) Serne, R. J.; Last, G. V.; Schaef, H. T.; Lanigan, D. C.; Lindenmeier, C. W.; Ainsworth, C. C.; Clayton, R. E.; LeGore, V. L.; O'Hara, M. J.; Brown, C. F.; Orr, R. D.; Kutnyakov, I. V.; Wilson, T. C.; Wagnon, K. B.; Williams, B. A.; Burke, D. S. *Characterization of Vadose Zone Sediment: Slant Borehole SX-108 in the S-SX Waste Management Area*; Project Report of Pacific Northwest National Laboratory, PNLL-13757-4; Richland, WA, 2002b.
(22) Knepp, A. J. *Field Investigation Report for Waste Management Area S-SX*; Project Report of Pacific Northwest National Laboratory, RPP-7884; Richland, WA, 2002.
(23) Zhao, H.; Harsh, J. B.; Flury, M.; Mashal, K. Abstracts, 222nd ACS National Meeting, August 26−30, 2002, Chicago, IL.
(24) Bickmore, B. R.; Nagy, K. L.; Young, J. S.; Drexler, J. W. *Environ. Sci. Technol.* **2001**, *35*, 4481−4486.
(25) Buddemeier, R. W.; Hunt, J. R. *Appl. Geochem*. **1998**, *3*, 535−548.
(26) Kaplan, D. I.; Bertsch, P. M.; Adriano, D. C.; Orlandini, K. A. *Radiochim. Acta* **1994**, *66/67*, 181−187.
(27) Kersting, A. B.; Efurd, D. W.; Finnegan, D. L.; Rokop, D. J.; Smith, D. K.; Thompson, J. L. *Nature* **1999**, *397*, 56−59.
(28) Sätmark, B.; Albinsson, Y.; Liang, L. *J. Contam. Hydrol.* **1996**, *21*, 231−241.
(29) Grindrod, P. *J. Contam. Hydrol.* **1993**, *13*, 167−181.
(30) Saiers, J. E.; Hornberger, G. M. *Water Resour. Res.* **1996**, *32*, 33−41.
(31) Noell, A. L.; Thompson, J. L.; Corapcioglu, M. Y.; Triay, I. R. *J. Contam. Hydrol.* **1998**, *31*, 23−56.
(32) Faure, M. H,; Sardin, M.; Vitorge, P. *J. Contam. Hydrol.* **1996**, *21*, 255−267.
(33) Hakem, N. L.; Al Mahamid, I.; Apps, J. A.; Moridis, G. J. *J. Radioanal. Nucl. Chem*. **2000**, *246*, 275−278.
(34) Serne, R. J.; Bjornstad, B. N.; Schaef, H. T.; Williams, B. A.; Lanigan, D. C.; Horton, D. G.; Clayton, R. E.; Mitroshkov, A. V.; LeGore, V. L.; O'Hara, M. J.; Brown, C. F.; Parker, K. E.; Kutnyakov, I. V.; Serne, J. N.; Last, G. V.; Smith, S. C.; Lindenmeier, C. W.; Zachara, J. M.; Burke, D. S. *Characterization of Vadose Zone Sediment: Uncontaminated RCRA Borehole Core Samples and Composite Samples*; PNNL-13757-1; Pacific Northwest National Laboratory, U.S. Department of Energy, Richland, WA, 2002.
(35) Jin, Y.; Chu, Y.; Li, Y. *J. Contam. Hydrol.* **2000**, *43*, 111−128.
(36) Cherrey, K. D.; Flury, M.; Harsh, J. B. *Water Resour. Res.* **2003**, 39, 1165, DOI: 10.1029/2002WR001944.
(37) van Genuchten, M. Th.; Alves, W. J. Analytical Solutions of the One-Dimensional Convective-Dispersive Solute Transport Equation. *U.S. Dept. Agric. Tech. Bull.* **1982**, *1661*.
(38) Toride, N.; Leij, F. K.; van Genuchten, M. Th. The CXTFIT code for estimating transport parameters from laboratory or field

tracer experiments, version 2.1, Research Report #137; U.S. Salinity Laboratory, U.S. Department of Agriculture, Riverside, CA, 1995.
(39) Atkins, P. W. *Physical Chemistry*, 4th ed.; Oxford University Press: Oxford, 1995; p 995.
(40) Sposito, G. *Soil Sci. Soc. Am. J.* **1980**, *44*, 652−654.
(41) Campbell, L. S.; Davies, B. E. *Appl. Geochem.* **1995**, *10*, 715−723.
(42) Comans, R. N. J.; Hallers, M.; De Preter, P. *Geochim. Cosmochim. Acta* **1991**, *55*, 433−440.
(43) Roy, S. B.; Dzombak, D. A. *Environ. Sci. Technol.* **1997**, *31*, 656−664.
(44) Um, W.; Papelis, C. *Environ. Geol.* **2002**, *43*, 209−218.
(45) Lu, L.; Conca, J.; Parker, G. R.; Leonard, P. A.; Moore, B.; Strietelmeier, B.; Triay, I. R. *Adsorption of Actinides onto Colloids as a Function of Time, Temperature, Ionic Strength, and Colloid Concentration*; Los Alamos National Laboratory Report LA-UR-00-51-21; 2000.
(46) Lu, N.; Cotter, C. R.; Kitten, H. D.; Bentley, J.; Triay, I. R. *Radiochim. Acta* **1998**, *83*, 167−173.

Received for review December 19, 2002. Revised manuscript received August 13, 2003. Accepted September 3, 2003.

ES0264504

Nitrate and colloid transport through coarse Hanford sediments under steady state, variably saturated flow

Kelly D. Cherrey, Markus Flury, and James B. Harsh

Department of Crop and Soil Sciences, Center for Multiphase Environmental Research, Washington State University, Pullman, Washington, USA

Received 27 December 2002; revised 18 February 2003; accepted 17 March 2003; published 24 June 2003.

[1] At the U.S. Department of Energy's Hanford Reservation, colloid-facilitated transport is a potential mechanism for accelerated movement of radionuclides like Cs-137. Here we investigate the transport of colloids through Hanford sediments under steady state, unsaturated flow conditions. We isolated colloids from Hanford sediments by dispersion and sedimentation and determined colloid breakthrough curves in packed sediment columns. A column system was developed with which we could control volumetric water contents with accuracy better than 0.01 effective saturation and the water potentials to better than 0.06 cm-H_2O. Inflow and outflow boundary conditions had to be meticulously controlled to ensure uniformity of water contents and water potentials inside the column. Colloid breakthrough curves were determined under a series of water contents ranging from 0.2 to 1.0 effective saturation. Colloids were mobile under all water saturations, but the total amount of colloids transported decreased with decreasing water saturation. Colloid behavior was described with the mobile-immobile model concept, including first-order deposition from the mobile phase only. *INDEX TERMS:* 1831 Hydrology: Groundwater quality; 1832 Hydrology: Groundwater transport; 1866 Hydrology: Soil moisture; 1875 Hydrology: Unsaturated zone; *KEYWORDS:* colloids, unsaturated flow, vadose zone

Citation: Cherrey, K. D., M. Flury, and J. B. Harsh, Nitrate and colloid transport through coarse Hanford sediments under steady state, variably saturated flow, *Water Resour. Res.*, *39*(6), 1165, doi:10.1029/2002WR001944, 2003.

1. Introduction

[2] Colloidal particles have been suspected and, in some cases shown, to facilitate the movement of contaminants through the subsurface [*McCarthy and Zachara*, 1989; *Kretzschmar et al.*, 1999]. While much information is available about colloid transport under water saturated conditions [*Kersting et al.*, 1999], much less is known about the behavior of colloids in the vadose zone. Results from the few studies conducted indicate that colloid movement under unsaturated conditions is less effective than under saturated conditions, with more and more colloids being removed from the fluid phase as the water content of the soil and sediments decreases. This has been demonstrated for inorganic silica colloids [*Lenhart and Saiers*, 2002], as well as organic colloidal bacteria [*Wan et al.*, 1994; *Schäfer et al.*, 1998; *Jewett et al.*, 1999] and viruses [*Chu et al.*, 2001].

[3] During saturated and unsaturated flow, colloids are deposited at the solid-liquid interface. For unsaturated flow, colloids are also removed from the fluid phase by two other major mechanisms: (1) attachment to the liquid-gas interface and (2) straining in liquid films that have thickness smaller than colloid diameters [*Wan and Tokunaga*, 1997; *Lenhart and Saiers*, 2002]. With decreasing water saturation, the liquid-gas interfacial area increases and the film thickness decreases, and consequently colloids are more likely to be deposited inside the porous medium. It has been postulated that capillary-based liquid pathways are effective conduits for colloid movement as long these conduits form connected pathways, and that at low water saturations these conduits become discontinuous causing an abrupt decrease in colloid transport [*Wan and Tokunaga*, 1997].

[4] Contaminants of particular concern for colloid-facilitated movement are the strongly sorbing radionuclides cesium, plutonium, and americium. At the Hanford Reservation in south-central Washington state, cesium-137 has been released to the vadose zone from leaking underground waste storage tanks [*Gephart and Lundgren*, 1998; *McKinley et al.*, 2001]. Cesium-137 is the major contributor to the radioactivity released by leaking waste tanks. The current depth distribution of cesium indicates that cesium has, at least in part, moved in accordance with a chromatographic model [*Zachara et al.*, 2002], but colloid-facilitated transport as an important transport mechanism cannot be ruled out. The geochemical conditions under leaking Hanford waste tanks is conducive to in situ colloid alteration and formation [*Bickmore et al.*, 2001; *Zhao et al.*, 2001]. It has been shown that the displacement of high ionic strength solutions by water of low ionic strength can induce in situ mobilization of native colloids from the Hanford sediments [*Blume et al.*, 2002; *Flury et al.*, 2002]. If these colloids can move large distances through the vadose zone at Hanford, there is a possibility for colloid-facilitated transport of radionculides. It has also been shown that mobilized colloids can be trapped by fine-textured sediment layers, resulting in a permeability reduction of the fine-textured sediments [*Blume et al.*, 2002]. In this study, we focus on colloid transport within a single, coarse-textured sediment layer only.

0043-1397/03/2002WR001944$09.00

[5] The goal of this study was the accurate measurement of colloid transport in unconsolidated Hanford sediments under well controlled saturated and unsaturated water contents at steady state fluxes. The experimental objective was the development of a laboratory column apparatus to control levels of effective saturation (S_e) at better than 0.01 error (σ_{S_e}). S_e is defined as

$$S_e = \frac{\theta_v - \theta_r}{\theta_s - \theta_r} \quad (1)$$

where θ_v is the volumetric water content, θ_r is the residual water content, and θ_s is the saturated water content. Breakthrough curves were done with a conservative $NaNO_3$ tracer, and two types of colloids: those removed from Hanford sediments and those modified by a simulated Hanford tank-waste solution [*Zhao et al.*, 2001].

2. Materials and Methods

2.1. Column Setup

[6] The experimental apparatus was designed [*Cherrey*, 2002] to accurately measure unsaturated colloid transport under steady state flux and unit hydraulic gradient (Figure 1). The column (acrylic, with internal diameter and length of 5 and 20 cm, respectively) was selected to minimize flow alterations around the tensiometers and along the wall edge. Five porous ceramic tensiometers (652X03-B1M3, 1 bar high flow, Soilmoisture Equipment Inc., Santa Barbara, CA) were equally spaced vertically and radially (i.e., equally on a helix). The water tension within each tensiometer was monitored by an electronic strain gauge pressure transducer (PX170-28DV, Omega Engineering, Stamford, CT). The average water content of the column was monitored gravimetrically with an electronic strain gauge load cell (PT1002, Precision Transducers Ltd., Castle Hill, Australia). This average water content was then transformed to effective saturation using equation (1).

[7] A sprinkler and peristaltic pump were used to supply influent to the column upper boundary. Flow through the sprinklers was controlled by a four channel peristaltic pump (Ismatec ISM760, Glattbrugg, Switzerland). Two different sprinkler heads were designed for high and low flow rate applications. Using three, two, or one of the pump channels, a high-flow sprinkler provided uniform flow rates from 90 mL min^{-1} down to 2–3 mL min^{-1}. A low-flow sprinkler was used for lower flow rates. Both sprinklers were designed with a low dead volume (≈0.2 mL) to minimize dispersion during influent switch-over. Tubing to the peristaltic pump and between the pump and the sprinkler was 1/16″ (1.6 mm) I.D. Tygon.

[8] The lower boundary condition was controlled at constant potential using a hanging water column [*Hillel*, 1998, *p. 167*] with a custom porous glass frit. The custom glass frit (ACE glass fiber disc, porosity C, 2.8 mm thick, 59.7 mm diameter, ACE Glass Inc., Vineland, NJ) was selected after testing against a porous stainless steel frit and nylon membranes. In contrast to the glass frit, colloids were captured in a stainless steel frit with pore diameter of ≈10 μm. The nylon membranes were susceptible to puncturing by the jagged Hanford sediments. The ACE frit carrys a negative charge, provides adequate mechanical support, has high hydraulic conductivity, and minimizes

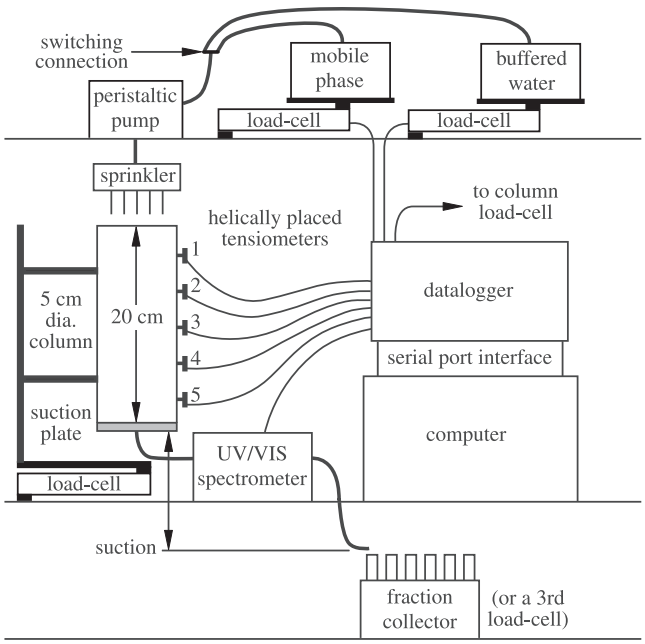

Figure 1. Schematic of experimental column setup.

colloid capture. The ACE frit had a bubbling pressure of ≈45 cm-H_2O (pressure when air bubbling begins) corresponding to a pore diameter of 65 μm. Saturated hydraulic conductivity of the ACE frit, measured by the falling head method [*Hillel*, 1998], was 0.11 cm min^{-1}. The ACE frit was epoxied to a Teflon sealing ring treated with FluoroEtch (Acton Technologies, Pittston, PA). This assembly was mated to acrylic column surfaces with flat Buna-N O-rings. When saturated, the ACE frit held 3.2 mL of water.

[9] The column outflow was measured in real-time using a Perkin Elmer LC95 UV/VIS spectrometer. The LC95 flow cell was modified for high flow rates (up to ≈90 mL min^{-1}). The flow cell (1/16″ I.D. = 1.6 mm) was constructed using a Torlon flow cylinder with quartz lenses and stainless steel tubing connections. All outflow tubing was 1/8″ (3.2 mm) I.D. Tygon.

[10] The weight of inflow, column, and outflow was monitored with electronic load cells. Within a laboratory temperature fluctuation of 21 to 25°C, the standard deviation of calibrated load cells (σ_w) was less than 0.4 g, and the standard deviation of calibrated pressure transducers (σ_h) was typically less than 0.02 cm-H_2O. These measurement errors were less than the design goals of $\sigma_w \approx 1.3$ g and $\sigma_h \approx 0.06$ cm-H_2O for $\sigma_{S_e} = 0.01$. Load cells and pressure transducers were calibrated prior to experimentation. Load cells, pressure transducers, and spectrometer were interfaced to a data logger (CR-7X, Campbell Scientific, Logan, UT).

2.2. Sediments and Sediment Treatment

[11] Sediments from the Hanford formation were obtained from the Submarine Site (218-E-12B) at the U.S. DOE Hanford Reservation in south-central Washington state. These coarse, unconsolidated sediments were air dried and filled into plastic buckets. These sediments are representative of the material underlying the S-SX (single-shell) tank farm in the 200 East Area (personal communication,

Bruce N. Bjornstad, September 2001, Pacific Northwest National Laboratories, Richland, WA). Detailed characterization data are reported by *Serne et al.* [2002a]. A 2-mm-square sieve was used to remove coarse particles from the sediments.

[12] To prevent colloid mobilization of residual colloids during the transport experiments, the sediments were treated to reduce the colloid fraction. Before treatment, Na^+ cation exchange was done to minimize cation exchange during breakthrough experiments. About 1 kg of sediment was packed into an acrylic column with internal diameter and length of 5 and 30 cm, respectively. Seven pore volumes of 1 M NaCl buffered at pH 10 (1.67 mM $NaHCO_3$ + 1.67 mM Na_2CO_3) were pumped through the column, followed only by pH 10 buffered water until the electrical conductivity of the outflow was less than 1 dS m^{-1}. The sediment was then removed from the column and simultaneously agitated and sonicated for at least five minutes in pH 10 buffered water. After settling through 10 cm of this pH 10 buffered water for about 16 hours the suspension was decanted and saved for the native colloid source. This process was repeated daily for 2 weeks, after which the sediment was packed into a column and additional colloids were removed by pumping through about 300 pore volumes of pH 10 buffered water. Approximately 6.5 g of colloids per kg of sediment were removed by sonication and sedimentation. Column mobilization removed another 3.5 g per kg of sediment.

[13] The solutions used for pretreatment and the following transport experiments were all buffered at pH 10 to prevent carbonate dissolution and to mimic Hanford tank farm conditions. The pH of the sediments used was 7.8 (in 1:1 w/w H_2O) and under the S-SX tank farm, the pH is in the range of 9 to 10 [*Serne et al.*, 2002b]. Our solutions were buffered to maintain a stable pH throughout the experiments.

[14] The particle size distribution of the treated sediment was determined by dry sieving. Petrographic thin sections were prepared and the primary minerals were determined with a petrographic microscope [*Cady et al.*, 1986].

2.3. Tracer and Colloidal Material

[15] Sodium nitrate ($NaNO_3$, 0.2 mM) was used as a conservative tracer to determine column parameters before infusing colloids. Colloid transport was measured with two types of colloids: native and modified. Native colloids were obtained from the colloid suspensions decanted during sediment treatment. Modified colloids were separated after reacting Hanford sediment with a simulated Hanford tank waste solution (1.4 *m* NaOH, 0.25 *m* $NaAlO_4$, and 3.7 *m* $NaNO_3$) at 50°C for 40 days [*Zhao et al.*, 2001]. This procedure was designed to mimic the reactions taking place in the subsurface after a Hanford tank leak [*Zhao et al.*, 2001]. Modified colloid suspensions were decanted from the reacted sediment after ≈16 hours of gravity sedimentation through a depth of 10 cm of suspension. Solids of both types of colloids were resuspended by sonication and decanted after settling for 2 weeks. The concentration of these suspensions (≈10 mg L^{-1}) remained stable for at least three days.

[16] Colloid mineralogy was characterized by X-ray diffraction (Philips XRG 3100, Philips Analytical Inc., Mahwah NJ) with Cu-Kα radiation [*Whittig and Allardice*, 1986]. Colloid particle size was determined by static light scattering (MasterSizer S, Malvern Instruments Ltd., Malvern, UK) and dynamic light scattering (Zetasizer 3000HSa, Malvern Instruments Ltd., Malvern, UK with a Helium-Neon laser at 633 nm wavelength). Electrophoretic mobility of the colloids was measured by the Zetasizer 3000HSa. All light scattering experiments were made with colloids suspended in 1.67 mM $NaHCO_3$ + 1.67 mM Na_2CO_3 pH 10 buffers (I = 6.67 mM).

2.4. Spectrometer Measurements

[17] Nitrate (NO_3^-) and colloid breakthrough concentrations were measured with a Perkin Elmer LC95 single wavelength UV/VIS spectrometer. Optimal wavelength for nitrate measurement was determined with the aid of an HP8452A full spectrum diode-array UV/VIS spectrometer. The HP8452A spectrometer showed uniform, monomodal peak shapes with regard to wavelength at nitrate concentrations lower than 0.2 mM. The LC95 spectrometer reproducibly detected these nitrate peaks when dialed to 204 nm from below. For reproducible colloid detection, the LC95 spectrometer was dialed to 300 nm from below. The wavelength of 300 nm was found to be optimal based on the absorption spectrum of the colloids; nitrate was essentially undetectable at 300 nm. Reproducible operation of the LC95 at these two wavelengths is necessary during the course of experimentation since nitrate, native colloid, and modified colloid breakthroughs were done in sequence at each water content. Calibration curves showed that nitrate concentration versus spectrometer response was slightly nonlinear and we fitted a quadratic function as calibration curve. Colloid concentration versus spectrometer response was linear. Analytical detection limits were 0.002 mM for nitrate and 0.2 mg L^{-1} for colloids.

2.5. Hydraulic Properties and Transport Experiments

[18] The column was packed by incrementally filling moistened sediments under flowing CO_2 gas. The background electrolyte solution (pH 10 buffered water) was pumped from the bottom to keep the sediments saturated. After the column was packed, about 20 pore volumes of pH 10 buffered water were pumped through to dissolve CO_2 gas bubbles and remove the dissolved CO_2. The pore volume of the saturated column was determined based on identically packed smaller cylinders, and independently verified by analysis of nitrate breakthrough curves. Saturated hydraulic conductivity of the packed sediments was measured by the constant head method, taking into account the saturated conductivity of the porous frit [*Hillel*, 1998]. Unsaturated hydraulic conductivities were obtained from the water flux and water potential measurements during the nitrate breakthroughs. The moisture characteristic of the sediments was measured by the hanging water column technique and confirmed during the nitrate breakthroughs.

[19] Nitrate and colloid breakthroughs were all buffered at pH 10 (1.67 mM $NaHCO_3$ + 1.67 mM Na_2CO_3). The experiments were run in a specific sequence, starting with the saturated column followed by incrementally lowering the water content. The column was uniformly desaturated by adjusting the inlet flow rate and the outlet suction. The

experimental goal was to uniformly decrease the effective water saturation S_e = 1.0, 0.9, 0.8, . . ., 0.1; however, it was not possible to uniformly desaturate the column at S_e = 0.9, 0.8, and 0.1.

[20] Water potential was predicted by fitting the van Genuchten equation, $S_e = [1 + (\alpha h)^n]^{(1/n-1)}$ [*van Genuchten*, 1980], to the measured moisture characteristic, where h is the water potential, α is the inverse of the air-entry potential, and n is a parameter related to the pore size distribution. Uniform water flux, water content, and water potential along the column was established at each water content. The high-flow sprinkler was used for $S_e \geq 0.3$, the low-flow sprinkler was used for $S_e < 0.3$.

[21] At each water content, first a nitrate breakthrough was performed, followed by a native colloid breakthrough, and finally a modified colloid breakthrough. The amount of colloid infused was minimized to prevent loading the column with colloids. The pH 10 buffered water was used to elute the nitrate and colloids, and to adjust the column to the next water content. Breakthroughs were reproducible and neither colloid breakthrough influenced subsequent breakthroughs.

2.6. Data Analysis

[22] The nitrate and colloid breakthroughs are modeled using the physical nonequilibrium mobile-immobile model (MIM). Steady state unsaturated flow has often been found to correspond to the MIM physical nonequilibrium concept [*Gaudet et al.*, 1977; *De Smedt and Wierenga*, 1984; *Bond and Wierenga*, 1990; *Padilla et al.*, 1999; *Gamerdinger and Kaplan*, 2000]. We assume that colloid deposition only occurs from the mobile water phase and is negligible in the immobile phase. First-order deposition coefficients are often found directly proportional to the pore water velocity [*Kretzschmar et al.*, 1999], so that deposition in the immobile phase will vanish. Under these assumptions, the dimensionless form of the MIM can be written as [*Toride et al.*, 1995]:

$$\beta \frac{\partial C_m}{\partial T} + (1-\beta)\frac{\partial C_{im}}{\partial T} = \frac{1}{Pe}\frac{\partial^2 C_m}{\partial Z^2} - \frac{\partial C_m}{\partial Z} - \mu_m C_m \qquad (2)$$

$$(1-\beta)\frac{\partial C_{im}}{\partial T} = \omega(C_m - C_{im}) \qquad (3)$$

where C_m and C_{im} are the scaled solute concentrations in the mobile and immobile water phases, respectively, $\beta = \theta_m/(\theta_m + \theta_{im}) = \theta_m/\theta$ is the ratio of mobile water content to total water content, $Pe = vL/D$ is the Peclet number, where v is the pore water velocity and L is the length of the column, $\omega = \alpha L/(\theta_m v)$ is a Dahmköhler number expressing the ratio of the mass transfer coefficient to the pore water velocity, $T = vt\theta_m/(\theta L)$ is the dimensionless time where t is the time, $Z = z/L$ is the dimensionless depth where z is the depth, and μ_m is the first-order deposition coefficient for colloids in the mobile region. The dimensionless deposition coefficient μ_m is defined as $\mu_m = L\theta_m\mu/(\theta v)$, where μ is the deposition coefficient with dimensions one over time. Scaled concentrations are defined as absolute concentrations divided by the concentration in the inlet. An analytical solution of (2) and (3) for a semi-infinite column with Dirichlet boundary conditions was fitted to the experimental data using CXTFIT 2.1 [*Toride et al.*, 1995]. For nitrate, we assumed that $\mu_m = 0$.

Table 1. Particle Size Distribution of Treated Hanford Sediments

Diameter, mm	Concentration, % (by weight)	Standard Deviation, % (by weight)
2.0–1.0	74.99	3.65
1.0–0.5	19.37	3.09
0.5–0.25	3.57	1.08
0.25–0.124	0.91	0.19
0.124–0.053	0.80	0.13
<0.053	0.33	0.10

3. Results and Discussion

3.1. Sediments and Colloid Characterization

[23] Treated sediments show a highly skewed particle size distribution peaked between 1 and 2 mm (Table 1). The primary minerals were mainly quartz, plagioclase, K feldspar, amphibole, sericite, pyroxene, magnetite, biotite, and muscovite. Native colloids consisted mainly of chlorite, smectite, vermiculite, kaolinite, illite, and quartz. Modified colloids were composed of similar mineral phases as the native colloids and contained new mineral phases. For modified colloids, the native mineral phases kaolinite and quartz have been partially or completely dissolved in the high alkaline environment of simulated Hanford tank waste, and the new mineral phases cancrinite and sodalite have been detected [*Zhao et al.*, 2001]. The resulting colloids consisted of a mixture of: (1) newly-formed phases (e.g., cancrinite and sodalite), (2) partially dissolved native soil minerals, and (3) unaltered native soil minerals. Electrophoretic mobilities were typically −4.0 and −4.5 ($\mu m\ s^{-1}$)/($V\ cm^{-1}$) for native and modified colloids, respectively. Particle size distributions of the two types of colloids were similar, with a mean Z-averaged diameter of 348 ± 14 nm for the native and 368 ± 16 nm for the modified colloids (Figure 2).

3.2. Hydraulic Properties

[24] The coarse-textured sediments show a pronounced air-entry pressure of about 7 cm-H_2O suction and reach their residual water content at suctions larger than about 30 cm-H_2O (Figure 3a). The narrow range of suctions needed to drain the sediments was explicitly considered in the design of the column system, and in particular for the accuracy needed for pressure transducers and load cells as well as for the selection of the porous plate (glass frit) to control the lower boundary condition. The hydraulic conductivities of the column are large, but decrease considerably as the column desaturates (Figure 3b). The parameters of the van Genuchten equation are $\alpha = 0.136$, $n = 4.776$, $\theta_r = 0.06$, and $\theta_s = 0.394$.

3.3. Water Contents and Water Potentials

[25] Water contents and water potentials need to be meticulously controlled and monitored to ensure uniform and constant hydraulic conditions during unsaturated transport experiments. Hydraulic conditions were generally more variable during colloid breakthroughs than during nitrate breakthroughs, possibly because of colloid capture in the sediment matrix and the porous plate. Water contents

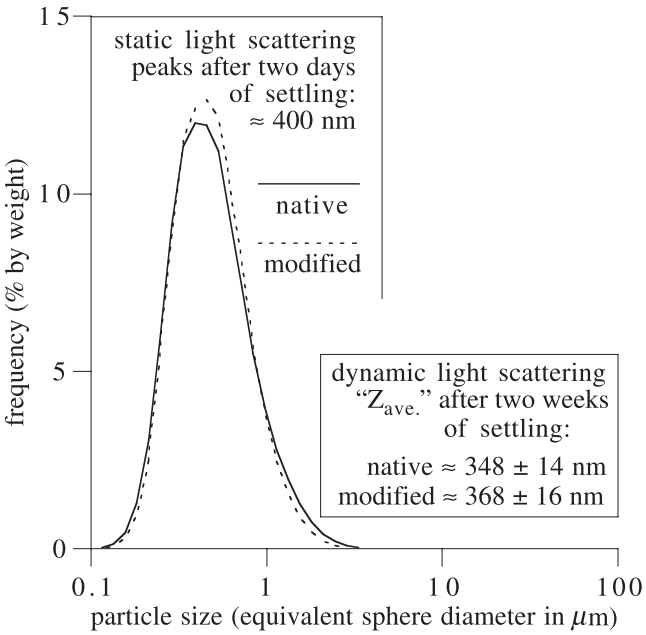

Figure 2. Particle size distribution of native and modified colloids in the inflow suspensions used for transport experiments.

remained constant during nitrate breakthroughs, and slightly increased during colloid breakthroughs (Figure 4). This effect was more pronounced as the water content of the sediments decreased. The weight increase with time (or pore volume) was clearly due to an increase in water content and not due to the mass of colloids captured inside the column. The mass of colloids captured inside the column (at most 1.5 mg during a colloid breakthrough curve) could not be resolved with our apparatus.

[26] The water potential measurements confirmed the observations from the water content measurements. During nitrate breakthrough, water potentials remained constant and very uniform, especially between tensiometers 2 and 4. For S_e = 0.7, the bottom tensiometer (tensiometer 5) indicated wetter conditions near the bottom plate than at the other parts of the column (Figure 5a), whereas for $0.7 > S_e \geq 0.2$, the water potentials were more uniformly distributed (S_e = 0.3 shown in Figure 5b is representative of the uniformity). During colloid breakthrough, the water potentials changed to slightly wetter conditions. This was most pronounced near the bottom of the column and with native colloids. After colloid breakthrough, tensiometer readings showed that the bottom of the column becomes drier again. This suggests colloid capture in the porous plate with some colloids released after influent is switched back to the colloid-free solution. These results show that it was not possible to maintain a unit hydraulic gradient mainly near the bottom of the column at all times and for all water saturations. Between tensiometers 2 and 4 the hydraulic gradient was no worse than 0.95, and typically much closer to one.

[27] Effective water saturations for the nitrate breakthroughs were S_e = 1.0, 0.69, 0.60, 0.50, 0.40, 0.30, 0.20, and 0.16. Uniform water contents were not achieved at S_e = 0.9 and 0.8 because of outflow restrictions, mainly due to the hydraulic conductivity and bubbling pressure of the suction plate. Effective saturations during the colloid breakthroughs were slightly higher, namely S_e = 1.0, 0.69, 0.61, 0.51–0.52, 0.41–0.42, 0.32–0.33, and 0.21–0.22, where, if a range is given, the first number denotes the native colloid breakthrough and the second number the modified colloid breakthrough. Mainly during colloid breakthrough, the bottom of the column (indicated by tensiometer 5) had a higher water content than the remainder of the column, but the water content between tensiometers 1 to 4 was uniform. Colloid breakthroughs at S_e = 0.16 are not reported because of highly variable colloid detection, possibly because of suction plate colloid mobilization and variable colloid concentration in the sprinkler.

3.4. Nitrate Transport

[28] Nitrate breakthrough curves under saturated conditions followed the classical advection-dispersion behavior

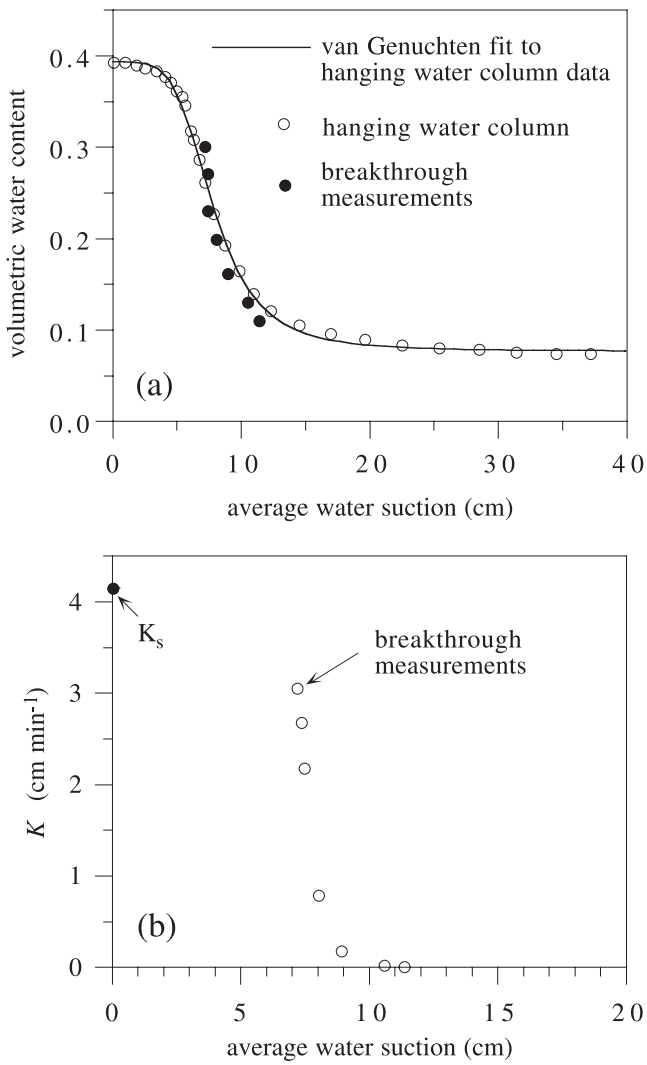

Figure 3. Hydraulic properties of sediments: (a) Moisture characteristic from sediments determined with hanging water column technique (open circles) and fitted van Genuchten equation (solid line); solid circles represent measurements obtained from column transport experiments. (b) Hydraulic conductivities measured during unsaturated transport experiments (open circles) and at saturation (solid circle).

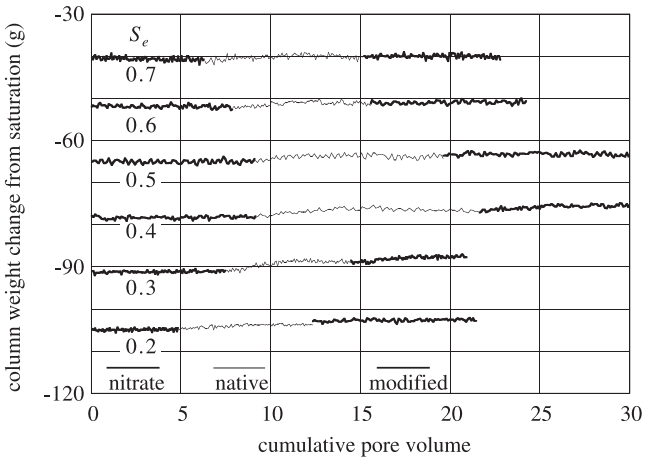

Figure 4. Column weight change during transport experiments at different water saturations. Ordinate indicates weight change referenced to the completely water-saturated column.

and the data were well described by the equilibrium advection-dispersion equation (ADE). Under unsaturated conditions, nitrate breakthrough curves show characteristic behavior in regard to initial tracer breakthrough and variance, as reported from other unsaturated tracer transport experiments [*Krupp and Elrick*, 1968; *Gaudet et al.*, 1977; *De Smedt and Wierenga*, 1984; *Padilla et al.*, 1999]: with decreasing water content, initial tracer breakthrough occurs earlier and breakthrough curve variance became larger (Figure 6). The unsaturated breakthrough data were well fitted with the MIM physical nonequilibrium model; measured and model parameters are summarized in Table 2. There was a substantial amount of immobile water present, which varied nonlinearly with the water saturation of the sediments. Whereas in the literature it was often reported that the fraction of immobile water increases with decreasing water content [*Gaudet et al.*, 1977; *Maraqa et al.*, 1997; *Griffioen et al.*, 1998; *Padilla et al.*, 1999], our analysis shows this was true only at high saturations—at low saturations the immobile water fraction decreased with decreasing water saturation (Figure 7). The increase in immobile water is usually attributed to the increase in film water and stagnant regions relative to the total water content [*Griffioen et al.*, 1998]. It appears that in our coarse sediments, immobile water regions develop as the system desaturates at high water contents, and that these regions themselves desaturate as the water content drops below $S_e = 0.5$.

[29] Model comparison showed that the mobile-immobile model was superior to the simple advection-dispersion model. As illustrated in Figure 8, the advection-dispersion equation was similar to the mobile-immobile model, and high-quality experimental data are necessary to distinguish between the two models. The conceptual difference between the two cases in Figure 8, however, is significant: the mobile-immobile model indicates that 27% of the water phase was immobile. Only one unsaturated result is shown

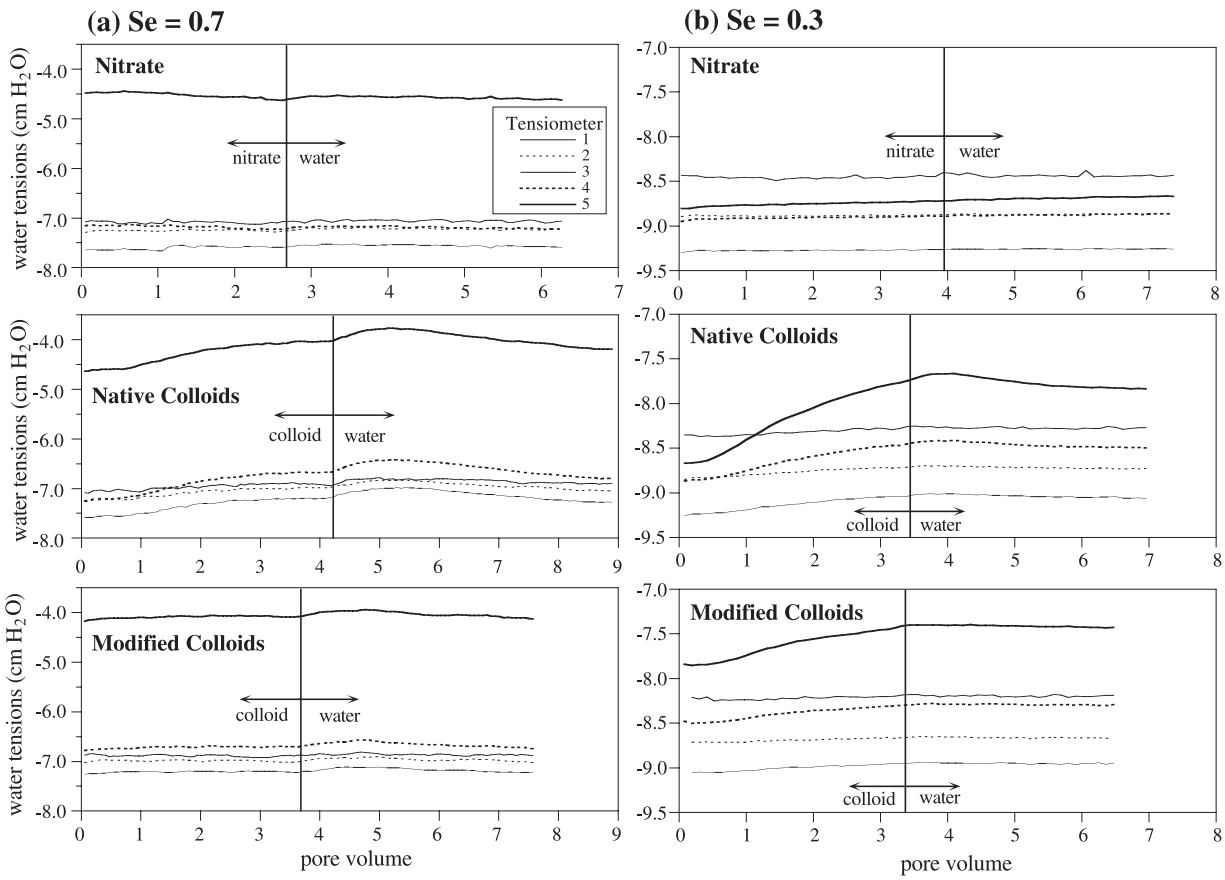

Figure 5. Tensiometer readings during transport experiments at effective water saturations of (a) S_e = 0.7 and (b) S_e = 0.3.

Table 2. Experimental and Modeling Summary for Nitrate Breakthroughs[a]

Measured Values				Mobile-Immobile Model Parameters					
S_e	θ, $m^3\ m^{-3}$	J_w, cm min^{-1}	v, cm min^{-1}	v, cm min^{-1}	D, $cm^2\ min^{-1}$	Pe	β	ω	Model R^2
1.0	0.40	4.107	10.16	10.08	5.857	33.2	–	–	0.999747
0.69	0.30	3.04	10.25	10.60	3.68	55.2	0.878	0.356	0.999952
0.60	0.27	2.68	10.05	10.41	4.05	49.2	0.810	0.487	0.999941
0.50	0.23	2.17	9.40	9.80	5.98	31.4	0.728	0.587	0.999885
0.40	0.20	0.783	3.99	4.19	3.34	34.0	0.730	0.623	0.999906
0.30	0.16	0.184	1.13	1.182	1.214	18.6	0.793	0.457	0.999885
0.20	0.13	0.022	0.178	0.183	0.184	19.0	0.804	0.392	0.998961
0.16	0.11	0.005	0.040	0.0368	0.054	13.1	0.841	0.184	0.996591

[a] S_e, effective saturation; θ, volumetric total water content; J_w, water flux; $v = J_w/\theta$, pore water velocity; D, hydrodynamic dispersion coefficient; Pe, Peclet number; β, fraction of mobile water content; ω, Dahmköhler number. Saturated water content $\theta_s = 0.40$; residual water content $\theta_r = 0.06$; column pore volume is 152.2 mL; column length is 19.15 cm.

in Figure 8; the remaining saturations gave very similar results.

3.5. Colloid Transport

[30] Native as well as modified colloids moved through the sediments at practically the same speed as the conservative nitrate tracer; however, the inflow concentrations were not reached during the injection pulse and the breakthrough curves show a plateau-like behavior (Figure 9). The modified colloid breakthrough plateau has a near-zero slope, but the native colloid breakthroughs show a more positive slope. Between $S_e = 1$ and 0.2, all breakthrough curves showed a smooth shape with monotonically increasing colloid concentrations during inflow and monotonically decreasing colloid concentrations during elution. At the lowest saturation for the modified colloids ($S_e = 0.22$), the elution portion of the breakthrough curve indicates that colloids were being eluted from the column and the concentrations did not return to zero as for the higher water saturations. This behavior is attributed either to in situ colloid mobilization or to release of colloids from the porous plate at the bottom of the column.

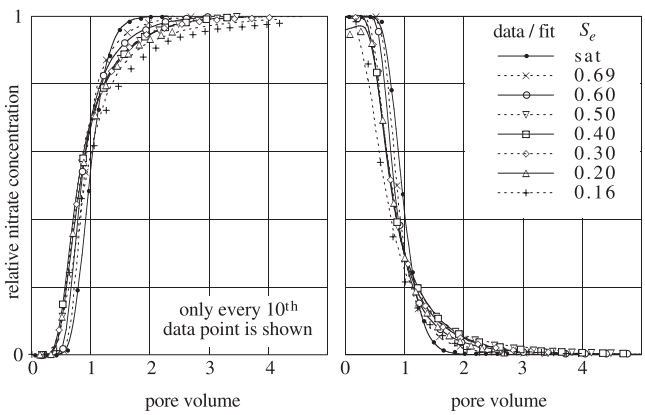

Figure 6. Breakthrough and elution limbs for the conservative tracer nitrate in Hanford sediments (2–2000 μm) under different effective water saturations S_e. Symbols are measured data; lines are model fits. The origin of each plot, i.e., pore volume = 0, indicates when nitrate was infused (breakthrough limb) and nitrate infusion was stopped (elution limb).

[31] All colloid breakthrough curves, except those at the lowest water saturation, were analyzed with the MIM. Fitted model parameters are listed in Table 3. The modified colloid behavior was well described with the MIM (Figure 9). The native colloid behavior, however, showed a more gradual increase of colloid concentration in the breakthrough limb than described by the MIM. This difference indicates that colloid deposition deviated from a first-order process, and is likely governed by a second-order process where colloid attachment sites are being blocked or filled up [*Chu et al.*, 2001; *Lenhart and Saiers*, 2002]. We attribute the different behavior of native and modified colloids to their different mineralogical composition and different electrophoretic mobility.

[32] The mass of colloids eluted from the column decreased in a nonlinear fashion with decreasing water saturation (Figure 10). At water saturations greater than $S_e = 0.5$, more than 80% of the infused colloids were eluted, but at $S_e < 0.5$, a considerable amount of colloids remained in the column. The increased colloid retention as the water

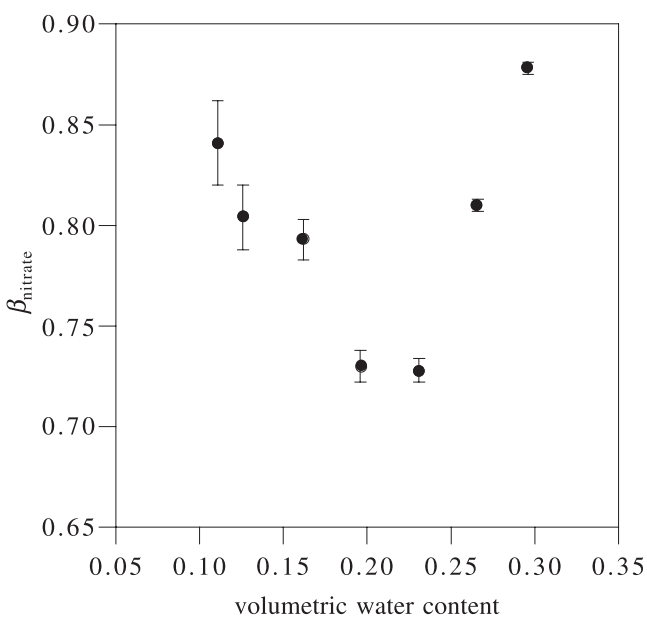

Figure 7. Fraction of mobile water $\beta = \theta_m/(\theta_m + \theta_{im})$ as a function of water content determined from nitrate data. Vertical bars represent ±1 standard deviation.

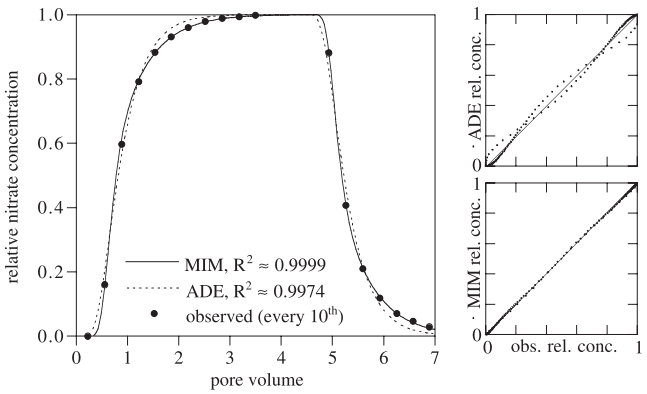

Figure 8. Comparison between fits of advection-dispersion equation (ADE) and mobile-immobile model (MIM) to nitrate breakthrough curve at $S_e = 0.5$. The subplots show the relation between ADE and MIM breakthrough data; the solid line is the 1:1 relation, shown as a guide to the eye.

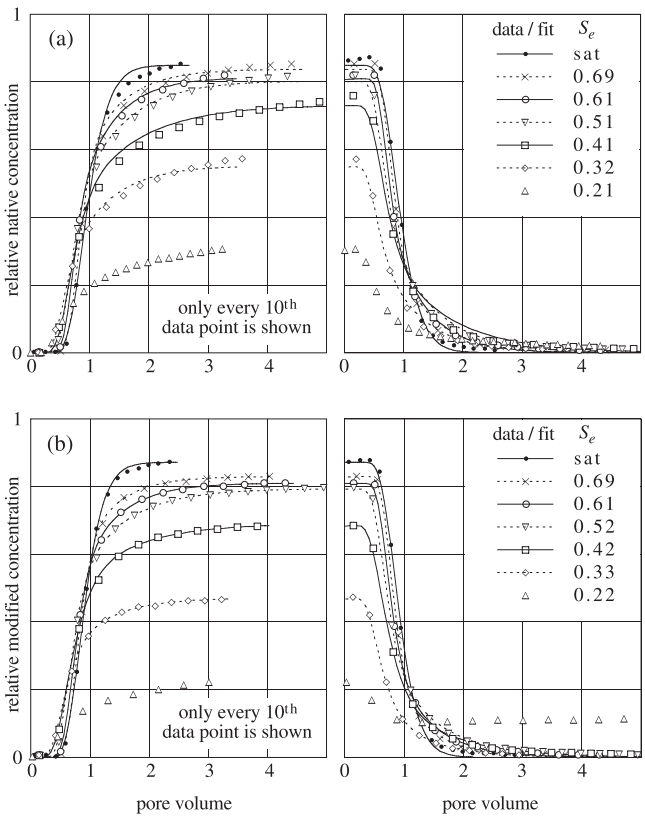

Figure 9. Breakthrough curves for (a) native and (b) modified colloids in Hanford sediments under different water saturations. Symbols are measured data; lines are MIM model fits. Data for the lowest water saturations were not fitted due to residual turbidity. The origin of each plot, i.e., pore volume = 0, indicates when colloids were infused (breakthrough limb) and colloid infusion was stopped (elution limb).

saturation decreases has been consistently observed by others [*Wan et al.*, 1994; *Wan and Tokunaga*, 1997; *Schäfer et al.*, 1998; *Lenhart and Saiers*, 2002]. The major mechanisms postulated for the enhanced colloid removal under unsaturated flow are attachment to the gas-liquid interface and straining in water films that have thickness smaller than the colloid diameters [*Wan and Tokunaga*, 1997; *Lenhart and Saiers*, 2002]. While our experiments do not determine the exact mechanisms of colloid removal inside the column, they do show a considerable change in colloid removal for both native and modified colloids as the water saturation drops below $S_e = 0.5$. This may be related to a change in the dominant colloid removal mechanism.

4. Implications

[33] At the Hanford Reservation, where radioactive materials have leaked from underground waste tanks, an ultimate concern is the mobility of the radionuclide Cs-137. Colloidal particles can potentially facilitate the movement of

Table 3. Experimental and Modeling Summary for Colloid Breakthroughs[a]

Measured Values				Mobile-Immobile Model Parameters						
S_e	θ, $m^3\ m^{-3}$	J_w, cm min^{-1}	v, cm min^{-1}	v, cm min^{-1}	D, $cm^2\ min^{-1}$	Pe	β	ω	μ_m	Model R^2
				Native Colloids						
1.0	0.40	4.09	10.12	9.89	7.78	24.0	–	–	0.085	0.99782094
0.69	0.30	3.02	10.16	9.57	3.61	50.8	0.805	0.408	0.178	0.99889992
0.61	0.27	2.67	9.98	9.71	3.99	46.6	0.750	0.600	0.208	0.99915235
0.51	0.23	2.17	9.25	8.60	5.26	31.3	0.686	0.615	0.221	0.99882561
0.41	0.20	0.78	3.89	3.33	3.49	18.3	0.688	0.473	0.318	0.99728774
0.32	0.17	0.18	1.10	1.10	1.07	19.6	0.673	0.694	0.612	0.99702499
0.21	0.13	0.022	0.17	NF	NF	NF	NF	NF	NF	NF
				Modified Colloids						
1.0	0.40	4.05	10.01	10.48	8.32	24.1	–	–	0.076	0.99924566
0.69	0.30	3.01	10.10	10.27	4.48	43.9	0.848	0.305	0.187	0.99984646
0.61	0.27	2.67	9.93	10.02	5.16	37.2	0.789	0.415	0.212	0.99980308
0.52	0.24	2.17	9.18	9.12	7.61	23.0	0.740	0.413	0.234	0.99971373
0.42	0.20	0.78	3.84	3.71	5.37	13.2	0.774	0.285	0.380	0.99969106
0.33	0.17	0.18	1.07	1.16	1.77	12.5	0.773	0.365	0.799	0.99981479
0.22	0.13	0.021	0.163	NF	NF	NF	NF	NF	NF	NF

[a] S_e, effective saturation; θ, volumetric total water content; J_w, water flux; v, pore water velocity; D, hydrodynamic dispersion coefficient; Pe, Peclet number; β, fraction of mobile water content; ω, Dahmköhler number; μ_m, deposition coefficient. Saturated water content $\theta_s = 0.40$; residual water content $\theta_r = 0.06$; column pore volume is 152.2 mL; column length is 19.15 cm. NF indicates not fitted because of residual turbidity.

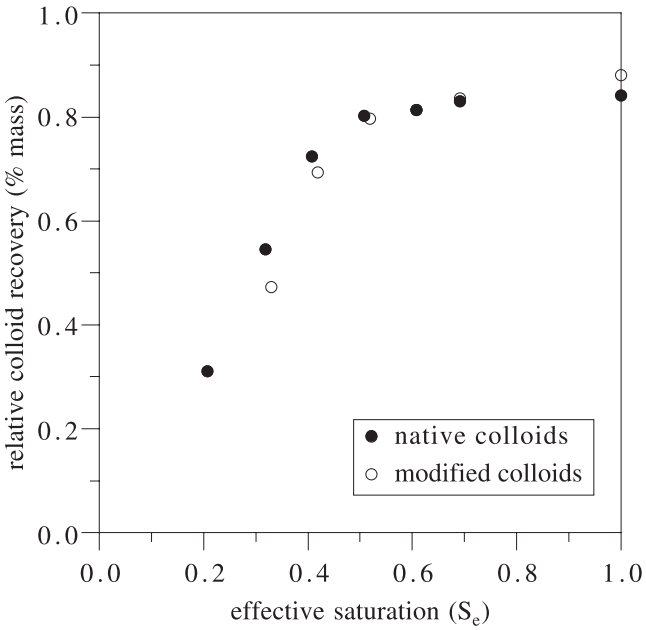

Figure 10. Mass of colloids recovered in outflow from Hanford sediments under different water saturations.

radionuclides like Cs-137, and colloid movement needs to be considered in long-term risk assessment and management of the waste at Hanford. In this study, we demonstrate that native colloids can move through natural Hanford sediments, but the amount of colloids transported strongly depends on the water saturation of the sediments. The presence of immobile water during steady state unsaturated flow leads to an earlier breakthrough and a larger dispersion of colloidal particles as compared to when immobile water is absent. No pore size exclusion, which results in increasing transport velocities, was observed for the colloids in the Hanford sediments.

[34] Analyses of boreholes drilled at the S-SX tank farm at Hanford indicate that the gravimetric water saturations in sediments of the Hanford formation in the vicinity the S-SX waste tanks range from 0.05 to 0.15 kg kg^{-1} [*Serne et al.*, 2002a]. These gravimetric water contents correspond to effective saturations S_e of 0 to 0.5 in our sediment column. Under these conditions colloid transport is possible, but not as effective as under higher water saturations.

[35] At the Hanford site, where the subsurface sediments consist of layered flood-deposits, it is possible that colloids released by a salinity change in the pore water are captured in finer-textured sediment layers as the colloids migrate downward [*Blume et al.*, 2002]. Such an effect would counteract colloid-facilitated transport if the trapped colloids are not remobilized at a later stage.

[36] **Acknowledgments.** This work was supported by the Environmental Management Science Program, U.S. Department of Energy under contract DE-FG07-99ER62882, Project Officers Frank Wobber and Chester Miller. We thank John Zachara and Jeff Serne (Pacific Northwest National Laboratory) for providing us with the Hanford sediments, Hongting Zhao for XRD analysis, and Szabolcs Czigány for the petrographic sediment characterization.

References

Bickmore, B. R., K. L. Nagy, J. S. Young, and J. W. Drexler, Nitrate-cancrinite precipitation on quartz sand in simulated Hanford tank solutions, *Environ. Sci. Technol.*, *35*, 4481–4486, 2001.

Blume, T., N. Weisbrod, and J. S. Selker, Permeability changes in layered sediments: Impact of particle release, *Groundwater*, *40*, 466–474, 2002.

Bond, W. J., and P. J. Wierenga, Immobile water during solute transport in unsaturated sand columns, *Water Resour. Res.*, *26*, 2475–2481, 1990.

Cady, J. G., L. P. Wilding, and L. R. Drees, Petrographic microscope techniques, in *Methods of Soil Analysis*, part 1, *Physical and Mineralogical Methods*, edited by A. Klute, pp. 185–218, Am. Soc. of Agron., Madison, Wis., 1986.

Cherrey, K. D., Laboratory column technique for the measurement of colloidtransport in variability-saturated porous media, M.S. thesis, Wash. State Univ., Pullman, Wash., 2002.

Chu, Y., Y. Jin, M. Flury, and M. V. Yates, Mechanisms of virus removal during transport in unsaturated porous media, *Water Resour. Res.*, *37*, 253–263, 2001.

De Smedt, F., and P. J. Wierenga, Solute transfer through columns of glass beads, *Water Resour. Res.*, *20*, 225–232, 1984.

Flury, M., J. B. Mathison, and J. B. Harsh, In situ mobilization of colloids and transport of cesium in Hanford sediments, *Environ. Sci. Technol.*, *36*, 5335–5341, 2002.

Gamerdinger, A. P., and D. I. Kaplan, Application of a continuous-flow centrifugation method for solute transport in disturbed, unsaturated sediments and illustration of mobile-immobile water, *Water Resour. Res.*, *36*, 1747–1755, 2000.

Gaudet, J. P., H. Jegat, G. Vachaud, and P. J. Wierenga, Solute transport, with exchange between mobile and stagnant water, through unsaturated sand, *Soil Sci. Soc. Am. J.*, *41*, 665–671, 1977.

Gephart, R. E., and R. E. Lundgren, *Hanford Tank Cleanup: A Guide to Understanding the Technical Issues*, 4th ed., Battelle, Columbus, Ohio, 1998.

Griffioen, J. W., D. A. Barry, and J. Y. Parlange, Interpretation of two-region model parameters, *Water Resour. Res.*, *34*, 373–384, 1998.

Hillel, D., *Environmental Soil Physics*, Academic, San Diego, Calif., 1998.

Jewett, D. G., B. E. Logan, R. G. Arnold, and R. C. Bales, Transport of Pseudomonas fluorescence strain P17 through quartz sand columns as a function of water content, *J. Contam. Hydrol.*, *36*, 73–89, 1999.

Kersting, A. B., D. W. Efurd, D. L. Finnegan, D. J. Rokop, D. K. Smith, and J. L. Thompson, Migration of plutonium in ground water at the Nevada Test Site, *Nature*, *397*, 56–59, 1999.

Kretzschmar, R., M. Borkovec, D. Grolimund, and M. Elimelech, Mobile subsurface colloids and their role in contaminant transport, *Adv. Agron.*, *66*, 121–193, 1999.

Krupp, H. K., and D. E. Elrick, Miscible displacement in an unsaturated glass bead medium, *Water Resour. Res.*, *4*, 809–815, 1968.

Lenhart, J. J., and J. E. Saiers, Transport of silica colloids through unsaturated porous media: Experimental results and model comparisons, *Environ. Sci. Technol.*, *36*, 769–777, 2002.

Maraqa, M. A., R. B. Wallace, and T. C. Voice, Effects of degree of water saturation on dispersivity and immobile water in sandy soil columns, *J. Contam. Hydrol.*, *25*, 199–218, 1997.

McCarthy, J. F., and J. M. Zachara, Subsurface transport of contaminants, *Environ. Sci. Technol.*, *23*, 496–502, 1989.

McKinley, J. P., C. J. Zeissler, J. M. Zachara, R. J. Serne, R. M. Lindstrom, H. T. Schaef, and R. D. Orr, Distribution and retention of Cs-137 in sediments at the Hanford Site, Washington, *Environ. Sci. Technol.*, *35*, 3433–3441, 2001.

Padilla, I. Y., T.-C. J. Yeh, and M. H. Conklin, The effect of water content on solute transport in unsaturated porous media, *Water Resour. Res.*, *35*, 3303–3313, 1999.

Schäfer, A., P. Ustothal, H. Harms, F. Stauffer, T. Dracos, and A. J. B. Zehnder, Transport of bacteria in unsaturated porous media, *J. Contam. Hydrol.*, *33*, 149–169, 1998.

Serne, R. J., et al., Characterization of vadose zone sediment: Uncontaminated RCRA borehole core samples and composite samples, *PNNL-13757-1*, Pac. Northwest Natl. Lab., U.S. Dep. of Energy, Richland, Wash., 2002a.

Serne, R. J., et al., Characterization of vadose zone sediment: Slant borehole SX-108 in the S-SX Waste Management Area, *PNNL-13757-4*, Pac. Northwest Natl. Lab., U.S. Dep. of Energy, Richland, Wash., 2002b.

Toride, N., F. J. Leij, and M. T. van Genuchten, The CXTFIT code for estimating transport parameters from laboratory or field tracer experiments, version 2.1, *Res. Rep. 137*, U.S. Salinity Lab., Riverside, Calif., 1995.

van Genuchten, M. T., A closed-form equation for predicting the hydraulic conductivity of unsaturated soils, *Soil Sci. Soc. Am. J.*, *44*, 892–898, 1980.

Wan, J. M., and T. K. Tokunaga, Film straining of colloids in unsaturated porous media: Conceptual model and experimental testing, *Environ. Sci. Technol.*, *31*, 2413–2420, 1997.

Wan, J. M., J. L. Wilson, and T. L. Kieft, Influence of the gas-water interface on transport of microorganisms through unsaturated porous media, *Appl. Environ. Microbiol.*, *60*, 509–516, 1994.

Whittig, L. D., and W. R. Allardice, X-ray diffraction techniques, in *Methods of Soil Analysis*, part 1, *Physical and Mineralogical Methods*, edited by A. Klute, pp. 331–362, Am. Soc. of Agron., Madison, Wis., 1986.

Zachara, J. M., S. C. Smith, C. Liu, J. P. McKinley, R. J. Serne, and P. L. Gassman, Sorption of Cs^{+} to micaceous subsurface sediments from the Hanford Site, USA, *Geochim. Cosmochim. Acta*, *66*, 193–211, 2002.

Zhao, H., J. B. Harsh, M. Flury, and K. Mashal, Alteration of mineralogical and surface properties of Hanford sediments contaminated with tank waste, paper presented at 222nd ACS National Meeting, Am. Chem. Soc., Chicago, Ill., 26–30 August 2001.

K. D. Cherrey, M. Flury, and J. B. Harsh, Department of Crop and Soil Sciences, Center for Multiphase Environmental Research, Washington State University, Pullman, WA 99164, USA. (flury@mail.wsu.edu)

Correction to "Nitrate and colloid transport through coarse Hanford sediments under steady state, variably saturated flow"

Kelly D. Cherrey, Markus Flury, and James B. Harsh

Received 31 January 2004; published 6 March 2004.

INDEX TERMS: 1831 Hydrology: Groundwater quality; 1832 Hydrology: Groundwater transport; 1866 Hydrology: Soil moisture; 1875 Hydrology: Unsaturated zone; 9900 Corrections; *KEYWORDS:* colloids, unsaturated flow, vadose zone

Citation: Cherrey, K. D., M. Flury, and J. B. Harsh (2004), Correction to ''Nitrate and colloid transport through coarse Hanford sediments under steady state, variably saturated flow,'' *Water Resour. Res.*, *40*, W03901, doi:10.1029/2004WR003066.

[1] In the paper "Nitrate and colloid transport through coarse Hanford sediments under steady state, variably saturated flow" by Kelly D. Cherrey, Markus Flury, and James B. Harsh (*Water Resources Research*, *39*(6), 1165, doi:10.1029/2002WR001944), the definitions of the dimensionless mass transfer coefficient ω and the dimensionless time T in paragraph 22 were incorrectly reported. The correct definitions should read:

$$\omega = \alpha L/(\theta v) \tag{1}$$

$$T = vt/L. \tag{2}$$

0043-1397/04/2004WR003066$09.00